

# 17.9% Efficiency Silicon Solar Cells by Using Spin-on Films Processes

**Yi-Yu Lee, Wen-Jeng Ho, Jhih-Kai Syu, Quan-Ru Lai, and Cheng-Ming Yu**

Institute of Electro-Optical Engineering, National Taipei University of Technology

1, Sec. 3, Chung-Hsiao E. Rd., Taipei 106, Taiwan

**Abstract**— We investigated the phosphorus diffusion process by using the spin-on film (SOF) and optimized rapid temperature annealing (RTA) techniques on single crystalline *p*-Si wafer to form a high-quality thin *n*<sup>+</sup>-Si emitter. We also studied a broad-band low-reflectance multi-layer ( $\text{SiO}_2/\text{TiO}_2/\text{TiO}_2$ ) AR-coating by using the SOF process. Furthermore, we successfully integrated both SOF processes for fabricating an *n*<sup>+</sup>-*p* Si solar cell with excellent photovoltaic performances. The improved performances show that  $V_{oc}$  of 0.56 V,  $I_{sc}$  of 5.35 mA,  $FF$  of 78.46%, and  $\eta$  of 17.91% are obtained.

## 1. INTRODUCTION

The high quality Shallow *n*<sup>+</sup>-emitter is one of the most important requirements in the fabrication of photovoltaic devices. Usually, diffusion process is accomplished by heat treatment in a conventional furnace at temperatures above 900°C for times ranging from minutes to hours [1].  $\text{POCl}_3$  diffusion in high temperature furnace diffusion has been reported in the previous study and in Si solar cell fabrication. Recently, using rapid thermal annealing (RTA) method for forming a shallow junction with a doped spin-on film has been reported in the shallow junction devices.

Anti-reflection coating is the function layer for reducing the light reflection at the air-semiconductor interface, which can be used to improve the efficiency of solar cell. A common method is used a single-layer with a thickness of quarter-wavelength for antireflection coating [2–4]. However, the conventional AR-coating is effective only for a specific wavelength, and with a narrow low-reflectance spectrum.

In this paper, the spin-on process for phosphorus diffusion and low reflection AR-coating are in depth study for solar cell fabrication. The quality of phosphorus-diffusion layer, the broad-band low-reflection spectrum of AR-coating, and the performance of the fabricated *n*<sup>+</sup>-*p* Si solar cell were characterization, respectively.

## 2. EXPERIMENT

The wafers used in the experiment are with 525  $\mu\text{m}$  thick, (100) oriented, resistivity in  $1 \sim 10 \Omega\text{-cm}$ , *p*-Si (boron doped). The samples are  $1 \times 1 \text{ cm}^2$  in size and the individual cell area is  $0.1296 \text{ cm}^2$ . The phosphorus-doped source embodies the dopant concentration of  $5 \times 10^{20} \text{ cm}^{-3}$ . After standard RCA cleaning, the samples are firstly coated with the phosphorus diffusion source by using the spin-on technique. The samples are spun at a speed of 6000 rpm for 20 s, followed by a prebaking at 200°C for 5 min and at 400°C for 10 min on the hot plate. Then the sample was held in RTA chamber at 900°C for 2 min for a diffusion process [5]. After phosphorus diffusion, four independent regions were formed by isolation etching. Next, an 200 nm Al-film was evaporated onto the back side and then annealed at 450°C as the back side electrode. Subsequently, the front electrode of Ti/Al (20/200 nm) film was formed by E-GUN evaporating and lifts-off processes, as shown in Figure 1. Finally,  $\text{SiO}_2/\text{TiO}_2/\text{TiO}_2$  multi-layer was deposited by spin-on film process on the surface of cell. The formation of multi-layer process can be categorized to three steps: step 1: spin a  $\text{TiO}_2$  film (43.6 nm) with a speed of 8000 rpm for 40 s and then baking at 300°C for 30 min, step 2: spin a second  $\text{TiO}_2$  film (49.6 nm) with a speed of 7000 rpm for 40 s and then baking at 250°C for 15 min, step 3: spin a  $\text{SiO}_2$  film (238.3 nm) upon second  $\text{TiO}_2$  layer with a speed of 2000 rpm for 40 s and then baking at 200°C for 15 min, the cells with 3-layer AR-coating as shown in Figure 2.

## 3. RESULTS AND DISCUSSION

Figure 3 shows the sheet resistance ( $R_s$ ) of *n*<sup>+</sup>-Si as a function of diffusion temperature, which the diffusion time is at 2–10 min and in  $N_2$  environment. The sheet resistance gives an estimation of the dopant element activation level. However,  $R_s$  values decrease with an increase in the diffusion temperature as shown in Figure 3. The behavior of the diffusion and subsequent activation of

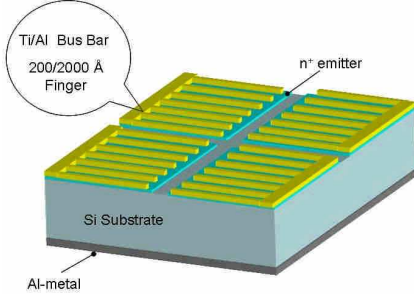


Figure 1: The schematic diagram of the fabricated solar cell.

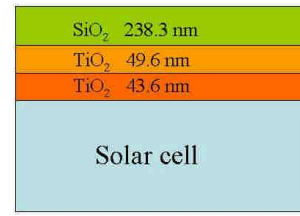


Figure 2: The schematic diagram of cell with 3-layers AR-coating.

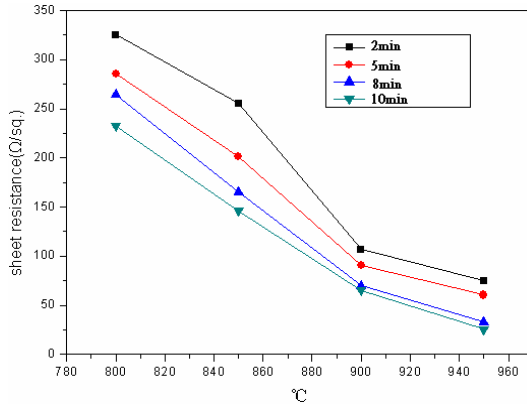


Figure 3: Sheet resistance versus RTA temperature.

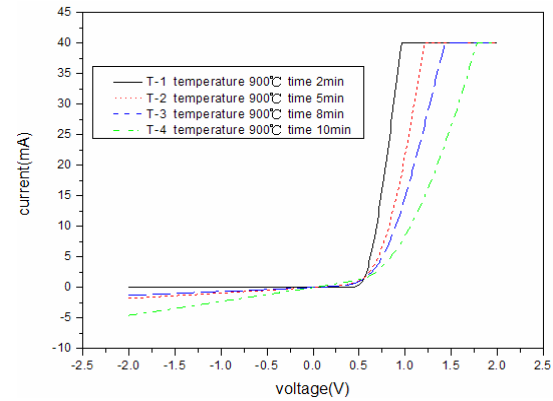


Figure 4:  $n^+$ - $p$  Si diodes dark I-V curves of different diffusion process temperature.

Table 1: Performance parameter of solar cell without AR-coating.

Sample	$V_{oc}$ (V)	$I_{sc}$ (mA)	FF (%)	$R_s$ ( $\Omega$ )	$R_{sh}$ ( $\Omega$ )	$\eta$ (%)
Si-1	0.54	3.83	77	9.34	18777	12.01
Si-2	0.54	3.78	76	9.3	33638	11.59
Si-3	0.54	3.57	69	8.75	25401	11.04
Si-4	0.54	3.67	73	7.56	32837	11.57

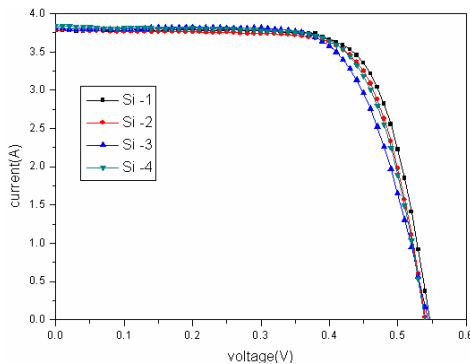


Figure 5: Photo I-V of solar cell without AR-coating.

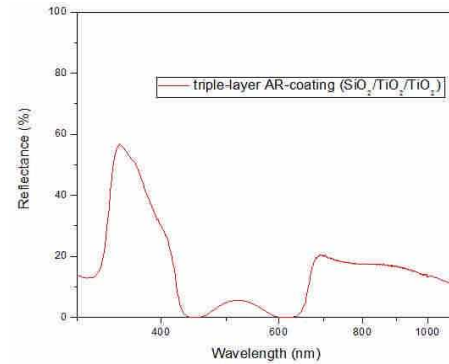


Figure 6: Reflectance spectrum of 3-layers AR-coating.

phosphorus atoms in  $p$ -type silicon were important factor for device fabrication. Thus, RTA seems to be very efficient for a shallow diffusion for using a spin-coating with a thin high-dopant layer [6, 7].

Table 2: The parameter of solar cell without and with AR coating.

Sample	$V_{oc}$ (V)	$I_{sc}$ (mA)	$J_{sc}$ (mA/cm <sup>2</sup> )	FF (%)	$R_s$ ( $\Omega$ )	$R_{sh}$ ( $\Omega$ )	$\eta$ (%)
Si-1 (without AR-coating)	0.54	3.83	29.55	77	9.34	18777	12.01
Si-1 (AR-coating with spinning $\text{SiO}_2/\text{TiO}_2/\text{TiO}_2$ )	0.56	5.35	41.28	78.64	8.45	25953	17.91

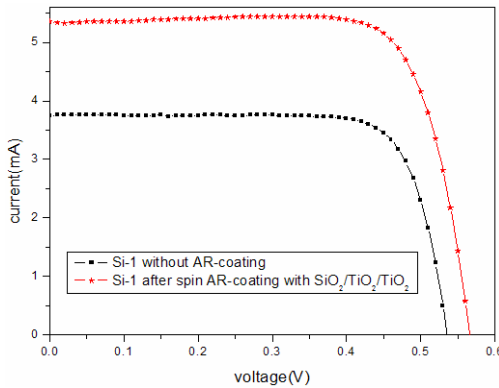


Figure 7: The illuminated I-V curve of without and with AR coating.

Four different diffusion temperatures are chosen to make  $p$ - $n$  diode, in this study. Figure 4 shows the I-V curve of the  $n^+$ - $p$  diodes. The best I-V curve of 900°C for 2 min was obtained due to the I-V characteristics more similar to the ideal  $p$ - $n$  diode [8]. The performance parameter of solar cells without AR-coating is listed in Table 1. The illuminated I-V curve of Si solar cells without AR-coating is shown in Figure 5. Under AM1.5G, 25°C, the cell without AR-Coating show that the open circuit voltage ( $V_{oc}$ ) of 0.54 V, short-circuit current ( $I_{sc}$ ) of 3.83 mA, fill factor (FF) of 77%, and conversion efficiency ( $\eta$ ) of 12.01% are presented. The reflectance spectrum of triple-layer AR-coating is shown in Figure 6. At wavelength from 500 nm to 650 nm, the reflectance of 5% is achieved. We applied such scheme on ARC solar cell to enhance the device's performances. The improved performances of cell with spin-on triple-layer ( $\text{SiO}_2/\text{TiO}_2/\text{TiO}_2$ ) AR-coating show that  $V_{oc}$  of 0.56 V,  $I_{sc}$  of 5.35 mA, FF of 78.46%, and  $\eta$  increased from 12.01 to 17.91% were obtained, as listed in Table 2. Finally, the measured I-V curve of cell without AR-coating and with AR-coating is also shown in Figure 7. Efficiency enhancement of 49% in this work was achieved due to the best diffusion processing [9] and high quality 3-layer AR-coating.

#### 4. CONCLUSION

We have successfully fabricated  $n^+$ - $p$  Si solar cell by spin-on processes for Phosphorus diffusion and 3-layer AR-coating. Short-circuit of 5.35 mA, open circuit voltage of 0.56 V, and fill factor of 78.64% are obtained. The results of the experimental show a cell with multi-layer AR-coating that the increasing in the short current from 3.83 mA to 5.35 mA, the efficiency increasing from 12.01% to 17.91% are obtained.

#### ACKNOWLEDGMENT

The authors would like to thank the financial support from the National Science Council under Grant NSC 99-2221-E-027-050.

#### REFERENCES

- Mathiot, D., A. Lachiq, A. Slaoui, S. Noël, J. C. Muller, and C. Dubois, "Phosphorus diffusion from a spin-on doped glass (SOD) source during rapid thermal annealing," *Materials Science*

- in Semiconductor Processing*, Vol. 1, 231–236, 1998.
- 2. Lee, D., M. F. Rubner, and R. E. Cohen, “All-nanoparticle thin-film coatings,” *Nano Letters*, Vol. 6, No. 10, 2305–2312, 2006.
  - 3. Bouhafs, D., A. Moussi, A. Chikouche, and J. M. Ruiz, “Design and simulation of antireflection coating systems for optoelectronic devices: Application to silicon solar cells,” *Solar Energy Materials and Solar Cells*, Vol. 52, 79–93, 1998.
  - 4. Tsai, T. H. and Y. F. Wu, “Wet etching mechanisms of ITO films in oxalic acid,” *Microelectronic Engineering*, Vol. 83, 536–541, 2006.
  - 5. Chen, B. C., “Development of Si bulk solar cell fabrication method by using non vacuum film deposition process,” National Taiwan University of Science and Technology, Taipei, 2008.
  - 6. Tec, S. T. and D. G. S. Chuan, “Diffusion profile of spin-on dopant in silicon substrate,” *Solar Energy Materials*, Vol. 19, 237–247, 1989.
  - 7. Oh, J., K. Im, C. G. Ahn, J. H. Yang, W. J. Cho, S. Lee, and K. Park, “Ultra shallow and abrupt  $n^+$ - $p$  junction formations on silicon-on-insulator by solid phase diffusion of arsenic from spin-on-dopant for sub 50 nm Si metal-oxide-semiconductor devices,” *Materials Science and Engineering*, Vol. 110, 185–189, 2004.
  - 8. Wang, J., D. Wheeler, Y. Yan, J. Zhao, S. Howard, and A. Seabaugh, “Silicon tunnel diodes formed by proximity rapid thermal diffusion,” *IEEE Electron. Devices Society*, Vol. 24, 93–95, 2003.
  - 9. Videira, R. S., R. M. Gamboa, J. Maia Alves, J. M. Serra, and A. M. Vallera, “Photo defined etching of on layers diffused on  $p$ -type silicon substrates,” *Applied Surface Science*, Vols. 138–139, 29–34, 1999.

## Switching of Dark Discrete Cavity Solitons

**Keivan Mahmoud Aghdami<sup>1</sup>, Reza Kheradmand<sup>2</sup>, and Roghayeh Karimi<sup>2</sup>**

<sup>1</sup>Physics Department, Payame Noor University, Tehran 19395-4697, Iran

<sup>2</sup>Research Institute for Applied Physics and Astronomy, University of Tabriz, Tabriz 51665-16, Iran

**Abstract**— The propagation of light in discrete system, such as waveguide arrays shows novel unique physical phenomena in comparison with beams propagating in usual continuous systems. Here we report various orders of dark discrete cavity solitons (DDCSs) in both self focusing and de-focusing regime. The possibility of writing, erasing and two by two transformations by appropriate control Gaussian beam (GB) are investigated and their co-existence is verified.

### 1. INTRODUCTION

The propagation of light in discrete system, such as waveguide arrays shows novel unique physical phenomena [1] in comparison with beams propagating in usual continuous systems [2]. For example, diffraction in this system can be controlled in both size and sign by the input condition. Such phenomena arise from the interplay between periodicity and nonlinearity in system. Discrete solitons have been predicted for cubic and saturable nonlinear waveguide arrays and their stability probed by linear stability analysis.

Unlike continuum system in discrete systems, dark and bright discrete solitons have been generated simultaneously in media with positive Kerr nonlinearities since the waveguide diffraction properties can be modified [3, 4]. Dark solitons consisting of a localized dip in a homogeneous background and require an effectively defocusing nonlinearity whereas bright soliton consisting of a localized peak in a homogeneous background and require an effectively selffocusing nonlinearity. In continuum system because of the unique sign of diffraction, dark soliton exist only in materials with a defocusing nonlinearity. In discrete system, normal holding beam leads to normal diffraction and to self-focusing nonlinearity in array and consequently to formation of bright soliton. By tilting the input beam, we can create the condition necessary to observe the anomalous diffraction and nonlinear self-defocusing at higher powers. Such condition leads to formation of dark soliton.

Discrete cavity solitons (DCSs) have been predicted in a waveguide array with dielectric mirrors at the end faces for Kerr [4], quadratic [5] and saturable [6] nonlinearities. In the present work, we focus on the investigate possibility of switch and co-existence of DCSs by appropriate control Gaussian beam (GB) in both selffocusing and self-defocusing regime.

The paper is organized as follows. In Section 2, we introduce the model describing light dynamics in an array of coupled cavities and in Section 3 we investigate the possibility of switch of discrete cavity solitons with holding beam. Finally, Section 4 concludes the paper.

### 2. THE MODEL

We consider an array of coupled cavities, driven by an external field (Fig. 1). The evolution of field at the output of each cavity obeys a discrete nonlinear Schrodinger (DNLS) equation:

$$i \frac{\partial u_n}{\partial T} + C(u_{n+1} + u_{n-1} - 2u_n) + (i + \Delta)u_n + \gamma |u_n|^2 u_n = \tilde{E}_{0n} e^{iqn} \quad (1)$$

where  $C$  and  $q$  correspond to the coupling constant and phase shift between adjacent cavities respectively. In this work,  $q = 0$  considered. Define the detuning from cavity resonance. The nonlinear Kerr coefficient  $\gamma$  rescaled to  $\gamma = \pm 1$ , ( $-1$  for the focusing and  $-1$  for the self-defocusing case respectively).  $\tilde{E}_{0n}$  is input field in the  $n$ th waveguide and assumed as a superposition of plane wave with the amplitude  $E_0$  and a GB with the amplitude  $E_1$

$$\tilde{E}_{0n} = \left( E_0 + E_1 e^{-\frac{n^2}{w^2}} e^{i\phi} \right) \quad (2)$$

where  $w$  and  $\phi$  specify the width and phase of GB respectively. The effective detuning  $\Delta_{eff} = \Delta_n + 2C(\cos q - 1)$  for different phase shift and coupling is kept constant. Newton iteration and Runge-Kutta methods are used to simulate the dynamics of discrete cavity solitons. In our previous works, switching of bright DSCs and the stability of them in different parameters has been investigated [7, 8]. Here we concentrate on switching of dark solitons with different orders in both regimes self-focusing and self-defocusing.

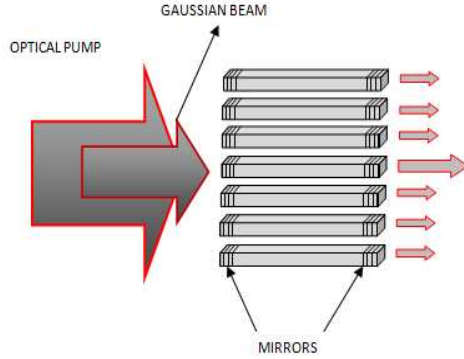
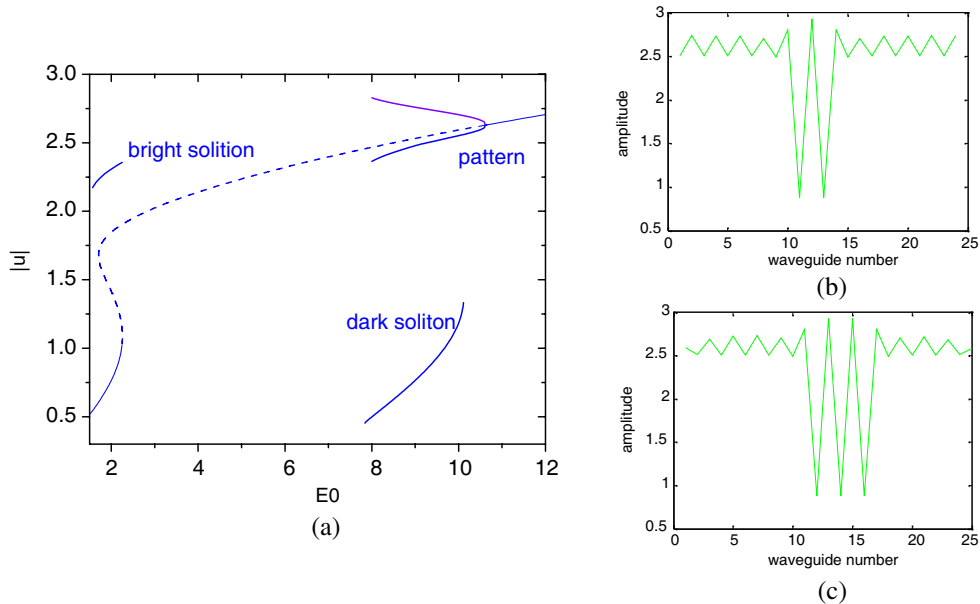


Figure 1: A array of coupled cavities that driven by a holding beam.

Figure 2: (a) Bistability curve for homogeneous solution, pattern and families of discrete cavity solitons in self-focusing case. Dashed part indicate modulation instability of homogeneous output. (b) Second order and (c) third order dark DCSs placed on a patterned background made by  $E_1 = 3$ ,  $W = 3$  and  $E_1 = 4$ ,  $W = 2$  GB at  $E_0 = 9.4$ . (Other parameters is:  $C = 1$ ,  $\Delta_{eff} = -3$ ,  $\gamma = 1$ ).

### 3. DARK DISCRETE CAVITY SOLITON

#### 3.1. Self-focusing Case

This system shows a bistability for homogeneous solutions and families of DCSs with respect to holding beam intensity,  $|E_0|^2$  (Fig. 2(a)). Linear stability analysis manifests some part of upper bistability branch is modulationally unstable then system cannot support dark solitons lie on a flat background. In a part of this domain a stable crinkle pattern emerges which its maximum intensity forms another branch. Different orders of dark DCSs have found within the pattern, with different shape and deep intensity. The fundamental dark DCSs has a deep onsite a cavity while the higher orders show multi deeps placed alternatively in neighbor sites (Figs. 2(b) and (2c)).

Dark DCSs can be written on patterned background by appropriate GB injection, in which GB and background are out of phase ( $\varphi = \pi$  in Eq. (2)). The phase and width of GB is chosen proportional to desired final order of DCS. Our simulation shows a successful writing takes place when the product of GB amplitude,  $E_1$ , and injection time exceeds a minimum which varies with the coupling constant,  $C$ . Fig. 3(a) shows the time evolution of writing process during the writing beam injection (red) and after it (blue) when the field profile relaxes to its final steady value.

This dark discrete cavity solitons formed into a stable periodic pattern, unlike other solitons which exist on a stable plane wave (PW) background. In these cases that the nonlinearity itself is self-focusing, the discrete dark solitons become staggered, i.e., the constant-intensity background

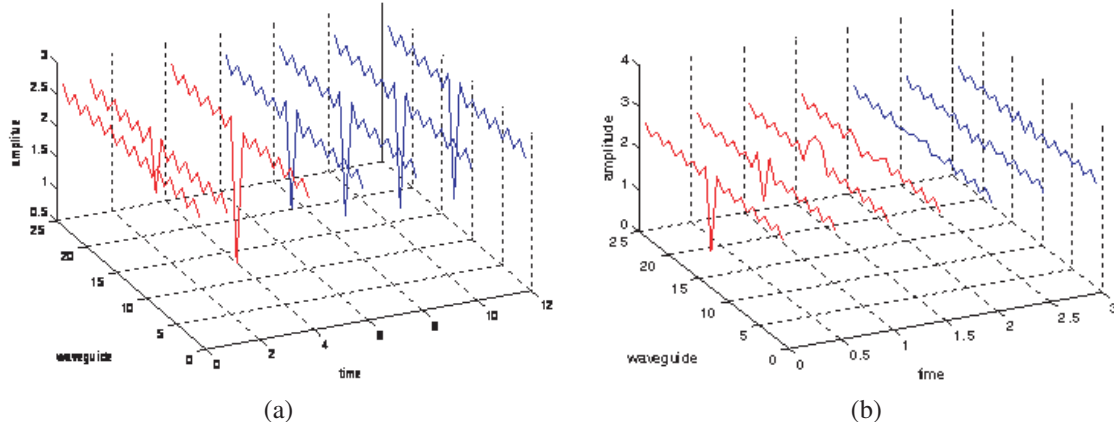


Figure 3: Plot (a) for dark discrete cavity soliton writing and (b) for erasing. Time evolution of output field during (red dash arrow) and after (blue solid arrow) GB injection; Parameters.  $q = 0$ ,  $E_1 = 3$ ,  $W = 1$ ,  $E_0 = 9.4$ ,  $C = 1$ ,  $\gamma = 1$ ,  $\Delta_{eff} = -3$ .

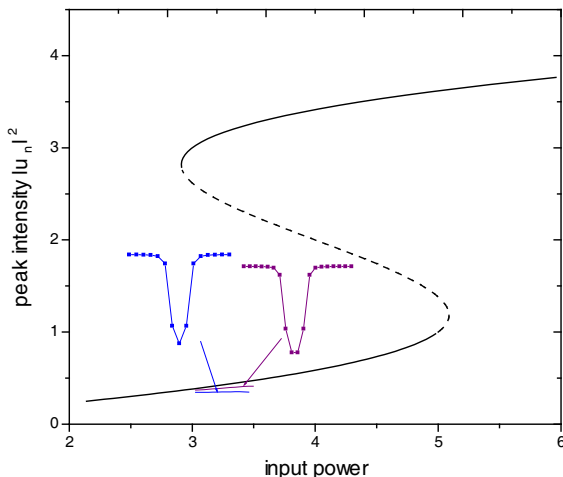


Figure 4: Bistability curve and families of discrete cavity solitons in self-defocusing medium,  $C = 0.25$ ,  $\gamma = -1$ ,  $\Delta_{\text{eff}} = 3$ .

has opposite phases at neighboring sites. We can also erase them unlike the writing, in which GB and background are in phase ( $\varphi = 0$ ) (Fig. 3(b)).

This dark DCSs have capability to switch different orders to each other by a control GB. The phase and width of GB is chosen proportional to desired final order of DCS ( $\varphi = \pi$  and  $\varphi = 0$  for switch of lower order to upper ones and vice versa, respectively).

### 3.2. Self-defocusing Case

Bistability curve and families of discrete cavity solitons in self-defocusing regime ( $\gamma = -1$ ) have shown in Fig. 4. In this regime, the upper branch of homogeneous solution is stable and dark solitons could form on a stable PW background. System provides two different orders of dark DCS distinguished by their width (Fig. 4-inset) as well as variety of bright DCSs from fundamental soliton with a site in its peak to very wide one with tens of cavity sites [7]. The writing and erasing of first order soliton is shown in Fig. 5 Width, intensity, injection time and phase of GB is chosen proportional to desired final order of DCS.

One of unique specifications of discrete systems in defocusing case is ability to provide bright and dark DCSs simultaneously. Fig. 6 shows the coexistence of dark and bright DCS. At the first a very wide bright DCS is created by a wide GB followed by an out of phase GB to make a deep on it evolve to a dark DCS. Another deep is created by a wider out of phase GB near to edge to make a bright DCS at the left. These two opposite DCSs are completely independent and could be switched separately.

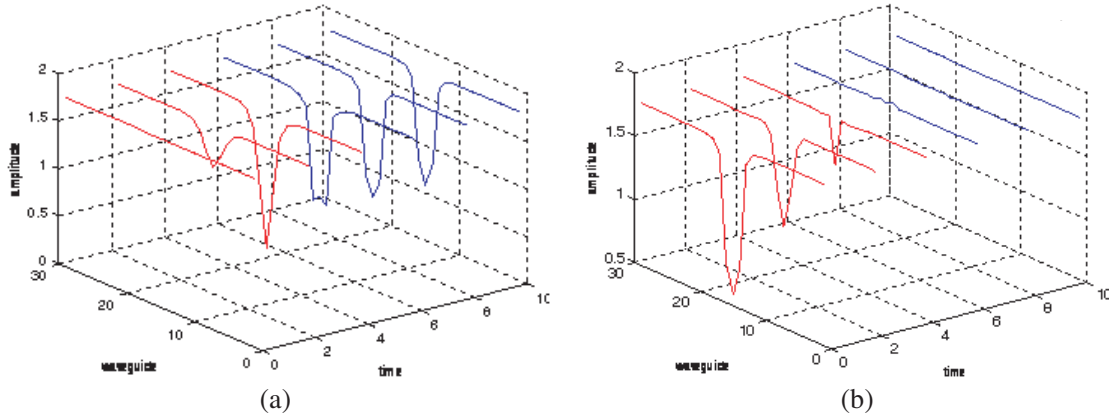


Figure 5: Time evolution of output field during (red) and after (blue) GB injection (a) for writing and (b) for erasing of dark discrete cavity soliton in self-defocusing; parameters.  $E_1 = 0.5$ ,  $w = 1.7$ ,  $E_0 = 1.8$ ,  $C = 0.25$ ,  $\varphi = \pi$ ,  $\gamma = -1$ ,  $\Delta_{eff} = 3$ .

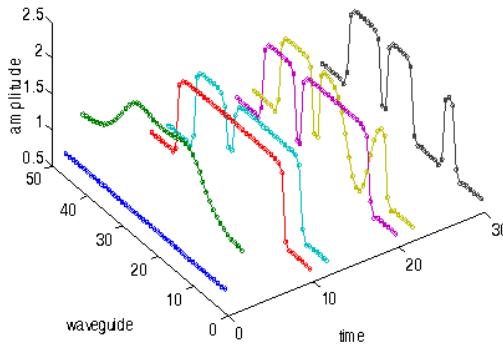


Figure 6: Coexistence of dark and bright DCS  $E_1 = 2$ ,  $w = 1$ ,  $E_0 = 1.8$ ,  $C = 0.25$ ,  $\varphi = \pi$ ,  $\Delta_{eff} = 3$ ,  $\gamma = -1$ .

#### 4. CONCLUSION

Various orders of dark discrete cavity solitons is reported in an coupled arrays of optical cavities containing a non absorbing Kerr medium driven by an external plane wave holding beam in self focusing and self-defocusing regime. We showed that any dark soliton could be successfully written, erased and switched to another by appropriate Gaussian control beam, if its amplitude and injection time product exceeds a threshold. Co-existence of bright and dark soliton is showed.

#### REFERENCES

1. Christodoulides, D. N., F. Lederer, and Y. Silberberg, *Nature*, Vol. 424, 817, 2003.
2. Kivshar, Y. S. and G. P. Agrawal, *Optical Solitons, from Fibers to Photonic Crystals*, 540, Academic Press, San Diego, 2003.
3. Susanto, H. and M. Johansson, *Phys. Rev. E*, Vol. 72, 016605, 2005.
4. Egorov, O. A., F. Lederer, and Y. S. Kivshar, *Opt. Express*, Vol. 15, 4149, 2007.
5. Egorov, O. A., U. Peschel, and F. Lederer, *Phys. Rev. E*, Vol. 71, 56612, 2005.
6. Yulin, A. V., A. R. Champneys, and D. V. Skryabin, *Phys. Rev. A*, Vol. 78, 011804, 2008.
7. Mahmoud Aghdami, K., R. Kheradmand, and R. Karimi, to be published in *Jap. J. Appl. Phys.*, Vol. 50, 2011.
8. Mahmoud Aghdami, K., R. Karimi, and R. Kheradmand, to be published in *Physica Status Solidi (c)*, 2011.

# EIT-based Coherent Control Effect Sensitive to Probe Frequency and Control Field Intensity in a Periodic Layered Medium

Teh-Chau Liau<sup>1</sup>, Jin-Jei Wu<sup>2</sup>, Jian Qi Shen<sup>3, 4</sup>, and Tzong-Jer Yang<sup>2</sup>

<sup>1</sup>Ph.D. Program in Engineering Science, College of Engineering  
Chung Hua University, Hsinchu 30012, Taiwan, China

<sup>2</sup>Department of Electrical Engineering, Chung Hua University, Hsinchu 30012, Taiwan, China

<sup>3</sup>Centre for Optical and Electromagnetic Research  
State Key Laboratory of Modern Optical Instrumentations

East Building No. 5, Zijingang Campus, Zhejiang University, Hangzhou 310058, China

<sup>4</sup>Joint Research Laboratory of Optics of Zhejiang Normal University and Zhejiang University

East Building No. 5, Zijingang Campus, Zhejiang University, Hangzhou 310058, China

**Abstract**— An EIT (electromagnetically induced transparency) material can exhibit a large number of intriguing quantum optical effects relevant to light wave manipulation, which are expected to be beneficial for developing new technologies in quantum optics and photonics. A periodic layered medium with unit cells consisting of a dielectric and an EIT atomic vapor is suggested for light propagation manipulation. Such an EIT-based periodic layered medium exhibits a flexible frequency-sensitive optical response, e.g., a very small change in probe frequency can lead to a drastic variation in reflectance and transmittance, since such an EIT atomic system interacts with both control and probe fields, and destructive quantum interference caused by two-photon resonance occurs. The present EIT-based periodic layered structure can also lead to controllable optical processes depending sensitively on the external control field. The tunable and sensitive optical response induced by quantum interference of the EIT atomic system has useful applications, such as new photonic device design (e.g., optical switches, photonic transistors, logic and functional gates).

## 1. INTRODUCTION

Over the past two decades, the effects of atomic phase coherence have exhibited a number of physically interesting phenomena such as electromagnetically induced transparency (EIT) [1] and the effects that are relevant to EIT [1]. For example, some unusual physical effects associated with EIT include inversionless light amplification [2], spontaneous emission cancellation [3], multi-photon population trapping [4], coherent phase control [5, 6], photonic resonant left-handed media [7], and light storage in atomic vapors [8–11], some of which are expected to be beneficial for developing new technologies in quantum optics and photonics. We shall in this paper suggest some new effects relevant to light propagation manipulation via EIT responses in an artificial periodic dielectric (EIT-based periodic structure). Such effects are caused because of the combination of EIT and photonic crystals. Since it shows extraordinary sensitivity to the frequency of the probe field (including an effect of tunable reflection and transmission induced by an external control field), it would be a new application of EIT for controllably manipulating light wave propagations. We believe that it can be used for designing sensitive quantum optical and photonic devices, and would have potential applications in many fields [12–16].

In this paper, we shall first address the optical property of an EIT medium, and then suggest a structure of periodic layered medium with unit cells consisting of a dielectric and an EIT atomic vapor. In Section 3, we present the behavior of frequency-sensitive reflectance and transmittance of the EIT-based periodic layered medium. In Section 4, we close the paper with some concluding remarks, where we will suggest that such a tunable and sensitive optical response would have useful applications, such as new photonic device design.

## 2. AN EIT SYSTEM AND AN EIT-BASED PERIODIC STRUCTURE

Here we shall address the quantum optical behavior of an EIT atomic vapor. Consider a three-level Lambda-configuration atomic system with two lower levels  $|1\rangle$ ,  $|2\rangle$  and one upper level  $|3\rangle$  (see Figure 1 for the schematic diagram). This atomic system interacts with the electric fields of the probe and control light waves, which drive the  $|1\rangle$ - $|3\rangle$  and  $|2\rangle$ - $|3\rangle$  transitions, respectively. In what follows, we are concerned with the influence of the external control field on the probe

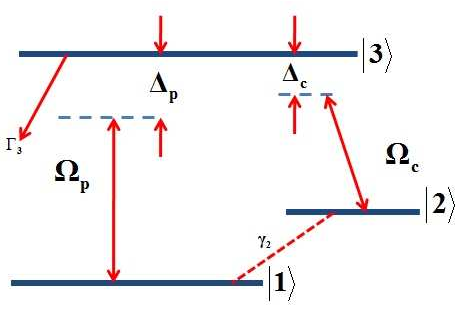


Figure 1: The schematic diagram of a three-level EIT atomic system. The control and probe laser beams drive the  $|2\rangle$ - $|3\rangle$  and  $|1\rangle$ - $|3\rangle$  transitions, respectively. Such a three-level system can be found in metallic alkali atoms (e.g., Na, K, and Rb).

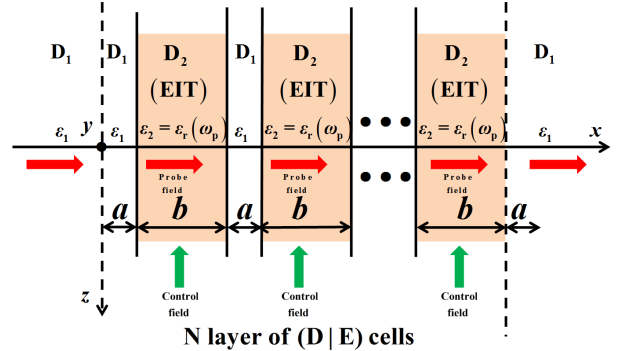


Figure 2: The 1D  $N$ -layer structure of  $(D|E)$  cells embedded in GaAs homogeneous dielectric. The dielectrics  $D_1$  and  $D_2$  stand for the GaAs and EIT atomic media, respectively. A  $(D|E)$  cell consists of GaAs dielectric ( $D$ ) and EIT medium ( $E$ ). The lattice constants of the  $(D|E)$  cells are chosen as  $a = b = 0.1 \mu\text{m}$ .

wave propagation inside the EIT-based periodic layered medium. The atomic microscopic electric polarizability of the  $|1\rangle$ - $|3\rangle$  transition in such a three-level system is given by [10, 11]

$$\beta = \frac{i|\varphi_{13}|^2}{\varepsilon_0 \hbar} \frac{\frac{\gamma_2}{2} + i(\Delta_p - \Delta_c)}{\left(\frac{\Gamma_3}{2} + i\Delta_p\right) \left[\frac{\gamma_2}{2} + i(\Delta_p - \Delta_c)\right] + \frac{1}{4}\Omega_c^*\Omega_c}. \quad (1)$$

Here,  $\Gamma_3$  and  $\gamma_2$  denote the spontaneous emission decay rate and the collisional dephasing rate, respectively. The Rabi frequency  $\Omega_c$  of the control field is defined as  $\Omega_c = \varphi_{32}E_c/\hbar$  with  $E_c$  the slowly-varying amplitude (envelope) of the control field. The two frequency detunings are defined as  $\Delta_p = \omega_{31} - \omega_p$ ,  $\Delta_c = \omega_{32} - \omega_c$  with  $\omega_p$  and  $\omega_c$  the mode frequencies of the probe and control fields, respectively. By using the Clausius-Mossotti relation (the local field effect due to the dipole-dipole interaction between neighboring atoms), the relative electric permittivity of the EIT vapor at probe frequency ( $\omega_p = \omega_{31} - \Delta_p$ ) is of the form

$$\varepsilon_r = 1 + \frac{N_a \beta}{1 - \frac{N_a \beta}{3}}, \quad (2)$$

where  $N_a$  denotes the atomic concentration (atomic number per unit volume) of the atomic vapor.

In Figure 2 we present the 1D periodic  $(D|E)$  cells that are composed of two kinds of media: GaAs dielectric with the relative refractive index  $n_1 = 3.54$  and a typical Lambda-configuration three-level EIT medium, of which the electric permittivity is determined by Equation (2). Here, the characters “D” and “E” in “ $(D|E)$ ” denote the dielectric (GaAs) and the EIT, respectively. The two materials are both homogeneous along  $y$ -direction (i.e.,  $\partial/\partial y = 0$ ) and the probe signal wave travels in the  $(\dots D|E|D|E \dots)$  structure always along  $x$ -direction. In the section that follows, we will address the reflection coefficient on the left side interface ( $x = 0$ ) of such an EIT-based periodic medium, which is in fact a 1D  $N$ -layer  $(D|E)$  layered structure bounded by the GaAs dielectric material [17].

### 3. FREQUENCY-SENSITIVE RESPONSE

We will show that the reflection coefficient of the EIT-based periodic medium would be sensitive to the probe frequency when it is tuned onto two-photon resonance ( $\Delta_p \rightarrow \Delta_c$ ). The typical atomic and optical parameters chosen for the numerical results are as follows: the atomic number density  $N_a = 5.0 \times 10^{20} \text{ m}^{-3}$ , the electrical dipole moment  $|\varphi_{31}| = 1.0 \times 10^{-29} \text{ C}\cdot\text{m}$ , the spontaneous emission decay rate  $\Gamma_3 = 2.0 \times 10^7 \text{ s}^{-1}$ , the frequency detuning of the control field  $\Delta_c = 0.5\Gamma_3 = 1.0 \times 10^7 \text{ s}^{-1}$ , and the dephasing rate  $\gamma_2 = 1.0 \times 10^5 \text{ s}^{-1}$ . The real and imaginary parts of the transmission coefficient  $t$  corresponding to  $N$ -layer  $(D|E)$  cells are presented in Figure 3 as an illustrative example, where the layer number  $N = 1, 2, 5, 10$ . It follows that the transmission coefficient changes drastically in the frequency detuning range of concern. It can be seen that  $t$  changes dramatically

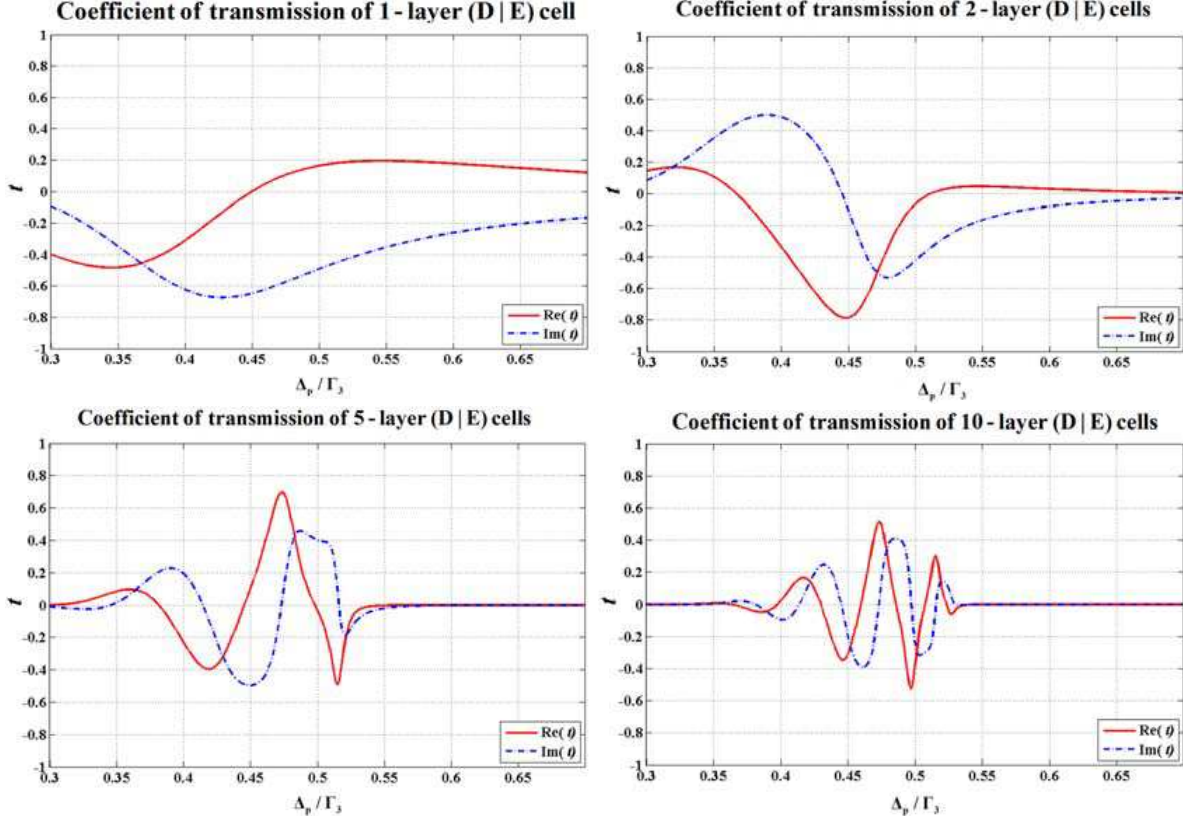


Figure 3: The real and imaginary parts of the transmission coefficient  $t$  versus the normalized probe frequency detuning  $\Delta_p/\Gamma_3$  in the frequency range of two-photon resonance caused by the destructive quantum interference between the  $|1\rangle-|3\rangle$  and  $|2\rangle-|3\rangle$  transitions (within  $\Delta_p = 0.4\Gamma_3 \sim 0.55\Gamma_3$ ). The layer number of the EIT-based periodic medium  $N = 1, 2, 5, 10$ . The control Rabi frequency is chosen as  $\Omega_c = 2.0 \times 10^7 \text{ s}^{-1}$ .

in the range of  $\Delta_p/\Gamma_3 \in [0.3, 0.7]$ , where the probe frequency detuning changes at the level of one part in  $10^8$  in the probe frequency  $\omega_p$  (the typical value of the probe frequency  $\omega_p \simeq 10^{15} \text{ s}^{-1}$ ). For example, the real and imaginary parts of  $t$  change from about  $-0.75$  to  $+0.75$  and from about  $-0.5$  to  $+0.5$ , respectively. Since the destructive quantum interference between the  $|1\rangle-|3\rangle$  and  $|2\rangle-|3\rangle$  transitions occurs [1], such a dramatic change in the coefficient of transmission is caused by the two-photon resonance. From Figure 3 we can conclude that the more layers there are in the dielectric-EIT cell structure, the more drastic change there would be in the transmission coefficient on the left-side interface of this EIT-based periodic layered medium. Therefore, the total number of valleys and peaks in the curve of the transmission coefficient  $t$  in a narrow band within  $\Delta_p \in (0.4\Gamma_3, 0.55\Gamma_3)$  becomes more and more when the total layer number  $N$  increases.

In addition to the probe *frequency-sensitive behavior*, the EIT-based periodic layered material can exhibit another effect, i.e., field-controlled tunable optical response, where the control field can be used to manipulate the photonic band structure, and therefore the transmission coefficient would vary as we tune the control Rabi frequency  $\Omega_c$ . From Figure 4 one can see that the tunable transmission coefficient of the EIT-based periodic layered medium is also sensitive to the Rabi frequency of the control field when the total layer number  $N$  increases. Hence, the incident probe signal is either reflected or transmitted depending quite sensitively on the intensity of the external control field (characterized by  $\Omega_c^*\Omega_c$ ). This means that such an effect in such an EIT-based periodic structure could be used for designing some sensitive photonic devices (e.g., tunable photonic transistors, optical switches, and photonic logic gates). Besides, a full controllability of reflection and transmission of the present EIT-based layered structure can also be indicated in Figure 4. It follows that both the real and imaginary parts of the transmission coefficient  $t$  are larger than 0.45, and hence the transmittance ( $T = [n_{\text{EIT}}/n_D] \cdot |t|^2$ ) approaches to unit (or almost one) when the normalized control Rabi frequency  $\Omega_c/\Gamma_3$  is taken to be certain values, such as at  $\Omega_c/\Gamma_3 = 6.0$   $|t| = 0.85$  (for  $N = 5$ ) and  $|t| = 0.75$  (for  $N = 10$ ). For this reason, a new photonic device, such as a field-intensity-sensitive switchable reflector (mirror), could be designed with such an EIT-based

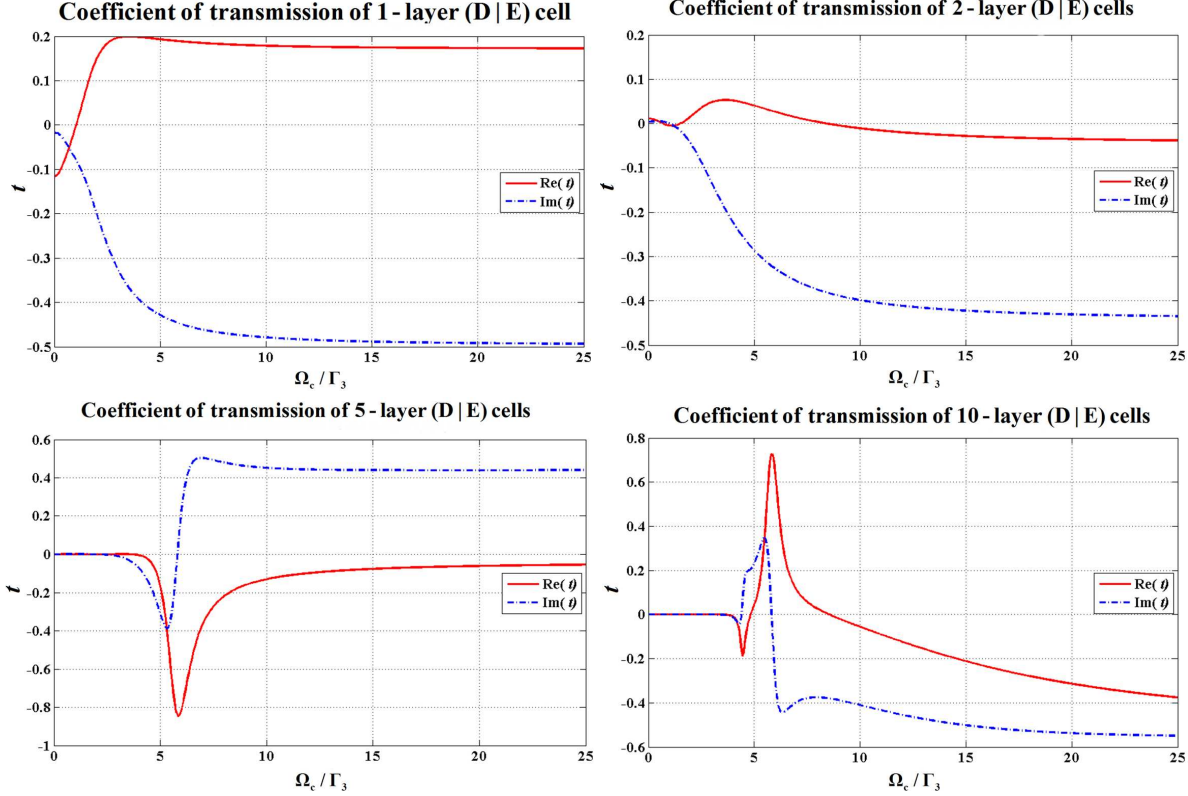


Figure 4: The real and imaginary parts of the transmission coefficient  $t$  versus the normalized Rabi frequency  $\Omega_c/\Gamma_3$  of the control field. The probe frequency detuning is  $\Delta_p = 2.0 \times 10^7 \text{ s}^{-1}$ . All the atomic and optical parameters such as  $\varphi_{31}$ ,  $\Gamma_3$ ,  $\gamma_2$ ,  $\Delta_c$ ,  $N_a$  are chosen exactly the same as those in Figure 3.

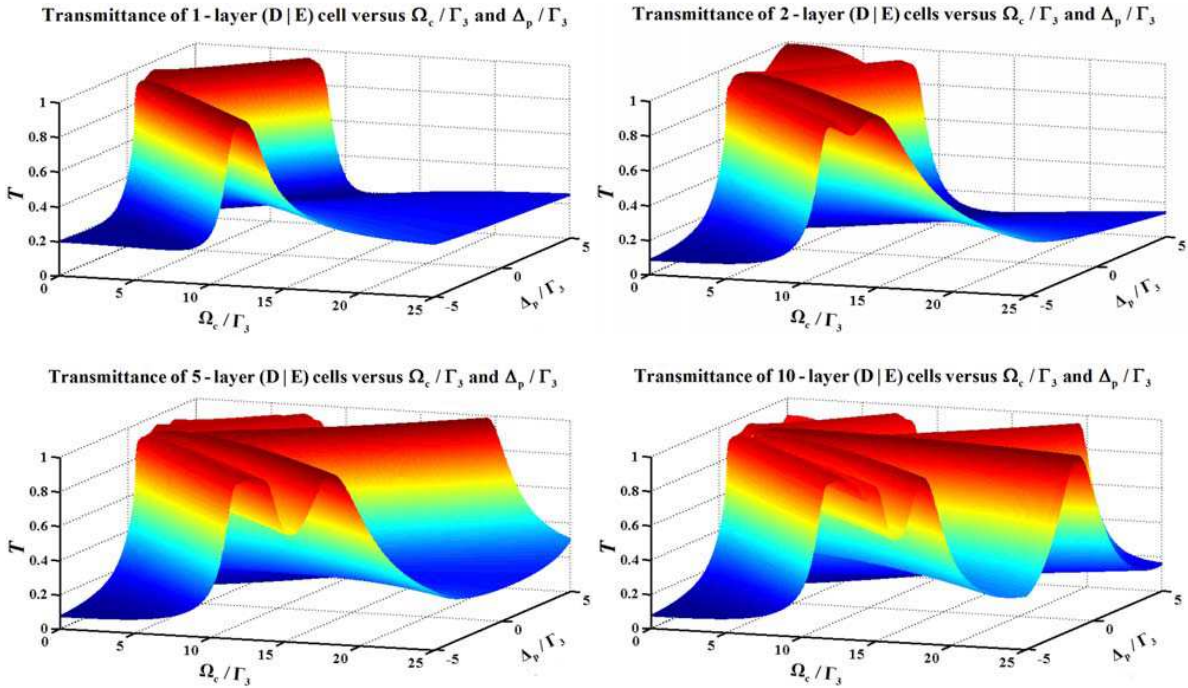


Figure 5: The three-dimensional behavior of the transmittance of the EIT-based layered medium versus the normalized control Rabi frequency  $\Omega_c/\Gamma_3$  and the normalized probe frequency detuning  $\Delta_p/\Gamma_3$ . All the atomic and optical parameters such as  $\varphi_{31}$ ,  $\Gamma_3$ ,  $\gamma_2$ ,  $\Delta_c$ ,  $N_a$  are chosen exactly the same as those in Figures 3 and 4.

layered structure that has a large total layer number  $N$  (e.g.,  $N > 10$ ). In Figure 5 we plot the three-dimensional behavior of the transmittance of the EIT-based periodic layered medium as both the control Rabi frequency  $\Omega_c$  and the probe frequency detuning  $\Delta_p$  change.

#### 4. CONCLUSIONS

We have shown that the reflectance and transmittance in an EIT-based periodic medium are quite sensitive to the probe frequency, since the microscopic electric polarizability as well as the electric permittivity of the EIT medium are caused by the atomic energy level transition processes from ground state to excited states, in which the quantum interference relevant to atomic phase coherence is involved. Such an EIT-based periodic layered material can also exhibit an effect of field-intensity-sensitive switching control (depending quite sensitively on the Rabi frequency of the control field) in the cases of large layer number. Thus, some new photonic devices (e.g., optical switches, photonic transistors, logic and functional gates, and other fundamental building blocks in, e.g., photonic microcircuits on silicon, in which light replaces electrons) would be realized with such an effect. The present scheme can be generalized to a four-level EIT system, where two control fields and one probe field drive the atomic level transitions. Obviously, the optical response in such an EIT photonic crystal would be more sensitive to the probe frequency than in a three-level EIT photonic crystal presented in this paper.

#### ACKNOWLEDGMENT

This work is supported by Taiwan Science Council under Grant Nos. NSC 99-2811-M-216-001 and NSC 99-2112-M-216-002, National Natural Science Foundation of China under Grant No. 60990320 and Natural Science Foundation of Zhejiang Province under Grant No. Y6100280. The author Shen is also grateful to the support of the Fundamental Research Funds for the Central Universities of China.

#### REFERENCES

1. Harris, S. E., “Electromagnetically induced transparency,” *Phys. Today*, Vol. 50, No. 7, 36–42, 1997.
2. Cohen, J. L. and P. R. Berman, “Amplification without inversion: Understanding probability amplitudes, quantum interference, and Feynman rules in a strongly driven system,” *Phys. Rev. A*, Vol. 55, 3900–3917, 1997.
3. Zhu, S. Y. and M. O. Scully, “Spectral line elimination and spontaneous emission cancellation via quantuminterference,” *Phys. Rev. Lett.*, Vol. 76, 388–391, 1996.
4. Champenois, C., G. Morigi, and J. Eschner, “Quantum coherence and population trapping in three-photon processes,” *Phys. Rev. A*, Vol. 74, 053404, 2006.
5. Zheltikov, A. M., “Phase coherence control and subcycle transient detection in . . . tering with ultrashort laser pulses,” *Phys. Rev. A*, Vol. 74, 053403, 2006.
6. Gandman, A., L. Chuntonov, L. Rybak, and Z. Amitay, “Coherent phase control of resonance-mediated. (2 + 1) three-photon absorption,” *Phys. Rev. A*, Vol. 75, 031401, 2007.
7. Krown, C. M. and J. Q. Shen, “Dressed-state mixed-parity transitions for realizing negative refractive index,” *Phys. Rev. A*, Vol. 79, 023818, 2009.
8. Shen, J. Q., “Negatively refracting atomic vapor,” *J. Mod. Opt.*, Vol. 53, 2195–2205, 2006.
9. Schmidt, H. and A. Imamoglu, “Giant Kerr nonlinearities obtained by electromagnetically induced transparency,” *Opt. Lett.*, Vol. 21, 1936–1938, 1996.
10. Wang, L. J., A. Kuzmich, and A. Dogariu, “Gain-assisted superluminal light propagation,” *Nature*, Vol. 406, 277–279, 2000.
11. Arve, P., P. Jänes, and L. Thylén, “Propagation of two-dimensional pulses in electromagnetically induced transparency media,” *Phys. Rev. A*, Vol. 69, 063809, 2004.
12. Shen, J. Q., Z. C. Ruan, and S. He, “Influence of the signal light on the transient optical properties of a four-level EIT medium,” *Phys. Lett. A*, Vol. 330, 487–495, 2004.
13. Sangu, S., K. Kobayashi, A. Shojiguchi, and M. Ohtsu, “Logic and functional operations using a near field optically coupled quantum-dot system,” *Phys. Rev. B*, Vol. 69, 115334, 2004.
14. Kawazoe, T., K. Kobayashi, S. Sangu, and M. Ohtsu, “Demonstration of a nanophotonic switching operation by optical near-field energy transfer,” *Appl. Phys. Lett.*, Vol. 82, 2957–2959, 2003.

15. Shen, J. Q., "Transient evolutional behaviours of double-control electromagnetically induced transparency," *New J. Phys.*, Vol. 15, 374–388, 2007.
16. Shen, J. Q. and P. Zhang, "Double-control quantum interferences in a four-level atomic system," *Opt. Express*, Vol. 15, 6484–6493, 2007.
17. Gharibi, A., J. Q. Shen, and J. Gu, "Tunable transient evolutional behaviours of a four-level atomic vapour," *J. Phys. B: At. Mol. Opt. Phys.*, Vol. 42, 055502, 2009.
18. Yeh, P., *Optical Waves in Layered Media*, Chapter 4–6, 83–143, John Wiley & Sons, Inc., New Jersey, 2005.

# Manipulating Photonic Nanojet Parameters of Micron-sized Dielectric Microspheres

**Yuri E. Geints, Ekaterina K. Panina, and Alexander A. Zemlyanov**

Zuev Institute of Atmospheric Optics SB RAS, 1 Zuev square, Tomsk 634021, Russia

**Abstract**— The results of our systematic theoretical investigations of spatial and amplitude characteristics of PNJ formed in the vicinity of transparent dielectric microspheres exposed to the laser radiation are presented. Based on the numerical calculation within the framework of the extended Mie theory for the optical radiation scattering on multilayered sphere, spatial and amplitude characteristics of the photonic jet of particles with a different size, optical properties, and structural composition were considered. In particular, for the first time the influence of the shell thickness and refractive index of composite two-layer microparticle on PNJ parameters were studied.

## 1. INTRODUCTION

The problem of overcoming the diffraction limit in the spatial resolution of wave microscopy devices, the necessity of a significant increase of the electromagnetic field strength in the region of its localization at the given radiation energy, and the micromanipulation of very small objects come recently to the forefront in connection with the development of nanophotonics studying optical fields and optical radiation behavior on a nanometer scale. One of the important aspects of this problem is the study of the structure of the optical field near a surface of slightly absorbing micron-sized particles from the viewpoint of the possibility of sub-diffraction focusing of the incident optical radiation. This effect, called the “photonic nanojet” (PNJ), was first noticed quite recently. The peculiarity of the PNJ from a spherical object is connected with the highest symmetry inherent to a sphere and providing for better focusing capability. Essentially, a PNJ corresponds to the specific spatial region within the external focal waist of the light wave diffracted on a transparent particle. It is located near the rear (shadow) side of the particle, extends to the distances of about several wavelengths in the environmental medium, and may have a sub-wavelength transversal dimension.

In this report we present the results of our systematic theoretical investigations of spatial and amplitude characteristics of PNJ formed in the vicinity of transparent dielectric microspheres exposed to the laser radiation. Based on the numerical calculation within the framework of the extended Mie theory for the optical radiation scattering on multilayered sphere, spatial and amplitude characteristics of the photonic jet of particles with a different size, optical properties, and structural composition were considered. In particular, for the first time the influence of the shell thickness and refractive index of composite two-layer microparticle on PNJ parameters were studied.

## 2. PNJ IN HOMOGENEOUS PARTICLES

The key parameters of PNJ (transverse dimension, length, peak intensity) formed in the vicinity of homogeneous dielectric microspheres and microcylinders under the exposure to laser radiation were studied theoretically in Refs. [1, 2]. These studies have shown that both the PNJ shape and intensity depend significantly on the size and optical properties of a generating microparticle.

Figure 2 shows the main parameters of PNJ of water particles with the variable size. It should be noted that all the three studied characteristics demonstrate the nearly linear growth at the increase of the drop radius. This regularity was found for the first time in our calculations. If we speak about the overcoming of the diffraction limit at the focusing of an optical wave by a particle, that is, consider the PNJ radius, then, as follows from figure (see the inset), it remains below the diffraction-limited value  $R_d = m_m \lambda / \sqrt{2}$  (in terms of the focal waist radius at the  $1/e^2$  level) only for drops with the radius  $a_0 \leq 3 \mu\text{m}$  or, more exactly, up to the particle diffraction parameter  $x_a \leq 35$ . Above this boundary, the PNJ radius is no longer sub-diffractive. Under this condition, the length of the photon jet  $L_{jet}$  does not exceed  $\sim 6\lambda$ , and the intensity growth in the jet at the peak is a little bit greater than two orders of magnitude.

At some values of the drop radius, the resonance excitation of whispering gallery modes (WGMs) was observed in our numerical experiments. The situations with WGM are marked by dark dots on the dependence  $R_{jet}(a_0)$ .

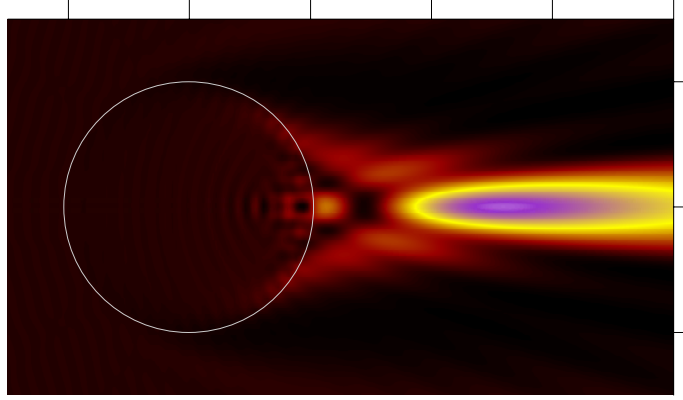


Figure 1: The spatial distributions of PNJ relative intensity formed in the vicinity of homogeneous particles with  $a = 2 \mu\text{m}$  and  $n = 1.1$  exposed to the radiation at  $\lambda = 0.532 \mu\text{m}$  (incident from the left).

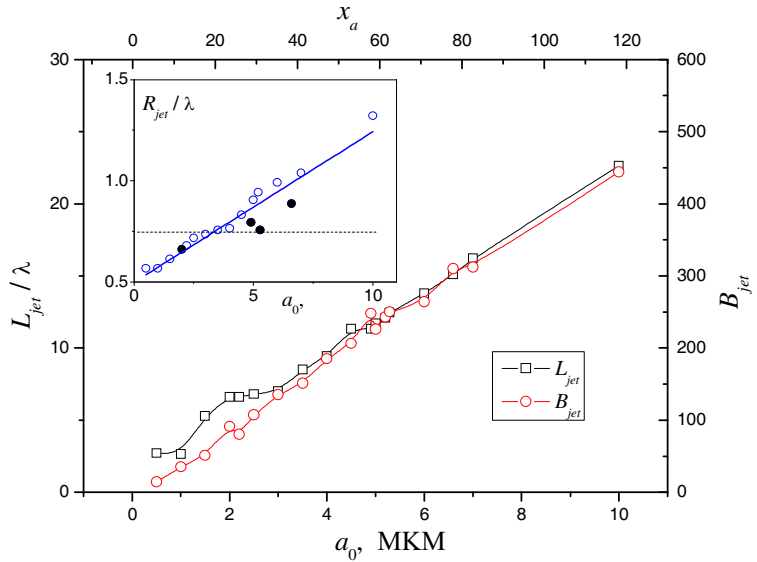


Figure 2: Parameters of PNJ of water drops with a different radius ( $\lambda = 0.532 \mu\text{m}$ ). The diffraction limit for the focal waist radius of the light beam  $R_d$  is shown by the dashed line in the inset.

Now let us analyze the influence of the refractive index on PNJ characteristics. Fig. 3 shows the characteristic length, half-width, and maximal intensity of PNJ from a 3-micron non-absorbing particle at the variable relative refractive index  $n_r = n_a/n_m$  (from here on, optical contrast).

The increase of the optical contrast of a particle relative to the medium, as is already known [3], is accompanied by the shortening of the characteristic length  $L_{jet}$  and the increase of the peak intensity  $B_{jet}$  of the photon jet. This is caused by the increase in the optical power of lens. A spherical particle plays the role of a lens for the incident light beam. As a result, starting from some value of  $n_r$ , the waist center of the external focus first falls on the particle surface, which corresponds to the maximum of the dependence  $B_{jet}(n_r)$  (see the inset in Fig. 3) and the minimal PNJ length of about  $2\lambda$ , and then shifts into the particle. In the last case, the photon jet “flowing out” of the particle has already the lower intensity than in the focal waist, but is characterized by the smoother decrease of the intensity with the distance from the particle, which is formally expressed in a somewhat increase of the parameter  $L_{jet}$ .

As can be seen from the figure, the PNJ half-width has the sub-diffraction value in rather wide range of variation of the optical contrast  $n_r = 1.317$ . Beyond this range, the parameter  $R_{jet}$  is greater than  $R_d$  either due to the weak focusing at the low contrast of the refractive index or due to the high angular divergence of the radiation after the focal waist lying inside the particle at the high optical contrast.

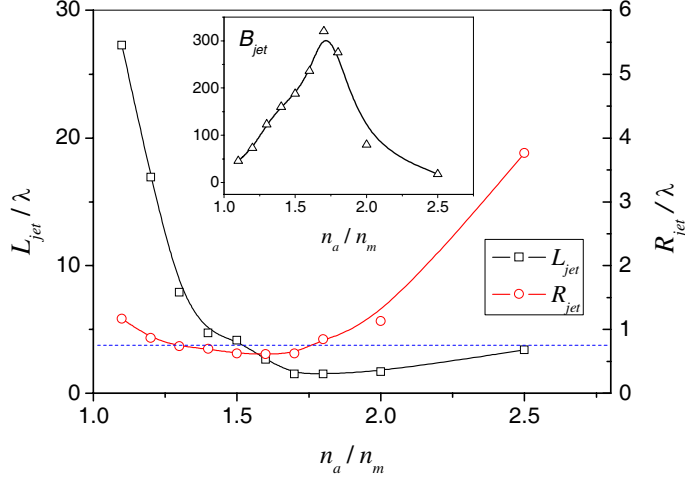


Figure 3: Length, half-width, and maximal intensity in Pijoli of a model spherical particle with  $a_0 = 3\text{ }\mu\text{m}$  at the variable relative refractive index (absorption is absent, the dashed straight line corresponds to the diffraction limit of the focal waist radius).

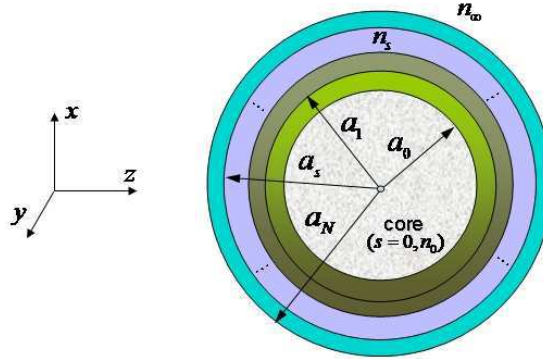


Figure 4: Model of a multilayer spherical particle.

### 3. Pijoli IN SHELLLED PARTICLES

If a sphere scattering the radiation is inhomogeneous in the radial direction and has a multilayer structure consisting of a core and several shells having a constant thickness (see Fig. 4), then the form of the Lorenz-Mie solution remains unchanged, but the number of boundary conditions increases. Below, we follow the equations of the modified Mie theory for layered spheres [4, 5]. These equations are adapted for the computer calculations. They are universal expansions of optical fields in every layer in the form and are presented below in the shortened form.

Inside every layer (and in the core), the electric and magnetic fields are written in the following universal form [4]:

$$\begin{aligned}\mathbf{E}^s(\mathbf{r}) &= \sum_{n=1}^{\infty} E_n \left[ i \left( a_n^s \mathbf{N}_{e1n}^{(3)} - d_n^s \mathbf{N}_{e1n}^{(1)} \right) - \left( b_n^s \mathbf{M}_{o1n}^{(3)} - c_n^s \mathbf{M}_{o1n}^{(1)} \right) \right] \\ \mathbf{H}^s(\mathbf{r}) &= \frac{k_s}{\omega} \sum_{n=1}^{\infty} E_n \left[ i \left( b_n^s \mathbf{N}_{o1n}^{(3)} - c_n^s \mathbf{N}_{o1n}^{(1)} \right) + \left( a_n^s \mathbf{M}_{e1n}^{(3)} - d_n^s \mathbf{M}_{e1n}^{(1)} \right) \right],\end{aligned}$$

where  $\omega = 2\pi c/\lambda$  is the circular frequency of the optical wave;  $c$  is the speed of light in vacuum. It is convenient to calculate the arrays of partial amplitudes  $a_n^s - d_n^s$  by passing first to generalized coefficients  $A_n^s - D_n^s$  and then using the following recursion for them [5]:

$$A_n^s = U_n^{s-1} C_n^s; \quad B_n^s = V_n^{s-1} D_n^s; \quad C_n^s = \prod_{t=s}^{N_s} P_n^t; \quad D_n^s = \prod_{t=s}^{N_s} Q_n^t$$

with the initial conditions  $C_n^{N_s+1} = D_n^{N_s+1} = \gamma$ , where  $\gamma = 1$ , if the total (incident + scattered) field is calculated, and  $\gamma = 0$ , if we are interesting only in the scattered field.

The functions  $U_n^s$  and  $V_n^s$  are connected with the field external with respect to the considered layer. The set of the functions  $P_n^s$  and  $Q_n^s$ , in their turn, are determined by the coefficients of expansion of the field inside a layer.

For reference, we write the equations for the spherical components of the electric field ( $E_r^s, E_\theta^s, E_\varphi^s$ ) at any spatial point at the incidence of a linearly polarized plane wave on a multilayer spherical particle:

$$\begin{aligned} E_r^s &= \sum_{n=1}^{\infty} \frac{iE_n}{(k_s r)^2} \cos \varphi \sin \theta n(n+1) \pi_n [a_n^s \xi_n(k_s r) - d_n^s \psi_n(k_s r)]; \\ E_\theta^s &= \sum_{n=1}^{\infty} \frac{E_n}{(k_s r)} \cos \varphi \{i\tau_n [a_n^s \xi'_n(k_s r) - d_n^s \psi'_n(k_s r)] + \pi_n [c_n^s \psi_n(k_s r) - b_n^s \xi_n(k_s r)]\}; \\ E_\varphi^s &= \sum_{n=1}^{\infty} \frac{-E_n}{(k_s r)} \sin \varphi \{i\pi_n [a_n^s \xi'_n(k_s r) - d_n^s \psi'_n(k_s r)] + \tau_n [c_n^s \psi_n(k_s r) - b_n^s \xi_n(k_s r)]\}. \end{aligned}$$

where  $\pi_n$  and  $\tau_n$  are angular functions expressed through the associated Legendre polynomials.

As an object of study, we took the most abundant configuration of a spherical particle consisting of a core with the radius  $a_{s=0} = 1 \mu\text{m}$  and one external layer. The thickness  $h = a_1 - a_0$  and the refractive index  $m_1$  of this layer were varied.

The series of plots in Fig. 5 demonstrates the results of our numerical calculations illustrating the influence of the shell thickness on the main characteristics of PNJ of a composite microparticle in the air: the maximal extent of the intensity increase in the optical field and the longitudinal and transverse dimensions of the photon nanojet. Two cases are considered, namely, a nonabsorbing quartz sphere ( $m_{s=0} \equiv m_a = 1.5 + i \cdot 0$ ) coated by a shell with the smaller refractive index, for example, a water shell ( $m_1 = 1.33 + i \cdot 0$ ), or by a more optically dense shell, for example, a germanium shell ( $m_1 = 2.0 + i \cdot 0$ ). The calculations are performed by equations of the modified Mie theory and are presented as a relative change in PNJ parameters as functions of the shell thickness:  $\delta L_{jet} = (L_{jet} - L_{jet}^0) / L_{jet}^0$ ,  $\delta R_{jet} = (R_{jet} - R_{jet}^0) / R_{jet}^0$ , and  $\bar{B}_{jet} = B_{jet} / B_{jet}^0$ , where the superscript 0 denotes the corresponding parameters of the jet of a homogeneous particle having the radius equal to the outer radius of the shelled particle.

The analysis of the plots indicates that the character of the shell influence on PNJ parameters is significantly different at different relations between optical properties of the core and the shell. Thus, in a particle with a shell having the higher refractive index, the photon jet widens and its peak intensity decreases. However, the jet length may increase drastically (see Fig. 5(a)). On the other hand, if the shell is made of a less optically dense material than the core, then an increase in the shell thickness affects weakly the PhNJ width and length, and only an increase in the intensity level is significant (see Fig. 5(c)).

The results obtained have a clear physical interpretation within the wave optics, if we do not consider the shell influence on the focusing properties of the core, but, to the contrary, how the

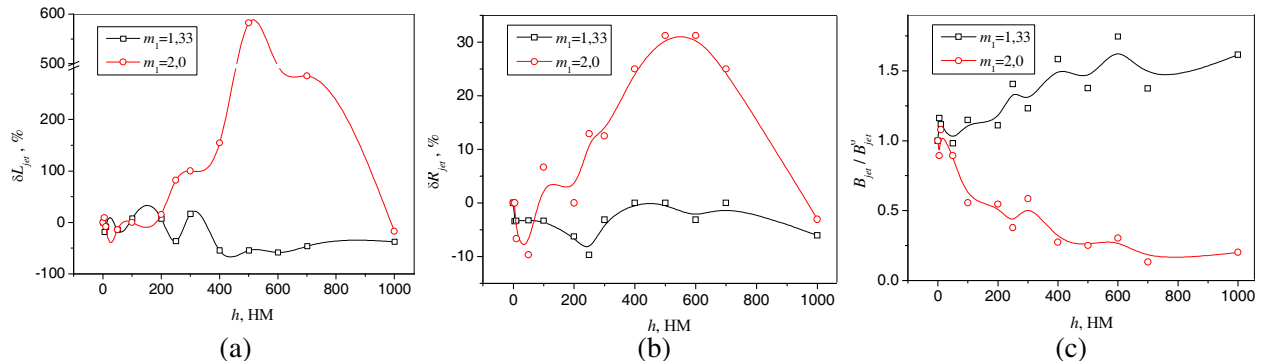


Figure 5: Relative change of the length (a), half-width (b), and relative intensity (c) in PNJ of a quartz particle ( $a_0 = 1 \mu\text{m}$ ) with a shell at a variable thickness.

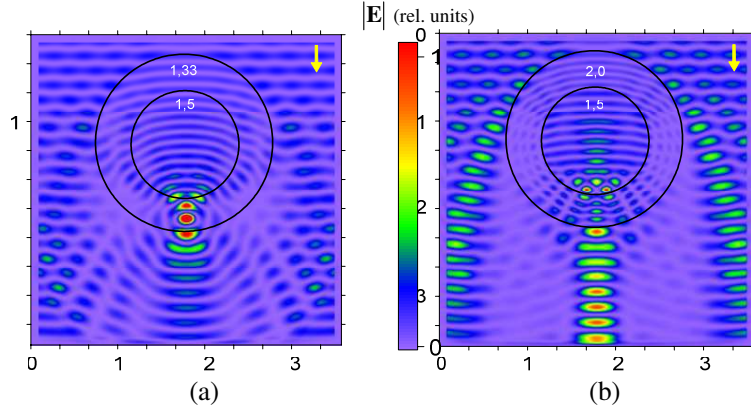


Figure 6: TFSF 3D-FDTD simulations of electric field amplitude  $|\mathbf{E}|$  spatial distribution in the vicinity of two-layered spherical particle (core+shell = 3  $\mu\text{m}$ ) with (a)  $m_a = 1.5$  and  $m_l = 1.33$  and (b)  $m_l = 2.0$  illuminated by a plane wave (532  $\mu\text{m}$ ). The incident wave propagates from the top. The value of  $|\mathbf{E}|$  in each figure is normalized to its maximal value.

core redistributes optical fluxes inside a larger-size particle. Let us consider Fig. 6, which shows the tone spatial distribution of the amplitude of the total electric field  $|\mathbf{E}|$  of a light wave in the plane  $xy$  passing through the center of a two-layer spherical particle. The calculations were performed by the technique of numerical solution of Maxwell differential equations (TFSF 3D-FDTD) through the construction of difference schemes based on the Yee cell. The source of the field was a plane monochromatic wave with  $E_0 = 1 \text{ V/m}$  generated at the upper boundary of the computational domain ( $200 \times 200 \times 200$  cells), which was enclosed by a system of perfectly matched layers (PMLs) to prevent the reflection from boundaries.

A plane wave incident on a composite particle first penetrates into the shell. The phase difference formed between different parts of the light wave leads to deformations of the wave front, which acquires the positive curvature favoring the radiation focusing. The further scenario of the wave propagation in the particle depends on the relation between the refractive indices of the core and the shell. If the core is more optically dense than the shell (Fig. 6(a)), an additional phase shift appears between the wave center (with respect to the main diameter of the particle) and its periphery. The curvature of the wave front of the radiation passing through the core increases, that is, the wave additionally focuses. As a result, the intensity at the focal waist for this composite spherical particle increases, while the characteristic dimensions (both longitudinal and transverse) shorten (see Fig. 5).

If, to the contrary, the radiation propagating in the shell meets the less optically dense material of the core (Fig. 6(b)), then the core straightens the phase front of the wave and thus defocuses the central part of the beam. This focusing system elongates the waist zone, leading to the smoother change of the wave intensity and decreasing the maximum.

The further increase of the shell thickness obviously reduces the core influence on the transformation of the photon flow inside the particle. This explains the maximum (Fig. 5) in the dependence of the PNP of the particle having the shell with the high refractive index on the shell thickness. The two-layer particle with a wide shell is close to a homogeneous particle in its optical properties, but with the higher effective value of  $m$ , which, according to Fig. 5, leads to the PNP localization in all spatial dimensions.

## REFERENCES

1. Heifetz, A., J. J. Simpson, S.-C. Kong, et al., *Optics Express*, Vol. 15, 17334, 2007.
2. Geints, Y. E., A. A. Zemlyanov, and E. K. Panina, *Optics Communications*, Vol. 283, 4775, 2010.
3. Itagi, A. V. and W. A. Challener, *J. Opt. Soc. Am. A*, Vol. 22, 2847, 2005.
4. Yand, W., *Appl. Opt.*, Vol. 42, 1710, 2003.
5. Xu, H., *Phys. Rev. B*, Vol. 75, 073405, 2005.

# Influence of Stokes Pulse Shapes on SBS Slow Light in Fibers

Shanglin Hou<sup>1</sup>, Hongbing Li<sup>1,2</sup>, Yunbo Shang<sup>1</sup>, Yanjun Liu<sup>1</sup>, and Yongzhao Xu<sup>3</sup>

<sup>1</sup>School of Science, Lanzhou University of Technology, Lanzhou, Gansu 730050, China

<sup>2</sup>School of Science, Nantong University, Nantong, Jiangsu 226007, China

<sup>3</sup>Institute of Electronic Engineering, Dong Guan University of Technology  
Dongguan, Guangdong 523808, China

**Abstract**— In order to increase time delay and decrease pulse broadening via Stimulate Brillouin Scattering slow light, the coupled amplitude equations of Stimulated Brillouin Scattering in optical fibers were solved with fourth-order Runge-Kutta formula and characteristics, the influence of the edge sharpness of injected stokes pulse on time delay and pulse broadening factor was investigated. A method of optimizing time delay and pulse broadening factor was represented, namely, increasing the sharpness of stokes pulse appropriately. Comparing with using Gaussian-shaped pulse as injected stokes pulse, the similar time delay and less pulse broadening factor were obtained by this method.

## 1. INTRODUCTION

Recently, more and more attention has been paid to slow down the group velocity of optical pulse (so-called slow light) because it has many applications [1–3], such as all-optical-buffer, data synchronization and signal processing, etc. Since comparing with other ways of implementing slow light, slow light via SBS has many advantages, such as being implemented at room temperature, tunable, compatibility with current communication system, etc. It is concerned more and more [1–6].

Slow light via SBS was first proposed by Gauthier in 2004 [7], and Song et al. [8] and Okawachi et al. [9] demonstrated it independently in 2005. Herraze et al. [10] increased the SBS gain bandwidth of single mode fiber from 40 MHz to 325 MHz by modulating the pump injection current with a Gaussian noise source. Then Zhu et al. [11] extended the bandwidth up to 12.6 GHz. Song et al. [12] achieved a bandwidth of 25 GHz by using a second broadened pump separated from the first one by the acoustic wave frequency, which made it possible to apply SBS slow light techniques to optical communication system with speed of dozens Gbit/s.

This paper is based on solving the three coupled amplitude equations via SBS in fibers by fourth-order Runge-Kutta formula [13] and characteristics [14, 15]. Considering the injected stokes pulse shape, the influence of its sharpness on delay time and pulse broadening factor was observed mainly, and its reason was analyzed. A way of reducing pulse broadening factor in the range of low frequency was proposed, which can afford some reference for the future design of optical equipments.

## 2. THEORY AND NUMERICAL MODEL

SBS in optical fibers occurs when a pump field and a counter-propagating stokes field interact with an acoustic wave. Its three coupled amplitude equations is described as [16, 17]

$$-\frac{\partial E_p}{\partial z} + \frac{n_g}{c} \frac{\partial E_p}{\partial t} = -\frac{\alpha}{2} E_p + i \frac{\gamma_e \omega_p}{2n_g c \rho_0} E_s \rho \quad (1a)$$

$$\frac{\partial E_s}{\partial z} + \frac{n_g}{c} \frac{\partial E_s}{\partial t} = -\frac{\alpha}{2} E_s + i \frac{\gamma_e \omega_p}{2n_g c \rho_0} E_p \rho^* \quad (1b)$$

$$\frac{\partial \rho}{\partial t} + \left[ \frac{\Gamma_B}{2} - i(\Omega_B - \Omega) \right] \rho = i \frac{\gamma_e q^2 \varepsilon_0}{8\Omega_B} E_p E_s^* \quad (1c)$$

where  $E_p(|E_p|^2 A_{eff})$ ,  $E_s(|E_s|^2 A_{eff})$  are the amplitudes (power) of the pump wave and stokes wave, respectively;  $A_{eff}$  is known as the effective mode area of fiber;  $\rho$  is acoustic matter-density field;  $\rho_0$  is the unperturbed density of medium;  $n_g$  is the group index of the fiber mode;  $c$  is the velocity of the light in vacuum;  $\alpha$  ( $\gamma_e$ ) is the loss (electrostriction) coefficient of the fiber;  $\omega_p(\Omega)$  are the angular frequencies of pump wave (acoustic wave);  $\Gamma_B$  is the full width at half maximum (FWHM) of the gain spectrum related to the phonon lifetime  $T_B$  as  $\Gamma_B = \frac{1}{T_B}$ ,  $\Omega_B$  is the Brillouin frequency;

$\epsilon_0$  is the vacuum permittivity. And we assumed that  $+(-)z$  direction is the transmission direction of stokes wave (pump wave).

On the assumption that pump wave is continuous wave and stokes field is sufficiently weak. We obtained that slow light rises from the group index which is the function of frequency written as [18]

$$n(\omega_s) = n_g + \frac{cg_B I_p}{\Gamma_B} \frac{1 - 4\delta\omega^2/\Gamma_B^2}{(1 + 4\delta\omega^2/\Gamma_B^2)^2} \quad (2)$$

where  $I_p$  is the optical intensity of pump wave;  $\delta\omega$  is the margin between the angular frequency of stokes pulse and the center angular frequency of the gain bandwidth;  $g_B = \frac{\gamma_e^2 \omega_p^2}{n_g v_B c^3 \rho_0 \Gamma_B}$  is the line-center gain factor which is associated with the material physical properties,  $v_B$  is the velocity of acoustic wave.

We define delay time as  $T_d$ , which is the difference of the arrival time when the output stokes pulse reach its maximum between when SBS happens and when SBS doesn't happen. We define  $T_{rd} = T_d/T$ ,  $T$  is the FWHM of the injected stokes pulse; We also define pulse broadening factor  $B$  as the proportion of input stokes pulse FWHM and output stokes pulse FWHM. According to the weak signal theory, delay and  $B$  are given by [18]

$$T_d = G/\Gamma_B \quad (3)$$

$$B = \sqrt{1 + \frac{16 \ln 2}{T^2 \Gamma_B^2}} G \quad (4)$$

where  $G = g_B I_p L$  is the weak signal gain parameter;  $L$  is the fiber length. For the purpose of indicating how much the pump wave energy contributes to the stokes wave energy, we define real gain as

$$G_r = \log(P_{out}/P_{in}) \quad (5)$$

where  $P_{out}$  and  $P_{in}$  are power of the output and input stokes wave, respectively.

We assume that injected stokes pulse is super-Gaussian shaped

$$U(t) = \exp\left(-\frac{1}{2}\left(\frac{t}{T_0}\right)^{2m}\right) \quad (6)$$

where  $t$  is the time of pulse transmission,  $U(t)$  is normalized amplitude,  $T_0$  is the half width of pulse (at 1/e-intensity point). The parameter  $m$  controls the degree of edge sharpness (for  $m = 1$ , it is Gaussian-shaped; for  $m > 1$ , it is super-gaussian-shaped, and the degree of edge sharpness is increased with  $m$ ). For different  $m$ , pulse with same FWHM can be written as

$$U(t) = \exp\left(-2^{2m}(\ln 2)\left(\frac{t}{T}\right)^{2m}\right) \quad (7)$$

### 3. NUMERICAL RESULTS AND DISCUSSION

We take the typical single mode fiber (SMF-28) as the transmission medium. Time delay and pulse broadening factor corresponding to different  $m$ , duration and power of injected stokes pulse are calculated numerically. In this paper, we assume that pump wave is continuous wave and input stokes pulses are super-Gaussian-shaped with no frequency chirp. We use the following parameters for our calculation:  $L = 50$  m,  $n_g = 1.45$ ,  $\alpha = 0.02$  dB/km,  $\lambda = 1550$  nm,  $A_{eff} = 50 \mu\text{m}^2$ ,  $\Gamma_B/2\pi = 40$  MHz,  $\Omega_B/2\pi = 10.8$  GHz and  $g_B = 5 \times 10^{-11}$  m/W, where  $\lambda$  is the wavelength of stokes wave.

We first consider the pulse time delay and pulse broadening factor as a function of parameter real gain for super-Gaussian-shaped pulse with different  $m$ , which is indicated in Fig. 1. In this case,  $T = 120$  ns,  $P_{in} = 0.1 \mu\text{W}$ . Fig. 1(a) shows that with the increase of  $G_r$ ,  $T_d$  increases accordingly and reaches its maximum. Then it decreases with further increasing  $G_r$ , even becomes negative. Comparing with different  $m$ , we can see that maximum  $G_r$  and the time when maximum  $G_r$  obtains decrease with  $m$  because when  $m$  changes from 0.5 to 3,  $T_d$  is equal to 0.5410, 0.6805, 0.7559 and 0.8705, respectively, i.e., for the same duration and apex, the super-Gaussian-shaped pulse with

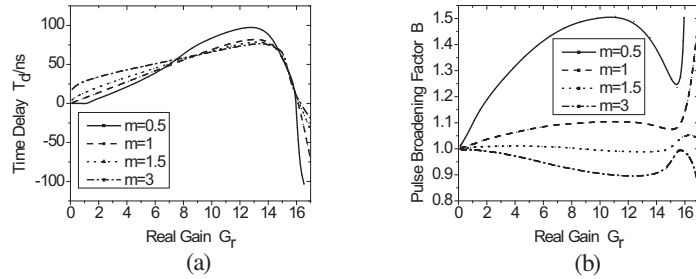


Figure 1: Parameters of output stokes pulse versus real gain for different parameter  $m$ . (a) Time delay  $T_d$  versus real gain; (b) Pulse broadening factor  $B$  versus real gain.

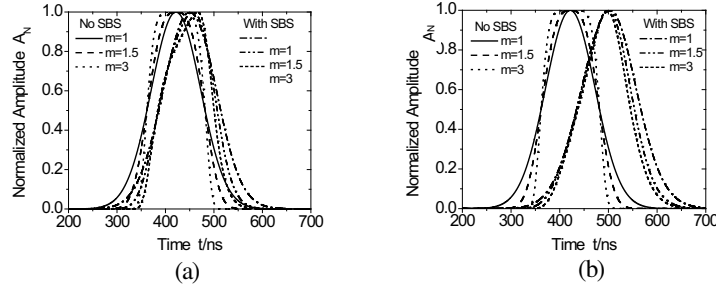


Figure 2: Output stokes pulse for different real gain. (a)  $G_r = 5$ ; (b)  $G_r = 13$ .

higher  $m$  is easier to reach gain saturation. And  $T_d$  when  $T_d$  reaches its maximum will decrease, which leads to the reducing of maximum  $T_d$ .

We observe an advantageous phenomenon for practical applications. When  $m = 1.5$ , pulse broadening factor  $B$  is close to 1. While  $m = 3$ ,  $B$  decreases with increasing  $G_r$  and reaches its peak value at gain = 13. Then it increase with  $G_r$  and reaches its maximum at  $G_r=15.5$ , it decrease with further increasing  $G_r$ . The reason why  $B$  has the rule can be explained well by Fig. 2. Considering SBS process and no SBS process, respectively, for three different  $m$ , the normalized output stokes pulses at  $G_r=5$  and  $G_r = 13$  are shown in Fig. 2, where  $t$  is the time axis. It is indicated from Fig. 2(a) that with increasing  $m$  the leading edge and the trailing edge of super-Gaussian-shaped pulse become steeper and steeper in time domain. So they will become broader and broader in the frequency domain. Considering Equation (2), we can conclude that the difference among the speeds of points at the leading edge will increase and the leading edge will be compressed more. Moreover, the increasing  $m$  leads to the increasing energy of pulse with same peak value. And most energy of pump wave is depleted in the leading edge of stokes pulse, the trailing edge only can get less energy from pump wave, the broadening of the trailing edge of stokes pulse is limited. All of this can contribute to decreasing  $B$  and result in  $B$  is almost close to 1 before stokes pulse is near saturation. When  $G_r$  increases to saturation gain step by step, the trailing edge gets more and more energy, resulting in broadening of the trailing, i.e.,  $B$  will increase, like shown in Fig. 2(b). When  $G_r$  go on increasing, it is out of the range of weak signal, the output stokes pulse is distortion seriously.

#### 4. CONCLUSIONS

According to the above numerical calculation and theory analysis, we find that using super-Gaussian-shaped pulse as the injected stokes pulse can contribute evidently to decreasing pulse broadening factor in low frequency. Selecting pretty  $m$  can get perfect delay time and pulse broadening factor. Though this adjusting effect will become weaker for a shorter pulse, this reform still takes advantage of decreasing the error rate of all-optical-buffer.

#### ACKNOWLEDGMENT

This work was supported by the Natural Science Foundation of Gansu Province (Grant No. 1010RJ-ZA036), the Natural Science Foundation of Guangdong Province (Grant No. 110451170003004948) and Dongguan Science and Technology Program (Grant No. 2008108101002).

## REFERENCES

1. Longdell, J. J., E. Fraval, M. J. Sellars, and N. B. Manson, “Stopped light with storage times greater than one second using electromagnetically induced transparency in a solid,” *Phys. Rev. Lett.*, Vol. 95, 063601–063604, 2005.
2. Yanik, M. F., W. Suh, Z. Wang, and S. Fan, “Stopping light in a waveguide with an all-optical analog of electromagnetically induced transparency,” *Phys. Rev. Lett.*, Vol. 93, 233903–233906, 2004
3. Zhu, Z., D. J. Gauthier, and R. W. Boyd, “Stored light in an optical fiber via stimulated Brillouin scattering,” *Science*, Vol. 318, 1748–1750, 2007.
4. Zhao, J., X. Yang, Y. Li, Z. Tong, Y. Liu, and Q. Zhao, “Stimulated Brillouin scattering slow light in photonic crystal fiber,” *Acta Optica Sinica*, Vol. 30, No. 8, 2437–2440, 2010.
5. Liu, Y., L. Ren, and S. Wang, “Theoretical study of stimulated brillouin scattering slow light and pulse-broadening reduction using double broadband pump in optical fibers,” *Acta Optica Sinica*, Vol. 28, No. 11, 2077–2082, 2008.
6. Ding, Y. and Y. Ren, “Latest developments of stimulated brillouin scattering slow-light pulse delays in optical fiber,” *Laser & Optoelectronics Progress*, Vol. 11, 51–57, 2009.
7. Gauthier, D. J., *Physics and Applications of Slow Light. Fitzpatrick Center for Photonics and Communication Systems*, Duke University, Durham, NC, 2004.
8. Song, K. Y., M. G. Herráez, and L. Thévenaz, “Observation of pulse delaying and advancement in optical fibers using stimulated Brillouin scattering,” *Opt. Express*, Vol. 13, 82–88, 2005.
9. Okawachi, Y., M. S. Bigelow, J. E. Sharping, Z. Zhu, A. Schweinsberg, D. J. Gauthier, R. W. Boyd, and A. L. Gaeta, “Tunable all-optical delays via Brillouin slow light in optical fiber,” *Phys. Rev. Lett.*, Vol. 94, 153902–153905, 2005.
10. González Herráez, M., K. Y. Song, and L. Thévenaz, “Arbitrary-bandwidth Brillouin slow light in optical fibers,” *Opt. Express*, Vol. 14, 1395–1400, 2006.
11. Zhu, Z., A. M. C. Dawes, D. J. Gauthier, L. Zhang, and A. E. Willner, “Broadband SBS slow light in an optical fiber,” *J. Lightwave Tech.*, Vol. 25, 201–206, 2007.
12. Song, K. Y. and K. Hotate, “25 GHz bandwidth Brillouin slow light in optical fibers,” *Opt. Lett.*, Vol. 32, 217–219, 2007.
13. Martijn de Sterke, C., R. J. Kenneth, and B. D. Robert, “Nonlinear coupled-mode equations on a finite interval: a numerical procedure,” *J. Opt. Soc. Am. B*, Vol. 8, No. 2, 403–409, 1991.
14. Damzen, M. J. and M. H. R. Hutchinson, “High-efficiency laser-pulse compression by stimulated Brillouin scattering,” *Opt. Lett.*, Vol. 8, No. 6, 313–315, 1983.
15. Parazzoli, C. G., W. W. Buehlnan, and R. D. Stultz, “Numerical and experimental investigation of a stimulated raman half resonator,” *IEEE J. Quantum Electron*, Vol. 24, No. 6, 872–880, 1988.
16. Kalosha, V. P., L. Chen, and X. Y. Bao, “Slow light of subnanosecond pulses via stimulated Brillouin scattering in nonuniform fibers,” *Phys. Rev. A*, Vol. 75, 021802–021805, 2007.
17. Kalosha, V. P., L. Chen, and X. Y. Bao, “Slow and fast light via SBS in optical fibers for short pulses and broadband pump,” *Opt. Express*, Vol. 14, 12693–12703, 2006.
18. Zhu, Z., D. J. Gauthier, Y. Okawachi, et al., “Numerical study of all-optical slow-light delays via stimulated Brillouin scattering in an optical fiber,” *J. Opt. Soc. Am. B*, (S0740-3224), Vol. 22, No. 11, 2378–2384, 2005.
19. Velchev, I., D. Neshev, W. Hogervorst, and W. Ubachs, “Pulse compression to the subphonon lifetime region by half-cycle gain in transient stimulated Brillouin scattering,” *IEEE J. Quantum Electron*, Vol. 35, 1812–1816, 1999.

# Measurement of the Verdet Constant in Different Mediums by Using Ellipsometry Technique

S. Suchat, P. Viriyavathana, P. Jaideaw, N. Haisirikul, W. Kerdsang, and S. Petcharavut

Physics Program, Faculty of Science and Technology  
Phranakhon Rajabhat University, Bangkok 10220, Thailand

**Abstract**— This experiment is designed to measure the Verdet constant  $V$  through Faraday Effect rotation of a polarized laser beam as it passes through different mediums, Flint Glass and water, parallel to the magnetic field  $B$ . As the  $B$  varies, the plane of polarization rotates and the transmitted beam intensity is observed. The angle through which it rotates is proportional to  $B$  and the proportionality constant is the Verdet constant times the optical path length. That by using ellipsometric parameters of under study was obtained. These are used to determine the Verdet constant for each medium and compared with standard known values. The experimental results are in good agreement with the corresponding theoretical analysis.

## 1. INTRODUCTION

The Verdet constant is an optical constant that describes the strength of the Faraday effect for a particular material. The phenomenon of the Faraday effect was first observed by Michael Faraday in 1845. He discovered the concrete evidence for the relationship between the major branches of optics, magnetism and atomic physics [1]. He found out that when a block of glass is subjected to a strong magnetic field, it becomes optically active. The effect occurs when the rotation of a linearly polarized wave passes through a thickness of a transparent medium. However, rotations of polarized light are not only limited to optically active materials, but also including some optically inactive materials exposed to high magnetic field. In magnetized medium the refractive indices for right- and left-handed circularly polarized light are different. This effect manifests itself in a rotation of the plane of polarization of linearly polarized light. This observable fact is called magneto optic effect. Magneto optic effects are those effects in which the optical properties of certain materials are affected by applied magnetic fields or the material's own magnetization. Magneto optic effects occur in gases, liquids, and solids.

In this work, we propose a new method for measurement of the Verdet Constant [2–4] in different mediums by using ellipsometry techniques limited only by the transmittance of the optical components and polarization ratio. The ellipsometry system [5, 6] has been studied by using the instrument to change the angle parameter of various materials, namely, Flint glass and water, when change magnetic field. The experimental values for wavelength of 635 nm are measurement and to compare its value to a theoretical calculated value.

## 2. THEORY

The Faraday effect is a magneto optic in which a plane of polarized light is rotated as it passes through a medium that is in a magnetic field. The amount of rotation is dependent on the amount of sample that the light passes through, the strength of the magnetic field and proportionality constant called the Verdet Constant. The Verdet constant is the proportionality constant between the angle of rotation  $\theta$  of plane polarized light and the product of the path length  $l$  through the sample and the applied magnetic field  $B$ . More explicitly, the Verdet constant  $V$  is the proportionality constant in Eq. (1).

$$\Delta = Vlb \quad (1)$$

The theory underlying why the Faraday Effect works lies in the quantum mechanical realm but can be understood on a more basic level using classical electrodynamics. The precession of the angular momentum of an electron orbiting the nucleus leads to different indices of refraction for right- or left- polarized light. This leads to a rotation of plane polarized light. To understand better how the Faraday Effect works, a classical electrodynamics approach gives an expression for the Verdet constant that is a function of the wavelength of light used in the experiment (the wavelength in a vacuum) and the change in index of refraction per change in wavelength. The verdet contant can be calculated from Eq. (2). This equation can be represented by the following empirical expression

$$V(\lambda) = \frac{\pi n^2(\lambda) - 1}{\lambda n(\lambda)} \left( A + \frac{B}{\lambda^2 - \lambda_0^2} \right) \quad (2)$$

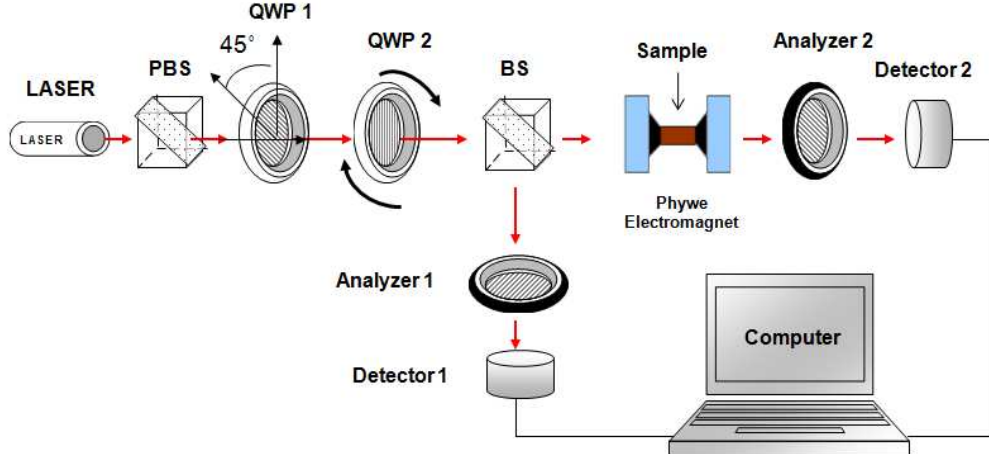


Figure 1: The experimental set up, QWP: Quarter wave plate, PBS: Polarizing beam splitter, BS: beam splitter.

where  $A$  is  $15.7116 \times 10^{-7}$  rad/T,  $B$  is  $6.3430 \times 10^{-19}$  m<sup>2</sup>·rad/T,  $n(\lambda)$  is index of refraction at a given wavelength,  $\lambda_0$  is 156.4 nm. The indices of refraction are given from Schott Optical Glass.

To analyze the process as shown in Fig. 1 the electric field  $\vec{E}$  of the output rotating linearly polarized light (after QWP2) can be represented by a vector, using Jones notation.

$$\vec{E}_1 = \begin{bmatrix} \cos \phi' \\ \sin \phi' \end{bmatrix} E_0 e^{i\varepsilon} \quad \text{where} \quad \phi' = \frac{1}{2} \left( \theta + \frac{\pi}{2} \right) \quad \text{and} \quad \varepsilon = \omega_0 t + \gamma \quad (3)$$

After the reflection at a sample surface with an incident angle of  $\phi_0$  the light beam then transverse an analyzer 2 with its axis at 45° to the plane of incidence. The change in polarization of light beam as a result of this, observed at the detector 2, can be described in terms of the product of Jones matrices as follows,

$$\vec{E}_2 = S \vec{E}_1 = \begin{bmatrix} t_p \cos \phi' \\ t_s \sin \phi' \end{bmatrix} E_0 e^{i\varepsilon} \quad (4)$$

When the Jones matrix of the sample ( $S$ ) written by  $S = \begin{bmatrix} t_p & 0 \\ 0 & t_s \end{bmatrix}$ . Therefore, the vector electric field through the sample ( $S$ ) to the polarizer at an angle  $\theta$  relation to the plane of incidence is as follows.

$$\vec{E}_{3,\theta} = P_\theta \vec{E}_2 = \begin{bmatrix} t_p \cos \phi' \cos^2 \theta - t_s \sin \phi' \cos \theta \sin \theta \\ t_p \cos \phi' \cos \theta \sin \theta - t_s \sin \phi' \sin^2 \theta \end{bmatrix} E_0 e^{i\varepsilon} \quad (5)$$

where  $t_p, t_s$  = Fresnel transmission coefficients, for the incident polarization  $p$ , parallel, and  $s$ , perpendicular, to the plane of incidence,  $\phi'$  = time-dependent azimuth of the polarization beam. When the polarizer angle 45° to the plane of incidence is written as.

$$\vec{E}_{3,45^\circ} = \begin{bmatrix} 1 \\ 1 \end{bmatrix} (t_p \cos \phi' - t_s \sin \phi') \frac{E_0}{2} e^{i\varepsilon} \quad (6)$$

Therefore, the intensity of light from the detector 2 is.

$$I_{45} = (\vec{E}_{3,45^\circ}) \cdot (\vec{E}_{3,45^\circ})^* = \frac{I_0}{2} [T_p \cos^2 \phi' + T_s \sin^2 \phi' - \sqrt{T_p T_s} \sin 2\phi' \cos \Delta] \quad (7)$$

Note that when light from the modulated parallel to the plane of incidence, intensity of light that the detector will be.

$$I_{\text{Parallel}} = (\vec{E}_{3,45,\phi'=0}) \cdot (\vec{E}_{3,45,\phi'=0})^* = \frac{I_0 T_p}{2} \quad (8)$$

Similarly, when the light is perpendicular to the plane of incidence. Intensity of light that can be

$$I_{\text{Perpendicular}} = (\vec{E}_{3,45,\phi'=\frac{\pi}{2}}) \cdot (\vec{E}_{3,45,\phi'=\frac{\pi}{2}})^* = \frac{I_0 T_s}{2} \quad (9)$$

When light at an angle to the plane of incidence angle is  $45^\circ$ , we can determine by

$$I_{45^\circ} = \left( \vec{E}_{3,45,\phi'=\frac{\pi}{4}} \right) \cdot \left( \vec{E}_{3,45,\phi'=\frac{\pi}{4}} \right)^* = \frac{I_0}{2} \left( \frac{T_p}{2} + \frac{T_s}{2} - \sqrt{T_p T_s} \cos \Delta \right) \quad (10)$$

When  $T_p$  and  $T_s$  is the intensity of light by Fresnel transmission. where  $T_p = |t_p|^2$ ,  $T_s = |t_s|^2$  and  $I_0$  is a constant. In ellipsometry measurements, the experimentally measured parameters  $\Delta$  and  $\Psi$  are related to the physical properties of the system by the relation where  $\tan \psi = |t_p|/|t_s|$  and  $\Delta = \delta_{rp} - \delta_{rs}$  are the ellipsometric angles.

### 3. EXPERIMENT AND RESULTS

The experimental set up system is shown in Fig. 1 light from a laser diode ( $\lambda = 635$  nm) is transformed into a circularly polarized beam by a quarter wave plate (QWP1). The light then is launched into the second quarter wave plate (QWP2). The function of the wave plate is to transform the output beams into two orthogonal circularly polarized beams with opposite handedness. This is equivalent to linear polarization state with an azimuth determined by the phase difference between the two circularly polarized beams. As the phase difference is modulated, the azimuth of polarization is modulated. A fraction of the output is sampled by a beam splitter passes thought an analyzer 1 orientated at a pre-determined direction and onto a detector 1 to form a reference signal. From this signal, the azimuth of polarization may be determined at any time. The main light beam is incident onto a sample at an angle of incidence  $\phi_0$ . The transmission light then propagates through an analyzer 2 with its transmission axis orientated at  $45^\circ$  to the plane of incidence, and onto detector 2 to provide the output signal. Both signals (detection and reference) then transferred to an online computer for analysis.

At the sample, the DC output 1.5 A of the power supply is connected via an ampere meter to the coils of the electromagnet which is in series. The electromagnet needed for the experiment is constructed from a laminaded U-shaped iron core, two 600-turn coils and the drilled pole pieces, the electromagnet then being arranged in a stable manner on the table on rod. After the flux-density distribution has been measured, the 30 mm long flint glass cylinder is inserted in the pole piece holes and the jack is raised so that the magnet is interpolated in the experimental set-up between the two polarization filters. Similarly, a water sample in a glass cuvette is placed in the gap and data is recorded

Since electromagnets were used to generate the magnetic field for this experiment, a correlation between the current supplied to the electromagnets and the average magnetic field in the space between the poles could be obtained by the curve fitting method. A linear curve was fit to the average magnetic field versus applied current 1.5A as shown in 60 mT (Phywe: LEB 2.0.6.01). In order to see how much the polarized beam is rotated as a function of the magnetic field strength, the relationship between the angles of rotation  $\Delta$ . The equations that fit the angle  $\Delta$  versus average magnetic field for wavelength of 635 nm it have shown that the angle of rotation of flint glass and water are 2.00 degree and 1.14 degree, respectively. The Verdet constant can be calculated from (1). From the results, they could be concluded that the Verdet constant for dense flint glass and water at 635 nm are 19.39 rad/T · m and 11.05 rad/T · m, respectively. Theoretically, the Verdet constant can be calculated from Eq. (2), the theoretical Verdet constant are revealed. For 635 nm, this theoretical value is 19.97 rad/T · m and 9.32 rad/T · m. The percentage errors of Verdet constant from this experimental are less than 2.9% for flint glass and 18.56% for water.

### 4. CONCLUSIONS

This experiment shows the measurement of the Verdet constant for the different mediums by using ellipsometry technique Included with using Faraday effect. However, in the future, the Faraday effect could be explored in a number of different ways. One way is to choose a different sample such as other liquid, for which the Verdet constant is known and find a way to increase the accuracy and precision of the apparatus used in order to get better experimental values. Furthermore, temperature dependence of the Verdet constant in diamagnetic glass should be determined because it may be significant in certain applications, such as high accuracy sensors.

### ACKNOWLEDGMENT

This work supported by the research fund for fiscal year 2009 of Faculty of Science and technology, Phranakhon Rajabhat University (**PNRU**).

**REFERENCES**

1. Jenkins, F. and H. White, *Fundamentals of Optics*, McGraw-Hill, Inc., New York, 1976.
2. Wen, H., M. A. Terrel, H. K. Kim, and M. J. F. Digonnet, “Measurements of the Birefringence and Verdet constant in an air-core fiber,” *Journal of Lightwave Technology*, Vol. 27, No. 15, 3194–3201, 2009.
3. Koerdt, C., G. L. J. A. Rikkenb, and E. P. Petrovc, “Faraday effect of photonic crystals,” *Applied Physics Letters*, Vol. 82, No. 10, 1538–1540, 2003.
4. Jain, A., J. Kumar, F. Zhou, L. Li, and S. Tripathy, “Simple experiment for determining Verdet constants using alternating current magnetic fields,” *Am. J. Phys.*, Vol. 67, No. 8, 714–717, 1999.
5. Suchart, S. and R. Chitaree, “A novel optical fiber ellipsometer,” *The IEEE Asia-Pacific Conference on Circuits and Systems*, 205–208, Chiangmai, Thailand, 1998.
6. Azzam, R. M. A. and N. M. Bashara, “Ellipsometric measurement of the polarization transfer function of an optical system,” *J. Opt. Soc. Am.*, Vol. 62, 336–340, 1972.

# Urban Impervious Surfaces Estimation from RADARSAT-2 Polarimetric Data Using SVM Method

Xinwu Li, Huadong Guo, Zhongchang Sun, and Guozhuang Shen

Center for Earth Observation and Digital Earth, Chinese Academy of Sciences, Beijing 100094, China

**Abstract**— Urban impervious surface area is a key environmental indicator in assessing urbanization’s impacts on urban environmental and ecological conditions, and it has therefore recently attracted more interest from the remote sensing community. The main objective of this investigation is to explore the potential to extract impervious surface coverage in dense urban areas from RADARSAT-2 full PolSAR data. To compare the results, SPOT-5 multispectral imagery is also used. A case study of a dense urban area (Beijing, China) is conducted by applying a support vector machine (SVM) algorithm to SPOT-5 imagery and RADARSAT-2 full PolSAR data. An accuracy assessment is performed using high-resolution WorldView images with a spatial resolution of 0.5 m. The root mean square error (RMSE), the mean absolute error (MAE), and the coefficient of determination ( $R^2$ ) are calculated to validate the accuracy of impervious surfaces derived from the SPOT-5 image and RADARSAT-2 PolSAR data. For the SPOT-5 imagery, the RMSE, MAE, and  $R^2$  are 17.03%, 12.99%, and 0.7641, respectively. The RADARSAT-2 full PolSAR data yield an RMSE of 13.18%, an MAE of 10.12%, and an  $R^2$  of 0.8173. The results indicate that RADARSAT-2 data allow for more accurate impervious surface estimation than SPOT-5. The results also demonstrate that bare soil or water can be easily separated from buildings or asphalt roads using RADARSAT-2 data, which is a difficult task for estimating impervious surfaces with optical remote sensing data. In addition, compared with optical images, impervious surfaces covered by tree crowns can be easily extracted from the RADARSAT-2 PolSAR data in sparse tree cover. Overall, our results demonstrate that PolSAR imagery can provide more efficient and useful polarimetric information and has enormous potential for extracting impervious surfaces.

## 1. INTRODUCTION

Impervious surfaces are usually defined as the entirety of surfaces through which water cannot pass, including roads, buildings, parking lots, railroads, squares, sidewalks or other urban infrastructure [3]. In recent years, impervious surface area has been recognized as a key environmental indicator in assessing urbanization’s impacts on the urban environmental and ecological conditions [6, 9, 17].

Due to their relatively low cost and suitability for large-area mapping, satellite remote sensing images have been widely applied for impervious surface estimation. Recently, optical imagery has been widely used to estimate the urban impervious surface area, but it has some limitations. (1) Because of the heterogeneity in the urban landscapes and the complexity of urban impervious surface materials, the mixed-pixel problem in urban landscapes has been recognized as a major problem, affecting the accuracy of impervious surface estimation [15, 18]. (2) Some existing materials have reflectance characteristics similar to impervious surfaces; for example, low albedo materials (such as water and shadows) often share similar reflectance characteristics with dark impervious surfaces (asphalt roads), while high albedo materials (such as dry soil, sand, and clouds) tend to be confused with bright impervious surfaces (building roofs). (3) For high spatial resolution optical images, the shadows caused by tall buildings or large tree crowns become a severe problem for extracting impervious surfaces [13]. In addition, the dark impervious surfaces in high spatial resolution imagery are difficultly separated from shadows or water. (4) In dense urban areas, many impervious surfaces (such as sidewalks and squares) are covered by tree crowns and cannot be extracted from optical imagery. InSAR images are very sensitive to buildings; therefore, man-made targets (e.g., buildings) can be discriminated from natural targets (e.g., bare soil) using InSAR data [11]. However, due to the low information content of individual SAR images, single-band SAR data do not provide highly accurate impervious surface estimation. To a certain extent, the synergistic use of medium and high spatial resolution images in urban impervious surface mapping can improve the accuracy of impervious surface extraction. Nevertheless, imagery co-registration becomes a key step, especially optical and InSAR image registration.

As an advanced earth observation technology, polarimetric synthetic aperture radar (PolSAR) backscatter from man-made structures in urban areas is quite different than backscatter from predominantly natural areas. Hence, based on polarimetric information, PolSAR data has been

successfully applied for target detection and image classification [1, 2, 4, 12, 14]. In order to compare the result, impervious surfaces will also be detected in SPOT-5 imagery. In addition, in our research, a robust algorithm, a support vector machine (SVM), was used for estimating impervious surface area. SVM is a modern machine learning method that offers improved generalization performance and can model complex nonlinear boundaries through the use of adapted kernel functions [5]. In recent years, for remote sensing studies, SVMs have been used for impervious surface estimation [7, 15]. SVMs method are well suited to handle linearly nonseparable cases by using the Kernel theory, and SVM training always finds a global solution [8]. Furthermore, SVM methods allow defining feature vectors with numerous and heterogeneous components and can obtain better results with less training datasets [10, 16]. SVM algorithms have been mostly applied to hyperspectral imagery, and a few studies have also been carried out on SAR data [12, 14]. The main objective of this investigation is to explore the potential to extract impervious surface area in dense urban areas (e.g., Beijing) from RADARSAT-2 full PolSAR data using support vector machine (SVM) method.

## 2. STUDY AREA AND DATASETS

### 2.1. Description of Study Area

Beijing Municipality, the capital of China, was chosen as the study area. Its urban area is located within  $39.82^{\circ}\text{N}$ – $40.12^{\circ}\text{N}$ , and  $116.25^{\circ}\text{E}$ – $116.63^{\circ}\text{E}$ , covering about  $1,300\text{ km}^2$ . Over the past three decades, Beijing has been one of the fastest growing urban areas in China, and has undergone intense urbanization that has seriously impacted the urban environment. Beijing's development pattern is a typical concentric expansion, showing a ring-shaped pattern moving from the inner city to the outskirts. The selected area consists of coverage of the central business district (CBD), high-density residential, low-density residential, vegetation, exposed soil, and water.

### 2.2. Datasets

RADARSAT-2 full PolSAR data (C-Band) acquired on 8 March 2009 were used. The slant range resolution is 12 m, and the azimuth resolution is 8 m. The incidence angles are  $39.25^{\circ}$  at near range and  $40.70^{\circ}$  at far range. Thirteen WorldView images (acquired on 11 February 2009) with a spatial resolution of 0.5 m were used for accuracy assessment. In order to compare the result, cloud-free SPOT-5 imagery (acquired on 12 January 2009) was used for extracting impervious surface area with three 10 m resolution visible and near infrared (VNIR) bands and one 20 m shortwave infrared (SWIR) band, but the 2.5 m panchromatic band was not used.

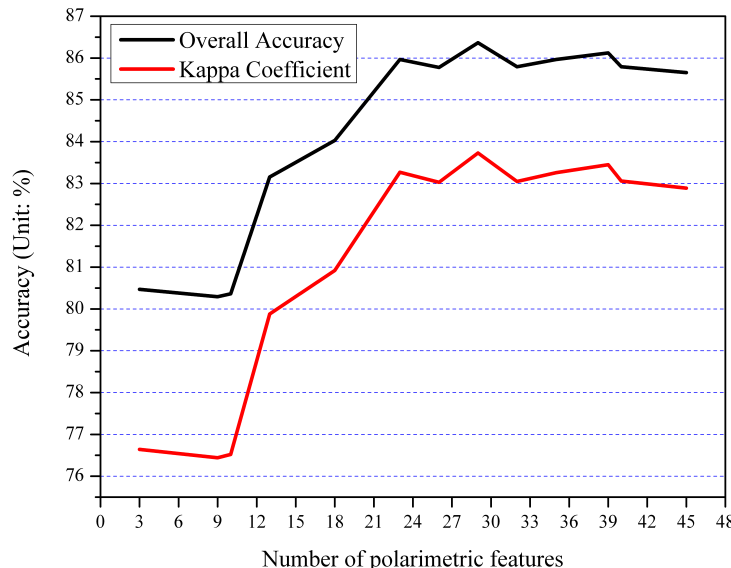


Figure 1: Contribution of classification accuracy when different polarimetric features are combined together.

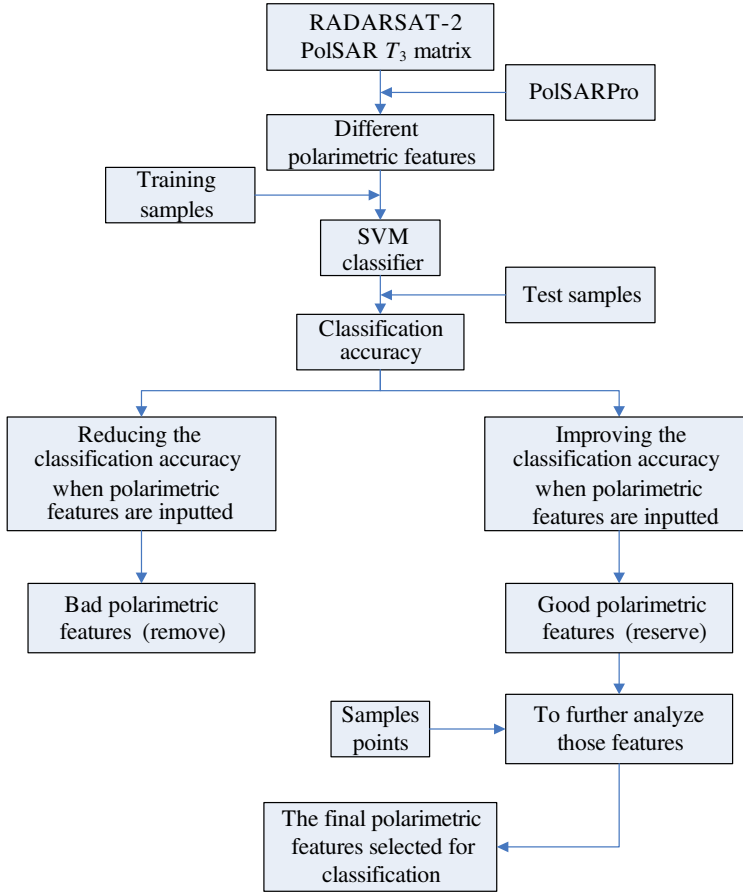


Figure 2: The flow chart of the detailed optimizing selection process.

### 3. METHODS

In our work, a total of 45 PolSAR features are extracted from the RADARSAT-2 full polarimetric data by the PolSARpro program and the authors of the program. However, too many PolSAR features will result in data redundancy and reducing classification accuracy. Therefore, the optimization of features is an important step for extracting impervious surfaces from PolSAR data. In our research, the various polarimetric features are selected through a stepwise process. As shown Figure 1, different classification accuracies are derived when different PolSAR features are inputted to the SVM classifier. When reducing the classification accuracy, the inputted features have adverse effect on classification and are removed; when improving the classification accuracy, the inputted features have a good effect on classification and are reserved. Then, the PolSAR features, improving the classification accuracy, are further statistically analyzed using the samples points of seven land use types. After statistical analysis for these features, the final polarimetric features are optimally selected for estimating the impervious surfaces. Figure 2 shows the flow chart of the detailed PolSAR features optimizing selection process. Through analysis for polarimetric parameters, the final polarimetric features selected for classification are listed in Table 1.

### 4. RESULTS AND DISCUSSIONS

Figure 3 illuminates the impervious surfaces extracted from the SPOT-5 image and RADARSAT-2 full PolSAR data using the SVM method in Beijing. The top two graphs show the percent impervious surfaces (PISs) images with values ranging from 0 to 1, while the bottom two graphs show the percent impervious surfaces images reclassified into six categories: high PIS (with values greater than 0.9), medium PIS (with values between 0.5 and 0.9), low PIS (with values less than 0.5), bare soil, vegetation (forest and crop) and water. Figure 4 shows impervious surface maps derived from SPOT-5 and RADARSAT-2 data using the SVM method in four selected sample sites corresponding to four areas (A, B, C and D) of Figure 3. In Figure 4, sample sites (A) and (B) illuminate the railroads and asphalt roads estimation, respectively, and sites (C) and (D) represent

Table 1: The final polarimetric features selected for classification through a stepwise process.

Numbers of polarimetric features	Polarimetric features	Description
3	$T_{ii} (i = 1, 2, 3)$	The diagonal elements of $T_3$ matrix
6	$I_{hv}/I_{hh} I_{hv}/I_{vv} I_{hh}/I_{vv}$	Intensities ratio
8	$\lambda\lambda_1$	Eigen-value parameters
12	$HA\alpha\alpha_1$	Entropy, anisotropy, $\alpha$ parameters
14	$k_{02}, k_{03}$	Barnes decomposition parameters
16	$K_S, K_D$	Krogager decomposition parameters
20	$P_S, P_D, P_V, P_C$	Yamaguchi decomposition parameters

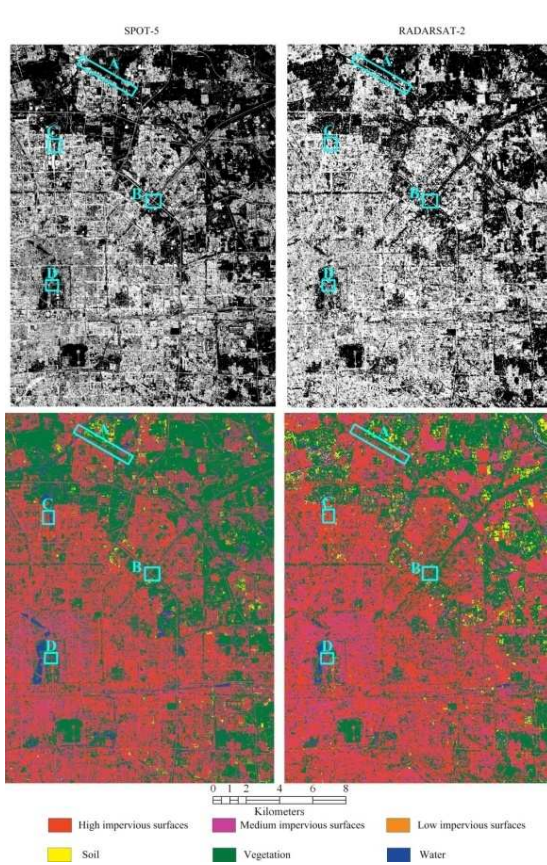


Figure 3: Impervious surfaces extracted from the SPOT-5 image and RADARSAT-2 full PolSAR data with SVM algorithms.

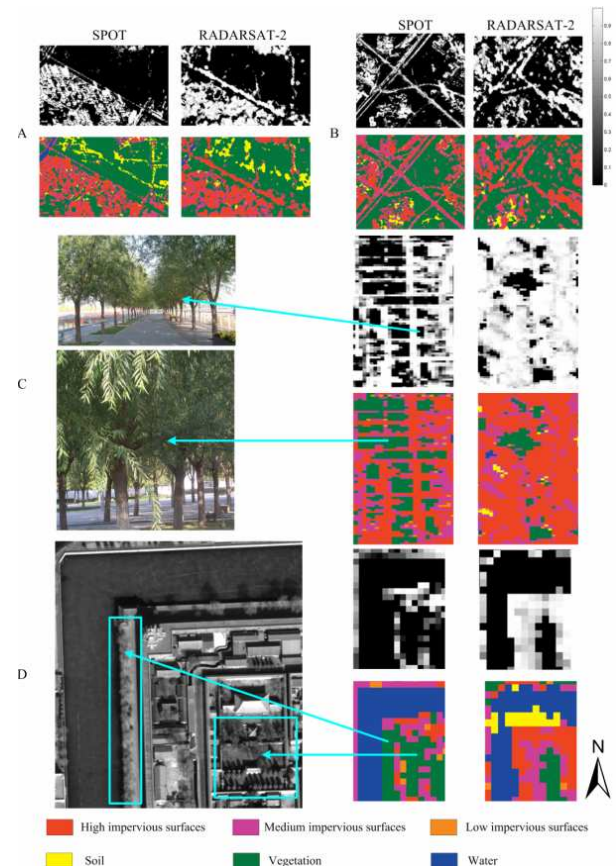


Figure 4: Impervious surface maps derived from SPOT-5 and RADARSAT-2 data using an SVM method in four selected sample sites corresponding to the four areas (A, B, C and D) of Figure 3.

extraction of the impervious surfaces covered by tree crowns. Looking at Figures 3 and 4, we see:

(1) In the PIS classification images, there is more bare soil in the PIS classification image derived from RADARSAT-2 data than that of the PIS classification image derived from SPOT-5 image (Figure 3). That is because RADARSAT-2 PolSAR (C-Band) has deeper penetration. On 8 March 2009, the main crop of the study area was small and short winter wheat. C-Band can penetrate winter wheat and detect bare soil.

(2) In selected sample area A (Figure 4(A)), because of stronger backscattering in SAR images, the railroads can be easily extracted from RADARSAT-2 full PolSAR data; while SPOT-5 imagery cannot extract them.

(3) For RADARSAT-2 data, as a significant part of urban impervious surfaces, the entire road area (such as asphalt roads and railroads) might be either occluded by shadows or covered by layover from adjacent buildings or trees. Hence, roads oriented along tracks sometimes cannot be

Table 2: Accuracy assessment of ISP estimation results.

Data	Statistical indicator		
	RMSE (%)	MAE (%)	$R^2$
SPOT-5	17.03	12.99	0.7641
RADARSAT-2	13.18	10.12	0.8173

seen at all in dense urban scenes. Compared with the PIS image derived from the SPOT-5 image, the urban roads derived from the RADARSAT-2 data are basically extracted, but some gaps are visible in a number of roads (Figure 4(B)). Intrinsic characteristics of SAR imagery, such as layover and shadow effects become a severe problem for extracting impervious surfaces, especially in dense urban areas. In our research, those characteristics were not considered.

(4) In dense urban areas, many impervious surfaces (such as sidewalks and squares) are covered by tree crowns and cannot be extracted from optical imagery. Because of its ability to penetrate vegetation, RADARSAT-2 full PolSAR data (C-Band), was used to investigate the potential for extracting urban impervious surfaces covered by tree crowns. In our study areas, two sample sites were selected to demonstrate this potential. One site was in Beijing's Olympic Park (Figure 4(C)); the other site was in Beijing's Imperial Palace (Figure 4(D)). In Figure 4(C), the two photos on the left were taken on the ground; and in Figure 4(D), the left image is a WorldView image (acquired on 11 February 2009) with a spatial resolution of 0.5 m. The right maps in the Figures 4(C) and (D) are urban impervious surface maps derived from SPOT-5 and RADARSAT-2 data using SVM. Figures 4(C) and (D) show that the impervious surfaces covered by tree crowns can be easily extracted from the RADARSAT-2 PolSAR data in sparse tree cover, while because of the limited of penetration, it is difficult for PolSAR data to extract the impervious surfaces covered by tree crowns in dense tree cover. For SPOT-5 imagery, however, it is impossible to extract the impervious surfaces covered by tree crowns in sparsely or densely wooded areas. Therefore, compared with optical imagery, PolSAR imagery has enormous potential for extracting the impervious surfaces covered by tree crowns in wooded areas, especially in those with sparse cover.

An accuracy assessment was performed to evaluate the results. RMSE, MAE, and  $R^2$  were calculated for the estimated ISP images derived from SPOT-5 imagery and RADARSAT-2 full PolSAR data using SVM. The results are summarized in Table 2 and show that RADARSAT-2 imagery generates better results than SPOT-5. RADARSAT-2 yields a RMSE of 13.18%, a MAE of 10.12%, and an  $R^2$  of 0.8173. SPOT-5 yields results with a RMSE of 17.03%, a MAE of 12.99%, and an  $R^2$  of 0.7641.

## 5. CONCLUSIONS

In this study, RADARSAT-2 full PolSAR data was applied to validate its potential to extract impervious surfaces based on an SVM method in dense urban areas. In order to compare the result, the impervious surfaces were also derived from SPOT-5 imagery. An accuracy assessment was performed against high-resolution WorldView images based on 150 samples of 100 m  $\times$  100 m. RMSE, MAE, and  $R^2$  were calculated for the estimated ISP images derived from RADARSAT-2 full PolSAR data and SPOT-5 imagery using SVM. The results show that RADARSAT-2 data can provide more accurate estimations than that of SPOT-5 in impervious surface estimation. The accuracy of RADARSAT-2 relative to SPOT-5 is due to the following factors. (1) The targets with different geometric surface structures can be discriminated using full PolSAR data, especially for the separation of bare soil from vegetated fields or buildings, but dry soil often shares similar spectral characteristics with bright impervious surfaces in optical imagery. In addition, it is difficult to distinguish asphalt roads from water in SPOT-5 imagery, while asphalt roads can be separated from water by extracted polarimetric features. (2) There were many shadows in our study area in the SPOT-5 imagery, which influences the accuracy of impervious surface estimation. (3) In dense urban areas, many impervious surfaces (such as sidewalks and squares) are covered by tree crowns and cannot be extracted from optical imagery. However, the impervious surfaces covered by tree crowns can be easily extracted from the RADARSAT-2 PolSAR data in sparse tree cover. Therefore, compared with optical imagery, PolSAR imagery has enormous potential for extracting the impervious surfaces covered by tree crowns in wooded areas, especially in sparsely wooded areas.

## ACKNOWLEDGMENT

The research in this paper was sponsored by the National Basic Research Program of China (No. 2009CB723906) and the graduate technological innovation program of the Chinese Academy of Sciences.

## REFERENCES

1. Ainsworth, T. L., D. L. Schuler, and J.-S. Lee, "Polarimetric SAR characterization of man-made structures in urban areas using normalized circular-pol correlation coefficients," *Remote Sensing of Environment*, Vol. 112, No. 6, 2876–2885, 2008.
2. Alberga, V., "A study of land cover classification using polarimetric SAR parameters," *International Journal of Remote Sensing*, Vol. 28, No. 17, 3851–3870, 2007.
3. Arnold, C. L. and C. J. Gibbons, "Impervious surface coverage: The emergence of a key environmental indicator," *Journal of the American Planning Association*, Vol. 62, No. 2, 243–258, 1996.
4. Borghys, D., C. Perneel, and M. Acheroy, "Automatic detection of built-up areas in high-resolution polarimetric SAR images," *Pattern Recognition Letters*, Vol. 23, No. 9, 1085–1093, 2002.
5. Burges, C. J. C., "A tutorial on support vector machines for pattern recognition," *Data Mining and Knowledge Discovery*, Vol. 2, No. 2, 121–167, 1998.
6. Conway, T. M., "Impervious surface as an indicator of pH and specific conductance in the urbanizing coastal zone of New Jersey, USA," *Journal of Environmental Management*, Vol. 85, No. 2, 308–316, 2007.
7. Esch, T., V. Himmller, G. Schorcht, M. Thiel, T. Wehrmann, F. Bachofner, C. Conrad, M. Schmidt, and S. Dech, "Large-area assessment of impervious surface based on integrated analysis of single-date Landsat-7 images and geospatial vector data," *Remote Sensing of Environment*, Vol. 113, No. 8, 1678–1690, 2009.
8. Han, J. and M. Kamber, *Data Mining Concepts and Techniques*, China Machine Press, Beijing, 2007.
9. Hu, X. and Q. Weng, "Estimating impervious surfaces from medium spatial resolution imagery using the self-organizing map and multi-layer perceptron neural networks," *Remote Sensing of Environment*, Vol. 113, No. 10, 2089–2102, 2009.
10. Huang, C., L. S. Davis, and J. R. G. Townshend, "An assessment of support vector machines for land cover classification," *International Journal of Remote Sensing*, Vol. 23, No. 4, 725–749, 2002.
11. Jiang, L., M. Liao, H. Lin, and L. Yang, "Synergistic use of optical and InSAR data for urban impervious surface mapping: A case study in Hong Kong," *International Journal of Remote Sensing*, Vol. 30, No. 11, 2781–2796, 2009.
12. Lardeux, C., P.-L. Frison, C. Tison, J.-C. Souyris, B. Stoll, B. Fruneau, and J.-P. Rudant, "Support vector machine for multifrequency SAR polarimetric data classification," *IEEE Transactions on Geoscience and Remote Sensing*, Vol. 47, No. 12, 4143–4152, 2009.
13. Lu, D. and Q. Weng, "Extraction of urban impervious surfaces from an IKONOS image," *International Journal of Remote Sensing*, Vol. 30, No. 5, 1297–1311, 2009.
14. Shimoni, M., D. Borghys, R. Heremans, C. Perneel, and M. Acheroy, "Fusion of PolSAR and PolInSAR data for land cover classification," *International Journal of Applied Earth Observation and Geoinformation*, Vol. 11, No. 3, 169–180, 2009.
15. Sun, Z., H. Guo, X. Li, L. Lu, and X. Du, "Estimating urban impervious surfaces from Landsat-5 TM imagery using multi-layer perceptron neural network and support vector machine," *Journal Applied of Remote Sensing*, Vol. 5, 053501, 2011.
16. Vapnik, V. N., *The Nature of Statistical Learning Theory*, Springer-Verlag, New York, 1995.
17. Weber, D. N. and R. Bannerman, "Relationships between impervious surfaces within a watershed and measures of reproduction in fathead minnows (*Pimephales promelas*)," *Hydrobiologia*, Vol. 525, Nos. 1–3, 215–228, 2004.
18. Weng, Q. and X. Hu, "Medium spatial resolution satellite imagery for estimating and mapping urban impervious surfaces using LSMA and ANN," *IEEE Transactions on Geoscience and Remote Sensing*, Vol. 46, No. 8, 2397–2406, 2008.

# New Method for the $\pi/4$ Compact Polarimetric SAR Mode

J. J. Yin<sup>1</sup>, J. Yang<sup>1</sup>, and Y. Yamaguchi<sup>2</sup>

<sup>1</sup>Department of Electronic Engineering, Tsinghua University, Beijing 100084, China

<sup>2</sup>Faculty of Engineering, Niigata University, Niigata 950-2181 Japan

**Abstract**— Compact polarimetric synthetic aperture radar (SAR) is a dual-polarimetric system, which shows promise of reducing the complexity, cost, mass, and data rate of a SAR system. It allows fully polarimetric information reconstructed from compact polarimetry (CP) under some constraints. Two assumptions are required here for the constructing, one is the reflection symmetry, and the other is a relationship model between the co-polarized and cross-polarized channels. In this paper, an improved reconstruction algorithm is proposed according to both the assumptions, and two improvements are accordingly proposed. Since the helix scattering component is always used to take account of the non-reflection symmetric circumstance which mostly appears in complex urban area, helix scattering should be considered in the reconstruction algorithm, especially for the regions with strong orientation angle effects. A modified four-component model-based decomposition algorithm is proposed with a new volume scattering model. Then using the decomposed powers of the four components, the relationship between the co-pol and cross-pol channels is developed instead of the original polarization state extrapolation model. Finally, a ESAR L-band polarimetric dataset over Oberfaffenhofen area is used to demonstrate the effectiveness of the proposed algorithm.

## 1. INTRODUCTION

Fully polarimetric SAR has many advantages, but it suffers from increments of the pulse repetition frequency and the downloading data rate. The downlink requirement versus the polarimetric resolution rather than polarimetry is the system design and the operation trade off. Thus, a dual polarization SAR system is the compromising choice between a full polarization system and a single polarization system. In order to obtain more information from the dual polarization, Souyris et al. proposed a new dual polarization mode, i.e., compact polarimetric (CP) [1, 2] SAR mode, based on one unique special transmitted polarization and two orthogonal polarizations in reception. In the fully polarimetric (FP) information reconstruction procedure, two assumptions are included: one is the well-known reflection symmetry assumption; the other is the polarization state extrapolation model. An iterative process was adopted by Souyris et al. and the reconstructed polarimetric data performs well to a certain degree [2].

However, the reflection symmetry is not always valid, e.g., the urban area, where the reconstructed results are far from the actual values. In order to derive more target information from compact polarimetry and accommodate the FP reconstruction scheme with the more general scattering case, an improved information reconstruction algorithm is proposed in this paper. The algorithm is based on a modified four-component model decomposition, in which a new volume scattering model is adopted. Using the proposed reconstruction algorithm, the helix scattering power can also be extracted from the  $2 \times 2$  CP covariance matrix.

## 2. THE FOUR-COMPONENT MODEL-BASED SCATTERING DECOMPOSITION

### 2.1. The Original Four-component Decomposition

The original four-component decomposition models the coherency matrix as the contribution of four scattering mechanisms: the surface scattering, the double-bounce scattering, the volume scattering and the helix scattering [3].

$$\langle \mathbf{T} \rangle = f_s \cdot \mathbf{T}_{\text{surface}} + f_d \cdot \mathbf{T}_{\text{double}} + f_v \cdot \langle \mathbf{T} \rangle_{\text{volume}} + f_c \cdot \mathbf{T}_{\text{helix}} \quad (1)$$

where  $f_s$ ,  $f_d$ ,  $f_v$ , and  $f_c$  correspond to the coefficients of the four scattering components, which are non-negative and proportional to their powers,  $\langle \dots \rangle$  denotes the ensemble averaging. The scattering

matrices are modeled as follows based on different scattering mechanisms.

$$\begin{aligned}\mathbf{T}_{\text{surface}} &= \begin{bmatrix} 1 & \beta^* & 0 \\ \beta & |\beta|^2 & 0 \\ 0 & 0 & 0 \end{bmatrix}, \quad |\beta| < 1; \\ \mathbf{T}_{\text{helix}} &= \begin{bmatrix} 0 & 0 & 0 \\ 0 & 1 & \pm j \\ 0 & \mp j & 1 \end{bmatrix}; \quad \mathbf{T}_{\text{double}} = \begin{bmatrix} |\alpha|^2 & \alpha & 0 \\ \alpha^* & 1 & 0 \\ 0 & 0 & 0 \end{bmatrix}, \quad |\alpha| < 1;\end{aligned}\tag{2}$$

where  $\mathbf{T}_{\text{surface}}$ ,  $\mathbf{T}_{\text{double}}$ , and  $\mathbf{T}_{\text{helix}}$  denote the surface scattering model, the double-bounce scattering model and the helix scattering model, respectively. There are three volume scattering models for  $\langle \mathbf{T} \rangle_{\text{volume}}$  [3], and the choice between them depends on the value of  $10 \cdot \log(|S_{VV}|^2/|S_{HH}|^2)$ . When the original four-component decomposition is applied to real POLSAR data, some scattering components' powers may become negative. To overcome this problem a modified decomposition is proposed with a power constraint. The basic principle is that if the decomposed power becomes negative, the power is forced to be zero and the sum of different components' powers is equal to  $\text{span}$ , denoted as  $\text{span} = 0.5|S_{HH} + S_{VV}|^2 + 0.5|S_{HH} - S_{VV}|^2 + 2|S_{HV}|^2$ .

## 2.2. Another Volume Scattering Model

The volume scattering can be regarded as the ensemble averaging of chaotic scattering states, and can't be characterized as a deterministic scattering process. Instead of the three volume models, another volume scattering model [4]  $\langle \mathbf{T} \rangle_{\text{vol}}$  is adopted in this paper.

$$\langle \mathbf{T} \rangle_{\text{vol}} = \begin{bmatrix} 1 & 0 & 0 \\ 0 & 1 & 0 \\ 0 & 0 & 1 \end{bmatrix}\tag{3}$$

One important reason for choosing this volume scattering model is that this model quite conforms to the polarization state extrapolation assumption, which is required in the compact polarimetry reconstruction architecture. Souyris et al. proposed a relationship between the linear coherence  $|\rho|$  and the average cross-polarization ratio [1]:

$$\langle |S_{HV}|^2 \rangle / (\langle |S_{HH}|^2 \rangle + \langle |S_{VV}|^2 \rangle) = \frac{1}{4}(1 - |\rho|)\tag{4}$$

where  $\rho = \langle S_{HH} S_{VV}^* \rangle / \sqrt{\langle |S_{HH}|^2 \rangle + \langle |S_{VV}|^2 \rangle}$ . This relationship is called the polarization state extrapolation model. The relationship is extrapolated from the case where the backscattered wave is either fully polarized or fully depolarized. For a fully polarized backscattered wave from a natural target,  $|\rho| \approx 1$ ; for a fully depolarized backscattered wave, the average powers received by the orthogonal antennas do not depend on their polarization states, i.e.,  $|\rho| \approx 0$  and  $\langle |S_{HH}|^2 \rangle \approx \langle |S_{VV}|^2 \rangle \approx 2\langle |S_{HV}|^2 \rangle$ . The three volume scattering models do not consist with the fully depolarized backscattering case, but the model (3) satisfies the hypothesis. Using the volume scattering model in (3), we have  $|\rho| = 0$ ,  $\langle |S_{HV}|^2 \rangle / (\langle |S_{HH}|^2 \rangle + \langle |S_{VV}|^2 \rangle) = 1/4$ . Both the values are consistent with the relationship model in (4) and the fully depolarized backscattered wave assumption.

## 2.3. Modified Four-component Decomposition

From the scattering models defined by (2) and (3), the coherency matrix can be decomposed into four scattering mechanisms. By comparing the measured data with both the sides of (1), we can derive the helix scattering power and the volume scattering power as shown in (5).

$$f_c = \text{Im} \langle (S_{HH} - S_{VV}) S_{HV}^* \rangle, \quad P_c = 2f_c; \quad f_v = 2 \langle |S_{HV}|^2 \rangle - f_c, \quad P_v = 3f_v\tag{5}$$

where  $P_v$ ,  $P_c$  denote the powers of the volume scattering and the helix scattering, respectively. The powers of both the components will be used in the following FP reconstruction algorithm.

## 3. FP INFORMATION RECONSTRUCTION FROM CP MODE

### 3.1. The $\pi/4$ Mode Compact Polarimetry

The scattering vector of the  $\pi/4$  mode is given by  $\vec{k}_{\pi/4} = [S_{HH} + S_{HV}, S_{VV} + S_{HV}]^T/\sqrt{2}$ . The covariance matrix of the  $\pi/4$  mode is given by (6), which can be regarded as the contributions

of three parts. Under the assumption of reflection symmetry, there is a complete decorrelation between the co-polarization and cross-polarization:  $\langle S_{HH}S_{HV}^* \rangle \approx \langle S_{VV}S_{HV}^* \rangle \approx 0$ . Regarding the third term in (6) as zero, we have an underdetermined system of three equations and four unknown variables,  $\langle |S_{HH}|^2 \rangle$ ,  $\langle |S_{HV}|^2 \rangle$ ,  $\langle |S_{VV}|^2 \rangle$  and  $\langle S_{HH}S_{VV}^* \rangle$ . In order to construct the fully polarimetric information, the pseudo deterministic trend (4) is used to relate the four unknowns.  $\langle |S_{HV}|^2 \rangle$  is the key to the solution and can be solved by iteration [1, 2].

### 3.2. Modification of Full Polarimetry Reconstruction Algorithm

In order to accommodate the reconstructed values for more general case and retain more information, it is

$$\begin{aligned} \mathbf{C}_{\pi/4} &= \frac{1}{2} \left\langle \begin{bmatrix} |S_{HH}|^2 & S_{HH}S_{HV}^* \\ |S_{VV}|^2 & \end{bmatrix} \right\rangle + \frac{1}{2} \left\langle |S_{HV}|^2 \right\rangle \begin{bmatrix} 1 & 1 \\ & 1 \end{bmatrix} \\ &+ \frac{1}{2} \left\langle \begin{bmatrix} 2\text{Re}(S_{HH}S_{HV}^*) & S_{HH}S_{HV}^* + S_{HV}S_{VV}^* \\ & 2\text{Re}(S_{VV}S_{HV}^*) \end{bmatrix} \right\rangle = \begin{bmatrix} C_{11} & C_{12} \\ & C_{22} \end{bmatrix} \quad (6) \\ F &= \text{Im}(S_{HH}S_{HV}^* + S_{HV}S_{VV}^*) \end{aligned}$$

necessary to consider the reconstruction according to pixels physical scattering mechanisms. From the third part of (6), we have  $\text{Im}\{\langle (S_{HH} - S_{VV})S_{HV}^* \rangle\} = \text{Im}\{\langle S_{HH}S_{HV}^* + S_{VV}S_{HV}^* \rangle\}$ , which is related to the helix scattering component, represented by  $F$ . Then, considering the polarization state extrapolation assumption, after the helix scattering component is added, we propose an improved average relationship based on the modified four-component decomposition. The values of  $\langle |S_{HV}|^2 \rangle / (\langle |S_{HH}|^2 \rangle + \langle |S_{VV}|^2 \rangle)$  and  $\rho$  should be calculated for the scattering models defined in (2) and (3), respectively. Assume that a coherence matrix of FP is decomposed into four components, and the corresponding powers are  $P_s$ ,  $P_d$ ,  $P_v$ , and  $P_c$ , respectively. In order to acquire the relationship between co-pol and cross-pol channels, the average values of the cross-pol ratio and the correlation coefficient of the four components are needed, i.e.,  $\langle |S_{HV}|^2 \rangle / (\langle |S_{HH}|^2 \rangle + \langle |S_{VV}|^2 \rangle) = (1/4 \cdot P_v + 1/2 \cdot P_c) / \text{span}$  and  $1 - |\rho| = P_v / \text{span}$ . Then the modified polarization state extrapolation model is derived by the division of the two parts,

$$\frac{\langle |S_{HV}|^2 \rangle}{\langle |S_{HH}|^2 \rangle + \langle |S_{VV}|^2 \rangle} = \frac{1 - |\rho|}{4} \left( \frac{P_v + 2P_c}{P_v + 2P_c + 2P_d} \right) \quad (7)$$

We also employ an iterative approach shown in (8) to solve the non-linear system numerically. By applying the four-component decomposition algorithm with the volume scattering model defined in (3), we can have a relationship that  $f_v$  is simply assigned by the evaluated  $\langle |S_{HV}|^2 \rangle$  and  $f_c$ . Due to the violations of the underlying assumption in iteration,  $|\rho_i|$  ( $i$  is the order of iteration) may become larger than one, or the power of the volume scattering may become negative. In both the cases, we regularize the approximation results to be the  $(i - 1)$ -th iterative results and then halt the iteration.

— Initializations :

$$\begin{aligned} &\left\{ \begin{array}{l} f_{c(0)} = |F_{(0)}| = 0 \\ \rho_{(0)} = \frac{C_{12}}{\sqrt{C_{11}C_{22}}} \end{array} \right. \\ \Rightarrow &\left\{ \begin{array}{l} \left\langle |S_{HV}|^2 \right\rangle_{(0)} = \frac{C_{11} + C_{22}}{2} \left( \frac{1 - |\rho_{(0)}|}{3 - |\rho_{(0)}|} \right) \\ \langle S_{HH}S_{VV}^* \rangle_{(0)} = \rho_{(0)} \times \sqrt{(C_{11} - \left\langle |S_{HV}|^2 \right\rangle_{(0)})(C_{22} - \left\langle |S_{HV}|^2 \right\rangle_{(0)})} \\ f_{c(0)} = |F_{(0)}| = |\text{Im}(C_{12} - \langle S_{HH}S_{VV}^* \rangle_{(0)})| \\ f_{v(0)} = 2 \left\langle |S_{HV}|^2 \right\rangle_{(0)} - f_{c(0)} \end{array} \right. \end{aligned}$$

— Iterations :

$$\begin{aligned}
 \rho_{(i+1)} &= \frac{C_{12} - \langle |S_{HV}|^2 \rangle_{(i)} - jF_{(i)}}{\sqrt{(C_{11} - \langle |S_{HV}|^2 \rangle_{(i)})(C_{22} - \langle |S_{HV}|^2 \rangle_{(i)})}} \\
 \langle |S_{HV}|^2 \rangle_{(i+1)} &= \frac{C_{11} + C_{22}}{2} \frac{(1 - |\rho_{(i+1)}|) (1 + 4f_c(i)/3f_{v(i)})}{2 + (1 - |\rho_{(i+1)}|) (1 + 4f_c(i)/3f_{v(i)})} \\
 \langle S_{HH} S_{VV}^* \rangle_{(i+1)} &= \rho_{(i+1)} \times \sqrt{\left( C_{11} - \langle |S_{HV}|^2 \rangle_{(i+1)} \right) \left( C_{22} - \langle |S_{HV}|^2 \rangle_{(i+1)} \right)} \\
 f_{c(i+1)} &= |F_{(i+1)}| = \left| \text{Im} \left( C_{12} - \langle S_{HH} S_{VV}^* \rangle_{(i+1)} \right) \right| \\
 f_{v(i+1)} &= 2 \langle |S_{HV}|^2 \rangle_{(i+1)} - f_{c(i+1)}
 \end{aligned} \tag{8}$$



Figure 1: Pauli-basis image of the original E-SAR Oberfaffenhofen FP data.

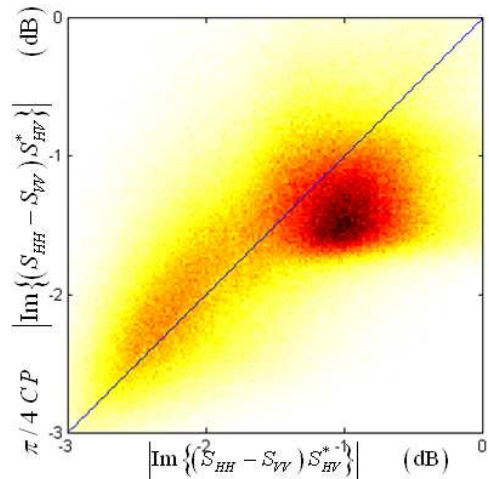


Figure 2: The helix scattering component reconstructed by the proposed method. The abscissa indicates the original data, whereas the ordinate indicates the reconstructed data.

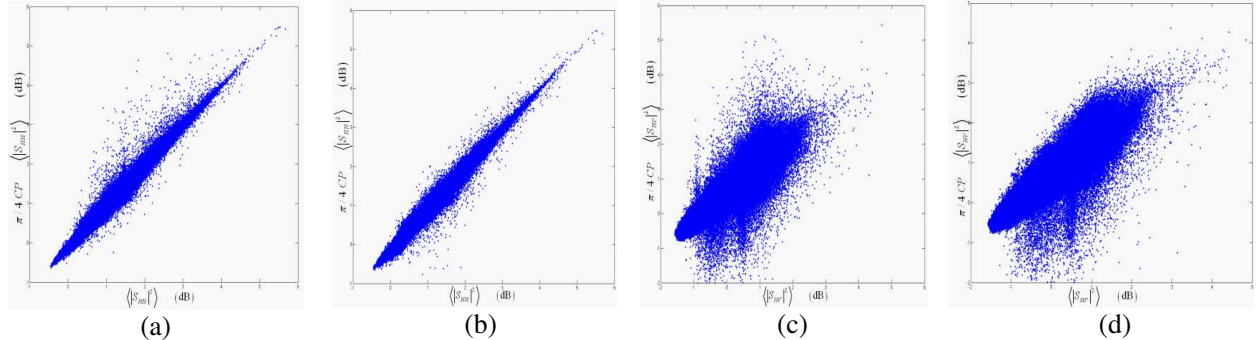


Figure 3: The reconstructed fully polarimetric data. On the abscissa are the original data; the ordinate indicates the reconstructed values. (a) and (c) are the performance of the original FP reconstruction algorithm. (b) and (d) are the performance of the proposed FP reconstruction algorithm. The scatter plots use all pixels of the Oberpfaffenhofen image.

#### 4. EXPERIMENTAL RESULTS

The proposed fully polarimetric information reconstruction algorithm was applied to the E-SAR L-band data acquired over the oberfaffenhofen area in Germany. The image size is  $1300 \times 1200$ . Figure 1 is the Pauli–basis image, from which we can see several kinds of terrain types such as an airport, the urban area, farmlands and forests. The  $\pi/4$  mode compact polarimetric data are generated from the original fully polarimetric data. The corresponding reconstructed results of the original method proposed by Souyris et al. [1], and the results of proposed method are shown in Figure 3, which shows the whole area scatter plots.

Figures 3(a) and (c) shows the original reconstructed results versus the actual radiometric values, and Figures 3(b) and (d) shows the modified reconstructed results versus the actual radiometric values. From the comparison of the two reconstruction algorithms, we can find that the reconstructed results of each channel are similar but the original method is somewhat inferior. Furthermore, the helix scattering type which is omitted in the original reconstruction algorithm by assuming the reflection symmetry is retained by the proposed method. Figure 2 demonstrates the reconstructed helix scattering power versus the actual helix scattering component decomposed by the modified four-component decomposition algorithm.

#### 5. CONCLUSION

Based on the modified four-component model decomposition, an improved fully polarimetric information reconstruction algorithm has been proposed in this paper. In the proposed reconstruction method, we considered the case that the reflection symmetry assumption does not hold, and recovered more information than the original fully polarimetric reconstruction method. Another volume scattering model which is more consistent with the assumption of polarization state was adopted in the modified four-component decomposition, replacing the original volume scattering models. Using the decomposed powers of the four components, we modified the assumed relationship between  $\langle |S_{HV}|^2 \rangle / (\langle |S_{HH}|^2 \rangle + \langle |S_{VV}|^2 \rangle)$  and  $|\rho|$  of compact polarimetry by an average extrapolation model. In summary, an algorithm which takes account of the non-reflection symmetry condition was developed for CP reconstruction architecture. The performance of the proposed FP information reconstruction algorithm was demonstrated by its implementations on real POLSAR images. The experimental results showed that the proposed method is effective.

#### REFERENCES

1. Souyris, J. C., P. Imbo, R. Fjørtoft, S. Mingot, and J.-S. Lee, “Compact polarimetry based on symmetry properties of geophysical media: The  $\pi/4$  mode,” *IEEE Trans. Geosci. Remote Sens.*, Vol. 43, No. 3, 634–646, Mar. 2005.
2. Nord, M. E., T. L. Ainsworth, J.-S. Lee, and N. J. Stacy, “Comparison of compact polarimetric synthetic aperture radar modes,” *IEEE Trans. Geosci. Remote Sens.*, Vol. 47, No. 1, 174–188, Jan. 2009.
3. Yamaguchi, Y., T. Moriyama, M. Ishido, and H. Yamada, “Four-component scattering model for polarimetric SAR image decomposition,” *IEEE Trans. Geosci. Remote Sens.*, Vol. 43, No. 8, 1699–1706, Aug. 2005.
4. An, W., Y. Cui, and J. Yang, “Three-component model-based decomposition for polarimetric SAR data,” *IEEE Trans. Geosci. Remote Sens.*, Vol. 46, No. 6, 2732–2739, Jun. 2010.
5. Xu, F. and Y.-Q. Jin, “Deorientation theory of polarimetric scattering targets and application to terrain surface classification,” *IEEE Trans. Geosci. Remote Sens.*, Vol. 43, No. 10, 2351–2364, Oct. 2005.

# Metamodel-based Adaptive Use of a Coherent Polarimetric Backscattering Simulator for the Characterization of Forested Areas at Low Frequencies

**A. Vasko<sup>1,4</sup>, L. Thirion-Lefevre<sup>2</sup>, S. Bilicz<sup>1,4</sup>, I. Champion<sup>3</sup>, M. Lambert<sup>1</sup>, and S. Gyimóthy<sup>4</sup>**

<sup>1</sup>L2S, UMR 8506, CNRS-SUPELEC, University Paris-Sud, France

<sup>2</sup>SONDRA/SUPELEC, France

<sup>3</sup>EPHYSE/INRA, France

<sup>4</sup>Budapest University of Technology and Economics, Hungary

**Abstract**— We present a new method for forest characteristics inversion, based on a surrogate model derived from a full wave electromagnetic simulator using kriging techniques. To illustrate the feasibility of this method, we consider a simple configuration for the forest and we use the polarimetric backscattering coefficients to retrieve both the age of the trunks and the ground moisture with different frequency bands. The benefit of polarimetry in this retrieval process is then studied.

## 1. INTRODUCTION

In the frame of forest observation, e.g., in the purpose of biomass retrieval, simple scattering models are used to perform inversion. For instance, the Random Volume over Ground (RVoG) model [1] derived from the work of Treuhaft et al. [2] is widely used to retrieve the mean height of the forest (see [3, 4]). However, the use of more complex scattering models (such as COSMO in [5]) for inversion appears to be difficult due to several bottlenecks, such as the high number of descriptive parameters and the computational cost of the simulation.

In this paper, we propose the combined use of a coherent polarimetric backscattering simulator and some adaptive metamodeling tools, which have already been used in electromagnetic nondestructive evaluation (e.g., [6]). We present the metamodeling tools and the surrogate model derived from the coherent polarimetric backscattering simulator (COSMO). Considering a set of polarimetric backscattering coefficients obtained for a given radar configuration and derived from the backscattered fields, we address the inverse problem of determining the forest age and the ground moisture by using the surrogate model. The impact of the radar parameters (frequency, incidence angle and also with special attention to the number of polarimetric channels) is investigated, namely to evaluate the accuracy we can expect on the retrieved quantities.

In the numerical study, we consider the case of a French temperate managed forest whose structure and radar response have already been widely studied in [5] and [7], respectively. For the illustration of the ability of the metamodeling tools to perform inversion, we propose herein to focus on a simple description of the forest: only the dielectric trunks standing on a rough and dielectric surface are considered. This can be seen as a rough, but acceptable approximation at the frequencies considered.

## 2. METAMODELING BY KRIGING

The main objective of metamodeling (or surrogate modeling) is to make a cheap-to-evaluate approximation for the response of a given, usually complex numerical simulator. For a formal description, let us denote the numerical simulation by the so-called forward operator  $\mathcal{F}$ :

$$\mathcal{F}\{\mathbf{x}\} = y_{\mathbf{x}}(\mathbf{t}) \quad \mathbf{x} \in \mathbb{X}, \mathbf{t} \in \mathbb{T}, \quad (1)$$

where  $\mathbf{x}$  is the vector of input variables and the output (response) of the forward operator is a function of the  $\mathbf{t}$  parameter. In our case,  $\mathbf{x} = [a, m_v]^T$  is the forest age  $a$  and ground moisture  $m_v$ , whereas  $\mathbf{t} = [f, \theta]^T$  is the applied frequency and incidence angle in the measurement setup. The domain  $\mathbb{X}$  is called the input space, whereas  $\mathbb{T}$  is the set of all feasible measurement parameters.

A common way of metamodeling is to evaluate the forward operator at certain values of the input parameters and to use interpolation to approximate the response at any unobserved values. Obviously, both the interpolator and the choice of the points where the forward operator is evaluated, highly influence the performance of the metamodel. In our study, we use the kriging technique [8] for interpolation, and the evaluation points are adaptively chosen.

## 2.1. Kriging Interpolation

Traditionally, kriging has been used to interpolate scalar functions, however, our forward operator yields functional data, thus a recent extension —called functional kriging, [9] — is used for this purpose. Functional kriging models the output data  $y_{\mathbf{x}}(\mathbf{t})$  by a functional Gaussian random process  $Y_{\mathbf{x}}(\mathbf{t})$ , and the observations are treated as its samples. Kriging then computes a linear prediction of the random process based on the set of samples  $Y_1(\mathbf{t}), Y_2(\mathbf{t}), \dots, Y_n(\mathbf{t})$  at the points  $\mathbf{x}_1, \mathbf{x}_2, \dots, \mathbf{x}_n$  as  $\hat{Y}_{\mathbf{x}}(\mathbf{t}) = \sum_{i=1}^n \lambda_i(\mathbf{x}) Y_i(\mathbf{t})$ , where the coefficients  $\lambda_i(\mathbf{x})$  are computed in a closed form based on the covariance of the modeling process, satisfying the criterion

$$s^2(\mathbf{x}) = \int_{\mathbb{T}} \mathbb{E} \left[ (\hat{Y}_{\mathbf{x}}(\mathbf{t}) - Y_{\mathbf{x}}(\mathbf{t}))^2 \right] d\mathbf{t} \rightarrow \text{the smallest, s.t. } \mathbb{E} [\hat{Y}_{\mathbf{x}}(\mathbf{t}) - Y_{\mathbf{x}}(\mathbf{t})] = 0, \quad \forall \mathbf{x} \in \mathbb{X}, \quad (2)$$

where  $s^2(\mathbf{x})$  is the so-called trace variance and  $\mathbb{E}$  stands for the expected value operator.

## 2.2. Adaptive Sampling

The performance of the kriging prediction obviously depends on the choice of the samples. The sample set should thus be an ideal discrete representation of the forward operator. Since we do not have any prior information on the behaviour of the latter, an adaptive sampling algorithm is needed. Our method is based on the step-by-step reduction of the uncertainty of the kriging prediction. The algorithm — presented in detail in [6] — consists in the following steps:

1. Choose  $n$  initial sample points in  $\mathbb{X}$  and evaluate  $\mathcal{F}$  there. These points are selected with the classical sampling method called the full-factorial sampling (i.e., in the nodes of regular grid);
2. Compute the kriging prediction over the input space based on the  $y_1(\mathbf{t}), y_2(\mathbf{t}), \dots, y_n(\mathbf{t})$  samples by computing the optimal coefficients  $\lambda_i(\mathbf{x})$  and substituting the observations of the modeling process  $Y_i(\mathbf{t})$  by the corresponding sample  $y_i(\mathbf{t})$ ;
3. Find the next sample point as  $\mathbf{x}_{n+1} = \arg \max_{\mathbf{x} \in \mathbb{X}} (\hat{s}^2(\mathbf{x}) \min_{i=1, \dots, n} \|\mathbf{x} - \mathbf{x}_i\|)$ . The first factor  $\hat{s}^2(\mathbf{x})$  is the variance from (2) predicted with the jackknife variance estimation, referring to the uncertainty of the prediction. The second factor is the Euclidean distance to the nearest sample in  $\mathbb{X}$ , introduced to enforce the balanced filling of  $\mathbb{X}$  by samples;
4. Add  $y_{n+1}(\mathbf{t}) = \mathcal{F}\{\mathbf{x}_{n+1}\}$  to the sample set, and increase  $n$  to  $n + 1$ ;
5. Go to step 2 until  $n$  reaches a given value.

## 2.3. Validation of the Model

In the frame of our studies, the forward operator yields the polarimetric backscattering coefficient, i.e.,  $\mathcal{F}\{\mathbf{x}\} = \sigma_p^{\mathbf{x}}(f, \theta)$  where  $p$  is the polarization channel (either VV, VH or HH). The goal of the metamodel generation is to find a good approximation of  $\mathcal{F}$  based on the  $\sigma_p^{\mathbf{x}}(f, \theta)$  functional observations. In our numerical studies, the  $\sigma_p^{\mathbf{x}}(f, \theta)$  functions are represented by a finite number of samples obtained at certain  $(f, \theta)$  values. For a proper representation, these scalar samples of each  $\sigma_p^{\mathbf{x}}(f, \theta)$  function are also adaptively chosen, i.e., a two-level adaptive sampling strategy is used. The *upper* level is the sampling of  $\mathcal{F}$ , where the observations are the  $\sigma_p^{\mathbf{x}}(f, \theta)$  *functions*, i.e., the sampling aims at choosing the best  $\mathbf{x}$  samples. The *lower* level is responsible for the representation of a *particular*  $\sigma_p^{\mathbf{x}}(f, \theta)$  function by the optimal choice of the  $(f, \theta)$  values. Both levels use the same adaptive sampling algorithm introduced in Section 2.2 but with different objective functions.

To illustrate the efficiency of the two-level adaptive sampling method, we compare the result of this method with a metamodel that was generated with a regular sampling. The mean interpolation error is calculated as  $\varepsilon_p(\mathbf{x}) = \sqrt{\frac{1}{\Delta f \Delta \theta} \int_{f_0}^{f_1} \int_{\theta_0}^{\theta_1} [\hat{\sigma}_p^{\mathbf{x}}(f, \theta) - \sigma_p^{\mathbf{x}}(f, \theta)]^2 d\theta df}$ . The results are presented in Fig. 1: the adaptive metamodel seems to outperform the regular one.

## 3. APPLICATION TO THE RETRIEVAL OF AGE AND GROUND MOISTURE

In this paper, we study the radar backscattering response of the Nezer forest, a pine trees forest, that has been widely described [7]. Its allometric equations have been derived [10], implying that we can describe it with a few parameters. Thus, it is now possible to retrieve some descriptive quantities of the forest using some radar observables. In a previous study [11], we have worked

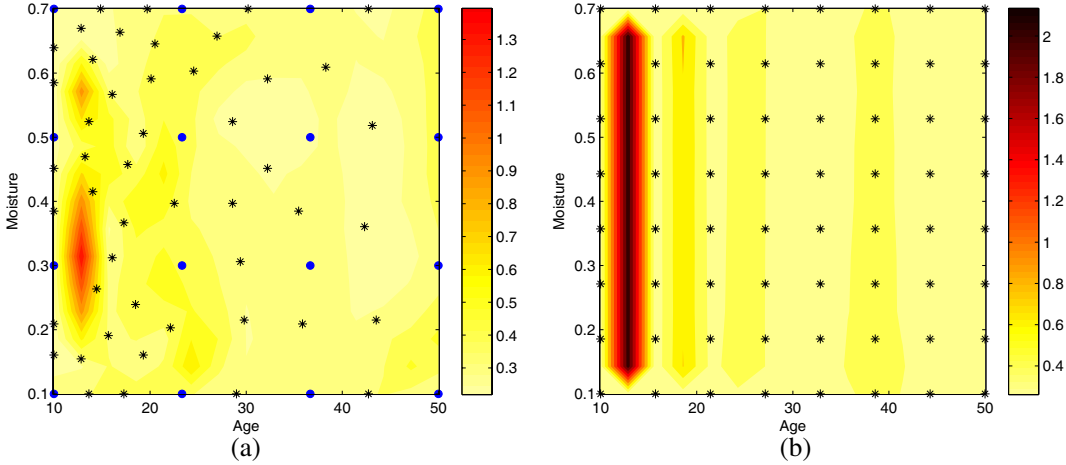


Figure 1: Interpolation error  $\varepsilon(\mathbf{x})$  of the adaptive and the regular metamodel. Both consist in 64 samples in the input space, and each sample is represented by 64 pairs of  $(f, \theta)$ . The regular model uses  $8 \times 8$  grids in both levels. The true values are computed on fine grids (involving totally 45200 simulations). (a) Adaptive metamodel (dots: initial samples, stars: sequentially added samples). (b) Regular metamodel.

with the polarimetric backscattering coefficients, the polarimetric interferometric heights, and the attenuation for the co-polarizations. In addition, we have simulated a whole forest (ground, trunks and branches), but for a given age of the forest and a constant gravimetric ground moisture  $m_v$  only. In order to illustrate the feasibility of our method, we consider here a simple forest configuration and we only use the polarimetric backscattering coefficients.

For simplicity, the forest under study is described only by its trunks. These trunks are modeled as almost vertical dielectric cylinders standing on a dielectric and rough ground. The age ( $a$ ) of the trunks varies between 10 and 50 years: each age corresponds to a height  $h$  and a diameter  $d$  (in meters). These quantities are derived using the allometric equations presented in [10]:  $h = 56.618 \times d + 0.646$  with  $d = 0.169 \times \log(a) - 0.257$ . The moisture of the trunks and the branches is assumed to be constant and around 0.54, the trees density is assumed also to be constant and regularly spaced (5 m distance, see [5] for details). As a consequence, two data are required to describe our scene: the age of the trees and the ground moisture  $m_v$ , which is assumed to vary between 0.1 and 0.7. The reference values of the polarimetric backscattering coefficients ( $\sigma$ ) are calculated with COSMO. The inversion is performed with our metamodel (Section 2.2). This example is simple as we actually need only two parameters to represent our simple forest. However, it is not expected to be the best case for the illustration of the benefit of polarimetry. Indeed, as the scatterers types are reduced, the polarimetric variety is weak.

To analyse the performance of inversion, we have selected four representative examples: the age is either 20 or 40 years and the ground moisture is equal either to 0.25 or 0.55. We present first error maps and then we comment some of our results.

### 3.1. Introduction to Error Maps

In Fig. 2, we have plotted four error maps, that represent the errors we obtained both on the retrieved  $m_v$  and  $a$  using  $\sigma$ . In this example,  $a = 40$  years and  $m_v = 0.25$ . Radar measurements between 1 GHz and 2 GHz and incidence angles between  $59^\circ$  and  $61^\circ$  are assumed. The white stars indicate for each polarization, the location of the true point ( $a = 40, m_v = 0.25$ ),  $\sigma$  being given for information. We observe in Fig. 2, that the best polarimetric channel (BPC) is VH (Fig. 2(b)), but we need the additional information brought both by VV and HH to obtain a better result (called CPC, for Combined Polarimetric Channels) (Fig. 2(d)). The drawn boxes represents the boundaries considered for inversion assuming an error of 1 dB. In this example, VH channel allows to estimate  $a$  such as  $a \in [37, 41]$ . There is an ambiguity on  $m_v$  and we can only estimate that  $m_v \in \{[0.14, 0.41] \cup [0.48, 0.7]\}$ , that is clearly not satisfying. When combining the full polarimetric information, the estimation of  $m_v$  is improved ( $m_v \in [0.17, 0.39]\}$ ).

### 3.2. A Focus on the Impact of Polarimetry on the Retrieval of $a$ and $m_v$

In this section, we investigate the role of polarimetry in the inversion of the trunks age and the ground moisture. It is obvious that the scattering mechanisms evolve with the frequency and so do the polarimetric mechanisms. As a consequence, we do not expect the same benefit of polarimetric

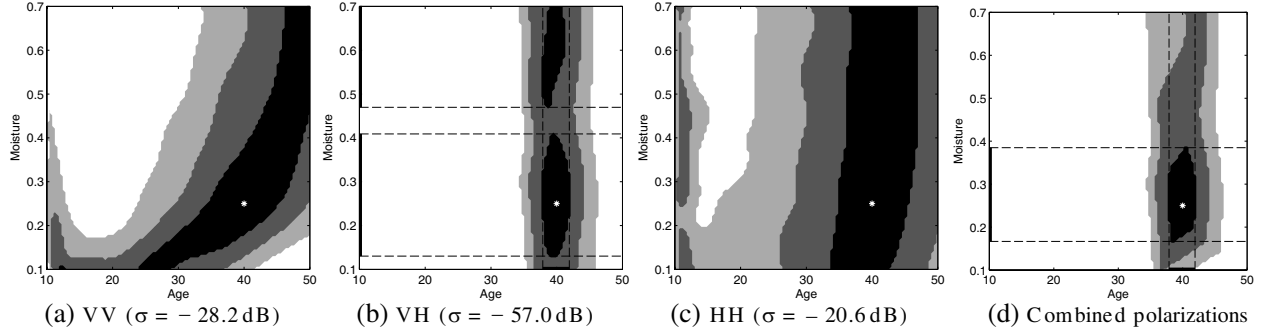


Figure 2: Illustration of error maps for  $(a = 40, m_v = 0.25)$ , frequency bandwidth=[1000, 2000] MHz and incidence angle range  $= [59, 61]^\circ$ . Black area refers to an error less than 1 dB, dark grey one to an error between 1 dB and 2 dB, and the light grey one between 2 dB and 3 dB. Boxes represent the boundaries we consider for inversion: VH is classified in this example as the best polarimetric channel.

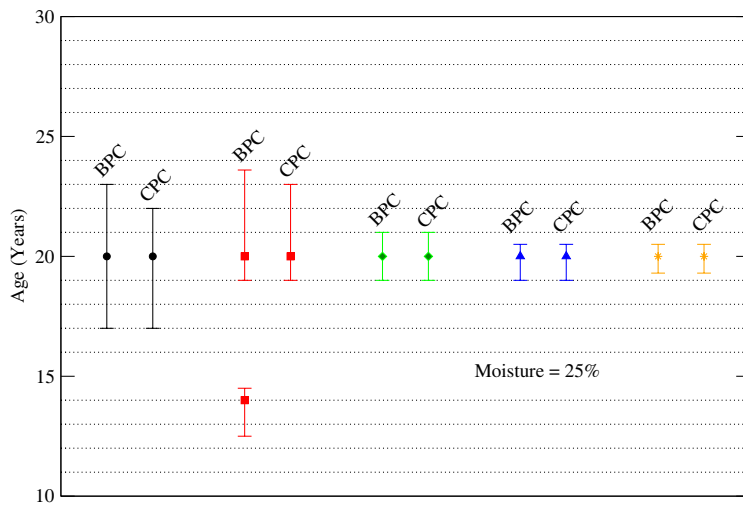


Figure 3: Age retrieval for different frequency bands and different polarimetric arrangements. The case to retrieve is  $(a = 20, m_v = 0.25)$ . For each frequency range, there are two cases: the best polarimetric channel results (BPC) either VV, HH or HV polarization; the combined polarimetric channels results (CPC) considering the three polarimetric channels. The bars represent the interval error.

information depending on the frequency range we consider. Therefore, we have defined five cases arranged in three groups: (1) some usual radar configurations [400, 470] MHz ( $\bullet$ ) and [1230, 1350] MHz ( $\square$ ); (2) enlarged low and hight frequency bands [350, 1000] MHz ( $\diamond$ ) and [1000, 2000] MHz ( $\triangle$ ) respectively; and finally (3) the whole frequency range, [350, 2000] MHz (\*).

### 3.2.1. Age Retrieval

In Fig. 3, we observe that polarimetric information does not contribute significantly to the inversion of the age. Error bars are about the same, either when considering the BPC or the CPC. On the contrary, the frequency range seems crucial: the larger it is, the more accurate is the retrieval of  $a$ . This trend is confirmed by additional results for other  $a$  and  $m_v$ , except that considering the whole frequency range does not always lead to the best case. However, as illustrated with the frequency range [1230, 1350] MHz ( $\square$ ), ambiguities may appear: is  $a \in [13, 15]$  or  $a \in [19, 24]$ ? Using CPC allows to suppress this uncertainty and even gives a little more accuracy with  $a \in [19, 23]$ .

### 3.2.2. Moisture Retrieval

For  $m_v$  retrieval (Fig. 4(a)), the roles of the frequency ranges and the polarimetry are not the same, a clear benefit of polarimetry enabling to suppress ambiguities and reducing significantly the error interval is shown. However, the quality of the inversion is not comparable: in the cases we have considered it is obviously more difficult to retrieve the ground moisture than the dimensions of the trunks. The additional results we obtained (see, e.g., Fig. 4(b)) lead us to think that polarimetry is mandatory when we do not obtain more accurate results with larger frequency range.

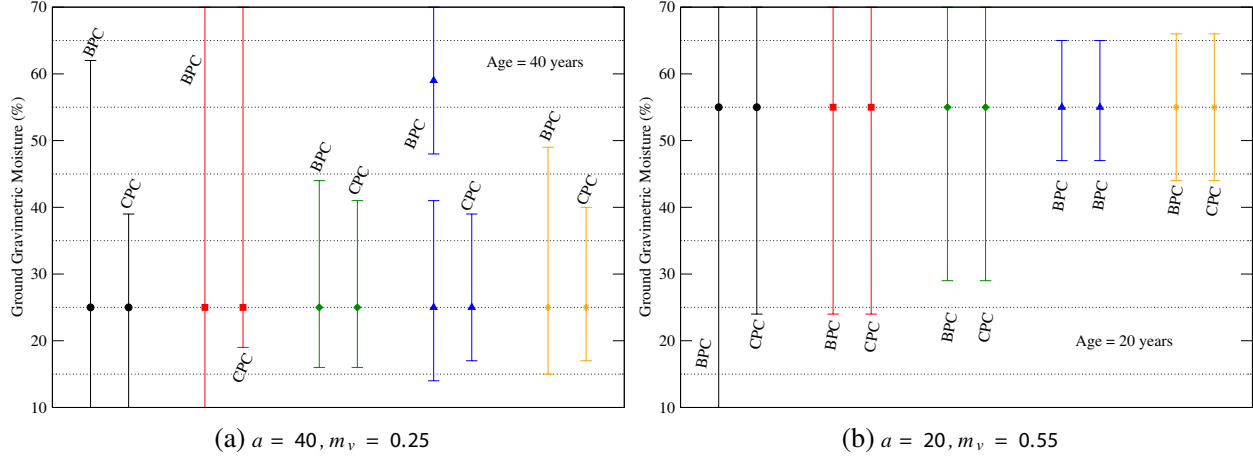


Figure 4: Ground moisture retrieval for different frequency bands and different polarimetric arrangements.

#### 4. CONCLUSION

We have presented in this paper a new method for forest characteristics inversion. We have considered a simple configuration for the forest, that is not considered as the best one to illustrate the benefit of polarimetry. We have used the polarimetric backscattering coefficients to retrieve both the age of the trunks and the ground moisture with different frequency bands. We have produced error maps, that illustrate the uncertainty we obtain and we have studied some examples. The very first results we have obtained lead us to conclude that we cannot state that only one polarimetric channel is sufficient to retrieve correctly our parameters. Actually, it dramatically depends on the variety of the measured scattering mechanisms. This variety is brought for instance by polarimetry or by frequency. But even in the case where the frequency range is large enough to provide this diversity, ambiguities may still remain, that require polarimetry in order to be suppressed.

#### REFERENCES

1. Cloude, S. R. and K. P. Papathanassiou, "Three-stage inversion process for polarimetric SAR interferometry," *Proc. Inst. Elect. Eng. Radar, Sonar Navig.*, Vol. 150, 125–134, 2003.
2. Treuhhaft, R. N., S. Madsen, M. Moghaddam and J. J. van Zyl, "Vegetation characteristics and underlying topography from interferometric data," *Radio Sci.*, Vol. 31, 1449–1485, 1996.
3. Garestier, F., P. Dubois-Fernandez, and K. P. Papathanassiou, "Pine forest height inversion using single-pass X-band Pol-InSAR data," *IEEE Trans. Geosci. Remote Sens.*, Vol. 46, 59–68, 2008.
4. Garestier, F., P. Dubois-Fernandez, and I. Champion, "Forest height inversion using high-resolution P-band Pol-InSAR data," *IEEE Trans. Geosci. Remote Sens.*, Vol. 46, 3544–3559, 2008.
5. Thirion, L., E. Colin, and C. Dahon, "Capabilities of a forest coherent scattering model applied to radiometry, interferometry and polarimetry at P- and L-bands," *IEEE Trans. Geosci. Remote Sens.*, Vol. 44, 849–862, 2006.
6. Bilicz, S., S. Gyimóthy, M. Lambert, and J. Pávó, "Adaptive kriging metamodels for expensive-to-run electromagnetic simulations," *Proc. 14th International IGTE Symposium on Numerical Field Calculation in Electrical Engineering*, 214–219, IGTE, Graz, Austria, 2010.
7. Sartore, M., et al., "Tree architecture in remote sensing analytical models: The Bray experiment," *Int. J. Remote Sens.*, Vol. 22, 1827–1843, 2001.
8. Chilès, J. and P. Delfiner, *Geostatistics, Modeling Spatial Uncertainty*, Wiley, 1999.
9. Delicado, P., R. Giraldo, C. Comas, and J. Mateu, "Statistics for spatial functional data: some recent contributions," *Environmetrics*, Vol. 21, 224–239, 2009.
10. Saleh, K., et al., "A forest geometric description of a Maritime pine forest suitable for discrete microwave models," *IEEE Trans. Geosci. Remote Sens.*, Vol. 43, 2024–2035, 2005.
11. Thirion-Lefevre, L., S. Bilicz, M. Lambert, and Sz. Gyimóthy, "On the use of an optimal database for radar forest observation," *8th European Conference on Synthetic Aperture Radar (EUSAR 2010)*, 873–876, 2010.

# Polarimetric Signature and the Temporal Variation Analysis for Deforestation Mapping in Southwest China

Fengli Zhang<sup>1</sup>, Maosong Xu<sup>2</sup>, Chou Xie<sup>1</sup>, Zhongsheng Xia<sup>3</sup>, Kun Li<sup>1</sup>, Aimin Cai<sup>1</sup>, Yun Shao<sup>1</sup>, Xuejun Wang<sup>2</sup>, and Ridha Touzi<sup>4</sup>

<sup>1</sup>State Key Laboratory of Remote Sensing Science, Institute of Remote Sensing Applications Chinese Academy of Sciences, #3 Datun Road, Chaoyang District, Beijing 100101, China

<sup>2</sup>Academy of Forestry Inventory, Planning and Designing, State Forestry Administration (SFA) Beijing 100714, China

<sup>3</sup>Forest Resource Management and Conservation Station, Guizhou 550001, China

<sup>4</sup>Canada Centre for Remote Sensing, 588 Booth Street Ottawa, Ontario, K1A0Y7, Canada

**Abstract**— In the southwest of China, Synthetic aperture radar (SAR) has been gradually adopted for forestry monitoring because the cloudy and rainy weather in this area has hindered the optical remote sensing too much. Polarimetric SAR data contains more information of targets and has been expected more helpful for forest mapping. In this paper, polarimetric signature and its temporal variation of deforestation areas caused by snow storm was analyzed using six polarimetric RADARSAT-2 images and taking Zhazuo area in Guizhou Province as the study area, and method for deforestation identification based on polarimetric SAR data was studied.

## 1. INTRODUCTION

Forest conservation and sustainable development is very important to human beings. However, the area of deforestation and natural loss of forest is about 13 million hectares per year at the global level in the last decade. China is one of the five most forest-rich countries in the world and forest mapping and protection has remained an important task. Dense forest distributes in southwest China where the weather condition is usually poor, with the annual clear days less than 50–100 days. Spaceborne Synthetic Aperture Radar (SAR) can be used for forest monitoring because of its all weather capabilities.

In the mid of 1990s, the Global Rain Forest Mapping (GRFM) project and Global Boreal Forest Mapping (GBFM) project were initiated and demonstrated the ability of L-band SAR data for forest mapping and monitoring [1]. Then, in order to map forest deforestation and improve forest monitoring results multi-temporal SAR data was adopted [2, 3]. Almeida-Filho et al. [4] concluded that only *HH* polarization data could not unambiguously identify areas in initial stage of deforestation. Tanase et al. [5] pointed out that C- and L-band cross polarization was better for burn severity evaluation in the Mediterranean environment. Polarimetric SAR data contains more information of targets and is expected more helpful for deforestation mapping. With the launch of RADARSAT-2 satellite, the polarimetric RADARSAT-2 data will be a promising tool for deforestation inventory under cloudy and rainy weather conditions. In this paper, polarimetric signature and its temporal variation of deforestation area caused by snow storm was analyzed using six polarimetric RADARSAT-2 images, and method for deforestation identification based on polarimetric SAR data was studied.

## 2. TEST SITE AND DATA SOURCES

Guizhou province was located in southwest of China, of Karst landform, mountainous and with less than 50 clear days per year. Zhazuo area is a representative of this province and is selected as the test site in our study. The climate of this region is mid-subtropical rainy and humid climate, with distinct seasonal variations, which is favorable to the growth of forest. The test site is covered with dense forests which are mainly coniferous forests. In early 2008, a severe snow storm not happened for last 50 years swept south China, and caused great damages to forest ecosystem in 18 provinces of China. Field investigations were carried out, and position and extent of deforestation area in the test site were surveyed. From November 2008 to October 2009, six RADARSAT-2 polarimetric SAR images were acquired respectively on November 4, 2008, February 8, 2009, July 26, 2009, August 19, 2009, September 12, 2009, and October 6, 2009, with the support of the Science and Operational Applications Research for RADARSAT-2 Program (SOAR).

### 3. METHODOLOGY

In this paper, the Polarimetric Workstation (PWS) [6] was used to extract backscattering coefficient, polarimetric signature, and Cloude's parameters, entropy ( $H$ ), anisotropy ( $A$ ),  $\alpha$  and  $\beta$  from each RADARSAT-2 image, and then the temporal variations were analyzed using the six polarimetric RADARSAT-2 images.

Polarimetric signature analysis is a general approach to visualize the signature of target as a function of the incident and backscattered polarizations, which is helpful to analyze backscattering mechanism of target. The pedestal height is related to the degree of polarization of a scattered wave, and also is a measure of the number of scattering mechanism types [7].

Cloude and Pottier [8] introduced several secondary polarimetric parameters, entropy ( $H$ ), Anisotropy ( $A$ ),  $\alpha$  and  $\beta$  to describe target's scattering mechanism.  $A$  is a parameter complementary to entropy  $H$  and measures the relative importance of the second and third eigenvalues.  $\alpha$  is closely related to physical scattering mechanism, determining the type of scattering.

The objective of polarimetric target decomposition is to make the scattering analysis of complex target change to the analysis of simpler scattering mechanisms and their contributions. Freeman-Durden decomposition is a kind of incoherent decomposition, and decomposes the total scattering into volume scattering, double-bounce scattering and surface scattering component [9]. In this paper, Freeman-Durden decomposition was ultimately used for deforestation identification.

## 4. RESULTS AND ANALYSIS

### 4.1. Temporal Variation of Backscattering Coefficient of Forest and Deforestation Area

Temporal variation of backscattering coefficient of deforestation caused by snow storm is similar to normal forest, yet the backscattering coefficient of deforestation area is generally lower than that of forest. For deforestation area, the  $HV$  polarization backscattering is much lower than  $HH$  and  $VV$  polarizations, and the difference between  $HV$  and  $HH$ ,  $VV$  polarizations is larger than normal forest, indicating less volume scattering from deforestation area.

### 4.2. Polarization Signature and Temporal Variation

Polarimetric signatures of normal forest and deforestation area extracted from RADARSAT-2 images on February 8, 2009 are shown in Figure 1. The pedestal height of forest is 0.63 in co-polarized signature and 0.53 in cross-polarized signature, indicating that there are several scattering mechanisms, and analysis based on  $H$ - $\alpha$  plot indicates that the scattering mechanisms from forest generally include volume scattering, rough surface scattering, and multi-scattering between canopy, trunk and the ground. Besides, the cross-polarized signature of damaged forest and normal forest also has no significant difference, but the co-polarized signature of damaged forest is different with that of normal forest. There are low values from orientation angle from  $\psi = 45^\circ$  to  $135^\circ$ , probably because the dihedral scattering formed by the sparse trees and the ground is more strong for deforestation area while for normal forest less C-band microwave can penetrate the canopy and then form dihedral scattering.

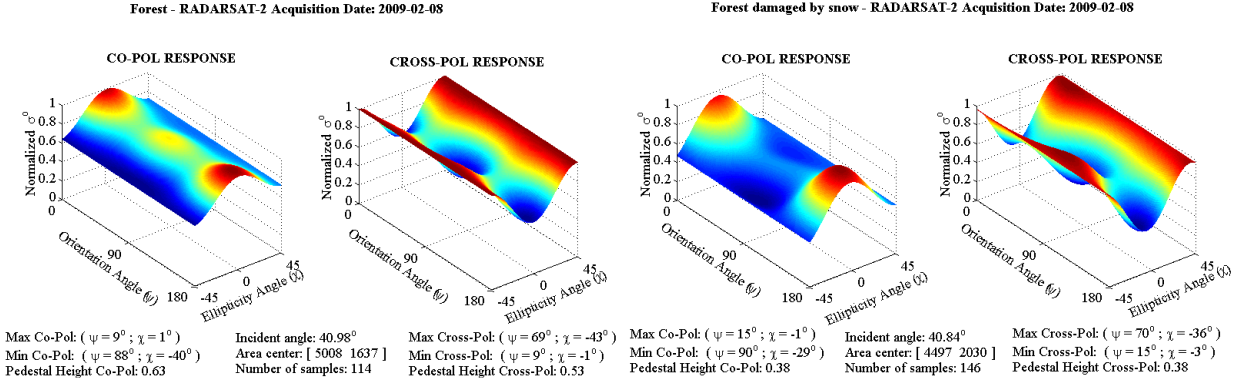


Figure 1: Polarimetric signatures of normal forest and deforestation area extracted from RADARSAT-2 image acquired on February 8, 2009.

Then, temporal variation of polarimetric parameters were extracted and analyzed using the six polarimetric RADARSAT-2 images. The temporal variations of  $A$  and  $\alpha$  for normal forest and forest damaged by snow are shown in Figure 2. The average entropy value  $H$  of normal forest and deforestation area is generally larger than 0.8, especially entropy of deforestation area damaged by snow storm is all higher than 0.9. The higher the anisotropy is, the larger the difference of the contribution between the second and third eigenvectors is. The anisotropy value  $A$  of normal forest is generally lower than that of deforestation area caused by snow storm, because for forest volume scattering is the dominant scattering mechanism and the difference between the second and the third principal scattering mechanism is little. For deforestation area, the anisotropy is generally higher than that of normal forest, because the second and the third principal scattering mechanism for normal and damaged forest both is rough surface scattering and multi-scattering, but in deforestation area contribution of rough surface scattering is much larger than that of normal forest area. Besides, in summer the difference of anisotropy between normal and damaged forest is small, and in autumn and winter, the difference is large. Temporal variation of  $\alpha$  of normal forest and deforestation area caused by snow storm is similar, with range of 40–50°, and the  $\alpha$  value of forest damaged by snow storm is generally higher than that of normal forest, because dihedral scattering formed by the erect trees, shrubs and the beneath ground is easier to appear. While for normal forest, dihedral scattering is hard to happen because of the weaker penetrating capability of C-band microwave.

#### 4.3. Deforestation Identification Based on Polarimetric Decompositon

Figure 3 shows the Pauli and Freeman-Durden decomposition result for deforestation areas using RADARSAT-2 image on February 8, 2009. In the Pauli decomposition composite image, deforestation area damaged by snow is not obvious, yet in the Freeman-Durden decomposition composite image, deforestation area takes on bright blue due to the high surface scattering. According to Freeman-Durden decomposition results, the double-bounce scattering, volume scattering and surface scattering are calculated and the results are listed in Table 1. It can be seen that for normal forest and deforestation area, volume scattering both is the dominant scattering mechanism, but surface scattering of deforestation area is  $-2.12$  dB, much higher than that of normal forest,  $-20.32$  dB, due to the presence of shrubs and grasses beneath the trees. For normal forest and deforestation area the double-bounce scattering both is moderate, with deforestation area a little higher than normal forest.

Table 1: Statistics of the three component scattering using the Freeman-Durden decomposition.

	Double-bounce scattering	Volum scattering	Surface scattering
Normal forest	$-20.7$ dB	$0.34$ dB	$-20.32$ dB
Forest damaged by snow	$-20.6$ dB	$-0.33$ dB	$-2.12$ dB

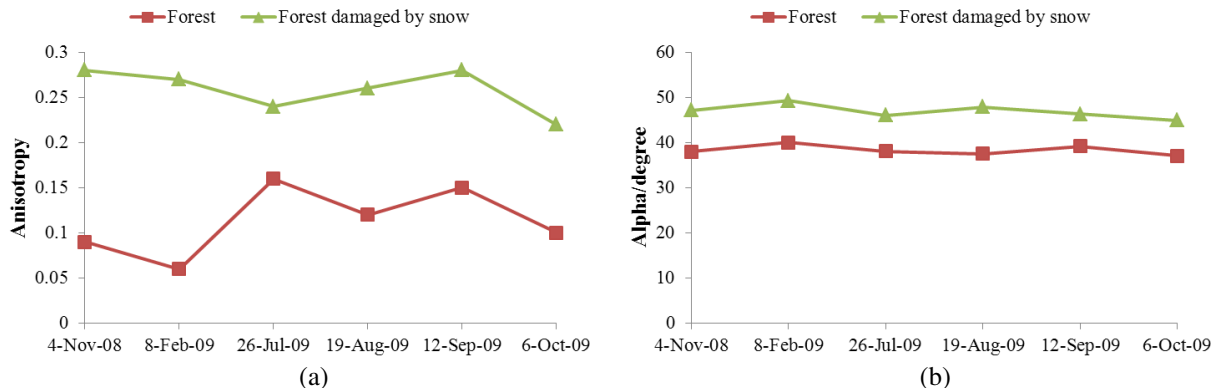


Figure 2: Temporal variation of polarimetric parameters, (a) represents  $A$ , and (b) represents  $\alpha$ .

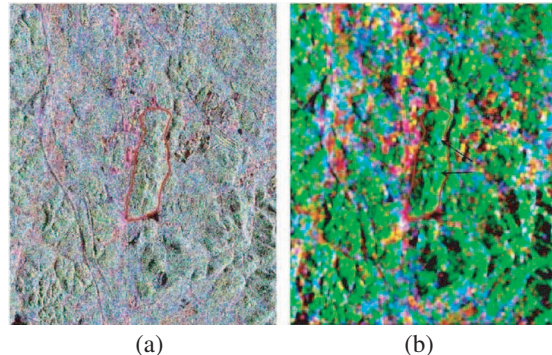


Figure 3: Deforestation identification based on Pauli and Freeman-Durden decomposition using RADARSAT-2 data on February 8, 2009, (a) is the Pauli decomposition composite image, and (b) is the Freeman-Durden decomposition composite image and the two arrows indicate the deforestation area damaged by snow storm.

## 5. DISCUSSIONS AND CONCLUSIONS

In this paper, polarimetric signature and its temporal variation of deforestation areas caused by snow storm was analyzed using six polarimetric RADARSAT-2 images and taking Zhazuo area in Guizhou Province as the study area, and method for deforestation identification based on polarimetric SAR data was studied. Backscattering coefficient of forest damaged by snow storm is significantly lower than that of forest not damaged, and the  $HV$  polarization backscattering of deforestation area is much lower, indicating much less volume scattering. And, the temporal variation of polarimetric parameters  $H$ ,  $A$  and  $\alpha$  value of forest damaged by snow storm is generally higher than that of normal forest. Freeman decomposition was proved more suitable for identification of deforestation area, because surface scattering of forest damaged by snow storm is higher than that of normal forest.

## ACKNOWLEDGMENT

This work was supported by the Knowledge Innovation Program of the Chinese Academy of Sciences (KZCX2-EW-320, Y0S04400KB) and the Project 41001213 supported by NSFC, and the National High Technology Research and Development Program of China (863 Program No. 2007AA12Z146).

## REFERENCES

1. Roseqvist, A., M. Shimada, B. Chapman, A. Freeman, G. De Grandi, S. Saatchi, and Y. Rauste, "The global rain forest mapping project — a review," *International Journal of Remote Sensing*, Vol. 21, No. 6, 7, 1375–1387, 2000.
  2. Bourgeau-Chavez, L. L., E. S. Kasischke, S. Brunzell, J. P. Mudd, and M. Tukman, "Mapping fire scars in global boreal forests using imaging radar data," *International Journal of Remote Sensing*, Vol. 23, No. 20, 4211–4234, 2002.
  3. Stankiewicz, K., "The use of microwave SAR images for forest decline monitoring in mountainous area," *Advances in Space Research*, Vol. 29, No. 1, 67–72, 2002.
  4. Almeida-Filho, R., A. Rosenqvist, Y. E. Shimabukuro, and R. Silva-Gomez, "Detecting deforestation with multitemporal L-band SAR imagery: A case study in western Brazilian Amazônia," *International Journal of Remote Sensing*, Vol. 28, No. 6, 1383–1390, 2007.
  5. Tanase, M. A., M. Santoro, J. Riva, F. Pérez-Cabello, and T. Le Toan, "Sensitivity of X-, C-, and L-band SAR backscatter to burn severity in Mediterranean pine forests," *IEEE Transactions on Geoscience and Remote Sensing*, Vol. 48, No. 10, 3663–2675, 2010.
  6. Touzi, R. and F. J. Charbonneau, "PWS: a friendly and effective tool for polarimetric image analysis," *Canadian Journal of Remote Sensing*, Vol. 30, No. 3, 566–571, 2004.
  7. Van Zyl, J. J., "Imaging radar polarization signatures: Theory and observation," *Radio Science*, Vol. 22, No. 4, 529–543, 1987.
  8. Cloude, S. R. and E. Pottier, "An entropy based classification scheme for land applications of polarimetric SAR," *IEEE Transactions on Geoscience and Remote Sensing*, Vol. 35, No. 1, 68–78, 1997.
  9. Freeman, A. and S. L. Durden, "A three-component scattering model for polarimetric SAR data," *IEEE Transactions on Geoscience and Remote Sensing*, Vol. 36, No. 3, 963–973, 1998.

# Rice Monitoring Using Touzi Decomposition Based on Polarimetric SAR Data in Southwestern China

Kun Li<sup>1</sup>, Yun Shao<sup>1</sup>, Ridha Touzi<sup>2</sup>, Brian Brisco<sup>2</sup>, and Fengli Zhang<sup>1</sup>

<sup>1</sup>Institute of Remote Sensing Applications, Chinese Academy of Sciences (IRSA, CAS), China

<sup>2</sup>Canada Centre of Remote Sensing (CCRS), Canada

**Abstract**— Rice is one of the three largest food grains in the world, providing food for more than one third of globe population. Researches on rice monitoring are of great significance and attract more attention of radar remote sensing communities. In this study, the Touzi target decomposition was investigated for rice monitoring. The results showed that the parameters of Touzi decomposition were sensitive to rice fields, especially the dominant symmetric scattering type amplitude. In addition, the dominant symmetric scattering type phase was the most sensitive to rice growth change and was very promising for rice monitoring.

## 1. INTRODUCTION

Rice is one of the three largest food grains in the world, providing food for more than one third of globe population. China is the largest rice producer with rough production of 193 million tons annually. Guizhou province is an important rice growing area in the southwest of China. However, due to its perennial cloud-coverage weather and undulating terrain, rice monitoring with remote sensing has great difficulties in this region. Synthetic Aperture Radar (SAR), with its all-weather, day-night imaging and high repeat coverage, has been proved to be a significant data source in rice monitoring [1–4]. With the emergence of full polarimetric SAR data and advanced methods for information extraction, monitoring rice in this region is more promising.

The Touzi target decomposition is a new method, which has been introduced for a roll and unique incoherent of target scattering [5]. It has been shown to be very promising in some applications, such as wetlands characterization [6, 7], forests discrimination [8] and ship identification [9]. However, researches on the Touzi decomposition's application in rice monitoring are really rare and still need further study. The objective of this paper is to evaluate the Touzi decomposition for rice monitoring and propose some parameters which are promising for rice identification and monitoring.

## 2. TEST SITE AND DATA SOURCE

The test site is located in Zhazuo, Guizhou, southwest China ( $26^{\circ}50'40.64''N$ ,  $106^{\circ}38'12.97''E$ ), with an area of  $93\text{ km}^2$ . This region is in the central of the highland, with the highest elevation 1607 m, lowest 900 m and relative relief 250–400 m. Paddy fields mainly distribute in the bottom of river valley and lowland among hills, with irregular shapes and great different sizes. The climate of this region is warm and humid, which is favorable for the growth of rice. There is one rice crop a year, from early May to early October. During this period, almost all farmlands in the test site are used for paddy rice cultivation.

Four Fine Quad-polarization RADARSAT-2 data were acquired in 2009, corresponding to the beginning of heading, milky, maturity stage and harvest, and the details were showed in Table 1. In addition, ground campaign was conducted from August 19 to 21 in 2009. Eight paddy fields were selected as the sample sites in this study, with the average size of about  $200,000\text{ m}^2$ . Crop calendar, phonological stage, variety, size and irrigation conditions were collected in each field. In addition, some sample sites, covering forest, urban and water, were select in the test site. All sample sites were geo-referenced using Global Positioning System (GPS).

## 3. METHODOLOGY

The Touzi decomposition is based on the characteristic decomposition of the coherency matrix  $[T]$ . For a reciprocal target, the coherency matrix  $[T]$  can be decomposed as follows [5, 7]

$$[T] = \sum_{i=1,3} \lambda_i [T]_i \quad (1)$$

Table 1: The details of polarimetric RADARSAT-2 data acquired in 2009.

Acquisition Time (mm-dd-yyyy)	Beam Mode	Look Direction	Pass	Incidence	Incidence	Product	Resolution (m)	
				Angle (Near Range)	Angle (Far Range)		Range	Azimuth
07-26-2009	FQ <sup>a</sup> 21	Right	Descending	40.18°	41.60°	SLC	12	8
08-19-2009	FQ21	Right	Descending	40.18°	41.60°	SLC	12	8
09-12-2009	FQ21	Right	Descending	40.18°	41.60°	SLC	12	8
10-06-2009	FQ21	Right	Descending	40.17°	41.60°	SLC	12	8

a:  $FQ = \text{Fine Quad-polarization}$ .

In (1),  $[T]_i$  represents the coherency matrix of each single scatter and  $\lambda_i$  denotes the contribution of the corresponding scatter.  $[T]_i$  can be expressed as function of the target vector  $\vec{k}_i$  as follows

$$[T]_i = \vec{k}_i \cdot \vec{k}_i^{*t} \quad (2)$$

where  $*t$  denotes the conjugate transpose. The three target vector  $\vec{k}_i$  ( $i = 1, 3$ ) denotes, in fact, the three eigenvectors of the coherency matrix  $[T]$ .

The Touzi decomposition uses the roll-invariant coherent scattering model for the parameterization of the target vectors of  $\vec{k}_i$ . The Touzi scattering vector [5] model is used as the basis of unique and roll-invariant coherent target scattering decomposition. It is derived using the projection of the Kennaugh-Huynen scattering matrix con-diagonalization into Pauli basis, which offers a more convenient way for scattering representation [7]. It is applied to each single-look pixel scattering  $[S]$  matrix.  $[S]$  is con-diagnolized and represented in terms of scattering vector model parameters  $\alpha_s$ ,  $\Phi_{\alpha_s}\psi$ ,  $\tau$  and  $m$ . These parameters, which do not depend on the wave polarization basis, are target characteristics and permit a unique and roll-invariant decomposition of coherent target scattering. The roll-invariant coherent target decomposition provides an unambiguous description of the symmetric target scattering using the complex scattering type parameters  $\alpha_s$  and  $\Phi_{\alpha_s}$ . The helicity  $\tau$  permits the measurement of the degree of target scattering symmetry. The combination of  $\tau$ , the maximum amplitude  $m$  and the orientation angle  $\psi$  leads to a full characterization of the maximum target return. In addition to the aforesaid five parameters, the normalized eigenvalue  $\lambda_i$  ( $\lambda_i = \eta_i / (\eta_1 + \eta_2 + \eta_3)$ ,  $\eta_i$  ( $i = 1, 3$ )) represents the eigenvalue of  $[T]$  that measures the relative energy carried by each single scatter is taken into account. Thus, each target vector  $\vec{k}_i$  is represented in terms of roll-invariant target scattering parameters as follows [5]

$$\vec{k}_i = (\lambda_i, m_i, \psi_i, \tau_i, \alpha_{si}, \Phi_{\alpha_{si}}) \quad (3)$$

Based on the polarimetric SAR data, Touzi and Cloude-Pottier decompositions were conducted using Polarimetric Workstation (PWS). Main parameters of the decompositions were obtained. And all the SAR parameter images derived from polarimetric decompositions were converted from slant to ground range, followed by an ortho-rectification. Then based on the ground data, rice fields were located on the images and various polarimetric parameters of rice were extracted. Figure 1 shows the flowchart of SAR data processing and all the parameters acquired.

#### 4. RESULTS AND DISCUSSION

By comparison the parameters aforementioned, it was found that the Touzi decomposition was more sensitive to rice than Cloude-Pottier decomposition, especially Dominant symmetric scattering type amplitude  $\alpha_{s1}$ . Figure 2 showed the images of Touzi- $\alpha_{s1}$  and Cloude average scattering angle  $\alpha$ . Rice fields on the image of Touzi- $\alpha_{s1}$  are much more clearly than that on the Cloude- $\alpha$ .

In addition, the parameters of Touzi decomposition are more sensitive to changes with rice growth. Their variations of with rice growth were displayed in Figure 3. It can be seen that  $\Phi_{\alpha_{s1}}$  and  $\alpha_{s1}$  decreased gradually with the growth of rice, showing more regularity.  $\Phi_{\alpha_{s1}}$  is the most sensitive parameters to rice growth. It decreased more than 32 degree from the heading stage to rice harvest and the variation showed a similar linear correlation with rice growth. As the period that from heading to harvest is a crucial stage for rice yield,  $\Phi_{\alpha_{s1}}$  maybe an important parameter for rice yield estimation. Moreover,  $\tau_2$  and  $\psi_1$  are also sensitive to rice growth, however, their variations are more random and the ranges of variation are both less than  $\pm 1.5$  degrees.

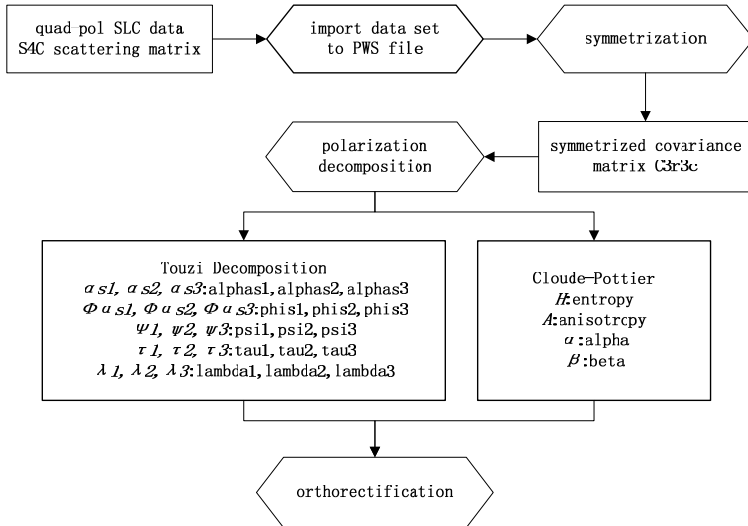


Figure 1: The flowchart of SAR data processing.

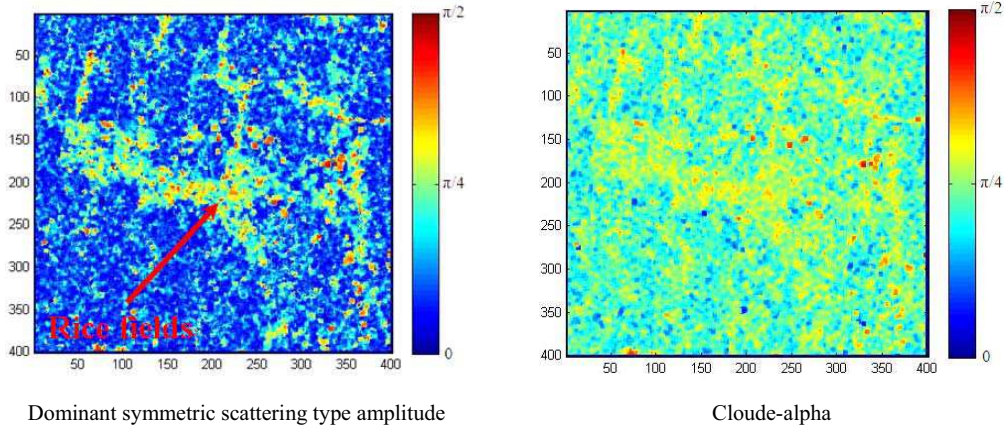
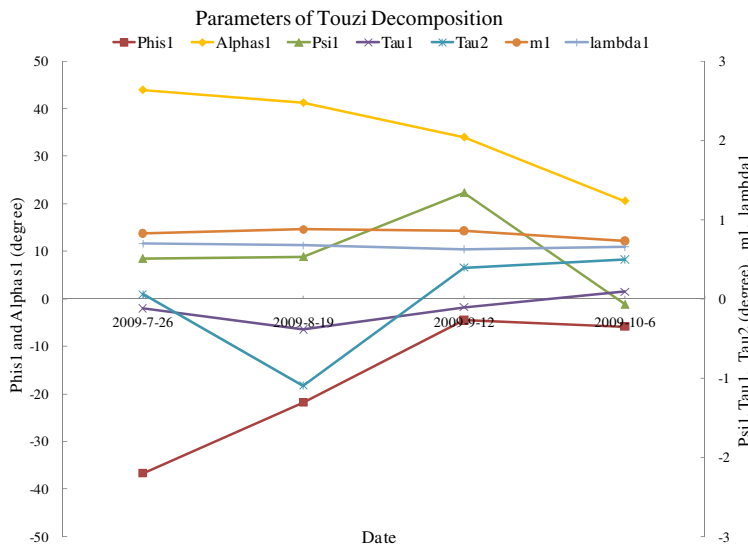


Figure 2: Rice fields on the images of Dominant symmetric scattering type amplitude and Cloude-alpha.

Figure 3: The variations of Touzi parameters with rice growth. (left) The values of  $\Alpha_{s1}$  and  $\Phi_{s1}$  are belong to the main axis; (right) other parameters' values are according to the secondary axis. The unit of all angles is degree.

## 5. CONCLUSION

In this paper, a multi-temporal Radarsat-2 polarimetric data set of a rice growing region in China was used to evaluate the Touzi decomposition for rice monitoring. The initial results showed that the Touzi decomposition were promising in rice identification and monitoring. The dominant symmetric scattering type amplitude was more sensitive to rice information. And the dominant symmetric scattering type phase is the most sensitive parameter to rice growth changes. In future, a controlled experiment with detailed ground truth on the distribution of plant biomass and water content in the rice canopy will be conducted to further develop the use of the Touzi decomposition for rice monitoring.

## ACKNOWLEDGMENT

This work was supported by the Knowledge Innovation Program of the Chinese Academy of Sciences (KZCX2-YW-313), the National High Technology Research and Development Program (2007AA12Z168) and State Key Laboratory of Remote Sensing Science, IRS/CAS. The author would like to thank CCRS for having licenced the PWS software for polarimetric image analysis.

## REFERENCES

1. Le Toan, T., F. Ribbes, L. F. Wang, N. Flouri, K. H. Ding, J. A. Kong, M. Fujita, and T. Kurosu, “Rice crop mapping and monitoring using ERS-1 data based on experiment and modeling results,” *IEEE Trans. Geosci. Remote Sens.*, Vol. 35, No. 1, 41–56, 1997.
2. Shao, Y., J. J. Liao, and C. Z. Wang, “Analysis of temporal radar backscatter of rice: A comparison of SAR observations with modeling results,” *Can. J. Remote Sens.*, Vol. 28, No. 2, 128–138, 2002.
3. Shao, Y., X. T. Fan, H. Liu, J. H. Xiao, S. Ross, B. Brisco, R. Brown, and G. Staples, “Rice monitoring and production estimation using multi-temporal RADARSAT,” *Remote Sens. Environ.*, Vol. 76, No. 3, 310–325, 2001.
4. Bouvet, A., T. Le Toan, and N. Lam-Dao, “Monitoring of the rice cropping system in the Mekong Delta using ENVISAT/ASAR dual polarization data,” *IEEE Trans. Geosci. Remote Sens.*, Vol. 47, No. 2, 517–526, 2009.
5. Touzi, R., “Target scattering decomposition in terms of roll-invariant target parameters,” *IEEE Trans. Geosci. Remote Sens.*, Vol. 45, No. 1, 73–84, 2007.
6. Touzi, R., “Wetland characterization using polarimetric RADARSAT-2 capability,” *Can. J. Remote Sens.*, Vol. 33, S56–S67, 2007.
7. Touzi, R., A. Deschamps, and G. Rother, “Phase of target scattering for wetland characterization using polarimetric C-band SAR,” *IEEE Trans. Geosci. Remote Sens.*, Vol. 47, No. 9, 3241–3261, 2009.
8. Touzi, R., R. Landry, and F. J. Charbonneau, “Forest type discrimination using calibrated C-band polarimetric SAR data,” *Can. J. Remote Sens.*, Vol. 30, No. 3, 543–551, 2004.
9. Touzi, R., R. K. Raney, and F. Charbonneau, “On the use of symmetric scatterers for ship characterization,” *IEEE Trans. Geosci. Remote Sens.*, Vol. 42, No. 10, 2039–2045, 2004.

# Dual-band Circularly Polarized CPW-fed Circular Slot Antenna with Two Opened-ground Rings for GPS and WLAN Applications

Sheau-Shong Bor<sup>1</sup>, Chia-Yen Wei<sup>2</sup>, Tian-Fu Hung<sup>2</sup>, Ji-Chyun Liu<sup>3</sup>, and Hai-Tao Sun<sup>1</sup>

<sup>1</sup>Department of Electrical Engineering, Feng-Chia University, Taichung, Taiwan, R.O.C.

<sup>2</sup>Program in Electrical and Communications Engineering, Feng-Chia University, Taichung, Taiwan, R.O.C.

<sup>3</sup>Department of Electrical Engineering, Ching Yun University, Chung-Li, Tao-yuan, Taiwan, R.O.C.

**Abstract**— This paper presents a novel dual-band circularly polarized CPW-fed circular slot antenna with two open-ground rings. The proposed antenna is constructed with two opened-ground rings facing in opposite directions and embedded in the circular slot and the enhanced feed strip of CPW. By way of adjusting the relevant parameters, we can obtain the dualband at 1.57 GHz and 2.46 GHz individually. A smaller frequency ratio of 1.56 is presented. The measured 10 dB return loss bandwidth are 380 MHz (24.68%) for 1.57 GHz band and 210 MHz (8.33%) for 2.46 GHz band. The measured 3 dB axial ratio bandwidth for 1.57 GHz and 2.46 GHz bands are 1338% and 8%, the polarization of radiation patterns are RHCP and LHCP for each band and the antenna gain are 3.72 and 3.21 dBiC respectively.

## 1. INTRODUCTION

Recently, coplanar waveguide (CPW) slot antenna has received considerable attention owing to its preferable characteristics, such as easy fabrication, low profile and wide bandwidths. In practice, several types of circularly polarized CPW-fed slot antenna have been developed [1–8]. The dualband CP operations can be realized by taking an inverted-L slit [1] or two spiral slots [2] in the ground plane. Various configurations include the band-notch antenna [3], the dual-monopole antenna [4–6], and the annular ring slot antenna [7]. Recently, the CPW-fed annular-ring slot antenna and with a pair of inverted-L grounded strips was proposed [7, 8]. In this paper, the improved CPW-fed circular slot antenna embedded with two open-ground rings is designed for achieving dual-band and circular polarizations. Both simulated and experimental results show the performance of the proposed antenna. It can be applied to WLAN and GPS systems.

## 2. ANTENNA CONFIGURATION

In Fig. 1, the proposed slot antenna is implemented on a commercial substrate. The ground plane under the substrate is square shape and dimension is  $W \times L = 70 \times 70 \text{ mm}^2$ . The  $50\Omega$  microstrip feed-line is excited with a SMA connector. The FR4 substrate with thickness 0.8 mm and relative permittivity 4.4 is used. The detail dimensions in Fig. 1(b) are  $R_0 = 20.0 \text{ mm}$ ,  $L_t = 10.0 \text{ mm}$ ,  $W_t = 4.2 \text{ mm}$ ,  $G_t = 0.3 \text{ mm}$ ,  $r_1 = r_2 = 13.0 \text{ mm}$ ,  $s_1 = s_2 = 2.0 \text{ mm}$ ,  $g_1 = g_2 = 2.0 \text{ mm}$ ,  $d_1 = 3.86 \text{ mm}$ ,  $d_2 = 5.14 \text{ mm}$  and  $\theta_1 = 57.0^\circ$ ,  $\theta_2 = 63.5^\circ$ .

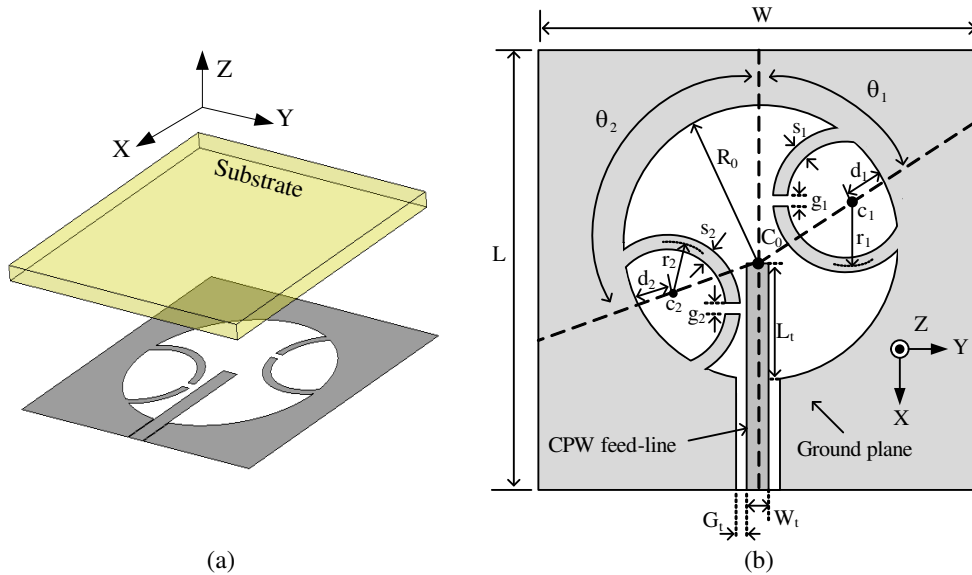


Figure 1: (a) Structure of the proposed antenna. (b) Geometry perspective of the proposed antenna.

### 3. SIMULATION AND EXPERIMENTS

The spectrums and radiation patterns are simulated by using commercial software of Ansoft HFSS [9]. The return loss spectrums of the proposed antenna are shown in Fig. 2. It is evident that the simulated and measured results of frequency responses are in good agreement. In measurement, while the reflection coefficient is smaller than -10dB, the frequency responses cover two bands, from 1.35 to 1.73 GHz (bandwidth = 380 MHz, 24.68%) and from 2.32 to 2.53 GHz (bandwidth = 210 MHz, 8.32%). Fig. 3 illustrates the axial ratio spectrums. The measured AR

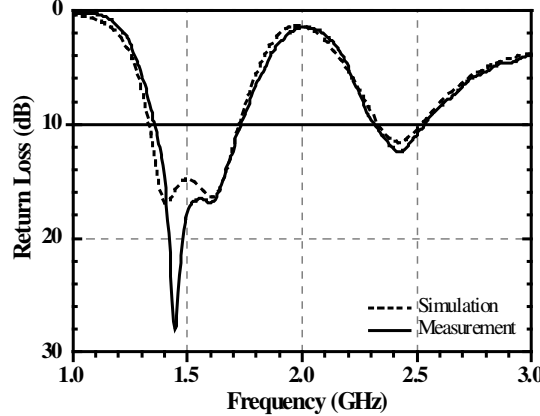


Figure 2: Return loss spectrums.

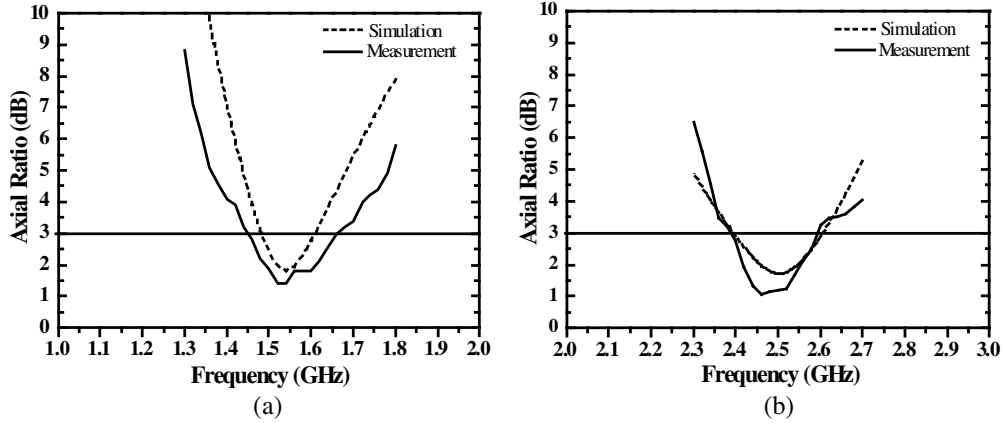


Figure 3: AR Spectrum. (a) 1.57 GHz, (b) 2.46 GHz.

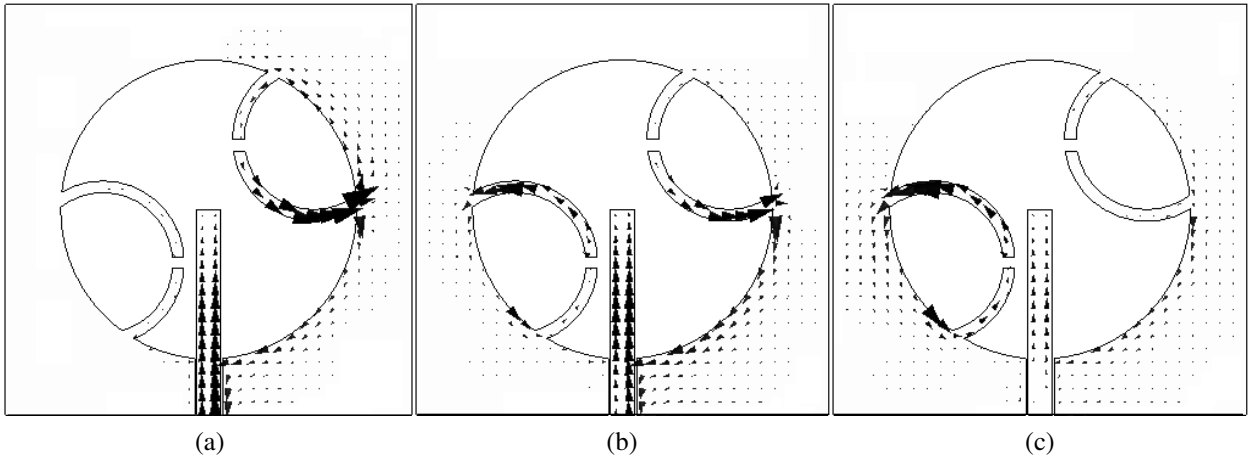


Figure 4: Simulated vector current distributions at 1.57 GHz. (a) 0 degree, (b) 45 degree, (c) 90 degree.

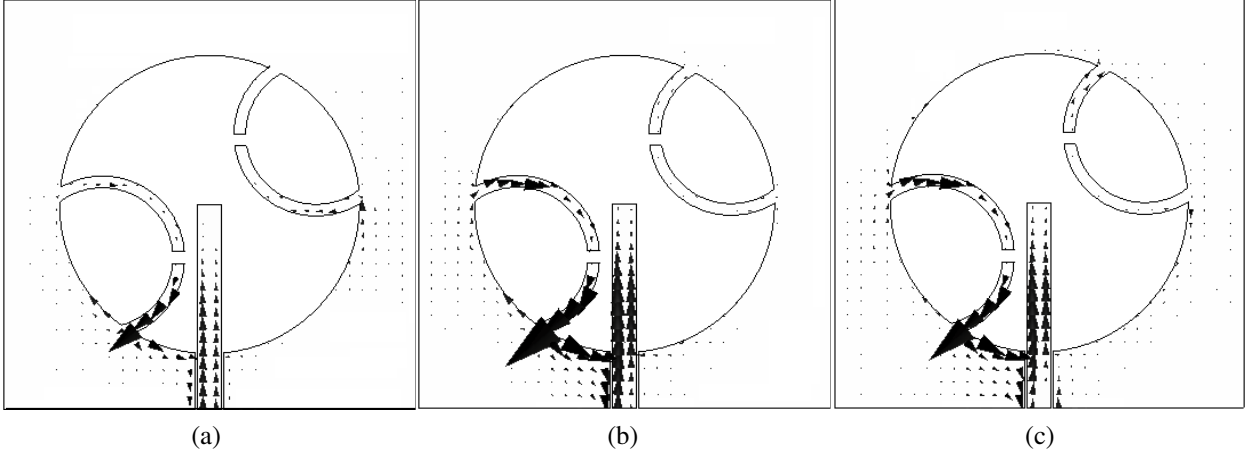


Figure 5: Simulated vector current distributions at 2.46 GHz. (a) 0 degree, (b) 45 degree, (c) 90 degree.

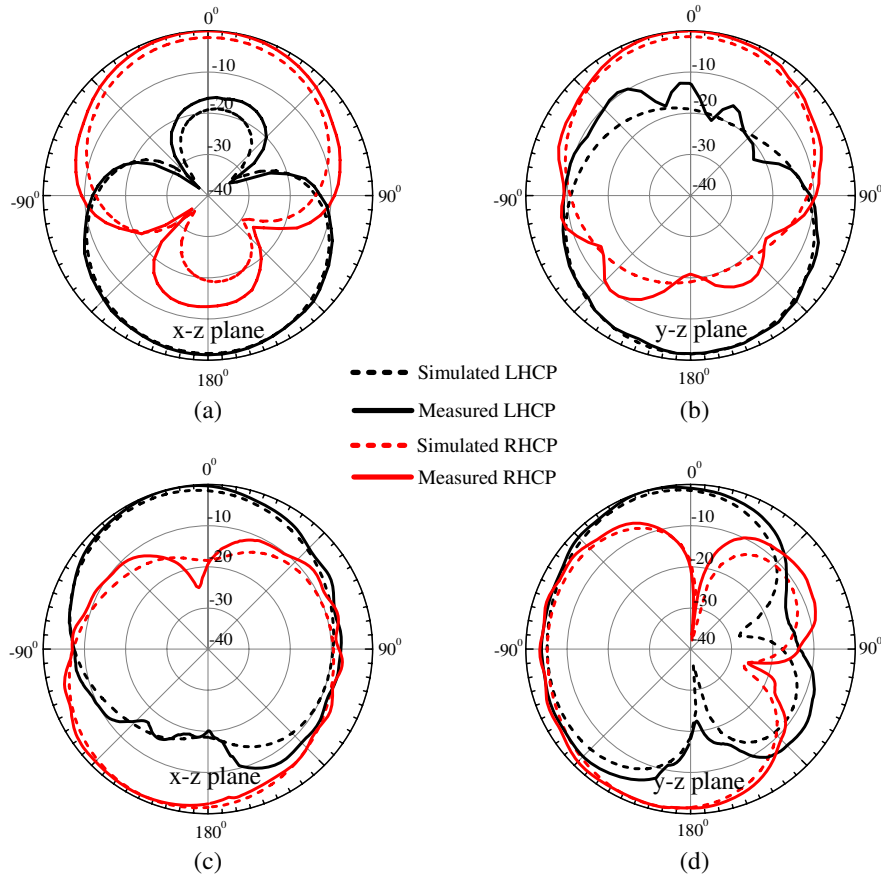


Figure 6: Radiation patterns. (a)  $x$ - $z$  plane at 1.57 GHz, (b)  $y$ - $z$  plane at 1.57 GHz, (c)  $x$ - $z$  plane at 2.46 GHz, (d)  $y$ - $z$  plane at 2.46 GHz.

bandwidths are 1338% (from 1.45 to 1.66 GHz) and 8.0% (from 2.391 to 2.59 GHz) for each band. CP characteristics are observed. The frequency ratio is 1.56 (1.57 GHz/2.46 GHz).

Both Fig. 4 and Fig. 5 exhibit the vector current distributions of the proposed antenna. They provide a physical insight on the CP of the antenna. The enhanced feed lines are excited with concentrating current distributions to induce the two opened-ground rings. Fig. 4 (a) shows that the right opened-ground ring is induced with left-band circularly polarized (LHCP) at  $0^\circ$  phase at first, and then the left opened-ground ring is expressed with RHCP at  $45^\circ$  and  $90^\circ$  phases in Figs. 4(b) and (c). Thus the 1.57 GHz band generates RHCP radiations mainly in the  $+z$  directions. Figs. 5(a) to (c) present that the left opened-ground rings are induced with LHCP at  $0^\circ$ ,  $45^\circ$  and  $90^\circ$  phases,

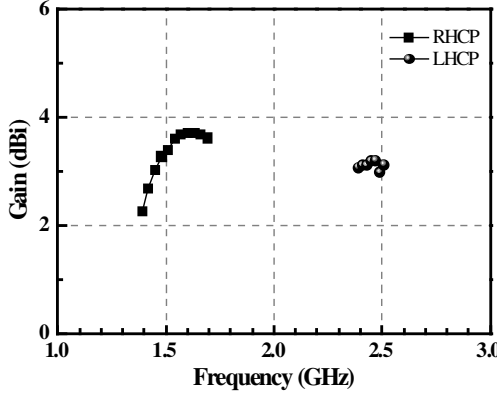


Figure 7: Measured antenna gains.

the 2.46 GHz band provide LHCp radiations in the  $+z$  directions.

In field analyses, Figs. 6(a) to (d) show the measured and simulated two-cut ( $x$ - $z$  plane and  $y$ - $z$  plane) radiation patterns at 1.57 GHz and 2.46 GHz, respectively. Both the measured and simulated radiation patterns are in good agreement. Since the planar antenna is a bidirectional radiator thus both sides of the antenna are opposite polarizations. Noted that the maximum fields tilt with  $-15^\circ$  to the  $+z$  directions at 2.46 GHz band In Fig. 7, the measured antenna gains deliver  $2.2 \sim 3.72$  dBic for 1.57 GHz band, and have approximately 3.21 dBic for 2.46 GHz band.

#### 4. CONCLUSIONS

A novel dual-band circularly polarized CPW-fed circular slot antenna with two open-ground rings is designed and measured. The two open-ground rings induce the performance of CP and wide AR bandwidth. The measured impedance and axial ratio bandwidths are 24.68% and 8.32% for the 1.57 GHz band, and 1338% and 8.0% for the 2.46 GHz band. The smaller 1.56 frequency ratio is obtained. The directional patterns with 3.72 dBic and 3.21 dBic peak power gains are obtained for 1.57 GHz and 2.46 GHz bands. The CP radiation patterns deliver RHCp and LHCp in the  $+z$  direction for 1.57 GHz and 2.46 GHz bands. For applications, the frequency responses of the proposed antenna are covered in the operation bands of WLAN and GPS bands.

#### REFERENCES

1. Jou, C. F., J. W. Wu, and C. J. Wang, "Novel broadband monopole antennas with dual-band circular polarization," *IEEE Trans. Antennas Propag.*, Vol. 57, No. 4, 1027–1034, Apr. 2009.
2. Chen, C. and E. K. N. Yung, "Dual-band dual-sense circularly-polarized CPW-fed slot antenna with two spiral slots loaded," *IEEE Trans. Antennas Propag.*, Vol. 57, No. 6, 1829–1833, Jun. 2009.
3. Lin, Y. C. and K. J. Hung, "Compact ultrawideband rectangular aperture antenna and band-notched designs," *IEEE Trans. Antennas Propag.*, Vol. 54, 3075–3081, Nov. 2006.
4. Chen, H. D. and H. T. Chen, "A CPW-Fed dual-frequency monopole antenna," *IEEE Trans. Antennas Propag.*, Vol. 52, No. 4, 978–982, Apr. 2004.
5. Kim, T. H. and D. C. Park, "CPW-fed compact monopole antenna for dual-band WLAN applications," *Elect. Lett.*, Vol. 41, No. 6, 291–293, Mar. 2005.
6. Liu, W. C. and C. F. Hsu, "Dual-band CPW-fed Y-shaped monopole antenna for PCS/WLAN application," *Elect. Lett.*, Vol. 41, No. 7, 390–391, Mar. 2005.
7. Chen, J. S., "Dual-frequency annular-ring slot antennas fed by CPW feed and microstrip line feed," *IEEE Trans. Antennas Propag.*, Vol. 53, No. 1, 569–571, Jan. 2005.
8. Sze, J. Y. and C. C. Chang, "Circularly polarized square slot antenna with a pair of inverted-L grounded strips," *IEEE Antennas and Wireless Propag. Lett.*, Vol. 7, 149–151, 2008.
9. HFSS version 11.0, Ansoft Software Inc., 2007.

# Compact Dual-band Monopole Antenna for WLAN/WiMAX Applications

Chia-Hao Ku<sup>1</sup>, Hsien-Wen Liu<sup>2</sup>, Di-Yu Lin<sup>1</sup>, and Yao-Xin Ding<sup>1</sup>

<sup>1</sup>Department of Electrical Engineering, Ming Chi University of Technology, Taipei, Taiwan, R.O.C.

<sup>2</sup>Technological Research Center, Auden Techno Corp., Taoyuan, Taiwan, R.O.C.

**Abstract**— A novel, compact dual-band monopole antenna for WLAN and WiMAX applications is proposed in this paper. This antenna with a key-like slot is fabricated using a 0.8 mm-thick FR4 substrate, which only occupies a small area of  $8(L) \times 8(W)$  mm<sup>2</sup> to be easily embedded inside a portable device as an internal antenna. By properly designing the key-like slot etched on the radiator, two operating frequency bands covering 2.39–2.51 GHz and 4.57–5.99 GHz can be achieved with our antenna. The resonant properties of the antenna are also tunable while various lengths and widths of the slot are adopted. Nearly omnidirectional coverage with stable receiving performance for actual applications can be obtained due to the antenna. Simulated and measured results are performed and analyzed. With a compact size, the proposed monopole antenna may well work as an internal antenna in a portable device for WLAN/WiMAX operations.

## 1. INTRODUCTION

Recently, increasing demands such as compact size and multi-mode operation in antenna design for wireless communication have attracted high attention. Many promising antennas to meet wireless local area network (WLAN: 2.4–2.483 GHz, 5.15–5.35 GHz and 5.725–5.85 GHz) and worldwide interoperability for microwave access (WiMAX: 5.25–5.85 GHz) operations have been studied in [1–8]. Several planar printed antennas using a wide-slot structure to achieve a wideband property for WLAN/WiMAX applications were discussed in [1, 2]. To serve more communication systems, some multiband antenna designs with open or symmetric slots have been presented in [3–8]. These antenna designs, however, can not be integrated within a portable device as an internal antenna due to their sizes. To this end, we propose a compact dual-band monopole antenna suitable for WLAN and WiMAX operations. By etching a key-like slot on the radiator, two resonant modes to operate at 2.4/5 GHz can be obtained in our antenna. For practical receiving application, the proposed antenna with a small size of  $8(L) \times 8(W)$  mm<sup>2</sup> can realize better radiation performance by tuning the length and width of the slot. Details of the antenna design are described in Section 2, and a fabricated prototype of the antenna is constructed and experimentally studied in Section 3. Finally, this paper will be concluded with a brief summary in Section 4.

## 2. ANTENNA DESIGN

Figure 1(a) depicts the whole geometry with detailed design parameters of the proposed dual-band monopole antenna, which is fabricated on a 0.8 mm-thick FR substrate with dielectric constant  $\epsilon_r = 4.4$  and loss tangent  $\tan \delta = 0.02$ . The overall dimension of the antenna is merely about  $8(L) \times 8(W)$  mm<sup>2</sup> to be easily embedded inside a portable device as an internal antenna. A constructed prototype of the proposed antenna for measurements is indicated in Fig. 1(b). In this study, a key-like slot is etched on the surface of the antenna to create two resonant modes for achieving 2.4/5 GHz operating bands. It is obvious that a longer meander strip on the top of the antenna is working for the lower band, as shown in Fig. 2(a). Different from conventional monopole antennas based on a multi-branch structure, the upper band of the antenna can be attained through an electromagnetic coupling. Figs. 2(b) and (c) respectively simulate the current distributions at 5.2 GHz and 5.8 GHz to observe the antenna resonance. We can find that the energy can be coupled from the feed point to the longer meander strip, so a wide bandwidth for upper band operation can be acquired in our design. By using such a coupling structure, the antenna size can be reduced as well. Moreover, both the length and width of the slot can be flexibly adjusted to control the coupling between the meander strip and the slot. Consequently, the effects about frequency shift caused by the antenna adjacent to the casing can be properly tackled. An electromagnetic software package, HFSS, has been used to construct the antenna model, whose electrical features and radiation performance are thoroughly analyzed as well. The design parameters optimized for the proposed antenna have been determined with  $L = 30$  mm,  $L_1 = 8$  mm,  $L_2 = 5$  mm,  $L_3 = 2$  mm,  $L_4 = 1.6$  mm,  $L_5 = 0.4$  mm,  $L_6 = 4.6$  mm,  $W = 35$  mm,  $W_1 = 18$  mm,  $W_2 = 8$  mm,  $W_3 = 17$  mm,  $W_4 = 0.4$  mm,  $W_5 = 2.6$  mm,  $W_6 = 0.4$  mm,  $W_7 = 0.4$  mm, and  $W_8 = 0.8$  mm.

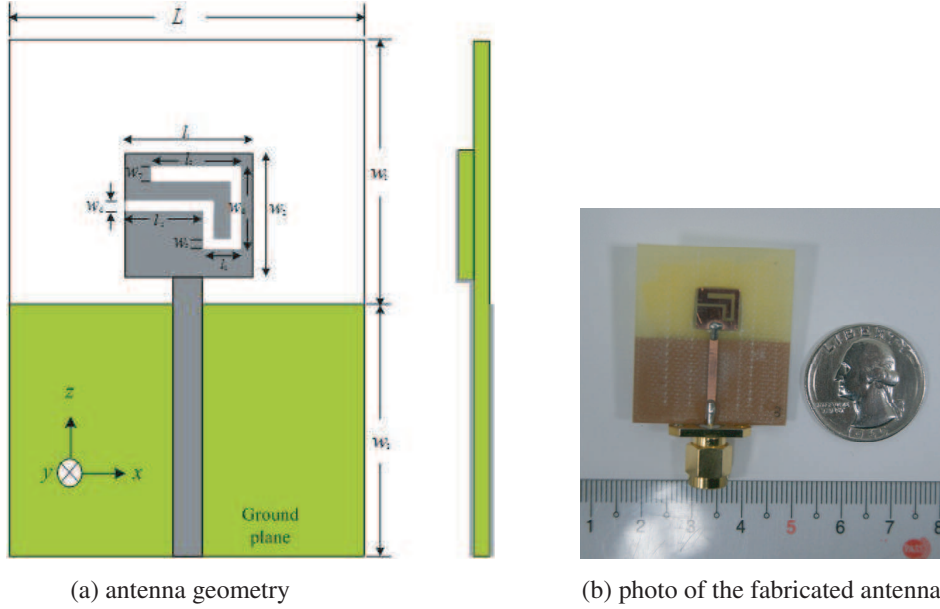


Figure 1: The proposed compact dual-band monopole antenna ( $L = 30$  mm,  $L_1 = 8$  mm,  $L_2 = 5$  mm,  $L_3 = 2$  mm,  $L_4 = 1.6$  mm,  $L_5 = 0.4$  mm,  $L_6 = 4.6$  mm,  $W = 35$  mm,  $W_1 = 18$  mm,  $W_2 = 8$  mm,  $W_3 = 17$  mm,  $W_4 = 0.4$  mm,  $W_5 = 2.6$  mm,  $W_6 = 0.4$  mm,  $W_7 = 0.4$  mm, and  $W_8 = 0.8$  mm).

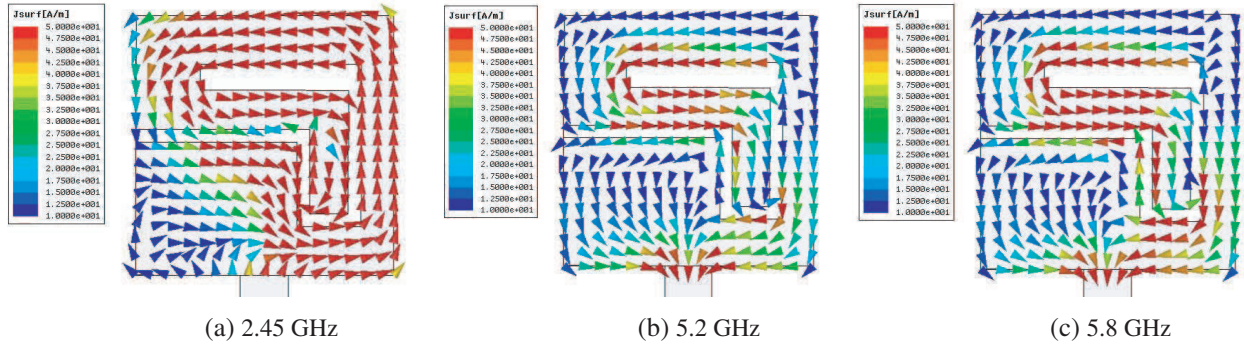


Figure 2: Simulated current distributions against three resonant frequencies of the proposed antenna.

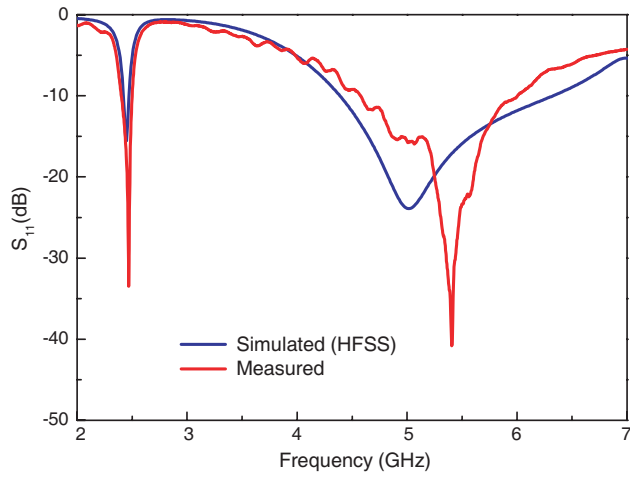


Figure 3: Simulated and measured return losses of the proposed antenna.

### 3. EXPERIMENTAL RESULTS AND DISCUSSION

A fabricated prototype of the proposed antenna was implemented and tested. The antenna performance was examined by using a vector network analyzer (Agilent 8362B). Fig. 3 illustrates the simulated and measured return losses against the frequency of the antenna. Fairly good agreement in the lower band has been achieved. A small difference in the upper band is mainly attributed to fabrication inaccuracy. According to 10 dB return loss, two measured impedance bandwidths have been determined to be about 2.39–2.51 GHz and 4.57–5.99 GHz, corresponding to 4.9% and 26.9%, respectively. It is noted that the WLAN of 2.4–2.483 GHz, 5.15–5.35 GHz and 5.725–5.85 GHz as well as WiMAX of 5.25–5.85 GHz can be satisfactorily covered. In this work, a suitable gap between the antenna and the ground plane is also critical for achieving better antenna performance. Fig. 4(a) reveals the simulated return losses with different gaps of the antenna. It is clear that good antenna performance can be received when the gap is larger than 0.5 mm.

On the other hand, several possible ground lengths for practical application of the antenna are simulated and compared in Fig. 4(b). Owing to the proposed antenna based on a monopole structure, it may work with stable performance if the ground length is longer than 7 mm. The measured far-field radiation patterns in the  $xz$ ,  $yz$  and  $xy$  planes at 2.45 GHz, 5.2 GHz and 5.8 GHz for the antenna are given in Fig. 5. Nearly good omnidirectional patterns in the  $xy$  plane have been received across these three frequencies. Fig. 6 exhibits the measured peak gains and radiation

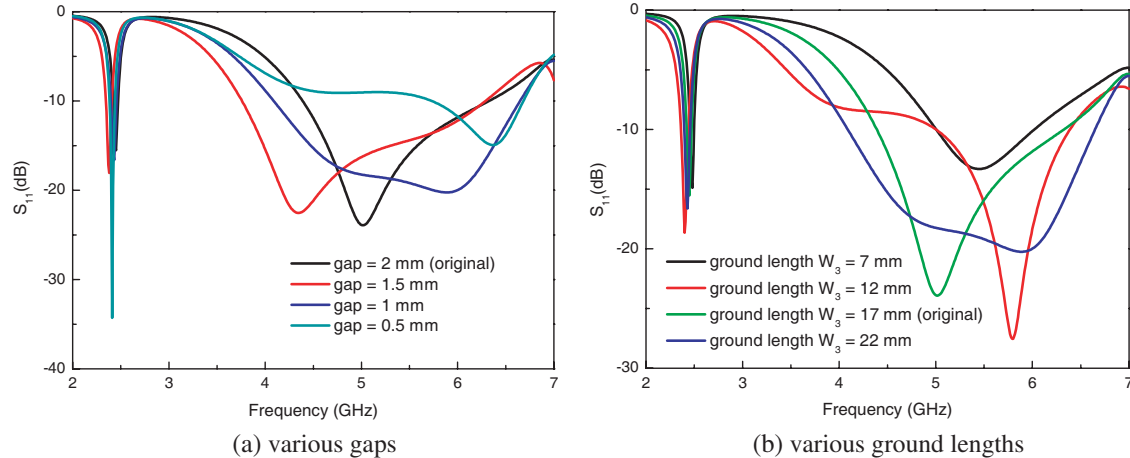
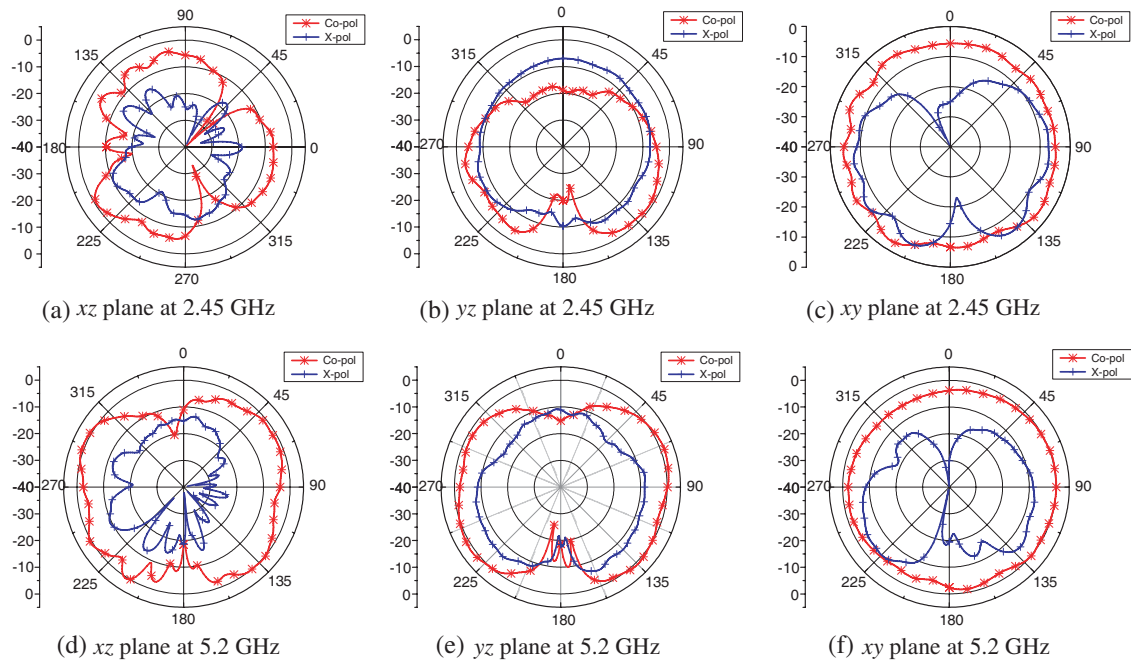


Figure 4: Simulated return losses with various gaps and ground lengths of the proposed antenna.



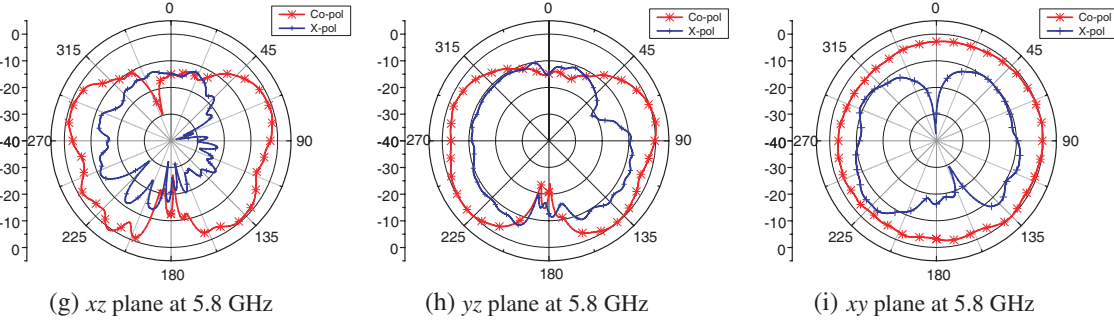


Figure 5: Measured radiation patterns at three definite frequencies of the proposed antnena.

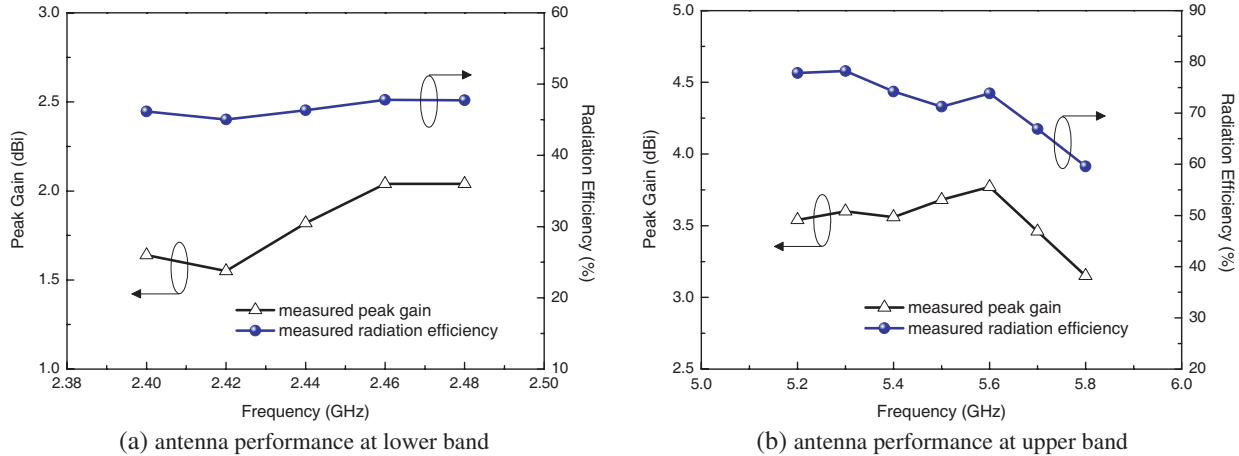


Figure 6: Measured peak gain and radiation efficiency of the proposed antenna.

efficiencies of the antenna. As shown in Fig. 6(a), the antenna gain varies from 1.55 to 2.04 dBi and the radiation efficiency is larger than 45% for the lower band. Referring to the upper band results shown in Fig. 6(b), the antenna can radiate with a gain range of 3.15–5.6 dBi and its efficiency is better than 60%. Good communication quality for WLAN/WiMAX operations can be thus acquired due to the proposed antenna.

#### 4. CONCLUSIONS

A compact printed monopole antenna for WLAN and WiMAX operations has been presented and studied in this paper. It simply uses a key-like slot etched on the radiator to achieve good dual-band property, in which the upper band is designed using an electromagnetic coupling. As for actual application, the antenna may tune its resonant properties to overcome the effects due to the antenna adjacent to the casing. Experimental results show that good omnidirectional coverage with stable gain variation can be achieved with our antenna design. For these reasons, the proposed planar dual-band monopole antenna with a small size will be a promising solution in a portable device as an internal antenna for WLAN/WiMAX applications.

#### REFERENCES

1. Liu, Y.-F., K.-L. Lau, Q. Xue, and C.-H. Chen, “Experimental studies of printed wide-slot antenna for wide-band applications,” *IEEE Antennas Wireless Propag. Lett.*, Vol. 3, No. 1, 273–275, 2004.
2. Jan, J.-Y. and J.-W. Su, “Bandwidth enhancement of a printed wide-slot antenna with a rotated slot,” *IEEE Trans. Antennas Propag.*, Vol. 53, No. 6, 2111–2114, Jun. 2005.
3. Chen, W.-S. and K.-Y. Ku, “Band-rejected design of the printed open slot antenna for WLAN/WiMAX operation,” *IEEE Trans. Antennas Propag.*, Vol. 56, No. 4, 1163–1169, Apr. 2008.
4. Chaimool, S. and K.-L. Chung, “CPW-fed mirrored-L monopole antenna with distinct triple bands for WiFi and WiMAX applications,” *Electron. Lett.*, Vol. 45, No. 18, 928–929, Aug. 2009.

5. Thomas, K. G. and M. Sreenivasan, "Compact triple band antenna for WLAN/WiMAX applications," *Electron. Lett.*, Vol. 45, No. 16, 811–813, 2009.
6. Kim, T.-H. and D.-C. Park, "Compact dual-band antenna with double L-slits for WLAN operations," *IEEE Antennas Wireless Propag. Lett.*, Vol. 4, 249–252, 2005.
7. Wu, C.-M., C.-N. Chiu, and C.-K. Hsu, "A new nonuniform meandered and fork-type grounded antenna for triple-band WLAN applications," *IEEE Antennas Wireless Propag. Lett.*, Vol. 5, 346–348, 2006.
8. Pan, C.-Y., T.-S. Horng, W.-S. Chen, and C.-H. Huang, "Dual wideband printed monopole antenna for WLAN/WiMAX applications," *IEEE Antennas Wireless Propag. Lett.*, Vol. 6, 149–151, 2007.

# Synthesizing a High Gain Planar Array Antenna for Volume Scanning Arrays

Fikret Tokan and Filiz Güneş

Department of Electronics and Communication Engineering, Faculty of Electrics and Electronics  
Yıldız Technical University, Yıldız 34349, Istanbul, Turkey

**Abstract**— In this work, a rectangular planar array antenna which can scan  $0^\circ \leq \theta \leq 60^\circ$  region in  $\phi = 0^\circ$  principal plane is synthesized to be used in volume scanning radars. Radiation patterns of each linear array constituting the rectangular planar array are steered to the determined directions in order to generate a super positioned  $60^\circ$  width radiation pattern. In this process, rectangular patch antennas are utilized in each of these linear antenna arrays. The radiation pattern designed for volume scanning in the desired region is verified by using FEKO, full-wave simulation software.

## 1. INTRODUCTION

In literature, Fourier transformation [1], Woodward-Lawson [2, 3] or Dolph-Chebyshev [4] analytical methods are extensively used in case radiation pattern distribution is demanded for a whole visible region. In our work, by utilizing Dolph-Chebyshev, a narrow main-beam and low side lobe level (SLL) synthesis method, we obtained low SLL radiation patterns of each linear arrays steered to the determined directions that constitutes the rectangular planar array, thus, a super positioned  $60^\circ$  width radiation pattern is generated.

The antenna array geometry we considered in this work is a planar array antenna formed in rectangular lattice as given in Fig. 1. As it is highlighted in Fig. 1, the patch antennas are symmetrically oriented along both  $x$ -axis and  $y$ -axis with an inter-element spacing of half-wavelength between the array elements.

As known a 3-D shaped array antenna pattern can be factorized as array factor and radiation pattern of a single element in case the array elements are identical and mutual coupling effects between these array elements are neglected. The array factor  $AF(\theta, \phi)$  can be defined as follows [5]:

$$AF(\theta) = 2 \sum_{m=1}^{N_y} \sum_{n=1}^{N_x} A_{mn} \cos \left[ \left( \frac{2n-1}{2} \right) (kd_x \sin \theta + \beta_{mx}) \right] \quad (1)$$

$$\beta_{mx} = -kd_x \sin \theta_{mo} \quad (2)$$

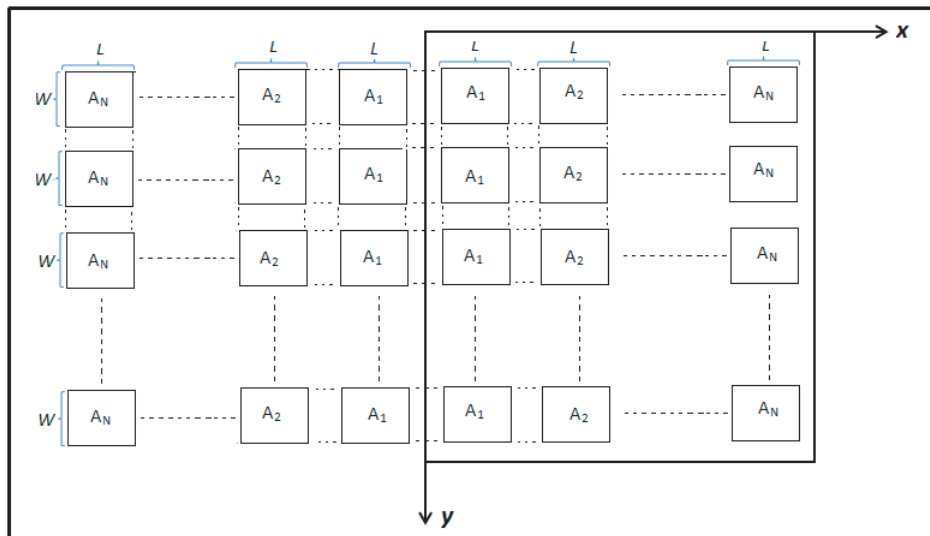


Figure 1: A rectangular planar patch antenna array.

where,  $A_{mn}$  is the excitation amplitude of the  $m$ th element and  $\beta_{mx}$  is the excitation phase of the  $m$ th element in the  $x$ th column of the planar array. Thus, the synthesis procedure given by (1) is reduced to determining the main beam direction of each sub-arrays  $\theta_{mo}$  to achieve the overall radiation pattern demand. Here, Dolph-Chebyshev method is selected to design linear sub-arrays. The radiation pattern designed for volume scanning in the desired region is verified by using the full-wave simulation software FEKO.

## 2. APPLICATION EXAMPLES

In this section we have synthesized two rectangular planar arrays formed by different number of antennas to achieve a flat top  $0^\circ \leq \theta \leq 60^\circ$  region in  $\phi = 0^\circ$  principal plane to be used in volume scanning radars. We have utilized Dolph-Chebyshev synthesis method to obtain low SLL radiation patterns of each linear arrays steered to the determined directions that form the rectangular planar array, thus, super positioned  $60^\circ$  width radiation patterns are generated.

In the first design example 4 sub-arrays located in  $x$ -plane, each including 10 rectangular patch antennas are considered. The microstrip antennas are designed using a substrate (RT/duroid 5880) with dielectric constant of 2.2,  $h = 1.58$  mm.  $W$ ,  $L$  of the antennas are 10.136 mm and 8.18 respectively, so as to resonate at 11.7 GHz. The main beams of sub-arrays are steered to  $7^\circ$ ,  $22^\circ$ ,  $37^\circ$  and  $47^\circ$  respectively to cover all the desired  $60^\circ$  width region. The maximum SLL (MSLL) of each radiation pattern is adjusted as  $-40$  dB using the appropriate Dolph-Chebyshev excitation amplitudes. These excitation amplitudes are given in Table 1. Besides, the radiation patterns of each sub-array are given in Fig. 2. The excitation phases of each antenna of the symmetrical configurationally rectangular array are also given in Table 2.

Table 1: Dolph-Chebyshev excitation amplitudes of 40 element planar antenna.

Each Sub-Array	$A_n(A)$	1.000	0.878	0.669	0.430	0.257
----------------	----------	-------	-------	-------	-------	-------

Table 2: The excitation phases of each antenna in the 40 element planar array.

Excitation Phases of Each Sub-Array	$\theta_{\max_1} = 7^\circ$	-10.96	-32.90	-54.84	-76.77	-98.71
	$\theta_{\max_2} = 22^\circ$	-33.71	-101.14	-168.57	-236	-303.43
	$\theta_{\max_3} = 37^\circ$	-54.16	-162.49	-270.81	-19.14	-127.47
	$\theta_{\max_4} = 47^\circ$	-65.82	-197.46	-329.1	-100.75	-232.39

Table 3: Dolph-Chebyshev excitation amplitudes of 120 element planar antenna.

Each Sub-Array	$A_n(A)$	1.000	0.958	0.880	0.772	0.646	0.512	0.381	0.264	0.166	0.118
----------------	----------	-------	-------	-------	-------	-------	-------	-------	-------	-------	-------

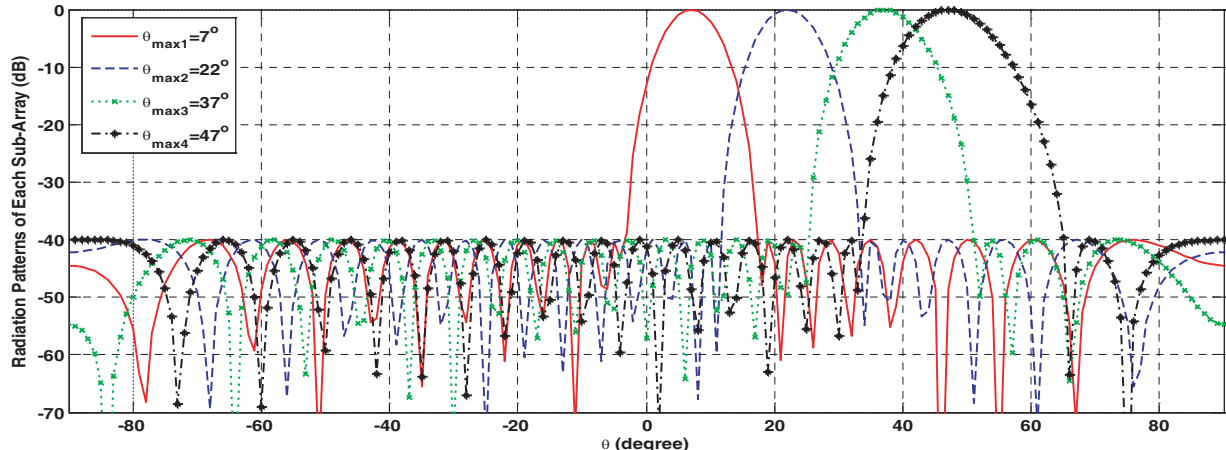


Figure 2: The radiation patterns of each sub-array obtained using the excitation amplitudes given in Table 1.

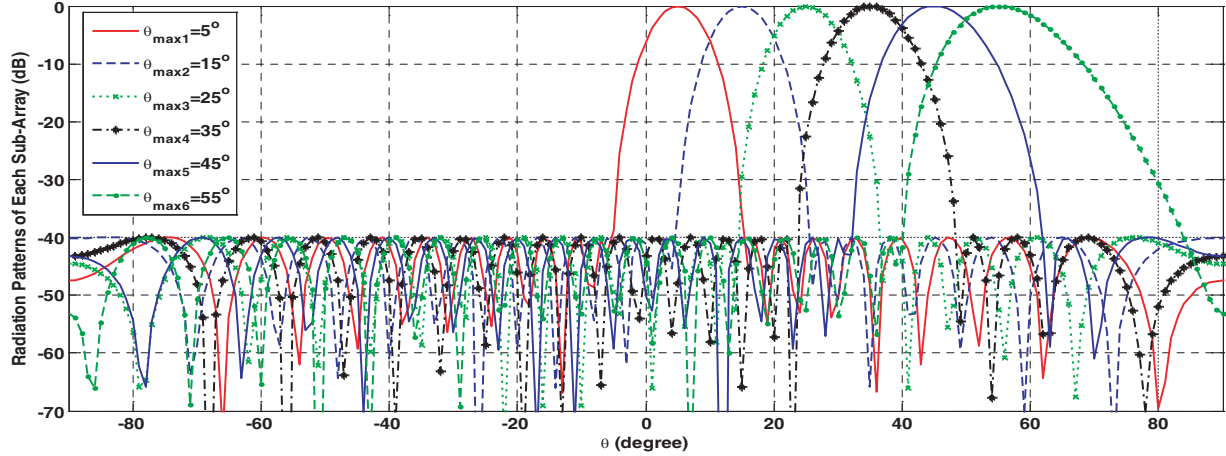


Figure 3: The initial radiation patterns of each sub-array obtained using the excitation amplitudes given in Table 3.

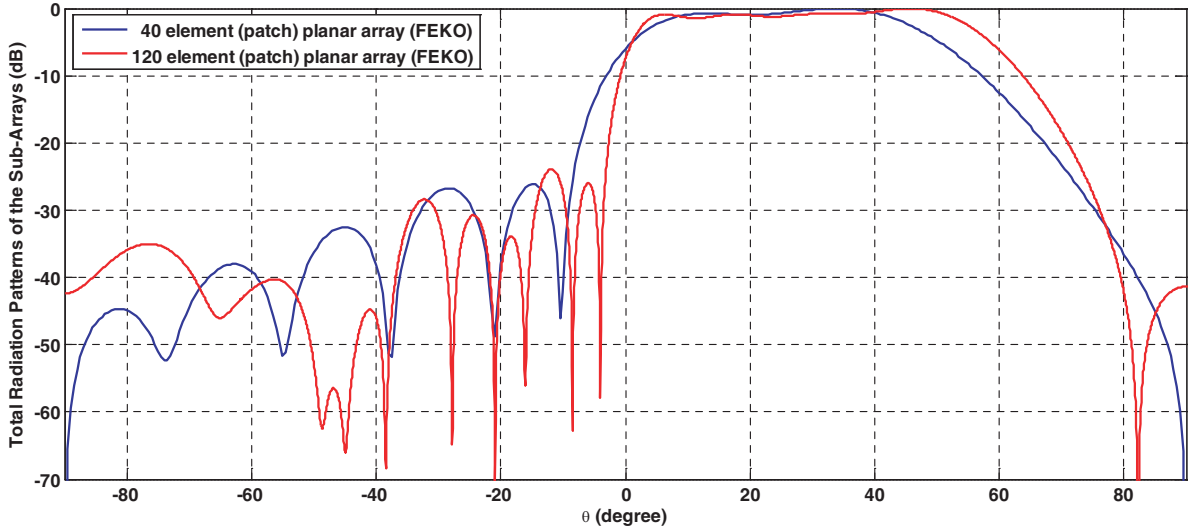


Figure 4: The FEKO simulations of the 40 element and 120 element planar arrays.

In order to state the effects of the number of antennas in a sub-array and the number of antennas in the planar array we have also designed a 120 element rectangular array which is formed by 6 sub-arrays located in  $x$ -axis each including 20 rectangular patches. The main beams of sub-arrays are steered to  $5^\circ$ ,  $15^\circ$ ,  $25^\circ$ ,  $35^\circ$ ,  $45^\circ$  and  $55^\circ$  respectively. The MSLL is also adjusted as  $-40$  dB using appropriate excitation amplitudes. The excitation amplitudes are given in Table 3. The radiation patterns of each sub-array steered to the determined directions are also given in Fig. 3.

The FEKO electromagnetic simulation software is utilized to obtain results of the total radiation patterns of the sub-arrays having 40 and 120 microstrip elements as given in Fig. 4. It is clear from Fig. 4 that, the increase in the number of sub-arrays and the number of antennas in each-sub array resulted in a better harmony with the desired radiation pattern. It can be concluded that when the number of antennas in the array increases, the resulted radiation pattern will approach to the exact desired pattern.

## REFERENCES

1. Booker, H. G. and P. C. Clemmow, "The concept of an angular spectrum of plane waves, and its relation to that of polar diagram and aperture distribution," *Proc. IEE (London)*, Radio Section, Vol. 97, 11–17, Paper No. 992, 1952.
2. Woodward, P. M., "A method for calculating the field over a plane aperture required to produce a given polar diagram," *J. IEE*, Vol. 93, 1554–1558, 1946.

3. Woodward, P. M. and J. D. Lawson, "The theoretical precision with which an arbitrary radiation pattern may be obtained from a source of finite size," *J. IEE*, Vol. 95, 363–370, 1948.
4. Dolph, C. L., "A current distribution for broadside arrays which optimizes the relationship between beamwidth and sidelobe level," *Proc. IRE*, Vol. 34, 335–345, 1946.
5. Stutzman, W. L. and G. A. Thiele, *Antenna Theory and Design*, John Wiley & Sons, New York, 1998.

# Design and Construction of UWB Antennas

**J. Sosa-Pedroza, E. Garduño-Nolasco, F. Martínez-Zúñiga, and M. Enciso**

Instituto Politécnico Nacional, SEPI-ESIME-Zacatenco, Edif. Z-4 3er Piso, CP 07738, México

**Abstract**— We present design results of two cases of Ultra Wide Band (UWB) quasi circular patch antennas, one with coplanar feeding (CPW) and the other one with microstrip feeding. Both antennas are an evolution from a circular patch structure softening the edges to improve the antenna performance, agreeing with the theory proposed Kraus. After the evolution there were improvements concerning reflection coefficient and number of resonant frequencies throughout the operating bandwidth. The operational frequency range is from 500 MHz to 15 GHz using a design frequency of 4.5 GHz. The antenna feeding impedance is proposed to be 50 ohms. The antennas with the best simulation response are constructed to test the practical performance of experiment.

## 1. INTRODUCTION

The technique to increase the bandwidth (BW) of circular antenna was proposed by Kraus in 1988 [1], by smoothing the transition between feed line and the antenna; this technique is easily applied to patch antennas with microstrip or coplanar feeding; radiator patch and ground plane can provide an almost constant input impedance over wide bandwidths

Radiating elements patches of printed antennas have a variety of forms, as triangular, rectangular, square, elliptical, circular, among others [2, 3]. However, it has been found that circular structures have smaller dimensions related with the operation frequency [4], Moreover, the circular structure offers another important advantage: the only control variable for the structure design is the patch radius, that is the reason circular or disk antennas are very popular and widely used nowadays.

Recently some techniques have been developed to improve BW of circular planar antenna, as introducing a slot into the circular patch, adding new resonant frequencies. We propose in this paper a smooth transition between the circular planar antenna and the ground plane and the microstrip feeding, as was originally established by Kraus in histheoretical volcano smoke antenna [1]. We start with the design of a circular patch antenna working in a frequency of 4.5 GHz.

## 2. GEOMETRICAL PARAMETERS

Both antennas were designed using CST and ADS commercial available software, comparing results to ensure the best performance. The only design parameter is the circular patch diameter, after obtain the initial diameter we smooth edges of circular patch with feeding and ground plane, until we get the best  $S_{11}$  parameter; after that, the best antenna was constructed. For the 4.5 GHz, selected frequency, the design patch radius was 11.24 mm, after use [5]:

$$R = \frac{F}{\sqrt{\frac{2h}{1 + \sqrt{\pi \varepsilon_{eff} F \left[ \ln \frac{F\pi}{2h} + 1.7726 \right]}}}} \quad (1)$$

where:

$$F = \frac{8.791 \times 10^9}{f_r \sqrt{\varepsilon_{eff}}};$$

$f_r$  = Resonant frequency in Hz;

$\varepsilon_{eff}$  = Dielectric effective constant;

$R$  = Patch radius in mm;

$h$  = Substrate thickness in mm.

On the other hand, the microstripline dimensions are obtained as [4]:

$$\frac{W}{d} = \begin{cases} \frac{8\ell^A}{\ell^2 A - 2}, & \frac{W}{d} < 2 \\ \frac{2}{\pi} \left[ B - 1 - \ln(2B - 1) + \frac{\varepsilon_r - 1}{2\varepsilon_r} \{ \ln(B - 1) + 0.39 - \frac{0.61}{\varepsilon_r} \} \right], & \frac{W}{d} > 2 \end{cases} \quad (2)$$

where  $\ell$  is the line length and:

$$\begin{aligned} A &= \frac{Z_0}{60} \sqrt{\frac{\varepsilon_r + 1}{2}} + \frac{\varepsilon_r - 1}{\varepsilon_r + 1} \left( 0.23 + \frac{0.11}{\varepsilon_r} \right) \\ B &= \frac{377\pi}{2Z_0\sqrt{\varepsilon_r}} \end{aligned} \quad (3)$$

For the CPW feeding line the design equations are [4]:

$$\frac{W}{d} = \begin{cases} x, & \sqrt{\varepsilon_r}Z_0 < 120 \\ 0.85 - \sqrt{0.6 - x}, & \sqrt{\varepsilon_r}Z_0 > 120 \end{cases} \quad (4)$$

where:

$$x = \frac{30\pi}{\sqrt{\varepsilon_r}Z_0} - 0.441 \quad (5)$$

### 3. CONSTRUCTION

Antennas were constructed over a substrate RF35-A with  $\varepsilon_r = 3.5$  and 0.762 mm thick, the sharp edges of the original circular patches were softened for both antennas following procedure outlined in [6]; Figure 1 shows the CPW circular patch, and Figure 2 the modified antenna, while Figure 3 shows the circular microstrip patch and Figure 4 the modified microstrip antenna.

### 4. EXPERIMENTAL AND NUMERICAL RESULTS

Both, simulation and measurements results are presented for reflection coefficient  $S_{11}$ , gain and field pattern, over a band from 500 MHz to 15 GHz, for circular and modified antennas. Following are simulated results comparison of circular patches with microstrip and CPW feeding and the corresponding modified antennas. Figures 5 and 6 show  $S_{11}$  parameter. We consider the 10 dB line the reference for good matching conditions.

Figures 7 and 8 show the response in gain and Figures 9, 10, 11 and 12 some field patterns at different frequencies.

As it is seen, there is a very good improvement for each parameter after smoothing edges of circular antennas. We also can compare results for the two feeding types: coupling is better for coplanar feeding, while gain is better for microstrip line. Field patterns are almost the same in both cases.

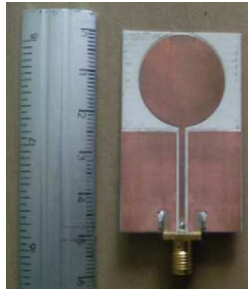


Figure 1: CPW circular patch.

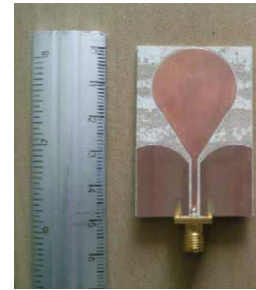


Figure 2: Modified CPW antenna.



Figure 3: Microstrip circular patch.

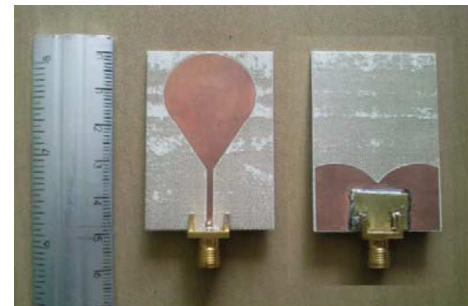


Figure 4: Modified microstrip antenna.

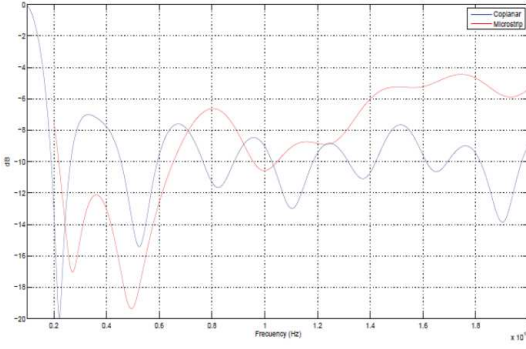
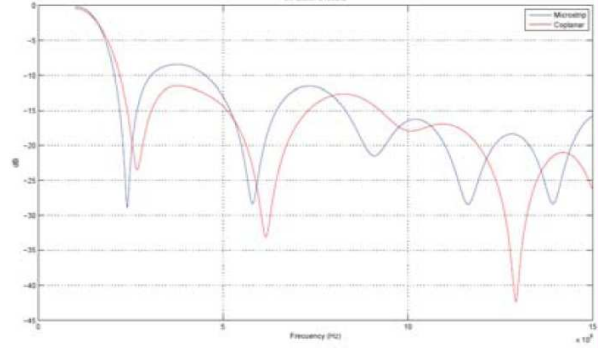
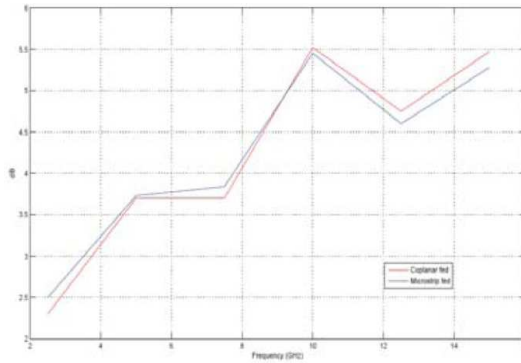
Figure 5:  $S_{11}$  for circular antennas.Figure 6:  $S_{11}$  for modified antennas.

Figure 7: Circular antenna gain.

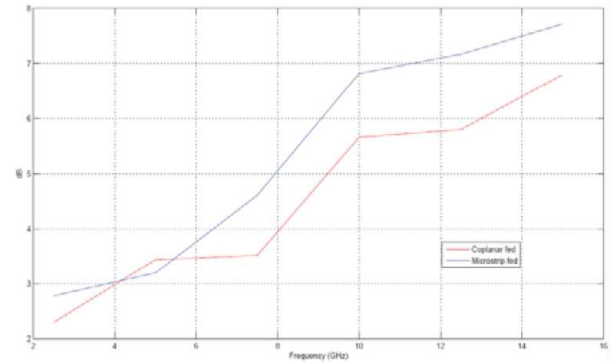


Figure 8: Modified antenna gain.

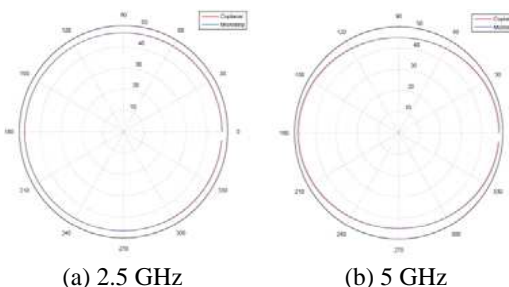


Figure 9: Patterns for circular patches.

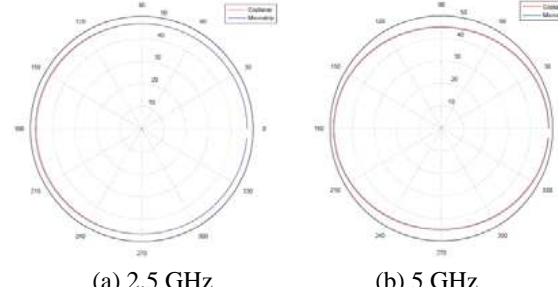


Figure 10: Patterns for modified patches.

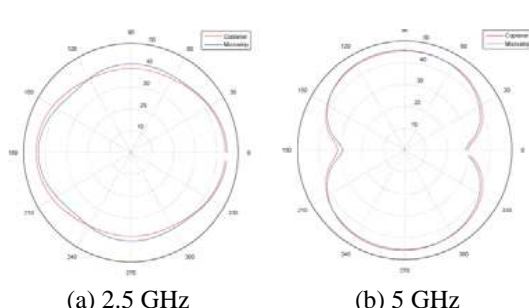


Figure 11: Patterns for circular patches.

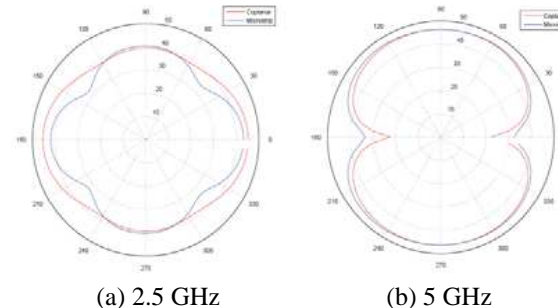


Figure 12: Patterns for modified patches.

In the same way we present the experimental results. Figures 13 and 14 show the  $S_{11}$  measured for the circular and modified antennas respectively.

Figures 15 and 16 show the measured gain for microstrip and CPW antennas respectively.

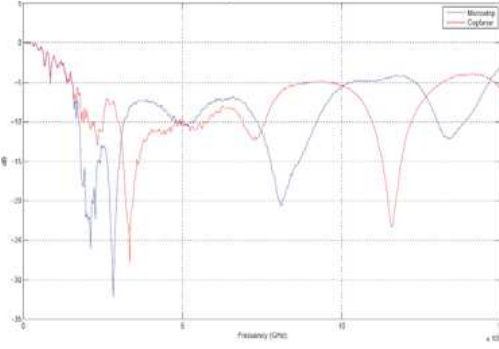
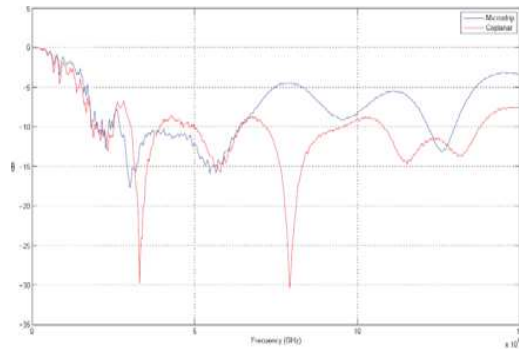
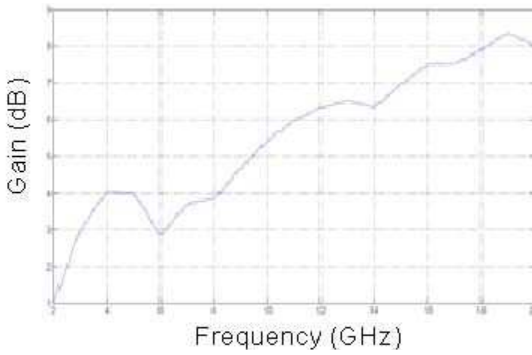
Figure 13:  $S_{11}$  for circular antennas.Figure 14:  $S_{11}$  for modified antennas.

Figure 15: Microstrip antenna gain.

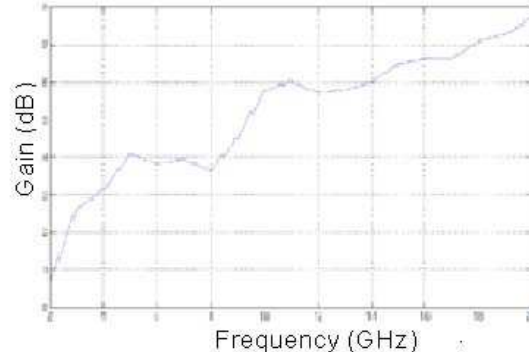


Figure 16: CPW antenna gain.

Comparing Figures 13 and 14, we can see that there is a good improvement for the the modified antennas, mainly in that of CPW feeding. It seems that construction of microstrip feeding antenna was not as good as what we expected, and we have to improve the way we did it. On the other hand, comparing Figures 15 and 16 with simulated gain response of Figure 8, we can see the good agreement between them;as it seen, microstrip feeding antenna shows a higher gain,compared with the CPW feed antenna but coplanar feeding antenna has better reflection coefficient in a softness curve.

## 5. CONCLUSION

We have applied the edge smoothing technique in the design of UWB antennas, improving reflection and gain parameter over a wide band for two different feeding techniques: microstrip and coplanar. Although practical results are not as good as they were expected, needing to improve our construction techniques, we conclude that the employed technique provide good results.

## REFERENCES

1. Kraus, J. D., *Antennas*, 2nd Edition, 692–694, McGraw Hill, New York, 1988.
2. Wong, K. L., *Compact and Broadband Microstrip Antennas*, 1st Edition, Chap. 1, 2 and Chap. 4, 144–154, Wiley Ed., 2006.
3. Martínez-Vázquez, M., O. Litschke, M. Geissler, D. Heberling, M. Antonio, and D. Martínez-González, “Integrated planar multiband antennas for personal communication handsets,” *IEEE Transactions on Antennas and Propagation*, Vol. 54, No. 2, February 2006.
4. Liang, J., C. C. Chiau, X. Chen, and C. G. Parini, “Printed circular disc monopole antenna for Ultrawideband applications,” *Electronics Letters*, Vol. 40, No. 20, September 30, 2004.
5. Pozar, D., *Microwave Engineering*, 2nd Edition, 162, University of Massachusetts at Amherst, John Wiley & Sons, 1998.
6. Garduño-Nolasco, E., J. R. Sosa-Pedroza, and H. Jardón-Aguilar, “An UWB microstrip feeding quasi circular antenna,” *7th International Congress on Electrical Computer Science and Automatic Control*, Tuxtla Gutiérrez, Chiapas, México, September 2010.

# Antennas for Compact Communication Systems

Dau-Chyrh Chang<sup>1</sup>, Hsiao-Bin Liang<sup>2</sup>, and Cheng-Wei Chen<sup>1</sup>

<sup>1</sup>Oriental Institute of Technology, Taiwan

<sup>2</sup>Climax Technology Co., Ltd, Taiwan

**Abstract**— The most important problems of nowadays compact communication systems are not only for the higher total radiation power (TRP), but also for the higher total isotropic sensitivity (TIS). The TIS of communication systems will be degraded by the electromagnetic interference (EMI) from other active parts of print circuit board (PCB). The smaller the size of compact communication system is, the serious problem of EMI will happen at receiver. Due to the EMI problem, the sensitivity of communication system will be degraded. In this paper, various kinds of small antennas are designed and developed for the compact size of communication systems. The antenna design should consider the compact size of communication system. The simulation tool for designing the antenna inside the compact size of communication system is by using commercial available General Electromagnetic Simulation (GEMS) [1]. The measurement results of TRP and TIS for various kinds of antenna and developed antenna for the compact communication system are compared.

## 1. INTRODUCTION

The paper designed the multi-band antennas applying to GSM communication systems. By using multiple-band dipole concept, the special meander line antenna is developed with frequency band including 850 MHz/900 MHz/1800 MHz/1900 MHz. Except for the passive antenna performances with or without size of communication are measured, the performances of TRP and TIS for GSM is also measured.

The simulated and measured results of the return loss and radiation patterns are in good agreements for applications in a communication system.

## 2. ANTENNA DESIGN

The proposed antenna is designed for operation at GSM850/900/1800/1900 bands for wireless security systems applications with return loss  $S_{11} < -10$  dB. Fig. 1 shows the simulation model structure of the multiband dipole antenna and main structure is made of copper.

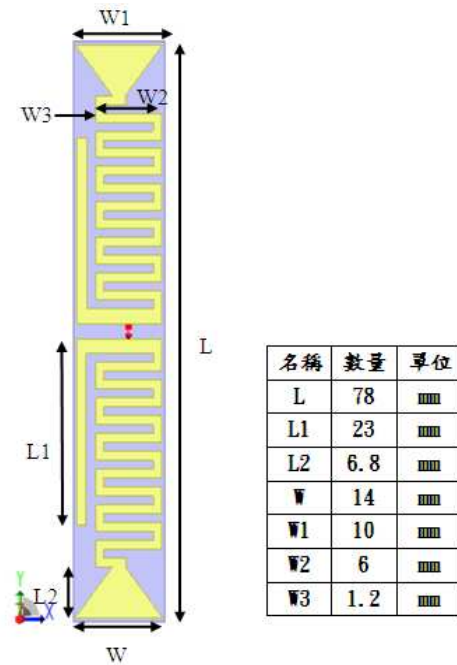


Figure 1: Simulation model of the multiband dipole antenna.

The multiband dipole antenna comprises of a meandering line and bow-Tie. The purpose of bow-tie is for bandwidth improvement at lower band. This structure is easily constructed by printing on a dielectric (FR4) substrate. Fig. 2 shows the prototype of fabricated multiband dipole antenna.

### 3. RESULTS OF SIMULATION AND MEASUREMENT

The antenna is mounted inside the case communication system is shown in Fig. 3. The return loss of multiband dipole antenna with and without compact communication systems are shown in Fig. 4. The worst case of return loss is 10 dB. The measured return loss with communication system will shift to higher frequency.

The radiation efficiency of multiband dipole antenna and antennas for compact communication systems are shown in Fig. 5. The measured radiation efficiency of antenna itself is about 70% for lower band and higher band. If with the communication case, the measured radiation efficiency degraded to 45% and 65% for lower and higher frequency.

The peak gain of multiband dipole antenna and antennas inside compact communication system are shown in Fig. 6. The multiband dipole antenna measured maximum antenna gain for operating frequencies across the 824 MHz ~ 960 MHz GHz band and 1710 MHz ~ 1990 MHz band are 0 dBi ~ 2 dBi.

The TRP and TIS are important for the GSM system. Except for the developed antenna, other market available antennas for the communication system are also measured and compared. The TRP and TIS are measured at the Communication Research Center of Oriental Institute of Technology. Figs. 7, 8, 9, and 10 are the TRP and TIS for frequency at 850 MHz, 900 MHz, 1800 MHz, and 1900 MHz respectively. The TRP and TIS of developed antenna with the communication sys-

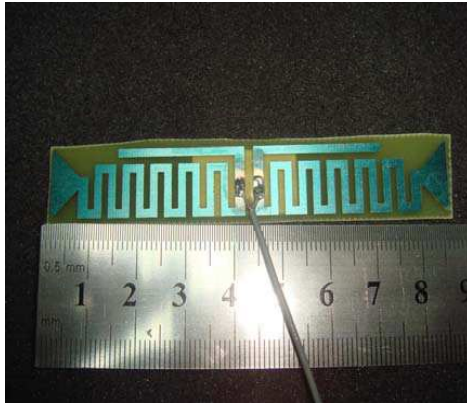


Figure 2: Prototype of the multiband dipole antenna.



Figure 3: Developed antenna for compact communication system.

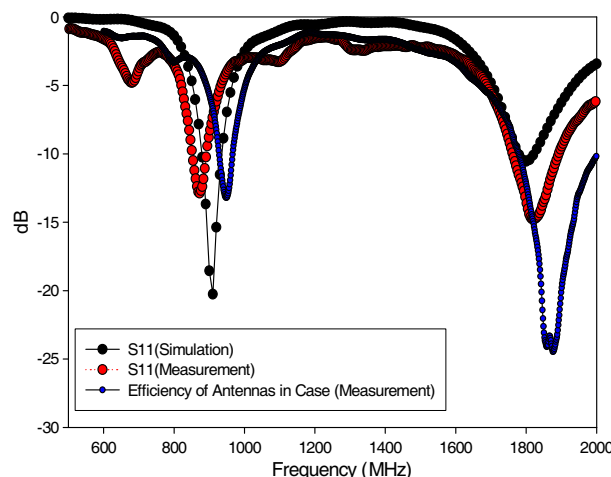


Figure 4:  $S_{11}$  of multiband dipole antenna.

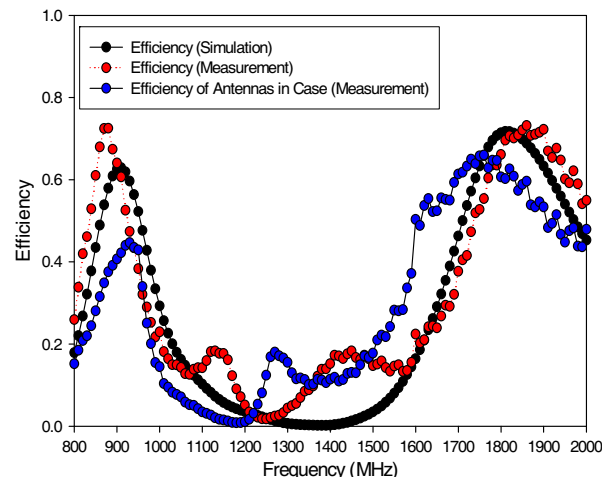


Figure 5: Radiation efficiency of multiband dipole antenna.

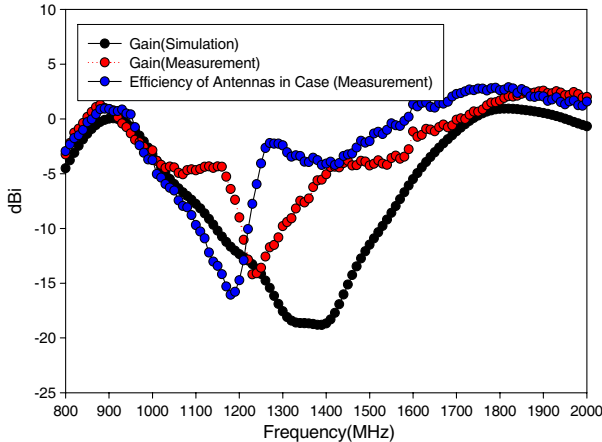


Figure 6: Peak gain of multiband dipole antenna.

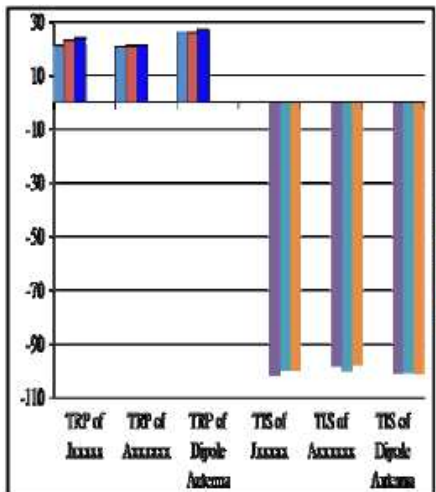


Figure 7: TRP and TIS of GSM850.

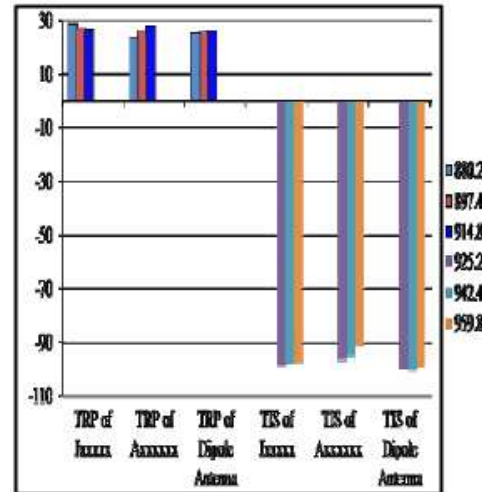


Figure 8: TRP and TIS of GSM900.

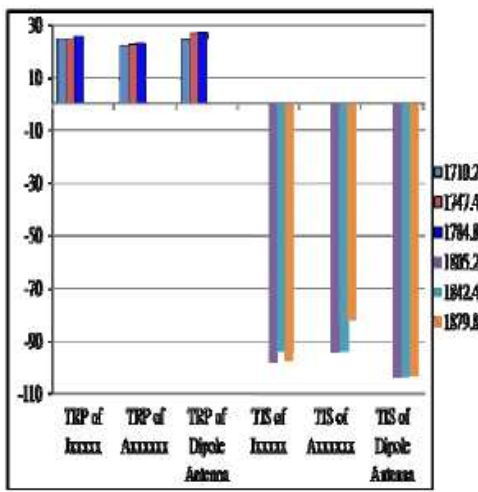


Figure 9: TRP and TIS of GSM1800.

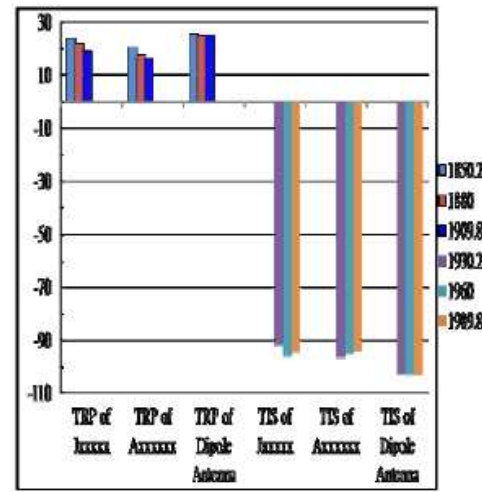


Figure 10: TRP and TIS of GSM1900.

tem are around 27 vdBm and  $-100$  dBm respectively for the four bands. Comparing the measured results of TRP and TIS, the performance of developed antenna is equal or better than that of market available antennas.

#### 4. CONCLUSIONS

When the antennas inside the compact communication systems, the operating frequency of antennas will be shifted to higher frequency, additionally, the efficiency and peak gain will be degraded because the antenna energy is absorbed or reflected by the compact communication systems.

The simulated and measured results of the return loss and radiation patterns are in good agreements. The TRP and TIS performances of GSM system with the developed antenna at the four bands are equal or better than that of commercial available two antennas.

#### REFERENCES

1. GEMS, 3-D High Performance parallel EM simulation Software, [www.2comu.com](http://www.2comu.com).

# A Dual Band Fractal Circular Microstrip Patch Antenna for C-band Applications

Nitasha Bisht and Pradeep Kumar

Department of Electronics and Communication Engineering  
Jaypee University of Information Technology, Solan, HP-173215, India

**Abstract**— This paper proposes the design of a circular patch antenna with fractals for C-band applications. The designed antenna has been fed with L probe feeding technique. The proposed circular patch antenna with fractals produces a dual band operation for the C-band applications. The designed model is simulated using CST microwave studio software based upon finite difference time domain method. The simulated results for various parameters like return loss, radiation pattern etc have been presented. The designed antenna operates for dual band at 6.6 GHz and 7.5 GHz with increase in Gain and Bandwidth. Such type of antennas is useful in Telecommunication, Wi-Fi, Satellite communication, Radar, Commercial and Military application.

## 1. INTRODUCTION

In modern wireless communication system and increasing other wireless applications, wider bandwidth, is required, traditionally each antenna operates at a single frequency band, where a different antenna is needed for different application. This will cause a limited space and place problem. In order to overcome this problem, multiband antenna can be used where a single antenna can operate at many frequency bands. One technique to construct a multiband antenna is by applying fractal shape into antenna geometries [1, 2].

Fractals: fractal shaped antenna have been proved to have some unique characteristics that are linked to geometrical properties of fractals. According to Webster dictionary a fractal is being derived from the Latin fractious meaning broken, uneven: any of the various extremely irregular curves or shapes that repeat themselves at any scale on which they are examined. Fractal geometry has unique geometrical features occurring in nature. It can be used to describe the branching of the tree leaves and plants, jaggedness of coastlines and many more examples in the nature. There are many benefits where we apply fractals to develop various antenna elements. By applying fractals to antenna elements: we can create smaller antenna size, achieve resonance frequency that are multiband, may be optimized for gain, achieved wideband frequency band [3, 4]. For most fractals, similarity concept can achieve multiple frequency band because of different of antenna are similar to each other at different scale. It has been found out that L-probe feed offer less dispersion at higher frequency and in broader matching as compare to micro strip feed. This paper presents the new L probe-fed circular patch multi-wideband antenna of compact size [5–7]. Such type of antenna is useful in Telecommunication, Wi-Fi, satellite communication, radar, commercial and military application.

In this paper, a design of dual band fractal microstrip antenna has been presented. The designed microstrip antenna in third iteration produces two bands at 6.7 GHz and 7.5 GHz for C-band applications. Rest of the paper is organized as follows: The geometrical configuration of the designed antenna is presented in Section 2. The simulated results and discussion are given in Section 3. Finally, Section 4 concludes the work.

## 2. ANTENNA GEOMETRY

The antenna structure based on fractal geometry shown in Fig. 1(a). This antenna has been designed on substrate dielectric constant  $\epsilon_r = 2.3$ , thickness = 4 mm with L-probe fed. A circular patch microstrip antenna of a radius  $a = 16$  mm has been taken as a base to construct fractal antenna. The 3rd iterative structure has been generated from this circular patch. In the 1st iteration shown in Fig. 1(b) we divide this circle into five smaller circle with radius = 5.1 mm and then removed the circle at the centre as the remaining circle is four. In the 2nd iteration shown in Fig. 1(c) we divide each remaining four circle into five circle with radius = 1.35 mm. Then drop the entire centre circle for each remaining circle. The reaming small circle for this stage is sixteen. In the 3rd iteration shown in Fig. 1(d) we divide each remaining sixteen circle into five with radius = 0.2 mm. The entire center circle for each remaining circle is being omitted. The

infinite iterative structure is not possible due to fabrication constraints. In this paper, 3rd iterative circular patch antenna has been finalized.

The antenna is fed with L-probe fed. To obtain a large bandwidth this type of feeding is used. In particular, an L shaped probe antenna has an excellent feeding structure suitable for wideband patch antenna with an air substrate. In general, this type of feed can be easily implemented by bending a straight strip or probe into an L-shape. The L-fed antenna not only performs better in respect of bandwidth but radiation pattern is also good [8–10]. It is also relevant to relative permittivity and thickness of substrate. In this paper,  $\epsilon_r = 2.3$  and thickness = 4 mm is used.

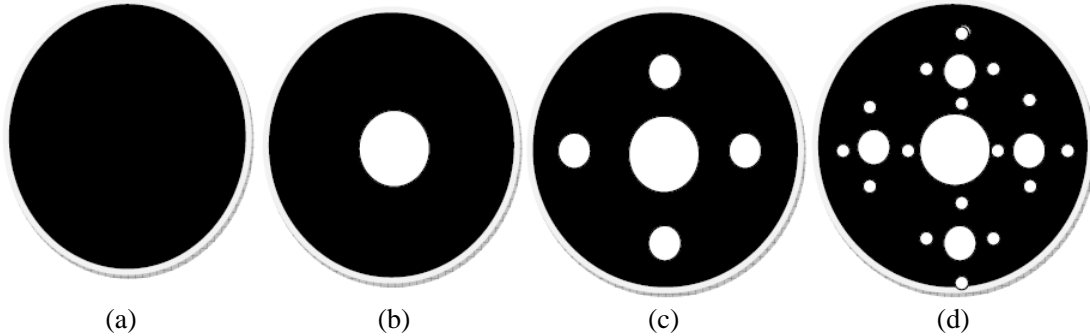


Figure 1: Geometry of the fractal antenna, (a) 0th iteration, (b) 1st iteration, (c) 2nd iteration, (d) 3rd iteration.

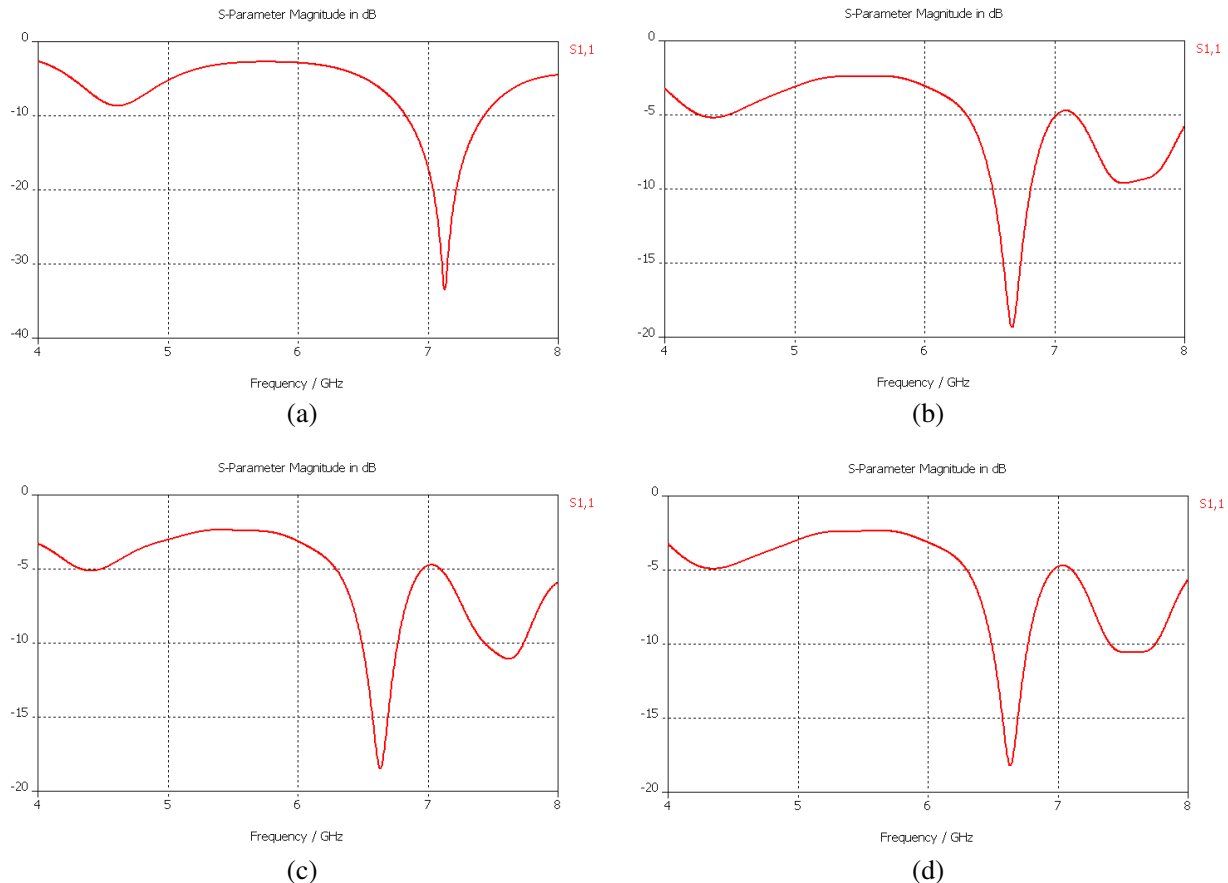


Figure 2: The return loss of the designed antenna, (a) 0th iteration, (b) 1st iteration, (d) 2nd iteration, (d) 3rd iteration.

### 3. RESULT AND DISCUSSION

As illustrated from Table 1, the bandwidth of antenna for 0 iteration is 0.6198 GHz (6.8243–7.4505), while for 1st iteration is 0.3003 GHz (6.524–6.8243), 2nd iteration are 0.2812 GHz (6.4989–6.7796) at lower band and 0.293 GHz (7.738–7.441) at upper band respectively as well as for 3rd iteration are 0.294 GHz (6.4856–6.7796) at lower band and 0.3706 GHz (7.3866–7.7572) at upper band. As the iteration increases the bandwidth is increases as well as it generates another resonant frequency at 7.5 GHz.

Table 1: Result the simulated circular patch antenna with fractals.

Circular patch antenna	Operating Frequency	Frequency band (GHz)	Bandwidth (GHz)
0th iteration	7.12 GHz	6.8243–7.4505	0.6198 (8.67%)
1st iteration	6.6 GHz	6.524–6.8243	0.3003 (4.5%)
2nd iteration	6.6 GHz	6.4984–6.7796	0.2812 (4.23%)
2nd iteration	7.5 GHz	7.738–7.441	0.293 (3.86%)
3rd iteration	6.6 GHz	6.4856–6.7796	0.294 (4.43%)
3rd iteration	7.5 GHz	7.3866–7.7572	0.3706 (4.9%)

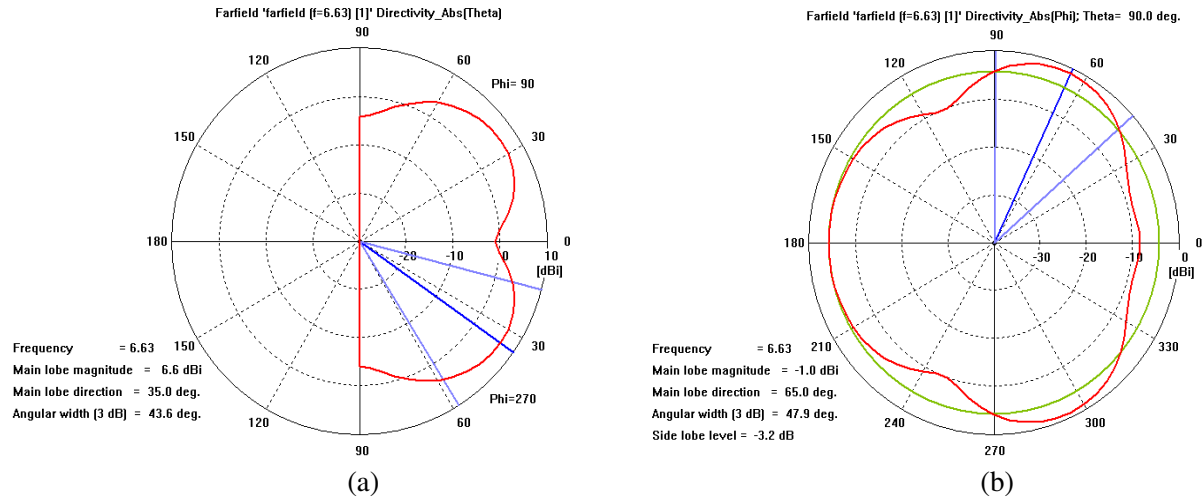


Figure 3: Radiation pattern of the antenna at 6.6 GHz, (a) theta plane, (b) phi plane.

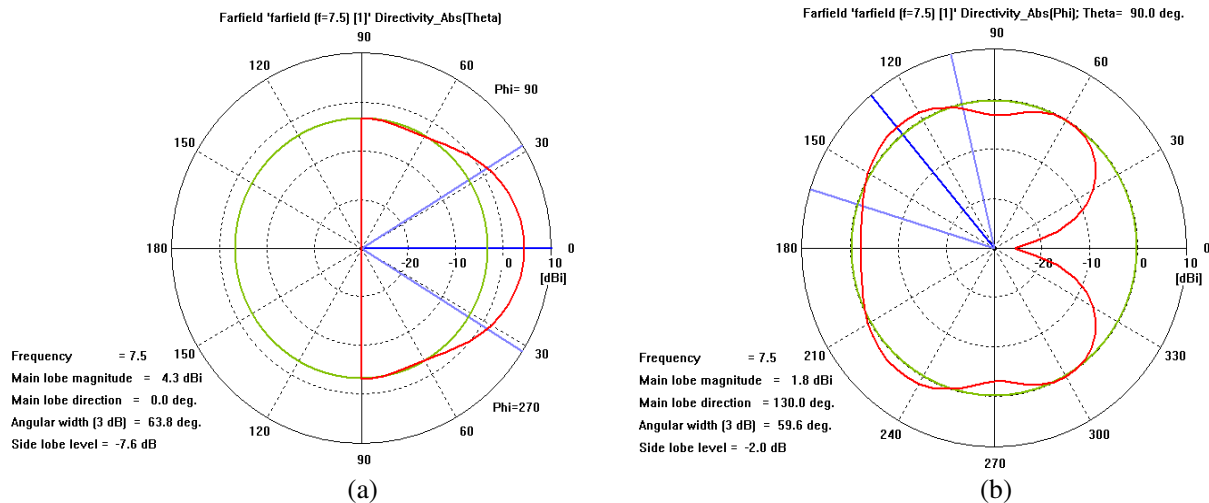


Figure 4: Radiation pattern of the antenna at 7.5 GHz, (a) theta plane, (b) phi plane.

Table 2: Simulated results for the designed antenna.

Circular patch antenna	Efficiency	Directivity	Gain (dBi)
0th iteration	0.9923	6.832	6.77
1st iteration	0.9776	6.429	6.28
2nd iteration	0.9807	6.422	6.29
2nd iteration	0.9987	7.636	7.62
3rd iteration	0.9720	6.454	6.27
3rd iteration	0.9904	7.615	7.54

The simulated radiation pattern of fractal antenna for 3rd iteration is shown in Fig. 3 and in Fig. 4. The gain result for simulated circular patch with fractal antenna at different iteration is shown in Table 2. From this table it is clear that the efficiency of the antenna is very high.

#### 4. CONCLUSIONS

The circular patch antenna with fractals has been designed to exhibit the dual band operation. This antenna offer increase in bandwidth and gain at all multiband. The designed antenna can be used for dual band applications in C band. Such type of antenna is useful for Telecommunication, Wi-Fi, Radar, Satellite communication, Military and commercial.

#### REFERENCES

1. Balanis, C. A., *Antenna Theory: Analysis and Design*, Wiley, 2005.
2. Bancroft, R., "Micro strip antenna design".
3. Azeri, A. and J. Rowan, "Ultra wideband fractal micro strip antenna design," *Progress In Electromagnetic Research C*, Vol. 2, 7–12, 2008.
4. Salmasi, M. P., F. H. Kashani, and M. N. Azarmanesh, "A novel broadband fractal Sierpinski shaped micro strip antenna," *Progress In Electromagnetic Research C*, Vol. 4, 179–190, 2008.
5. Khan, A. S. N., J. Hu, J. Xiong, and S. He, "Circular fractal monopole antenna for low VSWR UWB application," *Progress In Electromagnetic Research Letters*, Vol. 1, 19–25, 2008.
6. Lai, T. F., W. N. L. Mahadi, and N. Soin, "Circular patch micro strip array antenna for KU-band," *World Academy of Science, Engineering and Technology*, 48, 2008.
7. Saidatul, N. A., A. A. H. Azremi, R. B. Ahmad, P. J. Soh, and F. M. Malek, "Multiband fractal planar inverted antenna (F-PIFA) for mobile phone application," *Progress In Electromagnetic Research B*, Vol. 14, 127–148, 2009.
8. Liang, J., et al., "CPW-fed circular disc monopole antenna for UWB application," *IEEE International Workshop on Antenna and Technology: Small Antennas and Novel Met materials*, 505–508, Marina Mandarin, Singapore, March 7–9, 2005, ©2009 ACADEMY PUBLISHER.
9. Pirai, M. and H. R. Hassani, "L-probe fed circular polarized wideband planar patch antenna on cylindrical structure," *Progress In Electromagnetic Research C*, Vol. 3, 161–167, 2008.
10. Guo, Y. X., K. M. Luk, and K. F. Lee, "U-slot circular patch antennas with L-probe feeding," *Electronics Letters*, Vol. 35, No. 20, Sept. 30, 1999.

# Rectangular Microstrip Patch Antenna with Photonic Band Gap Crystal for 60 GHz Communications

R. N. Tiwari<sup>1</sup>, P. Kumar<sup>2</sup>, and Nitasha Bisht<sup>2</sup>

<sup>1</sup>School of Engineering and Technology, Bahra University, India

<sup>2</sup>Department of Electronics and Communication Engineering  
Jaypee University of Information Technology, India

**Abstract**— In this paper, the design of rectangular microstrip antenna with 2-D photonic band gap crystal as substrate (dielectric substrate with regular cylindrical periodic air-gap) for 60 GHz applications, has presented. The photonic band gap structure is used to enhance the radiation efficiency and the bandwidth of the antenna. The periodic structures designed to open up frequency bands within which the propagation of electromagnetic waves is forbidden irrespective of the propagation direction. The design is optimized using the Finite Difference Time Domain (FDTD) based CST microwave studio simulator. The designed periodic air-gap rectangular microstrip patch antenna gives a bandwidth up to 20.53% for 60 GHz applications. Various parameters like directivity of the antenna, efficiency of the antenna etc. are also shown.

## 1. INTRODUCTION

The microstrip patch antennas are having many advantages such as low profile, versatile, conformal and low-cost devices. The advantages of microstrip antennas make them suitable for various applications like, vehicle based satellite link antennas [1–3] global positioning systems [4] radar for missiles and telemetry and wireless communication devices [4]. However these antennas have limitation of narrow bandwidth. Some of the common techniques proposed by researchers for widening the bandwidth are; increasing the height of antenna substrate [4] using aperture coupling method [4, 5] or using stacked patch structure [5], using gap-coupling [6–8]. The great interests have been given to the photonic crystal whose photonic band gap has attracted considerable possibility [9, 10]. By using the strong confinement of the light by the photonic band gap, it is expected that waveguide devices whose size is of the order of the wavelength of light can be realized [9]. In fact, many microscale photonic crystal optical waveguide devices have been proposed [11–13].

There is always the demand of increasing the bandwidth and data rate of the wireless communication systems. The present wireless systems, generally uses approximately frequency band of 1 to 6 GHz [14]. The second demand in the wireless communications systems is to reduce the interference [14]. To overcome these problems, the millimeter wave systems are becoming increasingly important in many military and commercial applications. The frequency range around 60 GHz presenting a license free frequency band is one of the possible solutions for the development of radio frequency systems [14, 15]. The 60 GHz band has the bandwidth of approximate 7 GHz (57 to 64 GHz) worldwide, and 9 GHz (57 to 9 GHz) in Europe. So, 60 GHz license free frequency band is the solution to the problems in the present wireless systems because of very high frequency as compared to the present wireless system frequency band. Many more advantages of 60 GHz frequency band have been described in [16].

In this paper, we present a design of rectangular microstrip antenna for 60 GHz communication. The air gaps are incorporated in the substrate and the bandwidth of the antenna is increased. Various parameters of the antenna such as return loss, VSWR, radiation pattern, directivity, radiation efficiency etc. are presented; the return loss of the antenna is less than  $-10$  dB for the frequency range 51.83 GHz to 63.69 GHz. The presented antenna can be used for 60 GHz applications. Rest of the paper is organized as follows: the geometrical configuration of the designed antenna is given in Section 2. The simulated results with discussion are presented in Section 3. Finally, Section 4 concludes the work.

## 2. ANTENNA CONFIGURATION

The geometrical configuration of the designed rectangular microstrip antenna with photonic band gap structure is depicted in Fig. 1. The rectangular patch of length ' $L_p$ ' and width ' $W_p$ ' is placed on a substrate with photonic band gap structure as shown in Fig. 1. The height and relative permittivity of the substrate is ' $h$ ' and ' $\epsilon_r$ ', respectively. The separation between two consecutive air cylinders is ' $d$ ', and the radius of the each cylinder is ' $r$ '. The antenna is fed by microstrip line feeding technique. The length and width of the microstrip feed line is ' $L_s$ ' and ' $W_s$ ' respectively.

### 3. RESULTS AND DISCUSSION

The designed antenna configuration of Fig. 1 is simulated using the CST microwave studio simulator. Using this simulator, the designed model of the antenna is optimized. The optimized dimensions of the microstrip antenna are given in Table 1.

The return loss of the proposed antenna is shown in Fig. 2. The antenna has been designed for operation in the 60 GHz frequency band that ranges from 51.83 GHz to 63.69 GHz (20.53%) is achieved as shown in Fig. 2. The voltage standing wave ratio (VSWR) of the designed rectangular microstrip antenna is shown in Fig. 3. From Fig. 3, it can be seen that the 2 : 1 bandwidth is 20.53%. The radiation pattern of the designed antenna is shown in Fig. 4. The radiation pattern of the designed antenna shows the omnidirectional nature in the upper hemisphere as shown in Fig. 4. The directivity, radiation efficiency and total efficiency at various frequencies are shown in Table 2. The designed microstrip antenna can be used for 60 GHz applications.

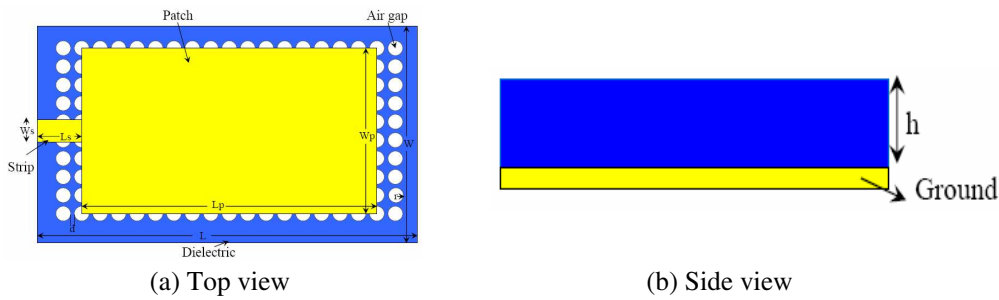


Figure 1: Geometrical configuration of rectangular microstrip antenna with photonic band gap structure.

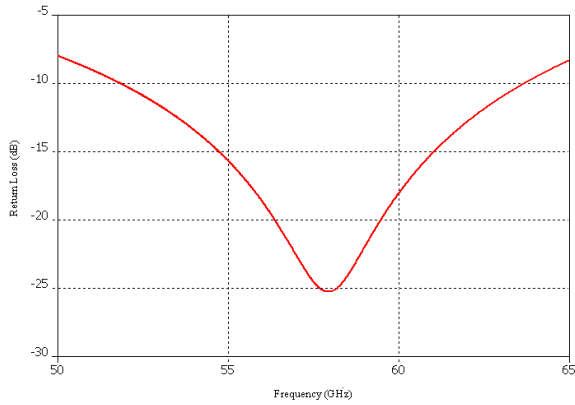


Figure 2: Return loss of the antenna.

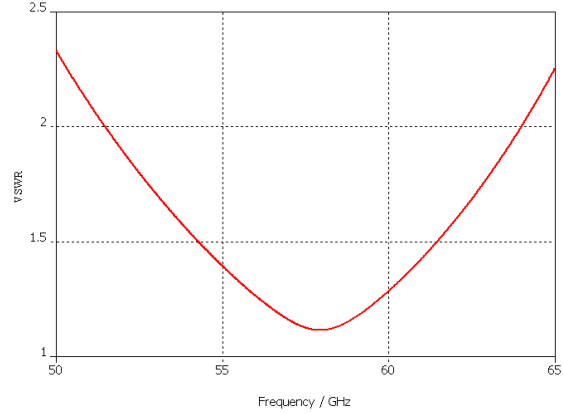


Figure 3: Voltage standing wave ratio (VSWR) of the antenna.

Table 1: Dimensions of the proposed microstrip antenna.

Parameter	Value
Length of the patch ( $L_p$ )	2.00 mm
Width of the patch ( $W_s$ )	0.80 mm
Dielectric substrate ( $\epsilon_r$ )	2.2
Distance between two air gap ( $d$ )	0.02 mm
Length of microstrip feed line ( $L_s$ )	0.45 mm
Width of microstrip feed line ( $W_s$ )	0.02 mm
Length of dielectric substrate ( $L$ )	2.50 mm
Width of dielectric substrate ( $W$ )	1.50 mm
Height of substrate ( $h$ )	0.40 mm
Radius of cylinder ( $r$ )	0.04 mm

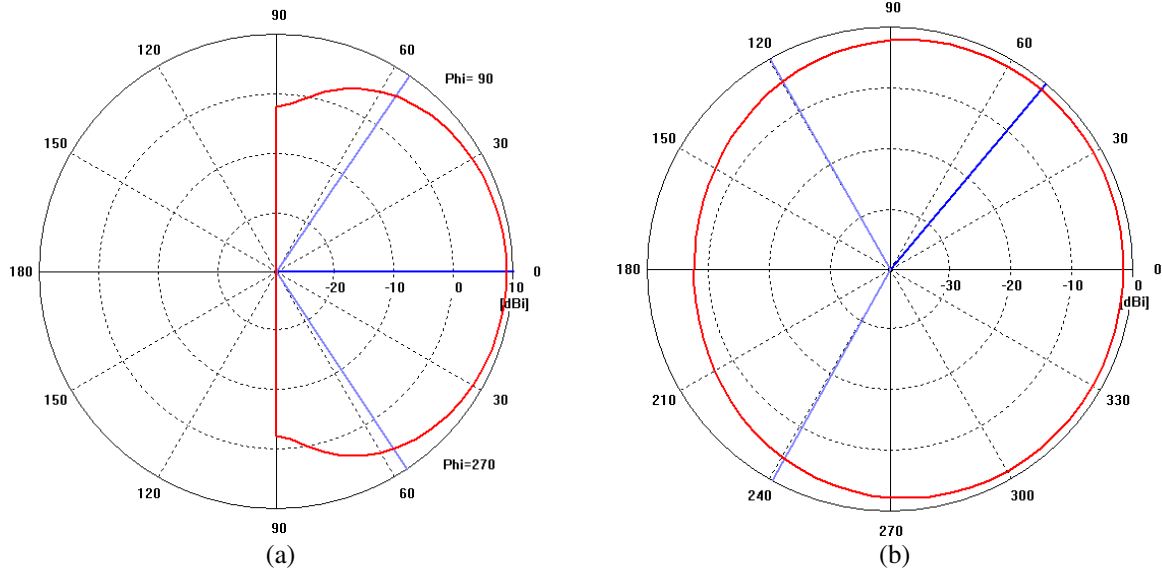


Figure 4: Radiation pattern of the antenna, (a) theta plane, (b) phi plane.

Table 2: Various parameters of the antenna.

Frequency	Directivity	Radiation Efficiency	Total Efficiency	3 dB Angular Width (theta plane)	3 dB Angular Width (phi plane)
57.5 GHz	8.937 dBi	0.7627	0.7599	112.1°	238.8°
57.9 GHz	8.970 dBi	0.7634	0.7611	112.4°	237.5°
60 GHz	9.143 dBi	0.7674	0.7553	114.1°	231.0°

#### 4. CONCLUSIONS

A design of rectangular microstrip antenna for 60 GHz communication has been presented. The photonic band gap structure is utilized to enhance the bandwidth and gain of the antenna. The designed antenna model has been optimized for 60 GHz applications using the CST Microwave studio. The return loss as well as the radiation pattern has been presented. The radiation pattern of the antenna shows the omnidirectional nature. The designed rectangular microstrip patch antenna with photonic band gap structure can be used for various applications of 60 GHz technology.

#### REFERENCES

1. Mailloux, R. J., et al., "Microstrip antenna technology," *IEEE Trans. Antennas and Propagation*, Vol. 29, 2–24, 1981.
2. Kumar, G. and K. P. Ray, *Broadband Microstrip Antennas*, Artech House Inc., MA, England, 2003.
3. Garg, R., P. Bhartia, I. Bahl, and A. Ittipoot, *Microstrip Antenna Design Handbook*, Artech House Inc., MA, England, 2001.
4. Pozar, D. M., "A review of aperture coupled microstrip antennas: History, operation, development, and applications," *IEEE Letters*, 1996.
5. Targonski, S. D., R. B. Waterhouse, and D. M. Pozar, "Design of wide band aperture coupled stacked microstrip antennas," *IEEE Trans. Antennas and Propagation*, Vol. 46, 1245–1251, 1998.
6. Kumar, P., G. Singh, T. Chakravarty, S. Bhooshan, S. Khah, and A. De, "Numerical computation of resonant frequency of gap coupled circular microstrip antennas," *Journal of Electromagnetic Waves and Applications*, Vol. 21, No. 10, 1303–1311, 2007.
7. Kumar, P. and G. Singh, "Theoretical investigation of the input impedance of gap-coupled circular microstrip patch antennas," *Journal of Infrared, Millimeter and Terahertz Waves*, Vol. 30, 1148–1160, 2009.

8. Kumar, P., G. Singh, S. Bhooshan, and T. Chakravarty, "Gap-coupled microstrip antennas," *Proc. of IEEE Sponsored International Conference on Computational Intelligence*, 435–438, Sivakasi, India, 2007.
9. Yablonovitch, E., "Inhibited spontaneous emission in solid-state physics and electronics," *Physical Review Lett.*, Vol. 58, 2059–2062, 1987.
10. Joannopoulos, J. D., P. R. Villeneuve, and S. Fan, "Photonic crystals: Putting a new twist on light," *Nature*, Vol. 386, 143–149, 1997.
11. Lin, S. Y., E. Chow, V. Hietala, P. R. Villeneuve, and J. D. Joannopoulos, "Experimental demonstration of guiding and bending of electromagnetic waves in a photonic crystal," *Science*, Vol. 282, 274–276, 1998.
12. Fan, S., P. R. Villeneuve, J. D. J. Oannopoulos, and H. A. Haus, "Channel drop tunneling through localized states," *Physical Review Lett.*, Vol. 80, 960–963, 1998.
13. Ikuno, H., Y. Naka, and A. Yata, "Analysis of optical waveguide devices using the FDTD method based on the principles of multidimensional wave digital filters," *Radio Science*, Vol. 35, 595–605, 2000.
14. Akkermans, J. A. G., "Planar beam-forming antenna array for 60-GHz broadband communication," *Technische Universiteit Eindhoven*, 2009.
15. Segura, N., et al., "On-wafer radiation pattern measurements of integrated antennas on standard BiCMOS and glass processes for 40–80 GHz application," *IEEE Int. Conference on Microelectronic Test Structures*, Vol. 18, 2005.
16. Koh, C., "The benefits of 60 GHz unlicensed wireless communications," *YDI Wireless Whitepaper*, 2004.

# Novel Shape of UWB Microstrip Patch Antenna with Enhanced Gain Using EBG Structure

Mohammed M. Mohanna<sup>1</sup>, Deena A. Salem<sup>2</sup>,  
Esmat A. F. Abdallah<sup>2</sup>, and Hadia M. S. El-Henawy<sup>3</sup>

<sup>1</sup>Ministry of Electricity & Energy, Egyptian Electricity Holding Company, Egypt

<sup>2</sup>Microstrip Department, Electronics Research Institute, Egypt

<sup>3</sup>Electronics and Communications Department, Ain Shams University, Egypt

**Abstract**— A novel shape of microstrip UWB planar monopole with enhanced gain using EBG structure is presented. The structure is composed of a rectangular patch fed by a microstrip line constructed on a  $22 \times 22 \text{ mm}^2$ , FR4 dielectric substrate. The patch is mitered at the corners of the first radiating slot ( $45^\circ$ ). Two slots were inserted in the partial ground plane lateral to the microstrip feed line. Mushroom-like circular EBG structures encircle the radiating patch. The operational bandwidth of this antenna extends from 3.5 to 13.5 GHz, with minimum return loss of 50 dB, with average directivity, gain and radiation efficiency of 7.5 dBi, 6.5 dBi, 82%, respectively. At the upper end of the spectrum, the gain increases to reach 11 dBi. Also due to using EBG structures, the antenna resonates at higher frequency range of 22 to 29 GHz, such that the design applications may be extended to other areas such as vehicular ones.

## 1. INTRODUCTION

The frequency band 3.1–10.6 GHz, was approved by the Federal Communications Commission (FCC) of USA in 2002 for unlicensed usage [1]. Since then, the interest in designing UWB antennas that operate over wide frequency range and that can be used for multiple channels or systems, has excelled. It enables high data transmission rates, low power consumption and simple hardware configuration in communication systems for different applications. Whereas, compact size and non-dispersion property are crucial issues that face these types of antennas.

Planar monopole antennas that consist of a rectangular patch loaded with slot(s) on both the patch and the ground plane were presented in literature and proved to be very good candidates for such applications [2, 3]. However, they have some disadvantages such as low directivity and low gain, that is attributed to the surface waves, which affects the radiation efficiency. To eliminate these surface waves EBG substrates were introduced in order to eliminate these effects [4]. In this paper, a new ultra wideband microstrip antenna with enhanced gain using EBG structure is presented, Fig. 1.

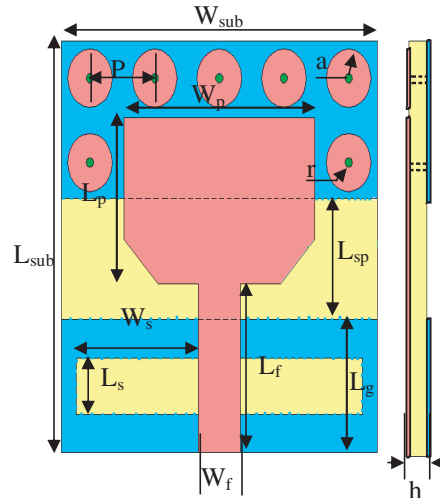


Figure 1: Geometry of the proposed antenna.

## 2. ANTENNA DESIGN

Figure 1 shows the configuration of the proposed ultrawide band antenna with enhanced gain using EBG structure. The proposed antenna is constructed on FR4 substrate with size  $W_{sub}xL_{sub} = 22 \times 22 \text{ mm}^2$ , thickness  $h = 1.5 \text{ mm}$ , relative dielectric constant = 4.65, and  $\tan \delta = 0.02$ .

The width,  $W_f$ , of the microstrip feed line is fixed at 2.9 mm to achieve  $50 \Omega$  characteristic impedance and the length,  $L_f$ , is 9 mm. On the upper surface of the substrate, a rectangular patch with size of  $W_p \times L_p = 13.3 \times 8.9 \text{ mm}^2$  mitered at the corners of the first radiating slot ( $45^\circ$ ); the cutting ratio equal 4.8%. On the lower surface of the substrate, there is a reduced ground plane with length  $L_g = 7 \text{ mm}$ , with two slots adjusted in the ground plane encasing the microstrip feeder, the dimensions of which is  $(W_s \times L_s)$ .

Adding these two slots, with dimensions  $(8.5 \times 3 \text{ mm}^2)$ , placed at a distance of about  $0.5W_f$  from the ground's center enhanced the impedance bandwidth. As illustrated in Fig. 1, the EBG structure is formed of circular small patches of radius  $a$ , placed symmetrically with respect to the center line of the structure around the radiating patch; with pins of radius  $r$ , penetrating the substrates, with periodicity  $P$ , to form a mushroom like surface. The EBG structure exists on a partial ground separated from the reduced ground by distance  $L_{sp}$ . The enhanced characteristics can be achieved by optimizing the parameters  $(a, r, P, L_{sp})$ .

## 3. RESULTS AND DISCUSSION

The simulated results are obtained using the Ansoft high frequency structure simulator (HFSS version 10). The design parameters,  $L_{sp}$ ,  $a$ ,  $r$  and  $P$ , are obtained using parametric analysis, the results of which are shown in Figs. 2–5. The optimized values are  $L_{sp} = 6.6 \text{ mm}$ ,  $r = 0.25 \text{ mm}$ ,  $a = 1.2 \text{ mm}$ ,  $P = 4.5 \text{ mm}$ , which maintains UWB bandwidth of 10 GHz, that extends from 3.5 to 13.5 GHz, Fig. 5.

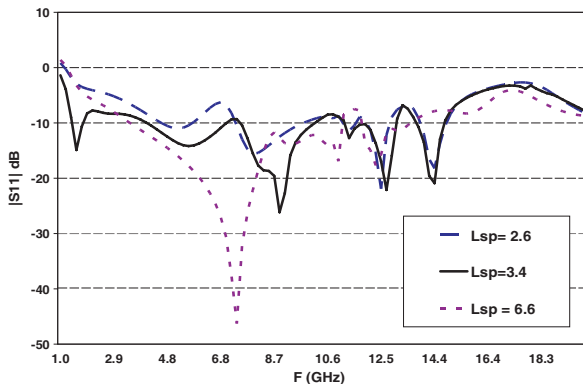


Figure 2: Parametric studies of parameter  $L_{sp}$  when  $a = 0.5 \text{ mm}$ ,  $r = 0.1 \text{ mm}$  and  $P = 4 \text{ mm}$  versus frequency.

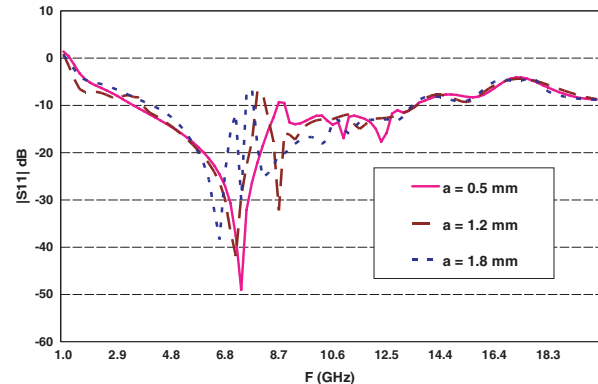


Figure 3: Parametric studies of parameter  $a$  when  $L_{sp} = 6.6 \text{ mm}$ ,  $r = 0.1 \text{ mm}$  and  $P = 4 \text{ mm}$  versus frequency.

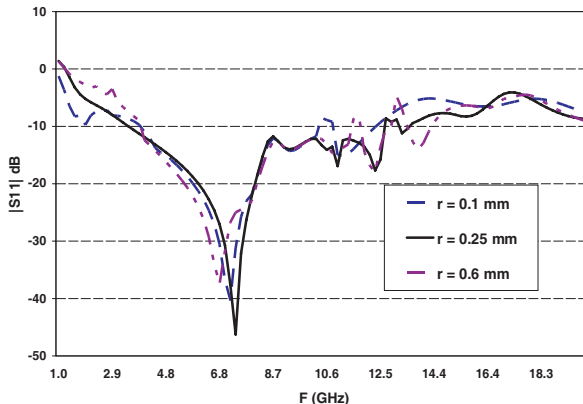


Figure 4: Parametric studies of parameter  $r$  when  $L_{sp} = 6.6 \text{ mm}$ ,  $a = 1.2 \text{ mm}$  and  $P = 4 \text{ mm}$  versus frequency.

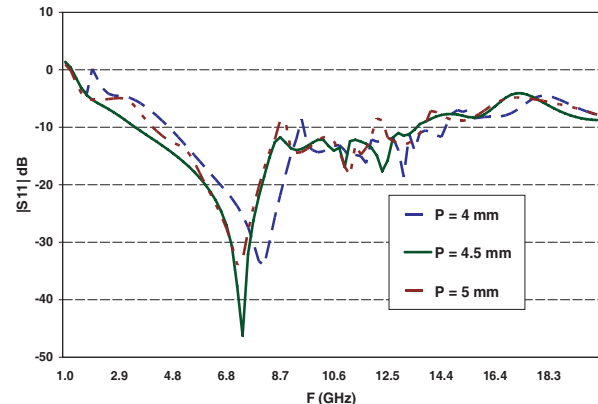


Figure 5: Parametric studies of parameter  $P$  when  $L_{sp} = 6.6 \text{ mm}$ ,  $a = 1.2 \text{ mm}$  and  $r = 0.25 \text{ mm}$  versus frequency

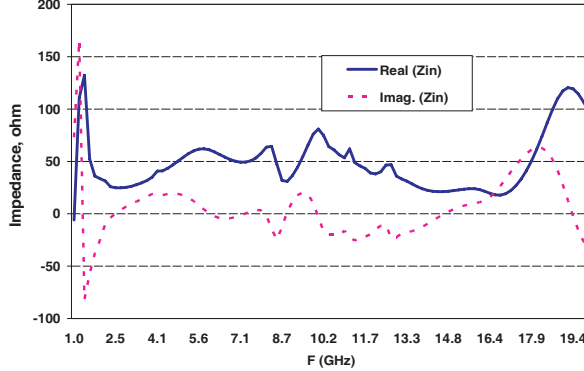


Figure 6: The simulated input impedance of the proposed antenna versus frequency.

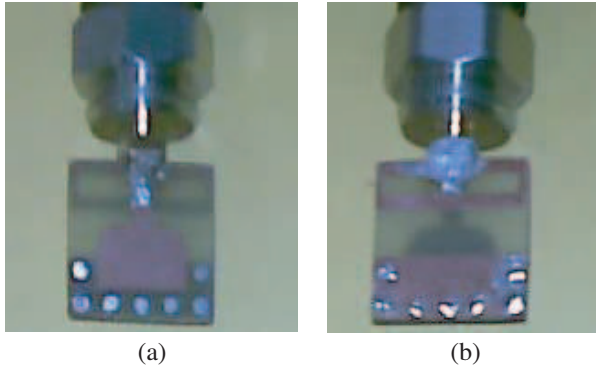


Figure 7: Fabricated antenna. (a) Bottom view. (b) Top view.

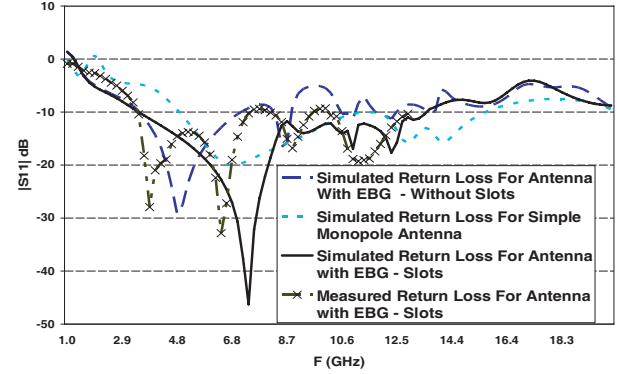
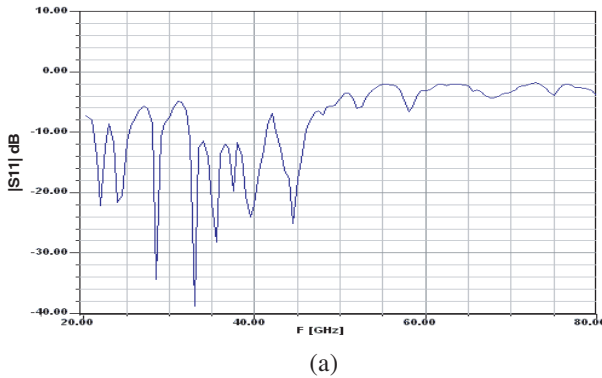
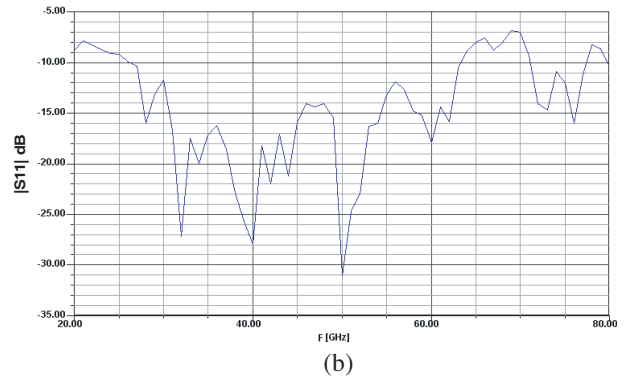


Figure 8: The measured and simulated return loss with and without EBG against frequency.



(a)



(b)

Figure 9: The simulated return loss of the proposed antenna. (a) Without EBG structure. (b) With EBG structure.

The input impedance, shown in Fig. 6, shows that the real part changes from 30 to 70 ohm, and the imaginary part changes from  $-20$  to 20 ohm, respectively. The return loss reduces to  $-50$  dB around 7 GHz. The proposed antenna was fabricated, Fig. 7. The measured and simulated return loss of the proposed antenna with the optimized dimensions with the EBG structure and without the EBG structure, are shown in Fig. 8.

Due to the pins of the EBG with its small dimensions, it can be considered as frequency selective surface FSS, so it resonates at higher frequencies [5], which extend from 26.5 to 63.5 GHz with bandwidth of 37 GHz, Fig. 9. It covers a wide range, 26.5–29 GHz, of the vehicular radar application which extends from 22–29 GHz.

The simulated *E*-plane and *H*-plane radiation patterns for the proposed antenna at 3.6, 6.6 and 11.8 GHz are shown in Fig. 10. It can be seen that the radiation patterns are bi-directional in the *E*-plane and almost Omni-directional in the *H*-plane, which indicates good monopole-like radiation characteristics are achieved over the operating bands.

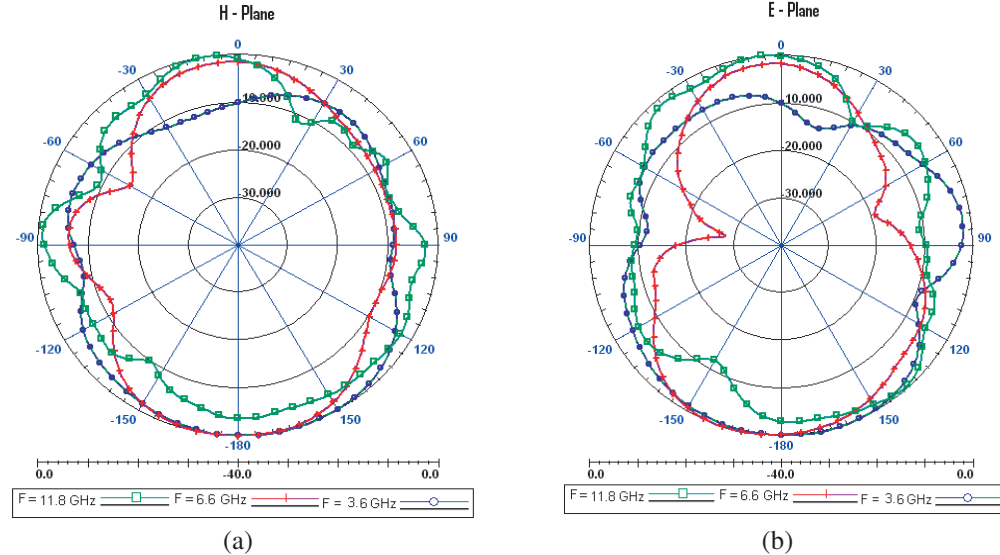


Figure 10: The radiation pattern of the proposed antenna at  $f = 3.6, 6.6, 11.8$  GHz. (a)  $H$ -plane. (b)  $E$ -plane.

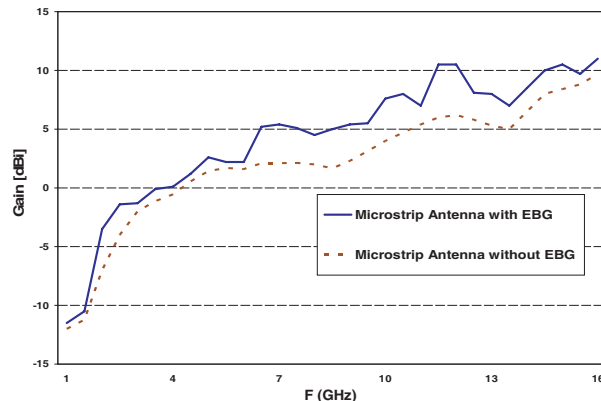


Figure 11: The simulated gain of the proposed antenna with and without EBG structure versus frequency.

Table 1: Comparison of the antenna parameters with and without EBG.

Antenna Type	Monopole antenna Without EBG structure	Monopole antenna with EBG structure
Bandwidth (GHz)	11	10
B.W (%)	161	146
Min. $S_{11}$ (dB)	-20	-50
Average radiation efficiency (%)	88	82
Average gain (dB)	4	6.5
Average directivity (dB)	4.5	7.5

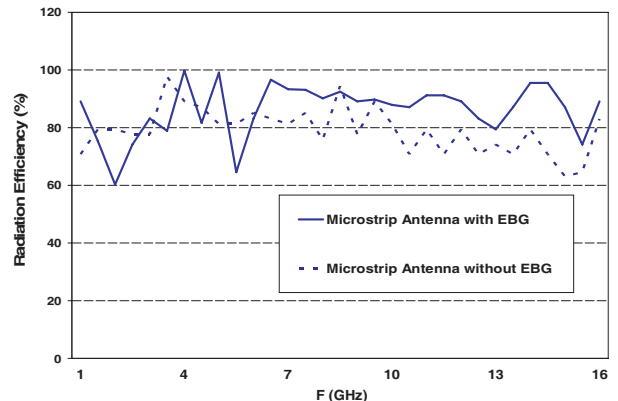


Figure 12: The simulated radiation efficiency of the proposed antenna with and without EBG structure versus frequency.

The gain of the proposed antenna with and without the EBG structure is shown in Fig. 11. For the antenna with and without EBG structure the average gain is 6.5 dBi, 4 dBi, respectively. The radiation efficiency of the proposed antenna is shown in Fig. 12 which equals 88% and 82%, for the two cases, and average directivity of 7.5 dBi and 4.5 dBi. Maximum gain reaches 11 dBi and 6 dBi, for the proposed antenna with and without the EBG structure, respectively throughout the

bandwidth. The overall comparison between the two cases, for different parameters is shown in Table 1.

#### 4. CONCLUSION

A new design of a modified UWB planar monopole antenna with high directivity and gain was presented using non periodic DGS and EBG structure. There are two inserted slots in the ground plane and an EBG structure placed symmetrically with respect to the center line of the structure around the radiating patch; with pins, penetrating the substrates of periodicity to form a mushroom like surface, which increased the impedance bandwidth of the antenna to 10 GHz. One of the advantages of this design is low cost compared to traditional EBG structures which uses two layers of substrates, this maintained the low profile of the planar structure with average directivity of 7.5 dB and average gain of 6.5 dB.

#### REFERENCES

1. FCC, “First report and order on ultra-wideband technology,” 2002.
2. Choi, S. H., J. K. Park, S. K. Kim, and J. Y. Park, “A new ultra-wideband antenna for UWB applications,” *Microwave and Optical Technology Letters*, Vol. 40, No. 5, 399, Mar. 5, 2004.
3. Zaker, R., C. Ghobadi, and J. Nourinia, “Novel modified UWB planar monopole antenna with variable frequency band-notch function,” *IEEE Antenna and Wireless Propagation Letters*, Vol. 7, 112–114, 2008.
4. Qu, D., L. Shafai, and A. Foroozesh, “Improving microstrip patch antenna performance using EBG substrates,” *IEE Proc. Microwave, Antennas Propag.*, Vol. 153, No. 6, 558–563, Dec. 2006.
5. Zhou, H., S. Qu, Z. Pei, J. Zhang, B.-Q. Lin, J. Wang, H. Ma, C. Gu, Z. Xu, P. Bai, and W.-D. Peng, “Narrow band frequency selective surface based on substrate integrated waveguide technology,” *Progress In Electromagnetic Research Letters*, Vol. 22, 19–28, 2011.

# Circularly Polarized Elliptical Slot Antenna with Enhanced Gain Using EBG Structure

Mohammed M. Mohanna<sup>1</sup>, Deena A. Salem<sup>2</sup>,  
Esmat A. F. Abdallah<sup>2</sup>, and Hadia M. S. El-Henawy<sup>3</sup>

<sup>1</sup>Ministry of Electricity & Energy, Egyptian Electricity Holding Company, Egypt

<sup>2</sup>Microstrip Department, Electronics Research Institute, Egypt

<sup>3</sup>Electronics and Communications Department, Ain Shams University, Egypt

**Abstract**— A circularly polarized elliptical slot antenna with enhanced gain using EBG structure is introduced. A new tapering profile that improves the matching and hence enhances the bandwidth is utilized. The tapering profile is based on the Willis-Sinha profile. The design is composed of an elliptical slot antenna on the upper side of a  $42 \times 42 \text{ mm}^2$ , FR4 dielectric substrate. On the lower side of the substrate, a Willis-Sinha tapered line feeds a modified U-shaped tuning stub. To enhance gain and bandwidth of the aforementioned antenna, mushroom like rectangular EBG structures were added to the lower side of the substrate to surround the projection of the U-shaped tuning stub. This new design exhibits a  $-10 \text{ dB}$  ultra wideband performance that extends from 2.7 to 16 GHz. Also it has average directivity, gain and radiation efficiency of 7.6 dBi, 6.7 dBi, 82%, respectively. At the upper end of the spectrum, the gain increases to reach 10.8 dBi, also it has a minimum axial ratio of 0.48 dB and axial ratio bandwidth extending from 8.2 to 11.6 GHz (35%).

## 1. INTRODUCTION

Recently, circularly polarized antennas are currently receiving much attention. Circular polarization is beneficial because current and future commercial and military applications (e.g., satellite, terrestrial communications) require the additional design freedom of not requiring alignment of the electric field vector at the receiving and transmitting locations.

On February 14, 2002, the Federal Communications Commission (FCC) of the United States adopted the First Report and Order that permitted the commercial operation of ultra wideband (UWB) technology [1], such that frequency range for UWB systems between 3.1 to 10.6 GHz.

Earlier, two novel designs of planar elliptical slot antennas were presented [2], which were printed on a dielectric substrate and fed by either microstrip line or coplanar waveguide with U-shaped tuning stub. The elliptical/circular slots exhibited an ultra wideband (UWB) behavior.

Besides, they showed nearly a unidirectional radiation pattern over a majority fraction of the bandwidth. Later, a printed elliptical slot antenna fed by different tapered microstrip line with U-shaped tuning stub and a circular ring-shaped tuning stub were proposed in [3] for UWB. The tapering improves the matching between the microstrip feed line and the tuning stub. All the above designs are adequate for UWB applications; however, some disadvantages exist, such as low directivity and low gain, besides the existence of surface waves, which affects directly the radiation efficiency.

In this paper, a new circularly polarized elliptical patch antenna with enhanced gain using EBG structure with a Willis-Sinha tapered line feeds a modified U-shaped tuning stub, on the lower side of the substrate is presented.

## 2. ANTENNA DESIGN

Figure 1 shows the configuration of the proposed circularly polarized antenna with enhanced gain using EBG structure. The proposed antenna is constructed on FR4 substrate with  $\tan \delta = 0.02$ , and size  $W_s \times L_s = 42 \times 42 \text{ mm}^2$ , thickness  $h = 1.5 \text{ mm}$  and relative dielectric constant of 4.65. As stated in [3], the dimension of the slot antenna is directly related to the lower edge of the impedance bandwidth. In the case of elliptical disc monopoles, it was reported that the optimal elliptical ratio  $A/B$  for obtaining a broader bandwidth lies in the range of 1.1 to 1.4 [4]. In our case and after optimization we found that the best value is  $A/B = 1.4$ , then it is obtained from [2] that  $A = 16 \text{ mm}$  and  $B = 11.5 \text{ mm}$ .

The dimensions of the U-shaped stub is obtained by using optimization technique and the dimensions that give the best values are:  $R_U = 5.9 \text{ mm}$ ,  $r_U = 2.9 \text{ mm}$ ,  $L_U = 6 \text{ mm}$  and  $W_U = 3 \text{ mm}$  [2]. Taper length is half wavelength ( $0.5\lambda_s$ ) in the case of linear and exponential tapers

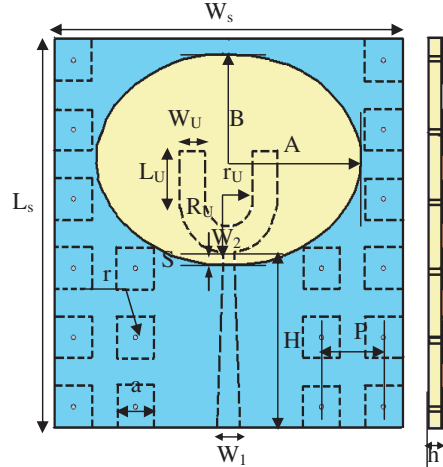


Figure 1: Geometry of the microstrip-fed printed elliptical slot antenna with EBG structure.

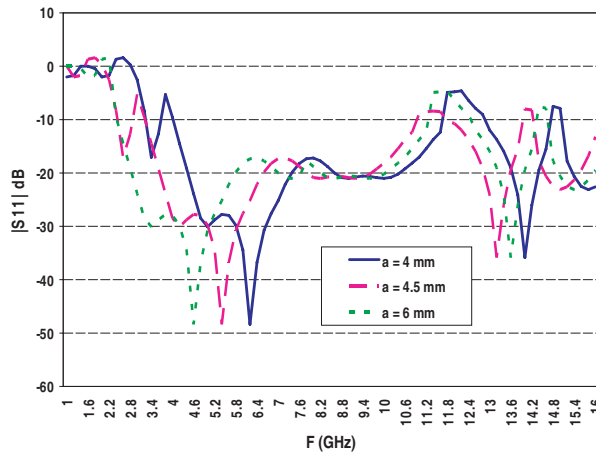


Figure 2: Parametric studies of parameter  $a$  when  $r = 0.25$  mm and  $P = 6.5$  mm.

and  $0.56\lambda_s$  where  $f_s = 3.1$  GHz in the case of Willis-Sinha taper,  $S = 1.6$  mm,  $W_1 = 2.72$  mm,  $W_2 = 1.26$  mm [3], with  $H = 19$  mm.

As illustrated in Fig. 1, the EBG structure is placed surround the Willis-Sinha tapered line feeds a modified U-shaped tuning stub on the lower side of the substrate, also is symmetrical with respect to the longitudinal direction. The EBG structure as a mushroom like surface i.e., periodic rectangular patches with via and it is considered as electromagnetic band gap materials and periodic dielectric which can stop the propagation of electromagnetic waves in certain directions, within certain frequency bands. The rectangular patches with length  $a$ , and via penetrating the substrate to the ground plane of radius  $r = 0.25$  mm which has periodicity  $P$ . The enhanced gain characteristic can be achieved by carefully choosing the parameters ( $a, P$ ).

### 3. RESULTS AND DISCUSSION

The simulated results are obtained by using the Ansoft high frequency structure simulator (HFSS) v.10. A parametric study has been done in order to get the optimum design by changing each parameter and fixing the others. The parameters to be changed are  $a, P$ , it affects the antenna bandwidth until reaching to the optimum design parameters.

The initial values  $a = 4$  mm,  $P = 6.5$  mm, changing  $a$  and fixing other parameters, it was clear that the optimum value of EBG small patches rectangular dimension  $a = 4.5$  mm,  $r = 0.25$  mm as shown in Fig. 2. Finally, changing  $P$  and fixing  $a_{new} = 4.5$  mm,  $r = 0.25$  mm, until obtaining  $P_{opt.} = 7.5$  mm,  $r = 0.25$  mm, which gives a  $-10$  dB bandwidth from 2.7 GHz to 13.3 GHz as shown in Fig. 3.

After Optimization the dimensions of a rectangular small patches are  $a = 4.5$  mm, with via penetrating the substrate to the ground plane of radius  $r = 0.25$  mm with periodicity  $P = 7.5$  mm. The optimized ratio of periodicity is  $a/P = 60\%$ . It is found that real part and imaginary part of

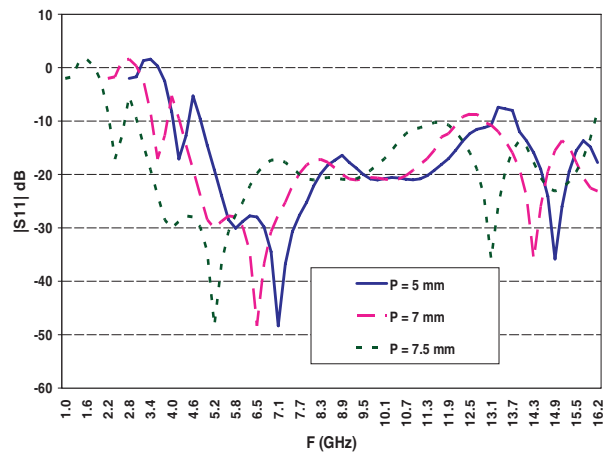


Figure 3: Parametric studies of parameter  $P$  when  $a = 4.5$  mm and  $r = 0.25$  mm.

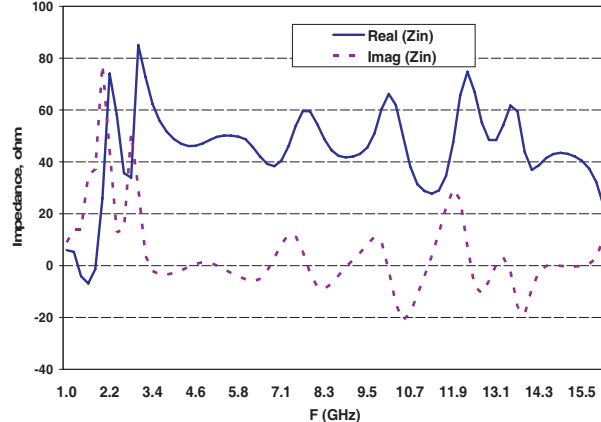


Figure 4: Input impedance of the elliptical antenna against frequency.

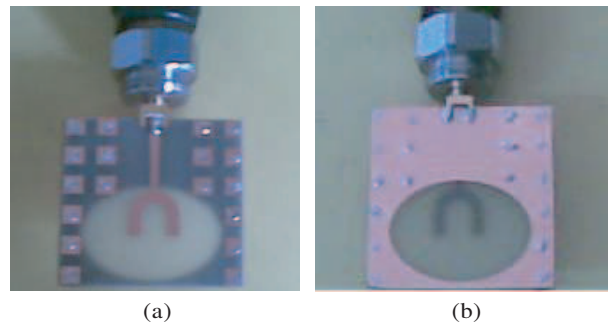


Figure 5: Fabricated antenna. (a) Bottom view. (b) Top view.

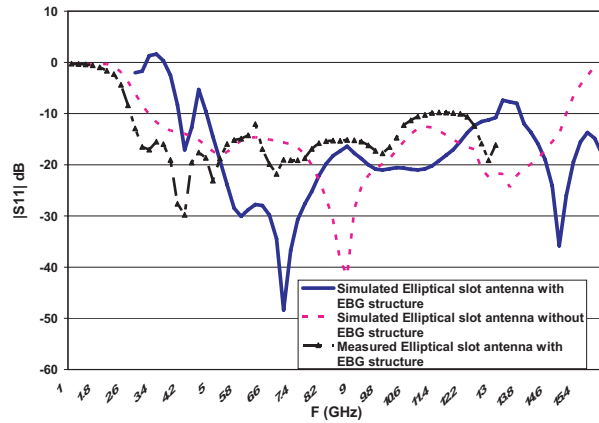


Figure 6: The measured and simulated return loss with and without EBG against frequency.

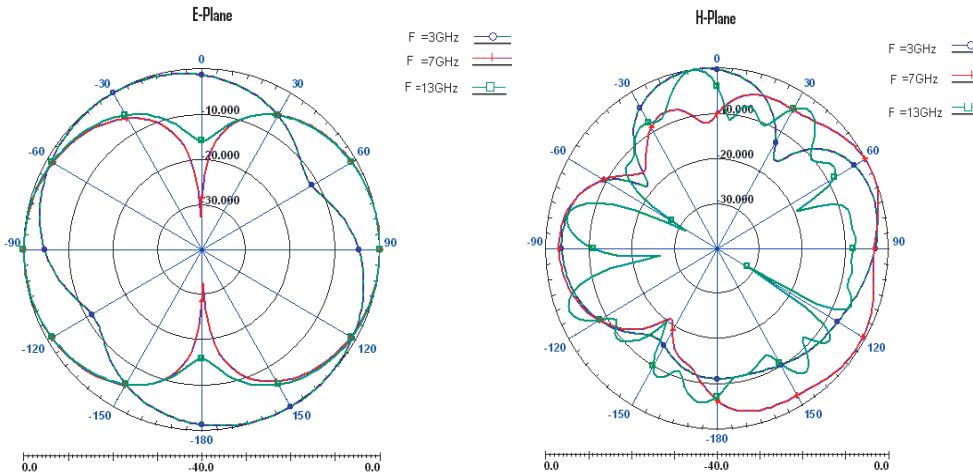


Figure 7: *E*-plane and *H*-plane radiation pattern of the proposed antenna at  $f = 3, 7, 13$  GHz.

the input impedance change from 35 to 85 and from  $-20$  to  $40$  ohm, respectively, as shown in Fig. 4. The input impedance may be accepted due to the large impedance bandwidth, but the real part of the input impedance along the bandwidth becomes higher than 50 ohm so it suffers acceptable reflection coefficient. The proposed antenna was fabricated, Fig. 5. The measured and simulated return loss results of the proposed antenna with optimized dimensions and its counterpart without loading the EBG structure is shown in Fig. 6.

The simulated normalized radiation patterns of the proposed antenna in *H*-plane (or  $x$ - $z$ ) and *E*-plane (or  $y$ - $z$ ) at the frequencies of 3, 7, and 13 GHz are plotted in Fig. 7. As shown in this figure, this design exhibits an omni-directional profile in lower frequencies for the  $x$ - $z$  plane and

bi-directional for the  $y$ - $z$  plane. As the frequency increases, the proposed antenna becomes more directive, but remains bidirectional.

The simulated gain of the proposed antenna with and without EBG structure is shown in Fig. 8. The average gain is 6.7 dBi, 4.8 dBi, respectively. Also the simulated radiation efficiency of the proposed antenna is shown in Fig. 9 which is equal to 82%, 80%, respectively, and leads to average directivity of 7.6 dBi, 5.8 dBi, respectively over the UWB bandwidth. The maximum gain reaches 10.8 dBi, 6.3 dBi, respectively over the bandwidth. The comparison between the values of the gain, directivity and radiation efficiency with and without EBG structure is shown in Table 1.

The axial ratio of EBG antenna is shown in Fig. 10 which shows a minimum axial ratio of 0.48 dB and gives axial ratio bandwidth extending from 8.2 GHz to 11.6 GHz (35%).

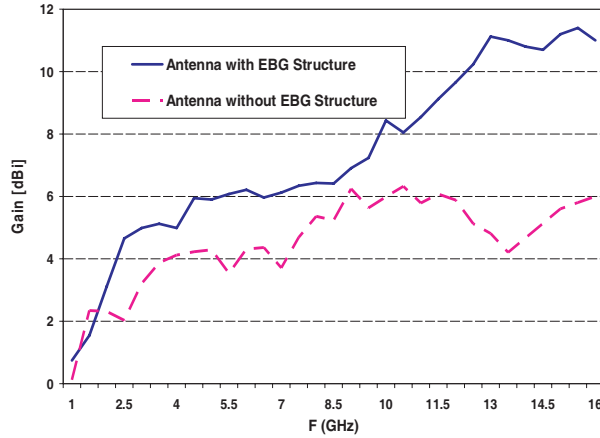


Figure 8: The simulated gain of the proposed antenna with-without EBG structure versus frequency.

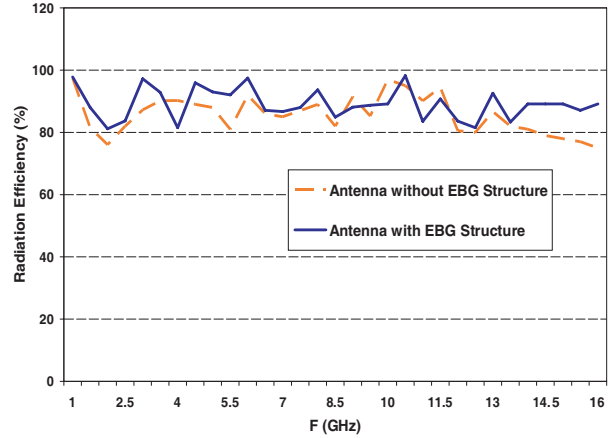


Figure 9: The simulated radiation efficiency of the proposed antenna with-without EBG structure versus frequency.

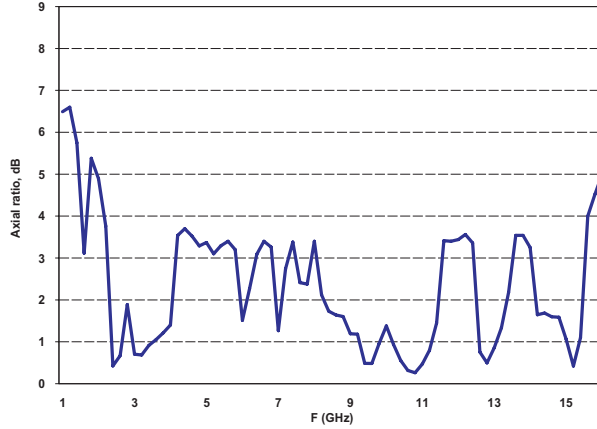


Figure 10: The simulated axial ratio of the proposed antenna.

Table 1: Comparison of antenna parameters with and without EBG.

Antenna Type	antenna without EBG	antenna with EBG
Bandwidth (GHz)	11.8	13.3
B.W (%) (-10 dB B.W)	172	194
Average radiation efficiency (%)	80	82
Average gain (dB)	4.8	6.7
Average directivity (dB)	5.8	7.6
Maximum gain (dB)	6.3	10.8

#### 4. CONCLUSION

A new modified elliptical slot antenna with U-shape tuning stub with high directivity and gain has been presented using EBG structure. The design takes into consideration the cost parameter of the antenna since it is fabricated on only one substrate not two layers substrate. This new design exhibits an ultra wideband performance that extends from 2.7 to 16 GHz and average directivity, gain and radiation efficiency of 7.6 dBi, 6.7 dBi, 82%, respectively. At the upper end of the spectrum, the gain increases to reach 10.8 dBi. Also it has a minimum axial ratio of 0.48 dB and gives an axial ratio bandwidth extending from 8.2 GHz to 11.6 GHz (35%).

#### REFERENCES

1. FCC, "First report and order on ultra-wideband technology," 2002.
2. Li, P., J. Liang, and X. Chen, "Study of printed elliptical/circular slot antennas for ultra wideband applications," *IEEE Trans. Antennas and Prop.*, Vol. 54, No. 6, 1670–1675, June 2006.
3. Abuhalima, S., E. Abdallah, and D. Mohamed, "Ultra wideband elliptical microstrip antenna using different taper lines for feeding," *11th WSEAS International Conference on Communications*, 144–149, Greece, July 26–28, 2007.
4. Agrawall, N. P., G. Kumar, and K. P. Ray, "Wide band planar monopole antennas," *IEEE Trans. Antennas and Prop.*, Vol. 46, No. 2, 294–295, February 1998.

# A New GL Anisotropic and Isotropic Invisible Cloak without Exceeding Light Speed Violation

Ganquan Xie, Jianhua Li, Lee Xie, and Feng Xie  
GL Geophysical Laboratory, USA

**Abstract**— In this paper, we propose a new GL EM anisotropic and isotropic invisible cloak class without exceeding light speed. The GL cloak material in this paper is different from our paper ArXiv 1050.3999. The radial dielectric and permeability of GL EM cloak in this paper are large than one. The refractive index of the GL cloak material,  $n(r)$ , is large than one or equal to one. A unconventional GL radial EM cloak modeling and inversion are proposed here. By searching in a distinctive class of the rational function of  $(h)$ ,  $h = r - R_1$ , the GL EM cloak modeling and inversion create GL EM invisible cloak class without exceeding light speed. The GL EM cloaks can be practicable by using conventional optical materials. The properties of our GL EM cloak and their proofs are presented in this paper. The novel EM wave propagation and front branching in the GL cloak by GL EM modeling are presented in this paper. The EM wave front propagation in GL cloak is behind of the front in free space. In the GL cloak, the wave front is curved as a crescent like and propagates slower than the light in free space. Its two crescent front peaks intersect at a front branching point. At the front branching point, the front is split to two fronts. The novel front branching and crescent like wave propagation are displayed in figures in this paper. A more exciting breakthrough progress is that we discovered GL isotropic invisible cloak without exceeding light speed. The isotropic relative dielectric and permeability parameter are proposed as (4)–(5) and (7) in our full paper. All copyright and patent of the GL EM cloaks and GL modeling and inversion methods are reserved by authors in GL Geophysical Laboratory.

## 1. INTRODUCTION

The new GL cloak without exceeding light speed in this paper is different from our paper [1]. The radial dielectric and permeability of GL EM cloak are large than one. The refractive index  $n(r)$ , is large than one or equal to one. In [2], Ulf Leonhardt referred almost all recent cloak publish papers, and wrote that “However, the realisation of electromagnetic cloaking suffers from a practical and a fundamental problem.”, he cited our paper [1] “ArXiv 1050.3999v1” as his reference [35], and wrote that “the preprint [35] proposes a different method for cloaking without superluminal propagation.” The detailed full paper and references are presented our GLGEO laboratory patent report [3]. The all contents of this paper are new and patented by GLGEO laboratory, any colleague downloads and refers this paper in his research work and paper, please cite our paper as reference.

A more exciting breakthrough progress is that we discovered GL isotropic invisible cloak without exceeding light speed. The isotropic relative dielectric and permeability parameter are proposed as (4)–(5) and (7) in our full paper. The description order of this paper is as follows: A new GL EM invisible cloak materials without exceeding light speed are proposed in Section 2. GL EM cloak modeling, and inversion and radial EM interal equations are proposed in Section 3 GL cloak properties are presented in Section 4. In Section 5, we give proof of the property 4. No scattering from GL cloak to disturb the exterior wave is proved in Section 6. In Section 7, by using GL EM modeling, we simulate full electromagnetic wave propagation through GL cloak and has no exceeding light speed propagation. The conclusion is presented in Section 8.

## 2. A NEW GL EM INVISIBLE CLOAK CLASS

### 2.1. GL EM Cloak without Exceeding Light Speed Wave

In this paper, we propose a new class of GL cloak without exceeding light speed which is used as outer layer in our GL double layer cloak. The inner cloak of our GL double layer cloak does no exceed light speed in [6] of [3]. In paper [13] of [3], we proved that there exist no Maxwell EM field can be excited by the source inside of the concealment, if the concealment is free space and cloaked by a single layer cloak. Therefore the double layer cloak is necessary for a normal EM environmental concealment. For overcoming the exceeding light speed difficulty, in this section, we propose a GL invisible cloak for outer layer of our double layer cloak [6] of [3]. In the concentric spherical annular  $R_1 \leq r \leq R_2$  cloaking device, we propose an GL cloaking material which consist

of the anisotropic dielectric diagonal matrix tensor  $\bar{\varepsilon}$  and permeability  $\bar{\mu}$  diagonal matrix tensor as follows:

$$\bar{\varepsilon} = \text{diag}(\varepsilon_r, \varepsilon_\theta, \varepsilon_\phi) \varepsilon_0 \quad (1)$$

$$\bar{\mu} = \text{diag}(\mu_r, \mu_\theta, \mu_\phi) \mu_0 \quad (2)$$

where  $\varepsilon_0$  is the basic dielectric parameter in free space,  $\varepsilon_r$  is the relative dielectric in  $r$  direction,  $\varepsilon_\theta$  is the relative dielectric in  $\theta$  direction,  $\varepsilon_\phi$  is the relative dielectric in  $\phi$  direction, similar explanation descriptions are for basic permeability  $\mu_0$  and for relative permeability parameters  $\mu_r, \mu_\theta, \mu_\phi$ . From the GL EM modeling [3] of [3] and inversion [5] of [3], we obtain a new anisotropic and isotropic form of the GL EM invisible cloak without exceeding light speed for all  $m > 0$  positive integral number. By GLGEO approving, we propose.

## 2.2. The GL Isotropic Invisible Cloak without Exceeding Light Speed Violation

By GL modeling, we are surprised to discover a new GL isotropic invisible cloak without exceeding light speed violation. The isotropic dielectric and permeability are proposed in (4)–(5) and (7). When condition (23) is satisfied, the relative dielectric and permeability are large than one. The GL invisible cloak can be practicable made by the conventional isotropic optical materials.

## 2.3. The Anisotropic Model GLM-2 EM Cloak

In this section, we propose a new GL EM invisibility GLM2 cloak as follows.

$$\begin{aligned} \varepsilon_r(r) = \mu_r(r) = & \frac{1}{2r^2} R_2 (3R_2 - 4R_1) - \frac{1}{r^2} \frac{(R_2 - 2R_1)}{R_2} \frac{4R_2^2 (r - R_1)}{G_2(R_1, R_2, R_2 - r)} \\ & + \frac{1}{2r^2} \frac{(3R_2 - 4R_1)}{R_2^5} \left( \frac{4R_2^2 (r - R_1)}{G_2(R_1, R_2, R_2 - r)} \right)^3 - \frac{1}{r^2} \frac{(R_2 - 2R_1)}{R_2^7} \left( \frac{4R_2^2 (r - R_1)}{G_2(R_1, R_2, R_2 - r)} \right)^4, \end{aligned} \quad (3)$$

and

$$\begin{aligned} \varepsilon_\theta(r) = \varepsilon_\phi(r) = \mu_\theta(r) = \mu_\phi(r) = & \frac{R_2}{\sqrt{r - R_1} \sqrt{G_2(R_1, R_2, R_2 - r)}} + \frac{4(R_2 - 2R_1) \sqrt{(r - R_1)R_2}}{(G_2(R_1, R_2, R_2 - r))^{\frac{3}{2}} F_2(R_1, R_2, (R_2 - r))}, \end{aligned} \quad (4)$$

where

$$\begin{aligned} G_2(R_1, R_2, R_2 - r) &= 3R_2 - 4R_1 + \sqrt{R_2^2 + 16(R_2 - R_1)(R_2 - r) - 8R_2(R_2 - r)}, \\ F_2(R_1, R_2, R_2 - r) &= \sqrt{R_2^2 + 16(R_2 - R_1)(R_2 - r) - 8R_2(R_2 - r)}, \end{aligned} \quad (5)$$

## 2.4. GL EM Anisotropic Cloak Class

For  $m > 0$  positive integral number, in the sphere annular  $R_1 \leq r \leq R_2$ , we propose a new practicable class of GL EM cloak without exceeding light speed wave.

$$\begin{aligned} \varepsilon_r(r) = \mu_r(r) = & \frac{1}{2r^2} R_2 ((2m - 1)R_2 - 2mR_1) + \frac{1}{r^2} \frac{(-(m - 1)R_2 + mR_1)}{R_2^{m-1}} \frac{2mR_2^m (r - R_1)}{G_m(R_1, R_2, R_2 - r)} \\ & + \frac{1}{r^2} \frac{(-(m - 1)R_2 + mR_1)}{R_2^{3m+1}} \left( \frac{2mR_2^m (r - R_1)}{G_m(R_1, R_2, R_2 - r)} \right)^{\frac{3m+2}{m}} + \dots, \end{aligned} \quad (6)$$

$$\varepsilon_\theta(r) = \varepsilon_\phi(r) = \mu_\theta(r) = \mu_\phi(r) = \frac{2R_2}{(2m(r - R_1))^{\frac{m-1}{m}} (G_m(R_1, R_2, R_2 - r))^{\frac{1}{m}}} + \dots \quad (7)$$

## 3. GL EM MODELING AND INVERSION IN SPHERICAL SYSTEM

Because the anisotropic dielectric and magnetic permeability electromagnetic parameters are radial dependence functions, In this section, we propose the three dimension and one dimension Maxwell equation in the spherical coordinate system with the anisotropic EM parameters.

### 3.1. Three Dimension Spherical Maxwell Equation

In this section, we propose the three dimension Maxwell equation in the spherical coordinate system with the anisotropic EM parameters:

$$\begin{aligned} & \frac{1}{r^2} \frac{\partial}{\partial r} \frac{1}{(\mu_\theta)} \frac{\partial}{\partial r} (r^2 \mu_r H_r) + \frac{1}{r^2} \frac{1}{\sin \theta} \frac{\partial}{\partial \theta} \sin \theta \frac{\partial}{\partial \theta} H_r + \frac{1}{r^2 \sin^2 \theta} \frac{\partial^2}{\partial \phi^2} H_r + \omega^2 \varepsilon_\theta \mu_r H_r \\ &= \frac{1}{\sin \theta} \left( \frac{\partial}{\partial \phi} (J_\theta) \right) - \frac{1}{\sin \theta} \frac{\partial}{\partial \theta} \sin \theta (J_\phi), \end{aligned} \quad (8)$$

$$\frac{1}{r^2} \frac{\partial}{\partial r} \frac{1}{(\varepsilon_\theta)} \frac{\partial}{\partial r} (r^2 \varepsilon_r E_r) + \frac{1}{r^2} \frac{1}{\sin \theta} \frac{\partial}{\partial \theta} \sin \theta \frac{\partial}{\partial \theta} E_r + \frac{1}{r^2 \sin^2 \theta} \frac{\partial^2}{\partial \phi^2} E_r + \omega^2 \mu_\theta \varepsilon_r E_r = S(J) \quad (9)$$

$$S(J) = (i\omega \mu_\theta) J_r - \frac{1}{r^2} \frac{\partial}{\partial r} \frac{1}{(i\omega \varepsilon_\theta)} \left( \frac{\partial}{\partial r} (r^2 J_r) \right) - \frac{1}{r^2 \sin \theta} \frac{\partial}{\partial r} \frac{\partial}{\partial \theta} \sin \theta \frac{r J_\theta}{(i\omega \varepsilon_\theta)} - \frac{1}{r^2 \sin \theta} \frac{\partial}{\partial r} \frac{\partial}{\partial \phi} \frac{r J_\phi}{i\omega \varepsilon_\phi}. \quad (10)$$

$$\frac{1}{r} \frac{\partial}{\partial r} \frac{1}{(i\omega \mu_\phi)} \frac{\partial r E_\theta}{\partial r} - (i\omega \varepsilon_\theta) E_\theta = - \frac{1}{r \sin \theta} \frac{\partial}{\partial \phi} H_r + \frac{1}{r} \frac{\partial}{\partial r} \frac{1}{(i\omega \mu_\phi)} \frac{\partial E_r}{\partial \theta} + J_\theta, \quad (11)$$

$$\frac{1}{r} \frac{\partial}{\partial r} \frac{1}{(i\omega \mu_\theta)} \left( \frac{\partial}{\partial r} (r E_\phi) \right) - (i\omega \varepsilon_\theta) E_\phi = \frac{1}{r} \frac{\partial}{\partial r} \frac{1}{(i\omega \mu_\theta) \sin \theta} \left( \frac{\partial E_r}{\partial \phi} \right) + \frac{1}{r} \frac{\partial}{\partial \theta} H_r + J_\phi, \quad (12)$$

$$\frac{1}{r} \frac{\partial}{\partial r} \left( \frac{1}{(i\omega \varepsilon_\phi)} \frac{\partial}{\partial r} r H_\theta \right) - (i\omega \mu_\theta) H_\theta = \frac{1}{r \sin \theta} \frac{\partial}{\partial \phi} E_r + \frac{1}{r} \frac{\partial}{\partial r} \left( \frac{1}{(i\omega \varepsilon_\phi)} \frac{\partial}{\partial \theta} H_r \right) + \frac{1}{r} \frac{\partial}{\partial r} \frac{r J_\phi}{i\omega \varepsilon}, \quad (13)$$

$$\frac{1}{r} \frac{\partial}{\partial r} \frac{1}{(i\omega \varepsilon_\theta)} \left( \frac{\partial}{\partial r} (r H_\phi) \right) - (i\omega \mu_\theta) H_\phi = \frac{1}{r} \frac{\partial}{\partial r} \frac{1}{(i\omega \varepsilon_\theta) \sin \theta} \frac{\partial}{\partial \phi} H_r - \frac{1}{r} \frac{\partial}{\partial \theta} E_r - \frac{1}{r} \frac{\partial}{\partial r} \frac{r J_\theta}{(i\omega \varepsilon_\theta)}, \quad (14)$$

where  $E_r$  is the radial component of the electric wave,  $E_\theta$  is the  $\theta$  component,  $E_\phi$  is the  $\phi$  component,  $H_r$  is the radial component of the magnetic wave,  $H_\theta$  is the  $\theta$  component,  $H_\phi$  is the  $\phi$  component.

### 3.2. One Dimensional Radial Maxwell Equation

In this section, we propose the one dimensional Maxwell equation in the spherical coordinate system with the anisotropic EM parameters. Suppose that the EM sources are located outside of the cloak, i.e.,  $r > R_2 + \delta$ , the  $\delta > 0$ , we consider the radial inhomogeneous Maxwell equations of the spherical Maxwell Equations (8)–(14). The general solution of these equations, for example, is as follows,

$$H_r(r, \theta, \phi) = \sum_{l=1}^{\infty} h_l(r) \sum_{m=-l}^l Y_l^m(\theta, \phi). \quad (15)$$

Substitute (15) for  $H_r$  in the radial inhomogeneous Maxwell equations of the spherical Maxwell Equations (8)–(14), we have

$$\frac{1}{r^2} \frac{\partial}{\partial r} \frac{1}{(\mu_\theta)} \frac{\partial}{\partial r} (r^2 \mu_r h_l) - \frac{l(l+1)}{r^2} h_l + (\omega^2 \varepsilon_\theta) (\mu_r h_l) = 0, \quad (16)$$

and

$$\frac{1}{r^2} \frac{\partial}{\partial r} \frac{1}{(\varepsilon_\theta)} \frac{\partial}{\partial r} (r^2 \varepsilon_r e_l) - \frac{l(l+1)}{r^2} e_l + (\omega^2 \mu_\theta) (\varepsilon_r e_l) = 0. \quad (17)$$

### 3.3. New Radial EM Integral Equation

In this section, we propose a new radial electromagnetic integral equation as follows:

$$\begin{aligned} r^2 \mu_r h_l(r) &= r^2 \mu_{r,b} h_{l,b} + \omega^2 \int_{R_1}^{R_2} r'^4 (\mu_r \varepsilon_{\theta,b} \mu_{r,b} - \mu_{r,b} \varepsilon_\theta \mu_r) G_{l,b} h_l dr' - l(l+1) \int_{R_1}^{R_2} r'^2 (\mu_r - \mu_{r,b}) G_{l,b} h_l dr' \\ &\quad - \int_{R_1}^{R_2} \left( \frac{1}{\mu_{\theta,b}} - \frac{1}{\mu_\theta} \right) \frac{\partial}{\partial r'} (r'^2 \mu_r h_l) \frac{\partial}{\partial r'} (r'^2 \mu_{r,b} G_{l,b}) dr', \end{aligned} \quad (18)$$

and its dual integral equation,

$$\begin{aligned} r^2 \mu_r h_l(r) = & r^2 \mu_{r,b} h_{l,b}(r) + \omega^2 \int_{R_1}^{R_2} r'^4 (\mu_r \varepsilon_{\theta,b} \mu_{r,b} - \mu_{r,b} \varepsilon_{\theta} \mu_r) G_l h_{l,b} dr' - l(l+1) \int_{R_1}^{R_2} r'^2 (\mu_r - \mu_{r,b}) G_l h_{l,b} dr' \\ & - \int_{R_1}^{R_2} \left( \frac{1}{\mu_{\theta,b}} - \frac{1}{\mu_{\theta}} \right) \frac{\partial}{\partial r'} (r'^2 \mu_{r,b} h_{l,b}) \frac{\partial}{\partial r'} (r'^2 \mu_r G_l) dr'. \end{aligned} \quad (19)$$

Similar integral equation and dual equation for the electric field  $e_l$ ,  $l = 1, 2, \dots$

### 3.4. New GL Modeling for Radial EM Wave Propagation

We propose a new GL modeling for radial electromagnetic wave propagation.

1 The interval  $[R_1, R_2]$  is divided into sub intervals  $\Omega_k = [r_k, r_{k+1}]$ , such that

$$[R_1, R_2] = \bigcup_{k=0}^N \Omega_k = \bigcup_{k=0}^N [r_k, r_{k+1}]. \quad (20)$$

2 Let  $h_{l,0}(r) = h_{l,b}(r)$ ,  $G_{l,0}(r', r) = G_{l,b}(r', r)$ , By induction, suppose that  $h_{l,k-1}$  and  $G_{l,k-1}(r', r)$  are found in the  $(k-1)$ th step, we solve the triangle Green's function integral Equations (18)–(19) in the sub domain  $\Omega_k$  to obtain  $G_{l,k}(r', r)$ .

3 Using the following new integral formula (19) in the sub domain  $\Omega_k$

$$\begin{aligned} r^2 \mu_r h_{l,k}(r) = & r^2 \mu_{r,b} h_{l,k-1}(r) + \omega^2 \int_{R_k}^{R_{k+1}} r'^4 (\mu_r \varepsilon_{\theta,b} \mu_{r,b} - \mu_{r,b} \varepsilon_{\theta} \mu_r) G_{l,k} h_{l,k-1} dr' \\ & - l(l+1) \int_{R_k}^{R_{k+1}} r'^2 (\mu_r - \mu_{r,b}) G_{l,k} h_{l,k-1} dr' \\ & - \int_{R_1}^{R_2} \left( \frac{1}{\mu_{\theta,b}} - \frac{1}{\mu_{\theta}} \right) \frac{\partial}{\partial r'} (r'^2 \mu_{r,b} h_{l,k-1}) \frac{\partial}{\partial r'} (r'^2 \mu_r G_{l,k}) dr', \end{aligned} \quad (21)$$

we calculate  $h_{l,k}(r)$ .

4 The steps (2) and (3) form a finite iterations,  $k = 1, 2, \dots, n$ . The  $h_{l,n}(r)$  is the solution of our GL method for radial magnetic Equation (16) with anisotropic EM material parameters. The GL method is used for solving radial electric wave Equation (17) and radial EM Equations (11)–(14).

## 4. PROPERTIES OF GL INVISIBLE CLOAK

In previous section, we proposed the GL class of the EM invisible cloak without exceeding light speed wave. The GL cloak properties are presented in this section.

**Property 1:** Assume that the GL relative cloak material  $\varepsilon_r(r)$  and  $\mu_r(r)$  are defined by (3) and (5) in the cloak,  $\varepsilon_r(r) = 1$  and  $\mu_r(r) = 1$  in the free space and concealment, then the relative radial dielectric parameter  $\varepsilon_r(r)$  and magnetic permeability  $\mu_r(r)$  are continuous in domain  $r > R_1$ , in particular, cross  $r = R_2$ , we have

$$\varepsilon_r(R_2) = \mu_r(R_2) = 1. \quad (22)$$

**Property 2:** Under the conditions in property 1 and if there is the additional assumption,

$$R_1 = \frac{(2m-1)(m-1)R_2}{2m^2} \quad (23)$$

then the first derivative of the dielectric and permeability are continuous in domain  $r > R_1$ , in particular, cross the outer boundary  $r = R_2$ ,

$$\frac{d}{dr} \varepsilon_r(R_2) = \frac{d}{dr} \mu_r(R_2) = 0. \quad (24)$$

**Property 3:** Assume that the EM relative transverse dielectric  $\varepsilon_\theta(r)$ ,  $\varepsilon_\phi(r)$  and permeability  $\mu_\theta(r)$ ,  $\mu_\phi(r)$  materials are defined by (4) and (5) in the GL cloak,  $\varepsilon_\theta(r) = \varepsilon_\phi(r) = 1$  and  $\mu_\theta(r) = \mu_\phi(r) = 1$  in the free space and concealment, then

$$\varepsilon_\theta(R_2) = \mu_\theta(R_2) = \varepsilon_\phi(R_2) = \mu_\phi(R_2) = 1, \quad (25)$$

the relative transverse dielectric parameter  $\varepsilon_\theta(r), \varepsilon_\phi(r)$  and magnetic permeability  $\mu_\theta(r), \mu_\phi(r)$  are continuous in domain  $r > R_1$ , in particular, cross outer boundary  $r = R_2$ .

**Property 4:** Under the conditions of the property 3, and if there is the additional assumption (23), then

$$\frac{d}{dr}\varepsilon_\theta(R_2) = \frac{d}{dr}\varepsilon_\phi(R_2) = \frac{d}{dr}\mu_\theta(R_2) = \frac{d}{dr}\mu_\phi(R_2) = 0. \quad (26)$$

the first derivative of the  $\varepsilon_\theta(r)$ ,  $\varepsilon_\phi(r)$ ,  $\mu_\theta(r)$ , and  $\mu_\phi(r)$  are continuous in domain  $r > R_1$ , in particular, cross outer boundary  $r = R_2$ .

**Property 5:** Under the conditions of the property 1 and 3, if there is the additional assumption (23), there exist EM wave  $E(r, \theta, \phi)$  and  $H(r, \theta, \phi)$  satisfy the Maxwell Equation (1), moreover, the grading  $\nabla E(r, \theta, \phi)$  and  $\nabla H(r, \theta, \phi)$  are continuous in the domain  $r > R_1$ , in particular, the exterior EM wave  $E(r, \theta, \phi)$ ,  $H(r, \theta, \phi)$  and their grading  $\nabla E(r, \theta, \phi)$  and  $\nabla H(r, \theta, \phi)$  are continuous cross the outer boundary  $r = R_2$ . Therefore, there is no scattering wave from the cloak to disturb the exterior EM wave.

**Property 6:** Under the conditions of the property 5, then the EM wave propagation  $E(r, \theta, \phi)$  and  $H(r, \theta, \phi)$  can not penetrate into the concealment.

**Property 7:** Under the conditions of the property 5, we have the refractive index

$$N(r) = \sqrt{\varepsilon_r(r)\mu_\theta(r)} = \sqrt{\varepsilon_\theta(r)\mu_r(r)} \geq 1, \quad (27)$$

in the all cloak domain  $R_1 \leq r \leq R_2$ .

**Property 8:** Under the conditions of the property 5, when the source and receiver are located outside of cloak, then

$$\begin{aligned} & \omega^2 \int_{R_1}^{R_2} r'^4 (\mu_r \varepsilon_{\theta,b} \mu_{r,b} - \mu_{r,b} \varepsilon_\theta \mu_r) G_{l,b} h_l dr' - l(l+1) \int_{R_1}^{R_2} r'^2 (\mu_r - \mu_{r,b}) G_{l,b} h_l dr' \\ & - \int_{R_1}^{R_2} \left( \frac{1}{\mu_{\theta,b}} - \frac{1}{\mu_\theta} \right) \frac{\partial}{\partial r'} (r'^2 \mu_r h_l) \frac{\partial}{\partial r'} (r'^2 \mu_{r,b} G_{l,b}) dr' = 0, \end{aligned} \quad (28)$$

i.e., there is no scattering wave from the GL EM cloak to disturb the incident EM wave in the free space

$$h_l(r) = h_{l,b} \quad (29)$$

when the source is located outside of cloak, and the receiver is located inside of the concealment then

$$\begin{aligned} & r^2 \mu_{r,b} h_{l,b} + \omega^2 \int_{R_1}^{R_2} r'^4 (\mu_r \varepsilon_{\theta,b} \mu_{r,b} - \mu_{r,b} \varepsilon_\theta \mu_r) G_{l,b} h_l dr' - l(l+1) \int_{R_1}^{R_2} r'^2 (\mu_r - \mu_{r,b}) G_{l,b} h_l dr' \\ & - \int_{R_1}^{R_2} \left( \frac{1}{\mu_{\theta,b}} - \frac{1}{\mu_\theta} \right) \frac{\partial}{\partial r'} (r'^2 \mu_r h_l) \frac{\partial}{\partial r'} (r'^2 \mu_{r,b} G_{l,b}) dr' = 0, \end{aligned} \quad (30)$$

i.e., the exterior EM wave can not propagate penetrate into the concealment, the concealment is invisible room, inside of the concealment,

$$h_l = 0. \quad (31)$$

Therefore GL EM cloak is complete cloak,

The radial component  $\varepsilon_r > 1$  and  $\mu_r > 1$  and tangential component  $\varepsilon_\theta > 1$  and  $\mu_\theta > 1$  are large than one in whole GL EM cloak domain. The refractive index  $N > 1$  in the whole GL EM cloak. Therefore GL EM cloak is practicable complete cloak without exceeding light speed wave through it.

## 5. THE PROOF OF THE PROPERTY 4

To calculate  $\frac{d}{dr}G_2(R_1, R_2, R_2 - R_2)$  and using condition (23),  $-3R_2 + 8R_1 = 0$ , we have

$$\frac{d\varepsilon_\theta(R_2)}{dr} = \frac{d\varepsilon_\phi(R_2)}{dr} = \frac{d\mu_\theta(R_2)}{dr} = \frac{d\mu_\phi(R_2)}{dr} = \frac{R_2}{(2(R_2 - R_1))^2} \left( -\frac{1}{2} + \frac{3}{16} + \frac{5}{16} \right) = 0 \quad (32)$$

The formula (32) is the formula (26) in property 4, therefore, we proved that the derivative of the transverse dielectric and magnetic permeability is continuous.

## 6. NO SCATTERING FROM GL CLOAK TO DISTURB THE EXTERIOR WAVE

### 6.1. The Continuous of the Solution of ODE with the Variable Coefficient

$$y'' + p(x)y' + q(x)y = 0, \quad (33)$$

$$\frac{d}{dx} \begin{bmatrix} y \\ y_1 \end{bmatrix} = \begin{bmatrix} 0 & 1 \\ -q(x) & -p(x) \end{bmatrix} \begin{bmatrix} y \\ y_1 \end{bmatrix}, \quad (34)$$

$$\begin{bmatrix} y \\ y_1 \end{bmatrix} = e^{-\int_a^x \begin{bmatrix} 0 & -1 \\ q(\xi) & p(\xi) \end{bmatrix} d\xi} \begin{bmatrix} C \\ C_1 \end{bmatrix}, \quad (35)$$

Therefore, when  $p(x)$  and  $q(x)$  are continuous or integrable, the solution  $y(x)$  of the second differential Equation (33) and its derivative function  $y'(x)$  are continuous.

### 6.2. No Scattering from GL Cloak to Disturb the Exterior Wave

The radial magnetic Equation (16) and the radial electric Equation (17) can be translated to the second linear differential Equation (33).

$$p(r) = P(\varepsilon_r(r), \frac{d}{dr}\varepsilon_r(r), \mu_r(r), \frac{d}{dr}\mu_r(r), \varepsilon_\theta(r), \frac{d}{dr}\varepsilon_\theta(r), \mu_\theta(r), \frac{d}{dr}\mu_\theta(r)), \quad (36)$$

$$q(r) = Q(\varepsilon_r(r), \frac{d}{dr}\varepsilon_r(r), \mu_r(r), \frac{d}{dr}\mu_r(r), \varepsilon_\theta(r), \frac{d}{dr}\varepsilon_\theta(r), \mu_\theta(r), \frac{d}{dr}\mu_\theta(r)), \quad (37)$$

In our patent report in <http://www.glgeo.com>, we proved the GL EM cloak material components and their derivative  $\varepsilon_r(r)$ ,  $\frac{d}{dr}\varepsilon_r(r)$ ,  $\mu_r(r)$ ,  $\frac{d}{dr}\mu_r(r)$ ,  $\varepsilon_\theta(r)$ ,  $\frac{d}{dr}\varepsilon_\theta(r)$ ,  $\mu_\theta(r)$ ,  $\frac{d}{dr}\mu_\theta(r)$  are continuous, from (36) and (37) we know the  $p(x)$  and  $q(x)$  are continuous. Therefore the radial magnetic wave  $h_l$  and radial electric wave  $e_l$  and their derivative functions are continuous. From the formula (15), we know that magnetic wave  $H_r(r)$  and electric wave  $E_r(r)$  and their derivative functions are continuous cross the outer boundary  $r = R_2$ . Therefore, no scattering wave from the GL EM cloak to disturb the exterior incident wave in free space. We can prove that when in the cloak,  $r$  going to  $R_1$ , the magnetic wave  $H_r(r)$  and electric wave  $E_r(r)$  and their derivative functions are continuous decay going to zero. The exterior EM wave can not be propagate penetrate into the concealment.

### 6.3. No Scattering from Coordinate Transform Cloak to Disturb the Exterior Wave

Assume that a cloak is made by coordinate transform, to substitute the coordinate transform  $r = f(r')$  into the EM equations in the spherical system (10) and (11), immediately, we obtain the EM equation in cloak media with anisotropic permittivity and permeability  $\varepsilon_r = \mu_r = (r'/r)^2 dr/dr'$ , and  $\varepsilon_\theta = \mu_\theta = dr'/dr$ . However, blow up coordinate transform cloak has “exceeding light speed” physical difficulty.

## 7. FULL ELECTROMAGNETIC WAVE PROPAGATION THROUGH GL CLOAK AND HAS NO EXCEEDING LIGHT SPEED PROPAGATION

In this section, using the GL EM modeling method, we simulate full electromagnetic wave propagation through GL cloak and has no exceeding light speed propagation. Let  $E_{z,b}$  denote the background electric intensity plane wave at source plane  $x = x_s$ ,  $x = -0.83$ , in the left side outside of the cloak in free space.,

$$E_{z,b}(x, x_s, t) = \delta(x - x_s)\delta(t). \quad (38)$$

The electric plane wave is denoted by vertical red line through red  $S$  in the figures in this paper. In Figure 1, at time step 84dt, the electric wave  $E_z$  inside of the GL EM cloak  $R_1 \leq r \leq R_2$

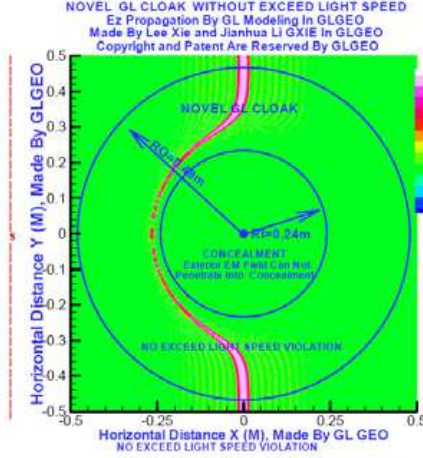


Figure 1: (color online) Electric wave  $E_z$  propagation at time step 84 dt.

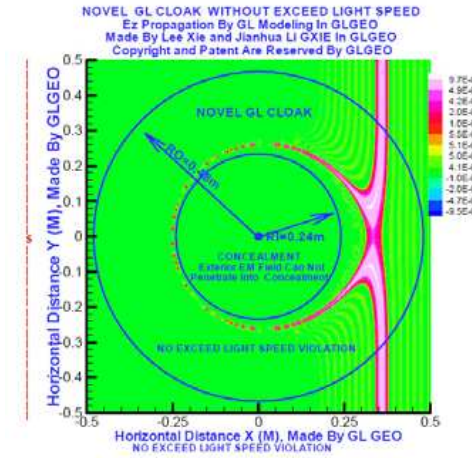


Figure 2: (color online) Electric wave  $E_z$  propagation at time step 94 dt.

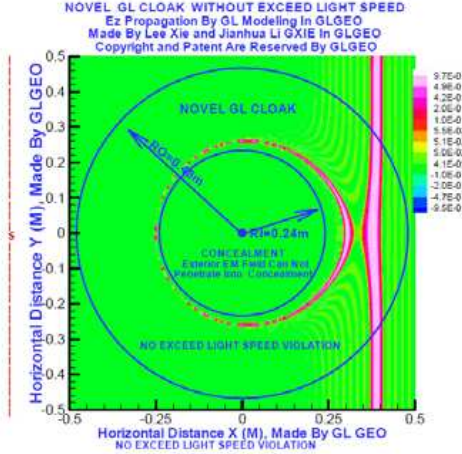


Figure 3: (color online) Electric wave  $E_z$  propagation at time step 123 dt.

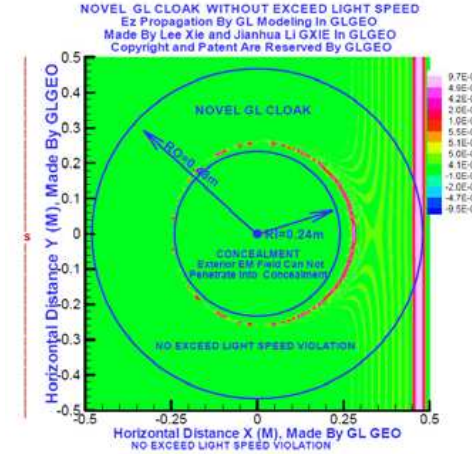


Figure 4: (color online) Electric wave  $E_z$  propagation at time step 131 dt.

propagates slower than light speed. In Figure 2, at time step 120 dt, electric wave  $E_z$  inside of the GL EM cloak  $R_1 \leq r \leq R_2$  propagates slower than light speed. The upside and downside parts of curved CRESCENT electric wave front are intersected at a branching point. These branching points form a 2D subsurface which depends on the source location. The vertical red dashing line cross red  $S$  denotes the incident electric plane wave  $E_{z,b}$  which is located in the left of the cloak. The front branching point is located in right of the concealment. The Figure 3 shows that at time step 123 dt,  $E_z$  electric wave front is split to two wave fronts, The outgoing front propagates forward to left and going to outer boundary  $r = R_2$ . The attractive front propagates and shrinks to the inner boundary. The two wave front propagate slower than light speed. In Figure 4, at time step 131 dt, the outgoing front of the electric wave  $E_z$  propagates on the outer boundary  $r = R_2$ , the attracting front rapid decay to zero and closes to the inner boundary of the cloak,  $r = R_1$ .

## 8. THE CONCLUSION

By the GL invisible cloak class properties in Section 4 and full EM propagation through the GL EM cloak, our GL EM invisible cloak without exceeding light speed that is verified. Compare the electric wave  $E_z$  propagation through GL cloak in Figure 1 and through Ps cloak in Figure 16 in [3] at 84 step time. It is obvious that the GL EM cloak has no exceeding light speed difficulty, but the Ps cloak has the infinite speed difficulty. Figure 17 in [3] shows that at 94 step time,  $E_z$  wave through Ps cloak exceeds light speed.

**ACKNOWLEDGMENT**

We wish to acknowledge the support of the GL Geophysical Laboratory and thank the GLGEO Laboratory to approve the paper publication. Authors thank to Prof. P. D. Lax, Prof. Michael Oristaglio, Prof. Yuesheng Li, Prof. Qin Jiang, and Prof. Hong Sheng Chen for their help and encouragements.

**REFERENCES**

1. Xie, G., J. Li, L. Xie, and F. Xie, arXiv:1005.3999.
2. Perczel, T. T. and U. Leonhardt, arXiv:1105.0164.
3. Xie, G., J. Li, L. Xie, and F. Xie, "New GL invisible cloak without exceeding light speed wave," GL Geophysical Laboratory patent report, <http://www.glgeo.com>.

# Increasing the Efficiency of Forward-backward Time-stepping Reconstruction Method

H. Zhou and H. J. Zhang

State Key Laboratory of Petroleum Resource and Prospecting

Key Laboratory of Geophysical Exploration of China National Petroleum Corporation

Department of Geophysics, China University of Petroleum, Changping, Beijing 102249, China

**Abstract**— The time-domain forward-backward time-stepping (FBTS) inversion method is a reconstruction technique being capable of reconstructing large objects. However its efficiency is affected by saving great amount of simulation data to hard disk and reading them from it. This paper proposes a method which need not save simulation data. In the proposed method, the simulation data is obtained by finite-difference time-domain (FDTD) method with perfect matched layer (PML) absorbing boundaries, and the simulation of the adjoint field is calculated using FDTD too, but random boundaries are used. In the random boundaries, the permittivity is randomly distributed and the adjoint fields caused by the random boundaries are uncorrelated. The adjoint field is calculated reverse in time, and the wave fields at 0 and  $\Delta t/2$  are saved to hard disk. The adjoint field at any time step is calculated from the saved initial conditions. As a result, the computation sequence of both fields is kept in the same forward time direction. A numerical reconstruction example is illustrated to compare inversion results using the conventional and the suggested methods. The reconstructed results by using these methods are almost the same, however, the calculation time of the suggested method is about 78% of the conventional method.

## 1. INTRODUCTION

Ground-penetrating radar (GPR) has been applied to various fields and solved many detection problems. As one kind of interpretation methods, the techniques to reveal quantitative properties of subsurface from GPR data have been investigated by many researches. Among these methods, there are inverse scattering reconstruction techniques in the frequency-domain [1, 2] and time-domain [3–5].

We have discussed a forward-backward time-stepping (FBTS) method to reconstruct electrical property profiles of objects using the time-domain electromagnetic data [4, 5]. The gradients of the cost functional with respect to unknown parameters (permittivity and conductivity) are expressed explicitly by introducing an adjoint vector field. In order to calculate the gradients, the wave field corresponding to a guessed model of the whole reconstruction space at all time must be saved to the hard disk. During the calculation of the gradients, the saved data are read from the hard disk and crosscorrelated with the adjoint field just calculated. As it is well known that the storage and read of data from hard disk is very time consuming, particularly for three-dimensional reconstruction problems because the amount of the guessed field is very huge. Low efficiency is the bottleneck of this reconstruction method for large scale practical applications.

This paper suggests a method for avoiding the storage and read of the large amount of simulation data in order to increase the efficiency of the reconstruction method.

## 2. RECONSTRUCTION METHOD WITHOUT SAVING LARGE AMOUNT OF DATA

The gradients of the cost functional of the FBTS inversion method with respect to unknown parameters (permittivity and conductivity) are expressed explicitly by introducing an adjoint vector field  $\mathbf{w}_m(\mathbf{p}; \mathbf{r}, t)$  as,

$$g_\varepsilon = 2 \int_0^{cT} \sum_{m=1}^M \sum_{i=1}^3 w_m^i(\mathbf{p}; \mathbf{r}, t) \frac{\partial v_m^i(\mathbf{p}; \mathbf{r}, t)}{\partial (ct)} d(ct) \quad (1)$$

$$g_\sigma = 2 \int_0^{cT} \sum_{m=1}^M \sum_{i=1}^3 w_m^i(\mathbf{p}; \mathbf{r}, t) v_m^i(\mathbf{p}; \mathbf{r}, t) d(ct) \quad (2)$$

where,  $c$  is speed of light in vacuum. The gradients are calculated by crosscorrelating  $\mathbf{w}_m(\mathbf{p}; \mathbf{r}, t)$  with  $\partial \mathbf{v}_m(\mathbf{p}; \mathbf{r}, t)/\partial t$  or  $\mathbf{v}_m(\mathbf{p}; \mathbf{r}, t)$ ,  $\mathbf{v}_m(\mathbf{p}; \mathbf{r}, t)$  is the wave field of the guessed model  $\mathbf{p}$  of the  $m$ th transmitter.  $\mathbf{v}_m(\mathbf{p}; \mathbf{r}, t)$  is calculated forward in time, however,  $\mathbf{w}_m(\mathbf{p}; \mathbf{r}, t)$  excited by residuals of

the observed and guessed data at the receivers' positions is calculated reverse in time. In order to calculate the gradients,  $\mathbf{v}_m(\mathbf{p}; \mathbf{r}, t)$  of the whole reconstruction space at all time must be stored to the hard disk when memory is insufficient. During the calculation of the gradients, the saved data are read from hard disk and crosscorrelated with  $\mathbf{w}_m(\mathbf{p}; \mathbf{r}, t)$  just calculated.

In this paper, the storage and read of  $\mathbf{v}_m(\mathbf{p}; \mathbf{r}, t)$  is avoided by using random boundaries surrounding the whole model. The random boundary is firstly proposed by Clapp for reverse-time migration [6]. Here we use it in waveform inversion. In the random boundaries the permittivity distributes randomly,  $\mathbf{w}_m(\mathbf{p}; \mathbf{r}, t)$  in this regions is scattered, and the scattered field is not coherent with  $\mathbf{v}_m(\mathbf{p}; \mathbf{r}, t)$ , consequently the gradient is not evidently affected by the wave field from the random boundary regions.  $\mathbf{w}_m(\mathbf{p}; \mathbf{r}, t)$  propagating in the guessed model with random boundaries is calculated at first from the largest time  $T$  to 0 by using FDTD method, and the electric field at 0

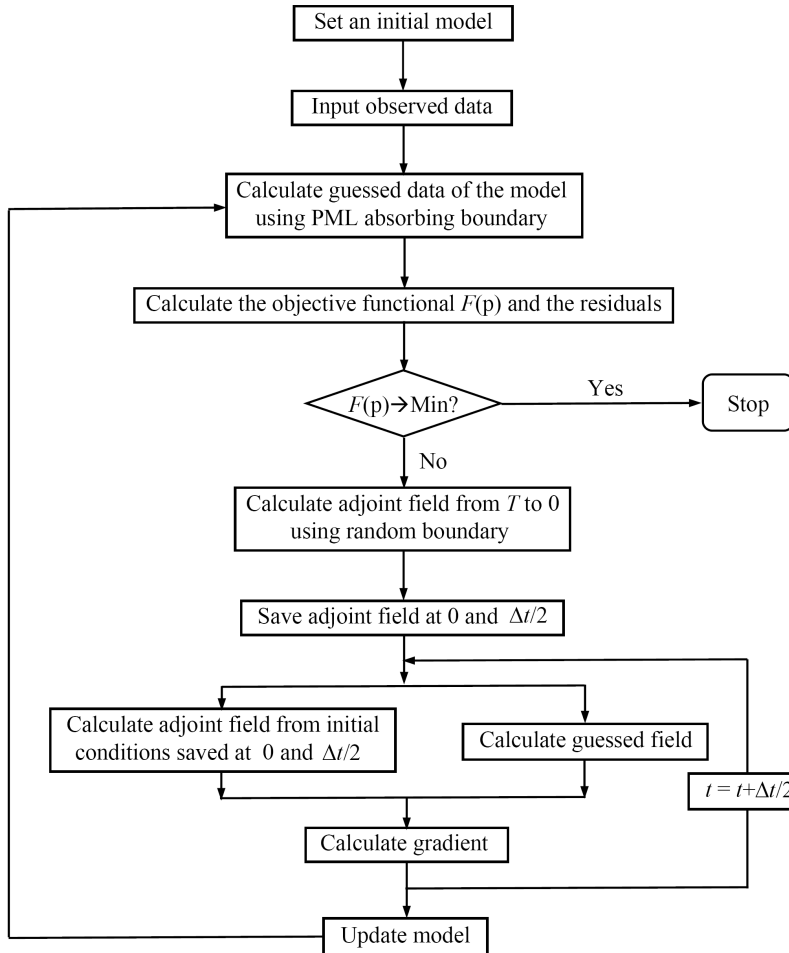


Figure 1: The flowchart of the FBTS method using the random boundaries in the calculation of the adjoint field.

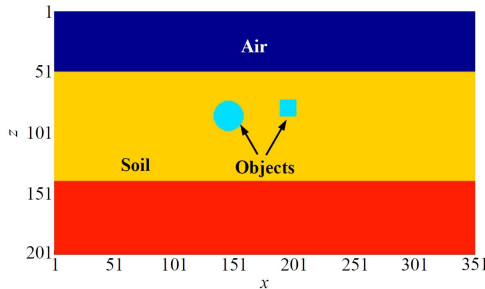


Figure 2: Actual model. The indexes of horizontal and vertical axes are grid number.

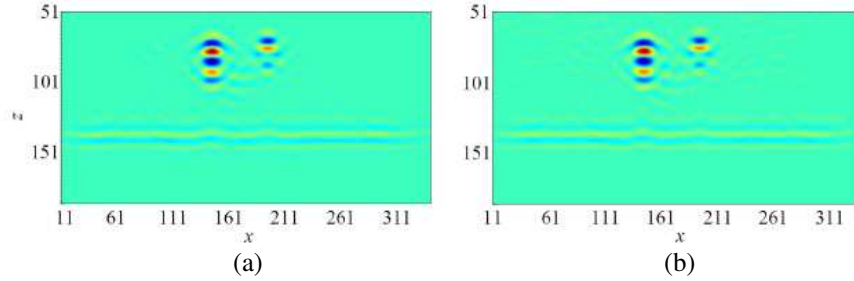


Figure 3: The gradient at 1st iteration calculated using the (a) conventional and (b) suggested method.

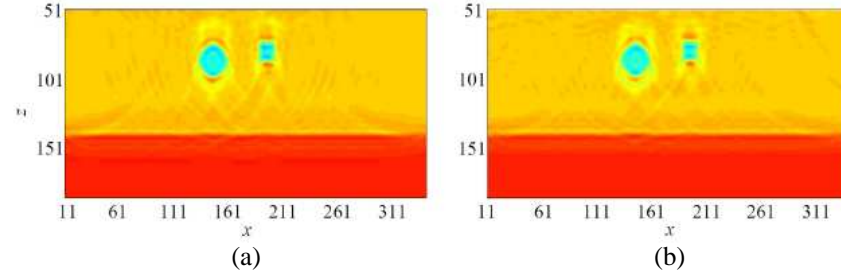


Figure 4: Reconstructed results at 60th iteration using the (a) conventional and (b) suggested method.

and the magnetic field at  $\Delta t/2$  are saved to the hard disk.  $\Delta t$  is time step. During the calculation of  $\mathbf{v}_m(\mathbf{p}; \mathbf{r}, t)$  by using FDTD method forward in time with PML absorbing boundaries,  $\mathbf{w}_m(\mathbf{p}; \mathbf{r}, t)$  is then also calculated from the saved data at 0 and  $\Delta t/2$  as initial conditions forward in time by using FDTD method with the random boundaries, and the gradient is then calculated using  $\mathbf{v}_m(\mathbf{p}; \mathbf{r}, t)$  and  $\mathbf{w}_m(\mathbf{p}; \mathbf{r}, t)$  at the same time sampling position.  $\mathbf{w}_m(\mathbf{p}; \mathbf{r}, t)$  at any time can be recovered by using FDTD method. The flowchart of the FBTS method using the random boundaries is illustrated in Figure 1. In this method only small amount of data need be stored to hard disk compared to the conventional method.

### 3. RECONSTRUCTION EXAMPLE

A 2-D reconstruction example is conducted by the conventional method with storage and read of  $\mathbf{v}_m(\mathbf{p}; \mathbf{r}, t)$ , and by the suggested method. Figure 2 shows the true model of relative permittivity, its size is  $351 \times 201$  which is called problem space. The indexes of horizontal and vertical axes are grid number, and the grid size is 1.2 cm.

There are two layers of soil, and their relative permittivity is 5 and 6. In the first layer there are two objects of relative permittivity of 3. The reconstruction region is 11–341 in horizontal direction and 51–188 in vertical direction. In the suggested reconstruction method, additional 100 grids, where the permittivity is random, surround the problem space in the calculation of the adjoint field. Figure 3 shows the gradients of the reconstruction region calculated by using the conventional and suggested method. It is seen that it is difficult to find the difference between them.

The reconstructed results by using the conventional FBTS reconstruction method in which guessed data are saved on hard disk and by using the proposed method are shown in Figure 4. The reconstructed results by using these methods are almost the same, however, the calculation time of the suggested method is about 78% of the conventional reconstruction method. The percentage is smaller if the reconstruction size and the number of transmitters are larger.

### 4. CONCLUSION AND DISCUSSION

The suggested method without saving large amount of data to hard disk can speed up the time-domain reconstruction method, and the influence from the random boundaries is very weak. Since the data storage and read are extremely reduced, the time-domain reconstruction method is very suitable for GPU (Graphic Processing Unit) parallel computation. By using the random boundary method and GPU parallel computation, the efficiency of the FBTS reconstruction method is expected to be greatly increased.

## ACKNOWLEDGMENT

This work was supported by National Natural Science Foundation of China (40974069), PetroChina Innovation Foundation (2009D-5006-03-01), National Key Basic Research Development Program (2007CB209601).

## REFERENCES

1. Abubakar, A., P. M. van den Berg, and B. Kooij, "A conjugate gradient contrast source technique for 3D profile inversion," *IEICE Trans. Electron.*, Vol. 83, 1864–1874, 2000.
2. Isernia, T., V. Pascazio, and R. Pierri, "On the local minima in a tomographic imaging technique," *IEEE Trans. Geosci. Remote Sensing*, Vol. 39, 1596–1607, 2001.
3. Ernst, J. R., A. G. Green, H. Maurer, et al., "Application of a new 2D time-domain full-waveform inversion scheme to crosshole radar data," *Geophysics*, Vol. 72, No. 5, 53–64, 2007.
4. Zhou, H., T. Takenaka, J. Johnson, and T. Tanaka, "A breast imaging model using microwaves and a time domain three dimensional reconstruction method," *Progress In Electromagnetics Research*, Vol. 93, 57–70, 2009.
5. Zhou, H., M. Sato, T. Takenaka, and G. Li, "Reconstruction from antenna-transformed radar data using a time-domain reconstruction method," *IEEE Trans. Geosci. Remote Sensing*, Vol. 45, No. 3, 689–696, 2007.
6. Clapp, R. G., "Reverse time migration with random boundaries," *SEG International Exposition and Annual Meeting*, 2809–2813, Houston, USA, 2009.

# Note on the Tangential Scattered Magnetic Field on a Perfectly Conducting Surface

Guyan Ni

College of Science, National University of Defense Technology, China

**Abstract**— In the paper, we consider an issue of the tangential component of the scattered field of a perfect conductor. Assume that the surface of the conductor is smooth and has a first-order smooth point. We prove that the tangential component of the scattered field at the point is infinite if the surface current density at the point is nonzero. By the boundary condition, we conclude that the surface current density at the point should be zero.

## 1. INTRODUCTION

Consider a plane wave  $(\mathbf{E}^i, \mathbf{H}^i)$  incident on a perfectly conducting object. The incident wave produces surface currents density  $\mathbf{J}_S$  on the conductor surface  $S$ , which generates a scattered electric field  $\mathbf{E}^s$  and a scattered magnetic field  $\mathbf{H}^s$ . The scattered electromagnetic field outside the current-carrying surface is often expressed in terms of a Green's function as [1–3]

$$\mathbf{E}^s(\mathbf{r}) = \frac{j\omega\mu_0}{4\pi} \int_S \frac{\exp(-jkR)}{R} \mathbf{J}_S(\mathbf{r}') dS' + \frac{j}{4\pi\epsilon_0\omega} \int_S \nabla \left( \frac{\exp(-jkR)}{R} \nabla' \cdot \mathbf{J}_S(\mathbf{r}') \right) dS' \quad (1)$$

$$\mathbf{H}^s(\mathbf{r}) = \frac{1}{4\pi} \int_S \nabla \left( \frac{\exp(-jkR)}{R} \right) \times \mathbf{J}_S(\mathbf{r}') dS' \quad (2)$$

where  $j = \sqrt{-1}$ ,  $R = |\mathbf{r} - \mathbf{r}'|$ . However, both (1) and (2) are invalid when  $\mathbf{r}$  is on  $S$ . Since the Green's function  $\exp(-jkR)/R$  becomes infinite when  $\mathbf{r}$  approaches  $\mathbf{r}'$ , so the integrals both (1) and (2) are improper. The divergent character of (1) and (2) is well known to the mathematician, since there are derivatives of  $\exp(-jkR)/R$  in the integrals.

Denote  $\hat{n}$  a unit normal to the surface  $S$  at  $\mathbf{r}$ . According to the boundary condition of the surface currents and the tangential component of the total field

$$\hat{n} \times (\mathbf{E}^i + \mathbf{E}^s) = 0, \quad \hat{n} \times (\mathbf{H}^i + \mathbf{H}^s) = \mathbf{J}_S, \quad (3)$$

we know that both  $\hat{n} \times \mathbf{E}^s$  and  $\hat{n} \times \mathbf{H}^s$  are finite on the surface in practice. Hence,  $\hat{n} \times \mathbf{H}^s(\mathbf{r})$  is always expressed as [1]

$$\lim_{\epsilon \rightarrow 0+} \frac{1}{4\pi} \int_S \hat{n} \times \left( \nabla \left( \frac{\exp(-jkR)}{R} \right) \times \mathbf{J}_S(\mathbf{r}') \right) dS', \quad (4)$$

where  $R = |\mathbf{r} + \epsilon\hat{n} - \mathbf{r}'|$ . A general viewpoint is that the integral (4) is convergent if the surface  $S$  is smooth [1, 2], and it is widely used in the magnetic-field integral equation (MFIE) [5, 6].

However, in this paper, we consider the tangential component of the scattered field at a first-order smooth point  $P$  of a conductor as in Figure 1. At the point, we show that the integral (4) is divergent if the surface current density at the point is nonzero. That is  $\hat{n} \times \mathbf{H}^s$  is infinite. Hence, by the boundary condition, the surface current density at the point should be zero.

## 2. MAIN RESULT

Since the convergence of (4) only depends on the convergence of the local integral of (4) around  $\mathbf{r}$ . Hence, we only consider the surface express around the  $\mathbf{r}$ . Suppose the surface  $S$  around the origin, as in Figure 2, is defined as

$$S : z = \begin{cases} \frac{\sqrt{x^2 + y^2}}{(\ln(x^2 + y^2))^{1/3}}, & \text{if } 0 < x^2 + y^2 \leq 1/2, \\ 0, & \text{if } x^2 + y^2 = 0. \end{cases} \quad (5)$$

In the section, we will prove that the surface  $S$  is smooth,  $\hat{n} \times \mathbf{H}^s(\mathbf{0})$  is infinite if the surface current density is nonzero, as well as, in general,  $\hat{n}(\mathbf{r}) \times \mathbf{H}^s(\mathbf{r})$  is finite if  $S$  is at least second-order smooth at  $\mathbf{r}$ .

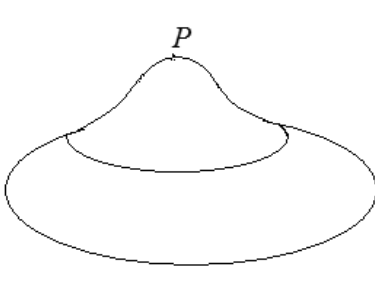


Figure 1: A conductor with a first-order smooth point.

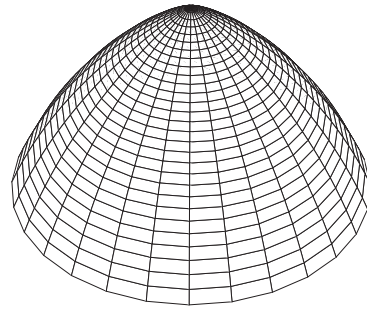


Figure 2: The surface  $S$  around the origin.

### 2.1. The Smoothness of the Surface $S$

We know that

$$\hat{n}(\mathbf{r}) = \left( \frac{\partial z}{\partial x}, \frac{\partial z}{\partial y}, 1 \right),$$

and

$$\begin{aligned} \frac{\partial z}{\partial x} &= \begin{cases} \frac{-2x}{3\sqrt{x^2+y^2}(\ln(x^2+y^2))^{4/3}} + \frac{x}{\sqrt{x^2+y^2}(\ln(x^2+y^2))^{1/3}}, & \text{if } 0 < x^2 + y^2 \leq \frac{1}{2}, \\ 0, & \text{if } x^2 + y^2 = 0. \end{cases} \\ \frac{\partial z}{\partial y} &= \begin{cases} \frac{-2y}{3\sqrt{x^2+y^2}(\ln(x^2+y^2))^{4/3}} + \frac{y}{\sqrt{x^2+y^2}(\ln(x^2+y^2))^{1/3}}, & \text{if } 0 < x^2 + y^2 \leq \frac{1}{2}, \\ 0, & \text{if } x^2 + y^2 = 0. \end{cases} \end{aligned}$$

It is clear that both  $\partial z / \partial x$  and  $\partial z / \partial y$  are continuous if  $0 < x^2 + y^2 < 1/2$ , and

$$\begin{aligned} \lim_{(x,y) \rightarrow (0,0)} \frac{\partial z}{\partial x} &= 0 = \left. \frac{\partial z}{\partial x} \right|_{(0,0)} \\ \lim_{(x,y) \rightarrow (0,0)} \frac{\partial z}{\partial y} &= 0 = \left. \frac{\partial z}{\partial y} \right|_{(0,0)}. \end{aligned}$$

Hence

$$\lim_{\mathbf{r} \rightarrow \mathbf{0}} \hat{n}(\mathbf{r}) = \hat{n}(\mathbf{0}) = (0, 0, 1) \neq (0, 0, 0).$$

So  $S$  is smooth.

### 2.2. The Tangential Component of the Scattered Field at the Origin

We know that the unit normal of  $S$  at  $\mathbf{0}$  is  $\hat{n} = (0, 0, 1)$ . The unit normal of  $S$  at  $\mathbf{r}$  is

$$\hat{n}(\mathbf{r}) = \frac{\left( -\frac{\partial z}{\partial x}, -\frac{\partial z}{\partial y}, 1 \right)}{\sqrt{\left( \frac{\partial z}{\partial x} \right)^2 + \left( \frac{\partial z}{\partial y} \right)^2 + 1}}.$$

So, the surface current density can be defined as

$$\mathbf{J}_S(\mathbf{r}) = (0, 1, \partial z / \partial y) \quad (\mathbf{r} \in S).$$

Then  $\mathbf{J}_S(\mathbf{r})$  is continuous and  $\mathbf{J}_S(\mathbf{0}) \neq \mathbf{0}$ . We claim that the tangential component of scattered magnetic field at the origin is infinite. Indeed, by (4),

$$\begin{aligned} \hat{n} \times \mathbf{H}^s(\mathbf{0}) &= \lim_{\epsilon \rightarrow 0^+} \int_S \frac{\exp(-jkR)}{4\pi R^3} (-jkR - 1) \hat{n} \times ((\epsilon \hat{n} - \mathbf{r}) \times \mathbf{J}_S(\mathbf{r})) dS \\ &= \lim_{\epsilon \rightarrow 0^+} \int_S \frac{\exp(-jkR)}{4\pi R^3} (-jkR - 1) [\hat{n} \cdot \mathbf{J}_S(\mathbf{r})(\epsilon \hat{n} - \mathbf{r}) - \hat{n} \cdot (\epsilon \hat{n} - \mathbf{r}) \mathbf{J}_S(\mathbf{r})] dS \quad (6) \end{aligned}$$

where  $R = |\epsilon\hat{n} - \mathbf{r}|$ . In order to prove (6) is infinite, we only prove the following limit

$$\lim_{\epsilon \rightarrow 0^+} \int_S \frac{1}{R^3} (\hat{n} \cdot \mathbf{J}_S(\mathbf{r})(\epsilon\hat{n} - \mathbf{r}) - \hat{n} \cdot (\epsilon\hat{n} - \mathbf{r})\mathbf{J}_S(\mathbf{r})) dS \quad (7)$$

is infinite. Since

$$\hat{n} \cdot \mathbf{J}_S(\mathbf{r})(\epsilon\hat{n} - \mathbf{r}) - \hat{n} \cdot (\epsilon\hat{n} - \mathbf{r})\mathbf{J}_S(\mathbf{r}) = \left( -x \frac{\partial z}{\partial y}, -y \frac{\partial z}{\partial y} - \epsilon + z, 0 \right).$$

It follows that (7) is infinite if and only if one of the following two limits

$$\lim_{\epsilon \rightarrow 0^+} \int_S \frac{-x}{R^3} \cdot \frac{\partial z}{\partial y} dS \quad (8)$$

or

$$\lim_{\epsilon \rightarrow 0^+} \int_S \frac{1}{R^3} \cdot \left( -y \frac{\partial z}{\partial y} - \epsilon + z \right) dS \quad (9)$$

is infinite.

For (8), the integrand is an odd function on  $x$ . So (8) is convergent and the integral value is zero.

For (9), we have

$$\begin{aligned} \lim_{\epsilon \rightarrow 0^+} \int_S \frac{1}{R^3} \cdot \left( -y \frac{\partial z}{\partial y} - \epsilon + z \right) dS &= \lim_{\epsilon \rightarrow 0^+} \int_S \frac{1}{R^3} \cdot \left( -\epsilon + \frac{2y^2}{3\sqrt{x^2+y^2}(\ln(x^2+y^2))^{4/3}} \right. \\ &\quad \left. - \frac{y^2}{\sqrt{x^2+y^2}(\ln(x^2+y^2))^{1/3}} + \frac{\sqrt{x^2+y^2}}{(\ln(x^2+y^2))^{1/3}} \right) dS. \end{aligned} \quad (10)$$

By the symmetry of  $S$ , we notice that for each positive  $\epsilon$

$$\begin{aligned} &\int_S \frac{1}{R^3} \cdot \left( \frac{2y^2}{3\sqrt{x^2+y^2}(\ln(x^2+y^2))^{4/3}} - \frac{y^2}{\sqrt{x^2+y^2}(\ln(x^2+y^2))^{1/3}} \right) dS \\ &= \int_S \frac{1}{R^3} \cdot \left( \frac{2x^2}{3\sqrt{x^2+y^2}(\ln(x^2+y^2))^{4/3}} - \frac{x^2}{\sqrt{x^2+y^2}(\ln(x^2+y^2))^{1/3}} \right) dS \\ &= \int_S \frac{1}{R^3} \cdot \left( \frac{\sqrt{x^2+y^2}}{3(\ln(x^2+y^2))^{4/3}} - \frac{\sqrt{x^2+y^2}}{2(\ln(x^2+y^2))^{1/3}} \right) dS. \end{aligned}$$

Substituting the above equation into (10), we have

$$\begin{aligned} &\lim_{\epsilon \rightarrow 0^+} \int_S \frac{1}{R^3} \cdot \left( -y \frac{\partial z}{\partial y} - \epsilon + z \right) dS \\ &= \lim_{\epsilon \rightarrow 0^+} \int_S \frac{1}{R^3} \cdot \left( -\epsilon + \frac{\sqrt{x^2+y^2}}{3(\ln(x^2+y^2))^{4/3}} + \frac{\sqrt{x^2+y^2}}{2(\ln(x^2+y^2))^{1/3}} \right) dS. \end{aligned}$$

Now, we will prove that

$$\lim_{\epsilon \rightarrow 0^+} \int_S \frac{1}{R^3} \cdot \left( -\epsilon + \frac{\sqrt{x^2+y^2}}{3(\ln(x^2+y^2))^{4/3}} \right) dS \quad (11)$$

is finite, but

$$\lim_{\epsilon \rightarrow 0^+} \int_S \frac{1}{R^3} \cdot \frac{\sqrt{x^2+y^2}}{2(\ln(x^2+y^2))^{1/3}} dS = -\infty. \quad (12)$$

Denote  $\rho = \sqrt{x^2+y^2}$ . Since

$$R = |\epsilon\hat{n} - \mathbf{r}| = \sqrt{x^2+y^2+(z-\epsilon)^2} > \sqrt{\rho^2+\epsilon^2}.$$

It follows that

$$\int_S \frac{\epsilon}{R^3} dS < 2\pi \int_0^{\sqrt{1/2}} \frac{\epsilon}{(\sqrt{\rho^2 + \epsilon^2})^3} \rho d\rho = 2\pi \left( 1 - \frac{\epsilon}{\sqrt{1/2 + \epsilon^2}} \right) \rightarrow 2\pi \quad (\epsilon \rightarrow 0^+). \quad (13)$$

Since  $R = |\epsilon\hat{n} - \mathbf{r}| = \sqrt{x^2 + y^2 + (z - \epsilon)^2} > \rho$ . It follows that

$$\int_S \frac{1}{R^3} \cdot \left( \frac{\sqrt{x^2 + y^2}}{3(\ln(x^2 + y^2))^{4/3}} \right) dS < 2\pi \int_0^{\sqrt{1/2}} \frac{1}{\rho^3} \cdot \frac{\rho^2}{3(\ln \rho^2)^{4/3}} d\rho = \frac{\pi}{\sqrt[3]{4 \ln 2}}. \quad (14)$$

By (13) and (14), we know that (11) is finite. Next, we will prove (12).

Since  $0 < x^2 + y^2 \leq 1/2$ , then  $0 < \frac{1}{-\ln(x^2+y^2)} < 2$ . Then

$$R = \sqrt{x^2 + y^2 + \left( \frac{\sqrt{x^2 + y^2}}{(\ln(x^2 + y^2))^{1/3}} - \epsilon \right)^2} < \sqrt{\rho^2 + (2\rho + \epsilon)^2}.$$

Hence,

$$\begin{aligned} & \int_S \frac{1}{R^3} \cdot \left( \frac{\sqrt{x^2 + y^2}}{3(-\ln(x^2 + y^2))^{1/3}} \right) dS \\ & > 2\pi \int_0^{\sqrt{1/2}} \frac{1}{(\sqrt{\rho^2 + (2\rho + \epsilon)^2})^3} \cdot \frac{\rho^2}{3(-\ln \rho^2)^{1/3}} d\rho \\ & = 2\pi \int_0^{\sqrt{1/2}} \frac{1}{\rho(\sqrt{1 + (2 + \epsilon/\rho)^2})^3} \cdot \frac{1}{3(-\ln \rho^2)^{1/3}} d\rho \\ & > 2\pi \int_{\epsilon}^{\sqrt{1/2}} \frac{1}{\rho(\sqrt{1 + (2 + \epsilon/\rho)^2})^3} \cdot \frac{1}{3(-\ln \rho^2)^{1/3}} d\rho \\ & > \frac{2\pi}{\sqrt{10}^3} \int_{\epsilon}^{\sqrt{1/2}} \frac{1}{3\rho(-\ln \rho^2)^{1/3}} d\rho \quad (\text{Since } 0 < \epsilon/\rho < 1) \\ & = \frac{2\pi}{\sqrt{10}^3} \left[ \frac{(\ln \epsilon)^{2/3}}{2^{4/3}} - \frac{(\ln \sqrt{1/2})^{2/3}}{2^{4/3}} \right] \rightarrow +\infty \quad (\epsilon \rightarrow 0^+). \end{aligned}$$

Thus, we have proved that (10) is infinite, which implies that (9) is infinite. Hence,  $\hat{n} \times \mathbf{H}^s(\mathbf{0})$  is infinite, which means that the tangential component of scattered magnetic field at the origin is infinite if  $\mathbf{J}_S(\mathbf{0}) \neq \mathbf{0}$ . This completes the prove.

By the boundary condition (3), it is not hard to deduce that  $\mathbf{J}_S(\mathbf{0}) = \mathbf{0}$ .

### 2.3. The Relationship between the Smoothness and the Convergency

Assume that the surface current of  $S$  is not zero. From above all, we find that  $\hat{n} \times \mathbf{H}^s(\mathbf{0})$  is infinite because

$$\lim_{\epsilon \rightarrow 0^+} \int_S \frac{\hat{n} \cdot \mathbf{r}}{R^3} dS$$

is divergent.

In general, for each  $\mathbf{r}_0 \in S$ , we also have that if

$$\lim_{\epsilon \rightarrow 0^+} \int_S \frac{\hat{n}(\mathbf{r}_0) \cdot (\mathbf{r} - \mathbf{r}_0)}{R^3} dS \quad (15)$$

is convergent then  $\hat{n}(\mathbf{r}_0) \times \mathbf{H}^s(\mathbf{r}_0)$  is finite, where  $R = |\mathbf{r} - (\mathbf{r}_0 + \epsilon\hat{n}(\mathbf{r}_0))|$ . Hence, a more smooth condition of  $S$  should be added to guarantee the convergence of (4). Indeed, if  $S$  is a second-order smooth surface, then there exists a positive number  $M$  such that

$$|\hat{n}(\mathbf{r}_0) \cdot (\mathbf{r} - \mathbf{r}_0)| \leq M|\mathbf{r} - \mathbf{r}_0|^2.$$

It follows that (15) is convergent, see Ref. [4]. We obtain the following result.

**Theorem.** Let  $S$  be a second-order smooth surface of a conductor,  $\mathbf{r}$  be a point on  $S$ ,  $\hat{n}(\mathbf{r})$  be an unit normal pointing outward from  $\mathbf{r}$ ,  $\mathbf{J}_S(\mathbf{r})$  be a continued surface current density. Then the tangential component of scattered magnetic field  $\hat{n}(\mathbf{r}) \times \mathbf{H}^s(\mathbf{r})$  is finite.

### 3. CONCLUSION

This paper proves that if a conductor has a first-order smooth point in its surface then the surface current density should be zero at the point. Otherwise, the tangential scattered magnetic field is infinite at the point. So we should consider the smoothness of the surface if we apply the magnetic-field integral equations (MFIE) to compute the electromagnetic scattering field. That is why the current distribution and the radar cross section (RCS) obtained by the MFIE are always not accurate when the geometry of the problem includes sharp edges or tips.

### ACKNOWLEDGMENT

This work was supported by China Postdoctoral Special Science Foundation (No. 200902662), the National Natural Science Foundation of China (No. 10871231), and Pre-research Foundation of Weapon and Equipment (No. 9140A31020609KG0170).

### REFERENCES

1. Tsang, L., J. A. Kong, K. H. Ding, and C. O. Ao, *Scattering of Electromagnetic Waves: Numerical Simulations*, John Wiley & Sons, Inc., 2000.
2. Bondeson, A., T. Rylander, and P. Ingelstrom, *Computational Electromagnetics*, Springer Science+Business Media, Inc., 2005.
3. Chew, W. C., M. S. Tong, and B. Hu, *Integral Equation Methods for Electromagnetic and Elastic Waves*, Printed in the United States of America, 2009.
4. Zorich, V. A., *Mathematical Analysis*, Springer-Verlag Berlin Heidelberg, 2004.
5. Geyi, W., “New magnetic field integral equation for antenna system,” *Progress In Electromagnetic Research*, Vol. 63, 153–170, 2006.
6. Hellicar, A. D., J. S. Kot, G. James, and G. K. Cambrell, “A comparison of higher order nodal- and edge-basis functions in the MFIE on rational Bézier geometries,” *IEEE Trans. Antennas and Propagat.*, Vol. 56, No. 6, 1812–1818, June 2008.

# Derivation of One-minute Rain Rate from Five-minute Equivalent for the Calculation of Rain Attenuation in South Africa

P. Owolawi

Department of Electrical Engineering, Mangosuthu University of Technology  
Umlazi, Kwazulu-Natal, South Africa

**Abstract**— This paper presents conversion of rain rate from 5-minute to equivalent 1-minute integration time. A proposed hybrid method is based on optimized existing conversion methods. The approach is considered because of mixed geographical/climatic conditions of the southern Africa. The results of the method are compared with the existing models which are geographically dependent.

## 1. INTRODUCTION

In accordance to International Telecommunication Union (ITU-R P.618-6 and P.530-8), estimation of rain attenuation need to be carried out at lower integration time, i.e.,  $\geq 1$  minute. The established conversion methods are grouped into three broad classes by Capsoni et al. [1] which physical, analytical and empirical model as classified with their respective examples in Table 1. Majority of the contributors tend to use the empirical method extensively to convert from higher integration time to lower equivalent because of its simplicity and experimental dependent. Studies which have applied this method in different regions include Ajayi and Ofoche [15] for Nigeria, Burgueno et al. [12] for Spain; Falvin [16] for Australia, Ong and Zhu [17, 18] for Singapore, Watson et al. [13] for Europe, Xiao et al. [19] for China, Chebil and Rahman [14] for Malaysia, and Segal [11] for Canada. In principle, the two main laws commonly used in empirical methods are the power law and the power-exponential law. In Emiliani et al. [20], the laws are expressed as follows:

$$R_1(P) = aR_T(P)^b \quad (1)$$

where  $R_1(P)$  and  $R_T(P)$  are, respectively, the rain rate for a one-minute integration time and any integration time ( $T$ ), at equal percentage of exceedence ( $P$ ). The other law is based on conversion factor as given by the expression:

$$CF(P) = \frac{R_1(P)}{R_T(P)}, \quad CF(P) = aP^b, \quad 0 < P < 1.0, \quad (2)$$

$$CF(P) = \frac{R_1(P)}{R_T(P)}, \quad CF(P) = aP^b + ce^{dp}, \quad 0 < P < 1.0, \quad (3)$$

where  $CF(P)$  is conversion factor at a particular percentage of exceedence,  $P$ , and  $a$  and  $b$  are constant values for parameters with respect to rain integration time  $\tau$ .

Table 1: Examples of different classes of rain rate integration time conversion models (RH = Rice-Holmberg [2], DD = Dutton-Dougherty [3], CM = Crane [4], ITU-R P.837-5 [5], EX = EXCELL [6], PS = Physical-Stochastic [7], MF = Moupfouma [8], KA = Karasawa [9], IH = Ito-Hosoya [10], SG = Segal [11], BG = Burgueno [12], WA = Watson [13], CR = Chebil-Rahman [14]).

<i>Physical model</i>	<i>Analytical models</i>	<i>Empirical model</i>
RH	MF	SG
DD	KA	BG
CM	IH	WA
ITU-R		
EX		
PS		

The extensive contribution of ITU-R study 3 which led to the revised ITU-R 837-5 [5] has given a good direction in resolving the issues around integration time, although the approach is based on the empirical method with limited climatological data from few regions in the world. In the proposal, the power law approach was considered for four different integration times which are 5 min, 10 min, 20 min and 30 min. Emiliani et al. [21] further reviewed ITU-R P.837-5 constants and suggests new global coefficients for the application of the power law conversion method. These proposed coefficients extend its application to rain rate conversion methods in temperate, tropical and cold climates. In addition, their contributions extend the ITU-R P.837-5 integration time from 5-, 10-, 20-, 30-minute to 60-minute interval.

In recent times, the group has put forward a revised recommendation with more data and analysis from many other regions in the world. Mathematically, two expressions are proposed to determine the global coefficients for the power laws (Equation (1)) as shown in the expressions below:

$$\begin{aligned} a &= 0.0002t^2 - 0.0189t + 1.0136 & R^2 &= 0.987 \\ b &= 0.0063t + 1.0366 & R^2 &= 0.97 \end{aligned} \quad (4)$$

## 2. EXPERIMENTAL MEASUREMENT FACILITIES/DATA PROCESSING

The details of experimental set-up and measurement methodology in the present work are presented in Section 2 as reported in [22]. Twenty-five data sites with master control site in Durban are used in the present study. In the case of distrometer, 92% of its data was processed and used while less than 2.8% of the data provided by South Africa Weather Services was not used. Table 2 shows few sites with their location names and longitude and latitudes and their precipitation characteristics. The parameters used are average annual total rainfall  $M$  (mm/yr), the highest monthly precipitation observed over 30 years  $M_m$  (mm/month), and the average number of thunderstorm days in a year  $D_{th}$  (day), which are extracted from World Meteorological Organization documents [23, 24]. The site cumulative distribution characteristics estimated over ten years are also presented with 0.01% percentage of exceedence of five-minute rain rate data collected over the South African regions and its islands.

Table 3 shows the yearly variation of mean bias error, correlation coefficient ( $R^2$ ) between the ten years' rain rate and individual year rain rate distribution at equal percentage of exceedence and rain rate values at 1%, 0.01% and 0.001% of exceedences at five-minute integration time. The table confirms a positive correlation across the years with the least value of 0.93 to the most significant value of 0.99. The results also show the yearly variation mean bias error of ten years rain rate distribution against each individual year. In 1996, 1997, 2000, 2003, and 2006, the percentage mean bias error is less than +9%, while for 1998, 1999, 2001, 2002 and 2005, the recorded percentage mean bias error is less than -17%. The exceptional years of 1995 and 2004 gave a percentage mean bias errors of +42% and -33%, respectively. Table 3 further shows the results of year-to-year variation of five-minute rain rate exceeded from 0.001% to 1% with their corresponding rain rate values. At 1% exceedance of rain rate, the recorded values remain approximately constant, while at 0.001% exceedance, the variation is relatively larger. In the case of 0.01% of exceedence, the variation of rain rate recoded falls in between the 1% and 0.01% percentages of exceedences. In years earlier than 1997, the rain rates recorded are relatively low compared with years later than

Table 2: Regional parameters used in estimating one-minute rain rate by hybrid method [24].

SITE/PARAMETERS	EASTERN CAPE		KZN	WESTERN-CAPE
	Port Alfred	Durban	Cape-Town	
Lat. (deg)	-33.5	-29.9	-33.9	
Long. (deg)	26.8	30.9	18.6	
$M$ (mm)	624	1009	515	
$D_{th}$ (day)	30	30	15	
$M_m$ (mm)	64	134	93	
$\beta$	0.721	0.688	0.609	
$R_{5\text{ min}}(0.01)$ (mm)	33.6	55.2	21.6	

Table 3: Yearly variation of 5-minute rain rate with their statistical characteristics.

Statistical Characteristics	<b>1995</b>	<b>1996</b>	<b>1997</b>	<b>1998</b>
% mean bias	42.01	4.34	4.62	-8.66
$R^2$	0.98	0.98	0.99	0.99
% exceedence 0.01%	26.4	48	48	62.4
% exceedence 0.001%	93.6	40.8	69.6	84
	<b>1999</b>	<b>2000</b>	<b>2001</b>	<b>2002</b>
% mean bias	-12.43	8.89	-16.61	-0.91
$R^2$	0.98	0.97	0.97	0.99
% exceedence 0.01%	52.8	50.4	55.2	57.6
% exceedence 0.001%	98.4	91.2	117.6	100
	<b>2003</b>	<b>2004</b>	<b>2005</b>	<b>2006</b>
% mean bias	2.24	-33.23	-2.41	3.49
$R^2$	0.99	0.99	0.97	0.93
% exceedence 0.01%	60	79.2	64.8	57.6
% exceedence 0.001%	110	151	146.4	93.6
	<b>2007</b>	<b>Ten years</b>		
% mean bias	-4.80	-		
$R^2$	0.99	-		
% exceedence 0.01%	67.2	55.2		
% exceedence 0.001%	93.6	93.6		

1997. This may be due to yearly cycles at the time of data collection. In the case of 2009 data, the table shows a negative percentage mean bias error with positive correlation coefficient. The rain rate at different percentage of exceedence is equal at both 1% and 0.001%, with a 22% increment in the 2009 rain rate data.

### 3. THE PROPOSED HYBRID METHOD

The hybrid method presented in this paper takes advantages of existing rain rate conversion methods with their inherent properties and adapts them for the region of interest by using a control site with at least one measured one-minute rain rate data to optimize the selected models. In the global model proposed by Ito et al. [10], an error band of  $\pm 20\%$  is considered acceptable for proper application of their proposed model worldwide, while Karasawa et al. [9] considered an improved error band of  $\pm 10\%$  for regional base estimation. The Hybrid model considers the later band range to select the optimized model for the region. The rationale of the model can be abridged as follows: assume that a cumulative distribution (CDF) of a region with measured one-minute rain rate with their coefficients can be mirrored in another site by simply adjusting the values of the coefficients to find the cumulative identity with the existing CDF. Here the regional precipitation properties will still be maintained and the variability of the site will be taken care of. Since several rain rate conversion models already exist, it is easy to tap into their properties and identify them with their region of interest using appropriate optimization methods. It is anticipated that a combined rain rate conversion method will give better performance than an individual model because of the dynamics of rain rate distribution especially in Africa where multiple regimes of rain can occur within one rain rate event.

Consider a hypothetical cumulative distribution of rain rate using different one-minute rain rate models. Let  $N$  be the number of models generating those one-minute rain rate cumulative distributions, i.e., rain rate distribution model 1 ( $N_1$ ), rain rate distribution model 2 ( $N_2$ ), ... up to rain rate distribution model ( $N_n$ ).

Let  $P$  represents the probability of rain rate exceedences using ITU-R's designations  $P_{0.001}$ ,  $P_{0.003}$ ,  $P_{0.01}$ ,  $P_{0.03}$ ,  $P_{0.1}$ ,  $P_{0.3}$ , and  $P_1$ . The conversion factors ( $CF$ ) for each class of  $N$  is given

by:

$$\begin{aligned} CF_{N=1,2,3,\dots,n} &= \left( \frac{R_{1,1}(P_{0.001})}{R_{T,1}(P_{0.001})} \right) + \left( \frac{R_{1,2}(P_{0.001})}{R_{T,2}(P_{0.001})} \right) + \dots + \left( \frac{R_{1,n}(P_{0.001})}{R_{T,n}(P_{0.001})} \right) \\ CF_{N=1,2,3,\dots,n} &= \left( \frac{R_{1,1}(P_{0.003})}{R_{T,1}(P_{0.003})} \right) + \left( \frac{R_{1,2}(P_{0.003})}{R_{T,2}(P_{0.003})} \right) + \dots + \left( \frac{R_{1,n}(P_{0.003})}{R_{T,n}(P_{0.003})} \right) \\ CF_{N=1,2,3,\dots,n} &= \left( \frac{R_{1,1}(P_1)}{R_{T,1}(P_1)} \right) + \left( \frac{R_{1,2}(P_1)}{R_{T,2}(P_1)} \right) + \dots + \left( \frac{R_{1,n}(P_1)}{R_{T,n}(P_1)} \right) \end{aligned} \quad (5a)$$

where  $N$  is the designation number assigned to each model used, i.e.,  $N = 1, 2, 3, \dots, n$ . Suppose we assume  $L_{i=0.001, 0.003, \dots, 1} = \frac{1}{N} \sum CF_{N=1,2,\dots,n,0.001}$ , and the Hybrid conversion factors for each percentage of exceedences are  $L_{0.001}, L_{0.003}, \dots, L_1$  respectively. Then, the generalized expression for the Hybrid conversion factor is given as:

$$L_{i=0.001, 0.003, \dots, 1} = \frac{1}{N} \sum CF_{N=1,2,\dots,n,0.001} \quad (5b)$$

where  $\sum CF_{N=1,2,\dots,n,0.001}$  is the sum of ratio of rain rates exceeded for a given percentage of time for rain gauges with integration times of  $T$  minutes and one minute for each number of distributions  $N$ . Also, the principle can be repeated for a case of a set threshold of rain rate at unknown percentage of exceedence, as follows:

$$\begin{aligned} CF_{N=1,2,3,\dots,n} &= \left( \frac{P_{1,1}(R_{0.001})}{P_{T,1}(R_{0.001})} \right) + \left( \frac{P_{1,2}(R_{0.001})}{P_{T,2}(R_{0.001})} \right) + \dots + \left( \frac{P_{1,n}(R_{0.001})}{P_{T,n}(R_{0.001})} \right) \\ CF_{N=1,2,3,\dots,n} &= \left( \frac{P_{1,1}(R_{0.003})}{P_{T,1}(R_{0.003})} \right) + \left( \frac{P_{1,2}(R_{0.003})}{P_{T,2}(R_{0.003})} \right) + \dots + \left( \frac{P_{1,n}(R_{0.003})}{P_{T,n}(R_{0.003})} \right) \\ CF_{N=1,2,3,\dots,n} &= \left( \frac{P_{1,1}(R_1)}{P_{T,1}(R_1)} \right) + \left( \frac{P_{1,2}(R_1)}{P_{T,2}(R_1)} \right) + \dots + \left( \frac{P_{1,n}(R_1)}{P_{T,n}(R_1)} \right) \end{aligned} \quad (5c)$$

Then Equation (5b) can be assumed where  $\sum CF_{N=1,2,\dots,n,0.001}$  refers to the sum of ratio of exceedences for a given rain rate measured using gauges with  $T$  minute and one minute integration times for each number of distributions  $N$ .

In this paper, the selected models for the Hybrid conversion method are: the Segal model (Singapore) model ( $N_1$ ); the Ito-Hosoya model ( $N_2$ ); the Burgueno models (Singapore) ( $N_3$ ); the Lavergnat-Golé model ( $N_4$ ); the Ajayi-Ofoche model ( $N_5$ ); the Migliora, Pontes and Mello model ( $N_6$ ); the ITU-R P.837-5 model ( $N_7$ ); the Australia model ( $N_8$ ); and the China model ( $N_9$ ). The mentioned models are selected because they consists location/region-based climatic parameters. The resulting hybrid integration time models will have mixed properties of selected climatic conditions that might similar to South Africa. South Africa has mixed tropical and temperate climates. The result of the mixed model approach is a Hybrid method whose coefficients are used to convert the available five-minute data to one-minute equivalent.

Figure 1 shows the relationship between the estimated one-minute (Hybrid method using nine rain rate models) and five-minute rain rate collected. Three different regression fits are applied, namely, the second order polynomial fit, the linear fit and the power fit. These regression fits are used to estimate the distributions of rain rate at two different integration times but at equal percentage of exceedence. The regression curve is based on equal percentage of exceedence at which rain rate is exceeded at a range between 0.001% and 1% with smaller unit intervals. The square value of correlation coefficients of the fits shows that the second order polynomial fit performs best; followed by linear fit, with the power fit performing worst.

Figure 1 also reveals that at lower rain rates, the three fits' distributions give a good correlation with the minimum percentage deviation of 0.33%; however, at a higher rain rate, the power law fit diverges slightly by a maximum percentage deviation of 7.87%.

Another approach to present the conversion method is to use conversion factors. This relates the ratio of rain rate at equal percentages of exceedence against its percentage of exceedence at each ratio of rain rate. Figure 2 is a graphic representation of conversion factor method using rain rate data for Durban. It shows the relationship between rain rate conversion factor and percentage of exceedence for each individual rain rate ratio. The second order polynomial, logarithm, and power

law fit distributions are considered. In Figure 2, the model rain rate conversion factor favours the second order polynomial fit using the square value correlation coefficient. It is noted that the square correlation coefficients were less than 0.5 and this poor correlation is common with other stations considered in this work. As a result of the weak square correlation coefficient shown in Figure 2, the expressions (polynomial, power and linear fit) in Figure 1 are adopted to convert rain rate from 5-minute integration time to 1-minute equivalent in Durban and other sites mentioned in this paper. The results of converted 5-minute cumulative distribution of rain rate using different fits are then compared with each other as well as the 1-minute measured data. The comparison includes ITU-R Recommendation P.837-5 conversion coefficients and the revised ITU-R P.837-5 results. The comparison is evaluated using a relative error method adopted by ITU-R and other authors.

Figure 3 shows the comparison of measured one-minute rain rate with three different hybrid fits. The different distribution fits used are the power fit, the second order polynomial fit, and the linear fit of Figure 1. As seen in the diagram, the three chosen fits seem to describe one-minute measured rain rate distributions well with little degree of deviation at a higher rain rate for the power fit. The resulting one-minute rain rates estimated by the three distribution fits derived by Hybrid method are tested against available one-year one-minute rain rate data.

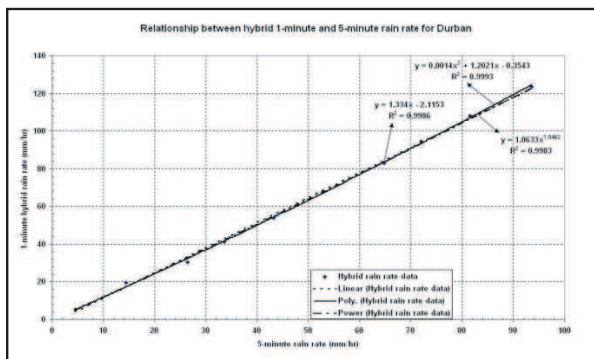


Figure 1: The hybrid 1-minute against 5-minute rain rate measured in Durban.

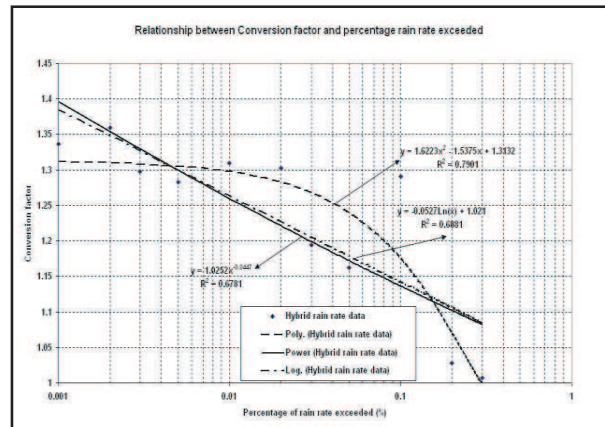


Figure 2: Relationship between the conversion factor and % of time rain rate exceeded.

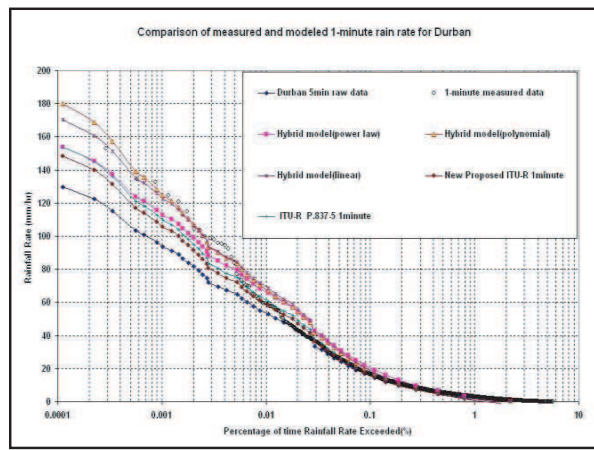


Figure 3: Comparison between modeled 1-minute and measured 1-minute rain rate for Durban.

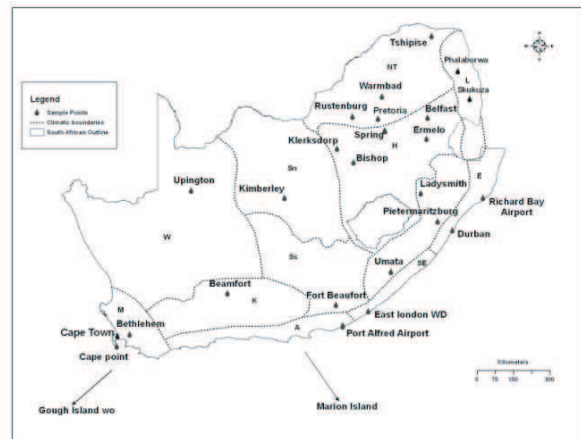


Figure 4: Climatic classification of South Africa and surrounding islands based on the Koppen classification.

#### 4. PERFORMANCE OF THE PROPOSED HYBRID MODEL AGAINST OTHER EXISTING MODELS

The first quantitative estimated errors are evaluated using relative error, which is a widely used error evaluation method, given by:

$$E_{\text{Rel},i}(\%) = 100 \left( \frac{R_{p,i} - R_{m,i}}{R_{m,i}} \right) \quad (6)$$

where  $R_p$  (mm/hr) and  $R_m$  (mm/hr) are predicted and measured 1-minute rain rates, respectively. It should be noted that the lower the values in Equation (6), the better the proposed model.

In this paper, the relative error is chosen for the first evaluation of the proposed model with actual measured data. In order to confirm the most suitable fit distribution to best describe Durban, the average standard deviation (STD) of the absolute relative error and root mean square (RMS) of relative error are determined as shown in Table 4. Table 4 confirms the best fit distribution that describes the proposed one-minute rain rate (Hybrid method) with measured one-minute rain rate. The average value of the absolute relative error is observed to be lowest when the polynomial fit of second order is used, while the maximum average error is recorded with power law fit. The same statistical trend is observed when STD and RMS of relative errors are used as performance criteria. At 0.01% percentage of exceedence, the power fit seems to be the best with 9.88% relative error, whereas the linear and polynomial fits give 14.79% and 12.28% of relative error, respectively. This is confirmed by the RMS value where the power fit records a value of 0.97%, while polynomial and linear fits record 1.5% and 2.1%, respectively. At 0.001% percentage of exceedence, the performance of the polynomial fit is the best with 0.072% of relative error, while the error for the linear fit is 1.68%, with highest relative error observed in power fit. Comparisons between ITU-R P.837-5 and the proposed new global power model using Durban's data shows that the percentage differences between the existing ITU-R and proposed ITU-R's global model in this study are 9.31%, 19.18%, and 8.85%, when using average value of absolute error, standard deviation of absolute value of error, and root mean square of absolute error, respectively. It is also noted from Table 4 and Figure 3 that both the ITU-R and proposed new ITU-R's global model describe the Durban cumulative distribution well at lower rain rate while at the higher rain rate, there is greater deviation. The performance of the polynomial fit of second order is considered the best for conversion of rain rate from five-minute to one-minute equivalent because the average error evaluation confirms the polynomial fit as overall best performing regression fit compared to its other counterparts.

In the second evaluation, the performance of the proposed model is observed. The Hybrid model has been tested against the measured one-minute rainfall data collected at Durban against the other 19 rainfall rate conversion models worldwide. The other 19 rainfall rate conversion models include the models used to derive the Hybrid model. The performance of the Hybrid model has been appraised through the following four error statistical figures using the probability level  $p$  between the ranges of 1% to 0.001%.

- The absolute percentage relative error, given by:

Table 4: Comparison between the different fit distributions for Durban using average, STD, and RMS values.

Model	Average value of absolute $E_{\text{Rel},i}$ (%)	STD value of absolute $E_{\text{Rel},i}$ (%)	RMS value of absolute $E_{\text{Rel},i}$ (%)
Linear Fit	11.72	12.38	16.69
Polynomial Fit (2nd order)	6.74	6.21	9.0
Power Fit	14.64	5.0	15.40
ITU-R P.837-5	10.85	7.05	12.80
New Proposed ITU-R	9.0	4.78	10.72

$$absolute \varepsilon(p) = \left| 100 \left[ \frac{R_e(p) - R_m(p)}{R_m(p)} \right] \right| \quad (\%) \quad (7)$$

where  $R_e(p)$  and  $R_m(p)$  are the estimated and measured rain rate values at equal probability of exceedence. The implication of this evaluator is that the less the absolute percentage error, the better the performance the tested model.

- The Root Mean Square error (RMS) as defined by Owolawi and Afullo [25]:

$$RMS = \sqrt{1/N \sum_{i=1}^N (X_{est,i} - X_{mea,i})^2} \quad (8)$$

where  $N$  is the number of data points, and  $X_{est}$  and  $X_{mea}$  are the estimated and measured quantities, respectively.

- The Average probability ratio (APR) as defined by Owolawi and Afullo [25]:

$$APR = \frac{1}{N} \sum_{i=1}^N \left( \frac{P_{est,i}}{P_{mea,i}} \right) \quad (9)$$

here  $P_{est}$  and  $P_{mea}$  denote the cumulative probabilities of estimated and measured quantities, respectively.

- The Chi-Square statistic as defined by Downie and Heath [25]:

$$\chi^2 = \sum_{i=1}^N \frac{(X_{est,i} - X_{mea,i})^2}{X_{est,i}} \quad (10)$$

In this work, absolute percentage relative error, RMS and APR are used to optimize and compare the propose Hybrid method against the existing models and the measured rain rate data. The Chi-square statistic is used to confirm the acceptance or rejection of the null hypothesis of the compared models. A good model should give an APR close to 1, a minimum  $absolute \varepsilon(p)$  and minimum RMS. It should also give a  $\chi^2$  statistic that is lower than the threshold  $t_\delta$  for a defined probability value  $\delta$  for  $N - 1$  degree of freedom (DF). In this work,  $\delta$  is chosen to be 5%.

In Table 5, the result of the evaluation defined over the interval of 1% to 0.001% is presented. From the table, the absolute relative error records its least value of 3.08% in the case of Hybrid model (Polynomial type) and worst in the case of Rice-Holmberg model with 63.22%. The other models that fall below 10% of absolute relative errors are Hybrid (Linear type), ITU-R P.837-5, Australia model, Hybrid (Power type), fitted Segal (Singapore) model, Lavergnat et al. model and Brazil model (Maritime tropical) in descending order error values. The reason for the lower relative error recoded may be due to similarity in the geographical patterns of the region especially in the case of Australia. Considering RMS and APR error for the same mentioned models, it seems that similar trends are observed. Using the  $\chi^2$  evaluation at 5% confidence interval, it is seen that up to 13 models could be used to convert from five-minute rain rate integration time to its one-minute equivalent. As inferred from Table 5, the proposed Hybrid model with polynomial fit performs better than the others.

## 5. INTEGRATION TIME COEFFICIENTS AND ITS VARIABILITIES

As a result of statistical evaluation presented in Table 5, the polynomial model is proposed for the conversion of rain rate from five-minute to one-minute equivalent for South Africa and surrounding islands with a simple general expression given as:

$$R_1(p_i) = aR_5(p_i)^2 + bR_5(p_i) + c \quad (11)$$

where  $a$ ,  $b$  and  $c$  are constants. In the case of Durban, it is observed that  $a = 0.0004$ ,  $b = 1.2833$  and  $c = -0.5282$ . The other expressions used in the equiprobable method are the power fit and linear fit, given as:

$$R_1(p_i) = d [R_5(p_i)]^e \quad (12a)$$

$$R_1(p_i) = f [R_5(p_i)] + g \quad (12b)$$

Table 5: Comparison between the measured data, proposed models and existing models of rain rate integration time.

Tested Models	Absolute % Relative Error	RMS	APR	CHI 5% (12.592)
Segal (Singapore)	9.00	8.67	1.00	5.27
Burgueno	9.64	7.99	0.99	4.89
Rice-Holmberg	63.22	47.15	2.94	171.31
Ito et al.	19.28	15.69	1.25	17.02
Lavergnat et al.	9.58	3.70	1.06	1.76
Ajayi et al. model	10.79	5.51	1.01	3.66
USA (Florida)	55.02	47.60	2.56	166.03
USA (Texas)	34.32	30.45	1.55	65.54
Canada (Montreal)	37.25	34.68	1.67	85.40
Italy (Rome)	23.33	21.63	1.31	32.03
Australia (Flavin)	7.16	3.73	1.04	1.40
China (Xiao et al.)	11.19	3.40	1.08	1.80
ITU-R P.837-5	6.59	8.09	1.02	4.45
Brazil model (Maritime Tropical)	9.62	4.95	0.91	3.32
Brazil model (Equatorial)	10.16	3.87	1.02	1.82
Brazil model (Inland tropical)	38.14	34.20	1.67	81.40
New propose ITU-R	14.08	10.31	1.18	7.50
Moupfouma Sub-tropic	32.51	10.03	0.85	27.18
Moupfouma Temperate	27.09	7.96	0.92	17.04
Hybrid (Power Law)	8.69	5.39	0.98	2.73
Hybrid (Linear Law)	5.89	5.05	0.98	2.73
Hybrid (Polynomial Law)	3.08	2.97	0.98	1.07

where  $d$ ,  $e$ ,  $f$  and  $g$  are constants with values for Durban given by 1.0615, 1.0506, 1.3183 and -0.9328, respectively. The second part of the expression uses the equal rain rate method rather than the equiprobable approach, and is summarized as follows:

$$CF(R_i) = h(p(R_i))^2 + I p(R_i) + j \quad (13a)$$

$$CF(R_i) = k [p(R_i)]^l \quad (13b)$$

$$CF(R_i) = m \ln [p(R_i)] + n \quad (13c)$$

where  $CF(R_i)$  and  $p(R_i)$  are, respectively, the conversion factor and percentages of exceedence at equal chosen rain rate value. The parameters  $h$ ,  $i$ ,  $j$ ,  $k$ ,  $l$ ,  $m$  and  $n$  are constants for Durban with values of 0.5232, -0.7278, 1.3113, 1.1419, -0.0244, -0.0292 and 1.1447, respectively.

Equations (13a) to (13c) are not adopted in this work because of the poor square correlation coefficient as shown in Figure 2, although the polynomial fit shows better square correlation value of 0.8053. The Hybrid approach is adopted to estimate one-minute rain rate for other provinces in South Africa and the surrounding islands.

In the earlier work by Seeber [26], South Africa was divided into 12 climatic regions using the Köppen climatic classification criteria. In the extension of classification to the present work, the study uses the same map but additional stations are added. Table 6 gives the description of each climatic zone as described by Seeber [26], with added data points. The graphical representation shown in Figure 4 represents the location and climatic region of autographic rainfall stations where data was collected. The details of designations are explained in Table 6 with their respective Köppen climate classifications. The map also includes Gough Island (2500 km from Cape Town) and Marion Island (1500 km from Port Elizabeth). Table 7 shows the coefficients of Equations (11) to (13) for South Africa with the square value of correlation coefficients.

Table 6: South African Köpen climatic regions from Seeber, 1995).

<i>Climatic classification for South African (Köppen climatic system)</i>		
<i>Site Designation</i>	<i>Köppen Classifications</i>	<i>Data points</i>
<b>W</b>	Northern Cape: Dessert climate. ( <b>BW</b> )	Upington
<b>M</b>	South-Western Cape: Mediterranean climate with winter rain. ( <b>Cs</b> )	Bethlehem, Cape Point
<b>K</b>	Karoo: Desert climate. ( <b>BW and BSk</b> )	Beaufort
<b>A</b>	Southern coastal belt: Rain during all seasons. ( <b>Cf</b> )	Port Alfred
<b>SE</b>	South-eastern coastal belt: Warm temperate with summer rain. ( <b>Cfw</b> )	East London
<b>E</b>	Eastern coast and Zululand: Sub-tropical with summer rain. ( <b>Cfw and Cfa</b> )	Durban, Richard Bay
<b>D</b>	Drekensberg and interior KwaZulu-Natal: Warm temperate with summer rain. ( <b>Cwb</b> )	Ladysmith, Umtata Pietermaritzburg
<b>L</b>	Lowveld (Northern province): Hot steppe with summer rain. ( <b>BShw</b> )	Skukuza
<b>NT</b>	Northern Province: Hot steppe with summer rain. ( <b>BShw</b> )	Tshipise, Warmbad, Rustenburg, Pretoria
<b>H</b>	Highveld (Mpumalanga, Gauteng and Free state): Warm temperate with summer rain. ( <b>Cwb</b> )	Spring, Bishop, Ermelo, Belfast
<b>Sn</b>	Northern Steppe (Free State and North-West): Steppe summer and autumn rain. ( <b>BSkw</b> )	Klerksdorp, Kimberley
<b>Ss</b>	Southern Steppe (Eastern Cape and Free state): Cold Steppe with autumn rain. ( <b>BSkw</b> )	Fort Beaufort

The observed coefficients reflect variability from one Köppen class to another. The variability noticed in all coefficients in Table 7 is peculiar with rain rate conversion method as testified by several authors (see for example [1, 20]). The discrepancy in the coefficients was brought to light by Emiliani et al. [20] when they observed variability in both the coefficients and the regions (such as temperate, tropical and moderate tropical). The variability trends of the coefficients are again found to increase as the integration time increases. In the work of Emiliani et al., they also confirmed very disperse values of coefficients both using percentage of exceedence approach and rain rate approach (conversion factor), even within the same climatic region. As shown in their example, the wide variations of these coefficients are not uncommon, ranging between  $-173\%$  and  $579.79\%$  in tropical subset, between  $-109\%$  and  $555.2\%$  in the temperate subset, and between  $-143\%$  and  $336\%$  in the cold subset [20].

In the case of the two Islands, the polynomial fit shows a positive value for the C coefficient, which differs from the trend shown in the South Africa region. Using the square correlation coefficient value, it is noted from the table that the polynomial and linear fits give a better performance than the power fit, though the result of the power fit distribution is acceptable because the average square correlation coefficient records its least value at 0.956. The implication of this is that using the equiprobable approach gives a better approximation than the conversion factor approach. Using the conversion factor method (at equal rain rate), the square correlation coefficient records its

worst value at 0.479 and the best value at 0.990. The polynomial and logarithm fits gave better approximations compared to the power fit. Gough and Marion islands classes are approximated using both the equiprobable method and conversion factor approach. Polynomial, power and linear fits perform very well under the equiprobable method in the two islands. Although the polynomial and linear fits seem to do better than power fit especially in the case of Gough Island, all the three chosen fits do very well in Marion Island. Under the conversion factor approach, none of the chosen fits seem to approximate the distribution well.

Table 7a: Average coefficient for Equations (11), (12) and (13) with their Köppen climate classifications for the South Africa region.

Site Designation/expression coefficients	W	M	K	A	SE	E
<b>Polynomial Fit <math>R_1(p)/R_5(p)</math></b>	$\rho = 1.000$	$\rho = 0.997$	$\rho = 0.999$	$\rho = 0.999$	$\rho = 0.996$	$\rho = 0.999$
<b>A</b>	0.002	0.001	0.002	0.0005	0.0004	0.0014
<b>B</b>	1.023	1.231	1.255	1.273	1.257	1.2021
<b>C</b>	-0.126	-0.503	-0.370	-0.646	-0.536	-0.3543
<b>Power Fit <math>R_1(p)/R_5(p)</math></b>	$\rho = 0.980$	$\rho = 0.971$	$\rho = 0.983$	$\rho = 0.999$	$\rho = 0.999$	$\rho = 0.9983$
<b>D</b>	1.993	1.547	1.850	1.087	1.064	1.063
<b>E</b>	0.829	0.931	0.867	1.041	1.044	1.046
<b>Linear Fit <math>R_1(p)/R_5(p)</math></b>	$\rho = 0.998$	$\rho = 0.997$	$\rho = 0.999$	$\rho = 0.999$	$\rho = 0.950$	$\rho = 0.998$
<b>F</b>	1.205	1.318	1.376	1.314	1.291	1.334
<b>G</b>	-2.007	-1.213	-1.331	-1.029	-0.839	-2.115
<b>Polynomial Fit (cf)</b>	$\rho = 0.797$	$\rho = 0.768$	$\rho = 0.750$	$\rho = 0.985$	$\rho = 0.766$	$\rho = 0.79$
<b>H</b>	1.284	1.042	1.912	1.820	1.789	1.622
<b>I</b>	-1.017	-0.885	-1.356	-1.257	-1.194	-1.537
<b>J</b>	1.134	1.284	1.328	1.286	1.265	1.313
<b>Power Fit (cf)</b>	$\rho = 0.990$	$\rho = 0.830$	$\rho = 0.730$	$\rho = 0.859$	$\rho = 0.721$	$\rho = 0.678$
<b>K</b>	0.930	1.064	1.084	1.085	1.080	1.025
<b>L</b>	-0.037	-0.035	-0.039	-0.030	-0.028	-0.044
<b>Logarithm Fit (cf)</b>	$\rho = 0.989$	$\rho = 0.839$	$\rho = 0.820$	$\rho = 0.868$	$\rho = 0.821$	$\rho = 0.688$
<b>M</b>	-0.038	-0.043	-0.048	-0.036	-0.033	-0.052
<b>N</b>	0.995	1.059	1.077	1.082	1.078	1.021

Table 7b: Average coefficient for Equations (11) to (12) for the two islands.

Location	Polynomial Fit $R_1(p)/R_5(p)$	a	b	c	Power Fit $R_1(p)/R_5(p)$	d	e	Linear Fit $R_1(p)/R_5(p)$	f	g
Gough Islands	$\rho = 0.997$	0.002	1.062	1.157	$\rho = 0.915$	4.567	0.667	$\rho = 0.998$	1.196	0.092
Marion Island	$\rho = 0.999$	0.001	1.110	0.524	$\rho = 0.999$	1.151	1.009	$\rho = 0.999$	1.199	-0.292
Location	Polynomial Fit (cf)	h	I	j	Power Fit (cf)	k	l	Logarithm Fit (cf)	m	n
Gough Islands	$\rho = 0.414$	0.301	0.351	1.191	$\rho = 0.012$	1.325	0.020	$\rho = 0.014$	0.026	1.329
Marion Island	$\rho = 0.115$	-0.617	0.330	1.158	$\rho = 0.0016$	1.199	0.008	$\rho = 0.0013$	0.007	1.119

Table 7c: Average coefficient for Equations (35), (36) and (37) with their Köpen climate classifications for the South Africa region.

Site Designation/expression coefficients	D	L	NT	H	Sn	Ss
<b>Polynomial Fit</b> $R_1(p)/R_5(p)$	$\rho = 0.999$	$\rho = 0.996$	$\rho = 0.997$	$\rho = 0.999$	$\rho = 0.999$	$\rho = 0.999$
<b>A</b>	0.0007	0.002	0.0025	0.0009	0.0014	0.0006
<b>B</b>	1.185	1.108	1.102	1.201	1.071	1.239
<b>C</b>	-0.483	-0.424	0.581	-0.252	-0.389	-0.615
<b>Power Fit</b> $R_1(p)/R_5(p)$	$\rho = 0.999$	$\rho = 0.998$	$\rho = 0.956$	$\rho = 0.980$	$\rho = 0.999$	$\rho = 0.999$
<b>D</b>	1.071	1.086	1.028	1.071	1.635	1.021
<b>E</b>	1.032	0.891	1.049	1.014	0.929	1.092
<b>Linear Fit</b> $R_1(p)/R_5(p)$	$\rho = 0.999$	$\rho = 0.998$	$\rho = 0.996$	$\rho = 0.999$	$\rho = 0.998$	$\rho = 0.999$
<b>F</b>	1.267	1.295	1.265	1.284	1.231	1.284
<b>G</b>	-1.322	-1.721	-1.405	-1.012	-1.645	-0.980
<b>Polynomial Fit (cf)</b>	$\rho = 0.809$	$\rho = 0.725$	$\rho = 0.584$	$\rho = 0.864$	$\rho = 0.824$	$\rho = 0.734$
<b>H</b>	1.123	1.383	1.014	1.259	1.606	2.686
<b>I</b>	-0.788	-0.716	-0.655	-0.956	-1.110	-1.548
<b>J</b>	1.224	1.218	1.204	1.289	1.187	1.247
<b>Power Fit (cf)</b>	$\rho = 0.698$	$\rho = 0.650$	$\rho = 0.506$	$\rho = 0.762$	$\rho = 0.979$	$\rho = 0.629$
<b>K</b>	1.086	1.383	1.083	1.103	0.993	1.044
<b>L</b>	-0.021	-0.016	-0.020	-0.023	-0.033	-0.031
<b>Logarithm Fit (cf)</b>	$\rho = 0.579$	$\rho = 0.782$	$\rho = 0.514$	$\rho = 0.772$	$\rho = 0.984$	$\rho = 0.659$
<b>M</b>	-0.025	-0.019	-0.023	-0.028	-0.037	-0.036
<b>N</b>	1.084	1.115	1.081	1.127	0.987	1.042

## 6. CONCLUSION

In this paper, a proposed Hybrid method for the conversion of five-minute integration time to one-minute equivalent is presented, as well as a comparison of the proposed model with two global models. In the proposed Hybrid method, the strength of each category of model classes were combined to produce a hybrid model. The selected model consists of regional parameters in order to characterize the rain rate pattern for a defined area. The resulting one-minute cumulative distribution of rain rate is fitted with polynomial, power, linear and logarithmic fits. The performance tests of these fits are optimized using standard deviation and root-mean square of absolute relative error at the control site of Durban. The results show that the equiprobable approach gives better results than the conversion factor approach. In addition, the second order polynomial fit performs relatively better than its other counterparts. The evidence of good performance by the second order polynomial fit makes it a good candidate for conversion of rain rate from five-minute to equivalent one-minute in South Africa and her Islands. The coefficients of hybrid models are categories using Koppen method and finally second order polynomial fit is adopted for the region with their respective coefficients.

## REFERENCES

1. Capsoni, C. and L. Luini, "1-min rain rate statistics predictions from 1-hour rain rate statistics measurements," *IEEE Trans. Antennas and Propagation*, Vol. 56, No. 3, March 2008.
2. Rice, P. and N. Holmberg, "Cumulative time statistics of surface-point rainfall rate," *IEEE Transactions on Communications*, 1772–1774, COM-21, October 1973.
3. Dutton, E. J., H. T. Dougherty, and R. F. Martin, Jr., "Prediction of European rainfall and link performance coefficients at 8 to 30 GHz," NTIS Rep ACC-ACO-16-17, 1974.
4. Crane, R. K., *Electromagnetic Wave Propagation through Rain*, John Wiley & Sons, Canada, 1996.

5. ITU-R P.837-5, “Characteristics of precipitation for propagation modelling, recommendation ITU-R P.837-5,” International Telecommunication Union, Geneva, Switzerland, 2007.
6. Capsoni, C., F. Fedi, C. Magistroni, A. Paraboni, and A. Pawlina, “Data and theory for a new model of the horizontal structures of rain cells for propagation applications,” *Radio Science*, Vol. 22, No. 3, 1726–1733, May 1987.
7. Lavergnat, J. and P. Golé, “A stochastic raindrop time distribution model,” *AMS Journal of Applied Meteorology*, Vol. 37, No. 8, 805–818, August 1998.
8. Moupfouma, F. and L. Martin, “Modelling of the rainfall rate cumulative distribution for the design of satellite and terrestrial communication systems,” *International Journal of Satellite Communications*, Vol. 13, No. 2, 105–115, 1995.
9. Karasawa, Y. and T. Matsudo, “One-minute rain rate distributions in Japan derived from AMeDAS one-hour rain rate data,” *IEEE Trans. Geosci. Remote Sensing*, Vol. 29, No. 6, 890–898, November 1991.
10. Ito, C. and Y. Hosoya, “Proposal of a global conversion method for different integration time rain rates by using M-distribution and regional climatic parameters,” *Electronics and Communications in Japan*, Part 1, Vol. 89, No. 4, 2006.
11. Segal, B., “The influence of rain gauge integration time on measured rainfall-intensity distribution functions,” *Journal of Atmospheric and Oceanic Technology*, Vol. 3, 662–671, 1986.
12. Burgueno, A. M., M. Puigcever, and E. Vilar, “Influence of rain gauge integration time on the rain rate statistics used in microwave communication,” *Ann. Telecomm.*, Vol. 43, No. 9–10, 522–527, 1988.
13. Watson, P. A., M. Gunes, B. A. Potter, V. Sathiaseelan, and J. Leitao, “Development of a climatic map of rainfall attenuation for Europe,” Final Report of ESA/ESTEC Contract No. 4162/79/NL/DG/(SC), Report 327, 1982.
14. Chebil, J. and T. A. Rahman, “Rain rate statistical conversion for the prediction of rain attenuation in Malaysia,” *Electronic Letters*, Vol. 35, No. 12, 1019–1021, 1999.
15. Ajayi, G. O. and E. Ofoch, “Some tropical rainfall rate characteristics at Ile-Ife for microwave and millimetre wave applications,” *Journal of Climate and Applied Meteorology*, Vol. 23, No. 4, 562–567, April 1984.
16. Flavin, R. K., “Rain attenuation considerations for satellite paths in Australia,” *Australian Telecommunications Research*, Vol. 16, 11–24, 1982.
17. Ong, J. and C. Zhu, “Rain rate measurements by a rain gauge network in Singapore,” *Electronics Letters*, Vol. 33, 240–242, January 1997.
18. Ong, J. and C. Zhu, “Effect of integration time in rain rate statistics for Singapore,” *Proceedings of 10th International Conference on Antennas and Propagation*, Conference Publication No. 436, 14–17, April 1997.
19. Xiao, J. M., D. H. Cheng, and L. J. Wang, “Rain rate statistics and analysis in Xian district,” *China Journal of Radio Science*, Vol. 2, No. 1, 39–48, 1987 (in Chinese).
20. Emiliani, L. D., L. Luini, and C. Capsoni, “Analysis and parameterization of methodologies for the conversion of rain-rate cumulative distributions from various integration times to one minute,” *IEEE Antennas and Propagation Magazine*, Vol. 51, No. 3, 71–84, June 2009.
21. Emiliani, L. D., L. Luini, and C. Capsoni, “Extension of ITU-R method for conversion of rain rate statistics from various integration times to one minute,” *Electronics Letters*, Vol. 44, No. 8, 557–558, April 2008.
22. Owolawi, P. A., “Rainfall rate probability density evaluation and mapping for the estimation of rain attenuation in South Africa and surrounding islands,” *Progress In Electromagnetics Research*, Vol. 112, 155–181, 2011.
23. World Meteorological Organization, *World Distribution of Thunderstorm Days*, No. 21, TP.6, WMO/OMM, Geneva, 1953.
24. World Meteorological Organization, *World Meteorological Organization Climatological Normal (CLINO) for Climate and Climate Ship Stations for the Period 1931–1960*, No. 117, TP.52, WMO/OMM, Geneva, 1962.
25. Owolawi, P. A. and T. J. Afullo, “Rainfall rate modelling and its worst month statistics for millimetric LOS links in South Africa,” *Radio Science*, Vol. 42, 2007.
26. Seeber, R. J., “An extreme value model of surface-point rain-rate distribution for the prediction of microwave rain attenuation in Southern Africa,” M.Sc. Thesis, University of Pretoria, 1995.

# Applications of the Natural Transform to Maxwell's Equations

R. Silambarasan<sup>1</sup> and F. B. M. Belgacem<sup>2</sup>

<sup>1</sup>M. S. Software Engg., V.I.T. University, Vellore, India

<sup>2</sup>Department of Mathematics, Faculty of Basic Education, PAAET, Shaamyia, Kuwait

**Abstract**— Electric and Magnetic Field solutions of Maxwell's equation describing TEMP waves traveling in conducting but lossy media are derived using the Natural Transform.

## 1. INTRODUCTION

In this paper, we apply the Natural transform to Maxwell's equations to determine the transient electric and magnetic fields solutions. Using the Sumudu transform, Maxwell's equations were solved by M. G. M. Hussain et al. [9] and F. B. M. Belgacem [5].

Now the Two sided Natural transform of the function  $f(t) \in (-\infty, \infty)$  may be defined on the both sides of real line  $t \in (-\infty, \infty)$ ,

$$\mathbb{N}[f(t)] = \int_{-\infty}^{\infty} e^{-st} f(ut) dt; \quad s, u \in (-\infty, \infty) \quad (1)$$

The Eq. (1) is defined precisely

$$\begin{aligned} \mathbb{N}[f(t)] &= \int_{-\infty}^0 e^{-st} f(ut) dt + \int_0^{\infty} e^{-st} f(ut) dt \\ &= \mathbb{N}^-[f(t)] + \mathbb{N}^+[f(t)] \\ &= \mathbb{N}[f(t)H(-t)] + \mathbb{N}[f(t)H(t)] \end{aligned}$$

Now for the function  $f(t)H(t)$  where  $H(t)$  is unit step function, the Natural transform of  $f(t) \in (0, \infty)$  is defined by [10]

$$\mathbb{N}^+[f(t)] = R(s, u) = \int_0^{\infty} e^{-st} f(ut) dt; \quad s > 0, u > 0 \quad (2)$$

provided the function  $f(t)H(t)$  is defined in the set

$$A = \left\{ f(t) \mid \exists M, \tau_1, \tau_2 > 0, |f(t)| < M e^{\frac{t}{\tau_j}}, \text{ if } t \in (-1)^j \times [0, \infty) \right\} \quad (3)$$

The integral Eq. (2) converges to Laplace transform [11] when  $u \equiv 1$  [10], and into Sumudu transform [1–4] for  $s \equiv 1$  [10]. The more details of Natural transform for its Multiple Shift, Heaviside's Expansion formula etc can be seen in [7].

Meanwhile, we take advantage to give certain properties of Natural transform [7] without proof which will be useful in Maxwell equation solving. The Natural transform of function derivative  $f(t)$  w.r.t 't',  $n$ -times

$$\mathbb{N}^+[f^n(t)] = R_n(s, u) = \frac{s^n}{u^n} R(s, u) - \sum_{k=0}^{n-1} \frac{s^{n-(k+1)}}{u^{n-k}} f^k(0) \quad (4)$$

The proof of Eq. (4) given in [7]. For  $n = 1, 2$  in Eq. (4) gives Natural transform of first and second derivative of  $f(t)$  w.r.t 't' [10]

$$\mathbb{N}^+ \left[ f'(t) \right] = R_1(s, u) = \frac{s}{u} R(s, u) - \frac{f(0)}{u} \quad (5)$$

$$\mathbb{N}^+ \left[ f''(t) \right] = R_2(s, u) = \frac{s^2 R(s, u) - s \cdot f(0)}{u^2} - \frac{f'(0)}{u} \quad (6)$$

Natural transform of Convolution of two functions [7]

$$\mathbb{N}^+[(f * g)] = uF(s, u)G(s, u) \quad (7)$$

The inverse Natural transform related with Bromwich contour integral [7]

$$\mathbb{N}^{-1}[R(s, u)] = f(t) = \lim_{T \rightarrow \infty} \frac{1}{2\pi i} \int_{\gamma-iT}^{\gamma+iT} e^{\frac{st}{u}} R(s, u) ds \quad (8)$$

Next we apply the above properties to Maxwell's equation.

## 2. MAXWELL'S EQUATIONS SOLUTION

The planar transverse electromagnetic wave (TEMP) propagate in  $z$  direction in lossy medium with constant permittivity  $\epsilon$ , permeability  $\mu$  and conductivity  $\sigma$ . The electric field vector  $\mathbf{E}$  and magnetic field vector  $\mathbf{H}$  are related by [5, 9]

$$\nabla \times E = -\mu \frac{\partial H}{\partial t} \quad (9)$$

$$\nabla \times H = \epsilon \frac{\partial E}{\partial t} + \sigma E \quad (10)$$

When the electric field vector is polarized along  $x$  direction thus  $E = E_x(z, t)$  and magnetic field along  $y$  direction  $H = H_y(z, t)$ . The Maxwell's equations of Eqs. (9) and (10) expressed in differential equation as

$$\frac{\partial E_x}{\partial z} + \mu \frac{\partial H_y}{\partial t} = 0 \quad (11)$$

$$\frac{\partial H_y}{\partial z} + \epsilon \frac{\partial E_x}{\partial t} + \sigma E_x = 0 \quad (12)$$

Application of Natural transform to the Eqs. (11) and (12) and setting  $\mathbb{N}^+[E_x(z, t)] = F(z, s, u)$ ,  $\mathbb{N}^+[H_y(z, t)] = G(z, s, u)$ , where  $(s, u)$  are Natural transform variables w.r.t. ' $t$ ', gives

$$\frac{\partial F(z, s, u)}{\partial z} + \frac{s\mu}{u} G(z, s, u) - \frac{\mu}{u} H(z, 0) = 0 \quad (13)$$

$$\frac{\partial G(z, s, u)}{\partial z} + \frac{s\epsilon}{u} F(z, s, u) - \frac{\epsilon}{u} E(z, 0) + \sigma F(z, s, u) = 0 \quad (14)$$

Differentiating Eq. (13) partially w.r.t. ' $z$ ' gives

$$\frac{\partial^2 F(z, s, u)}{\partial z^2} + \frac{s\mu}{u} \frac{\partial G(z, s, u)}{\partial z} = \frac{\mu}{u} \frac{\partial H(z, 0)}{\partial z} \quad (15)$$

Substituting Eq. (14) in Eq. (15) for  $\frac{\partial G(z, s, u)}{\partial z}$ , simplifying and arranging

$$\frac{\partial^2 F(z, s, u)}{\partial z^2} - \left[ \frac{s^2 \mu \epsilon}{u^2} + \frac{s \mu \sigma}{u} \right] F(z, s, u) = \frac{\mu}{u} \left[ \frac{\partial H(z, 0)}{\partial z} \right]_{t=0} - \frac{s \mu \epsilon}{u^2} E(z, 0) \quad (16)$$

Now we reduced to differential equation only in  $F(z, s, u)$ . Now substituting Eq. (12) in Eq. (16)

$$\frac{\partial^2 F(z, s, u)}{\partial z^2} - \left[ \frac{s^2 \mu \epsilon}{u^2} + \frac{s \mu \sigma}{u} \right] F(z, s, u) = - \left[ \frac{s \mu \epsilon}{u^2} + \frac{\mu \sigma}{u} \right] E(z, 0) - \frac{\mu \epsilon}{u} \left[ \frac{\partial E(z, 0)}{\partial t} \right]_{t=0} \quad (17)$$

Now consider the initial and boundary conditions

$$E_x(\infty, t) = \text{finite} \quad (18)$$

$$E_x(z, 0) = H_y(z, 0) = 0 \quad (19)$$

$$\frac{\partial E_x(z, 0)}{\partial z} = \frac{\partial H_y(z, 0)}{\partial z} = 0 \quad (20)$$

$$\left[ \frac{\partial E_x(z, 0)}{\partial t} \right]_{t=0} = \left[ \frac{\partial H_y(z, 0)}{\partial t} \right]_{t=0} = 0 \quad (21)$$

$$E(0, t) = f(t); \quad t \geq 0 \quad \text{and} \quad 0; t < 0 \quad (22)$$

Using the initial conditions Eqs. (19) and (21). The R.H.S of Eq. (17) is 0. Thus

$$\frac{d^2F(z, s, u)}{dz^2} - \left[ \frac{s^2\mu\epsilon}{u^2} + \frac{s\mu\sigma}{u} \right] F(z, s, u) = 0 \quad (23)$$

Substituting  $\gamma^2 = \frac{s^2\mu\epsilon}{u^2} + \frac{s\mu\sigma}{u}$ . And the resulting homogenous differential equation solution is

$$F(z, s, u) = A(s, u)e^{-\gamma z} + B(s, u)e^{\gamma z} \quad (24)$$

Using the boundary condition Eq. (22) gives  $B(s, u) = 0$  in Eq. (24)

$$A(s, u) = \mathbb{N}^+[f(t)] = f(s, u) \quad (25)$$

$$F(z, s, u) = f(s, u)e^{-\gamma z} \quad (26)$$

Now multiplying and dividing the R.H.S of Eq. (26) by the parameters  $su$

$$F(z, s, u) = \frac{su f(s, u) e^{-\gamma z}}{su} \quad (27)$$

By the application of Eq. (5) and Eq. (8)

$$F(z, s, u) = u \mathbb{N}^+[f'(t) + f(0)] \mathbb{N}^+ \left[ \frac{1}{2\pi i} \int_{\gamma-i\infty}^{\gamma+i\infty} \frac{e^{\frac{st}{u}} e^{-\gamma z}}{s} ds \right] \quad (28)$$

Applying inverse Natural transform on both sides of Eq. (28) and using the Convolution theorem Eq. (7),

$$E(z, t) = \int_0^t [f'(t-\tau) + f(0)] \frac{1}{2\pi i} \int_{\gamma-i\infty}^{\gamma+i\infty} \frac{e^{\frac{st}{u}} e^{-\gamma z}}{s} ds d\tau \quad (29)$$

which is the transient electric field  $E(z, t)$  of TEMP waves in lossy medium.

Similarly the transient solution of magnetic field  $H(z, t)$  of TEMP waves in lossy medium is given by

$$H(z, t) = \int_0^t [g'(t-\zeta) + f(0)] \frac{1}{2\pi i} \int_{\gamma-i\infty}^{\gamma+i\infty} \frac{e^{\frac{st}{u}} \cos \gamma z}{s} ds d\zeta \quad (30)$$

### 3. CONCLUSION

It should be noted that electric field solutions are real and magbetic field solutions are imaginary from their reduced homogenous differential equations as was expected.

### REFERENCES

1. Belgacem, F. B. M., A. A. Karaballi, and S. L. Kalla, “Analytical investigations of the Sumudu transform and applications to integral production equations,” *Mathematical Problems in Engineering*, No. 3, 103–118, 2003.
2. Belgacem, F. B. M. and A. A. Karaballi, “Sumudu transform fundamental properties, investigations and applications,” *Journal of Applied Mathematics and Stochastic Analysis*, 1–23, 2006.
3. Belgacem, F. B. M., “Introducing and analysing deeper Sumudu properties,” *Nonlinear Studies Journal*, Vol. 13, No. 1, 23–41, 2006.
4. Belgacem, F. B. M., “Sumudu transform applications to Bessel’s functions and equations,” *Applied Mathematical Sciences*, Vol. 4, No. 74, 3665–3686, 2010.
5. Belgacem, F. B. M., “Sumudu applications to Maxwell’s equations,” *PIERS Online*, Vol. 5, No. 4, 355–360, 2009.
6. Belgacem, F. B. M., “Applications of Sumudu transform to indefinite periodic parabolic equations,” *Proceedings of the 6th International Conference on Mathematical Problems & Aerospace Sciences, (ICNPAA 06)*, Chap. 6, 5160, Cambridge Scientific Publishers, Cambridge, UK, 2007.

7. Belgacem, F. B. M. and R. Silambarasan, "Theoretical investigations of the natural transform," In Pre-print, to Appear.
8. Belgacem, F. B. M. and R. Silambarasan, "Maxwell's equations solutions through the natural transform," In Pre-print, to Appear.
9. Hussain, M. G. M. and F. B. M. Belgacem, "Transient solutions of Maxwell's equations based on Sumudu transform," *Progress In Electromagnetics Research*, Vol. 74, 273–289, 2007.
10. Khan, Z. H. and W. A. Khan, "N-transform properties and applications," *NUST Jour. of Engg. Sciences*, Vol. 1, No. 1, 127–133, 2008.
11. Spiegel, M. R., *Theory and Problems of Laplace Transforms*, Schaums Outline Series, McGraw-Hill, New York, 1965.

# Miniaturized Patch Antennas with Ferrite/Dielectric/Ferrite Magnetodielectric Sandwich Substrate

Guo-Min Yang<sup>1</sup>, Ogheneyunume Obi<sup>2</sup>, Ming Liu<sup>2</sup>, and Nian X. Sun<sup>2</sup>

<sup>1</sup>Key Laboratory of Wave Scattering and Remote Sensing Information  
Department of Communication Science and Engineering  
Fudan University, Shanghai 200433, China

<sup>2</sup>Department of Electrical and Computer Engineering  
Northeastern University, Boston, MA 02115, USA

**Abstract**— Magneto-dielectric substrates with thin magnetic films show great potential in realizing electrically small antennas with enhanced bandwidth, improved directivity, and high efficiency. This is the first time to introduce 10- $\mu\text{m}$  thick self-biased NiCo-ferrite films as a practical means to tune a patch antenna by loading Ferrite/Rogers/Ferrite (F/R/F) sandwich structures. The central resonant frequency of the base line patch antenna with composite of Rogers and alumina substrate is 2460 MHz with a bandwidth of 42 MHz. However, with F/R/F loading of the alumina substrate, this frequency is down shifted to 2380 MHz with a greatly improved bandwidth of 74 MHz. In addition, the gain of the magnetic antenna with F/R/F sandwich structure is enhanced by 2.4 dB over the unloaded antenna.

## 1. INTRODUCTION

With the continuous growth of wireless communication technologies, design and manufacturing of miniaturized microwave components are among most critical issues in communication systems [1, 2]. In the RF front-end, patch antennas with small size and high performance are highly desirable. Planar device size can be minimized by using a substrate with high relative permittivity. However, antennas with high-permittivity substrates result in decreased bandwidth and the excitation of surface waves, leading to lower radiation efficiency and larger element coupling in arrays. It also becomes difficult to achieve impedance matching on high-permittivity substrates, due to large reactance of the coaxial probes used to feed the antenna.

Achieving relative permeability larger than 1 ( $\mu_r > 1$ ) in antenna substrates can lead to antenna miniaturization, enhanced bandwidth, tunable center frequency, polarization diversity, and beam steering [3–5]. Bulk ferrite materials, composites of ferrite particles in polymer matrix, metamaterials with embedded metallic circuits, etc., have been used as antenna substrates for achieving  $\mu_r > 1$ . However, these bulk ferrite materials or ferrite composites are too lossy to be used at frequencies  $> 600$  MHz under self-bias condition, i.e., no bias magnetic field is needed, and large biasing magnetic fields are needed for these antennas to operate at higher frequencies. In order to be practically feasible in miniature antenna applications, such as handheld wireless communication devices, where battery power and space for electronics are at a premium, it is important for antenna substrates to be comprised of self-biased magnetic materials, in which no external bias field is applied.

Magnetic thin films provide a unique opportunity for achieving self-biased magnetic patch antenna substrates with  $\mu > 1$  [6–8] and operating frequencies  $> 1$  GHz. The strong demagnetization field for magnetic thin films,  $H_{\text{demag}} = 4\pi M_s$ , allows for a self-biased magnetization with high ferromagnetic resonance (FMR) frequencies (up to several GHz), a necessary condition for multi-ferrite RF devices to operate in the cellular and WLAN bands.

Most recently, we have proposed to use novel magnetoelectric composite substrates for antennas with low-loss magnetic film materials and low-loss dielectric materials. In our previous work, new designs of electronically tunable patch antennas with magnetic metallic magnetic films were investigated [9], which showed that the bandwidth was increased by 50% over the non-magnetic antennas. Fielding addition, a new self-biased ferrite film of NiCo-ferrite was investigated and adopted in our recent research of antenna miniaturization [10, 11]. We have successfully achieved self-biased ring antennas at 1.7 GHz with a wide range of tunable resonant frequency with high quality self-biased ferrite films [11], which shows great potential in the applications of antenna miniaturization for mobile handheld wireless communication devices.

In this paper, we report on patch antennas miniaturized by using Ferrite/Rogers/Ferrite sandwich structures on the alumina substrate, thus essentially creating a magneto-dielectric substrate

for practical applications. The magnetic patch antennas were fabricated by loading the antenna with an F/R/F structure adjacent to the patch. These antennas show an enhanced bandwidth of up to 76% over the base line counterparts at 2.4 GHz, a large central resonant frequency tunability (190% of the  $-10\text{ dB}$  bandwidth), and a significantly enhanced gain by 2.4 dB over the non-magnetic antenna.

## 2. THE CHARACTERISTICS OF NICO-FERRITE FILMS AND DESIGN OF PATCH ANTENNAS

In this work, we used self-biased spinel NiCo-ferrite films fabricated by a low-cost spin-spray deposition process [8], a wet chemical synthesis process at a low-temperature of  $90^\circ\text{C}$ . NiCo-ferrite films with the composition of  $\text{Ni}_{0.23}\text{Co}_{0.13}\text{Fe}_{2.64}\text{O}_4$  were deposited onto both side of the Rogers material. As the surface of the Rogers material is very rough, it is possible to get the ferrite film with a thickness of  $10\text{ }\mu\text{m}$ , and this is the first time to get it. Since the ferrite films were deposited on both side of the Rogers substrate, the total thickness of the ferrite film is  $20\text{ }\mu\text{m}$ . A small sample was used for the characteristics measurement. The in-plane and out-of-plane magnetic hysteresis loops of the NiCo-ferrite films were measured with a vibrating sample magnetometer (VSM) with the external magnetic field applied in the film plane, out of the film plane, respectively. The in-plane hysteresis loop shows an in-plane coercivity of 165 Oe as well as the self-biased magnetization of the film under zero applied magnetic fields. There is a huge difference between the in-plane hysteresis and the out-plane hysteresis, indicating that the magnetization stays in the film plane under zero bias magnetic field. The NiCo-ferrite film showed an in-plane homogeneous magnetization with an in-plane relative permeability of  $\sim 10$ . The in-plane resistivity of the NiCo-ferrite film was measured to be  $5.6 \times 10^3\text{ }\Omega\cdot\text{cm}$ .

The geometry of the patch antenna is shown in Fig. 1. It is a conventional microstrip line-fed patch on a  $2'' \times 2''$  alumina substrate ( $\epsilon_r = 9.9$ ) with a thickness of 2 mm. This antenna is fed by an SMA connector mounted at the side of the substrate. The copper patch for this non-magnetic antenna has a length of  $L_2 = 20.0\text{ mm}$ , and a width of  $W_1 = 30.0\text{ mm}$ . The width of the feed-line is 2.0 mm and the length is 20.8 mm. The width of the inset is 2.0 mm and the length is 7.0 mm. The working frequency of the patch antenna without ferrite film is about 2.46 GHz in this paper, which means our designed antenna can work for the WLAN and Bluetooth bands. To our knowledge, this is the first time to demonstrate the advantages of NiCo-ferrite film to work at this frequency band.

## 3. EXPERIMENTAL RESULTS FOR THE PATCH ANTENNA WITH F/R/F SANDWICH STRUCTURES

The F/R/F sandwich structure was composed of Rogers Duroid6010 material with a very thin thickness of 10 mil. NiCo-ferrite films were deposited onto both side of Rogers material and the thickness of ferrite film on each side was about  $10\text{ }\mu\text{m}$ , thus one could get a Ferrite/Rogers/Ferrite (F/R/F) sandwich structure. This sandwich structure has the same surface dimension of  $2'' \times 2''$  as the alumna substrate. The side views of the antenna with Rogers material and magnetic antenna with F/R/F sandwich structure are shown in Figs. 2(a) and (b), respectively. The total thickness of sandwich structure (Ferrite/Rogers/Ferrite) is about 0.274 mm.

The measured reflection coefficient for the magnetic antenna with sandwich structure is plotted in Fig. 3, along with that of the base line patch with Rogers and alumina substrate for comparison. The base line patch antenna (composite Rogers and alumina only) shows a resonant frequency of

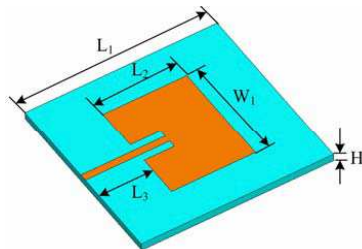


Figure 1: Geometry of the non-magnetic rectangular patch antenna.  $L_1 = 51\text{ mm}$ ,  $L_2 = 20.0\text{ mm}$ ,  $L_3 = 13.8\text{ mm}$ ,  $W_1 = 30.0\text{ mm}$  and  $H = 2.0\text{ mm}$ . The dimension of the inset is  $7.0 \times 2.0\text{ mm}^2$ .

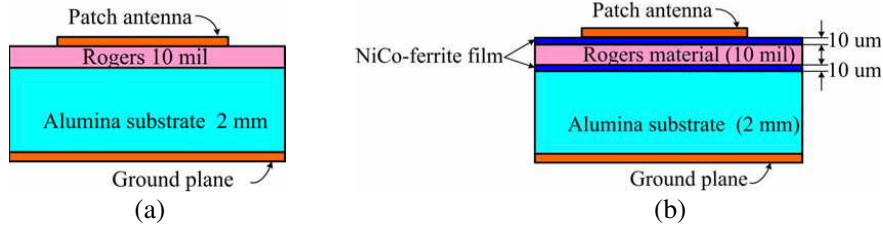


Figure 2: (a) Side view of the patch antenna with Rogers material. (b) Side view of patch antenna with Ferrite/Rogers/Ferrite sandwich structure loading.

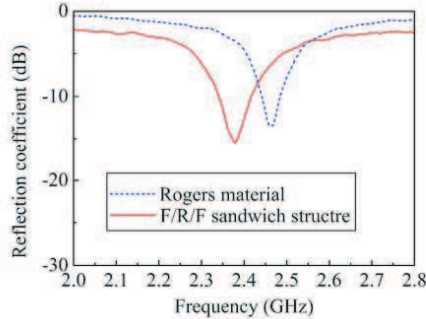


Figure 3: Measured reflection coefficient of the patch antennas with Rogers material and F/R/F sandwich structures.

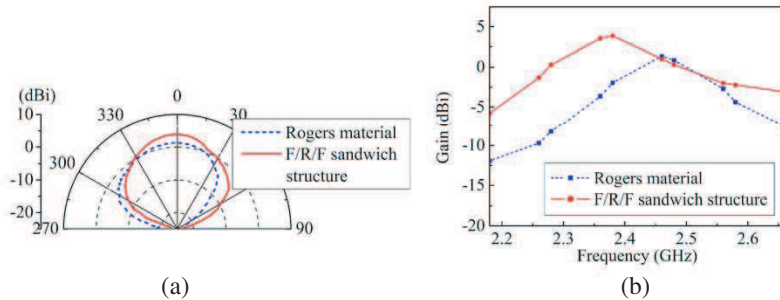


Figure 4: (a) Radiation patterns of *H*-plane. (b) Measured gains against frequency.

2460 MHz, and a 2 : 1 VSWR bandwidth of 42 MHz. When the F/R/F sandwich structure is added above the alumina substrate, the resonance shifts down to 2380 MHz. This indicates a frequency shifting of 80 MHz relative to the non-magnetic substrate, or equivalent to approximately 190% of the bandwidth, relative to the non-magnetic substrate. The antenna bandwidth is 74 MHz with the addition of the F/R/F, an increase of 76% relative to non-magnetic antenna, which is because of the magnetoelectric substrates could provide a higher ratio of relative permeability and relative permittivity than their dielectric counterpart. As shown in Fig. 3, the magnitude of the reflection coefficient at the resonant frequency is also improved with the ferrite film. Clearly the F/R/F sandwich loading leads to the enhanced bandwidth and improved impedance matching.

The antenna radiation patterns of *H*-plane and gains were measured in the anechoic chamber. The maximum detected power at the broadside is about 6.19 mW for the non-magnetic patch, which increases to 10.9 mW for the magnetic antennas. The gain comparison technique was used to determine the radiation patterns and gains of the antennas, which were plotted in Figs. 4(a) and (b), respectively. As we have indicated in the first section, the designed patch lies on the interface between two material half spaces, that is the free space above the patch and the substrate below the patch. The patch antenna acts like a generator that is driving two loads in parallel and the power split between the loads is inversely proportional to the ratio of the characteristic impedance. To deliver more power to the free space, the permeability of the substrate could be increased. For

the fabricated magnetic patch antenna in this paper, there is a Ferrite/Rogers/Ferrite sandwich structure between the rectangular patch and the alumina substrate, thus to improve the effective permeability of the whole substrate at GHz frequencies. As shown in Fig. 4(b), the fabricated magnetic antenna gain is enhanced by 2.4 dB at the central resonant frequency of 2.38 GHz over the non-magnetic antenna at the resonance of 2.46 GHz.

#### 4. CONCLUSION

Ferrite/Rogers/Ferrite sandwich structures have been introduced as a practical means to tune a patch antenna by loading a commercially available substrate. Measurements on magnetic patch antennas demonstrate that the central resonant frequency can be varied downward over a tuning of 190% of the antenna bandwidth, which indicates that the self-biased magnetic films do lead to minimized antennas by shifting down the resonance frequency. The working frequency bandwidth increased of 76% over the non-magnetic antenna, which shows that the designed magnetic antennas have significantly enhanced bandwidth. Also antennas with magnetodielectric substrates show significantly improved antenna gains at GHz frequency range.

#### ACKNOWLEDGMENT

This work is sponsored by ONR, NSF and Natural Science Foundation of Shanghai under Grant 11ZR1403500. The authors would like to thank Professor A. Farhat for allowing the use of the measurement facility. The authors would also like to thank X. Xing for her technical assistant and helpful discussion.

#### REFERENCES

1. Balanis, C. A., *Antenna Theory: Analysis and Design*, John Wiley, Hoboken, NJ, 2005.
2. Wong, K. L., *Planar Antennas for Wireless Communications*, John Wiley, Hoboken, NJ, 2003.
3. Mosallaei, H. and K. Sarabandi, “Magneto-dielectrics in electromagnetics: Concept and applications,” *IEEE Trans. Antennas and Propagat.*, Vol. 52, No. 6, 1558–1567, 2004.
4. Ikonen, P. M. T., K. N. Rozanov, A. V. Osipov, P. Alitalo and S. A. Tretyakov, “Magnetodielectric substrate in antenna miniaturization: Potential and limitations,” *IEEE Trans. Antennas Propag.*, Vol. 54, No. 11, 3391–3399, 2006.
5. Bell, J. M., M. F. Iskander, and J. J. Lee, “UWB hybrid EBG/ferrite ground plane for low-profile array antennas,” *IEEE Trans. Antennas Propagat.*, Vol. 55, No. 1, 4–12, 2007.
6. Wang, S. X., N. X. Sun, M. Yamaguchi, and S. Yabukami, “Sandwich films: properties of a new soft magnetic material,” *Nature*, Vol. 407, No. 9, 150–151, 2000.
7. Lou, J., R. E. Insignares, Z. Cai, K. S. Ziemer, M. Liu, and N. X. Sun, “Soft magnetism, magnetostriction, and microwave properties of FeGaB thin films,” *Appl. Phys. Lett.*, Vol. 91, No. 10, 18254, 2007.
8. Kondo, K., S. Yoshida, H. Ono, and M. Abe, “Spin sprayed Ni(-Zn)-Co ferrite films with natural resonance frequency exceeding 3 GHz,” *J. Appl. Phys.*, Vol. 101, 09M502, 2007.
9. Sun, N. X., J. W. Wang, A. Daigle, C. Pettiford, H. Mosallaei, and C. Vittoria, “Electronically tunable magnetic patch antennas with metal magnetic films,” *Electronics Lett.*, Vol. 43, No. 4, 434–435, 2007.
10. Yang, G. M., X. Xing, A. Daigle, M. Liu, O. Obi, S. Stoute, K. Naishadham, and N. X. Sun, “Tunable miniaturized patch antennas with self-biased multilayer magnetic films,” *IEEE Trans. Antennas Propag.*, Vol. 57, No. 7, 2190–2193, 2009.
11. Yang, G. M., X. Xing, A. Daigle, O. Obi, M. Liu, J. Lou, S. Stoute, K. Naishadham, and N. X. Sun, “Planar annular ring antennas with multilayer self-biased NiCo-Ferrite films loading,” *IEEE Trans. Antennas Propag.*, Vol. 58, No. 3, 648–655, 2010.

# Tunable High Frequency Permeability of Metamaterials

Shunlin Zhong, Mangui Han, Jianliang Xie, Difei Liang, and Longjiang Deng

State Key Laboratory of Electronic Thin Films and Integrated Devices

University of Electronic Science and Technology of China, China

**Abstract**— In this paper, an approach of tuning the magnetic permeability of split-ring resonator (SRR) has been presented. A varactor diode has been embedded into a SRR structure, and its capacity can be tuned by controlling the applied voltage. By this method, the resonance frequency and effective permeability are found to be easily tuned. Using the Finite-Difference-Time-Domain method and retrieval method, we have respectively simulated the tunability of permeability by changing the geometry of split and by changing the applied voltage of varactor diodes. The HFSS simulation results show that the resonance frequency of permeability shifts toward a higher value with increasing the size of split, while it is also found that the resonance frequency of permeability shifts toward a lower value by increasing the applied voltage.

## 1. INTRODUCTION

In recent decades, more attention has been given to the so-called metamaterials, which are believed that they will find many important applications in electromagnetic engineerings and materials engineering. In 1968, metamaterials firstly have been proposed based on the electromagnetic theory by a scientist named Veselago from the former Soviet Union, who had proved that a metamaterial can possess negative permittivity and negative permeability [1]. The vectors of electric field ( $E$ ), magnetic field ( $H$ ) and Poynting vector energy ( $K$ ) consistent with the left-handed coordinate system, therefore it is termed as the Left-Handed Materials. However, at that time, materials possessing both negative permittivity and permeability have not been found in nature, therefore the idea of metamaterial has attracted less attention. Until 1999, Pendry et al used two artificial structures; split-ring resonators [2] as well as plasmonic wires (PWs) [3], to prove that negative magnetic and negative electric permittivity can be obtained, respectively. In 2000, D. R. Smith et al. have fabricated a metamaterial based on the Pendry's theory, which show that both the permittivity and permeability are negative [4]. Since then, research on metamaterials booms. In this paper, we use the basic element of metamaterials (i.e., SRR) to study the possibility of tuning the permeability dispersion behaviors by two approaches: one is to change the dimensional size of SRR split. The other way is to embed a varactor diode into the SRR structure and tune its permeability by the biased voltage. Our results show that the latter one is more flexible and easier to tune the permeability, which will enable the metamaterials to deal with the increasingly complex electromagnetic environment.

## 2. PRINCIPLES OF DESIGN

When the wavelength of incident electromagnetic wave is much larger than the dimensions of SRR, SRR can be thought to exhibit the capacitive and inductive behaviors. According to the Faraday's law, when the propagation direction of incident EM wave is normal to the plane of SRR, the variation of magnetic field of EM wave will give rise to an induced-current in two SRR elements respectively. The current move to the same under an external magnetic field Lorenz forcecharges with different polarity will be produced and distributed between two SSR elements. Such an effect is equivalent that there is coupled capacitor ( $C_g$ ) between two SRR elements, as shown in Fig. 1. This capacitor and the distributed inductance will form a  $LC$  resonance circuit at a certain frequency. The resonance frequency is dependent on the values of capacitance and inductance. In this case, the effective permeability ( $\mu$ ) of SRR element can be described by the following equations [5]:

$$\mu(\omega) = 1 - \frac{F\omega^2}{\omega^2 - \omega_0^2 + i\Gamma\omega} \quad (1)$$

$$\omega_0 = 1/\sqrt{LC} \quad (2)$$

where  $\omega_0$  is the resonance frequency of SRR element,  $L$  and  $C$  is the effective inductance and capacitance,  $\Gamma$  is the damping factor due to metal losses,  $F$  is a factor related to the dimension of SRR element. Generally,  $\Gamma$  is so small that it can be neglected. Therefore, when the frequency

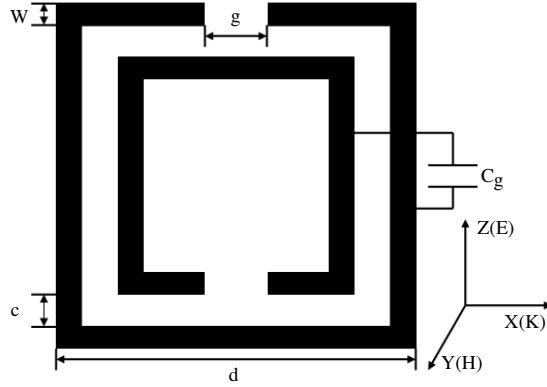


Figure 1: A single unite cell of SRR structure.

$(\omega)$  falls within the range of  $\omega_0 < \omega < \frac{\omega_0}{\sqrt{1-F}}$ , negative  $\mu(\omega)$  can be obtained. As indicated in Equation (2),  $\omega_0$  is proportion to the  $1/\sqrt{C}$ . Keeping other parameters constant, changing the effective capacitance will give us an approach to tune the resonance frequency and permeability.

### 3. SRR STRUCTURES DESIGN AND RESULTS DISCUSSIONS

#### 3.1. Permeability Tuned By Controlling Geometry of SRR

A straightforward method to tune the permeability of SRR is to vary the dimensions of a SRR element, for instance, the size of split of SRR, the space between the inside and outside SRR element, the perimeter of a SRR element. Here, we show how to tune the permeability of SRR by changing the size of split. A SRR element has been shown as Fig. 1. The substrate of SRR is Flame Resistant 4 (FR4), a type of material used for making a printed circuit board, whose relative permittivity is  $\epsilon \approx 4.4 + 0.001i$  and dimension is  $30\text{ mm} \times 30\text{ mm} \times 0.25\text{ mm}$  (thickness). The material of metallic ring is copper with a thickness of  $15\text{ }\mu\text{m}$ . The length ( $d$ ) of SRR outside arm is  $24\text{ mm}$ . The width ( $w$ ) of SRR is  $2.5\text{ mm}$ . The space ( $c$ ) between two SRR elements is  $3.5\text{ mm}$ . The split ( $g$ ) of SRR is  $2\text{ mm}$ . The conductivity ( $\sigma$ ) of copper is  $5.8 \times 10^7\text{ S/m}$ , FR4 with electric loss tangent  $\tan \delta_e \approx 0.02$ . The resonance frequency of SRR is  $f \approx 1.4\text{ GHz}$ . Its effective inductance ( $L$ ) is about  $23\text{ nH}$ . The effective resistance ( $R$ ) is about  $0.7\text{ }\Omega$ .

HFSS software is employed to simulate the response when the electromagnetic wave is propagating through the SRR structure. Due to the perfect magnetic conducting (PMC) and perfect electric conducting (PEC) boundaries, we are simulating a structure that is periodic and of infinite extent in the transverse plane. So in HFSS, two faces perpendicular to the  $Z$ -axis are PEC, two faces perpendicular to the  $Y$ -axis are PMC, the other two faces are wave ports.  $C_g$  about  $0.54\text{ pF}$  is the capacitance of the resonance ring, which is dependent on the capacitance of split and the capacitance between two metallic rings. This value can be obtained by the Ansoft Q3D Extractor simulation [5]. Based on the simulation results, we can get the microwave SRR scattering spectra. According to the Maxwell equations, electromagnetic wave can not propagate inside a medium with negative permeability, i.e., there will be an electromagnetic wave propagation forbidden band in the scattering spectra. As shown in Fig. 2 (Transmission spectra), an obvious peak can be seen around the resonance frequency for each split size, which also means that the reflection of electromagnetic wave is strongest around this frequency.

Figure 3 shows the dependence of resonance frequency ( $f_r$ ) on the split size of SRR. Clearly, with increasing the split size,  $f_r$  is monotonously increasing. When the split size (i.e. “ $g$ ” value in Fig. 1) is increased from  $0.5\text{ mm}$  to  $4\text{ mm}$ , the resonance frequency is increased from  $1.15\text{ GHz}$  to  $1.27$ . The tunable range  $\Delta f$  can be expressed as  $|f(0.5) - f(4)| \approx 100\text{ MHz}$ .

Using the retrieval method based on the Transfer matrix, the effective permeability can be extracted from the obtained  $S$  parameters [6, 7]. Compared with the experimental, the retrieval method can be obtained directly the effective permeability of SRR structures, however, it is very difficult to select the correct branch of the refractive index ( $n$ ), they suggested to measure more than one thickness to identify the correct branch [8, 9]. Equations (3) and (4) are the core formula of retrieval method [6].  $Z$  is the impedance of SRR.  $d$  is the thickness of SRR element.  $K$  is the

wave number of the incident wave.

$$n = \frac{1}{kd} \cos^{-1} \left[ \frac{1}{2S_{21}} (1 - S_{11}^2 + S_{21}^2) \right] \quad (3)$$

$$z = \sqrt{\frac{(1 + S_{11})^2 - S_{21}^2}{(1 - S_{11})^2 - S_{21}^2}}, \quad \mu = n/z \quad (4)$$

The extracted effective permeability dispersion spectra are shown in Fig. 4. The real parts of permeability are shown in Fig. 4(a). Within some frequency range, the negative  $\mu'$  has been obtained in the SRR elements. When the “g” value varies between 0.5–4 mm, the frequency with the minimum  $\mu'$  values can be tuned between 1.17 GHz–1.23 GHz. Besides, we also learn that the permeability of SRR element shows a typical resonance type dispersion behavior, which mean that  $\mu'$  value abruptly increase around some frequency then abruptly decrease to a negative value. Such a resonance type dispersion behavior can be commonly seen in metamaterials. The imaginary parts of permeability are shown in Fig. 4(b). Obviously, a dispersion peak can be observed in each  $\mu''-f$  spectrum. Since  $\mu''$  represent the magnetic loss arising from the material under study, the  $\mu''-f$  spectra in Fig. 4(b) manifest that there is a magnetic loss associated with the SRR element. For some applications, such as the electromagnetic wave absorption for stealth technology, large  $\mu''$  is necessary for dissipating the absorption of electromagnetic energy into the heat by means of magnetic losses.

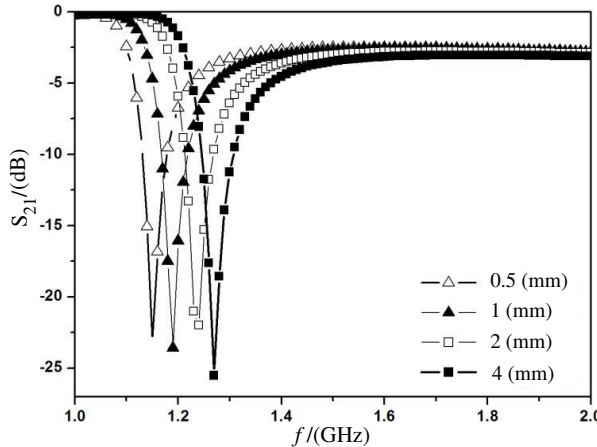


Figure 2: Microwave transmission spectra of SRR element with different split sizes.

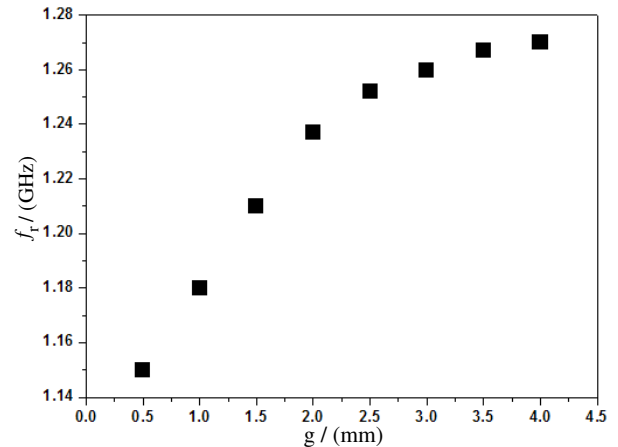


Figure 3: The resonant frequency of SRR element with different split sizes.

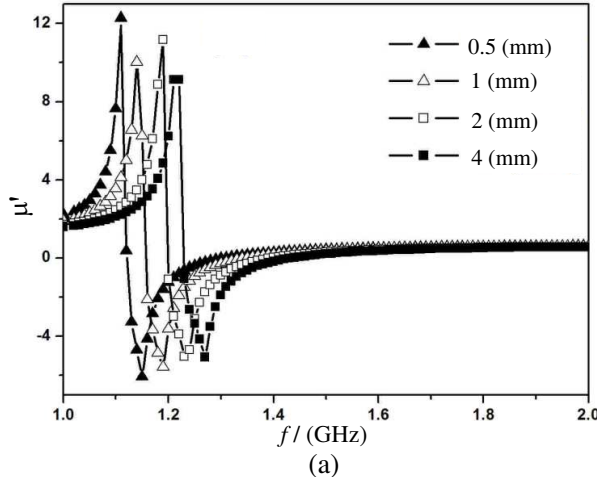
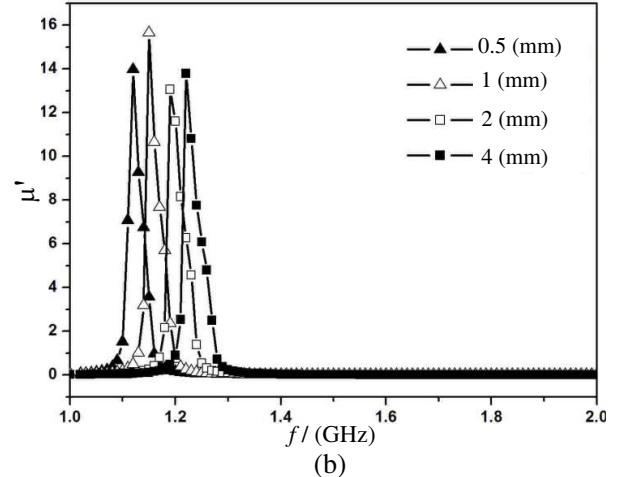


Figure 4: Permeability dispersion spectra tuned by selecting different split size. (a) Real parts, (b) imaginary parts.



### 3.2. Electric Tunability of Permeability

For this method, a diode with variable capacitance was introduced into the structure of SRR element. The basic idea is that applying difference voltage on a diode will change its capacitance, which will result in variable effective capacitance of SRR and final realization of variable permeability. The SRR shown in Fig. 5 has the same geometry as the one shown in Fig. 1. The split size ( $g$ ) of SRR is specified as 2 mm. Diode with variable capacitance are embedded into the outside ring, as indicated in Fig. 5(a). The diode used here is SMV-1408 manufactured by Alpha® [10]. According to the datasheet of SMV-1408 diode, its parasitic resistance ( $R_d$ ) is about  $0.6 \Omega$ . When the biased voltage varies between 0–30 V, its capacitance value is between 4.08–0.95 pF. The capacitance ratio ( $\tau$ ) is 4.1 ( $\tau = \frac{C_{\max}}{C_{\min}} = \frac{C_{(1v)}}{C_{(10v)}}$ ), which is a parameter describing the ability of capacitance to be tuned. The larger ratio  $\tau$  a diode has, the greater tunable frequency range.

Figure 5 shows the capacitance of varactor and the effective capacitance of SRR are connected in series, so the effective capacitance of SRR embedded with a diode is  $C = (C_g C_d) / (C_d + C_g)$ ,  $C_g$  is a constant for a specified SRR structure,  $C_d$  is the capacitance of the diode. Increasing biased voltage will result in the capacitance of diode to be decreased. Consequently, the effective capacitance of SRR will increase. According to Equations (1) and (2), the change of effective capacitance in Fig. 5 will give rise to the resonance frequency shifting toward lower values and will result in the permeability dispersion behaviors to be altered. Fig. 6 shows the dependence of resonance frequency on the biased voltage of diode. As shown,  $f_r$  monotonously decreases with increasing the biased voltage. When the biased voltage changes from 0 V–30 V,  $f_r$  changes from 1.67 GHz to 1.45 GHz.

The extracted effective permeability dispersion spectra are shown in Fig. 7. Negative  $\mu'$  value also can be obtained within some frequency range for the SRR element embedded with a diode. When the biased voltage changes between 0 V ~ 30 V, the frequency with the minimum  $\mu'$  values can be varied between 1.42 GHz–1.64 GHz. The permeability dispersion spectra are much like the

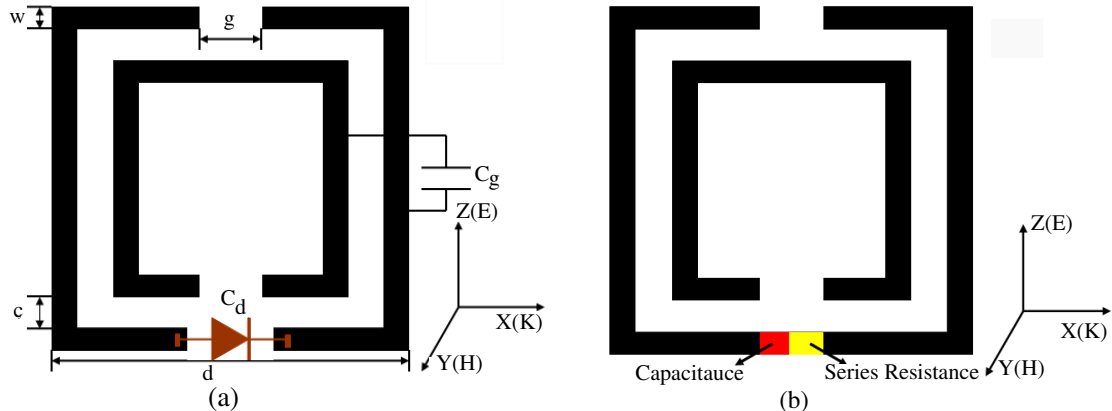


Figure 5: (a) A single unit cell of the varactor diode embedded in the SRR structures, (b) the HFSS model for the varactor diode loaded in SRR structure.

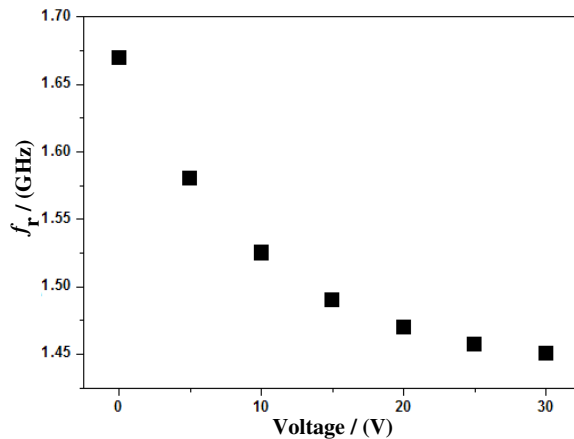


Figure 6: Dependence of resonance frequency of SRR on the biased voltage of diode.

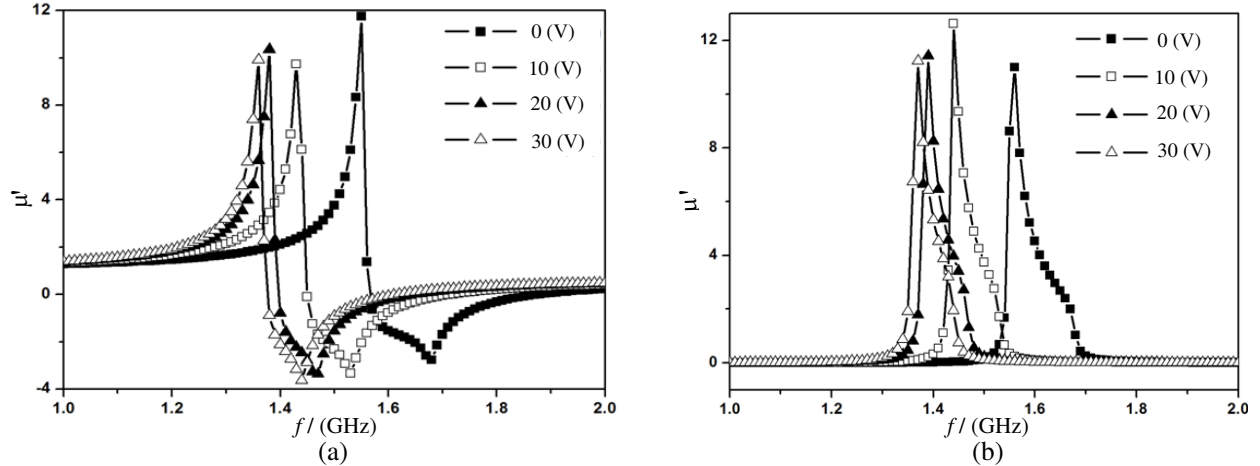


Figure 7: Permeability dispersion spectra tuned by the biased voltage. (a) Real parts, (b) imaginary parts.

ones shown previously in Fig. 4. The  $\mu'' \sim f$  spectra are given in Fig. 7(b). The dispersion peaks can also be found in the  $\mu'' \sim f$  spectra. Except that the dispersion peaks are wider than the ones found in Fig. 4(b). Comparing the above two approaches of tuning the permeability dispersion behaviors, the latter one is preferred in terms of convenient, active and effective.

#### 4. CONCLUSIONS

We have simulated the tunability of permeability of SRR structures by changing the geometry of split and by changing the biased voltage of varactor diodes, using the Finite-Difference-Time-Domain method and retrieval method. Accordance to the HFSS simulation results and retrieval data, we clearly justify that the resonance frequency of permeability shifts toward a higher value with increasing the size of split. It is also found that the resonance frequency of permeability shifts toward a lower value with the biased voltage increasing. Comparing these two structures, as can be seen, electrically controlling the diode is the better way to tune the permeability dispersion behaviors.

#### ACKNOWLEDGMENT

This work is financially supported by the National Basic Research Program of China (973 Project) (No. 2010CB334702), China National Funds for Distinguished Young Scientists (No. 51025208), the Fundamental Research Funds for the Central Universities (No. ZYGX2009J036) the International Collaboration Program of Sichuan Province (No. 2011HH0001) and the Basic Research Funds of National Defense Department (No. 9140A10030409DZ0228).

#### REFERENCES

1. Veselago, V. G., "The electrodynamics of substances with simultaneously negative values of  $\epsilon$  and  $\mu$ ," *Sov. Phys. Usp.*, Vol. 10, No. 4, 509–514, 1968.
2. Pendry, J. B., A. J. Holden, D. J. Robbins, and W. J. Stewart, "Magnetism from conductors and enhanced nonlinear phenomena," *IEEE Trans. Microwave Theory Tech.*, Vol. 47, No. 11, 2075–2084, 1999.
3. Pendry, J. B., A. J. Holden, W. J. Stewart, and I. Youngs, "Extremely low frequency plasmons in metallic mesostructures," *Phys. Rev. Lett.*, Vol. 76, No. 25, 4773–4776, 1996.
4. Smith, D. R., W. J. Padilla, D. C. Vier, S. C. Nemat-Nasser, and S. Schultz, "Composite medium with simultaneously negative permeability and permittivity," *Phys. Rev. Lett.*, Vol. 84, No. 18, 4184–4187, 2000.
5. Hand, T. H. and S. A. Cummer, "Frequency tunable electromagnetic metamaterial using ferroelectric loaded split rings," *J. Appl. Phys.*, Vol. 103, 066105.1–066105.3, 2008.
6. Smith, D. R., D. C. Vier, Th. Koschny, and C. M. Soukoulis, "Electromagnetic parameter retrieval from inhomogeneous metamaterials," *Phys. Rev. E*, Vol. 71, No. 3, 026617.1–036617.11, 2005.

7. Chen, X. D., T. M. Grzegorczyk, B. I. Wu, J. Pacheco, Jr., and J. A. Kong, "Robust method to retrieve the constitutive effective parameters of metamaterials," *Phys. Rev. E*, Vol. 70, No. 1, 016608.1–016608.7, 2004.
8. Smith, D. R., S. Schultz, P. Marko, and C. M. Soukoulis, "Determination of negative permittivity and permeability of metamaterials from reflection and transmission coefficients," *Preprint*, No. 1–5, 2002.
9. Chen, X. D., Doctoral Dissertation, Zhejiang University, 2005.
10. <http://www.alldatasheet.com/datasheet-pdf/pdf/55406/ALPHA/SMV1408-001.html>.

# Optical Single Sideband Modulation Using Feedback Technique Based on SBS Effect in Fiber

**P. H. Hsieh<sup>1</sup>, W. S. Tsai<sup>1</sup>, Z. S. Lin<sup>1</sup>, and H. H. Lu<sup>2</sup>**

<sup>1</sup>Department of Electrical Engineering, Ming Chi University of Technology  
84 Gungjuan Rd., Taishan, Taipei 24301, Taiwan

<sup>2</sup>Department of Electro-Optical Engineering, National Taipei University of Technology  
1, Sec. 3, Chung-Hsiao E. Rd., Taipei 10608, Taiwan

**Abstract**— We propose an optical single sideband (OSSB) modulation scheme using stimulated Brillouin scattering (SBS) to achieve OSSB modulation in fiber. Driving with 10.87 GHz RF signal into Mach-Zehnder modulator (MZM), due to the SBS effect, lower sideband of modulated signal is amplified and upper sideband is attenuated as well. By properly adjusting the phase shifter for phase difference between the two paths of electrical signal, output signal is OSSB format. After 25 km and 50 km SMF transmission, we can observe good system performances including sideband power ratio (SBPR) > 12 dB and 10 dB, phase noise < -71 dBc/Hz and < -65 dBc/Hz measured by an optical spectrum analyzer (OSA) and an electrical spectrum analyzer (ESA), respectively.

## 1. INTRODUCTION

Radio-on fiber (ROF) technology can be applied to a fiber network to transmit microwave signal. The communication system with ROF technology can transmit microwave signals over a long distance with high fidelity. Such technology can make effective usage of the broad bandwidth and low transmission loss characteristics of the fiber, and can solve the last mile problem as well as deliver the broadband data to the user by using microwave. In traditional intensity modulation, the optical carrier is modulated to generate an optical signal with double sideband (DSB) format.

DSB modulation produces two sidebands on both sides of the carrier. The beating components between the carrier and two sidebands induce interference at the receiver. Over a long haul fiber transmission, RF signal will cause severe power degradation due to chromatic dispersion [1]. In order to overcome RF power degradation due to fiber dispersion, optical single sideband (OSSB) modulation technique must be implemented. The fact that OSSB modulation can remove a half of the optical spectrum is expected to attain a dispersion benefit since the optical spectrum has been reduced by a factor of two. Several OSSB generation methods [2–5] have been proposed to solve dispersion-induced RF fading.

By eliminating one of the sidebands, OSSB modulation not only immunizes to fiber dispersion, but it also increases the spectral efficiency twice. One way for generating OSSB signals is to exploit the Hilbert transform [6]. For example, using a dual electrode Mach-Zehnder modulator can be reality to generate OSSB signal [7]. The other way to generate OSSB signals is to utilize narrow optical filter. The narrow optical filter at the end of the ODSB transmitter output eliminates one of the sidebands to achieve OSSB modulation. Nonlinear effects are interactions between light waves, which can cause noise and crosstalk. Stimulated Brillouin scattering (SBS) occurs when signal power reaches a level sufficient to generate tiny acoustic vibrations in the glass. Acoustic waves change the density of a material, and thus alter its refractive index. Since the light wave being scattered itself generates the acoustic waves, the process can cause input light degradation.

In this study, we propose an OSSB modulation scheme using SBS effect in fiber. The Brillouin frequency is about 10.87 GHz in 1550 nm region in SMF. We present a smart technique for OSSB modulation of the 10.87 GHz ROF system based on characteristics of SBS in fiber. The output wavelength with OSSB modulation format can prevent fiber dispersion induced RF signal fading. Using the SBS effect in fiber to enhance OSSB is realizable to implement. The results show that OSSB modulation performance is enhanced with this technique.

## 2. EXPERIMENTAL SETUP

The experimental system configuration of our proposed OSSB system using electroabsorption modulator laser (EML) associated with feedback light injection technique based on SBS effect in fiber is shown in Figure 1.

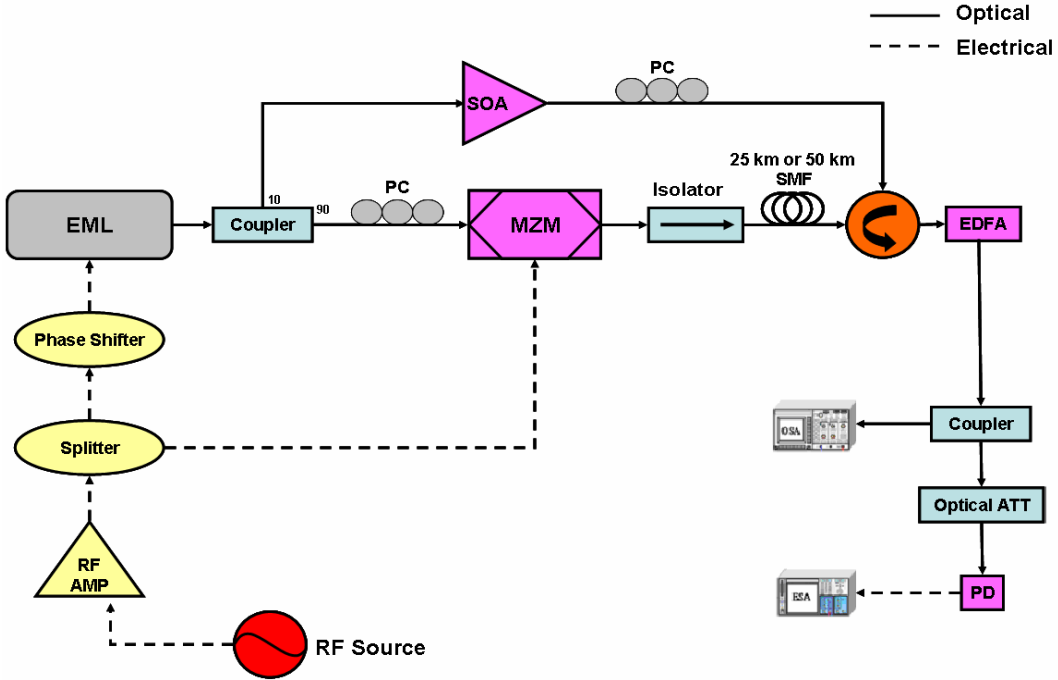


Figure 1: The OSSB system using feedback light injection technique based on SBS effect in fiber.

The main parts of transmitter consists of an EML, a microwave signal generator, a RF power amplifier, a RF power splitter, a phase shifter and a Mach-Zehnder modulator (MZM). The EML light source includes a single mode laser and an electro-absorption modulator (EAM). The wavelength of optical wave from EML is 1550.1 nm, and the operation current is 84 mA. RF signal is generated by a microwave signal generator then fed into a RF power amplifier to increase signal power. Amplified signal goes into a RF power splitter to split two copies. One copy of RF signal passes through a phase shifter then couples into EML. The other copy is feeds into MZM as modulating signal. EML output signal launches into a 10 : 90 coupler. 90% light is modulated by the microwave signal at 10.87 GHz via a MZM. The insertion loss of the MZM is about 7 dB.

Since MZM has the sensitive characteristic regarding the input light sources polarization state. A polarization controller (PC) needs to be added on in front of the MZM input section. This function is to adjust the state of polarization (SOP) of the input light.

The remaining 10% light acts as feedback light to enhance OSSB modulation. The modulated signal is launched into SMF and interacts with the feedback light from the circulator. For 25 km or 50 km SMF transmission, we use an optical spectrum analyzer (OSA) to measure optical spectrum. On the other hand, photo-detector (PD) transforms optical signal to electrical one, then we measure the frequency spectrum by using an electrical spectrum analyzer (ESA).

### 3. RESULTS AND DISCUSSION

Figure 2(a) shows the optical spectra of the DSB signal with 10.87 GHz modulation. When the laser diode is modulated by the small-current signals, the laser diode output exhibits frequency modulation (FM), which can be express as

$$E_{LD}(t) = \cos \cdot \left[ \omega_c t + \beta \int_t A \cdot \cos(\omega_m \tau + \varphi) d\tau \right] \quad (1)$$

where  $\omega_c$  is the angular frequency of the carrier,  $\beta$  is the FM index,  $A$  is the amplitude of the signal,  $\omega_m$  is the modulation angular frequency,  $t$  is time, and  $\varphi$  is the phase of the signal. The frequency-modulation EML output is remodulated by the signals at the MZM. Thus, the output of the MZM can be expressed with the aid of Bessel function as

$$E_0(t) = \sqrt{1 + m \cos(\omega_m t + \varphi + \theta)} \cdot \sum_n J_n(h) \cos(\omega_c t + n\omega_m t + n\varphi) \quad (2)$$

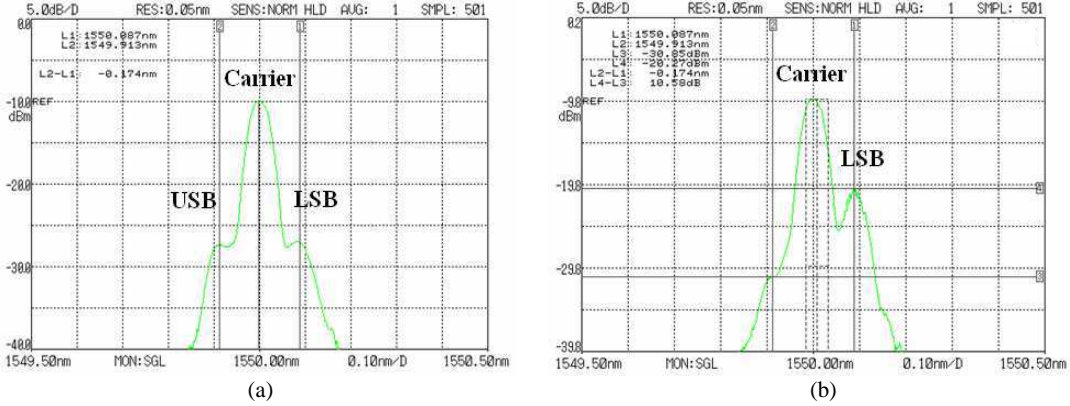


Figure 2: The measured optical spectra of DSB and SSB. (a) DSB signal with 10.87 GHz modulation. (b) SSB signal with 10.87 GHz modulation using feedback light injection.

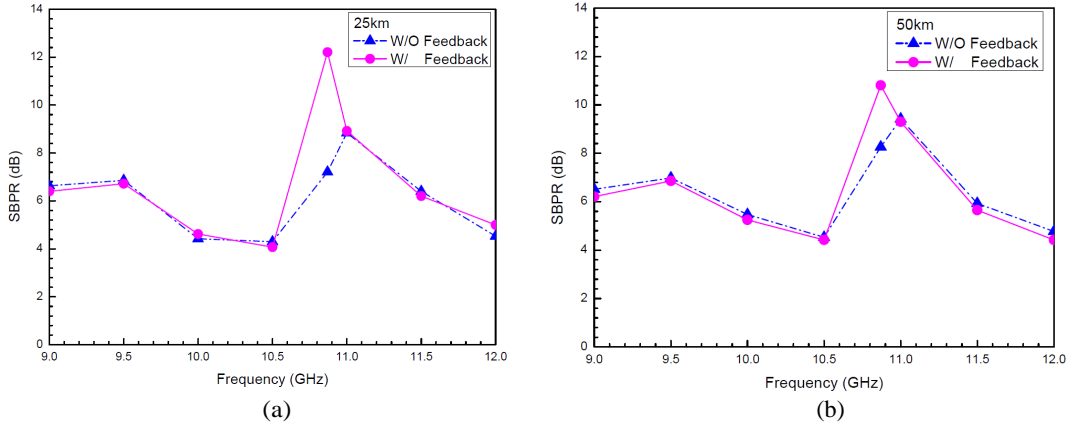


Figure 3: The SBPR as a function of RF signal modulation frequency with and without feedback light injection for (a) 25 km and (b) 50 km.

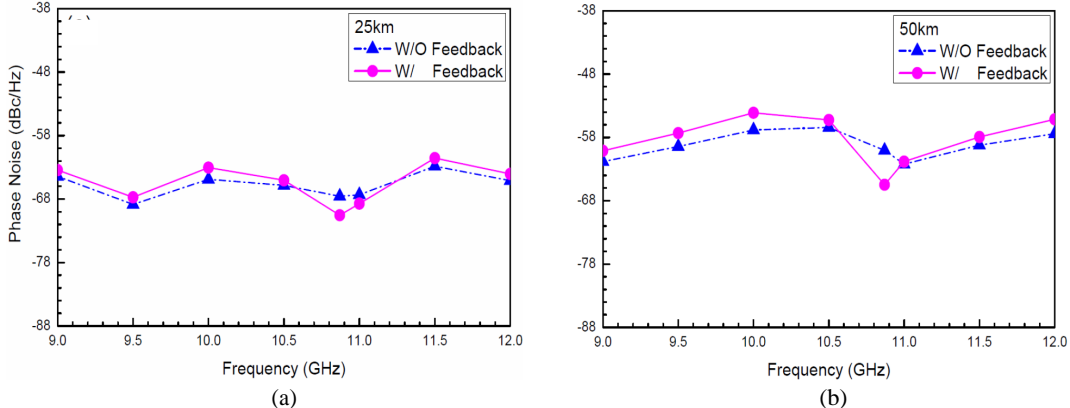


Figure 4: The phase noise as a function of RF signal modulation frequency with and without feedback light injection at 100 kHz offset frequency of 10.87 GHz for (a) 25 km and (b) 50 km.

where  $m$  is the amplitude modulation (AM) index, and  $\theta$  is the relative phase between FM and AM signals. Here, the lower sideband (LSB) is suppressed when  $\theta = 0$ , whereas the upper sideband (USB) is suppressed when  $\theta = \pi$ . Thus, by choosing proper  $\beta$ ,  $m$  and setting  $\theta$  to be 0 or  $\pi$ , OSSB modulation can achieve. In Figure 2(b), we use feedback light injection based on SBS effect to enhance OSSB modulation performance.

We launched electrical source at 10.87 GHz to EML and MZM. The Brillouin frequency of the fiber in 1550 nm region is about 10.87 GHz. The temperature coefficient of the Brillouin frequency is about 1.4 MHz/°C. The sideband power ratio (SBPR) is defined as power difference between

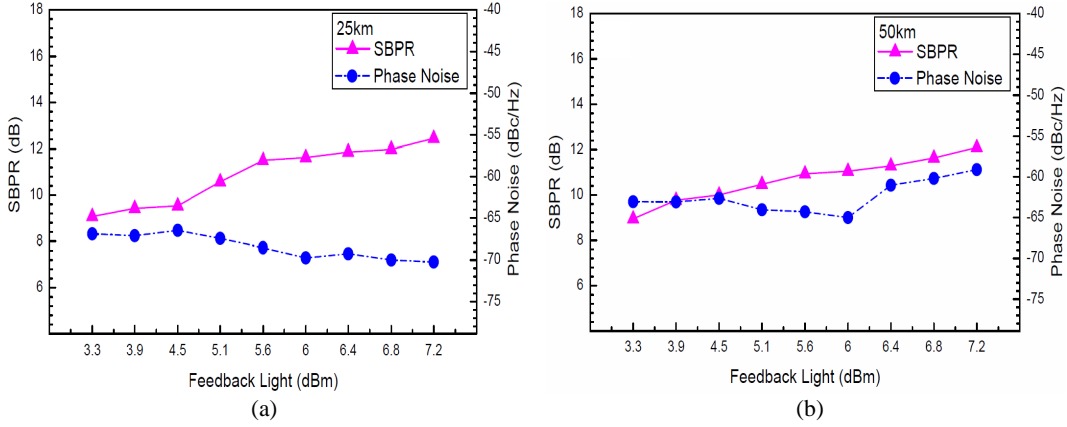


Figure 5: The SBPR and phase noise as a function of feedback light injection power at 10.87 GHz.

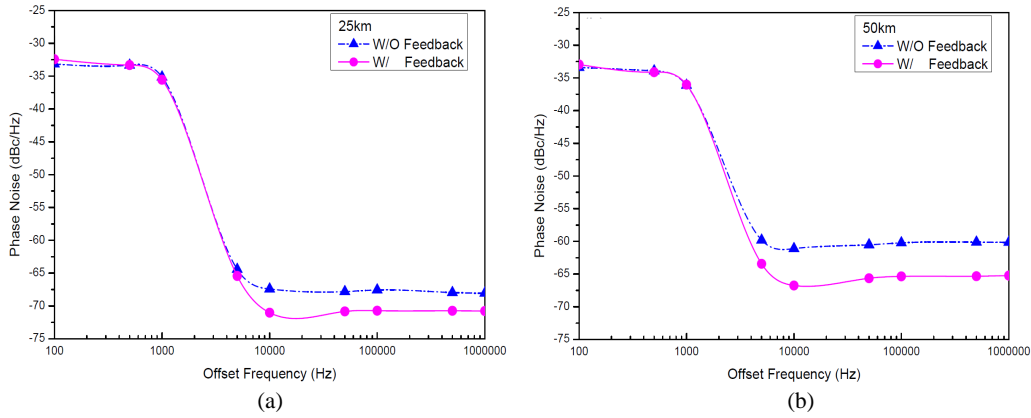


Figure 6: The phase noise with and without feedback light injection. Modulation frequency at 10.87 GHz for (a) 25 km and (b) 50 km.

LSB and USB. It indicates that SBPR can present the level of SSB.

Figures 3(a) and (b) show the SBPR as a function of RF signal modulation frequency with and without feedback light injection for 25 km and 50 km. For 25 km we can obtain the SBPR is 12 dB and 7 dB at 10.87 GHz with and without feedback light injection. When transmitting 50 km with and without feedback light injection technique, the SBPR is 11 dB and 8 dB. The SBPR can be improved 5 dB and 3 dB since the Brillouin frequency of the fiber in 1550 nm region is 10.87 GHz.

Figures 4(a) and (b) display the phase noise as a function of RF signal modulation frequency with and without feedback light injection at 100 kHz offset frequency of 10.87 GHz for 25 km and 50 km SMF. After 25 km transmission, the phase noise is measured to be  $-68$  dBc/Hz at 100 kHz offset without feedback light injection. With feedback light injection, the phase noise is measured to be  $-71$  dBc/Hz. The phase noise can be improved 3 dBc/Hz. After 50 km transmission, the phase noise is measured to be  $-60$  dBc/Hz at 100 kHz offset without feedback light injection. With feedback light injection, the phase noise is measured to be  $-65$  dBc/Hz. The phase noise can be improved 5 dBc/Hz. In Figures 4(a) and (b), the phase noise are almost the same as the modulation frequency are not at 10.87 GHz. The SBPR and phase noise as a function of feedback light injection power at 10.87 GHz are shown in Figures 5(a) and (b), respectively. When feedback light power is increased, the SBPR can be enhanced.

Figures 6(a) and (b) show the phase noise with and without feedback light injection at 10.87 for 25 km and 50 km, respectively. In Figures 6(a) and (b), we observe the phase noise can be improved 3 dBc/Hz and 5 dBc/Hz with feedback light injection technique for 25 km and 50 km SMF transmission.

#### 4. CONCLUSION

We propose an OSSB modulation scheme using SBS effects in fiber to enhance OSSB modulation performance. Using this method to construct the OSSB system can replace a complex circuit or

device to exploit the Hilbert transform of the conventional OSSB systems. Good performances can achieve that OSSB signals have  $> 12$  dB and 11 dB SBPR, phase noise  $< -71$  dBc/Hz and  $-65$  dBc/Hz on 10.87 GHz carrier over 25 km and 50 km SMF transmission. With feedback light injection, the SBPR and phase noise can be improved 5 dB and 3 dBc/Hz for 25 km SMF transmission. For 50 km with feedback light injection, the SBPR and phase noise can be improved 3 dB and 5 dBc/Hz, respectively. As the mention above, the OSSB modulation with feedback light injection based on SBS effect in fiber thus has potential applications in ROF systems.

## REFERENCES

1. Chi, H. and J. P. Yao, "Frequency quadrupling and upconversion in a radio over fiber link," *Journal of Lightwave Technol.*, Vol. 26, 2706–2711, 2008.
2. Sung, H. K., E. K. Lau, and M. C. Wu, "Optical single sideband modulation using strong optical injection-locked semiconductor lasers," *IEEE Photon. Technol. Lett.*, Vol. 19, 1005–1007, 2007.
3. Lee, U. S., H. D. Jung, and Sang-Kook, "Optical single sideband signal generation using phase modulation of semiconductor optical amplifier," *IEEE Photon. Technol. Lett.*, Vol. 16, 1373–1375, 2004.
4. Blais, S. R. and J. P. Yao, "Optical single sideband modulation using an ultranarrow dual-transmission-band fiber bragg grating," *IEEE Photon. Technol. Lett.*, Vol. 18, 2230–2232, 2006.
5. Fonseca, D., A. V. T. Cartaxo, and P. Monteiro, "Adaptive optoelectronic filter for improved optical single sideband generation," *IEEE Photon. Technol. Lett.*, Vol. 18, 415–417, 2006.
6. Takano, K., N. Hanzawa, S. Tanji, and K. Nakagawa, "Experimental demonstration of optically phase-shifted SSB modulation with fiber-based optical hilbert transformers," *Conference on Opt. Fiber Communication*, 1–3, 2007.
7. Hou, C., Y. Shao, X. Liu, X. Zheng, X. Li, S. Zou, and N. Chi, "Dual-level optical single side band modulation scheme for 0.1 tera Hz radio-over-fiber systems," *Communications and Photonics Conference*, Vol. 2009-Supplement, 1–6, 2009.

# Optical Single Sideband Modulation of 9-GHz RoF System Based on FWM Effects of SOA

P. H. Hsie<sup>1</sup>, W. S. Tsai<sup>1</sup>, C. C Weng<sup>1</sup>, and H. H. Lu<sup>2</sup>

<sup>1</sup>Department of Electrical Engineering, Ming Chi University of Technology  
84 Gungjuan Rd., Taishan, Taipei 24301, Taiwan

<sup>2</sup>Department of Electro-Optical Engineering, National Taipei University of Technology  
1, Sec.3, Chung-Hsiao E. Rd., Taipei 10608, Taiwan, R.O.C.

**Abstract**— We propose an optical single sideband (OSSB) modulation scheme using self-phase modulation (SPM), cross-phase modulation (XPM) and four-wave mixing (FWM) effects of SOA to achieve wavelength conversion. Drive with the 9 GHz RF signal into electro-absorption modulator laser (EML) and IM modulator. By properly adjust the phase shifter for phase difference between the two paths of electrical signal. FWM signal is OSSB format for a 25 km SMF transmission. Finally, we use an optical spectrum analyzer (OSA) to observe optical spectrum.

## 1. INTRODUCTION

In traditional intensity modulation, the optical carrier is modulated to generate an optical signal with double sideband (DSB) format. DSB modulation produces two sidebands on both sides of the carrier, and the beating components between the carrier and two sidebands induce interference at the receiver. Over a long haul fiber transmission, RF signal will cause severe power degradation due to chromatic dispersion [1]. This phenomenon will degrade systems' performance. In order to overcome RF power degradation due to fiber dispersion, optical single sideband (OSSB) modulation technique must be implemented [2]. The fact that OSSB modulation can remove a half of the optical spectrum is expected to attain a dispersion benefit because the optical spectrum has been reduced by a factor of two. Several OSSB generation methods [3–6] have been proposed. By eliminating one of the sidebands, OSSB modulation not only immunizes to fiber dispersion, but it also increases the spectral efficiency twice. One way for generating OSSB signals is to exploit the Hilbert transform [7]. Using a dual electrode Mach-Zehnder modulator can be reality to generate OSSB signal [8]. Another way to generate OSSB signals is to utilize narrow optical filter. The narrow optical filter at the end of the ODSB transmitter output can eliminate one of the sidebands to achieve OSSB modulation [9]. Optical amplifier plays an important role in a long haul fiber transmission system, the use of semiconductor optical amplifier (SOA) as an optical amplifier is very attractive since it can potentially be used to help upgrade fiber penetration, easily integrated and small compact. However, SOA also has several nonlinearity effects such as self-phase modulation (SPM), cross-phase modulation (XPM), self-gain modulation (SGM), cross-gain modulation (XGM) and four-wave mixing (FWM) that will degrade systems' performances. In this letter, we propose an OSSB modulation scheme using SPM, XPM and FWM effects of SOA to achieve wavelength conversion. The translation wavelength possessing OSSB modulation format can prevent fiber dispersion induced RF signal fading. Using the phase modulation effects in SOA to generate OSSB format is relatively simple to implement. It only needs SOA and electrical phase shifter to construct the OSSB system instead of a complex circuit or device to exploit the Hilbert transform of the conventional OSSB systems.

## 2. EXPERIMENTAL SETUP

The experimental system configuration of our proposed OSSB system to operate wavelength conversion based on SPM, XPM and FWM effects of SOA associated with electrical phase shifter is shown in Fig. 1. The main parts of transmitter consists of a tunable laser source as local oscillation light, a polarization controller (PC), a Mach-Zehnder modulator (MZM), a microwave signal generator with 9 GHz, a RF power splitter, a phase shifter, a RF power attenuator and an electro-absorption modulator laser (EML).

The MZM input light source is 1549.6 nm provided by a tunable laser source, because the optical modulator has the sensitive characteristic regarding the input photo source's polarization state. A PC needs to be added on in front of the MZM input section. This function is to maintain the input light at the specific polarization state when the light launches into the optical modulator.

9 GHz RF signal is generated by a microwave signal generator and fed into a RF power splitter to split two copies. One copy of RF signal passes through a phase shifter and adjusts optimal power with tunable RF power attenuator, then feeds into optical modulator. Another one copy of the RF source supplies to EML as modulating signal. Two paths of optical light are combined by an optical coupler. Passing through an optical power attenuator to adjust the suitable input power avoids the SOA output power saturation. Output signal launches into the band-pass filter to filter out the noise which provided by SOA. For a 25 km SMF transmission, we use an optical spectrum analyzer (OSA) to measure optical spectrum. On the other hand, PD transforms optical signal to electrical one, and measures the output frequency spectrum by using an electrical spectrum analyzer (ESA).

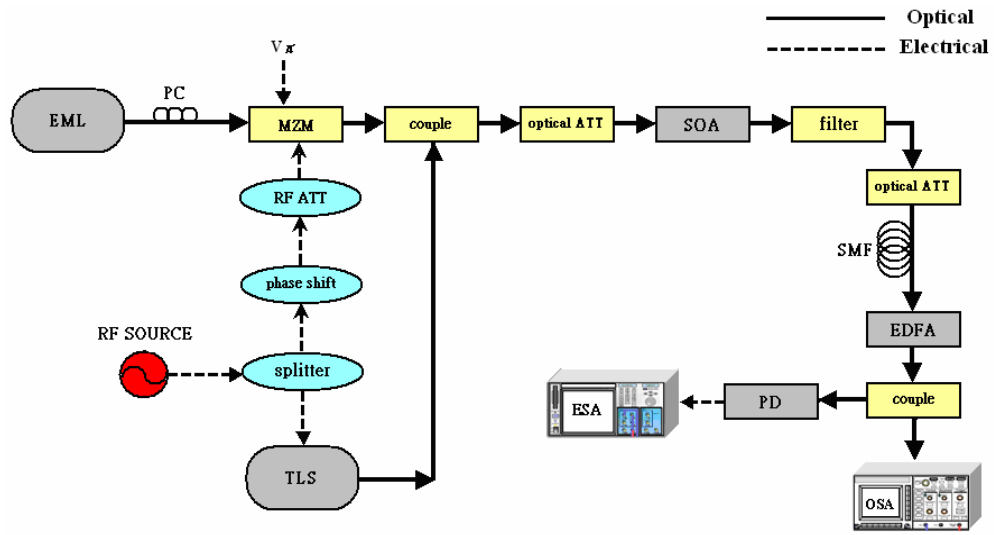


Figure 1: Experimental setup of OSSB modulation based on SPM, XPM and FWM effects of SOA.

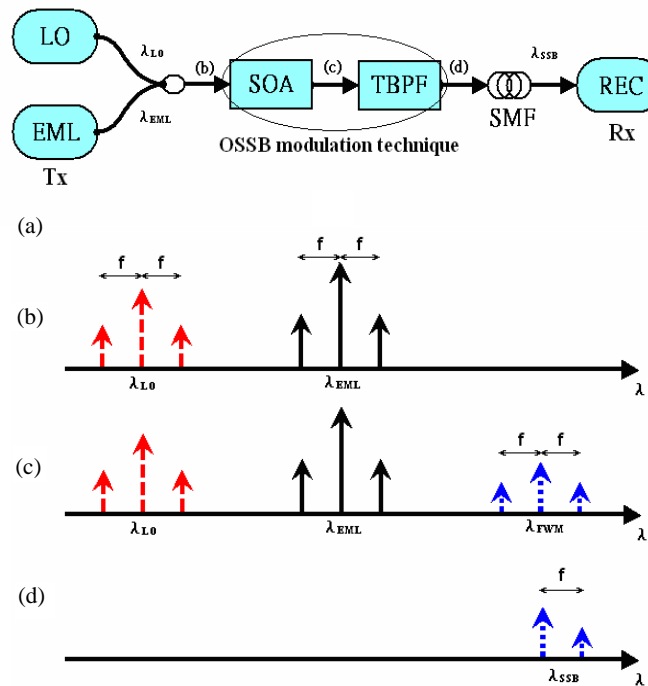


Figure 2: Conceptual diagram of (a) OSSB modulation system for wavelength conversion technique, (b) optical spectrum before passing through SOA, (c) optical spectrum after passing through SOA, (d) filtering out  $\lambda_{FWM}$  and adjusting parameters of system achieved OSSB signal.

### 3. RESULTS AND DISCUSSION

Figure 2(a) shows a conceptual diagram of OSSB modulation system for wavelength conversion technique using SOA and electrical phase shifter. Two optical signals,  $\lambda_{\text{EML}}$  and  $\lambda_{\text{LO}}$  are launched into SOA as shown in Fig. 2(b).

After passing through SOA, the FWM effect causes new optical signal ( $\lambda_{\text{FWM}}$ ) to appear shown in Fig. 2(c). In general situation, FWM is a bad noise disturbance item. However, this kind of non-linear effect can easily perform wavelength conversion. Filter out FWM and adjust parameters of system can realize OSSB system shown in Fig. 2(d).

In the case of a single RF tone modulation, the OSSB optical field can be written as [10]

$$E(t) = \left[ E_0 + \frac{Km_1}{2} \sin(\omega_m t) \right] \times \exp \left\{ i \left[ \omega_0 t + \frac{m_1 \alpha_1}{2} \sin(\omega_m t + \beta_1) \right. \right. \\ \left. \left. + \frac{Km_1 \alpha_2}{2} \sin(\omega_m t + \beta_2) + \frac{m_2 \alpha_3}{2} \sin(\omega_m t + \gamma) \right] \right\} \quad (1)$$

where  $\omega_0$  denotes the optical carrier frequency,  $\omega_m$  is the subcarrier frequency, and  $m$  is modulation index.  $k$ ,  $\alpha_1$ ,  $\alpha_2$ ,  $\beta_1$ , and  $\beta_2$  denote modulation decrease factor, prechirp parameter, SPM chirp parameter, phase difference of prechirp from AM modulating term and phase difference of SPM of SOA from AM modulating term, respectively.  $\alpha_3$  is a chirp parameter which is relevant to XPM,  $\gamma$  can be any value between 0 and  $2\pi$ .

In our experiment, we launched electrical source at 9 GHz to EML and IM modulator. The wavelength of optical wave from EML was 1550.8 nm. EML was biased to  $-0.1$  V, and the operation current was 75 mA. SOA operation current was 320 mA. Fig. 3 shows the optical spectrum in back of the optical coupler. Because 9 GHz RF signal is fed into EML and IM modulator, we can observe two optical carriers with DSB modulation format.

By the nonlinear effects of SOA, the optical spectrum can be observed in Fig. 4. In the Fig. 4,  $\lambda_{\text{FWM}}$  appears in the right side and it also has DSB modulation format. The FWM efficiency is defined as the FWM signal power at the SOA output divided by signal power at EML. When the input signal power is too much, the converted signal power decreased, which is due to the gain saturation of SOA. The conversion efficiency in our experiment is about  $-20$  dB.

Figures 5 and 6 show the  $\lambda_{\text{FWM}}$  from DSB format transformed to SSB format, when we tune the phase shifter and the operation current of SOA. We tune the phase shifter to adjust the phase difference between the two ways of electrical signal. When two orthogonal waves are modulated at the same single tone RF carrier, propagate in SOA. Due to SPM and XPM effects of SOA, the  $\lambda_{\text{FWM}}$  can reveal SSB modulation. In this way, we can observe the transformation of modulation format by tuning phase shifter.

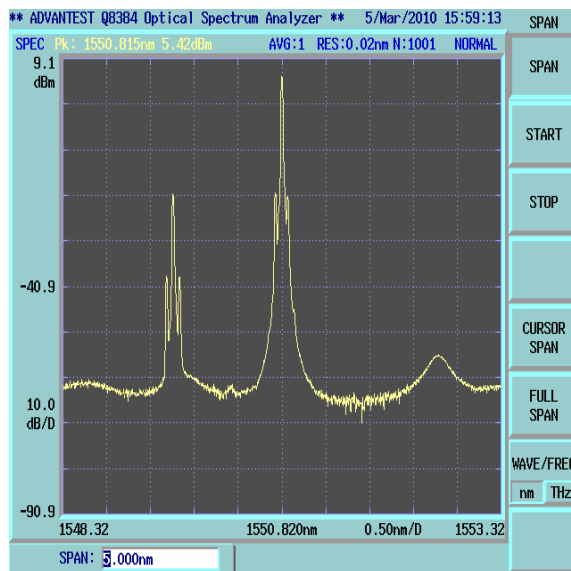


Figure 3: Measured optical spectrum in back of the optical coupler.

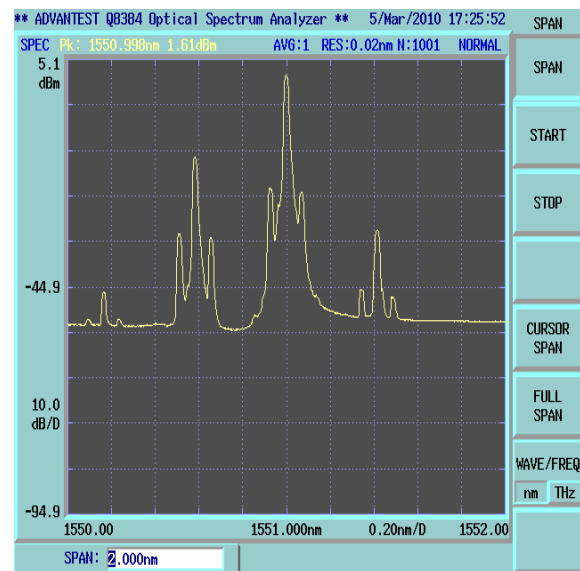


Figure 4: Measured optical spectra based on nonlinear effects of SOA.

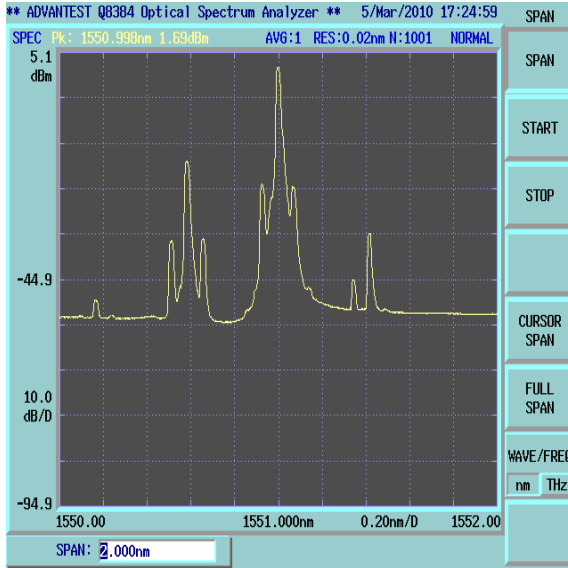


Figure 5:  $\lambda_{\text{FWM}}$  from DSB format transformed to SSB one at the upper sideband.

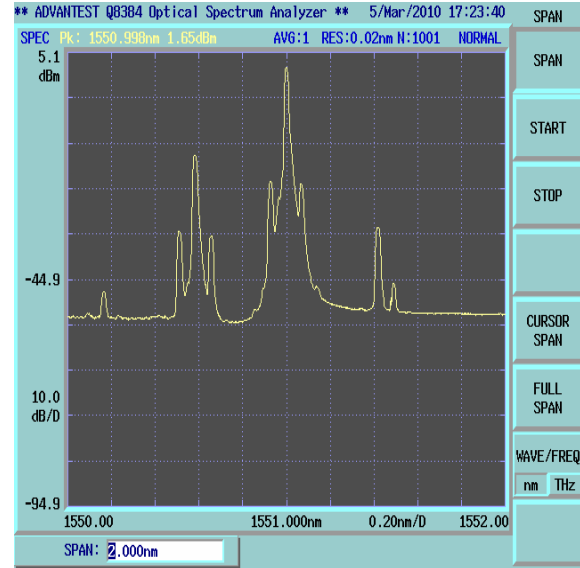


Figure 6:  $\lambda_{\text{FWM}}$  from DSB format transformed to SSB one at the lower sideband.

#### 4. CONCLUSION

We propose an OSSB modulation scheme using SPM, XPM and FWM effects of SOA to achieve wavelength conversion. Using this method to construct the OSSB system can substitute a complex circuit or device to exploit the Hilbert transform of the conventional OSSB system. In the future work, we can enhance the wavelength conversion efficiency and transmit digital signal in our proposed OSSB system.

#### REFERENCES

- Chi, H. and J. P. Yao, "Frequency quadrupling and upconversion in a radio over fiber link," *J. Lightwave Technol.*, Vol. 26, 2706–2711, 2008.
- Hong, C., C. Zhang, M. J. Li, L. X. Zhu, L. Li, W. W. Hu, A. S. Xu, and Z. Y. Chen, "Single-sideband modulation based on an injection-locked dfb laser in radio-over-fiber systems," *IEEE Photon. Technol. Lett.*, Vol. 22, 462–464, 2010.
- Blais, S. R. and J. P. Yao, "Optical single sideband modulation using an ultranarrow dual-transmission-band fiber bragg grating," *IEEE Photon. Technol. Lett.*, Vol. 18, 2230–2232, 2006.
- Fonseca, D., A. V. T. Cartaxo, and P. Monteiro, "Adaptive optoelectronic filter for improved optical single sideband generation," *IEEE Photon. Technol. Lett.*, Vol. 18, 415–417, 2006.
- Sung, H. K., E. K. Lau, and M. C. Wu, "Optical single sideband modulation using strong optical injection-locked semiconductor lasers," *IEEE Photon. Technol. Lett.*, Vol. 19, 1005–1007, 2007.
- Sun, X. Q., K. Xu, S. N. Fu, J. Q. Li, X. B. Hong, J. Wu, J. T. Lin, and P. Shum, "All-optical WDM subcarrier modulator for binary phaseshift keying (BPSK) with optical ssb format using aphase modulator loop mirror filter," *Conference on Opt. Fiber Communication*, 2009.
- Takano, K., N. Hanzawa, S. Tanji, and K. Nakagawa, "Experimental demonstration of optically phase-shifted SSB modulation with fiber-based optical hilbert transformers," *Conference on Opt. Fiber Communication*, 1–3, 2007.
- Hou, C., Y. Shao, X. Liu, X. Zheng, X. Li, S. Zou, and N. Chi, "Dual-level optical single side band modulation scheme for 0.1 tera Hz radio-over-fiber systems," *Communications and Photonics Conference*, 1–6, 2009.
- Fonseca, D. D., A. V. T., Cartaxo, and P. P. Monteiro, "Opto-electrical filter for 40 Gb/s optical single sideband signal generation," *Conference on Opt. Fiber Communication*, 2006.
- Lee, U.-S., H.-D. Jung, and S.-Kook, "Optical single sideband signal generation using phase modulation of semiconductor optical amplifier," *IEEE Photon. Technol. Lett.*, Vol. 16, 1373–1375, 2004.

# Dynamic Characterization of EDFA Based on ASE Selective-feedback and Gain-clamping Techniques

Jhe-Min Lin, Wen-Jeng Ho, and Chih-Yung Li

Institute of Electro-Optical Engineering, National Taipei University of Technology  
1, Sec. 3, Chung-Hsiao E. Rd., Taipei 106, Taiwan

**Abstract**— We experimental demonstrated a gain clamped C-band EDFA with a stable wide dynamic range performance by using the ASE selective-feedback gain-clamping technique. The gain of 16.2 dB with variation  $\pm 0.26$  dB for the input signal power from  $-35$  to  $-5$  dBm and the maximum NF of 6.6 dB for the input signal power from  $-35$  to  $-10$  dBm were obtained, respectively. Therefore, a wide dynamic range of the input signal of 25–30 dB can be achieved. We also applied a saturation tone signal (on/off) for simulating the 16-channels DWDM signals (add/drop) to investigate the gain variation for the probe signal. When the number of channel signals are added or dropped in our proposed C-band EDFA scheme, the gain variation is less than 0.13 dB for the signals wavelength range from 1530 to 1564 nm.

## 1. INTRODUCTION

In addition to enlarging the bandwidth of optical amplification in frequency domain, the optical amplifiers with wide-band uniform-gain characteristics are also play an important role in WDM systems with the optical add-drop multiplexers (OADM)s [1] and the optical cross-connects (OXCs) [2]. In the conventional WDM transport systems, the input optical powers of Erbium-doped fiber amplifier (EDFA) will change when transmission channels are adding or dropping. Since EDFA is usually operated in saturation region, so its saturation output power is invariable. However, Erbium-doped fiber has longer transition time, when the carriers are dropped from excited state to ground state. The total output optical power variation is depended on the number of signal channels working in the EDFA at all times. The gain of each channel signal is dependent on the present channel number. Both the gain and the output signal power of each channel will decline when the number of channels increases, this may degrade the signal reception. In contrast, both the gain and the output signal power of each channel will increase when the number of channels decreases, this will degrade the overall performance of the system due to nonlinear effects in fiber [3]. In recent years, there are three common methods to design gain clamping for optical fiber amplifiers: (1) using electro-optical feedback in pumping source to compensate [4], (2) by putting an additional compensation signal [5], (3) by an optical loop to compensate the gain [6]. In this paper, we refer to the third method and propose an alternative approach to achieve the gain clamping. We focus firstly on the cost-effective design of a gain-clamped C-band EDFA based on the ring-fiber laser cavity using a fiber Bragg grating (FBG) technique, then the gain flatness and variations, and the noise figure was characterization for the further WDM applications.

## 2. EXPERIMENTAL SETUP

An experimental setup of C-band EDFA with an ASE selective-feedback gain-clamping technique is shown in Fig. 1. It consisted of a C-band EDFA, a FBG with a 3-dB Bandwidth of 0.142 nm and centre wavelength at 1532.95 nm, a  $1 \times 2$  optical coupler, a 3-ports optical circulator (OC), and a variable optical attenuator (VOA). The ASE power spectrum of EDFA is also shown in Fig. 3. A specific wavelength signal from ASE spectrum was firstly reflected by FBG. Then the 1532.95 nm signal from the ASE was backed into EDFA through a circulator (Port 2 to Port 3), a VOA, and an optical coupler, in which the optical loop was form a ring cavity. The 1532.95 nm-wavelength signal was re-amplifying by the EDFA and traveling through the above mention optical loop that a 1532.95 nm-wavelength fiber laser was created. The key component FBG in this scheme serves as a laser feedback wavelength selector and also as a noise filter. The optical power of 1532.95 nm signal injected to EDFA was controlled by a VOA. A tunable laser source (TLS) was used to simulate a different input signals level at the wavelength of C-band. The input signal level, output signal level and gain of the proposed gain-clamping EDFA are characterized by using an Optical Spectrum Analyzer (OSA, ADVENTEST Q8384) with a resolution of 0.01 nm.

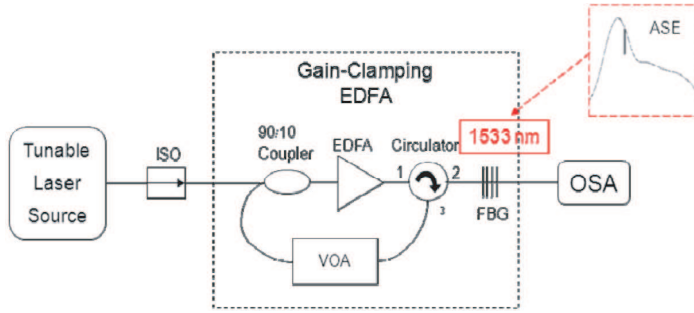


Figure 1: Experimental setup of the gain-clamping C-Band EDFA with an ASE selective-feedback.

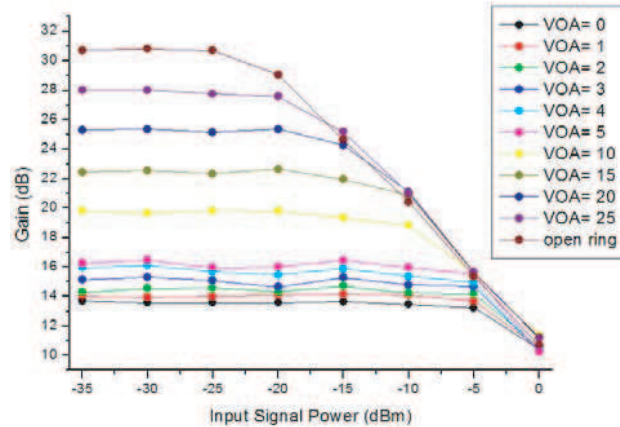


Figure 2: Optical gain characteristics versus various input signal power at different attenuation values.

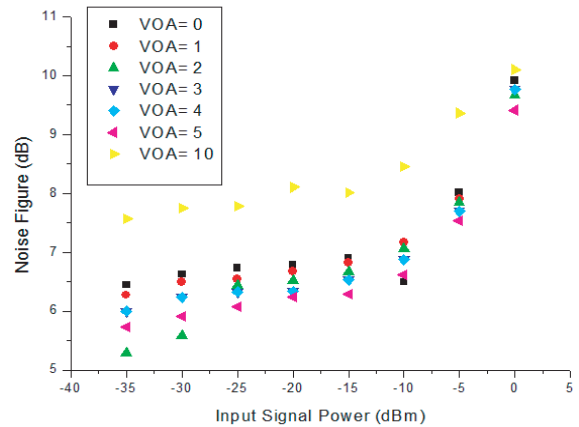


Figure 3: Noise figure as a function of the input signal power at different attenuation values.

### 3. RESULTS AND DISCUSSION

Figure 2 shows the optical gain characteristics versus various input signal power for a single-channel operating in open-ring and the gain clamped with different attenuation values ( $\text{VOA} = 0 \sim 25 \text{ dB}$ ). The gain-performance of amplifier working in open-ring ( $\text{VOA} = \infty$ ) is also shown in the figure. The power levels of input signal from  $-35 \text{ dBm}$  to  $0 \text{ dBm}$  at  $1550 \text{ nm}$  are employed in this study. The good gain-clamping trends were observed at low attenuation values (e.g.,  $\text{VOA} = 0 \sim 5 \text{ dB}$ ) for a closed-ring system, in which the gain curves were flat within a wide range of the optical power levels of input signal. The ring-fiber laser power of the proposed scheme was decreased as the attenuation value is increased. When attenuation was set at a higher value, the experiment scheme was similar to an open-ring case. If attenuation value  $\leq 5 \text{ dB}$ , however, the dynamic range of  $30 \text{ dB}$  with a flatting-gain-curve was achieved for the power of input signal from  $-35 \text{ dBm}$  to  $0 \text{ dBm}$ . Therefore, the optical power of the ring-fiber laser must be adjusted to an appropriate attenuation value to obtain the superlative gain clamping effect. Thus the gain clamped at  $16.2 \text{ dB}$  with a flatness of  $0.26 \text{ dB}$ , which having high gain and wide dynamic range, was obtained at  $\text{VOA} = 5 \text{ dB}$  and the input signal power levels from  $-35 \text{ dBm}$  to  $-5 \text{ dBm}$ . Fig. 3 shows the calculated noise figure at  $1550 \text{ nm}$  as a function of the input signal power at different attenuation values. Lower noise figure values were presented at  $\text{VOA} = 0 \sim 5 \text{ dB}$ . Noise figure  $\leq 7 \text{ dB}$ , in the proposed scheme, were obtained when the input signal power of  $-35 \text{ dBm}$  to  $-10 \text{ dBm}$ .

Optical gain of the gain-clamping EDFA versus the wavelength of input signal at different attenuation values is shown in Fig. 4. The gain of long wavelength was large than that of the short wavelength, in general, when the  $\text{VOA} < 5 \text{ dB}$ . The gain increases with the wavelength within the range from  $1540$  to  $1560 \text{ nm}$ . In contrast, the gain of the long wavelength ( $1540\text{--}1560 \text{ nm}$ ) is less than that of at the short wavelength of  $1533 \text{ nm}$  when the  $\text{VOA} > 5 \text{ dB}$ . In addition, the gain spectrum of the gain-clamping EDFA with the  $\text{VOA} = 5 \text{ dB}$  was flat than that of the  $\text{VOA} < 5 \text{ dB}$  and  $\text{VOA} > 5 \text{ dB}$ , respectively.

Figure 5 shows an experimental setup for investigating the gain-variation of probe-signal when a saturation tone signal was adding or dropping into the gain-clamping EDFA. The saturation tone

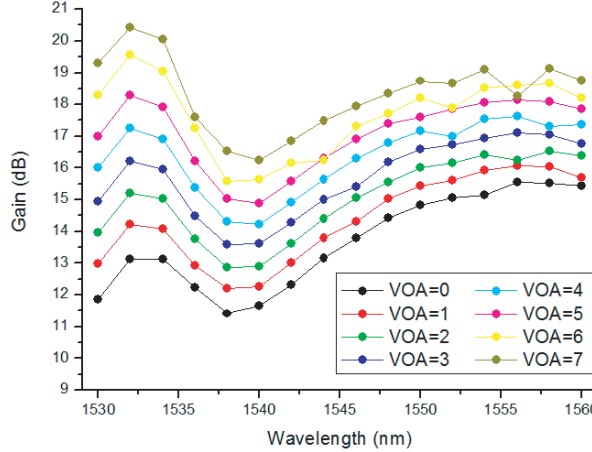


Figure 4: Optical gain versus the wavelength of input signal at different attenuation values.

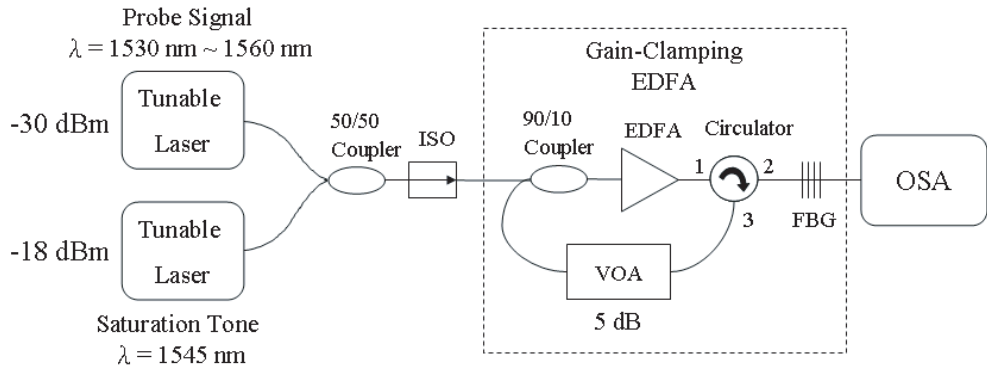


Figure 5: Experimental setup for investigating the gain-variation of probe-signal when a saturation tone signal was adding or dropping into the gain-clamping EDFA.

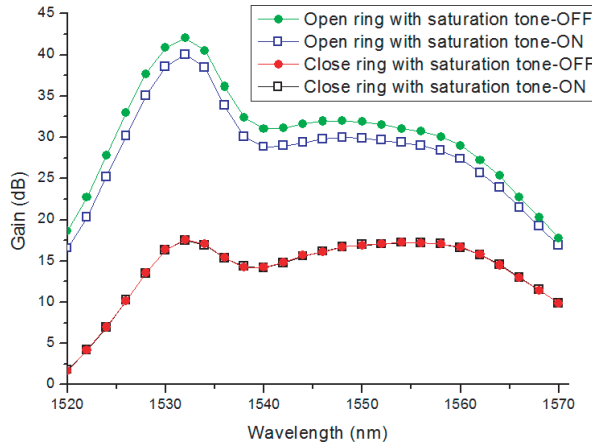


Figure 6: Gain spectrum of open ring and close ring with saturation tone signal adding or dropping.

signal, in this experiment, was used to simulate 16-channel signals in WDM system. The optical power of probe-signal was set at  $-30 \text{ dBm}$  for each channel ( $1530\text{--}1560 \text{ nm}$ ) and the optical power of the saturation tone signal of  $-18 \text{ dBm}$  at wavelength of  $1545 \text{ nm}$  was employed.

Figure 6 shows the gain spectrum of open ring and close ring with saturation tone signal at on-state (adding) and off-state (dropping), respectively. The attenuation value (VOA) was selected at  $5 \text{ dB}$  due to EDFA operating in wide-dynamic range and lower noise figure. A large difference of gain values of  $12.0 \text{ dB}$ , which the peak gain relative to the flat-region ( $1540\text{--}1560 \text{ nm}$ ), in the

open ring case was observed. However, the gain-spectrum was flat and with a minimum difference in gain values at C-band range (1530–1560 nm) was obtained in close ring case. Furthermore, the gain difference at wavelength of 1530 nm to 1564 nm of  $\leq 0.13$  dB was achieved when the saturation tone signal was added or dropped in the gain-clamping EDFA. The obtained results show that the proposed scheme is highly appropriate for the applications of wide-dynamic and stable gain-clamping.

#### 4. CONCLUSIONS

A gain clamped C-band EDFA has been proposed and demonstrated using an ASE selective-feedback gain-clamping technique. At attenuation value of 5 dB, the gain of amplifier was clamped about 16.2 dB with a gain variation of 0.26 dB when the input signal power levels of from –35 dBm to –5 dBm. The gain-clamped amplifier also has a flattest gain spectrum with gain variation  $\leq 0.13$  dB within the wavelength range from 1530 nm to 1564 nm. The gain spectrum is nearly unchanged when the input optical power fluctuates with the channels added or dropped. According to the above results, the proposed gain-clamping amplifier can endure large power variations for WDM systems.

#### ACKNOWLEDGMENT

The authors would like to thank the financial support from the National Science Council under Grant NSC 99-2622-E-027-030-CC3.

#### REFERENCES

1. Rhee, J. K., I. Tomkos, and M. J. Li, "A broadcast-and-select OADM optical network with dedicated optical-channel protection," *J. Lightwave Technol.*, Vol. 21, 25–31, 2003.
2. Le, H. C., H. Hasegawa, and K. I. Sato, "Cost evaluation of hybrid-hierarchical optical cross-connects based optical path networks," *The International Conference on Communications and Electronics 2010 (ICCE)*, 40–45, Nha Trang, Vietnam, 2010.
3. Keiser, G., *Optical Fiber Communication*, 3rd Edition, 379–414, McGraw-Hill, New York, 2000.
4. Tancevski, L., L. A. Rusch, and A. Bononi, "Gain control in EDFA by pump compensation," *IEEE Photonics Technology Letters*, Vol. 10, No. 9, 1313–1316, 1998.
5. Yeh, C. H., Y. W. Hsu, Y. J. Huang, C. C. Lee, and S. Chi, "Simultaneously gain-flattened and gain-clamped technique for erbium-doped fiber amplifiers by backward injection of a fabry-perot laser light," *Japanese Journal of Applied Physics*, Vol. 43, 4238–4239, 2004.
6. Ko, S. Y., M. W. Kim, D. H. Kim, S. H. Kim, J. C. Jo, and J. H. Park, "Gain control in erbium-doped fiber amplifiers by tuning centre wavelength of a fiber Bragg grating constituting resonant cavity," *Electronics Letters*, Vol. 34, 990–991, 1998.

# Generation and Transmission Characterization of Sub-picoseconds 1550 nm Optical RZ-pulse

Jheng-Jie Liu, Wen-Jeng Ho, Jhe-Min Lin, Yi-Chia Hsieh,  
Hsuan-Ming Tang, and Yu-Feng Yang

Institute of Electro-Optical Engineering, National Taipei University of Technology  
1, Sec. 3, Chung-Hsiao E. Rd., Taipei 106, Taiwan

**Abstract**— The paper experimentally demonstrated the 1550 nm optical return-to-zero (RZ) pulse using a 2.5 GHz radio frequency (RF) signals to drive a TO-can-packaged gain-switching distribution feedback (DFB) semiconductor laser, a fiber ring self-injection locking, and an non-return-to-zero on/off keying (NRZ-OOK) modulating techniques. The obtained RZ-pulse of 58.46 ps was transmitted and characterized in the optical fiber link. At  $\text{BER} = 10^{-9}$ , the receiver power of  $-21.9 \text{ dBm}$  and power penalty of 1 dB were obtained over a fiber link with a transmission distance of  $> 10 \text{ km}$ .

## 1. INTRODUCTION

To achieve high speed and high capacity operation in the telecommunication systems, e.g., high-bit-rate optical time division multiplexed/wavelength division multiplexed (OTDM/WDM) systems, the sub-picoseconds optical RZ-pulses play an important role for this goal. The multiplexed optical pulses with a sufficiently narrow width would greatly increase the transmission capacity. Especially in the OTDM system, the sub-channels in one communication channel can be simultaneously multiplexed and transferred more optical signals [1]. In previous studied, the performance of RZ-OOK format signal was preferred than that of NRZ-OOK format because the RZ-OOK formats are more robust to the nonlinear propagation distortions than the NRZ-OOK format [2]. However, it's well known that multiplexed optical pulses with a sufficiently narrow optical pulse width in the optical time-domain would increase the transmission capacity. The requirements of transmitted performances in the optical time domain for the pulse signal are not only having high peak power but also in the smallest timing jitter. When the pulses are generated during the turn-on time of gain-switch process, there are a few drawbacks such as a lower side mode suppression ratio (SMSR) and a larger timing jitter. The reduction of the SMSR under gain-switching conditions is due to the large fluctuations in the photon density, which cause by the strongly excited the side modes of diode lasing. As a consequence, the SMSR of gain-switching DFB laser was smaller than 25 dB. In contrast, the timing jitter of gain-switch diode laser can be mainly attributed to from the spontaneous noise [3].

Frequency injection-locking technique has a great capability to produce an optical pulse with very low jitter characteristics, SMSR improving and intrinsic bandwidth enhancing when a laser diode was with an optical injection [4, 5]. In this paper, a gain-switching DFB laser with fiber ring optical self-injection scheme to generate a high-quality single-mode and short optical RZ-pulse was proposed and experimental demonstrated. We also studied the transmission performances of the obtained RZ-pulse over an optical fiber link.

## 2. EXPERIMENTAL SETUP

Figure 1 shows the experimental setup for optical pulse generation using a fiber ring self-injection locking with a gain switching DFB laser. An RF signal and a DC bias current were combined through a Bias Tee to modulate a DFB laser and generate the pulse trains. The following Equations are the modulation current  $I(t)$  applied to the laser diode from both DC bias current  $I_{bias}$  and RF signal parts [3, 6]:

$$I(t) = I_{bias} + I_{mod} \sin 2\pi f(t) \quad (1)$$

$$M = I_{mod} / (I_{bias} - I_{th}) \quad (2)$$

where  $I_{mod}$  is RF signal current,  $I_{th}$  is laser diode threshold currents and  $M$  is modulation index  $M < 1$ , it was at the condition of small-signal modulation and operated in the linear region.  $M > 1$ , however, it is at the condition of gain-switching modulation.

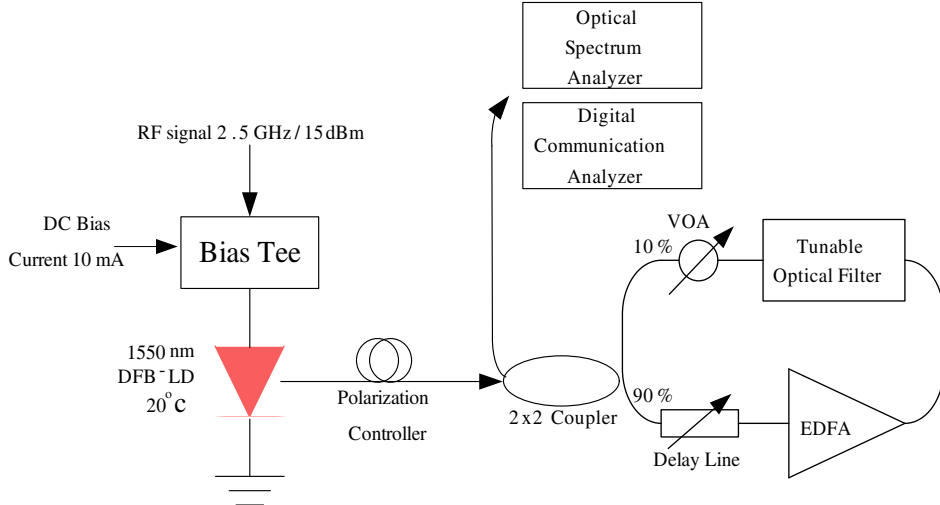


Figure 1: Experimental setup for gain-switching DFB-LD with a fiber ring optical injection.

In this experiment, a DFB laser operating in gain-switching was obtained by using a DC bias current biased at a linear region near the threshold point and a RF driving signal. The DC bias current is 10 mA and the RF signal frequency is 2.5 GHz with a power of 15 dBm, in this work. The optical pulses from the laser were coupled into a  $2 \times 2$  (90/10) coupler through a polarization controller (PC). The most parts of optical pulses were obtained from the 90% output port of  $2 \times 2$  coupler and went through an optical delay line (ODL) and then amplified by an erbium-doped filter amplifier (EDFA). The amplified optical-pulse signal was next filtered by a tunable optical filter (TOF) to eliminate the amplified spontaneous emission (ASE) noise. A variable optical attenuator (VOA) was used to control the optical amplified power which the power will be properly injected into a DFB laser. In addition the optical pulses can be further controlled by the ODL and a PC device to achieve an optimum re-injection. Finally, the time and the linear polarization state of the re-injection pulses were synchronized with the emitted pulses from the gain-switched DFB laser. The working principle of the proposed fiber ring, which consisted of PC, coupler, DL, EDFA, TOF, VOA Coupler and PC, was as same as an external cavity for compensating the photon density when the dynamic transient of the pulse is ON. The optical pulses in our experimental setup were characterized by an optical spectrum analyzer (ADVENTEST Q8384) with a resolution of 0.02 nm and a 40 GHz Digital Communication Analyzer (Agilent 86100C).

### 3. RESULTS AND DISCUSSION

The light-current (L-I) characteristics of a TO-can packaged DFB laser at temperature of 20°C is shown in Figure 2. The threshold current of DFB laser diode was 9.6 mA. To operate the device at the linear region, the DFB laser diode was driven at 10 mA, which was near a threshold point.

The frequency response of the TO-can packaged DFB laser was characterized with and without optical injection, as shown in Figure 3. The injection ratio (which, the injection optical power over laser the emission power) controlled by a VOA was 5 dB. The cutoff frequency of the free-running DFB laser was about 3.3 GHz at the DC bias current of 10 mA. However, the cutoff frequency of DFB laser can improve up to 5.45 GHz after an optical injection applied. A flat frequency response curve was also presented under the optical injection.

In frequency domain, the optical spectrum of gain-switching DFB laser with and without the fiber ring self-injection locking is shown in Figure 4. The peak power and center wavelength of a gain-switching DFB laser without optical injection were  $-18.96$  dBm and 1549.232 nm. In contrast, the peak power and center wavelength of a gain-switching DFB laser with a self-injection were  $-12.94$  dBm and 1549.349 nm. Furthermore, the SMSR improving of 34.3 dB (from 27.8 dB to 61.2 dB) and line-width reducing of 0.172 nm (form 0.361 nm to 0.189 nm) were obtained when the gain-switching DFB laser with a fiber ring self-injection.

The waveform of optical pulse without and with optical injection is shown in Figures 5(a) and (b) using a sampling oscilloscope. In time domain, very severe time jitter presented in the waveform of optical pulse is shown in Figure 5(a) when the gain-switching DFB laser without optical injection. The pulse RMS jitter of 1 ps, pulse-width of 58.46 ps and pulse peak power of 3.24 mV were obtained

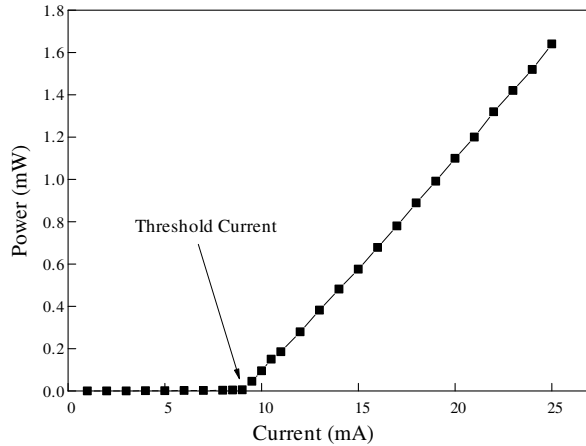


Figure 2: L-I curve of the used DFB laser diode at 20°C.

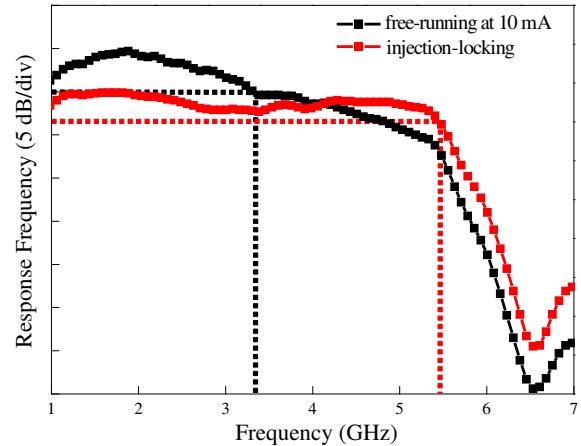


Figure 3: 3-dB frequency response of the used DFB-LD at free-running and optical injection.

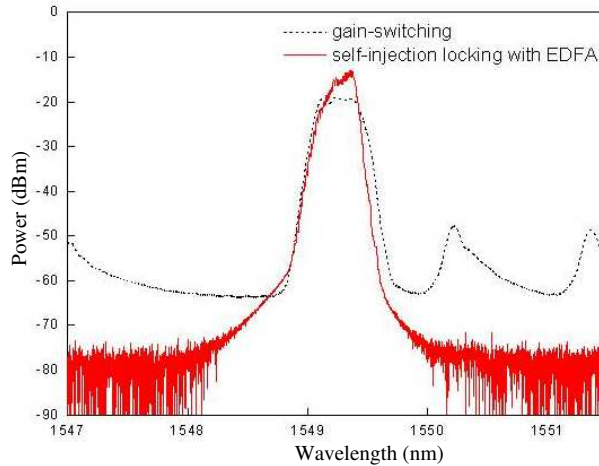


Figure 4: Optical spectrum of gain-switching DFB laser at free-running (Black curve) and with optical injection (Red curve).

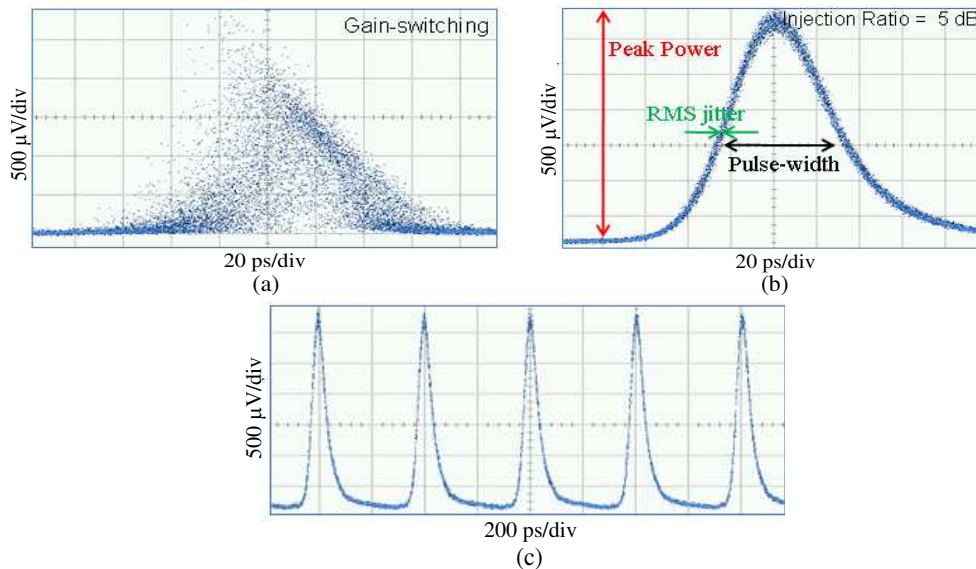


Figure 5: The optical pulse of gain-switching DFB. (a) Without optical injection. (b) With fiber ring optical self-injection. (c) The obtained optical pulse train with a fiber ring optical self-injection.

when the gain-switching DFB laser with optical injection. In addition, the generated 2.5 GHz optical pulse train and the round trip time of the pulse train of 403 ps are shown in Figure 5(c). Therefore, the performances of 2.5 GHz optical pulse generated from a gain-switching DFB laser with an optical self-injection were effectively improved in the proposed scheme.

The obtained 2.5 GHz optical pulse train (as mentioned above) was further transformed to an optical return-to-zero (RZ) pulse train for transmission characterization. In this study, the 2.5 GHz optical pulse was first coupled into MZM-modulator and the modulator subsequently modulated by a 2.5 Gbit/s PRBS electrical signal with the word length of  $2^7 - 1$  NRZ-OOK format data. Then a 2.5 Gbit/s RZpulse train was obtained at the output port of MZM-modulator. A sub-picoseconds width of the RZ pulse of 58.46 ps was achieved in the proposed scheme. Particularly, to generate a RZ-OOK format pulse train the data rates of NRZ-OOK signal have to match the frequency of 2.5 GHz RF signal. Finally, RZpulse signals were transmitted and characterized over a 10 km fiber link. The received power levels of  $-21.9$  dBm and power penalty of 1 dB at the BER of  $10^{-9}$  were achieved, respectively.

#### 4. CONCLUSIONS

In this paper, we have demonstrated a gain-switching TO-can packaged DFB laser with fiber ring optical self-injection to generate an optimum RZ-pulse. In frequency domain, the peak power of  $-12.94$  dBm, center wavelength of 1549.349 nm, line-width of 0.189 nm and SMSR of 61.2 dB were obtained. In contrast, the pulse characteristics in time domain show that the pulse RMS jitter of 1 ps, pulse-width of 58.46 ps and pulse peak power of 3.24 mV were also achieved. In addition, the optical RZ-OOK format pulse-signal generated by modulating the 2.5 Gbit/s NRZ-OOK format data was successfully transmitted over a 10 km SMF link. The received power levels of  $-21.9$  dBm and power penalty of 1 dB at the BER of  $10^{-9}$  were obtained, respectively. 10 Gbit/s optical RZ-pulse based on the above scheme are ongoing study in our laboratory.

#### ACKNOWLEDGMENT

The authors would like to thank the financial support from the National Science Council under Grant NSC 99-2622-E-027-030-CC3.

#### REFERENCES

1. Seo, S. W., K. Bergman, and P. Prucnal, "Transparent optical networks with time-division multiplexing," *IEEE Journal of Selected Areas on Communications*, Vol. 14, No. 5, 1039–1051, 1996.
2. Winzer, P. J. and R. J. Essiambre, "Advanced optical modulation formats," *Proceedings of the IEEE*, Vol. 94, No. 5, 952–985, 2006.
3. Sayin, M. and M. S. Ozyazici, "Effect of gain switching frequency on ultrashort pulse generation from laser diodes," *Optical and Quantum Electronics*, Vol. 29, 627–638, 1997.
4. Seo, D. S., D. Y. Kim, and H. F. Liu, "Timing jitter reduction of a gain-switched DFB laser by external injection-seeding," *Electronics Letters*, Vol. 32, No. 1, 44–45, 1996.
5. Guignard, C., P. M. Anandarajah, A. Clarke, L. P. Barry, O. Vaudel, and P. Besnard, "Experimental investigation of the impact of optical injection on vital parameters of a gain-switched pulse source," *Optics Communications*, Vol. 277, No. 1, 150–155, 2007.
6. Siegman, A. E., *Lasers*, Univ. Sci. Books, Mill Valley, CA, 1976.

# Efficient Generation of Broadband High-count Channels with Full Duty Cycle Amplitude Sampled Fiber Bragg Gratings

Xiaojun Zhu, Chinhua Wang, Jing Ge, and Shixin Liu

Key Lab of Modern Optical Technologies of Jiangsu Province

Institute of Modern Optical Technologies, Soochow University, Suzhou 215006, China

**Abstract**— A novel high-count-channel optical fiber filter in amplitude sampled fiber Bragg grating (ASFBG) based on full duty-cycle sampled function with spectral Talbot effect is proposed for dense-wavelength-division-multiplexing (DWDM) system applications. Under the Talbot conditions, the self-imaging phenomenon can be appeared with the refractive index modulation with Gaussian spatial profile is used within the total sampling period, and high-count channels, wider spectral range, and high energy in-band channels can be obtained with the reflection spectral covers the whole C band.

## 1. INTRODUCTION

Fiber gratings have found important applications in optical communication and fiber-sensing systems. Among the many applications, the increasing demand on the number of wavelength channels has attracted considerable interests in the design and implementation of multichannel devices based on sampled fiber Bragg gratings (SFBGs) [1]. Two types of sampled fiber Bragg gratings are most frequently employed in practice, i.e., amplitude sampled fiber Bragg grating (ASFBG) and phase-only sampled fiber Bragg grating (PSFBG). The main drawback of the conventional ASFBG is the trade-off between the spectral range and the channel energy efficiency according to Fourier transform in which the spectral range in frequency domain is inversely proportional to the duty cycle in each sampling period. An interleaved structure was proposed to improve the fiber utilizing efficiency by inserting two or three sets of wavelength shifted ASFBGs to the grating-absent portion [2]. Although the channel density can be increased by the interleaving structure, it does not improve the energy efficiency since duty cycle of each set of ASFBG does not change. The most attractive feature of phase-only sampled FBGs (PSFBGs) is the high energy efficiency [3]. It has been estimated that for phase-only SFBGs, the peak refractive index modulation  $\Delta n$  must be increased by a factor of  $\sqrt{N}$  only as opposed to  $N$  in the conventional ASFBGs in order to increase the number of wavelength channels  $N$  within a given bandwidth. The enhancement of the energy efficiency is, however, at the expense of increasing significantly the fabrication complexity. Recently, it has been shown that the multi-channel generation can be implemented by exploiting Talbot effect in sampled and chirped FBGs, in which the channel density (or free spectral range, FSR) can be effectively multiplied by changing the chirp coefficient with no need to change the sampling period as the case in conventional SFBGs [4]. However, when we examine the structure of an ASFBG used under condition of Talbot effect, it is found that the duty cycle of each sampling period must also be kept small ( $< 0.2\text{--}0.3$ ) in order to obtain clean multi-channel outputs [5, 6], which also results in low energy efficiency and the practical application is thus very limited. It is also noted that the energy enhancement in each channel in Talbot-based ASFBGs cannot be obtained by increasing the grating length due to the energy saturation caused by the grating chirp. The Talbot effect in PSFBGs for multi-channel generation has also been proposed [7] to enhance the energy efficiency with a limited fiber length. It is shown that, under the Talbot condition, the PSFBGs using less phase transitions is capable of generating superior high-count DWDM channels with high energy efficiency. Nonetheless, the manufacturing difficulty of PSFBGs still remains.

In this paper, we propose a novel ASFBG structure that has a full duty cycle (= 1) for efficient generation of broadband high-count channels operated under spectral Talbot effect. This structure integrates advantages of amplitude sampled FBGs (easy and straightforward making), phase-only sampled FBGs (high energy efficiency and short fiber length) and Talbot effect (inherit high efficiency in high-count channel output and arbitrarily FSR tuning). It is shown that the energy efficiency of the structure is almost comparable to that of the PSFBGs with the same fiber length (no Talbot). The direct use of a simple Gaussian beam profile or combination of Gaussian profile yields high uniformity, high isolation and high-count channel outputs.

## 2. FULL DUTY-CYCLE ASFBGS

In an ASFBG, the refractive index modulation  $\Delta n_0(z)$  of length  $L$  along the fiber axis  $z$  can be expressed as follows:

$$\Delta n_0(z) = \Delta n_0 s(z) \cos \left[ \frac{2\pi z}{\Lambda(z)} \right] \quad (1)$$

where  $\Delta n_0$  is the peak refractive-index modulation,  $\Lambda(z)$  is the grating period at  $z$  with  $\Lambda_0$  being the nominal grating period. The sampling function with a grating period of  $P$  can be written as:

$$s(z) = s_p(z) * \sum_{n=-\infty}^{+\infty} \delta(z - nP) \quad (2)$$

where  $s_p(z)$  is the sampling function in one period.  $\delta(x)$  is the delta function and symbol “\*” represents the operator of convolution,  $n$  is an integer. The ASFBG with a linearly chirped grating period,  $\Lambda(z) = \Lambda_0(1 + c_g z)$ , where  $c_g$  is the chirp coefficient. The Talbot condition among  $\Lambda_0$ ,  $P$  and  $c_g$  can be expressed as [4, 5]:

$$c_g = \frac{s}{m} \left( \frac{\Lambda_0}{P^2} \right) \quad (3)$$

where  $s$  and  $m$  are integers ( $m$  being positive), such that  $s/m$  is an irreducible rational number, the value of  $m$  decides if an integer or a fractional self-imaging Talbot effects occurs [5]. In the Talbot effect conditions, the FSR can be arbitrary modulated by,  $\delta\lambda = \Delta\lambda/m$ , where  $\Delta\lambda = \lambda_B^2/(2n_0 P)$ , and  $\lambda_B = 2n_0\Lambda_0$ ,  $n_0$  represents the average refractive index of the propagating mode. The drawback of conventional ASFBG with Talbot effect is the low reflectivity energy efficiency, because of Talbot effect phenomena can only be obtained when the spatial band width is much smaller than the spatial bandwidth as shown:

$$dc \ll \frac{m}{s} \frac{P}{L} \quad (4)$$

where  $dc = P_1/P$  is the duty cycle of the ASFBG. It means the Talbot effect can only be obtained when the duty cycle is very small (generally smaller than 0.1). In our work, we found that the Talbot effect limitation conditions can be expanded by:

$$\delta\lambda \geq \Delta\omega \quad (5)$$

where  $\Delta\omega$  is the bandwidth of discrete reflection bands as the whole grating length  $L$ . It means that the Talbot effect phenomenon can be obtained as long as the FSR is greater than or equal to the bandwidth of discrete reflection bands. Based on the conditions, a new ASFBGs structure that has a full duty cycle (= 1) for efficient generation of broadband high-count channels operated under spectral Talbot effect. In this way, Gaussian sampling function (GSF) is used for the full duty cycle structure:

$$s_p(z) = \exp \left[ -g \left( \frac{z}{P/2} \right)^2 \right] \quad -P/2 < z < P/2 \quad (6)$$

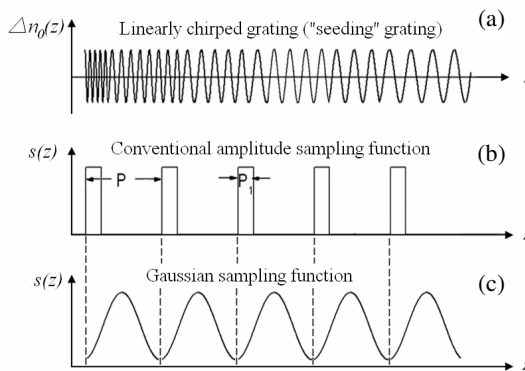


Figure 1: Schematic of the chirped CASFBG and Gaussian ASFBG.

where  $g$  is the coefficient of Gaussian. Fig. 1 shows the structure of the conventional amplitude sampling function (CASF) compared with the Gaussian sampling function (GSF). Fig. 1(a) shows the refractive index  $\Delta n_0(z)$  is linearly chirped along the fiber axis  $z$  corresponding with Eq. (3). Fig. 1(b) shows the CASF, in which the “unused” grating result in the low energy efficiency of the conventional. Fig. 1(c) is the ASFBG structure of GSF with the full duty cycle, in which the “unused” grating is totally taken up. Thus, the spectral reflectivity energy efficiency is highly improved, and the side lobes of the reflection channel can be efficiently diminished by the apodization of Gaussian function.

### 3. SIMULATIONDS AND DISSCUSSION

The simulation is based on the transfer-matrix method [8]. In our simulation, the following grating parameters are used:  $n_0 = 1.485$ ,  $\Lambda_0 = 521.8855$  nm, and the sampling period  $P = 1.0$  mm. Fig. 2 shows the multi-channel reflectivity spectra of the ASFBG with GSF (called as GSFBG). In the simulations, the following parameters are used:  $\Delta n_0 = 6.0e - 4$ ,  $g = 20$ , and grating length  $L = 40$  mm. In Fig. 2(a),  $s = 0$ ,  $m = 1$ ,  $c_g = 0$ , i.e., a uniform ASFBG, the FSR is  $\sim 0.8$  nm (100 GHz) only determined by the sampling period  $P = 1$  mm, as expected. In Fig. 2(b),  $s = 1$ ,  $m = 1$ ,  $c_g = 5.2188e - 4(1/mm)$ , the FSR is  $\sim 0.8$  nm (100 GHz), it is exactly an inverse integer spectral Talbot-effect. In Fig. 2(c),  $s = 1$ ,  $m = 2$ ,  $c_g = 2.6094e - 4(1/mm)$ , it is seen that the FSR is reduced by a factor of 2 to 0.4 nm (50 GHz) with the same sampling period  $P = 1$  mm. while in Fig. 2(d),  $s = 2$ ,  $m = 3$ ,  $c_g = 3.4792e - 41/mm$ , it is a direct fractional Talbot effect, the FSR is reduced by a factor of 3 to 0.27 nm (33 GHz). Fig. 2 shows that the self-imaging effect can be obtained in the GSFBGs.

Figure 3 shows the detailed comparison spectrum of the conventional ASFBG (CASFBG) with GSFBG under the Talbot effect condition. In the simulation, the Gaussian coefficient  $g = 8$  was

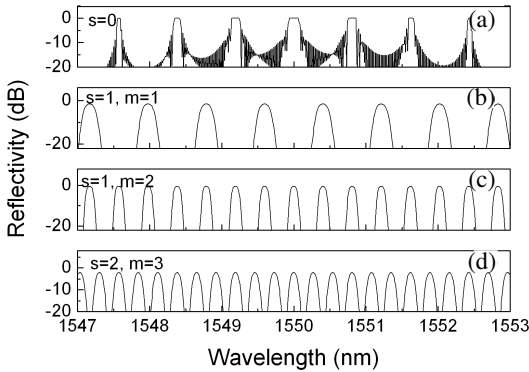


Figure 2: The multi-channel reflectivity spectra of ASFBG with Gaussian sampled function at different Talbot effect conditions. (a)  $s = 0$  ( $c_g = 0$ ); (b)  $s = 1$ ,  $m = 1$  ( $c_g = 5.2188e - 4/mm$ ); (c)  $s = 1$ ,  $m = 2$  ( $c_g = 2.6094e - 4/mm$ ); (d)  $s = 2$ ,  $m = 3$  ( $c_g = 3.4792e - 4/mm$ ).

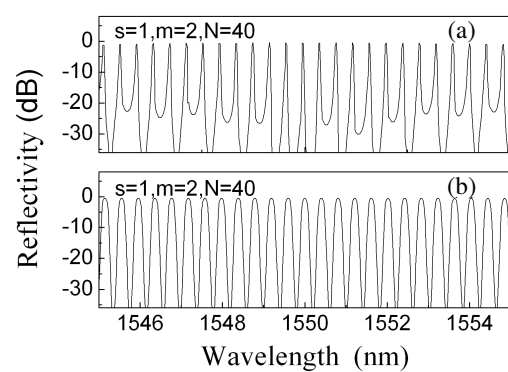


Figure 3: Comparison spectrum of the ASFBG with conventional sampled function and Gaussian sampled function under the Talbot effect condition. (a)  $s = 1$ ,  $m = 2$ ,  $N = 40$  ( $c_g = 2.6094e - 4/mm$ ); (b)  $s = 1$ ,  $m = 2$ ,  $N = 40$  ( $c_g = 2.6094e - 4/mm$ ).

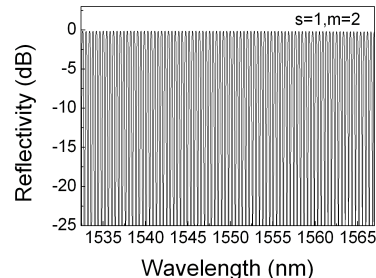


Figure 4: High-in-count channels obtained by ASFBG used Gaussian sampled function with Talbot effect.

used. Fig. 3(a) shows the spectrum of a CASFBG with Talbot effect, i.e., the grating length  $P_1 = 0.1$  mm, in which the FSR is  $\delta\lambda = 0.4$  nm. Fig. 3(b) shows the spectrum output of GSFBG. It is clearly seen from Fig. 3, the channels of GSFBG are much better than the CASFBG at the channel uniformity, the higher energy efficiency, and the higher channel isolation. These features of the Talbot effect based GSFBG are especially useful for generating broadband high-count-channel DWDM devices. Fig. 4 shows the capability of using GSFBG to generate 85 channels with a FSR of 0.4 nm. In the simulation, the following parameters are used:  $\Delta n_0 = 8.0e-4$ ,  $g = 15$ ,  $L = 10$  cm,  $c_g = 2.6094e-4(1/mm)$ . It very clear from Fig. 4 that, based on the Talbot effect, the GSFBG can generate high energy efficiency channels and very high-count channels which could cover the whole C band, breaking the limitations with CASFBG, in which only low energy efficiency channels and several channels can be obtained.

#### 4. CONCLUSIONS

In this paper, we obtained the high-count channels with a full duty-cycle amplitude sampled in the ASFBGs under spectral Talbot effect. GSF of ASFBGs is examined with various integer or fractional Talbot effects by using different Talbot conditions. It is shown that with the GSF, 85 channels that cover the whole C band is be obtained. The Talbot effect based on a full duty cycle which provides a novel method to generating high-channel-count FBG filters with great uniformity and higher energy efficiency by a convenience fabrication.

#### ACKNOWLEDGMENT

The funding supports from the Applied Research Program (Industry) of Suzhou Municipal Government (Contract No. SYJG0921), The Project Funded by the Priority Academic Program Development of Jiangsu Higher Education Institutions (PAPD), the open project of Key Lab of Modern Optical Technologies of Jiangsu Province (KJS0807), and Innovative Graduate Education Program of Jiangsu Province (ZY320034) are acknowledged.

#### REFERENCES

1. Eggleton, B. J., P. A. Krug, L. Poladian, and F. Oullette, “Long periodic superstructure Bragg gratings in optical fibres,” *Electron. Lett.*, Vol. 30, No. 19, 1620–1622, 1994.
2. Castro, J. M., J. E. Castillo, R. Kostuk, C. M. Greiner, D. Iazikov, T. W. Mossberg, and D. F. Geraghty, “Interleaved sampled Bragg gratings with concatenated spectrum,” *IEEE Photon. Technol. Lett.*, Vol. 18, No. 15, 1615–1617, 2006.
3. Li, H. P., M. Li, and J. Y. Hayashi, “Ultrahigh-channel-count phase-only sampled fiber Bragg grating covering the S, C, and L bands,” *Opt. Lett.*, Vol. 34, No. 7, 1938–1940, 2009.
4. Wang, C. H., J. Azaña, and L. R. Chen, “Spectral Talbot-like phenomena in one-dimensional photonic bandgap structures,” *Opt. Lett.*, Vol. 29, No. 14, 1590–1592, 2004.
5. Azaña, J., C. H. Wang, and L. R. Chen, “Spectral self-imaging phenomena in sampled Bragg gratings,” *J. Opt. Soc. Am. B*, Vol. 22, No. 9, 1829–1841, 2005.
6. Chen, L. R. and J. Azaña, “Spectral Talbot phenomena in sampled arbitrarily chirped Bragg gratings,” *Opt. Com.*, Vol. 250, Nos. 4–6, 302–308, 2005.
7. Lu, Y. L., X. J. Zhu, C. H. Wang, and G. J. Zhang, “Broadband high-channel-count phase-only sampled fiber Bragg gratings based on spectral Talbot effect,” *Opt. Express*, Vol. 16, No. 20, 15584–15594, 2008.
8. Kashyap, R., *Fiber Bragg Grating*, Academic, San Diego, 1999.

# Influence of Grating Period of Uniform Fiber Bragg Grating on Slow Light Delay

Shanglin Hou<sup>1</sup>, Yunbo Shang<sup>1</sup>, Yanjun Liu<sup>1</sup>, Jingli Lei<sup>1</sup>, and Yongzhao Xu<sup>2</sup>

<sup>1</sup>School of Science, Lanzhou University of Technology, Lanzhou, Gansu 730050, China

<sup>2</sup>Institute of Electronic Engineering, Dong Guan University of Technology  
Dongguan, Guangdong 523808, China

**Abstract**— On the basis of the coupled mode theory, the influence of grating period of uniform fiber Bragg grating on delay was investigated by using numerical simulation method. The result shows that grating period has a remarkable impact on the delay. The maximum value of the delay can be obtained by parameters optimization, which is 17.3013 μs occurs near the Bragg wavelength, but it decays exponentially.

## 1. INTRODUCTION

Fiber Bragg grating has developed dramatically and performed an important role in fiber communications and optical fiber sensing in recent 30 years [1, 2]. Recently, the introduction of slow light with a wide range of novel properties results in unique spectral characteristics of fiber Bragg gratings [3], especially slow light delay of fiber Bragg grating is studied emphatically. K. B. Rochford and S. D. Dyer [4] reported reconstruction of minimum-phase group delay from fiber Bragg grating transmittance or reflectance measurements. The results indicate that phase reconstruction is compared to exact solutions using the reflectance from a uniform grating. An intermediate windowing process improves the recovery accuracy. J. T. Mok, et al. [5] observed 0.68 ns pulses delayed by 4.7 pulse widths in a 30 cm silica FBG without pulse broadening. Improved slow-light delay performance of a broadband SBS system using fiber Bragg grating was reported [6]. Tunable delay slow-light in an active fiber Bragg grating was also studied [7]. These studies provide a very simple approach to control the light group delay. However, this approach requires very high power signal, which limits its practical implications.

In this work, based on the coupled theory, the effect of grating period on delay was studied by using numerical simulation method and slow light delay characteristics was demonstrated by parameters optimization. The results show that grating period has a remarkable influence on the delay induced by the fiber Bragg gratings, the maximum value of the delay can be reached um order, but its wavelength width is very narrow, and slow light delay decays exponentially.

## 2. THEORY

Fiber Bragg gratings are produced by exposing an optical fiber to a spatially varying pattern of ultraviolet intensity. For sake of simplicity, we studied an unchirped uniform fiber Bragg grating whose refractive index can be described as follows [8]

$$\delta n_{eff}(z) = \overline{\delta n}_{eff} \left[ 1 + v \cos \left( \frac{2\pi}{\Lambda} z \right) \right] \quad (1)$$

where  $\overline{\delta n}_{eff}$  is the “dc” index change spatially averaged over a grating period,  $v$  is the fringe visibility of the index change,  $\Lambda$  is the grating period and

$$\Lambda = \frac{L}{N} \quad (2)$$

where  $L$  is the grating length,  $N$  is the total number of the grating periods.

According to coupled mode theory, synchronous approximation and the boundary condition of the fiber Bragg grating [9–11]. The amplitude reflection coefficient can be expressed as

$$\rho = \frac{-\kappa \sinh \left( \sqrt{\kappa^2 - \hat{\sigma}^2} L \right)}{\hat{\sigma} \sinh \left( \sqrt{\kappa^2 - \sigma^2} L \right) + i \sqrt{\kappa^2 - \hat{\sigma}^2} \cosh \left( \sqrt{\kappa^2 - \hat{\sigma}^2} L \right)} \quad (3)$$

and the reflectivity

$$\gamma = |\rho^2| = \frac{\sinh^2(\sqrt{\kappa^2 - \hat{\sigma}^2}L)}{\cosh^2(\sqrt{\kappa^2 - \hat{\sigma}^2}L) - \hat{\sigma}^2/\kappa^2} \quad (4)$$

where  $\kappa = \pi v \bar{\delta n}_{eff}/\lambda$  is the “ac” coupling coefficient,  $\sigma = 2\pi \bar{\delta n}_{eff}/\lambda$  is the “dc” coupling coefficient,  $\hat{\sigma}$  is a general “dc” self-coupling coefficient and  $\hat{\sigma} = \delta + \sigma$ . The detuning  $\delta$  is defined as

$$\delta = \beta - \frac{\pi}{\Lambda} = 2\pi n_{eff} \left( \frac{1}{\lambda} - \frac{1}{\lambda_B} \right) \quad (5)$$

the Bragg wavelength  $\lambda_B$  is expressed as

$$\lambda_B \equiv 2n_{eff}\Lambda. \quad (6)$$

The delay of the reflected light induced by the fiber Bragg grating can be determined from Eq. (3). If we denote  $\theta_\rho = phase(\rho)$ , then at a local frequency  $\omega_0$ , we may expand  $\theta_\rho$  in a Taylor series about  $\omega_0$ . Since the first derivative  $d\theta_\rho/d\omega$  is directly proportional to the frequency  $\omega$ , this quantity can be identified as a time delay. Thus, the delay time  $\tau_\rho$  for reflected light of a grating is expressed as [12]

$$\tau_\rho = \frac{d\theta}{d\omega} = -\frac{\lambda^2}{2\pi c} \frac{d\theta_\rho}{d\lambda} \quad (7)$$

### 3. CALCULATED RESULTS AND ANALYSIS

Setting  $n_0 = 1.46$ ,  $\Delta = 0.002$ ,  $a = 5 \mu m$ ,  $\bar{\delta n}_{eff} = 0.0001$ ,  $v = 1$ ,  $L = 1.06252 \text{ cm}$  and  $\Lambda = 0.5314 \mu m$ , the delay-wavelength curve of uniform fiber Bragg grating can be obtained from Eq. (7). The curves of the delay as functions of the wavelength  $\lambda$  and the maximum values of delay in uniform fiber Bragg grating can be obtained by adjusting the grating period  $\Lambda$  and keeping the others parameters as constant as shown in Fig. 1 and Fig. 2. Fig. 1 shows the influence of  $\Lambda$  on the maximum delay  $delay_{max}$  as function of  $\Lambda$ . It can be seen that the  $delay_{max}$  decreases from 7.4083 fs to 7.1384 fs, with  $\Lambda$  increasing,  $\Lambda$  and the  $delay_{max}$  is approximately linear relationship.

In order to further study influence of grating period on delay characteristics in uniform fiber Bragg grating, we compared delay versus wavelength for four different values of grating period. As shown in Fig. 2, it can be seen that the delay curves are blue-shifted with  $\Lambda$  increasing from  $0.524 \mu m$  to  $0.553 \mu m$ , furthermore, the degrees of the deviation are remarkably different and large. In addition, the maximum value of delay is decreased. It shows that the grating period has a remarkable impact on delay-wavelength curves in fiber Bragg grating and such impact is apparently different.

Delay<sub>max</sub> curve of uniform fiber Bragg grating can be calculated by parameters optimization. Setting  $n_0 = 1.468$ ,  $\Delta = 0.0012$ ,  $a = 6.4 \mu m$ ,  $\bar{\delta n}_{eff} = 0.004$ ,  $v = 23$ ,  $L = 42.5008 \text{ cm}$  and  $\Lambda = 0.5317 \mu m$ . In this case, the reflection coefficient  $\gamma$  as functions of the wavelength  $\lambda$  with  $\Lambda = 0.5317 \mu m$  can be calculated from Eq. (4) as shown in Fig. 3. It can be seen that the reflection spectra is blue-shifted, peak top becomes much flattened and the bandwidth changes especially broaden. At the same time, the maximum values of reflection coefficient  $\gamma$  increased to 100%.

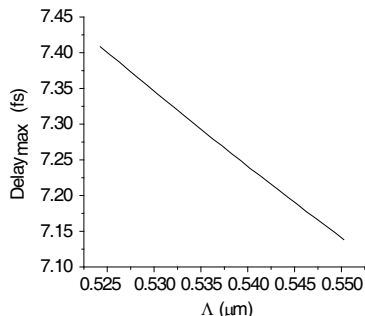


Figure 1: Influence of  $\Lambda$  on  $delay_{max}$ .

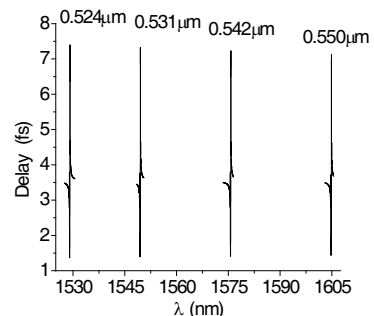


Figure 2: Delay versus wavelength for various  $\Lambda$  done.

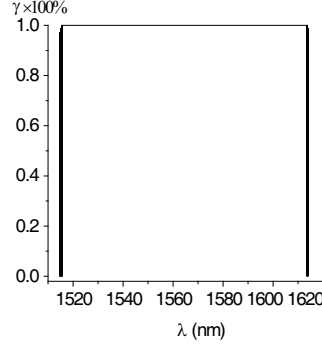


Figure 3: Reflection spectra as a function of wavelength with  $\Lambda = 0.5317 \mu\text{m}$ .

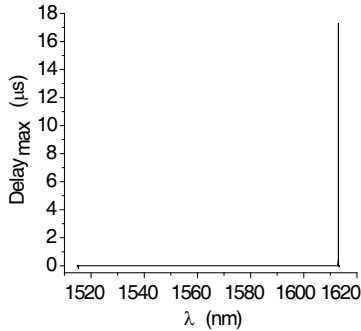


Figure 4:  $\text{Delay}_{\max}$  versus wavelength with  $\Lambda = 0.5317 \mu\text{m}$ .

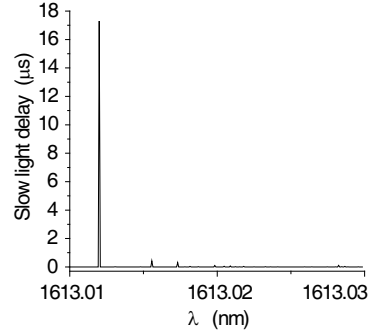


Figure 5: Influence of wavelength on slow light delay with  $\Lambda = 0.5317 \mu\text{m}$ .

As shown in Fig. 4, the  $\text{delay}_{\max}$ - $\lambda$  curve with  $\Lambda = 0.5317 \mu\text{m}$  can be given by parameters optimization. The  $\text{delay}_{\max}$  curve is also obviously blue-shifted and becomes flattened, especially the bandwidth has tends to 100 nm. The  $\text{delay}_{\max}$  increased to 17.3013  $\mu\text{s}$  occur at the Bragg wavelength, at the same time, the maximum value of delay corresponds to the minimum value of reflection coefficient.

Finally, Fig. 5 shows the influence of wavelength on slow light delay in uniform fiber Bragg grating with the others parameters optimization and  $\Lambda = 0.5317 \mu\text{m}$ . It can be seen that the slow light delay is an exponentially decaying of rapidly shocks, which is rapidly reduced to 0  $\mu\text{s}$  from 17.3013  $\mu\text{s}$ , especially shocks of the deviation is no more than 0.03 nm. On the whole, the grating period has a strong influence on the slow light delay of uniform fiber Bragg grating.

#### 4. CONCLUSION

The influence of grating period of uniform fiber Bragg grating on delay is discussed by using numerical simulation method based on the coupled mode theory and slow light delay characteristics is studied by parameters optimization. The calculated result shows that grating period has a remarkable impact on the delay this grating, between the reflection spectra and  $\text{delay}_{\max}$  curve are blue-shifted, peak top become flattened and the bandwidth change broaden, the maximum value of the delay is 17.3013  $\mu\text{s}$  occurs at the Bragg wavelength with  $\Lambda = 0.5317 \mu\text{m}$ , especially slow light delay is an exponentially decaying of rapidly shocks, they offer references for designing system.

#### ACKNOWLEDGMENT

This work was supported by the Natural Science Foundation of Gansu Province (Grant No. 1010-RJZA036), the Natural Science Foundation of Guangdong Province (Grant No. 1104511-70003004948) and Dongguan Science and Technology Program (Grant No. 2008108101002).

#### REFERENCES

- Hill, K. O. and G. Meltz, "Fiber Bragg grating technology fundamentals and overview," *J. Lightwave Technol.*, Vol. 15, No. 8, 1263–1264, 1997.

2. Kersey, A. D., "A review of recent developments in fiber optic sensor technology," *Optic. Fiber Technol.*, Vol. 2, No. 3, 219–317, 1996.
3. Mok, J. T., M. Ibsen, C. Martijn de Sterke, and B. J. Eggleton, "Slow light generation using fiber Bragg grating," *OFC/NFOEC*, Vol. 10, 1109–1112, 2008.
4. Rochford, K. B. and S. D. Dyer, "Reconstruction of minimum-phase group delay from fiber Bragg grating transmittance/reflectance measurements," *Electron. Lett.*, Vol. 35, No. 10, 838–839, 1999.
5. Mok, J. T., M. Ibsen, C. M. de Sterke, and B. J. Eggleton, "Dispersionless slow light with 5-pulse-width delay in fiber Bragg grating," *Electron. Lett.*, Vol. 43, No. 25, 1418–1419, 2007.
6. Myungjun, L., P. Ravi, and N. A. Mark, "Improved slow-light delay performance of a broadband SBS system using fiber Bragg gratings," *Applied Optics*, Vol. 47, No. 34, 6404–6415, 2008.
7. Kai, Q., L. Zhan, H. Li, X. Hu, J. Peng, L. Zhang, and Y. Xia, "Tunable delay slow-light in an active fiber Bragg grating," *Optics Express*, Vol. 17, No. 24, 22217–22219, 2009.
8. Erdogan, T., "Fiber grating spectra," *J. Light Wave Technol.*, Vol. 15, No. 8, 1277–1294, 1997.
9. Hou, S. L., C. Hu, X. M. Ren, Z. Xia, and Y. Q. Huang, "Influence of uniaxial crystal material cladding on reflectivity and dispersion of uniform fiber Bragg grating," *Optics Communications*, Vol. 271, No. 1, 109–115, 2007.
10. Kogelnik, H. and C. V. Shank, "Coupled-wave theory of distributed feedback lasers," *J. Appl. Phys.*, Vol. 43, No. 5, 2327–2335, 1972.
11. Kogelnik, H., "Theory of optical waveguides," *Guided-wave Optoelectronics*, T. Tamir, Ed., Springer-Verlag, New York, 1990.
12. Ball, G. A., W. H. Glenn, and W. W. Morey, "Programmable fiber optical delay line," *IEEE Photon. Technol. Lett.*, Vol. 6, No. 6, 741–743, 1994.

# Influence of SBS Gain Coefficient on Time Delay and Pulse Broadening in Fibers

Shanglin Hou<sup>1</sup>, Zhongyi Wang<sup>1</sup>, Yunbo Shang<sup>1</sup>, Yanjun Liu<sup>1</sup>, Jingli Lei<sup>1</sup>, and Yongzhao Xu<sup>2</sup>

<sup>1</sup>School of Science, Lanzhou University of Technology, Lanzhou, Gansu 730050, China

<sup>2</sup>Institute of Electronic Engineering, Dong Guan University of Technology  
Dongguan, Guangdong 523808, China

**Abstract**— The fiber-based stimulated Brillouin scattering coupled equations were solved by the method of implicit finite difference with prediction-correction. The influence of the Brillouin gain coefficient on time delay and pulse broadening was investigated within the gain range of 0~16. The result indicates that the time delay and the pulse broadening factor increase with increasing gain in the small signal regime and decrease in the gain saturation regime. However, the Stokes pulse will reach gain saturation at a larger gain for smaller gain coefficient and its maximum time delay is accordingly larger.

## 1. INTRODUCTION

Slow light based on stimulated Brillouin scattering (SBS) in optical fibers has attracted much more interests for its potential application in optical buffering, data synchronization, optical memories and optical signal processing. Compared with previously demonstrated slow-light techniques [1, 2], such as electromagnetically induced transparency (EIT) [3] and coherent population oscillations (CPO) [4], it has a lot of advantages, for instance, the simple, flexible and easy-to-handle SBS can be realized in room temperature; the optical fiber components based on it can easily integrated with the existing telecommunications infrastructure; the slow-light resonance can be tunable within the optical communications wavelength windows; the use of optical fiber allows for a relaxed pump-power requirement owing to long interaction length, small effective mode area and so on.

However, the SBS-induced group index change is always so small in standard single mode fiber and dispersion shift fibers (DSFs) [5] to delay the time very little. In order to explore suitable optical fibers served as slow light generation with much efficiency, some special optical fibers, such as chalcogenide fiber [6, 7], tellurite fiber [8], bismuth fiber [9] and so on, have been extensively studied, these kinds of optical fiber are usually with large gain coefficient and low loss coefficient. Though long pulse delay can be obtained using cascaded fiber segments joined by unidirectional optical attenuators to overcome pump depletion (gain saturation) and amplified spontaneous Brillouin emission (ASBE), it's always accompanied with serious pulse distortion [10]. So gain tailoring is used in pulse distortion management to keep a balance between time delay and pulse distortion [11–13]. To overcome the narrow band spectral resonance of SBS which limits the maximum data rate of the optical system, a simple and inexpensive pump spectral broadening technique is used in broadening the SBS slow light bandwidth [14–16], which paves the way towards real applications based on SBS slow light.

Numerical studies of SBS slow light focusing on different pulse parameters were also studied [17, 18], which provide an insight into the SBS slow light process, but we can't learn a lot about how the optical fiber structures and Brillouin gain parameters influence on the SBS process, the time delay and the pulse shape.

In this paper, the SBS model in optical fiber was described and the three coupled SBS equations were solved by the method of finite difference with prediction-correction, the effects of gain coefficient on time delay and pulse broadening were demonstrated. These results provide base for designing optical buffer, time delay line or other optical components based on the SBS slow light technologies.

## 2. NUMERICAL MODEL AND DISCUSSION

The process of SBS is the interaction of two counter-propagating waves, a strong pump wave and a weak Stokes wave. If a particular frequency relation is satisfied

$$v_{\text{pump}} = v_{\text{Stokes}} + v_B, \quad (1)$$

where  $v_{pump}$  and  $v_{Stokes}$  are the frequency of pump wave and stocks wave respectively,  $v_B$  is the Brillouin frequency. Then an acoustic wave is generated which scatters photons from the pump to the Stokes wave and the interference of these two optical waves in turn stimulates the process [19]. From a practical point of view, the process of SBS can be viewed as a narrowband amplification process, in which a continuous-wave pump produces a narrowband gain in a spectral region around  $v_{pump} - v_B$ . In this paper, the Stokes pulse is set on the SBS gain line center to achieve the maximum delay.

For simply describing the SBS process, assume: (1) Transverse field variations are neglected, Stokes and pump fields are assumed to vary with time  $t$  and space  $z$  only. (2) The slowly varying envelope approximation (SVEA) SBS model is used, i.e., the field amplitudes are assumed to vary slowly in time and space as compared with their temporal and spatial frequencies. (3) The initial ( $t = 0$ ) phonon field is zero and the Stokes output grows from an injected Stokes field at  $z = 0$ . (4) The frequency difference between the pump and Stokes wave is set to the Brillouin shift of the fiber, i.e., the Stokes pulse is on the SBS line center.

Considering a Brillouin amplifier where the pump wave counter-propagates through the fiber with respect to the Stokes pulse, the SBS process can be described by one-dimensional coupled wave equations involving a backward pump wave ( $-z$  direction), a forward Stokes wave ( $+z$  direction), and a backward acoustic wave. Under the slowly varying envelope approximation (SVEA) and neglecting the transverse field variations, the equations are written as follows [20]:

$$-\frac{\partial A_p}{\partial z} + \frac{n}{c} \frac{\partial A_p}{\partial t} = -\frac{\alpha}{2} A_p + ig_2 A_s Q, \quad (2)$$

$$\frac{\partial A_s}{\partial z} + \frac{n}{c} \frac{\partial A_s}{\partial t} = -\frac{\alpha}{2} A_s + ig_2 A_p Q^*, \quad (3)$$

$$\frac{\partial Q}{\partial t} + \frac{\Gamma_B}{2} Q = ig_1 A_p A_s^*, \quad (4)$$

where  $A_p$ ,  $A_s$ , and  $Q$  are the amplitudes of the pump wave, the Stokes wave, and the acoustic wave, respectively;  $n$  is the group refractive index when SBS is absent;  $\alpha$  is the loss coefficient of the fiber;  $\Gamma_B/2\pi$  is the bandwidth (FWHM) of the Brillouin gain;  $g_1$  is the coupled coefficient between the pump wave and the Stokes wave,  $g_2$  is the coupled coefficient between the pump (Stokes) wave and the acoustic wave,  $g_0 = 4 \frac{g_1 g_2}{\Gamma_B}$  is the peak value of the Brillouin gain coefficient.

According to the small signal steady state theory of stimulated Brillouin scattering, the pump power  $P_{critical}$  required to reach Brillouin threshold in a single pass scheme is related to the Brillouin gain coefficient  $g_0$  by the following equation:

$$g_0(P_{critical}/A_{eff})L_{eff} \cong 21, \quad (5)$$

where  $P_{critical}$  is the power corresponding to the Brillouin threshold,  $L_{eff}$  is the effective length defined as  $L_{eff} = \alpha^{-1}[1 - \exp(-\alpha L)]$ , from Eq. (5) we can obtain the threshold pump intensity:

$$I_{critical} = P_{critical}/A_{eff} \cong 21/(g_0 L_{eff}). \quad (6)$$

Once reaching the threshold pump intensity, a large part of the pump power is transferred to the Stokes wave, resulting in the generation of Stokes wave at the output depletes the pump seriously and leads to serious Stokes pulse distortion. In our simulations, we consider the pump intensity is near the Brillouin threshold and obtain the Stokes gain around 16 using the previous parameters, here the Stokes gain is defined as:

$$Gain = \log \left( \frac{P_{out}}{P_{in}} \right), \quad (7)$$

where  $P_{out}$  and  $P_{in}$  are the output and input of the Stokes power, respectively.

### 3. NUMERICAL SIMULATION RESULTS

The Eqs. (2)–(4) were numerically solved by the method of implicit finite difference with prediction-correction [21], setting fiber length  $L = 25$  m, pump wavelength  $\lambda = 1550$  nm, group refractive index  $n = 1.45$ , effect mode area  $A_{eff} = 50 \mu\text{m}^2$ , loss coefficient  $\alpha = 0.2 \text{ dB/km}$ , gain bandwidth (FWHM)  $\Gamma_B/2\pi = 40 \text{ MHz}$ , gain coefficient  $g_0 = 5 \times 10^{-11} \text{ m/W}$ . We assume the pump wave is CW and the

Stokes wave is Gaussian shaped with the peak power of  $0.1 \mu\text{W}$  and the FWHM pulse width of  $120 \text{ ns}$ .

The curves of the pulse delay and pulse broadening factor as a function of the gain with different gain coefficient  $g_0$  were shown in Fig. 1. It can be seen from Fig. 1 that the time delay increases linearly with Stokes gain when the gain is small ( $\leq 10$ ), that's because the pump isn't completely affected when the gain is small. For larger gain, pump depletion becomes more and more seriously, the time delay increases slowly with gain and reaches its maximum before decreasing with gain. At the same time, for larger gain coefficient, the time delay decreases with increasing gain more quickly and even leads to pulse advancement which can be explained by gain saturation. It can also be seen that the smaller gain coefficient reaches the gain saturation at a larger gain and the maximum time delay is accordingly larger, the gain saturation limits the maximum time delay for a Stokes pulse at a given input power.

The pulse broadening factor for different gain coefficients as a function of gain was shown in Fig. 2. It shows that the pulse broadening factor is also increasing linearly with gain when the small signal regime holds. As the gain further increases, the pulse broadening factor increases slowly with gain and then gradually decreases to less than 1, it means that the pulse become more and more narrower, the pulse with larger gain coefficient narrows more seriously than the smaller one. The time delay is always accompanied with pulse distortion, the Stokes pulse broadens a little in the small signal regime but can narrow largely in the gain saturation regime. Fig. 3 shows the normalized output pulse shapes with the gain coefficient  $g_0 = 5 \times 10^{-11} \text{ m/W}$  at gain = 0, 12, and 17, respectively. The output Stokes pulse with a maximum time delay  $\sim 45 \text{ ns}$  at gain = 12 with a little distortion while the output Stokes pulse is advanced by  $42.9 \text{ ns}$  at gain = 17 but is distorted substantially.

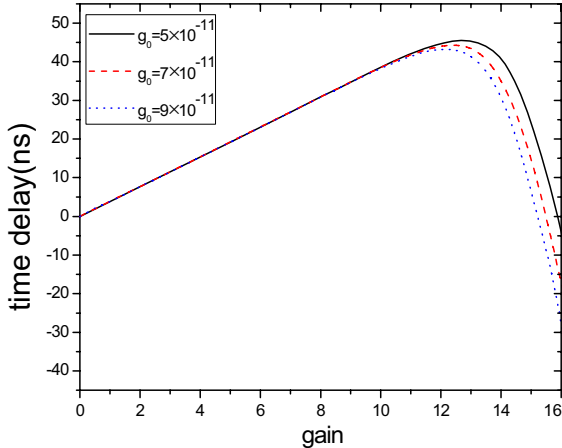


Figure 1: Time delay as a function of gain with different gain coefficients.

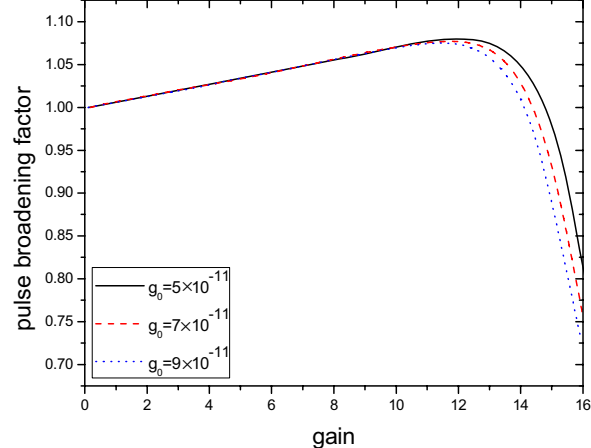


Figure 2: Pulse broadening as a function of gain with different gain coefficients.

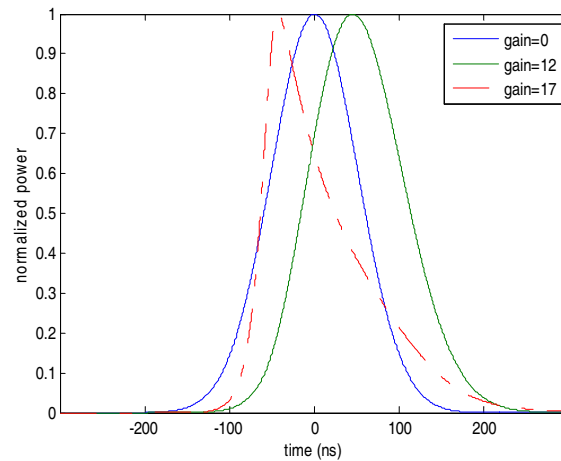


Figure 3: Normalized output Stokes pulse at gain = 0, 12, 17 with the gain coefficient  $g_0 = 5 \times 10^{-11} \text{ mW}$ .

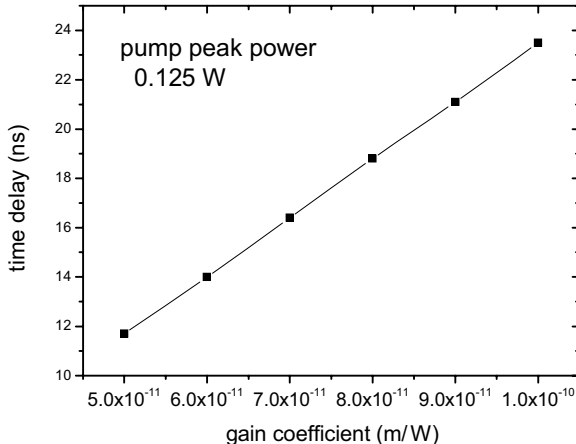


Figure 4: Time delay as a function of gain coefficient at a given pump power.

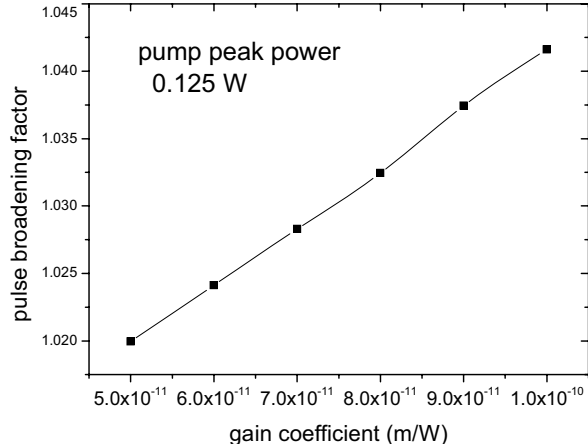


Figure 5: Pulse broadening as a function of gain coefficient at a given pump power.

Then we consider the time delay and pulse broadening factor varying with the gain coefficient at a given pump peak power 0.125 W shown in Fig. 4. We can see that the time delay increases with the increasing gain coefficient in a linear fashion. Fig. 5 shows that the pulse broadening factor also increases with the increasing gain coefficient. Note that the maximum gain parameter is 6.25 at the gain coefficient  $g_0 = 1 \times 10^{-10} \text{ m/W}$ , which satisfies the small signal condition.

#### 4. CONCLUSIONS

We make a numerical study of the SBS slow light in optical fibers, and consider the influences of gain coefficient on time delay and pulse broadening. In the small signal regime, we find that the time delay and the pulse broadening factor increase with the increasing gain coefficient. In the gain saturation regime, the pulse with larger gain coefficient decreases more quickly in the gain range of 0~16. For the gain larger than 16, the pulse advancement becomes more obviously and the distortion also becomes more seriously, which may render the delay useless. We also investigate the time delay and pulse broadening factor vary with the increasing gain coefficient at a given pump power whose gain parameter is in the small signal regime, and find that the time delay and pulse broadening factor are proportional to the gain coefficient.

#### ACKNOWLEDGMENT

This work was supported by the Natural Science Foundation of Gansu Province (Grant No. 1010RJZ A036), the Natural Science Foundation of Guangdong Province (Grant No. 110451170003004948) and Dongguan Science and Technology Program (Grant No. 2008108101002).

#### REFERENCES

1. Gehring, G. M., R. W. Boyd, A. L. Gaeta, D. J. Gauthier, and A. E. Willner, "Fiber-based slow-light technologies," *J. of Lightwave Techn.*, Vol. 26, No. 23, 3752–3762, 2008.
2. Zhu, Z., D. J. Gauthier, and R. W. Boyd, "Stored light in an optical fiber via stimulated Brillouin scattering," *Science*, Vol. 318, No. 5857, 1748–1750, 2007.
3. Hau, L. V., S. E. Harris, Z. Dutton, and C. H. Behroozi, "Light speed reduction to 17 metres per second in an ultracold atomic gas," *Nature*, Vol. 397, 594–598, 1999.
4. Bigelow, M. S., N. N. Lepeshkin, and R. W. Boyd, "Superluminal and slow-light propagation in a room-temperature solid," *Science*, Vol. 301, 200–202, 2003.
5. Song, K. Y., M. G. Herraez, and L. Thevenaz, "Observation of pulse delaying and advancement in optical fibers using stimulated Brillouin scattering," *Opt. Express*, Vol. 13, 82–88, 2005.
6. Abedin, K. S., "Observation of strong stimulated Brillouin scattering in single-mode As<sub>2</sub>Se<sub>3</sub> chalcogenide fiber," *Opt. Express*, Vol. 13, No. 25, 10266–10271, 2005.
7. Song, K. Y., K. S. Abedin, K. Hotate, M. G. Herraez, and L. Thevenaz, "Highly efficient Brillouin slow and fast light using As<sub>2</sub>Se<sub>3</sub> chalcogenide fiber," *Opt. Express*, Vol. 14, No. 13, 5860–5865, 2006.
8. Abedin, K. S. "Stimulated Brillouin scattering in single-mode tellurite glass fiber," *Opt. Express*, Vol. 14, No. 24, 11766–11772, 2006.

9. Jauregui, C., H. Ono, P. Petropoulos, and D. J. Richardson, "Four-fold reduction in the speed of light at practical power levels using Brillouin scattering in a 2-m bismuth-oxide fiber," *Conference on Optical Fiber Communication (OFC 2006)*, Paper PDP2, 2006.
10. Song, K. Y., M. G. Herraez, and L. Thevenaz, "Long optically-controlled delays in optical fibers," *Opt. Lett.*, Vol. 30, No. 14, 1782–1784, 2005.
11. Stenner, M. D., M. A. Neifeld, Z. Zhu, A. M. C. Dawes, and D. J. Gauthier, "Distortion management in slow-light pulse delay," *Opt. Express*, Vol. 13, No. 25, 9995–10002, 2005.
12. Schneider, T., R. Henker, K. U. Lauterbach, and M. Junker, "Comparison of delay enhancement mechanisms for SBS-based slow light systems," *Opt. Express*, Vol. 15, No. 15, 9606–9613, 2007.
13. Schneider, T., R. Henker, K. U. Lauterbach, and M. Junker, "Distortion reduction in slow light systems based on stimulated Brillouin scattering," *Opt. Express*, Vol. 16, No. 11, 8280–8285, 2008.
14. Herraez, M. G., K. Y. Song, and L. Thévenaz, "Arbitrary-bandwidth Brillouin slow light in optical fibers," *Opt. Express*, Vol. 14, No. 4, 1395–1400, 2006.
15. Zhu, Z., A. M. C. Dawes, D. J. Gauthier, L. Zhang, and A. E. Willner, "12-GHz-bandwidth SBS slow light in optical fibers," *Proc. of OFC 2006*, paper PD1, 2006.
16. Song, K. Y. and K. Hotate, "25 GHz bandwidth Brillouin slow light in optical fibers," *Opt. Lett.*, Vol. 32, No. 3, 217–219, 2007.
17. Zhu, Z., D. J. Gauthier, Y. Okawachi, J. E. Sharping, A. L. Gaeta, R. W. Boyd, and A. E. Willner, "Numerical study of all-optical slow-light delays via stimulated Brillouin scattering in an optical fiber," *J. Opt. Soc. Am. B*, Vol. 22, No. 11, 2378–2384, 2005.
18. Kalosha, V. P., L. Chen, and X. Bao, "Slow and fast light via SBS in optical fibers for short pulses and broadband pump," *Opt. Express*, Vol. 14, No. 26, 12693–12703, 2006.
19. Agrawal, G. P., *Nonlinear Fiber Optics*, Academic Press, California, 2002.
20. Damzen, M. J., V. I. Vlad, V. Babin, and A. Mocafanescu, *Stimulated Brillouin Scattering: Fundamentals and Applications*, IOP Publishing, 2003.

# Dual-concentric-core Photonic Crystal Fibers with Multi Outer Core Rings

I-Hung Tsai<sup>1</sup>, Der-Li Ye<sup>1</sup>, and Jui-Ming Hsu<sup>1, 2</sup>

<sup>1</sup>Department of Electro-Optical Engineering, National United University  
Miaoli, Taiwan 360, Taiwan R.O.C.

<sup>2</sup>Optoelectronics Research Center, National United University  
Miaoli, Taiwan 360, Taiwan R.O.C.

**Abstract**— To elastically design a dual-concentric-core photonic crystal fiber (DCC-PCF) for dispersion compensation, we use multi-layers of cladding holes as outer core rings. In previous study, the design of DCC-PCF with single outer core ring is difficult to give well consideration to wavelength-adjusting and maximum dispersion coefficient simultaneously. In this study, by using multi-layers of outer core ring, the maximum value of dispersion coefficient can be held and the adjustment of the compensated wavelength is unrestricted. The design-elasticity enlarges the negative chromatic dispersion significantly. The numeric results indicate that the minimum chromatic dispersion of the previous 1-ring DCC-PCF is about  $-7700 \text{ ps/km-nm}$  whereas that of the 3-ring DCC-PCF is about  $-10500 \text{ ps/km-nm}$  at around a wavelength of  $1.55 \mu\text{m}$ . Thus, the negative chromatic dispersion of the proposed structure is approximately 1.36 times larger than that of the previous one.

## 1. INTRODUCTION

In optical fiber communication systems, chromatic dispersion in single mode fibers (SMFs) induces temporal optical pulse broadening, resulting in serious restrictions in the transmission data rates. Currently, dispersion-compensating fibers (DCF) are extensively used to minimize the negative effects of chromatic dispersion. J. L. Auguste et al. reported a design of DCF by using a dual-concentric-core fiber (DCCF) structure. The dispersion coefficient of their DCCF was up to  $-1800 \text{ ps/nm-km}$  [1]. Recently, additional research involved altering the air hole size of a specific layer of PCF to design dual-concentric-core photonic crystal fibers (DCC-PCF) [2–5].

For previous studies, the DCC-PCF (referred to as 1-ring DCC-PCF in this study) was composed of two concentric cores to propagate two supermodes, which are named as inner and outer modes. To separate the two concentric cores, the cladding holes at a specific layer (which is referred to as outer core ring, OCR) in a DCC-PCF is reduced. Consequently, the mode-couple between inner and outer modes then results in a negative dispersion for the guiding mode. However, the size of holes at the OCR and in the cladding may all influence the value of dispersion coefficient and the compensated wavelength. Therefore, the design of DCC-PCF with single OCR is difficult to give well consideration to wavelength-adjusting and maximum dispersion coefficient simultaneously. In this work, to elastically design a DCC-PCF designing the compensated wavelength and the dispersion coefficient independently, we introduce three layers of OCR in a DCC-PCF structure (referred to as 3-ring DCC-PCF). Thus, the dispersion coefficient can be always kept at a maximum value when the compensated wavelength is adjusted.

## 2. SIMULATION MODELS AND THEORIES

Figures 1(a) and (b) show the cross-sectional views of the 1-ring and 3-ring DCC-PCFs respectively. The cladding of the photonic crystal fibers consists of a triangular lattice of air holes with a diameter of  $d = 1.350 \mu\text{m}$  and a pitch (center-to-center distance between the holes) of  $\Lambda = 1.500 \mu\text{m}$  in a background of undoped silica, whose refractive index can be estimated by using the Sellmeier equation [6]. The solid core is formed by removing a central air hole. The fourth layer of 1-ring DCC-PCF or the third, fourth and fifth layers of 3-ring DCC-PCF are with smaller air holes (with a diameter of  $d_r = 0.534 \mu\text{m}$ ,  $d_3 = 0.755 \mu\text{m}$ ,  $d_4 = 0.950 \mu\text{m}$  and  $d_5 = 0.755 \mu\text{m}$  respectively), which define the outer core ring, separate the cladding region into inner cladding and outer cladding.

Two types of structure can be considered for a 3-ring DCC-PCF, a symmetric type (with a diameter of  $d_3 = d_5$ ) and an asymmetric type ( $d_3 \neq d_5$ ). Fig. 2(a) depicts the relation between the effective indices and wavelength for 3-ring DCC-PCF of both types by using plane-wave expansion (PWE) method. The effective index curves of inner and outer modes are intersected at a phase-matching wavelength  $\lambda_0$ ,  $\lambda_0 \approx 1.55 \mu\text{m}$  in this work, which is designed as the operating wavelength

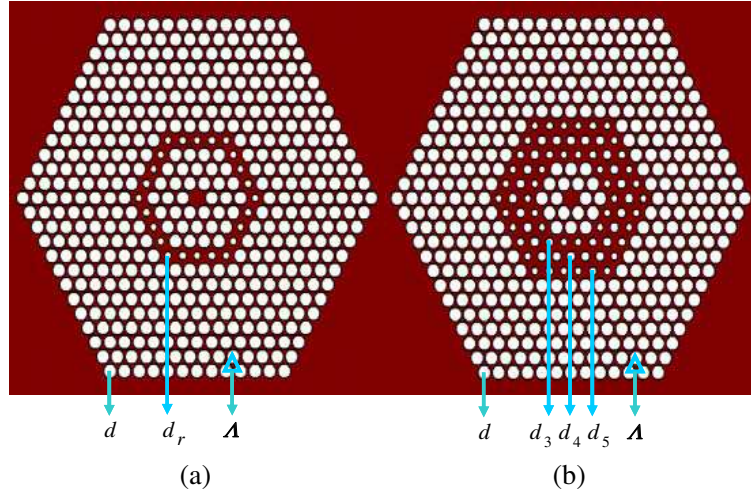


Figure 1: Cross-sectional view of (a) previous structure (1-ring DCC-PCF) and (b) proposed structure (3-ring DCC-PCF).  $\Lambda = 1.500 \mu\text{m}$ ,  $d = 1.350 \mu\text{m}$ ,  $d_r = 0.534 \mu\text{m}$ ,  $d_3 = d_5 = 0.755 \mu\text{m}$ ,  $d_4 = 0.950 \mu\text{m}$ .

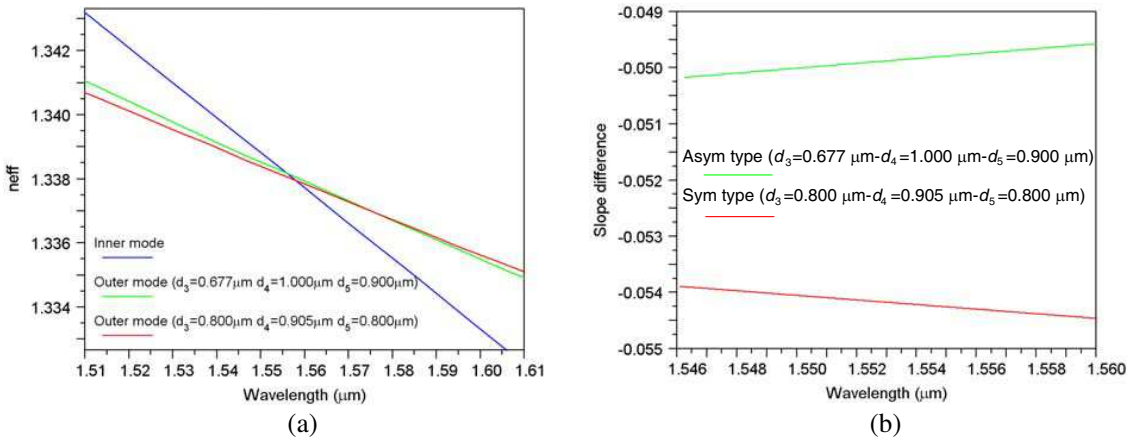


Figure 2: Relations of (a) the effective indices and (b) slope differences between outer and inner mode to wavelengths for symmetric and asymmetric type DCC-PCFs.  $\Lambda = 1.500 \mu\text{m}$ ,  $d = 1.350 \mu\text{m}$ .

for dispersion compensation. The fundamental mode coincides with the inner mode at wavelengths of  $\lambda < \lambda_0$ . Nevertheless, at wavelengths of  $\lambda > \lambda_0$ , the fundamental mode switches to the outer mode. The chromatic dispersion coefficient  $D$  is defined as

$$D = \frac{-\lambda}{c} \frac{d^2 n_{eff}}{d\lambda^2}, \quad (1)$$

where  $\lambda$  represents the wavelength,  $c$  is the speed of light in a vacuum, and  $n_{eff}$  is the effective indices of the fundamental modes guided in a fiber at various wavelengths. According to Equation (1), the chromatic dispersion coefficient  $D$  at  $\lambda_0$  signifies the transient rate of break, i.e., the slope difference between effective index curves of inner and outer modes. The inner mode distributions of symmetric and asymmetric types are identical. Therefore, the smaller the slope of outer mode curve, the larger the absolute value of  $D$ .

### 3. NUMERICAL RESULTS AND DISCUSSIONS

As shown in Fig. 2(a), the  $n_{eff}$ -curve of outer mode for the asymmetric type DCC-PCF ( $d_3 = 0.677 \mu\text{m}$  and  $d_5 = 0.900 \mu\text{m}$ ) is steeper than that of the symmetric one ( $d_3 = d_5 = 0.800 \mu\text{m}$ ). Fig. 2(b) shows the dependence of the slope difference between outer and inner mode on wavelengths for these two types. As shown in the figure, the slope difference of the symmetric type is larger than that of the asymmetric one. This predicts that the chromatic dispersion  $D$  of a symmetric type DCC-PCF is larger than that of the asymmetric one. Therefore, this study focuses on the symmetric OCR structure from now on.

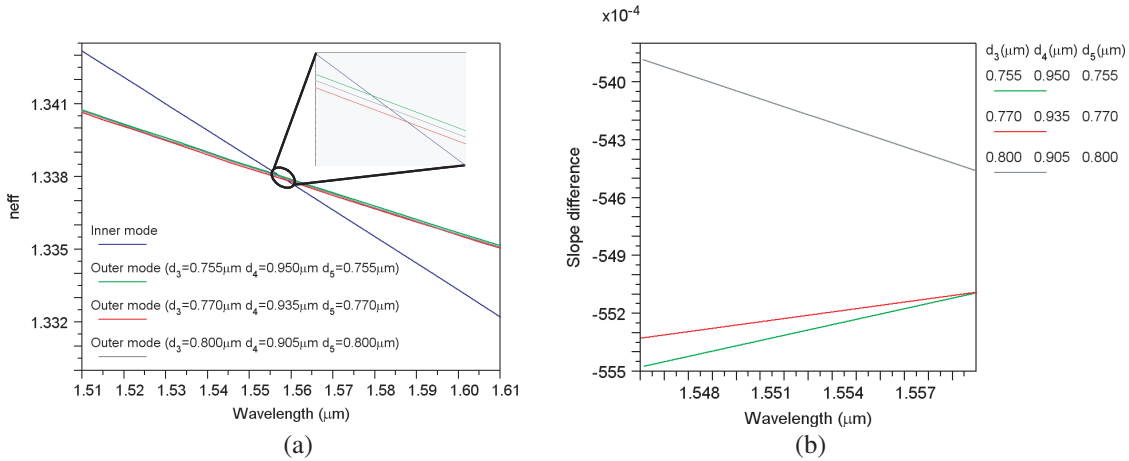


Figure 3: Dependence of the (a) effective indices and (b) slope difference between outer and inner mode on wavelengths for some structures.  $\Lambda = 1.500 \mu m$ ,  $d = 1.350 \mu m$ .

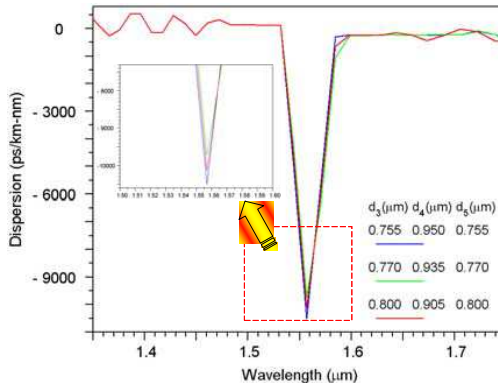


Figure 4: Dependence of the dispersion coefficient on wavelength for the structures previously mentioned in Fig. 3.  $\Lambda = 1.500 \mu m$ ,  $d = 1.350 \mu m$ .

Some tailor tendencies for OCR-design were generalized from several simulation results. For a symmetric OCR structure, tailoring the hole-size of middle OCR-layer (fourth layer) can alter the phase-matching wavelength  $\lambda_0$ , while the hole-size of both sides of OCR-layer (third and fifth layers) determines the slope of  $n_{eff}$ -curve of outer mode. Some symmetric OCR DCC-PCFs are simulated for  $\lambda_0 \approx 1.55 \mu m$ . Fig. 3(a) indicates the dependence of the effective indices on wavelengths for these structures; the inset is a magnified plot of a section. It is difficult to recognize which one of outer mode  $n_{eff}$ -curve is flatter in Fig. 3(a), thus the slope differences between outer and inner modes are estimated and shown in Fig. 3(b). As shown in Fig. 3(b), the slope difference of the DCC-PCF with  $d_3 = d_5 = 0.755 \mu m$  and  $d_4 = 0.950 \mu m$  is a largest one. This predicts that the chromatic dispersion  $D$  of this structure will be maximum. By substituting  $n_{eff}$  into Equation (1), we can evaluate the dispersion coefficient  $D$ . Fig. 4 indicates the dependence of the chromatic dispersion coefficient on wavelength for all of the structures mentioned above in Fig. 3. Just as expectancy, the dispersion coefficient  $D$  of the DCC-PCF with  $d_3 = d_5 = 0.755 \mu m$  and  $d_4 = 0.950 \mu m$  is the largest. Numerically, the minimum chromatic dispersion of the proposed multi-OCR DCC-PCF (with  $\Lambda = 1.500 \mu m$ ,  $d = 1.350 \mu m$ ,  $d_3 = d_5 = 0.755 \mu m$ ,  $d_4 = 0.950 \mu m$ ) is about  $-10500 \text{ ps/km-nm}$  at around a wavelength of  $1.55 \mu m$ .

To compare the proposed structure with a previous 1-ring DCC-PCF, the dispersion value of an optimum-designing 1-ring DCC-PCF is evaluated in this article. The hole diameter of  $d_r = 0.534 \mu m$  for the OCR in the 1-ring DCC-PCF is deliberately designed to locate the phase-matching wavelength at the wavelength of  $1.55 \mu m$ . Fig. 5 shows the dependence of the chromatic dispersion coefficient on wavelength for the previous (1-ring) and the proposed (3-ring) DCC-PCF. As shown in the figure, the 1-ring DCC-PCF has a minimum chromatic dispersion of about  $D \approx -7700 \text{ ps/km-nm}$  whereas the 3-ring DCC-PCF has a minimum chromatic dispersion of about  $D \approx -10500 \text{ ps/km-nm}$ .

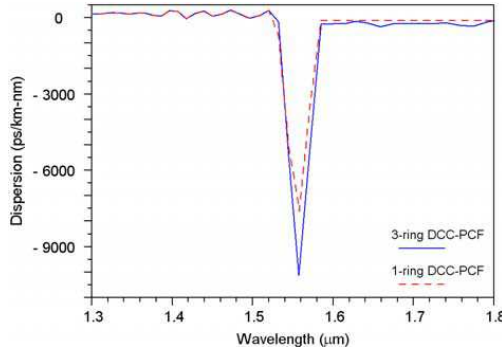


Figure 5: Dependence of the chromatic dispersion on wavelength for the previous (1-ring) and the proposed (3-ring) DCC-PCF.

nm at around a wavelength of  $1.55\text{ }\mu\text{m}$ . Thus, the negative chromatic dispersion of the proposed DCC-PCF is approximately 1.36 times larger than that of the previous one.

#### 4. CONCLUSIONS

This article proposes an elastic method for designing a DCC-PCF for dispersion compensation. In previous structure with single outer core ring, the design of DCC-PCF is difficult to give well consideration to wavelength-adjusting and maximum dispersion coefficient simultaneously. In this study, by using multi layers of outer core ring, the dispersion coefficient can be always kept at a maximum value when the compensated wavelength is adjusted. The numerical results exhibit that the negative chromatic dispersion coefficient for the proposed DCC-PCF is approximately 1.36 times greater than that of the previous work at around a wavelength of  $1.55\text{ }\mu\text{m}$ .

#### REFERENCES

1. Auguste, J.-L., J.-M. Blondy, J. Maury, B. Dussardier, G. Monnom, R. Jindal, K. Thyagarajan, and B. P. Pal, “Conception, realization, and characterization of a very high negative chromatic dispersion fiber,” *Opt. Fiber Technol.*, Vol. 8, No. 1, 89–105, 2002.
2. Gerome, F., J.-L. Auguste, and J.-M. Blondy, “Design of dispersion-compensating fibers based on a dual-concentric-core photonic crystal fiber,” *Opt. Lett.*, Vol. 29, No. 23, 2725–2727, 2004.
3. Ni, Y., L. Zhang, L. An, J. Peng, and C. Fan, “Dual-core photonic crystal fiber for dispersion compensation,” *IEEE Photon. Technol. Lett.*, Vol 16, No. 6, 1516–1518, 2004.
4. Varshney, S. K., K. Saitoh, and M. Koshiba, “A novel design for dispersion compensating photonic crystal fiber Raman amplifier,” *IEEE Photon. Technol. Lett.*, Vol. 17, No. 10, 2062–2064, 2005.
5. Fujisawa, T., K. Saitoh, K. Wada, and M. Koshiba, “Chromatic dispersion profile optimization of dual-concentric-core photonic crystal fibers for broadband dispersion compensation,” *Opt. Express*, Vol. 14, No. 2, 893–900, 2006.
6. Malitson, I. H., “Interspecimen comparison of the refractive index of fused silica,” *J. Opt. Soc. Am.*, Vol. 55, No. 10, 1205–1209, 1965.

# Polarization-maintaining Photonic Crystal Fiber with Ultra-high Modal Birefringence

Jui-Ming Hsu<sup>1,2</sup> and Der-Li Ye<sup>1</sup>

<sup>1</sup>Department of Electro-Optical Engineering, National United University  
Miaoli 360, Taiwan, R.O.C.

<sup>2</sup>Optoelectronics Research Center, National United University  
Miaoli 360, Taiwan, R.O.C.

**Abstract**— To achieve a polarization-maintaining photonic crystal fiber (PM-PCF) with ultra-high modal birefringence, three types of photonic crystal fiber geometric structure, named as 8 Large-Holes (type I), 10 Large-Holes (type II) and Air-Walls (type III) structures, are simulated and compared with each other. The numeric results indicate that the birefringence of type III is largest in the three types of structure, but the fabrication of the Air-Wall is quite difficult. The birefringence of type II is just less than that of type III slightly; nevertheless, its fabrication process is considerably simpler than that of type III. Therefore, type II can be chosen as a compromising approach. For the eventual design, the birefringence of the proposed PM-PCF (type II) at  $\lambda = 1544.6 \text{ nm}$  is up to  $26.98 \times 10^{-3}$ .

## 1. INTRODUCTION

In conventional single mode fibers (SMF), unpredictable birefringence brings about polarization-mode dispersion (PMD) and induces pulse broadening; results in serious restrictions in the data rates of high-speed optical communication links. Conventional polarization-maintaining fibers (PMF, such as elliptical core fibers, bowtie structured fibers, and PANDA fibers) with a modal birefringence about  $5 \times 10^{-4}$  typically, which are designed to significantly reduce the governing factor of small random birefringence fluctuations.

Recently many articles used photonic crystal fibers (PCF) to realize a polarization-maintaining photonic crystal fiber (PM-PCF) [1–6]. Modal birefringence of about  $10^{-3}$  order is achieved typically for PM-PCF at a wavelength of  $1.55 \mu\text{m}$ . T. P. Hansen et al. designed two neighboring solid rods to consist an asymmetric elliptical core [3]. T. Nasilowski et al. used three solid rods instead of using two rods to form a highly elliptical core [5]. M. Chen et al. used three solid rods and four big elliptical air-holes to replace the holes nearest the central rod [6].

In this study, three types of PM-PCF are simulated and compared with each other. Type I with three solid rods is similar to the structures of [5, 6]; nevertheless, eight larger holes are used near the elliptical core instead of cladding holes or big elliptical holes. Types II and III in this work are more novel structure. Finally, a compromising approach can be selected as a proposed PM-PCF with some tradeoff between birefringence and fabrication-difficulty.

## 2. SIMULATION MODELS

The cross-sectional views of three types of PM-PCF structure are shown in Figures 1(a), (b) and (c), respectively. Figure 1(a) indicates the type I, named as 8 Large-Holes in this study, structure with three solid rods and eight large holes near the elliptical core. The PCF consists of a triangular lattice of cladding holes with a diameter of  $d_S = 1.00 \mu\text{m}$ , and a pitch of  $\Lambda = 1.56 \mu\text{m}$ . The eight large holes (colored in yellow) with a diameter of  $d_L$  situated at both sides of the elliptical core. Figure 1(b) shows the structure of type II, which is named as 10 Large-Holes in this study. In this structure, five large-holes (colored in yellow) with a diameter of  $d_L$  at each side of the elliptical core touch side-by-side with each other inseparably. To compare the birefringence between these two types of PM-PCF structure, the diameters  $d_S$  and  $d_L$  are identical for types I and II. Therefore,  $w = 3\Lambda + d_L$  in Figure 1(a) must be equal to  $w = 5d_L$  in Figure 1(b); as a result,  $d_L = 3\Lambda/4 = 1.17 \mu\text{m}$ . Figure 1(c) exhibits the structure of type III, which is named as Air-Walls in this study. For the sake of comparing with types I and II again, two air-walls with a height of  $h = d_L$  and a width of  $w$ , which is equal to the  $w$  of types I and II, are used in place of four and five large holes in types I and II.

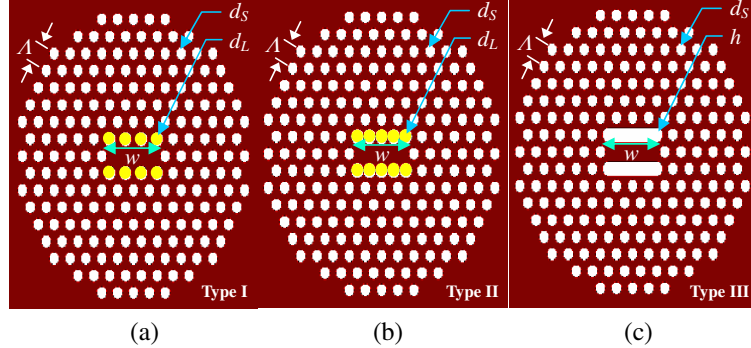


Figure 1: Cross-sectional views of PM-PCF with (a) 8 large-holes, (b) 10 large-holes and (c) air-walls structures.  $\Lambda = 1.56 \mu\text{m}$ ,  $d_S = 1.00 \mu\text{m}$ ,  $d_L = h = 1.17 \mu\text{m}$ .

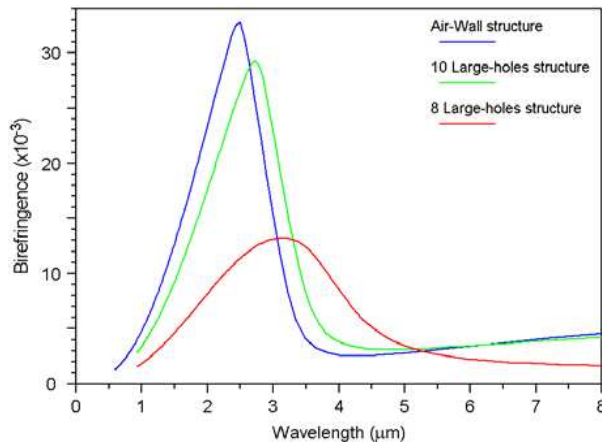


Figure 2: Dependence of birefringence on wavelength for PM-PCFs shown in Figure 1.

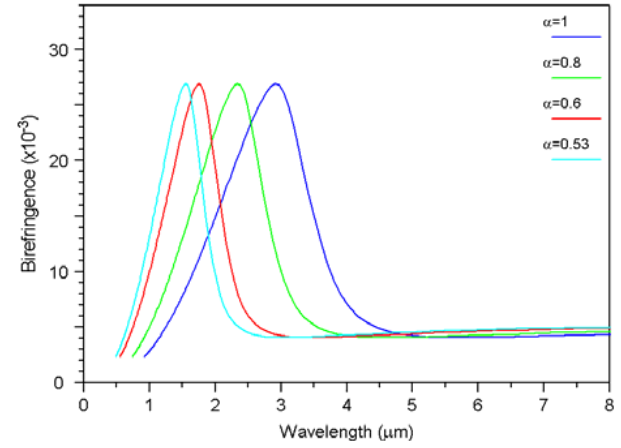


Figure 3: Relationship between birefringence and wavelength for the proposed PM-PCF (type II) with different shrink ratio  $\alpha$ .

### 3. NUMERICAL RESULTS AND DISCUSSIONS

The mode birefringence of a fiber is defined as the difference in effective refractive index of the slow mode and fast mode:

$$B = |n_{slow} - n_{fast}| \quad (1)$$

where  $B$  is the mode birefringence of a fiber,  $n_{slow}$  and  $n_{fast}$  represent the effective refractive index of the slow mode and fast mode, respectively. In this study,  $n_{slow}$  and  $n_{fast}$  can be evaluated by means of the plane-wave expansion (PWE) method to simulate each structure; the  $B$  values at a range of wavelength are then figured out by using Equation (1).

Figure 2 shows the dependence of birefringence on wavelength for three types of PM-PCFs shown in Figure 1. As shown in Figure 2, the birefringence value of type III is largest among the three types of structure. However, for carrying out the Air-Walls in the fiber is quite difficult. The modal birefringence of type II is just less than that of type III slightly. On the contrary, it is greatly larger than that of type I. Nevertheless, its fabrication process is considerably simpler than that of type III. Therefore, type II can be chosen as a compromising approach in this study.

For the structure of 10 Large-Holes, Figure 2 reveals that the maximum value of birefringence is occurred at a wavelength which is too far from the habitual wavelength of optical-fiber communications ( $1.55 \mu\text{m}$ ). To shift the maximum-birefringence wavelength toward a wavelength of  $1.55 \mu\text{m}$  while still keeping its birefringence at an original value, we attempted to shrink the whole structure with a scale-reduction factor  $\alpha$  ( $\alpha$  is named as shrink ratio in this work). For the sake of convenience, the  $\alpha$  is defined as a shrink ratio of geometric parameter while the structure is scaled down with the hole-diameters ( $d_S$ ,  $d_L$ ) and pitch ( $\Lambda$ ) in a same rate. Figure 3 indicates the relationship between the birefringence and wavelength for the proposed PM-PCF (type II) with different shrink ratio  $\alpha$ . For the case of  $\alpha = 1$ , the structure represents an unshrink PM-PCF of

type II. Therefore, the curve of birefringence for  $\alpha = 1$  (blue curve) shown in Figure 3 is identical to that of 10 Large-Holes structure (green curve) shown in Figure 2. As shown in Figure 3, the maximum values of birefringence for each shrunken structure are almost identical. However, the wavelength that a maximum birefringence occurred is shifted to a shorter wavelength when  $\alpha$  is decreased. Ultimately, an appropriate value of  $\alpha = 0.53$  is selected through several numerical calculations as shown in Figure 3. The geometric parameters of the proposed PM-PCF (10 Large-Holes structure) are recorded as follows: the pitch of  $\Lambda = 1.56 \times 0.53 \approx 0.83 \mu\text{m}$ , the cladding-holes diameter of  $d_S = 1.00 \times 0.53 = 0.53 \mu\text{m}$ , the large-holes diameter of  $d_L = 1.17 \times 0.53 \approx 0.62 \mu\text{m}$ . The birefringence value is up to  $26.98 \times 10^{-3}$  at a wavelength of 1544.6 nm.

#### 4. CONCLUSION

Three types of elliptical core polarization-maintaining photonic crystal fiber are compared with each other by their modal birefringence values. The Air-Walls structure (type III) has a largest birefringence among the three types of structure. However, the fabrication of the Air-Walls is quite difficult to achieve a PM-PCF of type III. The 8 Large-Holes structure (type I) is easy to realize, but its birefringence is smallest among the three types of structure. As a happy medium, the 10 Large-Holes structure (type II) not only has a large birefringence value close to an Air-Walls structure but is easy to carry out. For a 10 Large-Holes structure, to shift the wavelength for maximum birefringence occurred toward the habitual wavelength of optical-fiber communications ( $1.55 \mu\text{m}$ ), we shrink the whole structure with an appropriate ratio. Ultimately, the birefringence of the proposed PM-PCF with a pitch of  $0.83 \mu\text{m}$ , a cladding-holes diameter of  $0.53 \mu\text{m}$ , and a large-holes diameter of  $0.62 \mu\text{m}$  is up to an ultra-high value of about  $27 \times 10^{-3}$  at a wavelength of 1544.6 nm.

#### REFERENCES

1. Ortigosa-Blanch, A., J. C. Knight, W. J. Wadsworth, J. Arriaga, B. J. Mangan, T. A. Birks, and P. S. S. J. Russell, "Highly birefringent photonic crystal fibers," *Opt. Lett.*, Vol. 25, No. 18, 1325–1327, 2000.
2. Suzuki, K., H. Kubota, S. Kawanishi, M. Tanaka, and M. Fujita, "Optical properties of a low-loss polarization-maintaining photonic crystal fiber," *Opt. Express*, Vol. 9, No. 13, 676–680, 2001.
3. Hansen, T. P., J. Broeng, S. E. B. Libori, E. Knudsen, A. Bjarklev, J. R. Jensen, and H. R. Simonsen, "Highly birefringent index-guiding photonic crystal fibers," *IEEE Photon. Technol. Lett.*, Vol. 13, No. 6, 588–590, 2001.
4. Sun, Y. S., Y. F. Chau, H. H. Yeh, L. F. Shen, T. J. Yang, and D. P. Tsai, "High birefringence photonic crystal fiber with a complex unit cell of asymmetric elliptical air hole cladding," *Appl. Opt.*, Vol. 46, No. 18, 5276–5281, 2007.
5. Nasilowski, T., et al., "Temperature and pressure sensitivities of the highly birefringent photonic crystal fiber with core asymmetry," *Appl. Phys. B*, Vol. 81, 325–331, 2005.
6. Chen, M., S. G. Yang, F. F. Yin, H. W. Chen, and S. Z. Xie, "Design of a new type high birefringence photonic crystal fiber," *Optoelectron. Lett.*, Vol. 4, No. 1, 19–22, 2008.

# Toughened Epoxy Filled with Ferromagnetic Particles as High Temperature Resistant Microwave Absorbing Coating

Zhenjiang Song, Jianliang Xie, Jianing Peng, Peiheng Zhou, and Longjiang Deng

State Key Laboratory of Electronic Thin Films and Integrated Devices

University of Electronic Science and Technology of China, Jianshe Road, Chengdu 610054, China

**Abstract**— In this work, microwave absorbing coatings consisted of toughened epoxy and ferromagnetic particles were prepared. The epoxy groups and isocyanate groups were investigated by Fourier Transform Infrared (FTIR) spectroscopy. Mechanical properties of the coatings are effectively improved comparing with the one employing unmodified epoxy in room temperature. After heat treat at 150°C for approximate 100 hours, the coatings still have special impact strength between 45 and 50 Kg·cm according to Chinese National Standards GB 1732–1993 and flexibility about 2–3 mm according to Chinese National Standards GB 6742-2007. Complex permittivity  $\epsilon(f)$  and permeability  $\mu(f)$  of the ferromagnetic particles were measured using network analyzer in the frequency range from 2 to 18 GHz, to explain the reflection loss behavior of the coatings tested in microwave chamber. The morphology of ferromagnetic particles and their random dispersion in the coatings were observed by field emission scanning electron microscope (FESEM).

## 1. INTRODUCTION

Electromagnetic absorbing materials are used for a wide range of businesses [1], especially the kind of absorbing coatings because of their simple techniques and convenient operation. With good performance properties, such as size stability, creep resistance, and strength, epoxy resins are studied as an attractive material at coatings [2]. However, epoxy resins also have disadvantage at brittleness due to the reported three-dimension network [3]. Therefore, we toughened the epoxy resins with a prepolymer which were isocyanate-terminated in this work. After mixing with ferromagnetic particles, the microwave absorbing coatings are prepared.

## 2. EXPERIMENTAL

### 2.1. Materials and Fabrication of Polyurethane

Polyester with an average molecular weight of 1,000 g/mol was used to fabricate the polyurethane with 2,4-toluene diisocyanate (TDI) and pretreated by drying under a vacuum to remove moisture. Dibutyl tin dilaurate (DBTD) and other chemical reagents were used as-received. The isocyanate-terminated prepolymers of polyurethane (PU) were prepared by reaction between the hydroxyl of polyester and the isocyanate (NCO) of TDI. Firstly, 100 g polyester was added into 200 g dimethylbenzene as solvent in a three-necked glass flask in nitrogen atmosphere. After that, the flask was preheated to about 60°C in an oil bath. Then the mixture of the calculated TDI, 0.5 g DBTD, and dimethylbenzene were poured slowly into the flask with vigorous agitation. The temperature of polymerized was controlled at about 85°C for two hours. The progress of the reaction was monitored by measuring the content of NCO groups in the isocyanate-terminated prepolymers according to Chinese Chemical Industry-standard HG 2409-1992. When the content of NCO was almost constant, the reaction was considered to be complete. The chemical structure of isocyanate-terminated prepolymer is shown in Chart 1.

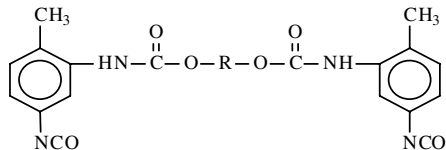


Chart 1 Schematic chemical structure of isocyanate-terminated prepolymer.

## 2.2. Preparation of Microwave Absorbing Coatings

Diglycidyl ether of bisphenol A epoxy resin (EP) having an epoxy value of about 0.02–0.04eq./100 g was a commercial product(supplied by Wuxi Resin Factory of Blue Star New Chemical Materials Co., Ltd.). Before used, the solid EP was dissolved in the mixture of butanone and cyclohexanone.

Microwave absorbing coatings was prepared by incorporating 80 wt.% ferromagnetic particles into the compound of EP and PU. The mixtures were poured into a mold and cured at room temperature for seven days. The specimen was cut to a thin sheet with thickness of 3.5 mm, and then processed into cylindrical toroidal shape with inner diameters 3.00 mm and outer diameters 7.00 mm, for relative complex permittivity ( $\epsilon_r = \epsilon' - j\epsilon''$ ) and permeability ( $\mu_r = \mu' - j\mu''$ ) test using the transmission/reflection coaxial line method.

For mechanical properties test, the mixtures were coated on a 5 mm × 5 mm metal plate for impact strength and adhesion test, and a 5 mm × 12 mm rectangular sectors for flexibility test through an air compressor by atomizing method.

## 2.3. Characterization

Fourier transform infrared (FTIR) spectra were obtained using Bruker Tensor 27 at transmission mode in the spectral range from 4000 to 400 cm<sup>-1</sup>. Firstly, the powder KBr was compressed into a pellet, then the liquid polmer were directly daubed onto the KBr pellet.

The ferromagnetic particles and their random dispersion in the coatings were observed by field emission scanning electron microscope (Model JSM-7600F, JEOL, Tokyo, Japan).

The moisture attaching to the ferromagnetic particles was analysed by thermo-gravimetric analyses (TG, Netzsch STA 449) carrying out from 40° to 800° with nitrogen protection, flow rate 22 ml/min, at the heating rate of 10 K/min · PU, EP, and toughened EP were examined by differential scanning calorimetry (DSC) also using STA 449 at the heating rate of 10 K/min under nitrogen atmosphere.

Agilent 8720 ET network analyser was used to measure the specimen of cured coating within the frequency range of 0.5–18 GHz.

Impact strength was tested according to Chinese National Standards GB 1732-1993 determination of impact resistance of film. Flexibility was tested according to Chinese National Standards GB/T 6742-2007 paints and varnishes-bend test (cylindrical mandrel). Adhesion was tested according to Chinese National Standards GB/T 5210-2006 paints and varnishes-pull-off test for adhesion.

## 3. RESULT AND DISCUSSION

### 3.1. The Chemical Structure of PU and the Toughened EP with PU

In Fig. 1, FTIR spectrum of NCO shows a broad and intense absorption at around 2270 cm<sup>-1</sup>. Besides, the N-H bands are characterized at 3298 cm<sup>-1</sup> and 1536 cm<sup>-1</sup>. The band around 1109 cm<sup>-1</sup> is attributed to the vibration of eater -C-O. The C = O from the chemical reaction of NCO and OH are observed at 1730 cm<sup>-1</sup> [4, 5]. Consequently, the desired preplymer is obtained (Chart 1).

From Fig. 2, we could speculate the main chemical strcture of the toughened EP. At the prime phase of mixing EP with PU, epoxy characteristic absorption at 910 cm<sup>-1</sup> and absorption

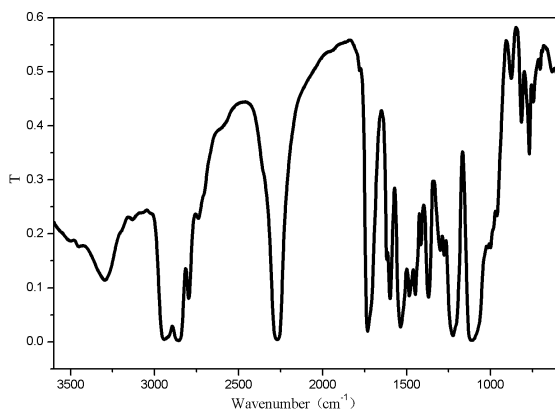


Figure 1: FTIR spectrum of the polyurethane composite.

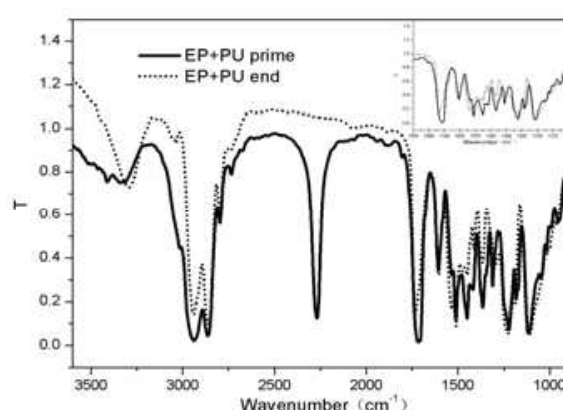


Figure 2: FTIR spectrum of the mixture of EP and PU.

at  $2270\text{ cm}^{-1}$  belonging to NCO group are distinct shown in Fig. 2. In the inset of Fig. 2, FTIR spectrum of the wavenumbers range of  $850$  to  $1900\text{ cm}^{-1}$  are given. After toughen process finished, the FTIR spectrum exhibits an intensive absorption band of urethane group at  $1730\text{ cm}^{-1}$ , with a drop of NCO group absorption at  $2270\text{ cm}^{-1}$ , and the pendant secondary hydroxyl groups (-OH) absorption on the epoxy resin spectrum at  $3470\text{ cm}^{-1}$  shifted to lower wavenumber, like the absorption band of N-H at  $3298\text{ cm}^{-1}$  [6]. The epoxy characteristic absorption at  $910\text{ cm}^{-1}$  also shifts to a lower wavenumber. The epoxy cycle does not react with NCO groups without a catalyst [6]. However, catalyst DBTD engaged in the prepared process of PU prepolymer may survive, so the reaction of oxazolidone formation may occur, and the main chemical groups reaction are shown in Chart 2.

### 3.2. The Microstructure of the Microwave Absorbing Coatings and Its Molecular Level Explain of High Temperature Resistance

Figure 3 shows the random dispersion of particles in as-prepared coatings. In Fig. 4, from DSC curve of the toughened EP, the exothermal peak in the range of  $150$ – $270^\circ$  belongs to the reaction of oxazolidone formation, which is the chemical structure for high temperature resistance [7]. Different from conventional epoxy resins which is rather brittle resulted from the three-dimension network, our EP toughened with PU exhibits excellent flexibility due to its semi-IPN structure [8]. We have tested the mechanical properties of the coatings, and listed in Table 1. Cured at room temperature for seven days, the coatings show good mechanical properties. Even high temperature treated, the coatings possess promising flexibility based on its molecular level thermal stability.

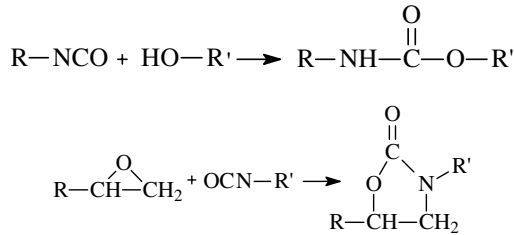


Chart 2 Urethane formation and oxazolidone formation.

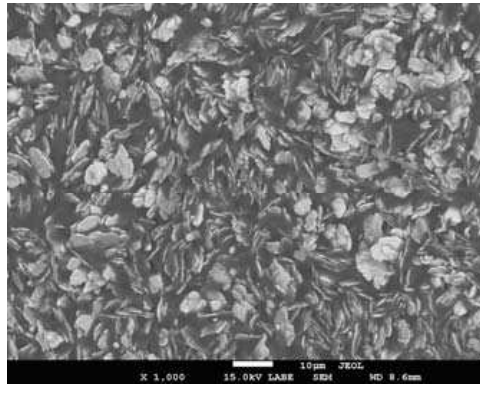


Figure 3: SEM of coating section.

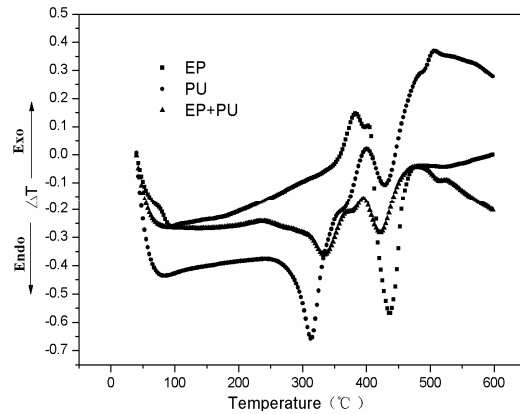


Figure 4: DSC of EP,PU, and the mixture of EP and PU.

Table 1: Mechanical properties of the microwave absorbing coatings.

	<i>Impact strength /Kg · cm</i>	<i>Flexibility /mm</i>	<i>Adhesion /MPa</i>
Coatings	50	2	14.78
Treated coatings	50	2–3	—

Coatings: cured at room temperature for seven days

Treated coatings: high temperature treated at  $150^\circ$  for 80 hours after cured completely.

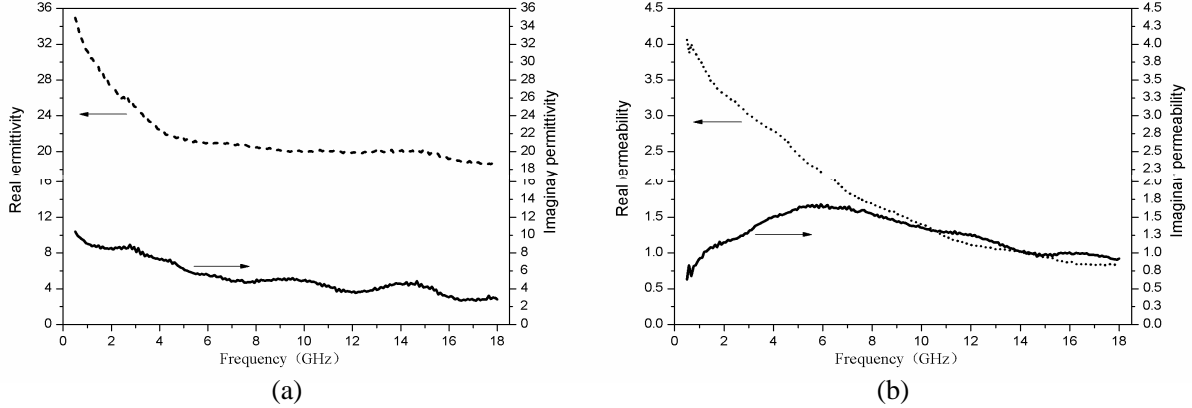


Figure 5: Electromagnetic parameters of the coatings: (a) complex permittivity  $\epsilon$ ; (b) complex permeability  $\mu$ .

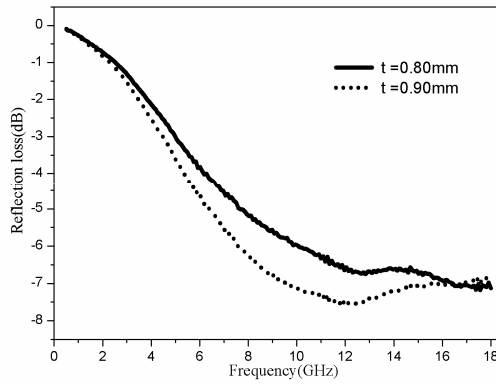


Figure 6: Reflection loss plot of coatings with thickness at 0.80 mm and 0.90 mm.

### 3.3. The Microwave Absorbing Property of the Microwave Absorbing Coatings

Based on the complex permittivity  $\epsilon(f)$  and permeability  $\mu(f)$  of the testing sample, we can obtain the reflection loss RL of this microwave absorbing coatings. The following equation is given for a single-layer absorbing layer [9]:

$$RL \text{ (dB)} = 20 \log |(Z_{in} - Z_0) / (Z_{in} + Z_0)| \quad (1)$$

$$Z_{in} = Z_0 \sqrt{(\mu_r / \epsilon_r)} \tanh \{j (2\pi f t / c) \sqrt{\mu_r \epsilon_r}\} \quad (2)$$

where  $Z_0$  is the impedance of free space,  $Z_{in}$  is the input impedance;  $\mu_r$  and  $\epsilon_r$  are the relative complex permeability and permittivity of the absorbing layer, respectively;  $f$  is the frequency of the electromagnetic wave;  $t$  is the coatings thickness;  $c$  is the velocity of light.

The complex permittivity and permeability of the specimen of the coatings are shown in Fig. 5.

Using the Equation (1), (2) and the parameters tested above, the RL can be evaluated as shown in Fig. 6. Microwave absorbing coatings with 0.80 mm and 0.90 mm thickness are designed. The RL values exceeding  $-6$  dB are achieved in the frequency range of 8 GHz to 18 GHz with the thickness 0.9 mm. So our prepared coatings may be applied as microwave absorbers for X- and Ku-band frequencies.

## 4. CONCLUSION

The toughened EP with PU are prepared and characterized by structural, compositional and morphological tests. Coatings with good mechanical properties are obtained, especially at high temperature resistance. Molecular level reasons for above merits of designed coatings are given. Electromagnetic parameters and RL of the microwave absorbing coatings indicate potential in practical application. This kind of coatings has light weight as well as excellent impact strength, flexibility, and adhesion.

**REFERENCES**

1. Vinoy, K. J. and R. M. Jha, *Radar Absorbing Materials*, Kluwer Academic Publishers, Boston, MA, 1996.
2. Lin, J., "High performance epoxy resin nanocomposites containing both organic montmorillonite and castor oil-polyurethane," *Polymer Bulletin*, Vol. 56, 377–384, 2006.
3. Iijima, T., S. Miura, W. Fukuda, et al., "Effect of cross-link density on modification of epoxy resins by n-phenylmaleimide-styrene copolymers," *European Polymer Journal*, Vol. 29, 1103–1113, 1993.
4. Hsieh, K. H. and J. L. Han, "Graft interpenetrating polymer networks of polyurethane and epoxy. I. Mechanical behavior," *Journal of Polymer Science: Part B: Polymer Physics*, Vol. 28, 623–630, 1990.
5. Rudolf, M., D. Lauerer, and M. Dahm, "IR spectroscopic studies of urethane foam formation," *Journal of Cellular Plastics*, Vol. 4, 262–275, 1968.
6. Kadurina, T. I., V. A. Prokopenko, and S. I. Omelchenko, "Curing of epoxy oligomers by isocyanates," *Polymer*, Vol. 33, 3853–3864, 1992.
7. Rudolf, M., "Synthesis of heterocyclic ring systems for heat-resistant plastics from polyisocyanates," *Angewandte Chemie International Edition in English*, Vol. 10, 294–301, 1971.
8. Thapliyal, P. C., "Interpenetrating polymer networks," *Composite Interfaces*, Vol. 17, 85–89, 2010.
9. Maeda, T., S. Sugimoto, T. Kagotani, et al., "Effect of the soft/hard exchange interaction on naturalresonance frequency and electromagnetic wave absorption of the rare earthironboron compounds," *Journal of Magnetism and Magnetic Materials*, Vol. 281, 195–205, 2004.

# Influence of Localized Surface Plasmon on Radiation Pattern of Nano-optical Antenna

S. F. Jiang, H. Gao, F. M. Kong, and K. Li

School of Information Science and Engineering, Shandong University, Jinan 250100, China

**Abstract**— Two optical dipole antennas (ODA) models comprised of a pair of gold nanorods (PNRs) and a pair of gold nanoellipsoids (PNEs) are introduced in this paper. Their far-field directivities at 600 nm are carefully studied by FDTD method. We find the radiation pattern of ODA is analogous to that of dipole antenna but the side-lobes occur more easily and earlier as the total length of ODA increases owing to existing of localized surface plasmon (LSP). In this paper, we present an analysis and explore on the influence of LSP on radiation pattern of ODA. Our results hold a great promise for improving the performance of optical antennas for various applications.

## 1. INTRODUCTION

Recent research in nano-optics and plasmonics has generated considerable interest in the optical antennas, and some studies are currently focused on how to transplant classical radio wave and microwave antenna theories into the optical frequency regime [1–7]. By analogy to classical antenna theory [8], the far-field directivity for an optical antenna is also a very important parameter because the appropriate far-field directivities are need for different applications. Taminiau et al. [9] only study the angular emission of a single emitter near a metallic nanoparticle by experiments and numerical calculation. Besides, Gao et al. [10] study two ODA models (PNRs and PNEs) and put forward an inference that surface plasmon polaritons might strongly influence the far-field directivity of ODA. In order to analysis and explore this inference, the far-field directivity of the two ODA models with the particles length increasing is carefully simulated and studied.

## 2. ANTENNA MODELS

In this paper, the two ODA models are similar to that of Gao et al. They are shown in Figure 1. The calculation regions are 2000 nm × 2000 nm × 2000 nm for both PNRs and PNEs. The dielectric constant of gold is approximated by modified Drude Model [11].

## 3. RESULTS AND DISCUSSION

We carefully study the far-field directivity of the above two ODA models with the particles length  $L$  increasing. Some important results are showed in Figure 2. Through the far-field directivity figures, we find that the far-field directivity of ODA become more directed with  $L$  increasing, and then when  $L$  increases to long enough, the dipole radiation pattern is lost and side-lobes occur, even main-lobe will change the ordination completely. Generally speaking, the changing tendency of the radiation patterns of ODA with the total antenna length increasing is analogous to that of dipole antenna, but has the difference that the tendency changes much faster with the increasing of the total antenna length. For example, Figures 2(i) and 2(j) show that apparent side-lobes occur for both PNRs and PNEs when the total length ( $2 * L + G$ ) is only 370 nm, which is much smaller than one wavelength.

The differences between the models of ODA and dipole antenna could be explained as below: First of all, metals are not perfect conductors at optical frequencies, but are instead strongly correlated plasmon described as a free electron gas. Incident radiation is no longer perfectly reflected from a metal's surface. Instead, radiation penetrates into the metal and gives rise to oscillations



Figure 1: Two ODA models used in FDTD calculation, where (a) stands for PNRs and (b) stands for PNEs. In the simulation,  $D = 40$  nm,  $G = 10$  nm,  $L$  changes from 40 nm to 200 nm with the step is 5 nm. Here, the wavelength of the incident light  $\lambda = 600$  nm.

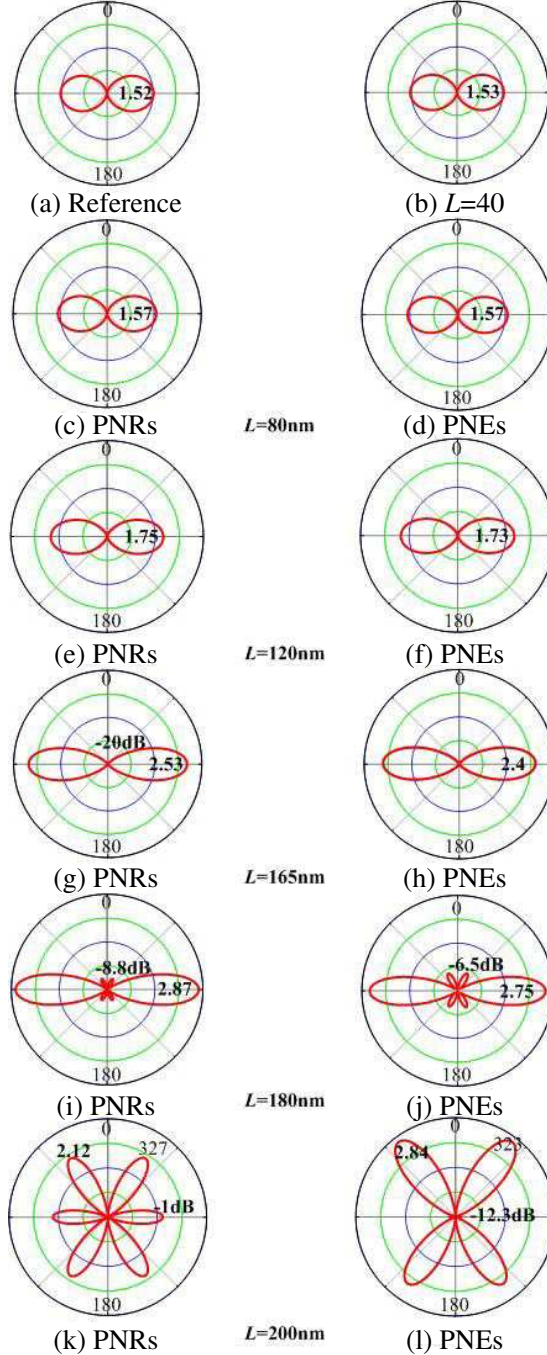


Figure 2: The far-field directivity figures for the two ODA models at the different  $L$ . (a) stands for radiation pattern of the dipole emitter as reference. (b) stands for that of a pair of spheres for both two models. (c), (e), (g), (i), and (k) stand for that of the PNRs model, while (d), (f), (h), (j), and (l) stand for that of the PNEs at the appropriate  $L$ .

of the free-electron gas. Here, oscillations of the free-electron gas on the surface of metallic nanoparticles are called localized surface plasmon (LSP). Secondly, optical antennas are typically fed by induced current of the local field of an electric emitter, not by real currents. So the local field distribution on the optical antenna will influence its induced current, and then influence its radiation pattern. Because LSP can strongly enhance local electric field of the particles [12–14], besides, the highly localized fields near the antenna make optical antennas can support higher-order multipolar modes in addition to the fundamental dipole mode [15, 16]. Therefore, we infer that LSP might influence the far-field directivity of ODA. Compared the Figure 2(i) with 2(j), larger side-lobes and less directivity are found in PNEs than that of PNRs at the same geometrical parameters. Xie et al. [17] simulate and illustrate that PNEs can excite much stronger LSP between two

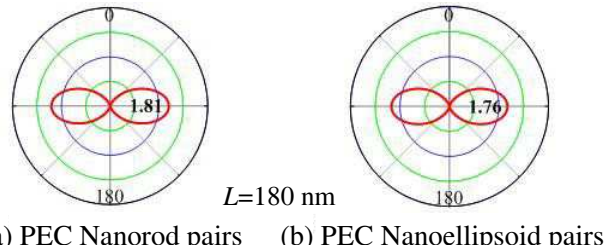


Figure 3: The far-field directivity figures for PEC nano-particles with the same geometric parameters as the PNRs and the PNEs at the  $L = 180$  nm.

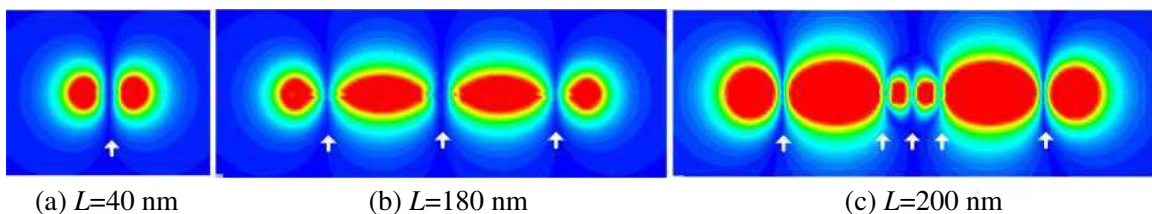


Figure 4: The field profile at the appropriate length  $L$ .

nanoparticles than PNRs with the same geometrical parameters. That implies that LSP does have an influence on the far-field directivity of ODA.

In order to verify the inference, based on the same geometrical parameters, we use a pair of perfectly electric conductor (PEC) nanoparticles, which do support LSP at the optical frequencies, to substitute the gold ones for two models. According to our inference, when  $L = 180$  nm, the PEC models will not occur side-lobes because the total antenna length ( $2 * L + G$ ) only is 370 nm, which much smaller than the incident wavelength. The far-field directivity figures are shown in Figures 3(a) and (b). Apparently, the results are consistent with our inference. This does illustrate the existing of LSP make higher-order multipolar modes be excited more easily and then influence the radiation pattern.

The existing of LSP make a standing surface charge wave appear on the surface of the nanoparticles [18]. In order to further explore the function and influence of LSP on ODA, the distributions of oscillating charges are obtained by recording the distributions of the amplitude of the electric field's normal component beside the nano-particles with  $L$  increasing. According to the Gauss's law, the electric field's normal component reflect the surface charge density, and then reflect the surface current. Here, take the PNRs models for example, we choose to record the field distribution in planes 4 nm off the side of the PNRs. We wound call this distribution "the field profile" hereafter. The field profiles at different  $L$  are recorded, several interesting results are shown in the Figure 4. In the field profiles figures, strong electric field can be seen at the nanorod's ends, indicating strong charge pileup there. These are signatures of LSP modes. When  $L$  is short ( $L = 40$  nm), there is one node (indicated by a white arrow) in the field amplitude, or equivalently in the surface charge density, along the nanorod. This means the LSP mode has an index of 1 (referred to as the  $m = 1$  mode hereafter). But when  $L$  is long enough ( $L = 180$  nm), there are three nodes in the charge density, which means this is the  $m = 3$  mode. When  $L$  continues to increase ( $L = 200$  nm), much higher order LSP mode ( $m = 5$ ) appears on the surface of the nano-particles. The field profile figures illustrate that higher-order LSP modes are excited when the particle length  $L$  is long enough, and much higher order LSP modes are excited with  $L$  increasing. In other words, higher-order LSP modes strongly influence the radiation pattern of ODA, or the existing of LSP excited at tips of the ODA make higher-order modes be excited more easily and then influence its far-field directivity.

#### 4. CONCLUSIONS

We carefully study the far-field directivity of two ODA models by calculating the far-field directivity and comparing the far-field directivity figures with the particles length  $L$  increasing. We find far-field directivity of ODA is analogous to that of dipole antennas. We find the changing tendency of the radiation patterns of ODA as the total antenna length increases is analogous to that of dipole

antenna but the critical condition which the side-lobes exist occurs more easily and earlier for ODA. In this paper, we carefully explore the appropriate field profile and verify that the existing of LSP make higher-order multipolar modes be excited more easily and then influence the radiation pattern. This paper illustrates that the appropriate angular directivity of ODA can be achieved by choosing nano-particles with proper length and controlling LSP excited at the particle tips. Our results also hold a great promise for improving the performance of the nano-optical antenna for various applications.

## ACKNOWLEDGMENT

This work was supported by the Reward Fund of Outstanding Youth and Middle Age Scientist of Shandong Province under Contract No. BS2009NJ002, the National Basic Research Program of China (973 Program) through Grant No. 2009CB930503, 2009CB930501, and 2007CB613203.

## REFERENCES

1. Aizpurua, J., P. Hanarp, D. S. Sutherland, M. Käll, G. W. Bryant, and F. J. Garcia de Abajo, “Optical properties of gold nanorings,” *Phys. Rev. Lett.*, Vol. 90, No. 5, 057401, 2003.
2. Mühlsgel, P., H.-J. Eisler, O. J. F. Martin, B. Hecht, and D. W. Pohl, “Resonant optical antennas,” *Science*, Vol. 308, No. 5728, 1607–1609, 2005.
3. Nehl, C. L., H. Liao, and J. H. Hafner, “Optical properties of star-shaped gold nano-particles,” *Nano Lett.*, Vol. 6, No. 4, 683–688, 2006.
4. Fischer, H. and O. J. F. Martin, “Engineering the optical response of plasmonic nanoantennas,” *Opt. Express*, Vol. 16, No. 12, 9144–9154, 2008.
5. Mohammadi, A., V. Sandoghdar, and M. Agio, “Gold nanorods and nanospheroids for enhancing spontaneous emission,” *New J. Phys.*, Vol. 10, No. 10, 105015, 2008.
6. Kühn, S., U. Hakanson, L. Rogobete, and V. Sandoghdar, “Enhancement of single-molecule fluorescence using a gold nanoparticle as an optical nanoantenna,” *Phys. Rev. Lett.*, Vol. 97, No. 1, 017402–4, 2006.
7. Agio, M., G. Mori, F. Kaminski, L. Rogobete, S. Kühn, V. Callegari, P. M. Nellen, F. Robin, Y. Ekinci, U. Sennhauser, H. Jäckel, H. H. Solak, and V. Sandoghdar, “Engineering gold nanostructures to enhance the emission of quantum emitters,” *Proc. SPIE*, Vol. 6717, 67170, 2007.
8. Stutzman, W. L. and G. A. Thiele, *Antenna Theory and Design*, John Wiley and Sons, New York, 1981.
9. Taminiau, T. H., F. D Stefani, and N. F. V. Hulst, “Single emitters coupled to plasmonic nano-antennas: Angular emission and collection efficiency,” *New J. Phys.*, Vol. 10, No. 10, 105005, 2008.
10. Gao, H., K. Li, F. M. Kong, H. Xie, and J. Zhao, (to be published).
11. Johnson, P. B. and R. W. Christy, “Optical constants of the noble metals,” *Phys. Rev. B*, Vol. 6, No. 12, 4370–4379, 1972.
12. Sherry, L. J., R. Jin, C. A. Mirkin, G. C. Schatz, and R. P. VanDuyne, “Localized surface plasmon resonance spectroscopy of single silver triangular nanoprisms,” *Nano Lett.*, Vol. 6, No. 9, 2060–2065, 2006.
13. Zhang, J., J. Yang, X. Wu, and Q. Gong, “Electric field enhancing properties of the V-shaped optical resonant antennas,” *Optics Express*, Vol. 15, No. 25, 16852–16859, 2007.
14. Muskens, O. L., V. Giannini, J. A. Sánchez-Gil, and J. Gómez Rivas, “Optical scattering resonances of single and coupled dimer plasmonic nanoantennas,” *Optics Express*, Vol. 15, No. 26, 17736–17746, 2008.
15. Hohenau, A., J. R. Krenn, G. Schider, H. Ditlbacher, A. Leitner, F. R. Aussenegg, and W. L. Schaich, “Optical near-field of multipolar plasmons of rod-shaped gold nanoparticles,” *Europhys. Lett.*, Vol. 69, 538–543, 2005.
16. Ditlbacher, H., J. R. Krenn, N. Felidj, B. Lamprecht, G. Schier, M. Salerno, A. Leiter, and F. R. Aussenegg, “Silver nanowires as surface plasmon resonators,” *Phys. Rev. Lett.*, Vol. 95, No. 25, 257403, 2005.
17. Xie, H., F. M. Kong, and K. Li, “The electric field enhancement and resonance in optical antenna composed of Au nanoparticle,” *Journal of Electromagnetic Waves and Applications*, Vol. 23, No. 4, 535–548, 2009.
18. Novotny, L., “Effective wavelength scaling for optical antennas,” *Phys. Rev. Lett.*, Vol. 98, No. 26, 266802, 2007.

# Supercontinuum Generation in Different Zero-dispersion Photonic Crystal Fibers

Yanrong Song<sup>1, 2</sup>, Jianyin Zhu<sup>1, 2</sup>, Xiao Zhang<sup>1, 2</sup>, Huihui Li<sup>1, 2</sup>, Lixiao Wei<sup>1, 2</sup>, and Pingxue Li<sup>3</sup>

<sup>1</sup>Institute of Information Photonics Technology, Beijing University of Technology, Beijing 100124, China

<sup>2</sup>College of Applied Sciences, Beijing University of Technology, Beijing 100124, China

<sup>3</sup>Institute of Laser Engineering, Beijing University of Technology, Beijing 100124, China

**Abstract**— The Supercontinuum spectrums were generated in different zero-dispersion photonic crystal fibers with 130 fs ultrafast laser pulses. The photonic crystal fibers of zero-dispersion point at 800 nm, 1060 nm and 2 μm were engaged. The Supercontinuum spectrums with different pulse energies and different central wavelengths were obtained and the difference between them were discussed.

## 1. INTRODUCTION

Supercontinuum (SC) could be used in optical frequency comb, sensor light sources and biological test, so it is very important to get a wide spectrum. Normally it was generated by injecting ultrashort pulses into micro-structure fibers, such as photonic crystal fibers (PCFs) or tapered fibers. In 1996, the first photonic crystal fiber was made successfully by J. C. Knight, T. A. Birk [1]. In 2000, Ranka's team first reported the SC generation in PCF with anomalous dispersion at 800 nm [2]. The SC generation in PCFs [3, 4] is influenced by dispersion, which included Grouped Velocity Dispersion (GVD), Third Order Dispersion (TOD), and by nonlinear effects, which include Self Phase Modulation (SPM), Self Steeping (SS), and Stimulated Raman Scattering (SRS) [5–7]. In these effects, the influence of the GVD is very important, so we discussed this effect by experiment.

In this paper, we used three different zero-dispersion PCFs to generate the SC by using an ultra-fast Ti:Sapphire laser with 130 fs pulse width with different conditions.

## 2. THEORETICAL MODEL

The effects of the dispersion and the nonlinear terms in the PCF is usually discussed by the modified Nonlinear Schrödinger equation (NLSE) as below [5]:

$$\frac{\partial A}{\partial z} + \frac{\alpha}{2} A + \frac{i\beta_2}{2} \frac{\partial^2 A}{\partial T^2} - \frac{\beta_3}{6} \frac{\partial^3 A}{\partial T^3} = i\gamma \left[ |A|^2 A + \frac{i}{\omega_0} \frac{\partial}{\partial T} \left( |A|^2 A - T_R A \frac{\partial |A|^2}{\partial T} \right) \right] \quad (1)$$

where,  $A$  is the slowly varying pulse envelope;  $z$  is the pulse propagation distance;  $\alpha$  is the effects of fiber losses;  $\gamma$  is the nonlinear parameter;  $\beta_2$  is second order dispersion parameter;  $T$  is measured in a frame of reference moving with the pulse at the group velocity;  $\beta_3$  is third order dispersion parameter;  $\omega_0$  is the central wavelength of the pulse;  $T_R$  is Stimulated Raman Scattering parameter. These parameters have important significance on effecting the SC generation in fibers.

In order to see the effect of the GVD, we calculate the SC in normal and anomalous dispersion conditions. The parameters are: for normal dispersion condition:

$$\begin{aligned} \beta_2 &= 6.43 \text{ ps}^2 \text{ km}^{-1}, & \beta_3 &= 0.1 \text{ ps}^3 \text{ km}^{-1}, & \gamma &= 0.075 \text{ (mW)}^{-1}, \\ T_0 &= 100 \text{ fs}, & P_0 &= 2 \text{ kW}, & Tr &= 5 \text{ fs}, & z &= 10 \text{ cm}. \end{aligned}$$

For anomalous dispersion condition:

$\beta_2 = -5.69 \text{ ps}^2 \text{ km}^{-1}$ ,  $\beta_3 = 0.06 \text{ ps}^3 \text{ km}^{-1}$ , others are as same as normal condition.

Figures 1 and 2 are the spectra when the pulses with central wavelength 800 nm propagate through the fibers. As is shown in Figure 1, the spectrum range is from 700 nm to 1000 nm with the parameters of fiber No. 1 in the normal GVD. Figure 2 shows that the spectrum range is from 680 nm to 1780 nm in anomalous GVD of fiber No. 2. Compared with the two figures, the supercontinuum range in anomalous GVD is much wider than the one in normal GVD. This means the zero-dispersion point is very important in SC.

### 3. EXPERIMENTS

Figure 3 is the setup of the experiment. We used a Mira-900 Ti:Sapphire pulsed laser pumped by a Verdi-V6, the output pulses (800 nm, 130 fs, 80 MHz) are guided into the PC fibers by using an objective lens. A Faraday rotator is used to prevent the CW light from going back to the pump laser.

From the Figure 4, we could see when the pulsed energies increase, the SC spectrum became wider and flatter.

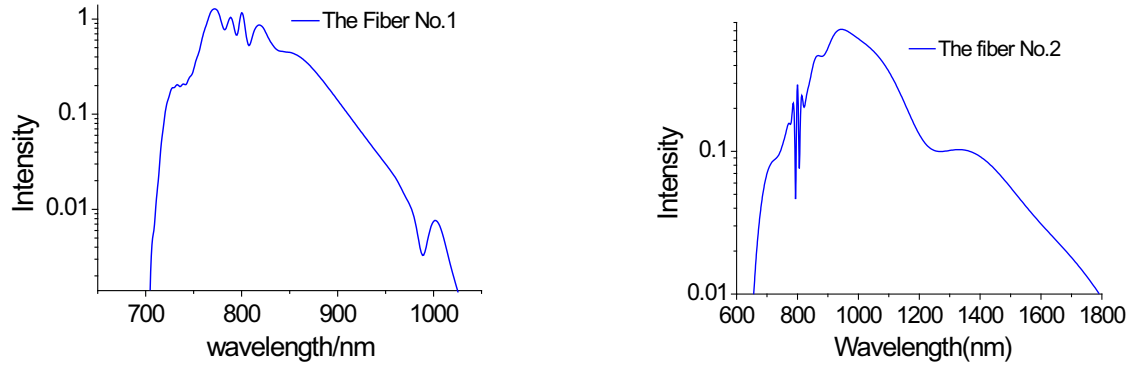


Figure 1: SC generates in the normal GVD area.

Figure 2: SC generates in anomalous GVD area.

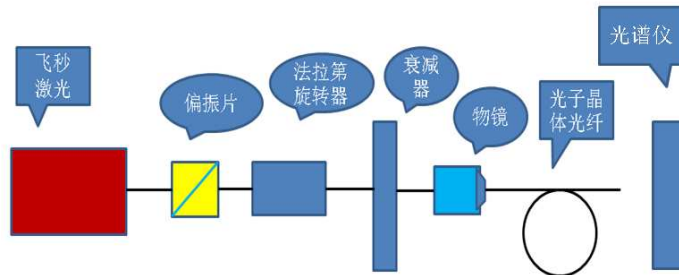


Figure 3: Setup of the experiment.

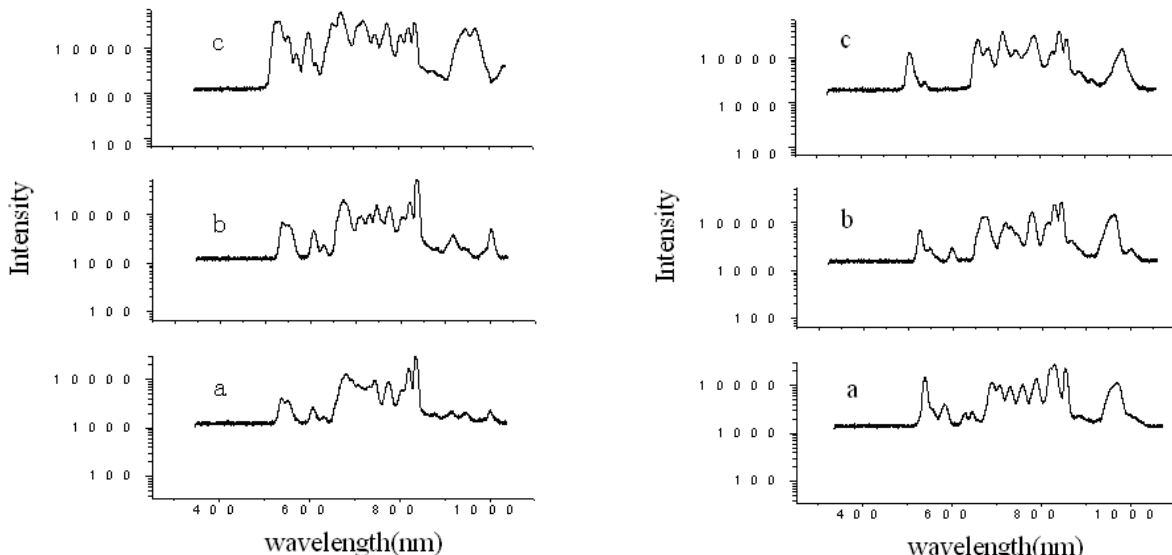


Figure 4: SC with different pulse energies. line a is with 8.75 nJ, line b is with 11.2 nJ, line c is with 13.75 nJ.

Figure 5: SC with different pump central wavelength. Line a is with 810 nm, Line b is with 820 nm, and line c is with 830 nm.

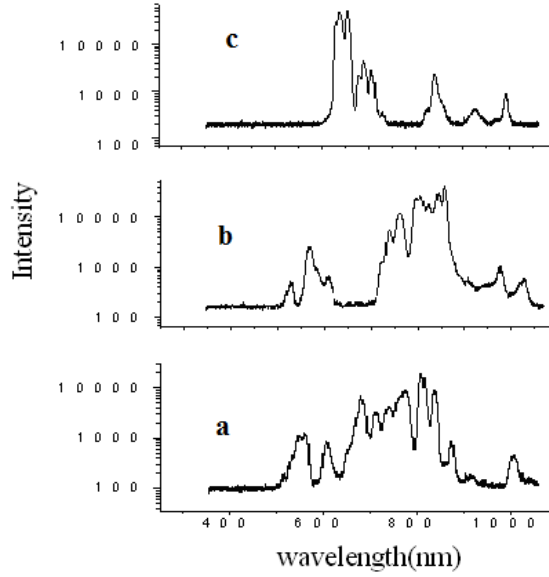


Figure 6: SC with different zero-dispersion photonic crystal fibers. Line a is with 800 nm, Line b is with 1060 nm, and line c is with 2000 nm.

From Figure 5, we can see there is no big difference between these three spectrum. The reason is that the zero-dispersion point of the PCFs is at 1060 nm, which is much far from the central wavelength of the pump laser.

Figure 6 is the SC with different zero-dispersion photonic crystal fibers. Line a is with 800 nm, Line b is with 1060 nm, and line c is with 2000 nm. From Figure 6 we can see, the shorter the wavelength is, the wider the SC is. This is because the pump light source is near 800 nm, the PCFs of 1060 nm and 2000 nm is at normal dispersion, the SC is narrow. Next step, we would do more experiment with different zero-dispersion point of the PCFs.

#### 4. CONCLUSIONS

We discussed the Supercontinuum spectrums generated in different zero-dispersion photonic crystal fibers with 130 fs ultrafast laser pulses. The photonic crystal fibers of zero-dispersion point at 800 nm, 1060 nm and 2  $\mu$ m were engaged. The shorter the wavelength is, the wider the SC is. At the same time, the SC was discussed with different pump energies and different wavelength. The higher the pump source, the wider the SC is.

#### REFERENCES

1. Knight, J. C., T. A. Birk, et al., "All-silica single-mode optical fiber with photonic crystal cladding," *Opt. Lett.*, Vol. 21, 1547, 1996.
2. Randa, J. K., R. S. Windeler, and P. S. J. Russell, "Visible continuum generation in air-silica microstructure optical fibers with anomalous dispersion at 800 nm," *Opt. Lett.*, Vol. 25, 25, 2000.
3. Russell, P., "Photonic crystal fibers," *Science*, Vol. 358, 299, January 17, 2003.
4. Wadsworth, W. J., A. Ortigosa-Blanch, J. C. Knight, T. A. Birks, T. P. Martin Man, and P. St. J. Russell, "Supercontinuum generation in photonic crystal fibers and optical fiber tapers: A novel light source," *J. Opt. Soc. Am. B*, Vol. 19, No. 9, September 2002.
5. Agrawal, G. P., *Nonlinear Fiber Optics*, 3rd Edition, Academic Press, New York, 2001.
6. You, H., S. M. Hendrickson, and J. D. Franson, "Analysis of enhanced two-photon absorption in tapered optical fibers," *Phys. Rev. A*, Vol. 78, 053803, University of Maryland, Baltimore County, Baltimore, Maryland 21250, USA, 2008.
7. Spillane, S. M., G. S. Pati, K. Salit, M. Hall, P. Kumar, R. G. Beausoleil, and M. S. Shahriar, *Phys. Rev. Lett.*, Vol. 100, 233602, 2008.

# Measurement of Weak Magnetic Fields

L. Kadlcik, J. Mikulka, and E. Gescheidtova

Department of Theoretical and Experimental Electrical Engineering  
Brno University of Technology, Kolejni 4, Brno 612 00, Czech Republic

**Abstract**— In the paper, the principle is described of measuring magnetic fields with very low levels of magnetic induction, of the order of unities of  $\mu\text{T}$ . The method described in the paper aims to ascertain the presence of a small amount of ferromagnetic material on a small area. It can, however, be also applied when examining the homogeneity of weak magnetic fields. The most important part of the device proposed here is the detection element, which evaluates the changes in magnetic properties of the surrounding environment, and interacts with the given ferromagnetic material. An integral part of the device is the demodulator, which processes the detected signal, from which only the part carrying useful information is selected. The useful information is deformed by convolution distortion and thus the signal must be reconstructed in an appropriate way. The reconstruction is associated with the decoder, which facilitates obtaining additional information in cases when the results of reconstruction are not unambiguous. A detailed analysis of the functions of detectors working on different principles has shown that our requirements are best satisfied by a simple ferromagnetic probe with a core of small diameter. The detecting part is designed in the form of a pen complemented with an oscillator with a resonance frequency of 300 kHz. The demodulator is implemented in the form of two PLL phase detectors, which are followed by a third-order low-pass filter with a cut-off frequency of 1 kHz. The circuitry terminates in a high-pass filter with a cut-off frequency of 0.34 Hz, which removes the dc component of the signal. The proposed meter will be used to establish the homogeneity of a weak magnetic field in biomedical applications.

## 1. INTRODUCTION

If the detector of a reading head is moved over a surface on which a thin layer of ferromagnetic material has been deposited, then in the ideal case the amount of ferromagnetic material  $c$  along the detector path  $r$  is a function of  $c(r)$ . The sensitivity of ideal detector to the ferromagnetic material is concentrated in one point but in practice this condition is not fulfilled. The magnetic field is dispersed over the surrounding environment and thus an actual detector reacts to all ferromagnetic materials present in its vicinity. This fact is described by the point spread function (PSF)  $h(r)$ . This is a spatial analogy to the Dirac pulse. The PSF of detectors actually comes close to the Gauss curve (1), which is manifested by sloping or even overlapping signal edges,

$$h(r) = K_{0,s} \frac{1}{\sigma \sqrt{2\pi}} e^{-\frac{r^2}{2\sigma^2}}, \quad (1)$$

where  $K_{0,s}$  is the detector sensitivity,  $\sigma$  is the dispersion, which gives the spread of detector sensitivity in the surrounding environment. In practice we try to design the detector such that its point spread function is as narrow as possible, coming close to the Dirac pulse. The shape of PSF depends, above all, on the area of the detector front; we endeavour to make this area as small as possible. The detector behaves like a linear system: the output signal is a convolution of the amount of ferromagnetic material and PSF

$$y(r) = h(r) * c(r). \quad (2)$$

In the spatial region, the detector behaves like a low-pass filter; the higher frequencies are suppressed and this is manifested as chamfered edges of the signal. The spatial frequency response of the distorting filter is given by the Fourier transform of PSF

$$H_r(\omega_r) = \int_{-\infty}^{+\infty} K_{0,r} \frac{1}{\sigma \sqrt{2\pi}} e^{-\frac{r^2}{2\sigma^2}} e^{-j\omega_r r} dr = K_{0,s} e^{-\frac{\omega_r^2 \sigma^2}{2}}. \quad (3)$$

Detector attenuation increases fast with increasing spatial frequency  $\omega_r$ ; the larger the dispersion  $\sigma$  is, the lower the cut-off spatial frequency of the filter and the steeper the filter. Electronic filters

work in the time domain; for the transition from the space domain to the time domain, the law of motion will be employed: path  $r$  equals the product of velocity  $v$  and time  $t$

$$r = vt. \quad (4)$$

The frequency response of the distorting filter can then be expressed by the relation

$$H(\omega) = \frac{1}{v} H_r\left(\frac{\omega}{v}\right), \quad (5)$$

from which it is apparent that the frequency response of the distorting filter depends on the velocity of detector motion.

There are two basic types of detector [1]: induction detector operating on the principle of Faraday's induction law, and inductive detector, which detects the presence of ferromagnetic material by changing the detector coil inductance. In the course of motion over a magnetized material, alternating voltage is induced in the induction coil, whose waveform corresponds to the distribution of magnetic induction. The principle is simple but inapplicable in our case; the induction near the surface of ferromagnetic layer is very low, lower than the induction of the Earth's magnetic field. To obtain a signal whose level would make it applicable, the coil surface would have to be large, which is in contradiction with the demand for low dispersion. Common detectors of weak magnetic fields are single and double ferromagnetic probes [1, 2]. The field coil and the current source are intentionally designed such that the core is being oversaturated. The waveform of magnetic induction is detected by the coil winding, in which the voltage induced passes through a band-pass filter tuned to the second harmonic. The voltage after the band-pass filter is rectified. The spectrum does not contain the even harmonics and thus there is zero voltage on the probe output. If the coil core is inserted into an external magnetic field, its intensity in the half-wave of one polarity will be added up with the magnetic field of the field coil and subtracted in the other half-wave. The core in one half-wave will thus be oversaturated more than in the other. The waveform of magnetic induction in the core will be asymmetrical, and so will the waveform of induced voltage [2]. The asymmetrical waveform contains the even harmonics; the second harmonic passes through the band-pass filter and is rectified by a rectifier. On the probe output there will be a voltage whose magnitude depends on the induction of external magnetic field. The band-pass filter must be sufficiently selective because we try to extract from the induced voltage the second harmonic in the presence of the much more pronounced fundamental frequency [2]. The sensitivity of the simple ferromagnetic probe is sufficient for our purposes. When testing the function of the meter we have fabricated we used as a reference detector the FLC 100 ferromagnetic probe manufactured by Stefan Meyer Instruments. The manufacturers claim that a magnetic field of  $50 \mu\text{T}$  induction will change the voltage on the probe output by 1 V.

## 2. DESIGN AND IMPLEMENTATION OF THE SENSOR

The fabricated device consists of an appropriate detector, demodulator, reconstruction circuit, and decoder, as shown in Fig. 1.

### 2.1. Detector

In the design of the sensor the detection element chosen was the oscillator, which is an LC circuit complemented with an amplifier, which makes up for the energy losses and thus the circuit becomes a source of permanent oscillations. A positive feedback guarantees that the amplitude and phase conditions are fulfilled. In the design of the oscillator we endeavoured to minimize the effect of

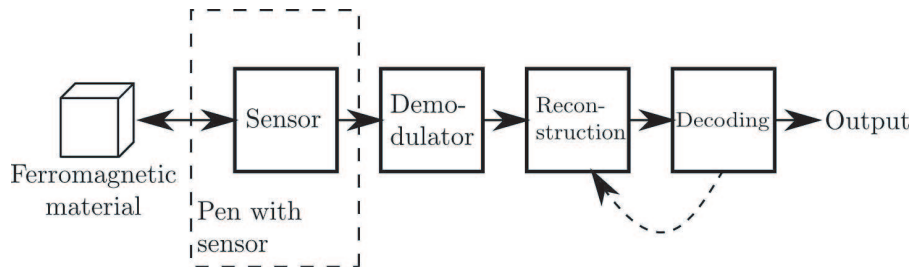


Figure 1: Block diagram.

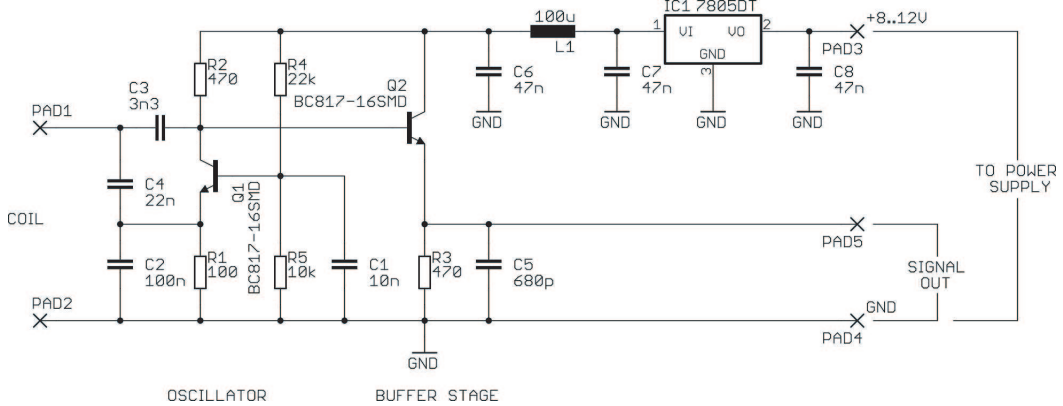


Figure 2: Schematic of detection oscillator.

surrounding signals. The barrier capacitances of the semiconductor employed mistune the supply voltage, which results in parasitic frequency modulation. This may lead to a feedback being formed through the supply voltage distribution, and the circuit need not be stable. Large capacitances will be used in the LC circuit and this will reduce the proportion of barrier capacitances in the total capacitance. We also tried hard to make the coupling between the circuit and the amplifier as loose as possible — the LC circuit is connected via a capacitive divider.

Both the coil inductance and the capacitance of the capacitors employed are temperature-dependent. The temperature dependence of the capacitance is primarily given by the type of capacitor dielectric [3, 4]. The temperature dependence of the inductance is given by the thermal expansivity of the coil and also by the temperature dependence of the permeability of its core. The temperature dependence of the frequency will be reduced if the thermal coefficients of the capacitance and of the inductance compensate each other. If the oscillator amplifier is excited up to the non-linear part of its transfer characteristic, the oscillator may be pulled by an interfering signal. Interference propagating through the supply voltage distribution can be prevented by an LC low-pass filter. For the convolution distortion to be attenuated as much as possible it is necessary to choose the detector with the narrowest possible spatial pulse response; the response width is directly proportional to the size of the detection area. The oscillator is assembled using SMD components on a small board, which is connected to the demodulator by a coaxial cable (shielded two-wire line) terminating in a connector.

## 2.2. Demodulator

An integral part of the device is the demodulator, which processes the signal detected, from which only the part that carries useful information is selected. This information is deformed by convolution distortion so that the signal must first be reconstructed in an appropriate way.

The phase detector measures the phase shift between two signals and produces a voltage on its output a certain characteristic of which (the mean value, for example) corresponds to this phase shift. The phase detector output signal is usually rectangular and the information about the phase shift is carried by the mean value, which we obtain by filtering. In the simplest case the loop filter is a first-order low-pass filter [5, 6]. The transfer function of the filter markedly influences the dynamic properties of PLL.

The demodulator supply voltage is 12 V; an IC3 stabilizer produces a smooth stable supply voltage for PLL. Connectors for the supply intake have intentionally a great number of pins; at the prototype stage its further extension was taken into account, in which case some further circuits might also require different supply voltages. The prototype can be further extended.

## 3. EXPERIMENTAL RESULTS

The device was implemented according to the description given above. The detection coil itself is a winding of several tens of turns on a ferrite core of 2 mm in diameter; it is placed on the detector board and connected to the oscillator. An implemented device is shown in Fig. 5.

The reference detector employed to test the function of the whole facility was the FLC 100 ferromagnetic probe (Stefan Meyer Instruments). The manufacturers claim that a magnetic field of 50  $\mu$ T induction generates on the probe output a voltage change of 1 V [7].

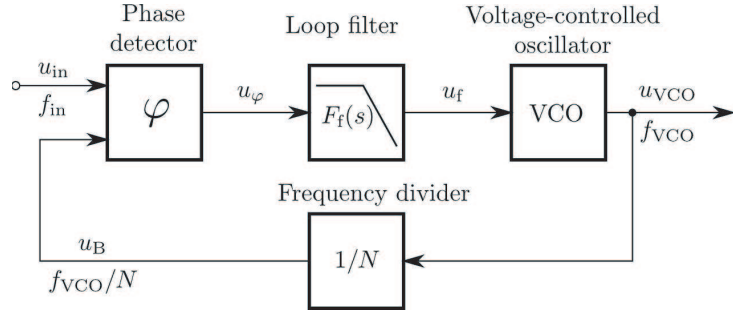


Figure 3: Block diagram of phase lock.

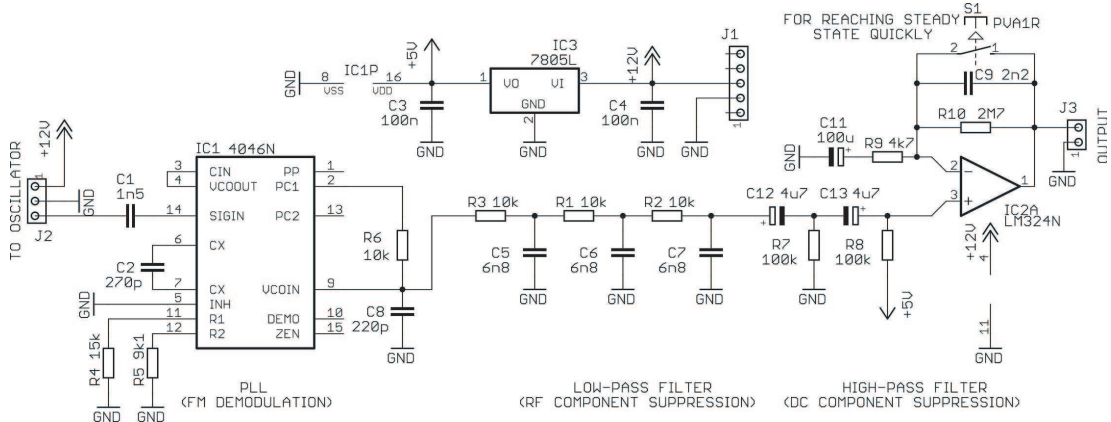


Figure 4: Schematic of demodulator.

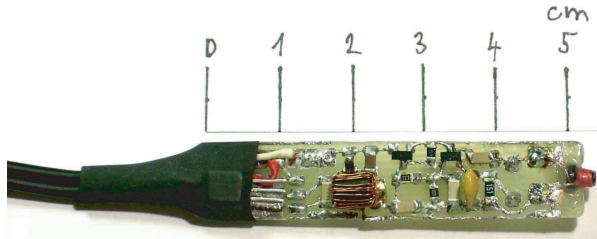


Figure 5: Implemented device.

In the verification, we used a substance with a deposited layer of ferromagnetic ink, which was magnetized by applying a strong permanent magnet. On the reference probe output we obtained a signal with 20 mV amplitude. This means that the magnetic induction of magnetized ink is  $1 \mu\text{T}$ . With the bar code not applied, the detection oscillator oscillates on the frequency  $f_1 = (311698 \pm 95)$  Hz. Applying one wide bar of magnetic ink directly to the front of the detection coil core of the designed detector reduced the frequency by  $f = (97 \pm 5)$  Hz, or  $f = (-312 \pm 16)$  ppm. The results of measuring on the demodulator are as follows. At rest the control voltage VCO  $U_{f_1} = (2.196 \pm 0.002)$  V).

After applying a 5 mm wide magnetic bar the voltage drops by  $-U_f = (-2.95 \pm 0.45)$  mV, i.e.,  $U_f = (-1340 \pm 210)$  ppm.

After amplification, the amplitude swing of the signal acquires a value of ca. 1 V (Fig. 6 in [20]). The convolution distortion can be observed clearly on the signal. If the detection is performed by the edge of the coil core, the amplitude swing of the signal is smaller (approximately 0.7 V, Fig. 7 in [21]), but the convolution detection is manifested to a lesser extent (because the surface of the edge is smaller). The output signal exhibits 50 Hz mains interference, as can be seen from the voltage waveforms in Fig. 6.

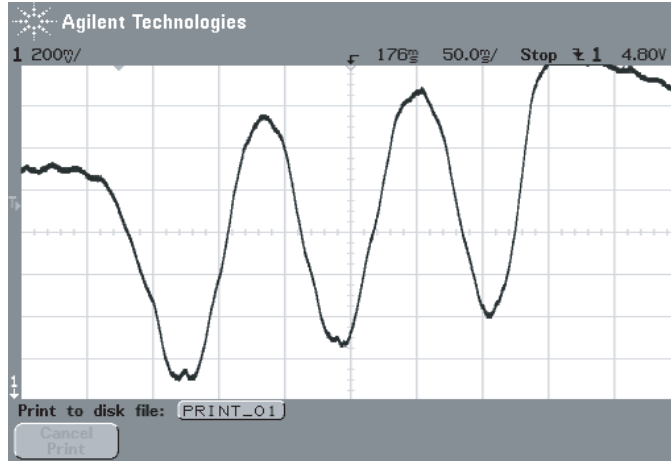


Figure 6: Output signal of demodulator.

#### 4. CONCLUSION

The device described in the paper can be used with advantage to establish the presence of a small amount of ferromagnetic material. It can also be used to examine the homogeneity of weak magnetic fields. The most important part of the device is the detection element, which assesses the changes in the magnetic properties of the surrounding environment when the element is moved over a source of magnetic field, and which interacts with the ferromagnetic material present. A simple ferromagnetic probe, FLC 100 (Stefan Meyer Instruments), can be used to this purpose but the detection is not very sharp. Detection by the detection oscillator that we designed and implemented is sharper but still leaves scope for improvement. It would be of advantage to use a coil core of less than 2 mm in diameter.

#### ACKNOWLEDGMENT

This work was supported within the framework of projects No. 102/11/0318 of the Grant Agency of the Czech Republic and the research plan MSM 0021630516.

#### REFERENCES

1. Draxler, K., P. Kaspar, and P. Ripka, *Magnetické prvky a měření*, CVUT, Praha, 1999 (in Czech).
2. Dufek, M., J. Hrabak, and Z. Trnka, *Magneticka merení*, SNTL, Praha, 1964 (in Czech).
3. Shellhammer, S., D. Goren, and T. Pavlidis, “Novel signal-processing techniques in Barcode scanning,” *IEEE Robotics & Automation Magazine*, Vol. 6, 57–65, 1999.
4. Smith, J., *Modern Communication Circuits*, McGraw-Hill Book Company, New York, 1986.
5. Curtin, M. and P. O’Brien, “Phase locked loops for high-frequency receivers and transmitters — Part 3,” *Analog Dialogue* [online], Vol. 33, No. 1, 18–22, 1999. URL: <http://www.analog.com/library/analogdialogue/cd/vol33n1.pdf>.
6. NXP Semiconductors, *HEF4046B Phase-locked Loop* [online], URL: [http://www.nxp.com/documents/data\\_sheet/HEF4046B.pdf](http://www.nxp.com/documents/data_sheet/HEF4046B.pdf).
7. Stefan Mayer Instruments, *Magnetic Field Sensor FLC 100* [online], URL: <http://www.stefan-mayer.com/Data%20sheet%20FLC%20100.pdf>.

# Ultrasonic-assisted Condensation of Chitosan with Salicylaldehyde and the Adsorption of Cr(VI) Ions in Magnetic Field

Lihong Duan<sup>1</sup>, Siyuan Guo<sup>2</sup>, and Qiongjuan Zheng<sup>1</sup>

<sup>1</sup>Institute of Polymer Science, College of Chemistry and Chemical Engineering

Sun Yat-sen University, Guangzhou 510275, China

<sup>2</sup>Light Industry & Chemical Engineering Research Institute, Food College

South China University of Technology, Guangzhou 510640, China

**Abstract**— In order to synthesis more efficient adsorbant of heavy metal ions, the condensation reaction of chitosan (CS) with salicylaldehyde (SD) to form Schiff base(SB) in ethanol using a ultrasonic liquid processor was studied and was contrasted with conventional method. The IR spectra of condensed chitosan from the two methods showed that their molecular structures were identical. The reaction conditions such as the kind of solvents, power density and irradiation time of ultrasonic, the pH condition and the reactant ratio were optimized using an orthogonal design. It was found that a shorter reaction time and a higher product yield could be got for the ultrasonic-assisted synthesis than that of traditional method. A condensation degree of 89.63% could be achieved under the optimization conditions: using 180 kW ultrasonic, taking 95% ethanol as solvent, at pH 4.0, with the SD/CS ratio of 6 : 1, ultrasonic irradiating for 60 min. The adsorption of Cr (VI) ions onto chitosan and its condensation with salicylaldehyde was investigated in magnetic field. Batch adsorption experiments were carried out as a function of magnetic power and reacted time. The results showed that, magnetic field strengthen the adsorption capacity, especial for Schiff bases.

## 1. INTRODUCTION

Chitosan (CS) is a partially N-deacetylated product from chitin and is particularly attractive linear polysaccharide, which has radicals of not only  $-\text{OH}$  but also  $-\text{NH}_2$ . There are many interesting properties with chitosan, such as biocompatibility, biodegradability, antibacterial, and wound-healing activity [1–3]. The degradation products of CS are non-toxic, non-immunogenic and non-carcinogenic [4–6]. Therefore chitosan was widely applied in many fields, such as biomedicine, waste water treatment, fabric and textiles, cosmetics, nutritional enhancer, and in food processing, especially for the adsorption of transition metal ions [7–11]. However, chitosan is the basic polysaccharides of which the  $-\text{NH}_2$  can form to be  $-\text{NH}_3^+$  in acidic condition. In addition, the  $-\text{NH}_2$  can not entirely take part in the coordination with metal ions which may limit its adsorbed capabilities and be disadvantaged for regeneration. Recently there was a growing interest in chemical modification of CS to improve its water-solubility and strengthen its adsorbed capabilities [12–16]. The  $-\text{NH}_2$  of CS can react with aldehyde or ketone to form imine (Schiff base) which has an excellent chelated ability with metal ions. It was reported hat the Schiff base of CS and 2, 4-pentanedione have a strong chelating property with  $\text{Cu}^{2+}$  and  $\text{Co}^{3+}$  [17].

However, a long reaction time and low condensation degree may accompany with traditional method. Recently, the ultrasonic-assisted technology was applied in organic synthesis [18–21]. It can not only ameliorate reaction conditions and quicken reaction rate as well as increase yield, but also enable for some reactions taken part hardly. Especially, it can obviously promote heterogeneous reactions. In order to synthesis more efficient adsorber of heavy metal ions, the condensation reaction of CS with salicylaldehyde (SD) can form Schiff base(SB). The reaction was studied for enhancing using a ultrasonic liquid processor and was compared with conventional method. The parameters of effecting condensation degree were investigated using orthogonal design. In addition, the adsorption of Cr (VI) ions onto chitosan and its condensation with salicylaldehyde was investigated in magnetic field through studying the effect of magnetic power and reacted time. And a satisfied result was obtained.

## 2. EXPERIMENT

### 2.1. Reaction Mechanism

In the preparation of Schiff base (SB), chitosan can be acting as the primary amine and react with aromatic aldehyde to produce the corresponding derivative. The preparation reaction of Schiff base can be presented as Figure 1.

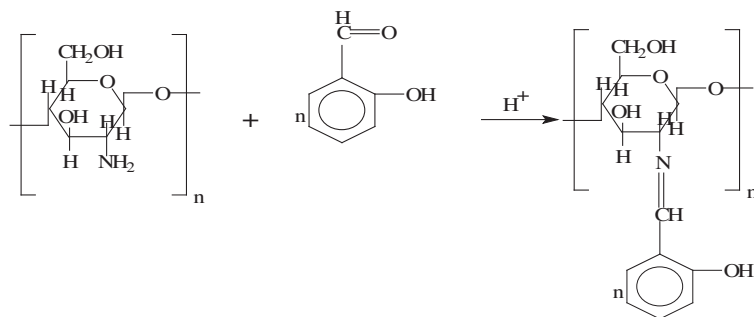


Figure 1: The condensation reaction of chitosan with salicylaldehyde.

Table 1: Characteristic IR bands of chitosan and product Schiff base.

Sample	Infrared ( $\text{cm}^{-1}$ )						
	$\gamma_{C=O}$ (amide I)	$\delta_{NH}$ (amide II)	$\gamma_{C=N}$ (imine I)	$\delta_{CH}$ (aromatic ring)	$\gamma_{antis}$ (bridge CO-C)	$\gamma_{C-O}$ (phenolic)	$\gamma_{C=C}$ (aromatic ring)
CS	1655.9	1602.8	Absent	Absent	1154.2	Absent	Absent
SB	nd	nd	1631	757;894	1153	1277	1582

CS: Chitosan; SB: Schiff base; nd: not detected;  $\gamma$ : stretching;  $\delta$ : axial deformation.

## 2.2. Adsorption Studies

In order to study the chromium sorption in magnetic field studies, 100 mg sorbent was brought into contact with 5 ml of Cr (VI) solutions and putted in magnetic field at constant intensity at room temperature. After centrifuging the solutions, the concentration of unadsorbed Cr (VI) in the toppler was analyzed. The amount of adsorption was calculated based on the difference of Cr (VI) concentration in aqueous before and after adsorption. The effect of intensity on metal adsorption was studied by adjusting the magnetic intensity over the range of approximately 0.1–1 T. The effect of reacted time was also evaluated to study the metal sorption kinetics.

## 3. RESULTS AND DISCUSSION

### 3.1. Infrared Spectroscopy

The most significant bands found from the IR spectra of chitosan and the product Schiff bases were showed in Table 1. The main bands observed in the IR spectra of the chitosan sample were: an amide band (amide I) at 1655.9  $\text{cm}^{-1}$ ; N-H angular deformation at 1602.8  $\text{cm}^{-1}$  (amide II).

The IR spectra of the product Schiff bases presented a strong absorption band at 1631  $\text{cm}^{-1}$ . It could be attributed to the  $C = N$  vibrations characteristic of imines. The absorption at 1582  $\text{cm}^{-1}$  could be attributed to the  $C = C$  stretching in the aromatic ring of the aldehyde. On the other hand, there was no evidence of the characteristic band related to free aromatic aldehydes group near 1665  $\text{cm}^{-1}$ . The imine formation was confirmed by the IR spectroscopy.

### 3.2. Orthogonal Experiment of Ultrasonic-assisted Synthesis

There are many factors which effected on the condensation reaction assisted with ultrasonic. In order to optimize the conditions, orthogonal design of four factors and three levels was investigated and the results were shown as Table 2.

It can be known from Table 7 that primary factors effecting the preparation assisted by ultrasonic were acidity and solvent. The ratio of reactants and ultrasonic irradiation time were in the next place. The reaction condition of ultrasonic-assisted synthesis was optimized as follows: 89.63% condensation degree could be achieved by using 180 kW ultrasonic in 95% ethanol at pH 4.0, with SD/CS ratio of 6 : 1, and for 60 min of ultrasonic irradiation time.

Table 2: The result of orthogonal design  $L_9(3^4)$ .

	Factors				Condensation degree(%)
	Acidity(pH)	Solvent	Irradiation time (min)	SD/CS	
1	3	water	60	4:1	68.01
2	3	95% ethanol	90	5:1	76.31
3	3	ethanol	120	6:1	67.41
4	4	water	90	6:1	84.82
5	4	95% ethanol	120	4:1	77.82
6	4	ethanol	60	5:1	80.04
7	5	water	120	5:1	83.32
8	5	95% ethanol	60	6:1	88.25
9	5	ethanol	90	4:1	69.35
$K_1$	211.73	236.15	236.30	215.18	
$K_2$	242.68	242.38	230.58	239.67	
$K_3$	240.92	216.80	228.55	240.48	
$k_1$	70.58	78.72	78.77	71.73	
$k_2$	80.89	80.79	76.86	79.89	
$k_3$	80.31	72.27	76.18	80.16	
$R$	10.31	8.52	2.59	8.43	

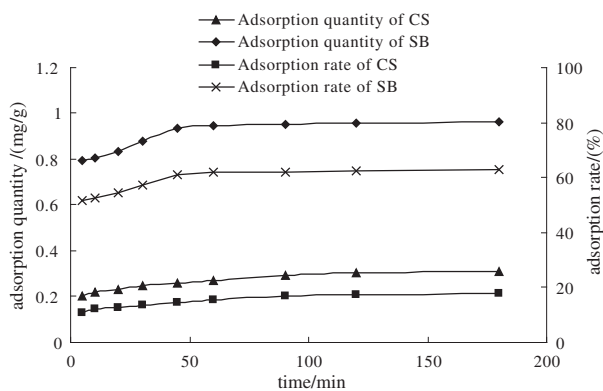


Figure 2: The adsorption kinetic curves in non-magnetic field.

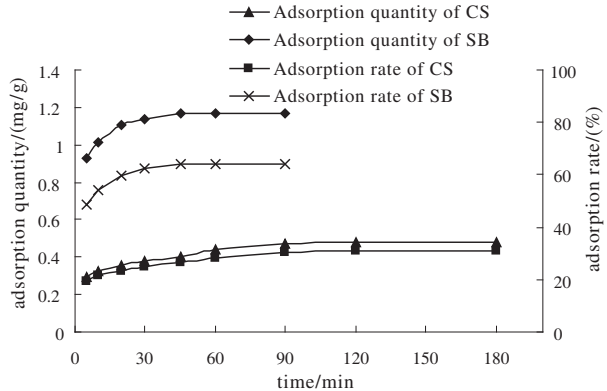


Figure 3: The adsorption kinetic curves in magnetic field.

### 3.3. Effect Parameters of the Adsorption of Cr (VI) Ions

#### 3.3.1. The Adsorption Kinetics in Non-magnetic Field

The adsorption kinetic curves of CS and SB were shown in Figure 2. According to the Figure 2, the changes of the adsorption quantities and absorption rates over time were similar for CS and SB. It was increasing with the extension of adsorption time and being almost constant when the time was up to a certain value and achieving ultimate equilibrium. It must spend 120 min to achieve the equilibrium for the CS. However, the equilibrium time of the SB was about 60 min. It was obvious that the absorption rate of SB was larger. It also could be seen that the absorption quantity and absorption rate of the SB were higher than the CS in the corresponding period.

#### 3.3.2. The Adsorption Kinetics in Magnetic Field

Figure 3 showed the adsorption kinetic curves of CS and SB in magnetic field of 400 kA/m and the changes disciplinarian was similar with the adsorption kinetic curves without magnetic field treatment. Whereas the adsorption equilibrium period of CS and SB were both shortened. The equilibrium periods of CS and SB were 90 min and 30 min respectively. Comparing Figure 2 and Figure 3, in the case with magnetic treatment, both of the absorption quantity and absorption rates of CS and SB were more than that of without magnetic treatment in any corresponding adsorption period. Namely their adsorption capabilities were enhanced by the magnetic field treatment.

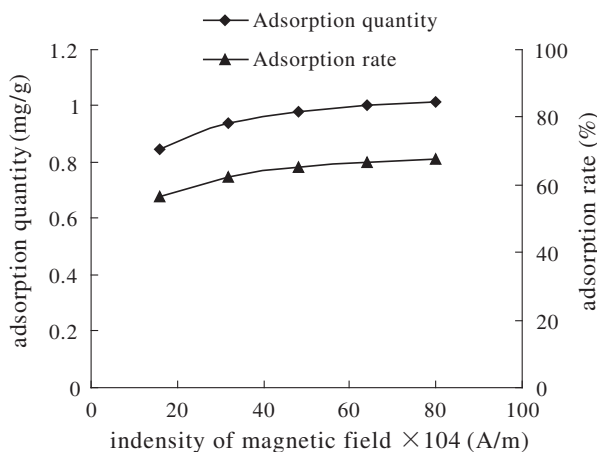


Figure 4: The effect of intensity of magnetic field on adsorption.

### 3.3.3. Effect of Magnetic Field Intensity on Adsorption

The effect of magnetic field intensity on adsorption was shown in Figure 4.

In the light of Figure 4, the adsorption capability of SB in the magnetic field was enhanced by a treatment with magnetic intensity from 160 kA/m to 800 kA/m for 30 min. Ranging from 160 kA/m to 480 kA/m, the absorption quantity and absorption rate were increasing dramatically. However, after that the changes became slight. Taking into account energy conservation, the magnetic field strength of 480 kA/m was recommended for the adsorption enhancement.

## 4. CONCLUSION

The chitosan can be modified to produce an efficient adsorbant of heavy metal ions, chitosan Schiff base, by the condensation reaction of chitosan with salicylaldehyde. The reaction can be promoted with a ultrasonic assisted technology. The reaction time can be shortened observably by ultrasonic-assisted from 8 h to 1 h and resulted in a condensation degree of 89.63% under the following conditions: with the reactant ratio (SD/CS) of 6, taking 95% ethanol as solvent, adjusting the solution at pH 4.0, using ultrasonic treatment for 60 min.

The adsorption property of chitosan (CS) can be improved by the condensation reaction with benzaldehyde to form a Schiff base. The chitosan-benzaldehyde Schiff base (SB) has an excellent adsorption capability to Cr (VI). It can take two times more adsorption amount and a half shorter saturation adsorption period for SB than that for CS. The adsorption can be expressed with the Langmuir isotherm equation.

The adsorption capability, including adsorption amount and adsorption rate can be enhanced by a suitable magnetic field treatment. For example, with the treatment of magnetic intensity of 480 kA/m, the adsorption equilibrium period for Cr (VI) on SB can be shortened from 60 min to be 30 min. And the minimum SB dose for 30 mg/L Cr (VI) solution can be saved more 43% than the normal process. However, the mechanism of magnetic treatment on the adsorption system is still to be studied.

## ACKNOWLEDGMENT

The authors are thankful to the financial support from the Doctoral Discipline Special Foundation of Education Ministry (20050561014) and National “863” Science & Technology Project of China (2007AA100405 ).

## REFERENCES

- Schuetz, Y. B., R. Gurny, and O. Jordan, “A novel thermoresponsive hydrogel based on chitosan,” *European Journal of Pharmaceutics and Biopharmaceutics*, Vol. 68, 19–25, 2008.
- Kim, I.-Y., S.-J. Seo, H.-S. Moon, et al., “Chitosan and its derivatives for tissue engineering applications,” *Biotechnology Advances*, Vol. 26, 1–21, 2008.
- Kim, T.-H., H.-L. Jiang, D. Jere, et al., “Chemical modification of chitosan as a gene carrier in vitro and in vivo,” *Prog. Polym. Sci.*, Vol. 32, 726–753, 2007.

# Microscopic Image Processing in Studying Diverticular Disease

J. Mikulka

Department of Theoretical and Experimental Electrical Engineering, Brno University of Technology  
Kolejni 2906/4, Brno 612 00, Czech Republic

**Abstract**— This article deals with initial research of designing microscopic image processing methods in studying diverticular disease. In previous medical research a functional and structural changes were found in tissues of persons affected by diverticular disease. The acquired images were processed manually. The goal of image processing methods research for automatic or semiautomatic processing followed by manual supervising is to simplify and speed-up the image processing and evaluation of objects parameters. In addition to speed-up the processing the goal is to increase the accuracy of evaluating the tissues properties.

## 1. INTRODUCTION

This article deals with initial research of designing microscopic image processing methods in studying diverticular disease [1]. The aim of the image processing is increasing the accuracy and speed-up the processing. First step to increase the accuracy was to obtain more images representing several regions of the same tissue to averaging the results of densities in each image. Second step to increase the accuracy was to change the approach in area measurement of monitored regions because traditional manual methods are influenced by error (up to 50%).

The article describes design of particular methods for processing of first kind of images. The set of images represents smooth muscle layer in which the goal is to evaluate number (density) of cell nuclei in area of the whole image. The second set of images represents myenteric plexus layer. The goal in this kind of images is to evaluating the ganglionic areas followed by determination of neurons or glial cells density. The third set of images represents interstitial cells of cajal (ICC). The goal of this kind of images processing is to evaluating number (density) of cells in observed area. The ICC's are monitored in smooth muscle layer and in myenteric plexus layer. In the first mentioned layer is evaluated the density of cells in whole image, in the second layer is evaluated density only inside the ganglionic area.

The aim of research is to design and implement image processing plug-ins which will be used as tools for speed-up the processing of huge sets of images and providing more information compared to manual processing.

## 2. PROPOSED APPROACH

The circular and the longitudinal muscle layer images are of sufficient contrast to use simple segmentation methods. Thus, no contrast enhancement is required. The cells detection algorithm consists of seven steps:

1. Resizing: the first processing consists of resizing to 50% their original size in order to speed up the processing.
2. Splitting the color channels: The red (R), green (G) and blue (B) color channels and the grayscale image (Y) obtained by transformation of all channels (by means of the following equation  $Y = 0.3 \cdot R + 0.59 \cdot G + 0.11 \cdot B$ ) were analyzed. In each type of image the best color channel to next processing was found. The circular and longitudinal muscle layer images have the best contrast in the red channel [2, 3].
3. Smoothing: To suppress the problem with interrupted boundaries of cells smoothing method is required. The best results were obtained by means of median filtering with mask size of 10 [2, 3].
4. Thresholding: After smoothing the image, it is segmented by a thresholding method. The threshold is established by triangle autothreshold method [4].
5. Skeletonization: After the image is binarized, it follows skeletonizing of objects in binary image and detection of crossed cells with refinement of the skeletons [2, 3].
6. Counting: The number of skeletons representing the cells is established.

resizing the image	splitting the color channels	median smoothing	thresholding	skeletonize and refinement	counting	supervising
--------------------	------------------------------	------------------	--------------	----------------------------	----------	-------------

Figure 1: Algorithm for extraction of cells from images of circular and longitudinal muscle layer.

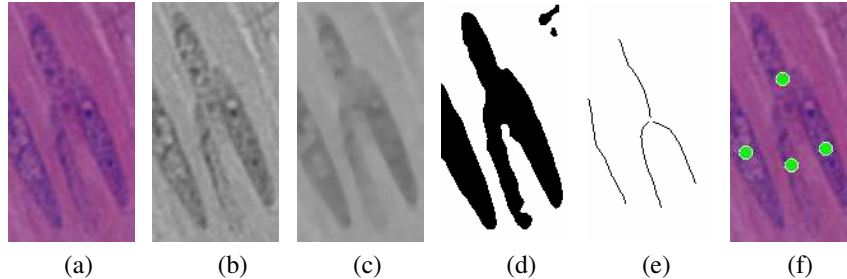


Figure 2: Intermediate results of the cut of circular muscle layer image processing; (a) original image, (b) red channel, (c) red channel after median filtering, (d) segmented image, (e) refined skeletons, (f) final result.

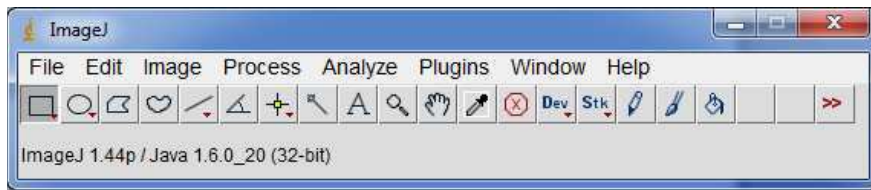


Figure 3: ImageJ application window for interactive image processing.

Table 1: Comparison of image processing duration.

	manual processing	automatic processing followed by manual supervising
processing time of 1 image	3 minutes	4 sec. + 20 sec. for supervising
processing time of 26 initial set images	78 minutes	10.4 minutes
processing time of 13 × 5 images of extended set	6.5 hours	52 minutes

7. Supervising: The previous result can be manually supervised. Two kinds of errors can exist:

Miss detection: a cell is not automatically detected and must be manually added.

False detection: a cell is automatically detected and must be manually removed.

The whole algorithm is shown in Figure 1. The intermediate results are shown in Figure 2.

### 3. IMAGEJ IMPLEMENTATION

ImageJ [5] is a public domain Java image processing program. It can calculate area and pixel value statistics of user-defined selections. It can measure distances and angles. It can create density histograms and line profile plots. It supports standard image processing functions such as contrast manipulation, sharpening, smoothing, edge detection and median filtering. It is suitable for this application of image processing. The application windows is shown in Figure 3.

### 4. EXPERIMENTAL RESULTS

The whole image processing was accelerated. In Table 1, is shown a comparison of manual processing and automatic processing followed by manual supervising in the case of 1 image and in the case

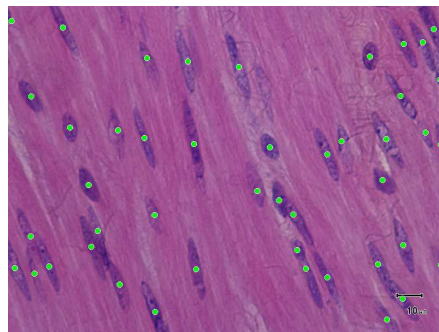


Figure 4: Result of image processing by ImageJ after manual supervising; green dots mark all the cell nuclei.

of a set of images. It is clear that the proposed automatic image processing approach save much time.

In Figure 4 area shown results of the processing by ImageJ tool after manual supervising. Green dots mark all the cells nuclei. The algorithm can recognize the overlapped cells in many cases. The manual supervising allow adding the marks and erasing the marks, as well. Processing of one image takes about 4 seconds (Intel Core i3, 4 GB RAM, Windows XP). The average time of manual supervising (adding and erasing of the marks) takes about 20 seconds.

## 5. CONCLUSION

The article shown the basic research in the field of microscopic image processing tools implementation. The aim is to simplify, speed-up, and increase the accuracy in image processing in studying the diverticular disease. The proposed approach can find the cell nuclei, it can recognize the overlapped cells and it allow manual supervising of the results. The manual processing of one image takes about 3 minutes and the automatic processing takes about 4 seconds, 24 seconds with manual supervising.

## ACKNOWLEDGMENT

This work was supported within the framework of the research plan MSM 0021630513 and projects ME10123 and GACR 102/11/0318.

## REFERENCES

1. Wedel, T., et al., "Diverticular disease is associated with an enteric neuropathy as revealed by morphometric analysis," *Neurogastroenterol Motil*, 2009.
2. Serra, J., *Image Analysis and Mathematical Morphology*, Vol. I, 600, Ac. Press, London, 1982.
3. Serra, J., *Image Analysis and Mathematical Morphology — Vol. II: Theoretical Advances*, 411, J. Serra, Ed., Academic Press, London, 1988.
4. Zack, G. W., W. E. Rogers, and S. A. Latt, "Automatic measurement of sister chromatid exchange frequency," *J. Histochem. Cytochem.*, Vol. 25, No. 7, 741–53, PMID 70454, 1977.
5. Image Processing and Analysis in Java (ImageJ) software documentation, on the website: <http://rsbweb.nih.gov/ij/>.

# Accuracy of Volumetry Depending on Smoothing Level

J. Mikulka, E. Gescheidtová, and K. Bartušek

Department of Theoretical and Experimental Electrical Engineering, Brno University of Technology  
Kolejni 4, 612 00 Brno, Czech Republic

**Abstract**— To imaging soft tissues is usually used tomography by magnetic resonance. Ideally, several tissue slices in three orthogonal planes (sagittal, coronal, transverse) are acquired. With slices in three planes is following reconstruction of shape of examined tissues most accurate. In case of acquired slices only in one plane the high spatial information lost occurs by image acquisition. Then it is necessary the shape of tissue appropriately reconstruct. At first the images are segmented and with use of particular segments the three dimensional model is composed. The reconstructed model has step-surface. There are several methods for smoothing the shape. In this article are discussed the methodology for shape smoothing. The results of volumetry with use of several smoothing levels are compared. Impact of shape smoothing to quality of reconstruction is discussed.

## 1. INTRODUCTION

Image processing in biomedical applications is strongly developing issue. There were described many methods and approaches for image preprocessing, segmentation and visualizing. In many cases it is useful to evaluate volume of examined objects and monitor its development in time. Typical example of examined object are tumors in human organs and monitoring their development depending on time and efficiency of treatment. To imaging mentioned soft tissues is usually used tomography by magnetic resonance. It is necessary the shape of tissue appropriately reconstruct. At first the images are segmented and with use of particular segments the three dimensional model is composed. The reconstructed model has step-surface. There are several methods for smoothing the shape. In this article the methodology for shape smoothing are discussed. The results of volumetry with use of several smoothing levels are compared. Impact of shape smoothing to quality of reconstruction is discussed. It is shown that high level of smoothing suppress the step-surface but the edge information is lost. Conversely the low smoothing level leads to poor reconstruction with visible slicing.

## 2. SHAPE RECONSTRUCTION

In figure 1 is shown set of slices of mandibular disc. The slices were segmented by active contours (edge-based level set approach) and the mandibular disc was extracted [1, 2]. The segmentation method is described by:

$$F(\varphi) = \lambda \int_{\Omega} g\delta(\varphi) |\nabla\varphi| dx dy + \nu \int_{\Omega} gH(-\varphi) dx dy \quad (1)$$

where the first term means the length of the zero level curve of  $\Phi$  (level set distance function) and the second term is called weighted area of  $\Omega_{\Phi}^-$ .  $\lambda, \nu$  are the weighted coefficients of the mentioned terms,  $\delta(\varphi)$  is the Dirac function and  $H$  is the Heaviside function. The  $g$  function is the edge indicator defined by

$$g = \frac{1}{1 + |\nabla G_{\sigma} * I|^2}, \quad (2)$$

where  $I$  is the original image and  $G_{\sigma}$  is the Gaussian kernel with standard deviation  $\sigma$ .

By calculus of variation, the first variation of the functional in (2) can be written as

$$\frac{d\varphi}{dt} = \mu \left[ \Delta\varphi - \operatorname{div} \left( \frac{\nabla\varphi}{|\nabla\varphi|} \right) \right] + \lambda\delta(\varphi) \operatorname{div} \left( g \frac{\nabla\varphi}{|\nabla\varphi|} \right) + \nu g\delta(\varphi). \quad (3)$$

This gradient flow is the evolution equation of the level set function  $\Phi$ . The second and third term in the Equation (3) correspond to the length and area energy functional. The first term penalizes the deviation of the level set function from a signed distance function during its evolution.

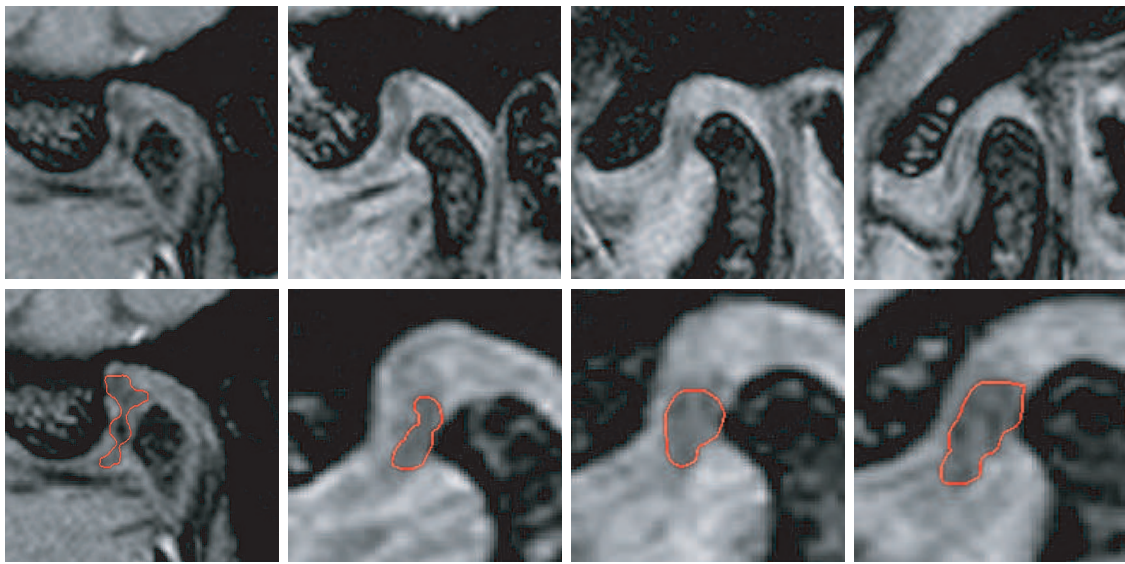


Figure 1: Selected slices of mandibular disc obtained by MR tomography and result of segmentation.

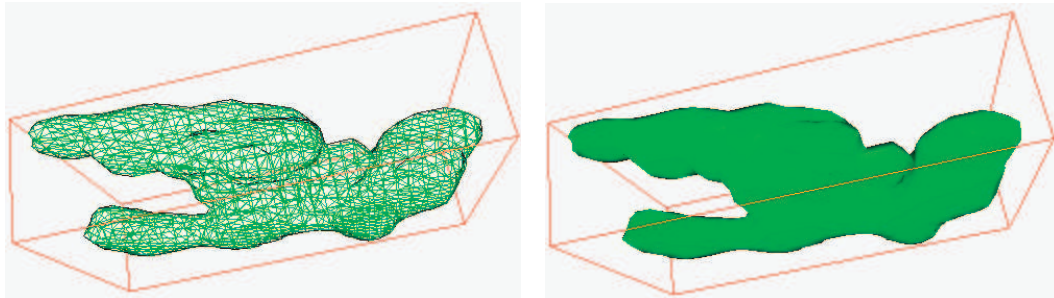


Figure 2: Reconstruction of mandibular disc with smoothing level 2.

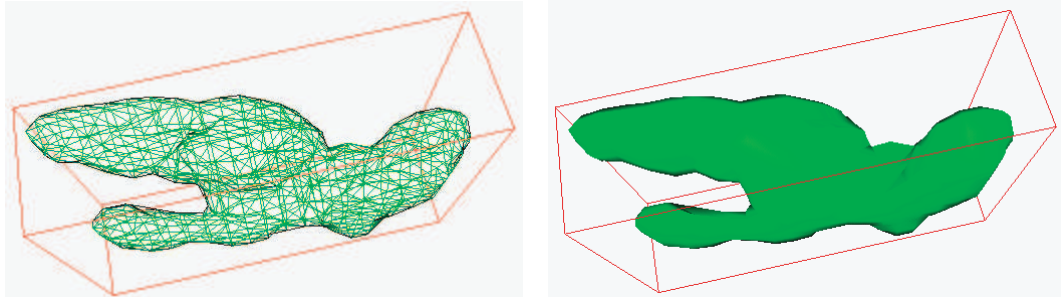


Figure 3: Reconstruction of mandibular disc with smoothing level 3.

In Figure 2 is shown result of shape reconstruction of mandibular disc with smoothing level of 2. In Figure 3 is shown result of shape reconstruction of mandibular disc with higher smoothing level of 3. The surface of the second model is smoother and the net model is created by less number of triangles. Three-dimensional models were created by ImageJ open-source software [3].

### 3. VOLUMETRY

The accuracy of volumetry was tested on images of liver tumor [4]. It was segmented manually at first and by automated process as well. Automatic processing is the very fast but the value of volume depends of the plane of obtained images. It is because of active contours segmentation methods principle. This approach has a filtering ability and the steady-state contour does not bound the edge of tumor exactly.

Table 1: Segmentation results of the edge-based level set method.

		Plane		
		Sagittal	Coronal	Transverse
<b>Sum of pixels [·]</b>		3147	2631	3171
<b>Pixel dimension [mm]</b>		0.811	0.777	0.811
<b>Total area [mm<sup>2</sup>]</b>		2069.848	1588.411	2085.633
<b>Slice thickness [mm]</b>		7	7	7
<b>Tumor volume [cm<sup>3</sup>]</b>	<b>automatic segmentation</b>	14.49	11.12	14.60
	<b>manual tracing</b>	9.70	10.00	10.10
<b>Approximate time of processing [s]</b>	<b>automatic segmentation</b>	20	25	30
	<b>manual tracing</b>	80	100	120

#### 4. CONCLUSIONS

The results obtained by edge-based segmentation approach is better then result obtained by region-based segmentation method. It is possible to use the results directly to creation of three dimensional model of the mandibular disc.

The impact of smoothing level on shape reconstruction by ImageJ tool was tested. The lowest smoothing level preserves the edges and small spatial details. The higher value of smoothing level suppress the aliasing caused by tomography slicing but the small details are lost.

In the case of volumetry the compromise between speed and accuracy of processing must be found. The manual processing can be more accurate than the automatic processing. It is very depending on human factor. The automatic processing is much faster than manual processing. It is best to use the automatic processing followed by manual supervising the results (area segmentation, spatial model creation).

#### ACKNOWLEDGMENT

This work was supported within the framework of the research plan MSM 0021630513 and projects ME10123 and GACR 102/11/0318.

#### REFERENCES

1. Mikulka, J., E. Gescheidtová, K. Bartusek, and Z. Smékal, “Processing of MR slices of temporomandibular disc for 3D visualization,” *PIERS Online*, Vol. 6, No. 3, 204–206, 2010.
2. Aubert, G. and P. Kornprobst, *Mathematical Problems in Image Processing: Partial Differential Equations and the Calculus of Variations*, 2nd Edition, Springer Science + Business Media, LLC, New York, 2006, ISBN 0-387-32200-0.
3. Image Processing and Analysis in Java (ImageJ) software documentation, on the website: <http://rsbweb.nih.gov/ij/>.
4. Mikulka, J., E. Gescheidtova, and K. Bartusek, “Processing of MR slices of human liver for volumetry,” *PIERS Proceedings*, 202–204, Xi'an, China, March 22–26, 2010.

# Synthesis of Arc Ladder Filters with Transmission Zeros for Using in the Feed Back of the Phase Lock Loop

Martin Friedl, Lubomír Fröhlich, and Jiří Sedláček  
Brno, FEEC BUT, UTEE, Kolejní 2906/4, Brno 612 00, Czech Republic

**Abstract**— In the field of a measurement of the fast one shot processes there is necessary to use special frequency filters. This frequency filter is usually connected in the feed back circuit of the phase lock loop (PLL), where performs a fine tuning of the frequency. Therefore the synthesis and optimization of the ARC ladder filters with transmission zeros based on frequency dependent negative resistors (FDNR) was elaborated. Frequency filters designed using approximation functions with transfer zeros (like Inverse Tchebyschev or Cauer functions) exhibit in comparison to approximation functions with monotonic magnitude response in stop band essential higher steepness of magnitude response in area of transitive band of filter. Active RC filters synthesized using modern active elements grown from passive RLC filter prototypes with very small sensitivity on passive elements can be in comparison to their RLC prototypes realized relative easily. These filters designed using active FDNR blocks as LP (low pass) filters or using SI (Simulated inductors) active blocks in case of HP (high pass) filters can be designed with minimum active and passive elements. During resulting optimization filter design process must be an influence of real lossy active blocks (FNDR, SI) on resulting filter response respected. In contribution here are presented some possibilities of filter optimization from this point of view. There are also discussed and in some examples prescribed ways of filter synthesis with account of influence of lossy active blocks on resulting filter magnitude response in case of Inverse Tchebyschev and Cauer filter of LP and HP filters of higher (from 3rd to 7th) filter orders.

## 1. INTRODUCTION

The realization of filters with transmission zeros requires only a small increase in complexity. The zero transfer in the transmission function of the filter is obtained by creating an additional resonant circuit in the classical ladder filter structure. Thereby will achieve an increase steepness of the transmission filter characteristics and significantly suppress the specific area (zero transmission) [1].

The presented paper describes possible to use of lossy FDNR elements in the filters with transmission zeros. There are advisedly used FDNR elements, by reason that by useful optimization the value of the filter element can be achieved almost the same transmission characteristics as with lossless blocks, however using half the number of OAs. In this paper also lossy FDNR blocks were studied and determine the limits of the lossy.

## 2. LOSSY FDNR BLOCKS

By the design of frequency RLC filters is the biggest problem with the quality, size and price of coils. Consequently, for low and medium frequencies, RLC filters are preferably replaced by active filters RC (ARC). Their basic principle consists in replacement the coil through the use of an active element with resistors and capacitors [2, 3]. One of the suitable method is solution consists in the creation the ARC circuit with transfer function of the 2nd order, which is equal to transfer functions of RLC filter through the use of FDNR blocks or SI blocks. FDNR elements are preferably used for low pass filters. Filters with FDNR elements replace coils indirectly using Bruton's transformation [4], which transforms the initial RLC structure into equivalent behaving the CRD structure (Fig. 1). This new structure does not contain an element of inductive character, but uses the properties of the synthetic element FDNR.

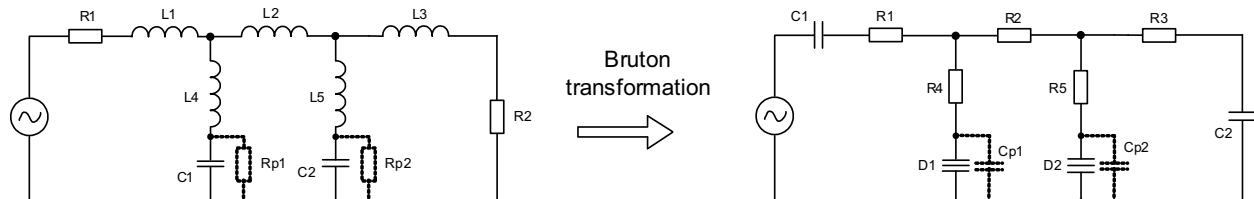


Figure 1: Design principle of active LP filter of the 3rd order with transfer zero.

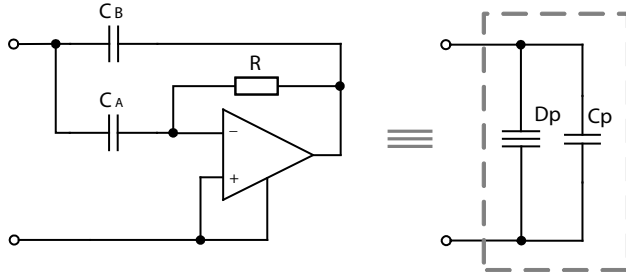


Figure 2: Grounded FDNR block with parallel lossy.

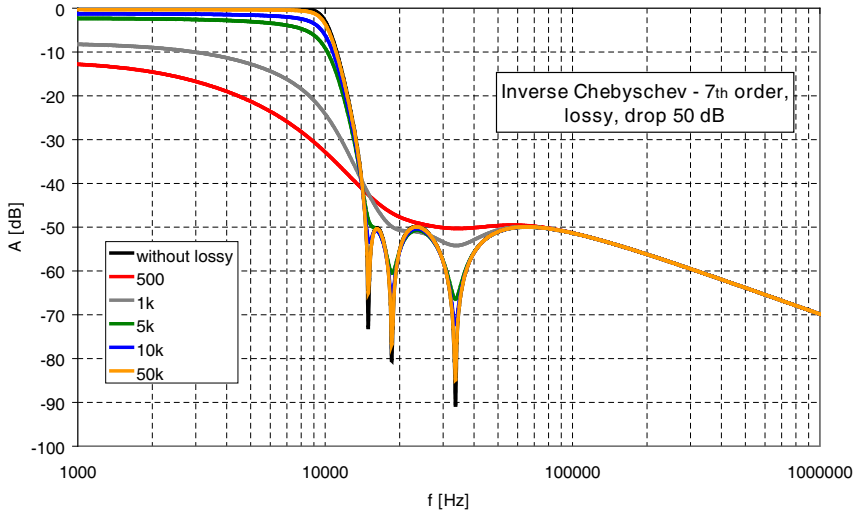


Figure 3: Magnitude response of filter with lossy resistors 0–10 kΩ.

The active circuits realized of the FDNR elements can be separated into different types according to their basic circuit characteristics [3]. The lossy FDNR grounded circuit (Fig. 2) can be realized by the use one active element (OA) [5]. In this circuit the losses are represented by a parallel capacitor. These losses correspond to resistors  $R_{p1}$  and  $R_{p2}$  parallel connected to capacitors in the initial circuit of the RLC filter (Fig. 1). Thus it is very easy these lossy to simulate and to investigate filter response to different values of the resistors  $R_{p1}$  and  $R_{p2}$ .

### 3. SIMULATIONS OF LOSSY IN LOW PASS FILTER

The circuit simulations of the influence of lossy FDNR blocks with lossy resistors  $R_{p1}$  and  $R_{p2}$  in the RLC filter (Fig. 1) were realized for inverse Tchebyschev low-pass filter. The different values of the lossy resistors were reflected in the final transmission characteristics of filter (Fig. 3). The simulations were realized for 3rd, 5th and 7th filter order for three values of minimum suppression of the filter. The below inserted transmission characteristics in Fig. 3 correspond to 7th filter order and the minimum value of the suppression filter 50 dB.

In the case that the lossy resistors in RLC filter (Fig. 1) modify the transfer function, due to shifting of the cut-off frequency filter. The following graph (Fig. 4) shows the lossy influence for the 7th filter order and the minimum suppression filter 30, 50 and 70 dB.

From the all simulations result these conclusion. The lossy resistors in circuit of the RLC filter (Fig. 1), simulating the lossy of the FDNR element, significantly deform the final transfer of the filter. The resulting distortion of the transfer characteristic of the filter (compared to the ideal structure of the RLC filter) increases in case of the decrease values of the lossy resistors  $R_{p1}$  and  $R_{p2}$  — there is a drop in the pass-band filter, to suppress the transmission zeros and to cut-off frequency shift. Cut-off frequency shift depends on the value of the minimum drop filter (Fig. 4). On the Fig. 5 is showed for better lucidity 3D transfer characteristics of low-pass filter of the 5th order (Fig. 1) in dependence on the lossy resistors  $R_{p1}$  and  $R_{p2}$ . The transfer drop in pass-band of the filter, suppressing of the transfer zeros and cut-off frequency shift are clearly visible with increasing lossy.

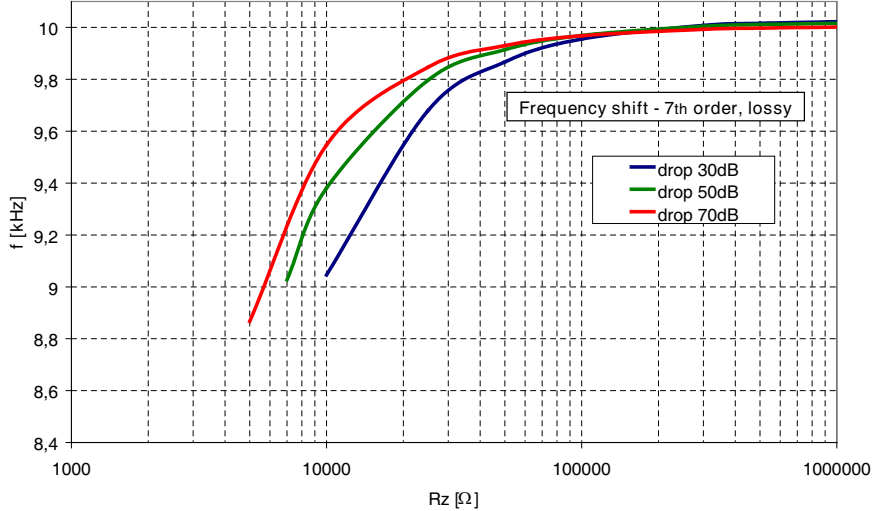


Figure 4: The frequency shift in depending on lossy.

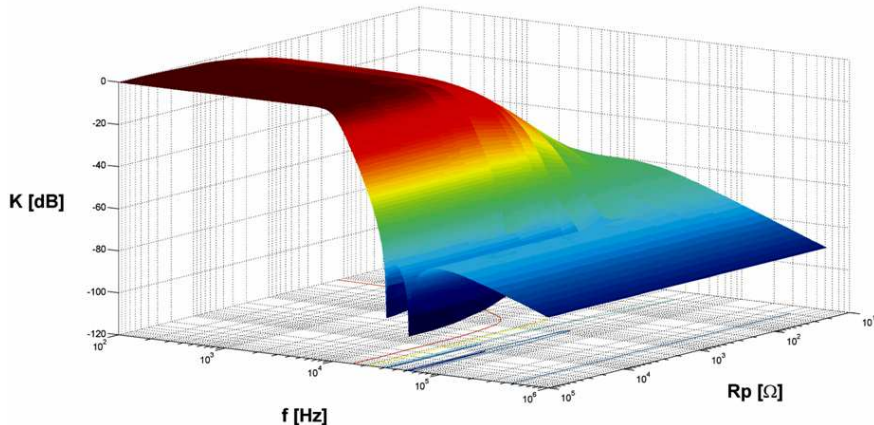


Figure 5: The 3D transfer characteristic of low-pass filter of the 5th order.

Table 1: Limit of lossy resistors.

Filter order	3rd	5th	7th
Rz min [W]	2	4	6
Frequency [kHz]	9.68	9.04	8.35

The RLC ladder structure of the filter shows that the higher order of the filter causes the higher lossy, briefly the more lossy resistors will affect the filter characteristics. The number of lossy resistors is equal to number lateral branches of the ladder filter considering the lossy after using Bruton transformation and subsequent FDNR element replacement puts into effect in just lateral branches, the expression is valid:

$$N = \frac{n-1}{2}, \quad (1)$$

where  $n$  means an odd filter order and  $N$  means the number of lateral branches, thus the lossy resistors. From the previous results that the influence of the lossy resistor will be the smallest in the 3rd order filter and the largest at the 7th order filter. The resulting limits were defined to drop 2 dB compared to pass-band filter and are shown in the table bellow.

The defined limits of the lossy resistors ensure enough emphasis of the transfer zeros yet. The relatively high cut-off frequency shift is not critical because the frequency shift can be easily calculated in advance and corrected in the optimization step of filter design.

#### 4. CONCLUSIONS

In this paper have been investigated the effect of lossy influence in the structure of the RLC filter. All the resulting transfer characteristics were shifted by 6 dB higher — thereupon impact of the terminating resistors was suppressed, with the view of the better comparison all transfer characteristics in the Fig. 3. The resulting limits of the lossy influence for three filter orders of the low-pass filter by inverse Tchebyschev approximation are shown in Table 1. The defined limits of the lossy resistors ensure enough emphasis of the transfer zeros yet and the relatively high cut-off frequency shift can be corrected in the optimization step of filter design. The influence of the lossy resistors could be guide by the design of active filters with lossy FDNR elements and help for first early information to the designer what the lossy resistor will have an impact to resulting filter characteristics. The designed filters are specifically established for use in the feedback phase coupling (PLL). It becomes clear, that in area of the lossy FDNR element design, it will be in some cases difficult to meet the acceptable limits of the lossy resistors. The unrealistic values of components in the lossy FDNR element are the reason for it. Therefore, further research will be focused on the optimization of the filters with lossy FDNR elements [6, 7].

#### ACKNOWLEDGMENT

This work has been supported by the project of the BUT Grant Agency FEKT-S-11-5.

#### REFERENCES

1. Pactitis, S., *Active Filters: Theory and Design*, CRC Press, USA, 274 str., 2008, ISBN 978-1-4200-5476-7.
2. Sedláček, J. and K. Hájek, *Kmitočtové Filtry*, 1. vydání, 535s, Praha, BEN, technická literatura, 2002, ISBN 80-7300-023-7.
3. Friedl, M., *Synthesis of Modern Structures Frequency Filters*, 21s, Pojednání k disertační práci, Brno university of technologyFaculty of Electrical Engineering and Communication, Department of Theoretical and Experimental Electrical Engineering, Brno, 2010.
4. Bruton, L. T., *RC-Active Circuits Theory and Design*, Englewood Cliffs, Prentice-Hall, Inc., New Jersey, 1980, ISBN 0-13-753467-1.
5. Hájek, K., V. Michal, J. Sedláček, and M. Steinbauer, “A simple method of goal — directed lossy synthesis and network optimization,” 249–253, ADVANCES in Electrical and Electronic Engineering, Žilina, 2006, ISSN 1336-1376.
6. Friedl, M., L. Fröhlich, and J. Sedláček, “Modified approximation types for lossy building blocks,” *PIERS Proceedings*, 521–525, Xian, China, March 22–26, 2010.
7. Hájek, K. and J. Sedláček, “Lossy LC ladder prototypes and their use for ARC filter optimization,” *WSEAS Transactions on Electronics*, Vol. 2, No. 3, 94–99, July 2005, ISSN 1109–9445.

## A 3D Magnetic Measurement for S/N < 0.01

Z. Roubal and T. Kříž

Department of Theoretical and Experimental Electrical Engineering, Brno University of Technology  
Kolejní 2906/4, Brno 612 00, Czech Republic

**Abstract**— The authors describe the process of developing a 3D meter designed for magnetic field mapping in MR Image Reconstruction (MREIT). As the anticipated application of MREIT involves the factor of an environment with strong electromagnetic disturbance, it is necessary to use a measurement method insensitive to such conditions. The most significant spurious signals affecting the process of measurement come from the supply mains and switched supply sources. In order to suppress these influences, the authors utilize the principle of synchronous detection in a lock-in amplifier; the amplifier facilitates the suppression of these spurious disturbing signals and enables the selection of the required ones. In the designed 3D magnetic field meter, Hall probes are used for the measurement of magnetic induction. At the beginning of the measurement, the measuring device automatically corrects the reference signal phase shift for the maximum amplitude of the output direct voltage; also, the influence of Earth's magnetic field is compensated. The magnetic field map measured using the 3D meter is used for the reconstruction of material properties of the measured sample.

### 1. INTRODUCTION

The EIT problem [1] recovers conductivity distribution satisfying the continuity equation

$$\operatorname{div} \mathbf{J} = 0. \quad (1)$$

Current density  $\mathbf{J}$  in a linear medium with interior conductivity  $\sigma$  can be obtained from electric field  $\mathbf{E}$  or the corresponding potential distribution  $\Phi$

$$\mathbf{J} = \sigma \cdot \mathbf{E} = -\sigma \cdot \operatorname{grad} \Phi \quad (2)$$

Further, we assume the electric field in a very thin layer of an electrically conductive medium which can be described by the surface current density  $\mathbf{K}$ . Magnetic flux density  $\mathbf{B}$  corresponding to  $\mathbf{K}$  can be obtained according to the Biot-Savart Law

$$\mathbf{B} = \frac{\mu_0}{4\pi} \int_S \frac{\mathbf{K} \times \mathbf{R}}{R^3} dS \quad (3)$$

For further numerical simulations, we divided the sample into  $NE$  triangle elements with centers  $[x_t, y_t, z_t]$ . We suppose that current density  $\mathbf{K}$  is constant on each element. Magnetic field in the general point given by coordinates  $[x_i, y_i, z_i]$  can be calculated using the superposition principle

$$\mathbf{B}_i \approx \frac{\mu_0}{4\pi} \sum_{j=1}^{NE} \frac{\mathbf{K}_j \times \mathbf{R}_{ij}}{R_{ij}^3} \Delta S_j \quad (4)$$

Vector  $\mathbf{R}$  represents the distance between the centre of the actual element  $[x_t, y_t, z_t]$  and the point  $[x_i, y_i, z_i]$ . If we know certain components of the magnetic field, we can obtain the current density distribution; see [5]. If we need to obtain the  $NE$  values of  $K_x$  and  $K_y$  components of surface current density  $\mathbf{K}$ , we have to know, for example, the same number of  $B_x$  and  $B_y$  components of the magnetic field

$$B_{ix} = \frac{\mu_0}{4\pi} \sum_{j=1}^{NE} R_{ijz} \frac{\Delta S_j}{R_{ij}^3} K_{jy}, \quad B_{iy} = -\frac{\mu_0}{4\pi} \sum_{j=1}^{NE} R_{ijz} \frac{\Delta S_j}{R_{ij}^3} K_{jx}, \quad i = 1, \dots, NE$$

The matrix notation for these  $2 \cdot NE$  algebraic equations is

$$\begin{bmatrix} B_{koefx} & 0 \\ 0 & B_{koeffy} \end{bmatrix} \begin{bmatrix} K_x \\ K_y \end{bmatrix} = \begin{bmatrix} B_x \\ B_y \end{bmatrix} \Leftrightarrow \mathbf{B}_{koeff} \mathbf{K} = \mathbf{B} \quad (5)$$

From system (5), we can obtain very easily the required current density distribution [1]

$$\mathbf{K} = \mathbf{B}_{koeff}^{-1} \mathbf{B} \quad (6)$$

## 2. MAGNETIC FIELD SENSORS

In order for a map of the magnetic field outside the measured sample to be created, the magnetic induction must be measured (if possible) in a small volume, pointwise. Therefore, it is not possible to utilize measuring coils or ferromagnetic probes. After considering all requirements related to the measurement, we selected a magnetic field sensor using a Hall probe (Figure 1), which is characterized by its applicability in a wider range of magnetic induction. The probe employs the Hall effect and is mostly composed of a thin semiconducting platelet based on GaAs, Si or InSb. Direct current  $I$  passes through current-carrying contacts  $C_1$  and  $C_2$ . A magnetic field of induction  $B$  acts on the moving charge carriers through the Lorentz force, which deflects them in a direction perpendicular to the passing current and the magnetic induction vector. On opposite sides at the platelet there generates the Hall voltage  $U_H$  measured on contacts  $S_1$  and  $S_2$ . The voltage magnitude is given by

$$U_H = \frac{R_H}{t} \cdot I \cdot B \quad (7)$$

where  $R_H$  is the Hall constant,  $I$  is the current passing through the semiconducting plate,  $t$  is the plate thickness, and  $B$  the magnetic field induction perpendicular to the plane of the semiconducting platelet. Today, all the sensor electronics together with the Hall probe are usually integrated in a single chip. The selected A1302 EUA-T Hall sensor is distinguished by its easy availability and low noise.

An amplifier providing for the Hall voltage amplification as well as an automatic offset compensation are already integrated in the sensor. With  $B = 0\text{T}$ , there is a half-value of the supply voltage on the sensor output; therefore, with the recommended supply voltage of 5 V, the output shows the voltage of 2.5 V. Typical sensitivity for  $25^\circ\text{C}$  is  $1.3\text{ mV}/100\text{ }\mu\text{T}$ . If a low-pass filter having the bandwidth of 10 kHz is used, noise voltage on the output equals to  $150\text{ }\mu\text{V}$ , which is consistent with the magnetic induction minimum measurable value of  $11\text{ }\mu\text{T}$ . The measurement of all three components of magnetic induction was conducted by the help of three mutually orthogonal sensors. In order to prevent undesirable interaction (such as that generated by a magnetic field induced around the feeding conductor) between the sensors during measurement, it is necessary to scan individual components of the magnetic field in a time multiplex; the unused sensors are not fed.

## 3. SYNCHRONOUS DETECTION USING A LOCK-IN AMPLIFIER

The measured sample is excited by a source of sinusoidal-wave alternating current. Thus, we have at our disposal a reference signal having a frequency identical with that of the measured signal. Advantageously, the synchronous detection principle can be used to facilitate measurement of the required signal below the environment disturbance level. The basics of a lock-in amplifier utilizing synchronous detection are shown in Figure 2. The measured signal is amplified in an input amplifier; on its output, then, the signal is led to the analogue multiplexer, which switches between the amplified signal and its inversion having the frequency of the reference signal. If we assume the special case when a non-disturbed signal on the analogue multiplexer input is in phase with the reference signal, then on the output there is a two-way rectified signal. This signal is then filtered through a low-pass filter, with the output direct voltage proportional to the measured signal mean value. If both the input and the reference signal have the same period  $T$  and the input signal (compared to the reference signal) shows a phase delay with a time interval of  $\Delta t$ , the output

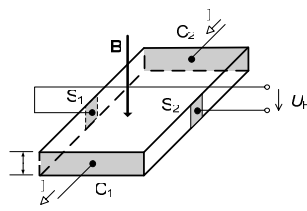


Figure 1: Principal connection of the hall probe.

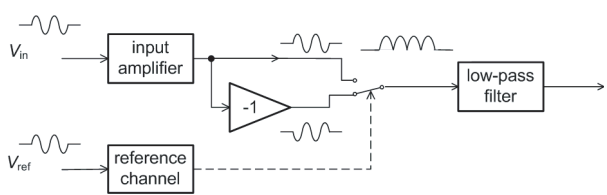


Figure 2: A lock-in amplifier.

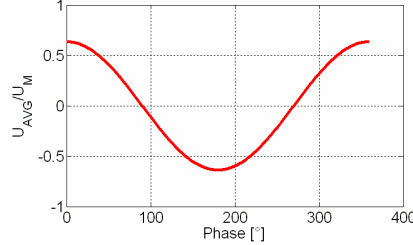


Figure 3: Theoretical dependence of the output signal mean value mean value on phase shift.



Figure 4: The measured signal spectrum before synchronous detection [1].

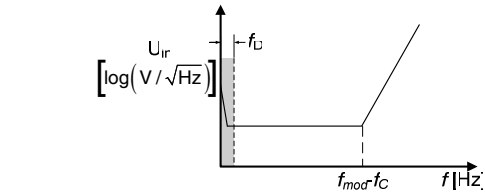


Figure 5: The measured signal spectrum after synchronous detection [1].

voltage mean value equals to

$$U_{\text{out}} = \frac{1}{2 \cdot T} \cdot \int_{0-\Delta t}^{\frac{T}{2}-\Delta t} u_{\text{in}}(t) dt + \frac{1}{2 \cdot T} \cdot \int_{\frac{T}{2}-\Delta t}^{T-\Delta t} -u_{\text{in}}(t) dt \quad (8)$$

While the output voltage is maximal for the phase shift of  $(0 + k \cdot 360)^\circ$  between the measured and the reference signal, it is zero for  $(90 + k \cdot 180)^\circ$ . The relation for  $\varphi$  between  $0^\circ$  and  $360^\circ$  can be seen in Figure 3.

Through the measuring configuration indicated in Figure 2, the independence of the output signal on the direct component is reached as the direct component is added to the measured signal in the first half-period and deducted from it in the second half-period. Therefore, the oscillations in Earth's magnetic field and the direct disturbance from the Hall sensors supply have no effect on the measured mean value of magnetic induction.

Synchronous detection also brings a positive influence on the suppression of noise  $1/f$ . The Hall probe shows the  $1/f$  noise below frequency  $f_c$ , which amounts to approximately 300 Hz–5 kHz [2]. The measured signal is modulated on a frequency which is not a multiple of mesh frequency within the range of several hundreds of Hz to several kHz. The signal spectrum before synchronous detection can be seen in Figure 4, whereas the state after synchronous detection is shown in Figure 5 [1]. Thus, if we select  $f_{\text{mod}} < f_k$ , the  $1/f$  noise is suppressed. With the low-pass bandwidth of  $f_D = 20$  Hz, the Teslameter sensitivity will rise to the value of  $B_{\min 20\text{Hz}}$

$$B_{\min 20\text{Hz}} = \frac{B_{\min 10\text{kHz}}}{\sqrt{10\text{ kHz}}/\sqrt{20\text{ Hz}}} = \frac{11\text{ }\mu\text{T}}{22,36} = 0.49\text{ }\mu\text{T} \quad (9)$$

#### 4. THE LOW-PASS FILTER

For the Sallen-Key low-pass filter, we applied the Gaussian approximation owing to the good response to momentum discontinuity [3, 4]. The break frequency for the bandwidth of 6 dB was determined to be 20 Hz, with the filter order of 10. The filter bandwidth constitutes a compromise between the rate (speed) of measurement and sensitivity to weak magnetic fields. With the jump change of input voltage, the output becomes stable after 0.6 s. Figure 6 shows a simulation voltage transfer  $K_U$  of the designed filter; frequency characteristics measured by the help of the Bode 100 analyzer are indicated in Figure 7. In order to suppress the direct offset influence, we used the high-quality OP27 operational amplifier in the filter.

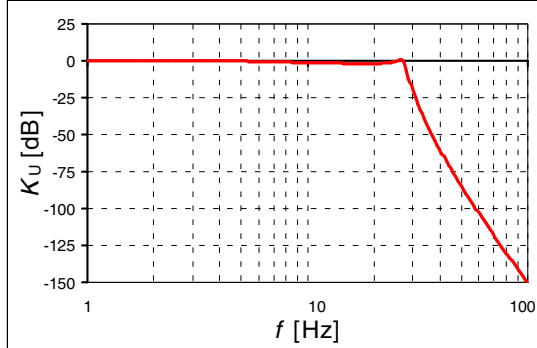
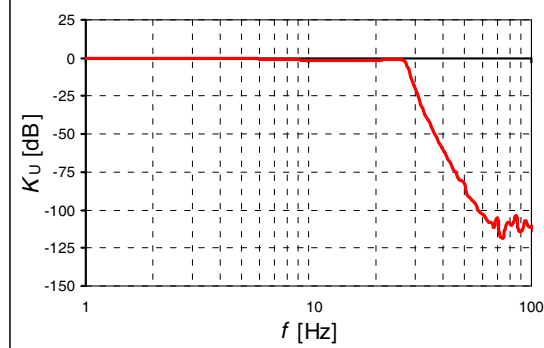
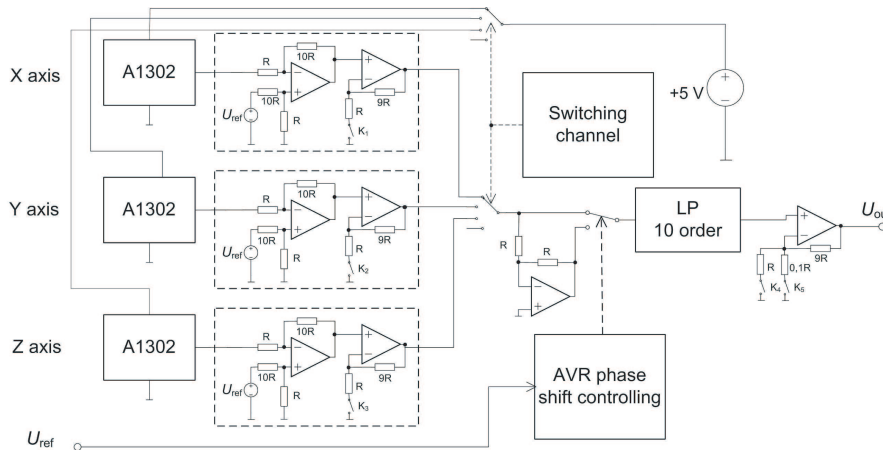
Figure 6: Simulation  $K_U$  through the low-pass filter.Figure 7: The measured  $K_U$  through the low-pass filter.

Figure 8: Principal diagram 3D Teslameter.



Figure 9: Internal configuration 3D Teslameter.

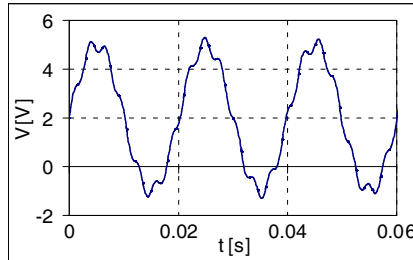


Figure 10: Disturbed input signal.

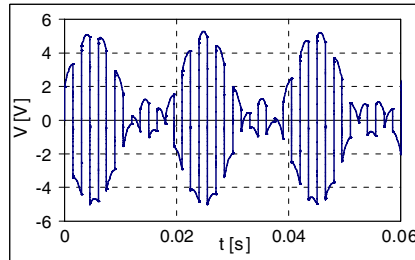
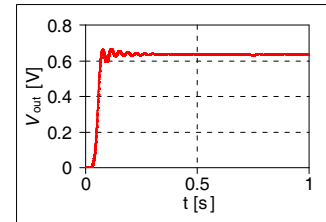


Figure 11: The output of a synchronous rectifier.

Figure 12: Response to the output ( $S/N = -40 \text{ dB}$ ).

## 5. OVERALL CONNECTION OF THE 3D MAGNETIC FIELD METER AND THE MEASURED DATA

Each A1302 sensor has its own preamplification stage, on whose input there is a difference amplifier compensating for the direct shift of the sensor (2.5 V in magnitude) and amplifying the signal 10 times.

By means of the direct shift elimination, any possible saturation in the measurement chain is prevented. Through the  $K_1$  to  $K_4$  relays, we select the measurement range. The switching between channels is realized using an Agilent measuring centre. The reference signal phase shift controlling takes place through the AVR Atmega8A microcontroller; during calibration at the start of the measurement, the output voltage is tuned to the maximum (the condition of  $\varphi = (0 + k \cdot 360)^\circ$  is satisfied). The principal diagram can be found in Figure 8, with the internal configuration indicated in Figure 9. Figure 10 shows a disturbed input signal with the spurious mesh frequency, having an amplitude of 3 V; the measured signal with the frequency of 333 Hz has an amplitude of 0.3 V. At

Table 1: Depend  $U_{str}/U_M = f$  (S/N).

S/N [dB]	$U_{Noise}$ [V]	$U_{str}/U_M$
0	0.002	0.635
-20	0.02	0.635
-40	0.2	0.635
-60	2	0.5

higher disturbance levels there occurs the saturation and related overloading of the measurement chain.

Figure 11 describes the output of a synchronous rectifier and the Table 1 contains a summary of the results for various relations of the measured and the spurious signals. The output voltage response to the momentum discontinuity is shown in Figure 12.

## 6. CONCLUSION

The designed 3D magnetic field meter globally eliminates external influences of electromagnetic disturbance and further reduces the effects generated by the noise of the applied sensor and active amplifying elements. The use of the meter for the purposes of MREIT will enable not only the verification of this novel method, but also the evaluation of its applicability for determining the properties of an examined material. The measurement requirement for  $S/N < 0.01$  was effectively satisfied: It is possible to measure up to  $S/N > 0.001$ .

## ACKNOWLEDGMENT

The work described in the paper was financially supported by the research plan MSM 0021630516, research plan MSM 0021630513, and project of the BUT Grant Foundation FEKT-S-11-5.

## REFERENCES

1. Ostanina, K., J. Dědková, and T. Kříž, "Utilization of boundary conditions in MR image reconstruction," *PIERS Proceedings*, 665–668, Marrakesh, Morocco, Mar. 20–23, 2011.
2. Pastre, M., M. Kayal, and H. Blanchard, "A hall sensor analog front end for current measurement with continuous gain calibration," *IEEE Sensors Journal*, Vol. 7, No. 5, 860–867, May 2007.
3. Popovic, D. R., S. Dimitrijevic, M. Blagojevic, P. Kejik, E. Schurig, and R. S. Popovic, "Three-axis teslameter with integrated hall probe free from the planar hall effect," *Proceedings of the IEEE Instrumentation and Measurement Technology Conference*, 1812–1815, Apr. 24–27, 2006.
4. Sedlacek, J. and M. Friedl, "Optimization of ARC component filter sensitivity," *PIERS Proceedings*, 526–530, Xi'an, China, Mar. 22–26, 2010.
5. Hájek K., J. Sedláček, *Kmitočtové Filtry*, BEN, Praha, 2002.

# The Study of Transport of Substances in the Plant Stems

Michaela Burdková and Tomáš Kříž

Department of Theoretical and Experimental Electrical Engineering  
Brno University of Technology, Kolejni 4, Brno 612 00, Czech Republic

**Abstract**— Monitoring of tissue structures of Euphorbia plants in non-destructive manner is possible using nuclear magnetic resonance-based tracking of angular momentum and the responses of nuclei placed in a magnetic field with defined induction and interaction with high-frequency electromagnetic waves. Characteristics of the response are dependent on the method of application of series of radiofrequency pulses. After the finish of phenomenon the resulting signal is detected by the receiving coil of tomograph. Measured plant is sensed by magnetic resonance imaging in several slices oriented perpendicular to the axis of the stem of the plant. The slices are designed in the same distances between them from the bottom of the root to the top edge of the plant. There is only part of the plant in the working area of the tomograph during the measurement. The measurements are chosen using sensing techniques called spin echo and inversion recovery method. The acquired images are weighted by relaxation times  $T_1$  for spin echo method respectively by  $T_2$  for inversion recovery method. Pictures weighted by relaxation times are evaluated in the program Marevisi manually to determine vascular structure of plants. Longer relaxation times correspond to places where there is a greater presence of water. Contrasts in the image correspond to the chemical bonds in nutritive substances, viscosity agents and mobility of molecules.

## 1. INTRODUCTION

For the study of substances in the tissues using tomographic imaging, there are several types of instruments. This article focuses only on magnetic resonance imaging (MRI). Physical principle of MRI is based on the fact that protons and neutrons have their own specific angular momentum, called spin, which makes the whole nucleus acquires a magnetic moment [1]. MRI is used to display tomographic tissue especially in medicine, but also in other fields which is closely related to medicine, biology, for example for plant tissue cultures and determination of its morphology, which is the main objective of this article. MRI is one of the non-destructive imaging techniques for observing tissue. The main advantages of MRI are non-existence of harmful radiation and adverse effects of the object, another advantage is the high image contrast in soft tissues. MRI slices are obtained from a certain area of plant tissue that shows the spatial distribution of spins, and these pictures are weighted by relaxation times  $T_1$  and  $T_2$ . Based on the obtained images the reconstructed image is made and the internal structure of Euphorbia plants is determined from it. Higher intensity of the reconstructed image point corresponds to the higher  $T_1$  relaxation time [2]. The aim of this project is a reconstructed image with recognizable morphology of vascular tissues in stem section slices of plants, carried out using the methods of spin echo and inversion recovery method with the chosen parameters.

## 2. SPIN ECHO AND INVERISON RECOVERY METHOD

The method of Spin Echo (SE) consist of two consecutive RF pulses with phases  $90^\circ$  and  $180^\circ$ , their duration is in order of several milliseconds. By applying the first pulse the magnetization vector flips to the transverse plane and the  $T_2$  relaxation begins to appear then occurs the phasing out. The application of second impulse leads to flip individual spins from the transverse plane by  $180^\circ$ , and the re-phasing occurs and by the receiving coil the ECHO signal is detected, whose amplitude is dependent on the tissue's  $T_2$  time. Image contrast can be adjusted by weighting relaxation times.

Method of Inversion Recovery (IR) consists of a sequence of RF pulses of  $180^\circ$ ,  $90^\circ$  and  $180^\circ$ . The first pulse inverts the magnetization vector. Then begin to apply the  $T_1$  relaxation and the magnetization vector returns to its original equilibrium state. A subsequent second pulse reverses the magnetization vector in the transverse plane. In the receiving coil the FID signal, whose amplitude is dependent on the relaxation time  $T_1$  of the shown tissue, is detected. The IR is suitable method for measuring of the relaxation time  $T_1$  and the SE is suitable method for relaxation time  $T_2$  [3, 4].

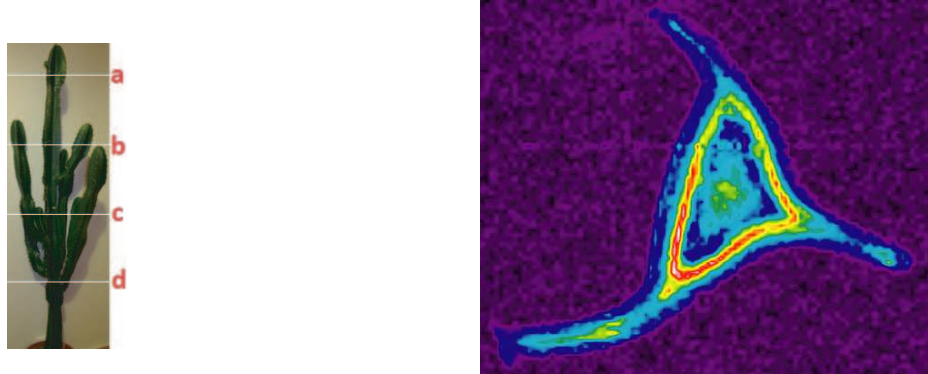


Figure 1: The layout of the slices of individual sections of Euphorbia cactus.

Figure 2: Non-weighted image of the stem cactus slice.

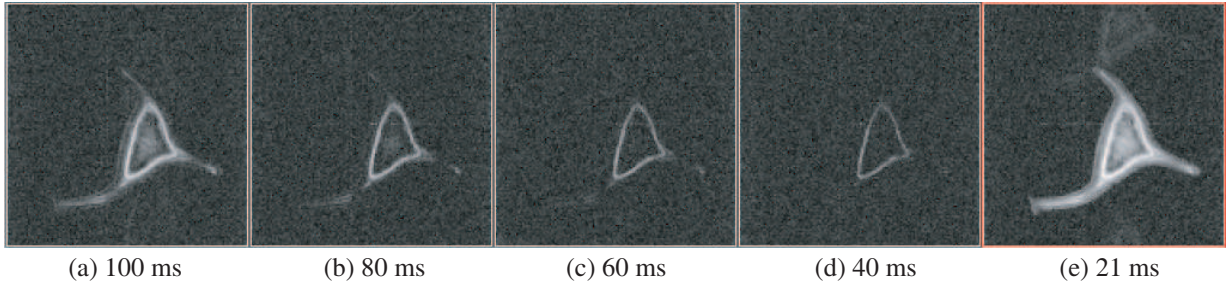


Figure 3: A series of slices with different times  $T_E$ .

### 3. EXPERIMENTAL MEASUREMENETS

MRI images were recorded at 4.7 T MRI system/75 mm (200 MHz) at ÚPT AV CR, v.v.i. in Brno. Scanned images were  $256 \times 256$  pixels large and the size of the operation point was  $26 \times 26$  mm. System resolution was 0.1 mm/pixel. MRI images were measured perpendicular to the axis of the stem of Euphorbia cactus in several slices, which were at different heights from the root to the upper part of the plant (Figure 1).

The evaluation of pictures taken by the IR method with measurements of the  $T_1$  relaxation time is done manually in the program Marevisi. The color in the image corresponds to the intensity that is proportional to the number of proton nuclei in the place of the cactus stem. In the middle of the Figure 2 you can see two light spots, which indicate higher water content (presence of vascular bundles). The images made from the intensities obtained by tomography are weighted by relaxation times  $T_1$  and  $T_2$ .

To measure the individual slices were selected following times TE: 21 ms, 40 ms, 60 ms, 80 ms and 100 ms (Figure 3).

A series of frames is then weighted by Equation (1).

$$y = \rho \left( 1 - 2e^{\frac{-T_E}{T_2}} \right) \quad (1)$$

which is obtained by weighting the resulting image (Figure 4), on which are indicated points 1 to 6. In these points is implied the presence of blood vessels. Each selected point in the image corresponds to a measured relaxation time captured in the Table 1.

The IR method shows that the longer relaxation time corresponds to a higher intensity of the point. Selected items 2, 3 and 4 are non-zero relaxation time  $T_1$ , which indicates a large amount of water (vascular tissue), the remaining points with zero value of relaxation time become a place where water level is zero (no vascular tissue).

Evaluation of  $T_2$  relaxation time measured using the SE method was performed similarly to the time  $T_1$ . To measure the individual slices were selected following times  $T_E$ : 21 ms, 50 ms, 100 ms, 500 ms and 1500 ms (Figure 5).

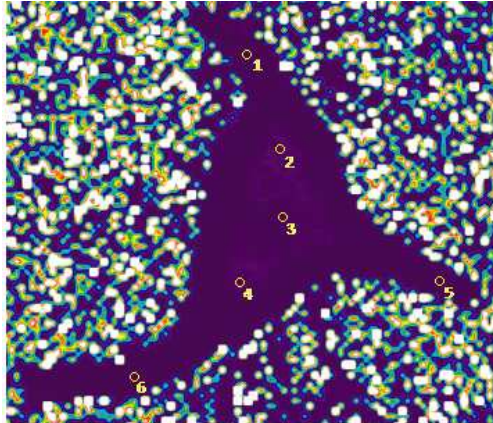


Figure 4: Plotted individual points of relaxation times  $T_1$ .

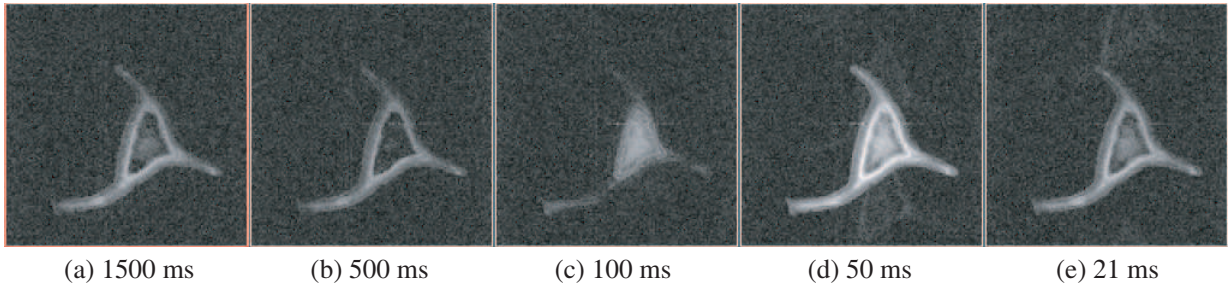


Figure 5: A series of slices with different times  $T_E$ .

Table 1: The resultant values of relaxation times  $T_1$ .

Selected point in the image	Relaxation time $T_1$ [ms]
1	0
2	35,455
3	51,553
4	17,186
5	0
6	0

Table 2: The resultant values of relaxation times  $T_2$ .

Selected point in the image	Relaxation time $T_1$ [ms]
1	28,939
2	37,406
3	68,657
4	19,204
5	17,441
6	35,890

A series of frames is then weighted by Equation (2).

$$y = \rho \left( e^{\frac{-t}{T_2}} \right) \quad (2)$$

On the final weighted image (Figure 6) are selected points 1–6, in which a finding of vascular tissue is expected. Each selected point in the image corresponds to a measured relaxation time captured in Table 2.

The value of  $T_2$  relaxation times depends on the amount of water in the plant site. A nonzero value of relaxation time reflects the fact that the site is located in vascular tissue. Since the points

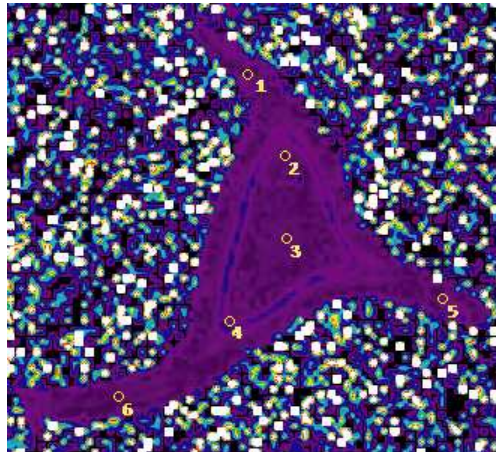


Figure 6: Plotted individual points of relaxation times  $T_2$ .

with a nonzero value are found all over the plant, then it follows that the plant has vascular tissue all over the selected area.

#### 4. CONCLUSIONS

The objective was to determine the morphology of cactus plants. Its exact structure was determined on the basis of MRI measurement methods SE ( $T_E$ : 21 ms (best contrast), 40 ms, 60 ms, 80 ms a 100 ms) and IR ( $T_E$ : 21 ms, 50 ms (best contrast), 100 ms, 500 ms a 1500 ms) then weighted by relaxation times  $T_1$  and  $T_2$ . Comparing Tables 1 and 2 the more sensitive method is SE (for the IR method the zero values of relaxation time occurs), also the resulting weighted image obtained by SE method better captures the structure of plant and has more contrast for detailed view of tissue culture. The plant was scanned in four sections, each section of the reconstructed images and relaxation times were similar.

#### ACKNOWLEDGMENT

This work was supported within the framework of the research plan FEKT-S-11-5/1012, research plan No. MSM 0021630513 ELCOM, and research plan No. MSM 0021630516.

#### REFERENCES

1. Vlaardingerbroek, M. T. and J. A. Den Boer, *Magnetic Resonance Imaging*, Springer-Verlag, Berlin, 1999, ISBN 3-540-64877-1.
2. Van As, H., T. Scheenen, and F. J. Vergeldt, "MRI of intact plants," *Photosynth. Res.*, 2009, Doi: 10.1007/s11120-009-9486-3.
3. Van As, H., "Intact plant MRI for the study of cell water transport membrane permeability, cell-to-cell and long distance water transport," *J. Exp. Bot.*, Vol. 58, 743–756, 2007.
4. Doubek, V., "Study of substances transport in plants stalks," Bachelor Thesis, Brno: Vysoké Ucení Technické v Brně, Fakulta Elektrotechniky a Komunikacních Technologií, 2010.

# The Frequency Source for Precision Synchronous Triggering

Z. Roubal and R. Kadlec

Department of Theoretical and Experimental Electrical Engineering, Brno University of Technology  
Kolejní 2906/4, Brno 612 00, Czech Republic

**Abstract**— A significant factor in demanding applications where precise synchronized triggering pulses ( $\Delta t < 1 \text{ ns}$ ) are required consists in the use of high-quality oscillators operating at frequencies in the order of hundreds of MHz. The Butler crystal oscillator in connection with a common collector is suitable for this frequency range, not least because of the fact that the noted device is not prone to spurious oscillation. This article presents an investigation into the optimization of amplification margin at the oscillation frequency, the maximization of short-term frequency stability, and the minimization of power dissipation on the crystal section. For nonlinear analysis of the oscillator, the harmonic balance method is used. Based on the method, we obtain the dependence of the crystal dissipated power on the damping resistor. The designated phase noise is recalculated to the crystal oscillator short-term stability, which constitutes a decisive point for the precise synchronization of triggering pulses.

## 1. INTRODUCTION

In certain special applications there has emerged the need of establishing precision synchronization of triggering pulse. For the purposes of the application described in this paper it is required that there exist at least two connected triggering devices which, at the beginning of the process, are phase- and frequency-synchronized. After the disconnection, the mutual detuning of the frequency and phase must not be greater than that specified in the concrete application. The detuning determines the indefiniteness of the triggering pulse ( $\Delta t < 1 \text{ ns}$ ) between both triggering devices, with an identical time preset and independent operation of the oscillators for the period of  $T_{\min} = 60$  minutes. Under strict input conditions, we designed a block diagram of the triggering devices and optimized the crystal oscillator. Based on its phase noise, the oscillator short-term frequency characteristics can be determined; then, from these characteristics, we can deduce whether the crystal oscillator satisfies the input criteria.

## 2. A BLOCK DIAGRAM FOR SYNCHRONOUS TRIGGERING

The fundamental part of every triggering device is a precise crystal oscillator. In the designed block diagram, the first triggering device includes a reference crystal oscillator. The oscillator is placed in a thermostat, which prevents the dependence of the oscillation frequency on the temperature of the environment. The oscillator output frequency is divided by means of binary dividers. The outputs of each monostable circuit in the individual dividers are led to a binary comparator; here, these outputs are compared with the required set value. In the case of agreement, a triggering pulse is generated.

In order for the second triggering device to generate the pulse synchronously with the first one, it is synchronized at the start of the process through the use of a phase-locked loop (PLL). The controlled crystal oscillator in the second triggering device is fine-tuned by the PLL operating voltage. In less complicated situations, this voltage can be used as controlling for the varicap (the voltage-controlled capacity diode). If more intensive requirements are placed on the short-term frequency stability, we may select fine-tuning realized via the change of temperature of another thermostat, which can be found inside the first one. In such cases, we do not apply the quality factor of the used varicap. However, the time constant of this type of regulation is longer by several orders when compared with the direct varicap fine-tuning; that is also why we opted for the varicap-based controlling. During the disconnection of both triggering devices, the phase-locked loop disconnects too, and therefore it is necessary to memorize the last value of the tuning voltage. In the reference triggering device, a generator of sampling pulses is used; this generator samples the low-pass filter output. At the moment of triggering circuits disconnection, the last tuning voltage is stored through the use of an analogue memory or, more efficiently, by means of the chain of an A/D converter, a memory, and a D/A converter.

### 3. THE BUTLER CRYSTAL OSCILLATOR

One of the most widely used crystal oscillators, which operates at the higher harmonic level of the crystal, is the Butler oscillator. There are two connection variants: In the first variant, the transistor operates in connection with the common base (Figure 2), while the other option involves operation with the common collector (Figure 3). The oscillation frequency of this oscillator ranges slightly above the crystal series resonance. Here, the crystal behaves as a highly selective resistor. In order to apply the oscillations, we first need to perform correct tuning of the resonant circuit  $L_1$  and capacity divider  $C_1, C_2$ . The less frequently used connection of the Butler oscillator with the common collector provides a lower output performance; at the same time, however, the presetting of the direct operating point shows a very low degree of criticality, and there is no spurious oscillation. From the perspective of the alternating signal, the coil  $L_1$  is earthed through the lock-in condenser  $C_F$ . Intensive requirements are placed on the transistor  $T_1$ ; for utilization purposes, its transit frequency  $f_T$  ought to be 10 times the amount of the oscillation frequency. Thus, we will achieve not only a negligible phase shift caused by the transistor, but also the minimization of its effect on the frequency stability. However, with the SB connection, this margin may generate spurious oscillation modes, and that is why the SC connection is more suitable. Spurious capacities of electrodes of the applied transistor as well as the capacities of its semiconductor junctions ought to be minimal so as not to affect the oscillation condition. Another requirement (which is nevertheless seldom guaranteed by the manufacturer) consists in the minimum noise of the  $1/f$  transistor. This noise increases the phase noise of the crystal oscillator, thus worsening its short-term frequency stability.

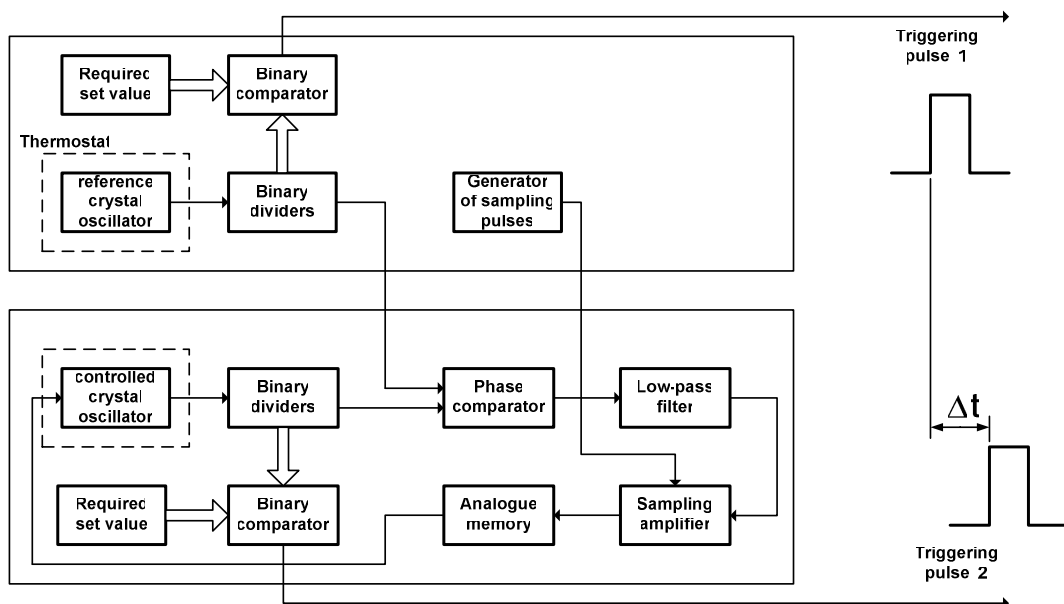


Figure 1: The triggering device block diagram.

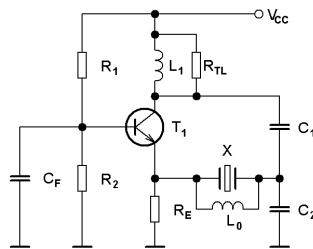


Figure 2: The butler oscillator in the SB connection.

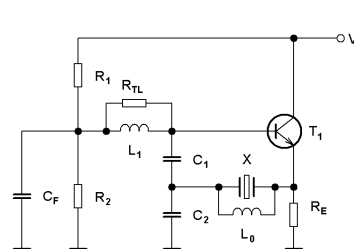


Figure 3: The butler oscillator in the SC connection.

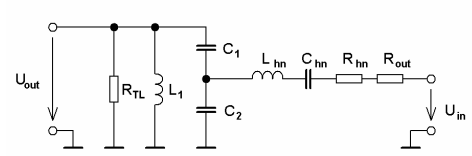


Figure 4: The feedback circuit.

#### 4. THE BUTLER OSCILLATOR FEEDBACK BRANCH: AN ANALYSIS

For an easy understanding of the design of individual components of the feedback circuit it is suitable to utilize the voltage transfer  $K_U(s)$  of the feedback branch. Inductivity  $L_0$ , together with the static capacity of crystal  $C_0$ , is tuned into resonance; therefore, we need not assume these components. Resistor  $R_E$  shows a value greatly exceeding the output impedance of the emitter follower, which enables us to neglect it. In a contrary situation, the resistor would be paralelly matched with this output impedance. Output impedance  $R_{out}$ , with the SC connection will be assumed as purely real owing to the multiply higher boundary frequency  $f_T$ . Then, the impedance can be included in the equivalent series resistance of the crystal unit to total resistance of  $R_T = R_{hn} + R_{out}$ . The feedback circuit is shown in Figure 4.

$$\begin{aligned}
 A &= C_1 \cdot C_{hn} \cdot L_1 \cdot R_{TL} \\
 B &= R_{TL} \cdot C_{hn} + R_{TL} \cdot C_1 + R_{TL} \cdot C_2 \\
 C &= C_1 \cdot L_1 + C_2 \cdot L_1 + C_1 \cdot C_{hn} \cdot R_T \cdot R_{TL} + C_2 \cdot C_{hn} \cdot R_T \cdot R_{TL} + C_{hn} \cdot L_1 \\
 D &= C_2 \cdot C_1 \cdot L_1 \cdot R_{TL} + C_1 \cdot C_{hn} \cdot L_1 \cdot R_{TL} + C_2 \cdot C_{hn} \cdot L_{hn} \cdot R_{TL} \\
 &\quad + C_1 \cdot C_{hn} \cdot R_T \cdot L_1 + C_2 \cdot C_{hn} \cdot R_T \cdot L_1 + C_1 \cdot C_{hn} \cdot L_{hn} \cdot R_{TL} \\
 E &= C_2 \cdot C_1 \cdot C_{hn} \cdot R_T \cdot L_1 \cdot R_{TL} + C_2 \cdot C_{hn} \cdot L_{hn} \cdot L_1 + C_1 \cdot C_{hn} \cdot L_{hn} \cdot L_1 \\
 F &= C_2 \cdot C_1 \cdot C_{hn} \cdot R_T \cdot L_1 \cdot R_{TL} \\
 K_U(s) &= \frac{s^2 \cdot A}{B + s \cdot C + s^2 \cdot D + s^3 \cdot E + s^4 \cdot F}
 \end{aligned} \tag{1}$$

The selected transistor was a BFR92A with  $f_T = 4\text{ GHz}$ , which is a readily available type. Further, a custom-made crystal having the AT cut, parameters of  $R_{h5} = 50\Omega$ ,  $C_{h5} = 1\text{ fF}$ ,  $C_0 = 6,02\text{ pF}$  and  $f_s = 2^{26}\text{ Hz}$ , and working at the fifth overtone was used. Utilizing the procedure described in [3], we designed initial values of individual components. The impedance module  $C_2$  has a lower or identical value as  $R_h$ .  $L_1$  was selected from the batch E12 220 nH,  $C_1$  a  $L_1$  are approximately in a resonance; quality  $Q$  of the coil  $L_1$  was lowered to 10 using the resistor  $R_{TL}$ . Inductivity  $L_0$  and capacity  $C_0$  are in a resonance.

$$C_2 \geq 47\text{ pF} \quad L_1 = 220\text{ nH} \quad C_1 = 26\text{ pF} \quad R_{TL} = 1\text{ k}\Omega \quad L_0 = 1,02\text{ }\mu\text{H}$$

The feedback branch amplitude frequency characteristics are shown in Figure 5; the phase characteristics can be seen in Figure 6. The parameter is the damping resistance  $R_{TL}$ ; other components have the initial values. It is obvious that, with the decreasing  $R_{TL}$ , the gain margin decreased while the phase characteristic passage through zero increased in steepness.

The oscillation condition, with the neglection of phase shift in the transistor, is satisfied if the feedback circuit phase shift equals to  $0^\circ$ . The aim of the optimization is to achieve the highest possible steepness of phase characteristics during the passage through zero. Furthermore, the value of condenser  $C_1$  was stepped together with several values of the resistor  $R_{TL}$ . Figure 7 shows the dependence of voltage transfer  $|K_u|$  with the satisfied oscillation condition; the phase characteristics steepness dependence is given in Figure 8. The ratio of oscillation frequency to the series resonance frequency of the crystal unit is indicated in Figure 9. Using this ratio, we are able to determine the necessary shift of the custom-made crystal series resonance.

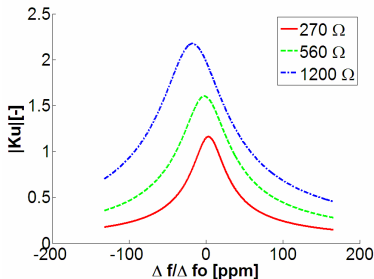


Figure 5: Amplitude frequency characteristic for parameter  $R_{TL}$ .

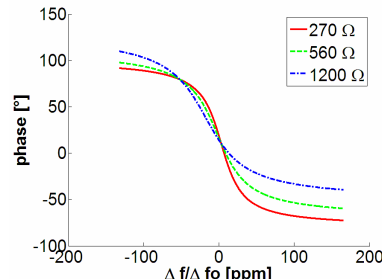


Figure 6: Phase frequency characteristic for parameter  $R_{TL}$ .

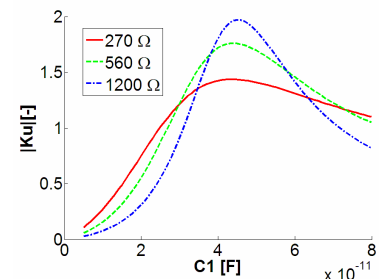


Figure 7:  $|K_u|$  in realized oscillation condition for parameter  $R_{TL}$ .

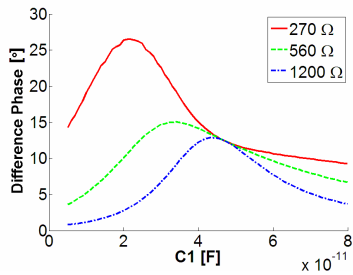


Figure 8: Difference phase for detuning around 5 ppm oscillation frequency for parameter  $R_{TL}$ .

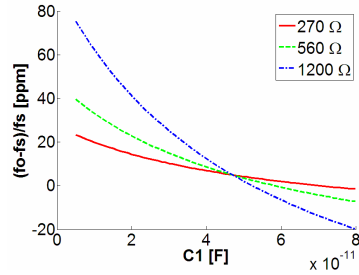


Figure 9: Rate variation oscillation frequency to series resonance crystal frequency.

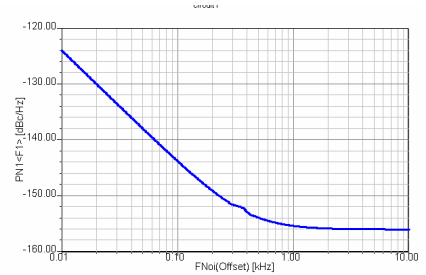


Figure 10: Phase noise  $L(f)$  in the output.

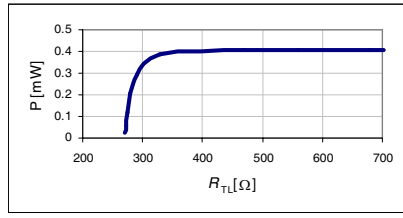


Figure 11: Power dissipation in the crystal unit without limiting diodes.

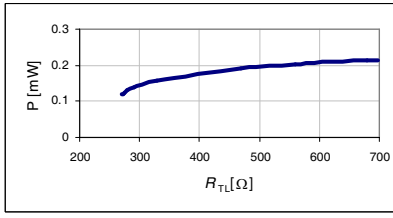


Figure 12: Power dissipation in the crystal unit with a vf dual diode HSMS-2822.

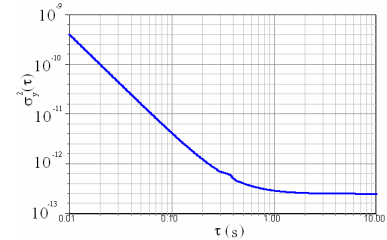


Figure 13: Short-term stability.

## 5. THE CRYSTAL UNIT POWER LOAD

The crystal unit resonance frequency is influenced by its power load. In order to obtain good medium-term frequency stability, we must not exceed the maximum value indicated by the manufacturer; contrary to that, in the making of the design, we ought to attempt to achieve the related minimum value. for small excitation levels, there (approximately) holds that the proportional change of resonance frequency equals to

$$\frac{\Delta f}{f_s} = B \cdot I_h^2 \quad (2)$$

Constant  $B$  for the common AT cut is equal to  $0.17410^{-9}$ . Using the Ansoft Designer program, we simulated the crystal unit power load on the damping resistor  $R_{TL}$  (Figure 11). This load was further decreased by diodes connected antiparalelly to the coil  $L_1$  in accordance with [3]. Advantageously, we used a vf dual Schottky diode HSMS-2822, which has a low treshold voltage (the result is shown in Figure 12). The crystal unit power load decreased (approximately) by a half. These results are beneficial to the desing of the Butler oscillator as they have not been published to date.

## 6. SHORT-TERM FREQUENCY STABILITY OF THE CRYSTAL OSCILLATOR

The short-term stability can be determined from the phase noise using the Allan variance. The recalculation relation is given by [1].

$$\sigma_y^2(\tau) = 2 \cdot \int_0^{f_h} 2 \frac{f^2}{\nu_0^2} L(f) \cdot \frac{\sin^4(\pi \tau f)}{(\pi \tau f)^2} df. \quad (3)$$

The recalculated short-term stability obtained from the phase noise (Figure 10) is shown in Figure 13. The required maximum time for the triggering pulse generation is about 60 minutes, which corresponds with the time interval of  $\tau = 3600$  s. The resulting short-term frequency stability for this time satisfies the requirements of the setting..

## 7. CONCLUSION

The concept of a precise synchronous triggering source was realized. Further, the Butler oscillator was optimized for the maximum short-term stability and a minimum load of the crystal unit. From the calculated spectrum of phase noise of the crystal oscillator, its related short-term stability was determined. Thus, the requirements of the setting were satisfied.

## ACKNOWLEDGMENT

The work described in the paper was financially supported by research plan MSM 0021630513, research plan MSM 0021630516 and project of the BUT Grant Foundation FEKT-S-11-5.

## REFERENCES

1. Odyniec, M., *RF and Microwave Oscillator Design*, Artech House, Boston, 2002.
2. Zelenka, J., *Piezoelektrické Rezonátory a Jejich Použití*, Academia, 1983.
3. Matthys, R. J., *Crystal Oscillators Circuit*, Krieger Publishing Company, 1991.
4. McClelland, T., C. Stone, and M. Bloch, “100 MHz crystal oscillator with extremely low phase noise,” *Frequency and Time Forum, 1999 and the IEEE International Frequency Control Symposium, 1999, Proceedings of the 1999 Joint Meeting of the European*, Vol. 1, 331–334, 1999.
5. Frerking, M., *Crystal Oscillator Design and Temperature Compensation*, Van Nostrand Reinhold, 1978.
6. Čajka, J. and J. Kvasil, *Teorie Lineárních Obvodů*, SNTL Praha, 1979.

# Evaluation of Characteristics of HV Electrometric Amplifier with Low Input Current

Z. Roubal and R. Kadlec

Department of Theoretical and Experimental Electrical Engineering, Brno University of Technology  
Kolejní 2906/4, Brno 612 00, Czech Republic

**Abstract**— In certain special applications, for example in various fields of chemistry, it is necessary to measure voltage in the order of hundreds of volts from a high-impedance source. Standard electrometric operational amplifiers cannot be used as their input range is limited to the maximum of ten volts. Furthermore, it is impossible to increase the input range by a voltage divider in situations when the required input resistance is, for example,  $10^{14} \Omega$ . A common resistive divider in the input of an operational amplifier typically shows the maximum input resistance of  $10^{12} \Omega$ .

A special circuit arrangement can be used in which the amplifier supply voltage is dynamically shifted with the input voltage. This configuration saves the high input resistance of the applied electrometric amplifier and extends the input voltage range to the desired value. In our configuration, the extended range is  $\pm 300$  V. The proposed design of an HV electrometric amplifier utilizes a high-voltage differential amplifier, which regulates the high-voltage source supplying the electrometric operational amplifier. The general feedback loop has to be frequency-compensated, and this compensation is designed using the Pspice simulator. Characteristics of the HV electrometric amplifier were confirmed by the measurement of freezing potentials.

## 1. INTRODUCTION

In the field of research into biochemical substances there has emerged the need to measure the electric potential of phase changes upon solidification of aqueous solutions. This potential is referred to as freezing potential or Workam-Reynolds phenomenon [1–6]; the effect is caused by an unequal distribution of ions between the solid and liquid phases. At this point, it is necessary to note that the results obtained by the related researchers differed in respect to the applied measuring method, measurement system configuration, and methodology.

There are at least 15 crystalline phases of ice, which have been observed under different conditions. Most of them can be seen in the ice-water phase diagram (Figure 1).

Even though, at first sight, ice does not appear to be an electrical material, a steady current can flow in it according to Ohm's law. The observed current is generated by a flow of protons and the process is similar to electronic conduction in semiconductors. Therefore, ice is sometimes referred to as a "prototypic semiconductor". However, its static conductivity ( $6 \cdot 10^{-10} \text{ S m}^{-1}$  for pure ice at  $-10^\circ\text{C}$ ) is too small in comparison with the static conductivity of water ( $5 \cdot 10^{-6} \text{ S m}^{-1}$ ). The conductivity of ice may be increased through an addition of specific dopants [1]. The polarization and electrical conduction in ice are possible only if, in the related lattice, there are few points where

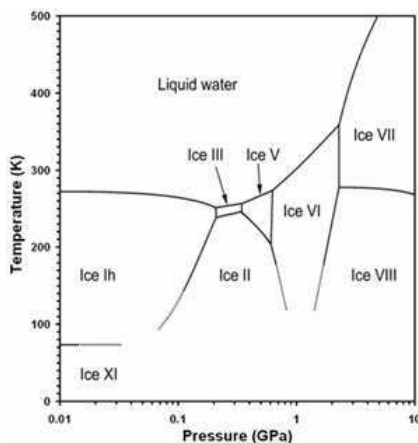


Figure 1: The ice-water phase diagram [1].

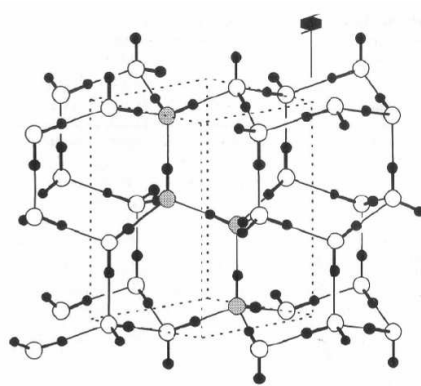


Figure 2: The crystal structure of ice Ih [1].

the ice rules are locally violated [1]. If the ice rules were strictly obeyed, the simplest change in the orientation of a molecule would require the directions of all the bonds in the lattice to reverse simultaneously.

This would involve large activation energy, and the overall polarization would not change. Once these violations of ice rules, also known as protonic point defects, are present, their motion induces the reorientation of molecules and jumps of protons from one water molecule to another. The motion of protonic point defects causes the electrical conduction and polarization of ice [1]. The water molecules are linked to one another by hydrogen bonds in such way that oxygens are tetrahedrally surrounded by four other oxygen atoms at the distance of 2.764 Å. Each molecule offers its hydrogens to two other molecules and accepts hydrogen bonds from yet another pair of molecules, and thus there is only one hydrogen between each pair of oxygen atoms (“ice rules”).

## 2. THE MEASURING APPARATUS

The basic research was materialized in laboratory conditions showing a lower degree of repeatability. For this reason, we designed and built a new measuring apparatus (Figure 3(a)); the original apparatus is shown in Figure 3(b). When designing the innovated model (as compared to the original version), we applied the principles of active shielding and reduced the leakage of the measurement apparatus; significantly, these structural steps enabled us to obtain higher measured values of freezing potential.

The entire measuring device is positioned in a thermally insulated vessel where liquid nitrogen will be produced (nitrogen boiling temperature equals to  $-195.80^{\circ}\text{C}$ ). The lower section of the vessel shows a shape and configuration enabling high-quality accumulation and transfer of heat (with cooling realized by means of liquid nitrogen); simultaneously, however, the vessel facilitates the elimination of problems resulting from the change in linear expansion. In the shielded vessel having a hot and a cold section there exists free, gas-filled space that prevents the occurrence of air humidity freezing. At the very initial stage of measurement, the head housing a capillary as well as the sample to be tested is inserted in an overcooled duralumin monobloc; thus, a repeatable refrigeration process starts. At the moment of the sample insertion in the overcooled space, the tested sample phase begins to change and the fluid — solid phase interface progressively moves upwards; now, freezing potential is measured. Following the phase change reach of the other electrode, freezing potential will discharge itself.

## 3. HV ELECTROMETRIC AMPLIFIER

In the process of designing an electrometric amplifier there may occur a certain technical problem concerning high input voltage [7, 8]. As a consequence, the measured voltage value can range within several hundreds of volts. A standard solution consists in applying a resistor divider at the input, Figure 4. In electrobiology, however, we can not use this type of solution as the signal source contains capacity in orders of pF; even when special high-ohm  $100\text{ G}\Omega$  resistors are used, the discharge time constant of the circuit ranges within orders of tenths of seconds. It is therefore obvious from the description that the discussed solution does not help us to meet the desired target.

One of the proposed methods of solution to the problem lies in the application of an electrometric amplifier not equipped with any input divider; in this type of amplifier, then, we assume

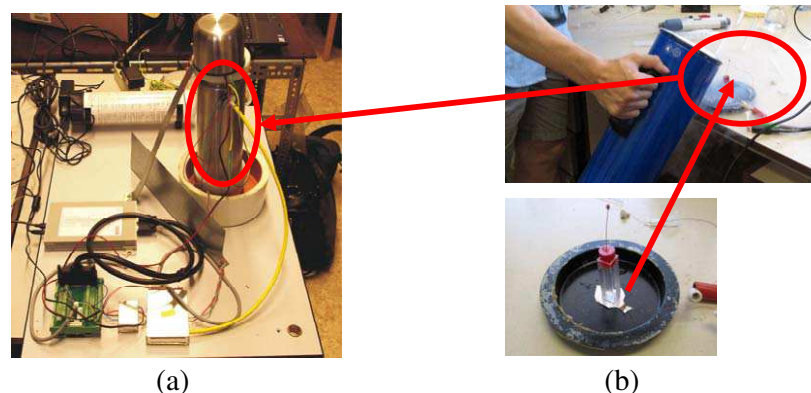


Figure 3: (a) The assembled apparatus. (b) The original apparatus for the measurement method verification.

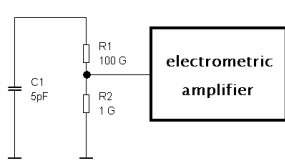


Figure 4: Resistor divider at the input.

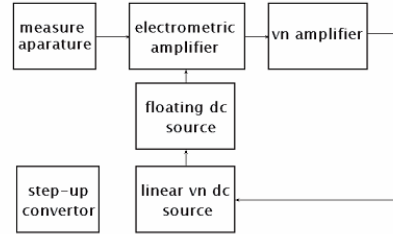


Figure 5: The block diagram of an electrometric amplifier with floating power supply.

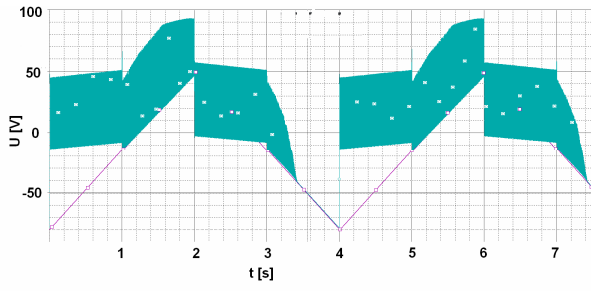


Figure 6: A floating supply electrometric amplifier: An instance of oscillation.

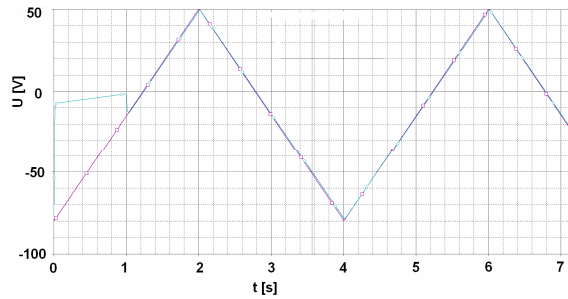


Figure 7: A frequency compensated amplifier.

floating power supply in relation to the input voltage. Figure 8(a) shows the diagram of such an amplifier. Here, the input voltage is amplified by an electrometric amplifier supplied from a floating source. The related output is connected to a high-voltage amplifier supplied by a raising voltage changer. This output manages a high-voltage straight line source, which shifts voltage levels of the electrometric amplifier. The input voltage is read at the high-voltage source output. The internal resistance of this configuration is defined only by the electrometric amplifier volume resistivity and may reach up to  $10^{14}\Omega$ . The discharge time constant is, with inner capacity of the signal source, approximately 1000 s, which will not affect the measured values of freezing potential.

A diagram of this type of electrometric amplifier has been designed and simulated using Spice. In the design, a LMC6041 operational amplifier was utilized as an electrometric amplifier; typically, its input current is 2 fA. Figure 5 presents the overall diagram. Operational amplifiers having the input voltage of 300 V are generally not available, and therefore we built a high-voltage amplifier based on discrete hv transistors. Owing to the connection sensitivity to oscillation, it is necessary to use correct values of capacitor  $C_1$ . With respect to the maximum input resistance, the amplifier does not have input protection. This problem is solved through the application of RC filter(s)  $R_{10}$  and  $C_2$ . The filter restrains voltage spikes at the input and the amplifier is capable of monitoring the changes occurring at its own input.

Figure 6 provides an example of possible oscillations: the input voltage is shown as the violet course, while the output voltage pertains to the dark green course. Figure 7 illustrates the situation following compensation. At the beginning of the measurement, the amplifier input must be short-circuited in order to facilitate stabilization of the initial conditions. Simulation in the Pspice environment indicates input resistance at  $10^{14}$  ohm. The amplifier input current is markedly represented by the charging of capacitor  $C_2$  during the input voltage changes. The configuration of the input part of an HV electrometric amplifier is shown in Figure 8(b).

#### 4. THE MEASURED DATA

Using a special electrometric amplifier as well as measurement apparatuses, we measured the potentials of chemical solutions. At the initial stage of the experiments, the measurement was degraded by an electric charge in certain parts of the measuring apparatus. The effects on the concerned parts manifested themselves adversely during the experiment evaluation. Voltage surge caused by the freezing of the solution occurred non-repeatedly and its amplitude showed different character-

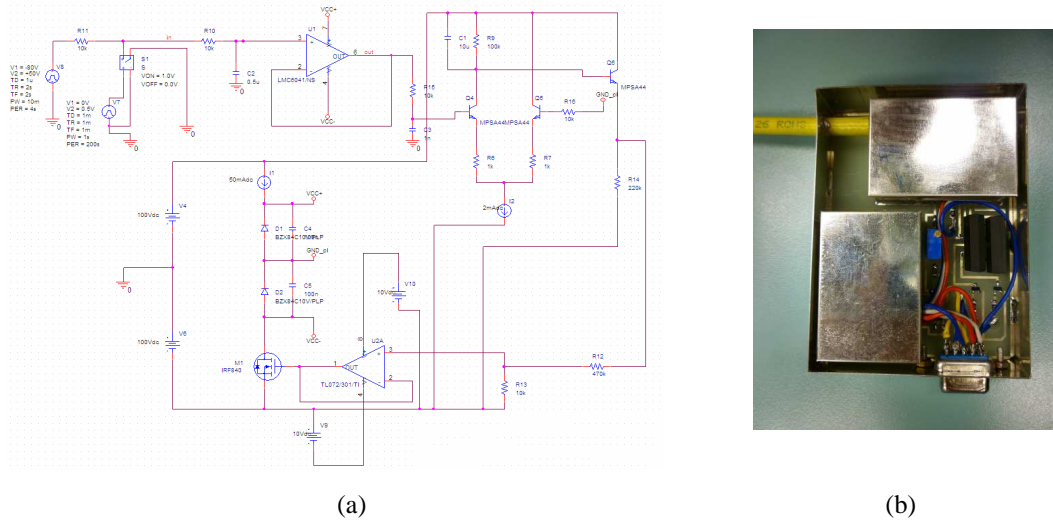


Figure 8: (a) A concrete diagram of a floating supply electrometric amplifier (after compensation). (b) The configuration of an HV electrometric amplifier.

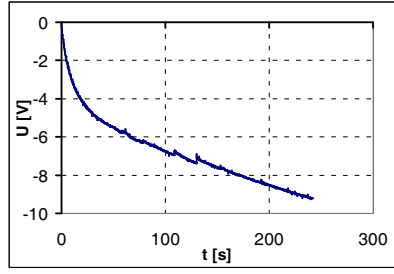


Figure 9: Only the charging of spurious capacities.

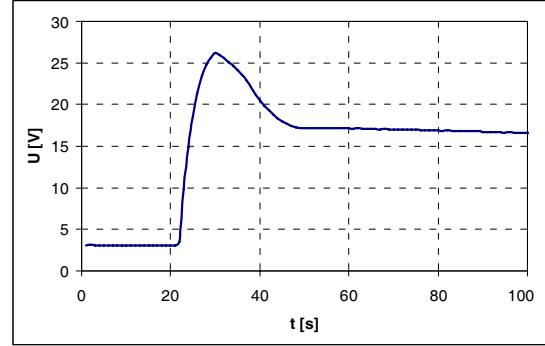


Figure 10: Time dependence: the freezing potential of water.

istics. The situation is described in Figure 9, which shows the charging of spurious capacities. After realizing the above-described structural modifications, we conducted the measurement of the freezing potential of different solutions. An example of a freezing potential time behaviour is shown in Figure 10.

## 5. CONCLUSION

A special HV electrometric amplifier was designed and frequency-compensated. In the process of realizing the design, we utilized in full the principles of active shielding, and connected the apparatus by means of a triaxial cable [9]. The amplifier is capable of performing measurement in the order of hundreds of volts with a large input resistivity. By the help of the measuring apparatus, we measured potential at the interface of the sample phase change. The measured data show that this potential can be repeatedly measured using a structurally modified apparatus.

## ACKNOWLEDGMENT

The work described in the paper was financially supported by the research plan MSM 0021630516, research plan MSM 0021630513, and project of the BUT Grant Foundation FEKT-S-11-5.

## REFERENCES

1. Petrenko, V. F. and R. W. Whitworth, *Physics of Ice*, Oxford University Press, USA, 1999.
2. Peterson, S. W. and H. A. Levy, “Proton positions in  $\text{CuCl}_2 \cdot 2\text{H}_2\text{O}$  by neutron diffraction,” *J. Chem. Phys.*, Vol. 26, 220–221, 1957.

3. Sola, M. I. and H. R. Corti, "Freezing included electrical potentials and Ph charges in aqueous electrolytes," *An. Asoc. Quím Argent.*, Vol. 81, No. 6, 483–498, 1993.
4. Lefebvre, V., "The freezing potential effect," *J. Colloid Interfacing Sci.*, Vol. 25, No. 2, 263–269, 1967.
5. Bronshteyn, V. L. and A. A. Chernov, "Freezing potentials arising on solidification of dilute aqueous solutions of electrolytes," *J. Crystal Growth*, Vol. 112, No. 1, 129–145, 1991.
6. Robinson, C., C. S. Boxe, M. I. Guzmán, A. J. Colussi, and M. R. Hoffmann, "Acidity of frozen electrolyte solutions," *J. Phys. Chem. B*, Vol. 110, No. 15, 7613–7616, 2006.
7. Roubal, Z. and M. Steinbauer, "Design of electrometric amplifier for aspiration condenser measurement," *PIERS Proceedings*, 1430–1434, Xi'an, China, Mar. 22–26, 2010.
8. Drexler, P. and P. Fiala, "Methods for HP EM pulse measurement," *IEEE Sensors Journal*, Vol. 7, No. 7, 1006–1011, 2007.
9. *Low Level Measurements Handbook: Precision DC Current, Voltage, and Resistance Measurements*, 6th Edition, Keithley Instruments Inc., Cleveland, Ohio, 2004.

# Special High Voltage Function Generator

P. Marcon, P. Fiala, M. Steinbauer, and M. Cap

Department of Theoretical and Experimental Electrical Engineering  
Brno University of Technology, Kolejni 2906/4, Brno 612 00, Czech Republic

**Abstract**— Goal of this project was to design, realize and test a special high voltage function generator. This generator was designed for special testing of soft tissues. The aim of this project was to generate electric field of defined shape. In course of design of the generator the properties of the output electrode voltage was the key element. In this article the construction and parameters measuring of the high voltage function generator is discussed.

## 1. INTRODUCTION

The generator was designed for special tests of soft tissues. Possibilities of the soft issue testing are described in literature (1). In this work the aim is to test the soft tissues in high voltage electric field. Tissues are exposed to defined shape electric field up to 20 kV. Voltage of the output electrode of the realized generator is possible to regulate in range 0 kV to 20 kV. Shape of the output voltage is possible to choose as sine, square or ramp. Frequency capabilities of this voltage source start on 0 Hz and reach 300 Hz.

## 2. HV GENERATOR FUNCTION SCHEME

The high voltage generator has two basic parts: a low voltage and a high voltage part. The low voltage part include a power source, isolation transformer, control module, optical isolation and function generator. Second part is the HV module. In the HV module a HV transformer as a border between low and high voltage part is the main part. The HV voltage transformer is designed as a flyback. Block diagram of the HV generator you can see in Fig. 1. Output voltage 20 kV is stabilized by the feedback signal FB — the voltage from HV output is connected through the high voltage divider and optocoupler to the control module. According to the feedback signal the control module use a PWM signal for transistor and primary coil of the HV transformer switching.

Frequency and shape of the HV output signal is possible to change by the low voltage output signal of the function generator. Function generator signal is connected to the control module where will be actively integrated and through the optical isolation connected to the PWM controller.

## 3. LOW VOLTAGE PART

Basic part of the low level part is the control module. Line voltage pass through the separating transformer 230 V/230 V and consequently is in switching power supply regulated to 24 V. The switching power supply need to be designed according to maximal output current for primary coil excitation. Primary coil voltage is switched by the PWM controlled MOSFET transistor. Used PWM controller precisely controls output voltage according to the signal on this circuit comparator. Due to this design, the circuit is quickly react to the output current changes and is able to decrease

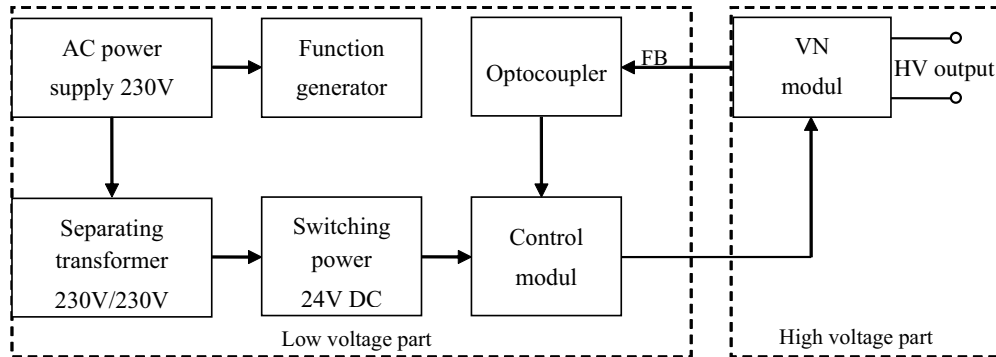


Figure 1: Block diagram of the high voltage generator.

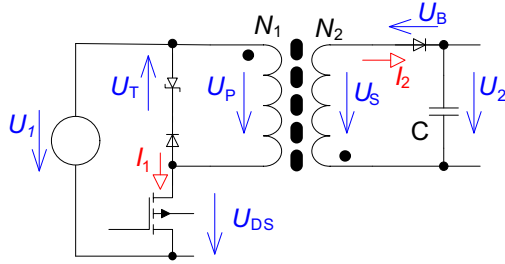


Figure 2: Scheme of the flyback convertor :  $U_1$  — Source voltage,  $U_2$  — Output voltage,  $U_p$  — primary voltage,  $U_s$  — secondary voltage,  $U_T$  — transil reverse voltage,  $U_{DS}$  — collector voltage of the transistor,  $U_B$  — diode reverse voltage,  $I_1$  — primary current,  $I_2$  — secondary current.

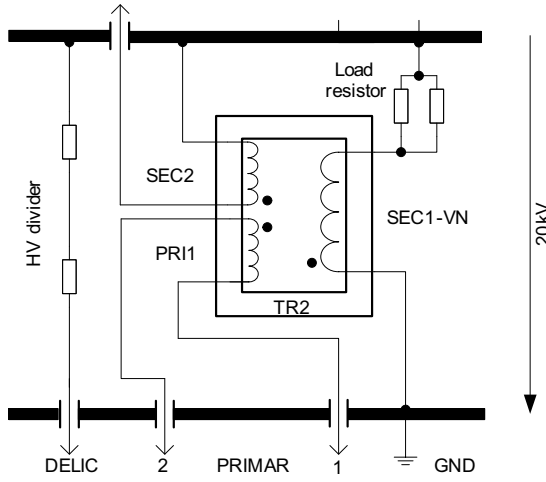


Figure 3: Block diagram of the high voltage part.

output current and voltage. This is very important for life protection in case of accidental touch. Setting of the output frequency is done by resistor and capacitor on the resonant frequency of the transformer. Comparator inside the PWM controller is comparing the current voltage with value of the requested voltage on the output electrode. High voltage is by HV divider decreased from 20 kV to 1 V on the input control unit. Comparison of the regulation and the output voltage is provided by an operation amplifier (OA). The operation amplifier work as a differential amplifier of the regulation deviation. OA is also compensating a voltage spikes from the HV divider. The voltage spikes could have influence on the device function and cause distortion of the output voltage.

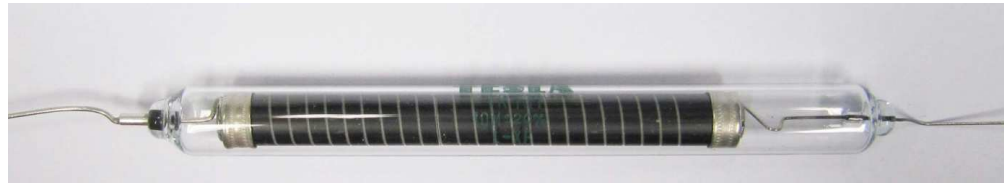
The border between low and high voltage part is the HV transformer connected as a flyback convertor. Scheme of the flyback converter is shown in Fig. 2. Using of this schematic circuit is possible to calculate number of loops of the primary and secondary coil. Calculations are published in [6, 9, 11].

#### 4. HIGH VOLTAGE PART

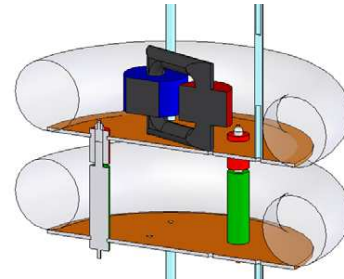
Block diagram of the high voltage part is in Fig. 3. The main part of the HV block is HV transformer TR2 working as a flyback converter. Inside the transformer a rectifier diode is connected. Secondary winding SEC2 is possible to link to next module for multiplying of the output voltage. Resistor 1 G $\Omega$  and the power resistor are as the HV divider connected between the output electrodes. Exceeding of the 20 kV output voltage value cause on the 1 G $\Omega$  resistor voltage drop higher then 1 V and consequently a change of pulse ratio of the PWM signal.

Limitation of the output current in case of direct contact is realized by pair of the 10 M $\Omega$  load resistors, Fig. 4. Maximal voltage rating of these resistors is 20 kV. Output current is limited to 4 mA.

Frame of the electrode is made from polystyrene ring. Design of the ring you can see in on the left Fig. 5. Homogenizer of the electromagnetic field is made by covering the ring by the aluminum foil.

Figure 4: High voltage load resistor  $-10 \text{ M}\Omega$ .

(a)

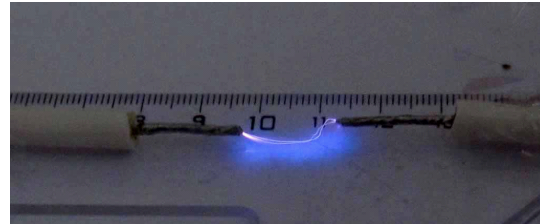


(b)

Figure 5: (a) Homogenizer of the electromagnetic field with cuprexit board. (b) Linking of two modules by the isolated spacing element.

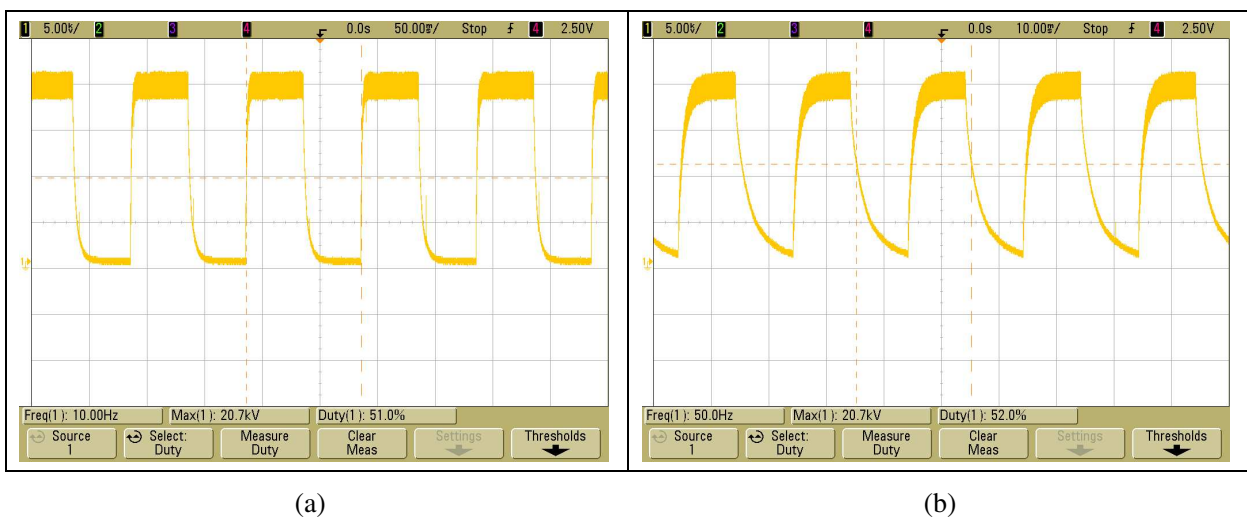


(a)



(b)

Figure 6: (a) Realized VN module. (b) Electric Discharge. Electrode distance is approximately 1.5 cm.

Figure 7: (a) HV generator output voltage,  $U_{gen} = 1\text{V}_{pp}$  and  $f_{gen} = 10\text{Hz}$ . (b) HV generator output voltage,  $U_{gen} = 1\text{V}_{pp}$  and  $f_{gen} = 50\text{Hz}$ .

Cuprexit board is conductively connected to the electromagnetic field homogenizer. By the linking of the five 20 kV modules is possible to design the 100 kV generator. Linking of two modules you can see in Fig. 5.

## 5. REALIZED HV GENERATOR

Realized HV generator, in detail ring electrodes,  $1\text{ G}\Omega$  resistors and flyback transformer you can see in Fig. 6. On the top the high voltage cable is connected. Voltage limit of this cable reach 30 kV. HV generator test is in Fig. 6. As you can see, discharge distance is approximately 1.5 cm.

## 6. HV GENERATOR PARAMETERS MEASUREMENT

Low voltage generator AGILENT was connected into the feedback loop of the flyback converter. Output square-wave voltage of the generator was set to  $1V_{pp}$ . Frequencies were changed in range from 1 Hz to 3 kHz. The control unit is changing the PWM signal in an effort to obtain the same shape of the secondary voltage as is the shape of the primary voltage. Amplitude of the output voltage is approximately 20 kV.

## 7. RESULTS AND CONCLUSIONS

The measurement confirms that the output voltage is possible to regulate in range from 0 V to 20 kV. Frequencies of the output voltage could be changed in range from 1 Hz to 3 kHz with low distortion. Frequencies over 300 Hz are under influence of the parasitic capacities. Voltage on the output electrode needs to be soft for soft tissue testing. The output voltage of the generator can be seen in Fig. 7. Input voltage has  $1V_{pp}$  amplitude and frequency in range 10 Hz to 50 Hz. Square-wave input signal is under influence of parasitic capacities changed. The influence is dependent on the frequency of the input signal. In addition, over 100 Hz the output voltage amplitude is decreasing and signal start to have offset.

## ACKNOWLEDGMENT

The research described in the paper was financially supported by project of the BUT Grant Agency FEKT-S-11-5/1012, research plan No. MSM 0021630513 ELCOM, and research plan No. MSM 0021630516.

## REFERENCES

1. Gasparov-Grekhov, A. V. and V. L. Granenstein, *Applications of High-Power Microwaves*, Artech House, Boston, London, 1994.
2. Kalousek, V., F. Stanek, and J. Schieblova, *Technika Vysokých Napěí*, Skripta VUT FEKT v Brne, Brno, 1989.
3. Krejcirik, A., *Napajecí Zdroje II — Integrovane Obvody ve Spinanych Zdrojich*, BEN, technicka literatura, Praha, 1997, ISBN 80-86056-03-1.
4. Krejcirik, A., *Napajecí Zdroje I — Zakladni Zapojeni Analogowych a Spinanych Napajecich Zdroju*, BEN, technicka literatura, Praha, 1997, ISBN 80-86056-02-3.
5. Krejcirik, A., *Napajecí Zdroje III — Pasivni Soucastky v Napajecich Zdrojich a Preregulatory*, BEN, technicka literatura, Praha, 2002, ISBN 80-86056-56-2.
6. Faktor, Z., *Transformatory a Cívky*, BEN, technicka literatura, Praha, 1999, ISBN 80-86056-49-2.

## Filter for Processing of NMR Signal

**Martin Friedl, Jiří Sedláček, Lubomír Fröhlich, and Radek Kubásek**  
 Brno, FEEC BUT, UTEE, Kolejní 2906/4, Brno 612 00, Czech Republic

**Abstract**— One of the fields of science, where is going forward continual development, is the area of nuclear magnetic resonance (NMR). Bulk of the NMR issues concerns on signal processing in analog and digital form in NMR signal. In this paper is focused our attention on design of active analog filter with frequency dependent negative resistor (FDNR). There is designed active ARC filter based on ladder structure of the LRC filter, then the filter DCR is made through the use of Bruton transformation and finally the DCR filter is converted to the filter with FDNR elements. The designed and realized filter is used as a low pass filter, which aims to filter out the noise of NMR signal. The filter is placed behind the mixer, which converts the useful NMR signal to baseband. The designed and realized filter performs role of the anti-aliasing filter before the A/D converter.

### 1. INTRODUCTION

The paper deals with the design of low-pass filter with lossy FDNR element. The purpose of the using the filter is as anti-aliasing filter in NMR spectrometer signal path, see Fig. 1. Signal of resonant nucleus detected by probe can be expected at  $\mu\text{V}$  level. Low noise preamplifier will increase the level of NMR signal before mixer. The mixer bring useful signal to base-band. Inter-frequency signal required to be filtered by low-pass filter with appropriate order. There is possible to use Bessel or Butterworth approximation. Filter has to have low noise parameters. In general, noise parameters are the most significant in all signal path design.

### 2. FILTER DESIGN

There is by the design of frequency RLC filters the biggest problem with the quality, size and price of coils. Consequently, for low and medium frequencies, RLC filters are preferably replaced by active filters RC (ARC). Their basic principle consists in replacement the coil through the use of an active element with resistors and capacitors [1]. One of the suitable method is solution consists in the creation the ARC circuit with transfer function of the 2th order, which is equal to transfer functions of RLC filter through the use of FDNR blocks [2]. The filters with FDNR elements replace coils indirectly using Bruton's transformation [3], which transforms the initial RLC structure into equivalent behaving the CRD structure (Fig. 2). This new structure does not contain an element of inductive character, but uses the properties of the synthetic element FDNR, which are preferably used for low pass filter.

The active circuits realized of the FDNR elements can be separated into different types according to their basic circuit characteristics [4]. The lossy FDNR grounded circuit (Fig. 3(b)) can be realized by the use one active element (OA) and in this circuit the lossy are represented by a parallel

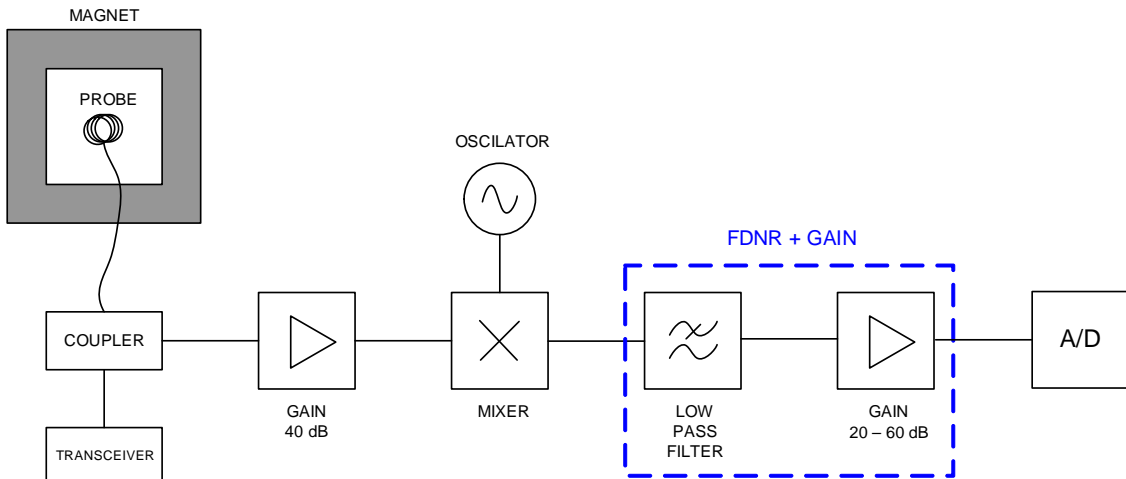


Figure 1: The anti-aliasing filter for mirror band after mixer and noise suppression.

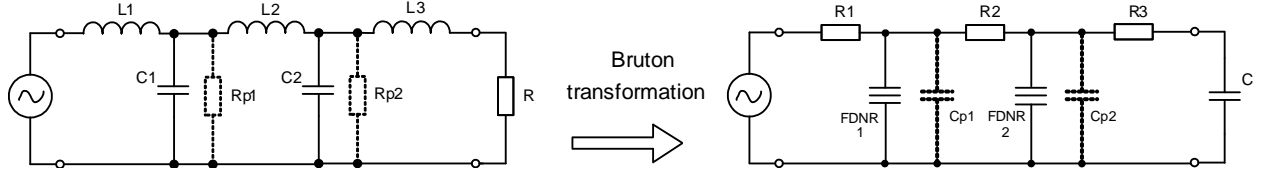


Figure 2: Principle of the active LP filter design.

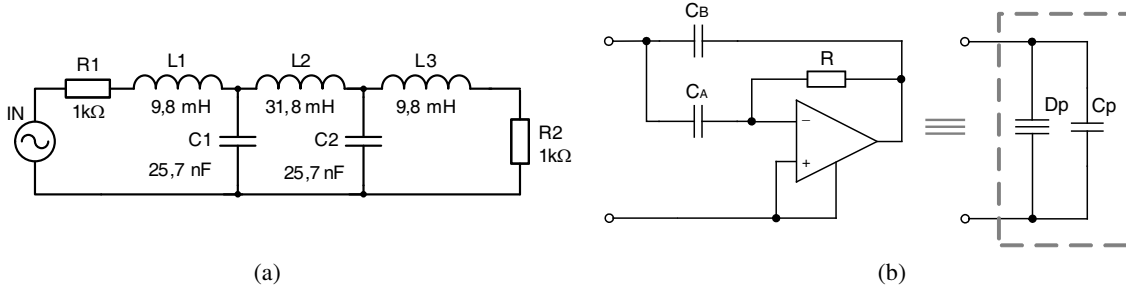


Figure 3: (a) The LRC low pass 5th order, (b) the grounded FDNR with the parallel lossy.

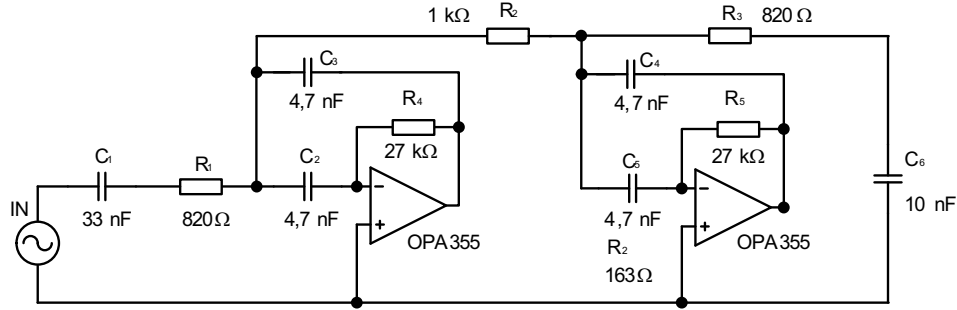


Figure 4: The optimized ARC filter with the lossy FDNR blocks.

capacitor. These lossy correspond to resistors Rp1 and Rp2 parallel connected to capacitors in the initial circuit of the RLC filter (Fig. 2). Thus it is very easy these lossy to simulate and to observe filter response to different sizes of the resistors Rp1 and Rp2.

The final design of the low-pass RLC filter of the 5th for cut-off frequency 10 kHz is on Fig. 3(a). Through the use Bruton's transformation and grounded lossy FDNR element (Fig. 3(b)) we obtain circuit of the ARC filter with lossy FDNR elements.

The results of the simulation (Fig. 6) show that parallel lossy of FDNR elements have highly influence to the resulting characteristic (the black curve). Therefore the optimization [5–7] was done and the resulting transfer characteristic of ARC filter with the real OA (OPA355) [8] corresponds to the red curve. It is clear that by the using of the optimization was achieved almost the same characteristic as it is at the RLC filter (the blue curve). There is possible of the using the optimization to reach almost identical transfer as with the lossless FDNR elements with the lossy FDNR elements. The optimization consists in spreading lossy from the lateral branch of the filter to the whole circuit.

The resulting realization of the filter is on the Fig. 5. The measuring was done with the help of vector analyzer Bode 100, by company OMICRON Lab [9]. During parameters verifying of designed circuit was also searched the characteristic sentence of real active elements. Very crucial is mainly sufficient width of the OA band, which is one of the key presumptions of the distortion-less function of the filter in demanded band-pass and it is necessary to solve it with the regard to cut-off frequency of the filter with the sufficient reserve, minimally one or two orders higher [10]. Very good results were achieved by OA by company Texas Instrument [8] OPA355, which are determined also for active filters and they have sufficient width of the band (GBW 200 MHz). The designed low-pass filter was completed with the three amplifiers for processing of NMR signal.

At first, the transfer characteristic of the filter was measured (Fig. 6 — the green curve) and after the transfer characteristic of the filter with amplifiers (Fig. 7) consequently there is obvious gain 22 dB.



Figure 5: The realized filter with the amplifiers.

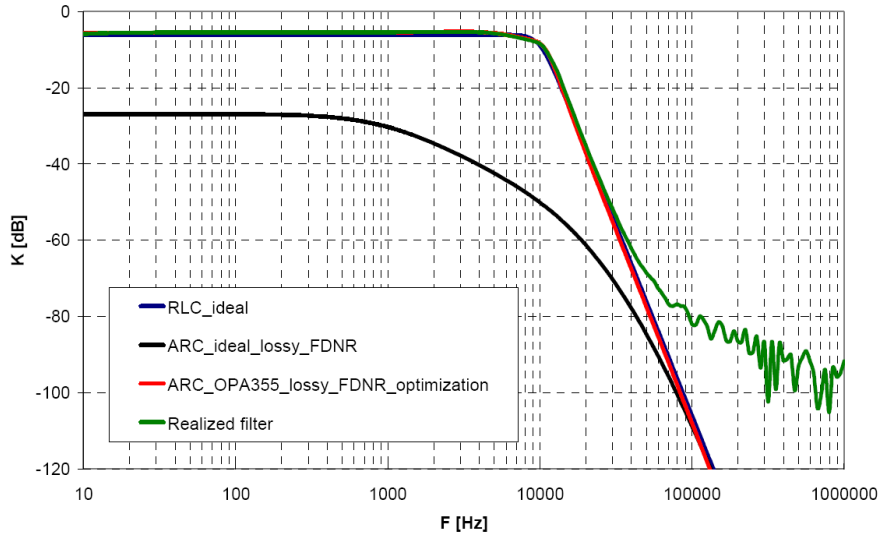


Figure 6: The magnitude response of the filters: LRC, ARC, ARC optimization and the realized filter.

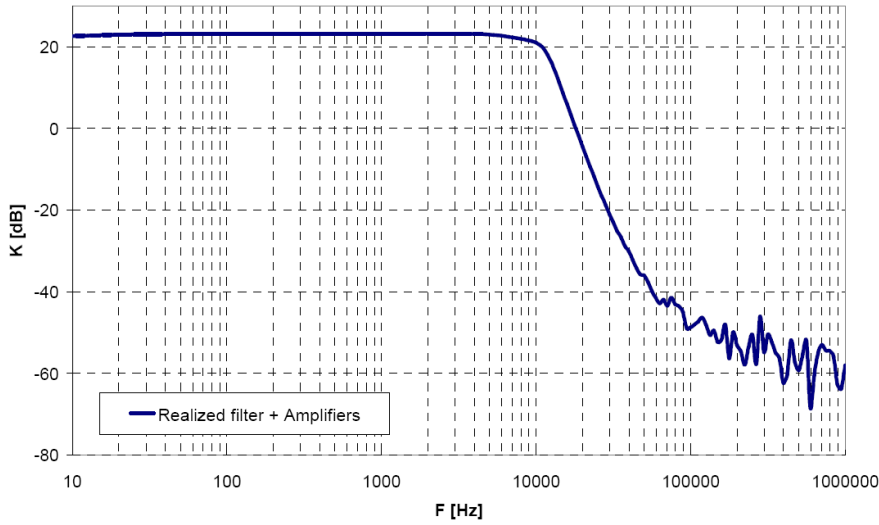


Figure 7: The measured magnitude response of the filter with amplifiers.

### 3. CONCLUSIONS

This contribution deals with synthesis and optimization of ARC low pass filter based on modified simple and economic lossy building blocks (FDNR). The designed frequency filter will be used for pre-processing of analogue signals before digitalization in the NMR signal processing area whereas the resulting characteristics of the designed and measured filter show, that it is possible using it with utilize of the optimization.

The quick progress of modern technologies enables realization of modern structures of analogue frequency filters. In this context, there is necessary to evolve the synthesis and optimization meth-

ods of these structures with regard to the possibilities of the modern active components (voltage OA with GBW approximately 1 GHz, current conveyors, transimpedance OA). In the future research, it will focused on optimization of the basic building block of 2nd order and their characteristics with the modern active elements above they will be analyzed from the point of view of their usage in circuits of higher orders and area of higher frequencies.

## ACKNOWLEDGMENT

This work has been supported by the project of the BUT Grant Agency FEKT-S-11-5.

## REFERENCES

1. Sedláčk, J. and K. Hájek, *Kmitocové Filtry*, 1. vydání, Praha, 535s, BEN — Technická Literatura, 2002, ISBN80-7300-023-7.
2. Pactitis, S. *Active Filters: Theory and Design*, CRC Press, 274 str., USA, 2008, ISBN 978-1-4200-5476-7.
3. Bruton L. T., *RC-active Circuits Theory and Design*, Prentice-Hall, Inc., Englewood Cliffs, New Jersey, 1980, ISBN 0-13-753467-1.
4. Friedl, M., *Synthesis of Modern Structures Frequency Filters*, 21s, Dizertací Práce, Department of Theoretical and Experimental Electrical Engineering, Faculty of Electrical Engineering and Communication, Brno University of Technology, Brno, 2010.
5. Hájek, K. and J. Sedláčk, “Lossy LC ladder prototypes and their use for ARC filter optimization,” *Wseas Transactions on Electronics*, Vol. 2, No. 3, 94–99, July 2005, ISSN1109-9445.
6. Friedl, M., L. Fröhlich, and J. Sedláčk, “Modified approximation types for lossy building blocks,” *PIERS Proceedings*, 521–525, Xi'an, China, March 22–26, 2010.
7. Hájek, K., V. Michal, J. Sedláčk, and M. Steinbauer, “A simple method of goal-directed lossy synthesis and network optimization,” *Advances in Electrical and Electronic Engineering*, 249–253, Zilina, 2006, ISSN1336-1376.
8. *Focus.ti*, OPA355, Dostupné z, [online], 2010 [cit. 2010-04-28], [www:http://focus.ti.com.cn/cn/lit/ds/sbos195d/sbos195d.pdf](http://focus.ti.com.cn/cn/lit/ds/sbos195d/sbos195d.pdf).
9. *Omicron-lab*, Vector Network Analyzer, Bode 100 Extended frequency range 1 Hz–40 MHz. Dostupné z, [online], 2010 [cit. 2010-04-28], [www:http://www.omicron-lab.com/](http://www.omicron-lab.com/).
10. Baker, C., *Chyba Zisku U Operaccích Zesilovacu*, www.Pandatron.cz: Elektrotechnický Magazín, Dostupný z, [online], 2010 [cit. 2011-01-31], [www:http://pandatron.cz/?1382&chyba\\_zisku\\_u\\_operacnich\\_zesilovacu](http://pandatron.cz/?1382&chyba_zisku_u_operacnich_zesilovacu).

# Universal Arc Filters for Arc Oscillators with Automatic Sequential Filtration

Lubomír Frölich, Jiří Sedláček, and Martin Friedl

Brno, FEEC BUT, UTEE, Kolejní 2906/4, Brno 612 00, Czech Republic

**Abstract**— There are situations, when it is not possible to use standard types of filters, mainly because of demands on using of digital tuning of complex filter and concurrently usage of higher amount of transfer functions, which can be low pass-LP, high-pass-HP, band-pass-BP, band-reject-BR, but also low or high-pass notch-LPN/HPN and all-pass-AP. For this purpose, we mostly use 2nd order ARC filters, which contain three or more operational amplifiers (OA). Concerning these blocks, tuning or control of this filter is usually the easiest.

Except very familiar known filters as Akerberg-Mossberg, Kerwin-Huelsman-Newcomb or Towa-Thoma, there is a further amount of circuit connections of universal ARC filters, which enable to realize the transfer function of biquad. The article mainly deals with some other circuits, which are not so familiar, but can be also successfully used as universal filters. These filters realizing required circuit functions with the possibility of tuning of basic parameters of the circuit have been used in special circuits with ARC oscillators for very low distortion with maximum suppression of third harmonics.

## 1. INTRODUCTION

In area of low-frequency oscillators, ARC oscillators are used more and more often. Its parts can be also in certain kind of connection also universal tuned filters see Fig. 1 and Fig. 2. On the Fig. 1, you can see the way of decreasing of alternation with the help of improved filtration and also bigger suppression of higher harmonic elements, just during usage of universal filter ARC 2nd order with the output LP. Another advantage of the connection on this figure is gaining neap signal (output BP). Another way how to achieve decreased harmonic alternation is creating of realizing of the filter with zero transfer LPN, see Fig. 2. In this connection, it is possible to set the zero frequency in dependence on the fact which of the higher harmonic elements on the output of regenerative stabilization member dominant [1].

For usage of the suitable universal filter in connection of ARC oscillators, it is necessary to work out the synthesis of universal filters ARC 2nd order. There are many kinds of universal ARC filters and in most cases these can realize transfer function  $H(s)$  in biquad form (1):

$$H(s) = K \frac{N(s)}{D(s)} = K \frac{b_2 s^2 + b_1 s + b_0}{a_2 s^2 + a_1 s + a_0} = K \frac{s^2 + s\omega_z/Q_z + \omega_z^2}{s^2 + s\omega_0/Q_0 + \omega_0^2}. \quad (1)$$

One of the most used universal circuits in practice is Akerberg-Mossberg, Kerwin-Huelsman-Newcomb or Towa-Thomas. The first two listed filters enable current realization of filters of type low-pass (LP), high-pass (HP), band-reject (BR), band-pass (BP), but also low-pass or high-pass notch (LPN/HPN) and all-pass (AP). The tuning for these filters is realized by parallel change of elements  $R_1-R_2$  a  $C_1-C_2$ . Both filters are characterized by an independent setting of individual parameters and by usage of the band up to 10 MHz. Below stated filters and their qualities will be mainly compared with these filters, which already found their usage in practice.

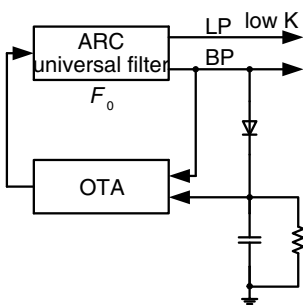


Figure 1: Principle of ARC oscillator.

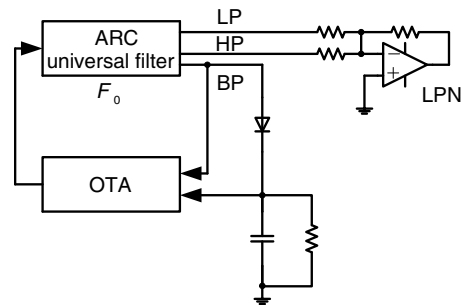


Figure 2: Principle of ARC oscillator.

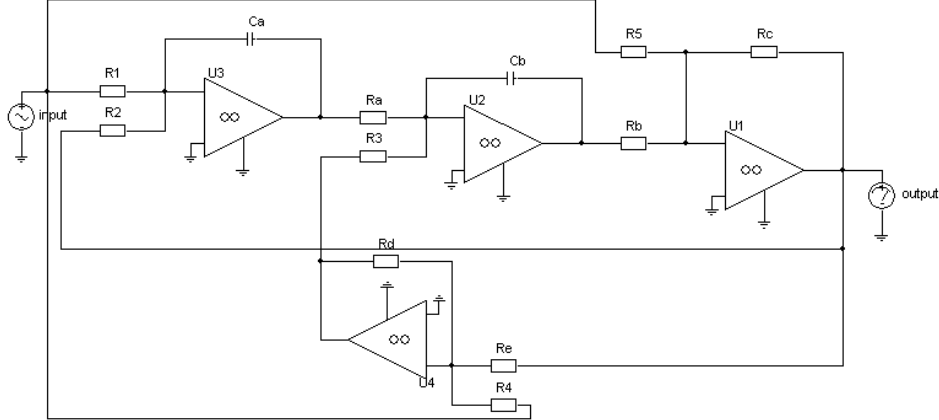


Figure 3: An illustration of the universal filter with 4OA [2, 5].

## 2. THE SYNTHESIS OF UNIVERSAL FILTERS

On the Fig. 3, there is a connection of a universal filter, which contains 4 operational amplifiers (OA) and enables to realize transfer functions of type LPN, HPN, BR, LP, HP and BP. Possibilities of tuning or retuning can be also realized with the help of capacitors  $C_A$  and  $C_B$  or resistors  $R_1$  and  $R_2$  where we have to consider dependence on  $Q$ -factor, by a change of the resistor  $R_Q$ .

For derivation of transfer characteristics for individual outputs in OA in a circuit, we used SNAP program, which is able to display function for a required output. A modified function for OA U1 can be seen in the following formula (2):

$$H(s) = \frac{N(s)}{D(s)} = \frac{-R_2 R_3 R_4 R_5 R_C R_E - s(R_1 R_2 R_5 R_A R_C R_D R_E C_A) - s^2(R_1 R_2 R_3 R_4 R_A R_B R_C R_E C_A C_B)}{+R_1 R_3 R_4 R_5 R_C R_E + s(R_1 R_2 R_4 R_5 R_A R_C R_D C_A) + s^2(R_1 R_2 R_3 R_4 R_5 R_A R_B R_E C_A C_B)}. \quad (2)$$

For a modification of the function (2), it is necessary to choose suitable initial circuit conditions, which can be the following ones:  $R_a = R_b = R_c = R_d = R_e = R$ ,  $C_a = C_b = C_{lad}$ ,  $R_1 = R_2 = R_{dig}$ ,  $R_3 = R_Q$ .

In a modified transfer function (3),  $R_{dig}$  is equal to  $R_1$ ,  $R_2$  and  $C_{lad}$  is equal to  $C_A$ ,  $C_B$ , these elements enable fine or coarse tuning of a frequency circuit:

$$H(s) = \frac{N(s)}{D(s)} = -\frac{R_C}{R_5} \frac{s^2 + s \frac{R_5 R_D}{R_3 R_4 R_B C_B} + \frac{R_5}{R_1 R_A R_B C_A C_B}}{s^2 + s \frac{R_C R_D}{R_3 R_B R_E C_B} + \frac{R_C}{R_2 R_A R_B C_A C_B}} = -\frac{R}{R_5} \frac{s^2 + s \frac{R_5}{R_Q R_4 C_{lad}} + \frac{R_5}{R_{dig} R^2 C_{lad}^2}}{s^2 + s \frac{1}{R_Q C_{lad}} + \frac{1}{R_{dig} R C_{lad}^2}}. \quad (3)$$

From denominator of the function  $D(s)$  (3), we can derive relations for a frequency  $f_0$  (4) and  $Q$ -factor (5):

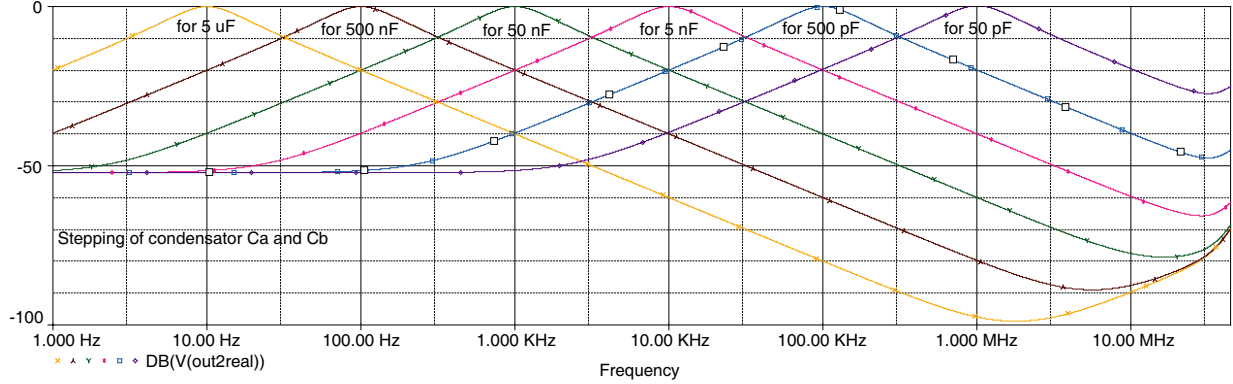
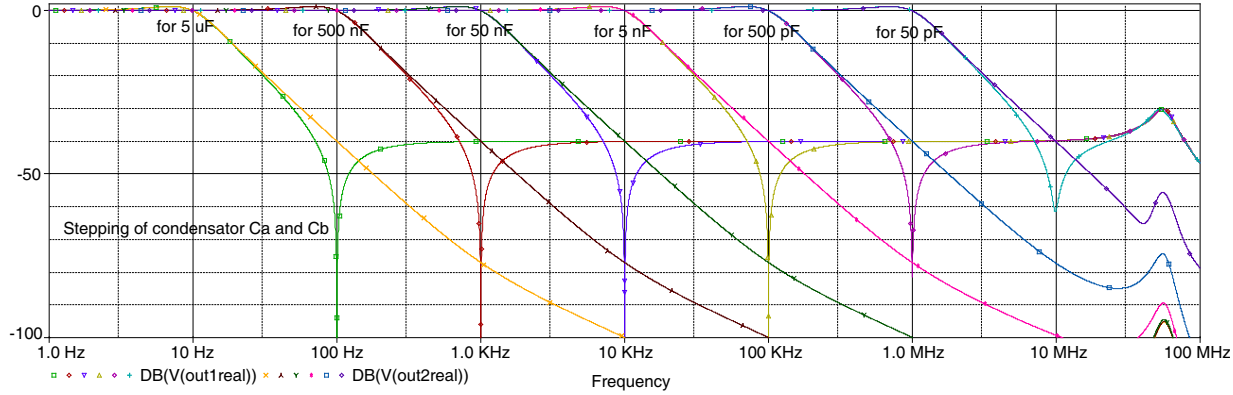
$$f_0 = \frac{1}{2\pi} \frac{1}{C_{lad}} \sqrt{\frac{1}{R_{dig} R}}, \quad (4)$$

$$Q_0 = R_Q \sqrt{\frac{1}{R_{dig} R}}. \quad (5)$$

From the function (5), we can see dependence of setting of  $Q$ -factor by a resistor  $R_Q$  on the resistors  $R_1$  and  $R_2$ , which serve for a fine setting of a circuit frequency.

From numerator of the function  $N(s)$  (3) for an output of operational amplifier U1 at initial conditions  $R_a = R_b = R_c = R_d = R_e = R$ ,  $C_a = C_b = C_{lad}$ ,  $R_1 = R_2 = R_{dig}$ ,  $R_4 = \infty$ ,  $R_3 = R_Q$  is accepted relation for LPN, HPN and BR:

$$N(s) = -\frac{R}{R_5} \left( s^2 + s \frac{R_5}{R_3 R_4 C} + \frac{R_5}{R_{dig} R C^2} \right) = -\frac{R}{R_5} \left( s^2 + \frac{R_5}{R} \frac{1}{R_{dig} R C_{lad}^2} \right). \quad (6)$$

Figure 4: Simulation of BP output U2\_CLC440/CL,  $Q = 1$ .Figure 5: Simulation of LP and LPN output U2 and U1\_CLC440/CL,  $Q = 1$ .

For frequency notch of transfer  $f_N$  is accepted relation  $R_5 = (R \cdot f_n^2)/f_0^2$ .

For transfer of OA U2 it is possible to create transfer function of type LP (7) and BP (8) at initial conditions for LP:  $R_4 = R_5$  and for BP:  $R_a = R_b = R_c = R_d = R_e = R_5 = R$ :

$$N(s) = \frac{R_2 R_3 R_4 R_B R_E (R_5 - R_C)}{R_1 R_2 R_3 R_4 R_5 R_A R_B R_E C_A C_B} + s \frac{R_1 R_2 R_A R_B R_D C_A R (R_5 - R_4)}{R_1 R_2 R_3 R_4 R_5 R_A R_B R_E C_A C_B} = \frac{(R_5 - R)}{R_5} \frac{1}{R_{dig} R C_{lad}^2} \quad (7)$$

$$N(s) = \frac{R - R_4}{R_4} s \frac{1}{R_Q C_{lad}}. \quad (8)$$

On the output of operational amplifier U3 it is possible to obtain LP and BP. However, there is a problem with the fulfilling of the basic conditions from the relations (4) and (5). Because of these reasons, it is not possible to use these transfer functions.

On the output of the last OA, or U4 after a derivation, we obtain functions for HP (9), LP (10) a BR (11), under conditions for HP:  $R_4 = R$  for LP:  $R_4 = R_5 = R_{45}$  and for BR at  $R_5 = R$ :

$$N(s) = -s^2 \frac{(R_5 - R_4)}{R_5} = -\frac{(R_5 - R)}{R_5} s^2, \quad (9)$$

$$N(s) = \frac{(R_4 - R)}{R_4} \left( \frac{1}{R_{dig} R C_{lad}^2} \right), \quad (10)$$

$$N(s) = \frac{(R_4 - R)}{R_4} \left( \frac{1}{R_{dig} R C_{lad}^2} + s^2 \right). \quad (11)$$

Out of above mentioned relations, it is possible to design complex values for individual components and with the help of SPICE program we can verify the function of the entire filter. Some examples of simulation are stated on the Figs. 4 to 5. One of the disadvantage of this circuit is a big scatter of a value of the resistor  $R_5$  for transfer functions LPN, HPN and BR.

This resistor decides about a given function and his value lies at intervals from several  $\Omega$  up to  $M\Omega$ . Another inconvenient factor can be also scatter of resistors  $R_{dig}$ , which we need as smallest as

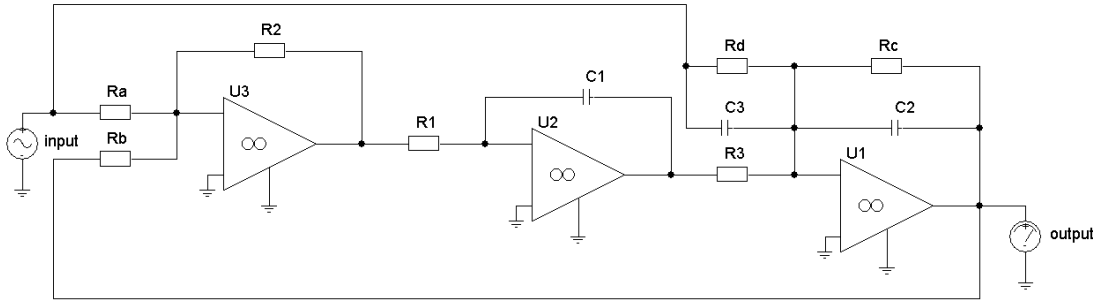


Figure 6: Example of universal filter with 3OA [2, 5].

possible for tuning with the help of digital potentiometers, regarding usage of circuits for the biggest possible frequency. Thus, for a design  $R_{dig} \max = 1\text{ k}\Omega$  we obtain unrealized  $R_{dig} \min = 10\Omega$ . According to stated simulations, this circuit can be used maximally up to 1 MHz. On higher frequencies, there is a significant characteristic deformation.

### 3. OTHER TYPES OF THE FILTERS

The example of other universal filter is on the Fig. 6.

At this circuit, there is not stated a complex synthesis of a circuit, but only a brief description of the circuit. The circuit on the Fig. 6 is able to realize transfer functions of type LPN, HPN and BR on the output of operational amplifier U1, on the output of OA U2 is gaining LP and BR and for the output of U3 we have HP or BP. In the same way as at the above mentioned circuit, the tuning of a frequency  $f_0$  with the help of resistor dependent on a  $Q$ -factor and another disadvantage is a relation  $C_3/C_{lad}$  for setting of a frequency of a transfer notch. The initial conditions are  $R_a = R_b = R_2 = R$ ,  $C_1 = C_2 = C_{lad}$ ,  $R_1 = R_3 = R_{dig}$ ,  $R_c = R_Q$ .

### 4. CONCLUSIONS

The introduction of the article tried to show the usage of universal tuned filters in practice, particularly in ARC oscillators. In these circuits, the universal filters A-M and K-H-N are used the most often. Both these filters can realize parallel demanded transfer functions, see Fig. 1 and Fig. 2. They both enable independent setting of parameters and possibilities of digital tuning. However, this article describes the synthesis of less known filters, which could be considered as universal filters, under certain conditions. For the set circuits, there is a problem with the fact, that it is not possible to create the realization of the filters with the parallel output of the set transfer functions, as it is showed on the Fig. 1 and Fig. 2, but also creating of individual transfer functions is also very difficultly realized with the help of retuning of individual parameters. The circuits enable to create digital tuning of the resonance frequency with the help of capacitors  $C_{lad}$  to frequency decades. Fine tuning inside the frequency decades is able to be realized with help of  $R_{dig}$  resistors. Here we come to a problem of dependence on the  $Q$ -factor. Apart from the mentioned problems, these circuits have big scatter of the building elements. At the end, it can be said that the described circuits cannot be used for the connections on the Fig. 1 and Fig. 2. It can be used in less demanding connections, where the usage of transfer function is not demanded and where we need the frequency to be digitally tuned, only roughly to frequency decades. The circuits were simulated with OA CLC 440/CL and maximum frequency scatter is about 1 MHz, when the  $Q$ -factor is 10. For the circuit design, the complete synthesis was created with the help of the programs SPICE and SNAP.

### ACKNOWLEDGMENT

This work has been supported by the project of the BUT Grant Agency FEKT-S-11-5.

### REFERENCES

1. Sedláček, J. and K. Hájek, "Kmitočtové filtry. 1. vydání," Praha: BEN-Technická Literatura, 535, 2002, ISBN 80-7300-023-7.
2. Galiamichev, I. P., A. A. Lanne, V. Z. Lundin, and V. A. Petrakov, *The Synthesis of Active RC Network*, 296, Moscow, Izdatel'stvo Sviaz', 1975 (in Russian).

3. Hájek, K., "Přeladitelný Nízkofrekvenční Generátor s Velmi nízkým Zkreslením," OA 277259, 1992.
4. Sedláček, J. and K. Hájek, "ARC oscillators with ultra low distortion," *Proc. Of Int. Symp. on Nonlin. Theory and Appl. NOLTA'98*, Vol. 3, 1201–1204, Crans-Montana, Sep. 1998.
5. Fröhlich, L., "Active frequency filters for higher frequencies," *Pojednání K Disertační Práci*, 22, Brno University of Technology, Faculty of Electrical Engineering and Communication, Brno, 2010.

# Visualization of Plant Fibres via Diffusion Tensor Imaging

E. Gescheidtová<sup>1</sup>, P. Marcon<sup>1</sup>, and K. Bartusek<sup>1,2</sup>

<sup>1</sup>Department of Theoretical and Experimental Electrical Engineering

Brno University of Technology, Kolejní 2906/4, Brno 612 00, Czech Republic

<sup>2</sup>Institute of Scientific Instruments, Academy of Sciences of the Czech Republic  
Kralovopolska 147, Brno 612 64, Czech Republic

**Abstract**— The paper deals with MR imaging of plant fibres via Diffusion weighted imaging (DWI) and Diffusion tensor imaging (DTI). Imaging plant fibres helps to better understand the process of nourishing the plants, and also to come to know the internal structure of plants without damaging them. To measure diffusion in the plant specimen, the well-known NMR method was used, currently referred to as the Pulsed field gradient spin-echo (PFGSE). Experimental measurement was conducted on an MR tomograph system with the gradient field  $B_0 = 4.7\text{ T}$ . Onion and dill were used as specimens to be measured. The values obtained by the PFGSE method were used to calculate diffusion weighted images (DWI). The measurement of diffusion weighted images was performed in 6 directions of the gradients ( $x, y, z, xy, xz, yz$ ) and the data obtained served to calculate the DTI image of the specimen being measured.

## 1. INTRODUCTION

Efforts aimed at obtaining in-depth knowledge of the way plants are nourished lead to the application of NMR measuring methods, which enable non-invasive measurement of the structure of the fibres that nourish plants. Frequently, we are interested in how matter (nutrients, particles) is transferred. By the Stokes-Einstein equation this motion of particles depends on temperature and on the so-called diffusion coefficient of the substance [1]. This coefficient is denoted by the letter  $D$  and physically, it expresses the degree of particle mobility. E. O. Stejskal and J. E. Tanner described the spectroscopic measurement of diffusion coefficients with the aid of the NMR technique in 1965 [2]. The PFGSE (Pulsed Field Gradient Spin Echo) method was successively improved and applied to the measurement of diffusion weighted images, DWI.

The data obtained by the PFGSE method are used to calculate  $ADC$  (Apparent Diffusion Coefficient). One  $ADC$  value represents one pixel in the DWI image. In the calculation of  $ADC$  (more frequently denoted  $D$ ) the following calculation is used:

$$\frac{S}{S_0} = e^{-bD}, \quad (1)$$

where  $b$  is the so-called  $b$ -factor, which is calculated from the properties of gradient pulses that are used in the PFGSE sequence [3, 4]. The quantity  $S$  describes an image weighted by the signal intensity from a specimen that was obtained using the PFGSE sequence with gradient pulses in a certain direction of the coordinate system. The quantity  $S_0$  denotes an image weighted by the signal intensity without the application of gradient fields. Equation (1) is correct only for isotropic materials or for measuring diffusion along one coordinate axis. To measure diffusion in plant fibres, where the medium is anisotropic, it is necessary to use the following relation:

$$\frac{S}{S_0} = e^{-\mathbf{b} \cdot \mathbf{D} \cdot \mathbf{b}^T}, \quad (2)$$

where  $\mathbf{b}$  is a vector containing information not only about the size of the gradient but also about its orientation. Matrix  $\mathbf{D}$  represents a symmetrical tensor that contains diffusion coefficients  $D$  calculated from the measurement along six independent coordinate directions. For the calculation of diffusion it is also necessary to measure a seventh image, and this time without using gradient pulses. When imaging a diffusion tensor, one voxel is in our case imaged by means of an ellipsoid. To form the ellipsoid it is necessary to know the eigenvalues  $\lambda$  and eigenvectors  $\mathbf{v}$ . These are obtained from tensor  $\mathbf{D}$  by means of the “diagonalization” process, as can be seen in Equation (3).

$$\mathbf{D} = \begin{bmatrix} D_{xx} & D_{xy} & D_{xz} \\ D_{yz} & D_{yy} & D_{yz} \\ D_{zx} & D_{zy} & D_{zz} \end{bmatrix} \xrightarrow{\text{diagonalization}} \lambda_1, \lambda_2, \lambda_3, \mathbf{v}_1, \mathbf{v}_2, \mathbf{v}_3. \quad (3)$$

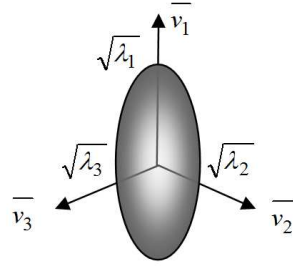


Figure 1: Ellipsoid which depicts the diffusion tensor according to relation (3).

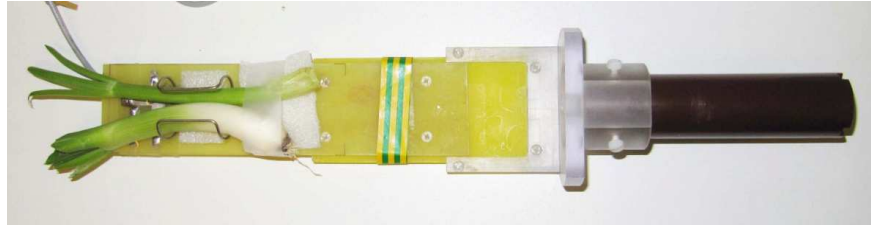


Figure 2: NMR probe with specimen (onion and dill).

Figure 1 shows imaging the ellipsoid on the basis of the knowledge of eigenvectors and eigenvalues. The eigenvalues determine the ellipsoid magnitude in individual directions, which are given by eigenvectors  $\mathbf{v}$ .

## 2. EXPERIMENTAL

To measure diffusion in plant specimens the well-known NMR method was used, which is referred to as the Pulsed field gradient spin echo (PFGSE). The experiment was conducted on an MR tomograph system with the magnetic field  $B_0 = 4.7 \text{ T}/120 \text{ mm}$  (i.e., 200 MHz for  $^1\text{H}$  nuclei). Actively shielded gradient coils yield a maximum gradient field magnitude of 180 mT/m [5–7]. Onion and dill were used as specimens. The values measured by the PFGSE method were used to calculate the diffusion weighted image (DWI). Each image voxel has an image intensity that reflects a single best measurement of the rate of water diffusion at that location. The measurement was conducted without and with gradients in axes  $x$ ,  $y$ ,  $z$ . However, the direction of fibres that nourish the plant cannot be seen from these DWI images. The data measured were therefore added up with the data measured with gradients in axes  $xy$ ,  $yz$  and  $xz$  and the diffusion tensor was calculated according to relations (2) and (4). The diffusion tensor was imaged with the aid of small ellipsoids. Each image point, called voxel, is thus formed by an ellipsoid.

Rewriting relation (2) led to the following equation, which was used to calculate individual diffusion coefficients:

$$\mathbf{b} \cdot \mathbf{D} \cdot \mathbf{b}^T = [\sqrt{b_x}, \sqrt{b_y}, \sqrt{b_z}] \cdot \begin{bmatrix} D_{xx} & D_{xy} & D_{xz} \\ D_{yz} & D_{yy} & D_{yz} \\ D_{zx} & D_{zy} & D_{zz} \end{bmatrix} \cdot \begin{bmatrix} \sqrt{b_x} \\ \sqrt{b_y} \\ \sqrt{b_z} \end{bmatrix}. \quad (4)$$

In the experiment, the following combination of gradients was used:  $[0, 0, 0]$ ,  $[1, 0, 0]$ ,  $[0, 1, 0]$ ,  $[1, 0, 1]$ ,  $[\frac{1}{\sqrt{2}}, \frac{1}{\sqrt{2}}, 0]$ ,  $[\frac{1}{\sqrt{2}}, 0, \frac{1}{\sqrt{2}}]$ ,  $[0, \frac{1}{\sqrt{2}}, \frac{1}{\sqrt{2}}]$ . The magnitudes of gradients were set such that  $b_x = b_y = b_z = \sqrt{b_x} \cdot \sqrt{b_y} = \sqrt{b_x} \cdot \sqrt{b_z} = \sqrt{b_y} \cdot \sqrt{b_z} = 221.5 \text{ mm}^2/\text{s}$ . This makes the calculation of diffusion coefficients  $D$  simpler.

## 3. RESULTS AND DISCUSSION

The procedure of processing the data measured is indicated in Fig. 4. By the application of PFGSE, measurement data were obtained that represented the intensity of images in the so-called  $k$ -space. These data represent a matrix of  $64 \times 64$  pixels and to obtain a resultant image, they must be transformed using the Fourier transform as, for example, in Fig. 4 (here the measurement

was performed without gradients). The data are then filtered for pulse noise and the images are calculated by the DWI and DTI methods.

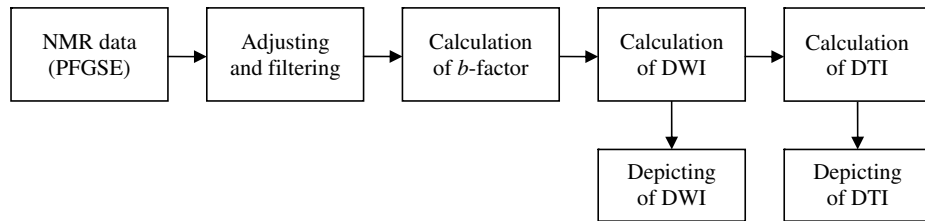


Figure 3: Algorithm for processing the data measured.

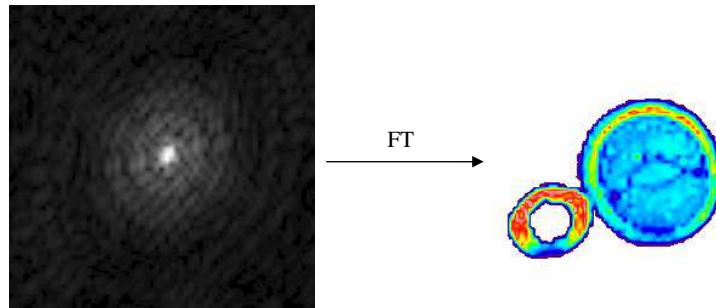


Figure 4: Left: values measured in  $k$ -space obtained from tomograph system. Right:  $S_0$  image transformed via FT.

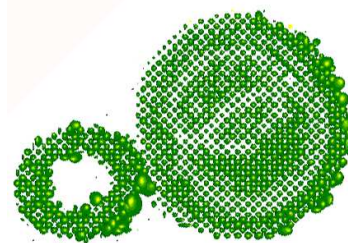


Figure 5: NMR probe with specimen (onion and dill).

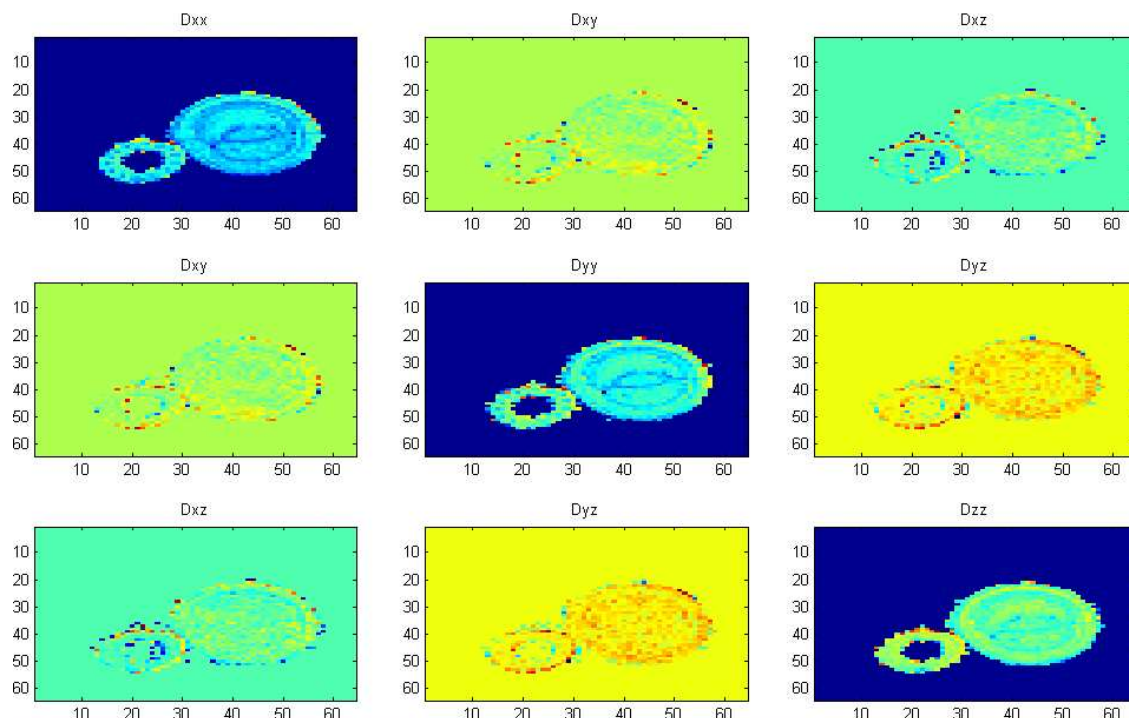


Figure 6: Calculated DWI images corresponding to individual elements in tensor  $\mathbf{D}$ .

The DTI image was calculated in the Matlab program, using relation (3) [8]. In Fig. 5 the measured specimen of dill and onion is depicted in transversal slice, obtained by the DTI method. It can be seen that the image in this 2D slice is made up of ellipsoids, which determine not only the direction of the particle diffusion but also its magnitude.

Figure 6 shows nine diffusion weighted images of a transversal slice of the specimen being measured. These images correspond to individual elements in matrix  $\mathbf{D}$ . As is obvious from the images, the highest resolution can be seen in the image measured with only the gradient in axis  $x$  being used. The structure of the specimen measured can best be seen here. In the remaining images, the structure can also be discerned on the main diagonal. When using gradients in two axes we obtain weaker signals outside the diagonal; here, the plant structure is less pronounced.

#### 4. CONCLUSION

To image via DTI the specimens measured, we used the PFGSE method and obtained images of  $64 \times 64$  px in size. We chose this resolution in order to obtain a higher intensity of the signal being measured. To get a more accurate image of the structure of plant fibres it would be better to choose a higher image resolution (e.g.,  $128 \times 128$  px). However, even with the resolution used, it was possible to obtain images of the fibre structure by means of ellipsoids, which give the magnitude of the diffusion coefficient and also the diffusion direction. Putting together several 2D images of ellipsoids we obtain a 3D structure from which curves can be plotted using the method of traction anisotropy [1, 2] that will characterize directly the fibres in the plant. These problems will be the subject of further works.

#### ACKNOWLEDGMENT

This work was supported within the framework of projects No. 102/11/0318 of the Grant Agency of the Czech Republic and the research plan MSM 0021630516.

#### REFERENCES

1. Johansen-Berg, H. and T. E. J. Behrens, *Diffusion MRI: From Quantitative Measurement to in Vivo Neuroanatomy*, Elsevier, China, 2009.
2. Stejskal, E. O. and J. E. Tanner, “Spin diffusion measurements: Spin echoes in the presence of a time-dependent field gradient,” *The Journal of Chemical Physics*, Vol. 42, No. 1, 10–28, 1965.
3. Basser, P. J., J. Mattiello, and D. Le Bihan, “MR diffusion tensor spectroscopy and imaging,” *Biophysical Journal*, Vol. 66, 259–267, 1994.
4. Bartusek, K. and E. Gescheidtova, “MRI method of diffusion measurement in heterogeneous materials,” *Measurement Science and Technology*, Vol. 19, 2008.
5. Marcon, P. and K. Bartusek, “Errors in diffusion coefficients measurement,” *PIERS Proceedings*, 1035–1039, Cambridge, USA, July 5–8, 2010,
6. Bartusek, K. and E. Gescheidtova, “Testing the quality of magnetic gradient fields for studying self-diffusion processes in biological specimens by magnetic resonance methods,” *Measurement Science and Technology*, Vol. 17, 2256–2262, 2006.
7. Barmpoutis, A., B. C. Vemuri, and J. R. Forder, “Tensor splines for interpolation and approximation of DT-MRI with application to segmentation of isolated rat hippocampi,” *IEEE TMI: Transactions on Medical Imaging*, Vol. 26, No. 11, 1537–1546, 2007.
8. Barmpoutis, A. and B. C. Vemuri, “A unified framework for estimating diffusion tensors of any order with symmetric positive-definite constraints,” *Proceedings of ISBI10: IEEE International Symposium on Biomedical Imaging*, 358–3188, April 14–17, 2010.

# Dielectric Properties of Water Solutions with Small Content of Glucose in the Millimeter Wave Band and the Determination of Glucose in Blood

B. M. Garin, V. V. Meriakri, E. E. Chigrai, M. P. Parkhomenko, and M. G. Akat'eva

Kotel'nikov Institute of Radio Engineering and Electronics RAS, Fryazino Branch

Fryazino, Moscow Region 141190, Russia

**Abstract**— The dielectric properties of 0.9% NaCl in water with small content of sugar and glucose, as well as of human skin, were measured in the millimeter (MM) waves range.

The measurement methods were chosen so that one could use them for the nondestructive control of glucose content (i.e., measurement only reflection of an electromagnetic wave, without penetrating into the medium). To determine  $\epsilon'$  and  $\epsilon''$ , of lossy materials one usually measures the power reflection coefficient and the phase of the reflected wave with the help of sophisticated and expensive network vector analyzers. We developed a sufficiently simple method and scheme, which consists in measuring the minimum of the power reflection coefficient  $R(f) = R_{\min}(f_{\min})$  and its frequency  $f_{\min}$  in the cases of corresponding to this minimum from the following structures: a specially chosen plane-parallel matching plate made of a low-loss dielectric or resonator — a medium under measurement with high losses (solution, blood, skin). This method was realized in the MM waves range. Dielectric properties of glucose solutions in water and in a 0.9% NaCl solution (physiological solution) have been measured. Also was measured dielectric properties of human skin. The values of  $\epsilon'$  and  $\epsilon''$  have been measured near the elbow joint in the frequency range from 30 to 80 GHz. Above 40 GHz, these data have been obtained for the first time, whereas, at frequencies of 30–40 GHz, the values of  $\epsilon''$  obtained in our experiments are higher than those available in the literature. Our method allows a real-time noninvasive determination of glucose content in blood by measuring reflection on skin. We established a clear correlation between glucose content  $W$  and the measured value of reflection coefficient as  $W$  increases after an oral glucose tolerance test (OGTT) on an empty stomach. The functions  $R_{\min}(W)$  show similar but individual behavior for each test person. It was established a correlation between glucose content  $W$  after OGTT and the properties of skin. The results of the measurements described can be used to implement real-time, including noninvasive, measurements of small glucose (sugar) content in water, physiological solution, and blood.

## 1. INTRODUCTION

Investigations of the dielectric properties of sugar in water solutions, as well as blood imitators and blood, in the millimeter (MM) wave range allow one to obtain valuable information on the possibility of real-time control of glucose concentration in blood using MM waves, which is of huge interest for diabetics [1, 2]. These investigations are also of interest for other applications such as determination content of water solutions [3].

## 2. RESULTS AND DISCUSSION

Investigations of the dielectric properties of glucose in water solutions, as well as blood imitators and blood, in the millimeter (MM) wave range allow one to obtain valuable information on the possibility of real-time control of glucose concentration in blood using MM waves. These investigations are also of interest for other applications such as determination content of water solutions. We investigated using methods described in [4] dielectric properties of glucose solutions in blood imitator (0.9% NaCl in water). Results are presented in Table 1.

Also we investigated dielectric properties of skin in the MM region. Table 2 presents results for forearm, joint at frequencies from 30 to 80 GHz. Above 40 GHz, these data have been obtained for the first time, whereas, at frequencies of 30–40 GHz, the values of  $\epsilon''$  obtained in our experiments are higher than those available in the literature [5].

For measurements dependence of reflection from skin on glucose content we used the matching insert consisting of the resonant cavity based on rectangular waveguide. (Fig. 3.) Directional coupler measures the reflection coefficient  $R$  of the cavity back wall of which is the object of study (in our case the skin). Operating frequency ranged from 30 to 35 GHz. The dimensions of the walls of the waveguide  $a = 7, 2$  mm,  $b = 3, 4$  mm. The ratio of the calculations was found to be 0.31. The size of a diaphragm was 2.28 mm. Fig. 1 presents measurement set up.

Table 1: Dielectric properties of glucose solutions in blood imitator.

$\epsilon', \epsilon''$	28,1 ГГц	31,3 ГГц	37,0 ГГц	42,7 ГГц	48,1 ГГц	62,6 ГГц	83,5 ГГц	92,7 ГГц
$\epsilon'_\phi$	19,9	23,0	15,1	14,5	14,5	9,35	8,73	7,83
$\epsilon'_{0,5}$	20,0	23,0	14,8	14,4	14,4	9,25	8,29	7,81
$\epsilon'_3$	20,3	22,7	14,4	13,6	13,9	9,16	8,02	7,60
$\epsilon''_\phi$	31,7	32,0	26,1	25,1	25,0	18,57	14,13	12,94
$\epsilon''_{0,5}$	31,4	31,5	25,8	25,0	24,8	18,51	14,05	12,85
$\epsilon''_3$	29,7	29,7	24,8	23,7	23,7	17,74	13,90	13,30
T, °C	18	17	19	17,5	17,5	20	19	19

Table 2: Dielectric properties of skin in the MM region.

	$f=29,8$ GHz	$tg \delta$ $\alpha$	$f=42,6$ GHz	$tg \delta$ $\alpha$	$f=66$ GHz	$tg \delta$ $\alpha$	$f=77,4$ GHz	$tg \delta$ $\alpha$
Water: 37 °C	$\epsilon =$ 34,05+i3 4,3	1,0 14, 5	$\epsilon =$ 23,1+i30, 5	1,3 2 21, 3	$\epsilon =$ 13,87+i2 3,29	1,6 8 30, 9	$\epsilon =$ 11,74+i20, 7	1,8 34, 4
$d =$ $c/4\pi\kappa f$	0,30 nm		0,20 nm		0,14 nm		0,12 nm	
Skin	$\epsilon =$ 13,0+i34, 2	2,6 3 18, 7	$\epsilon =$ 10,6+i23, 5	2,2 21, 4	$\epsilon =$ 7,86+i12, 7	1,6 2 22, 9	$\epsilon =$ 7,6+i10,3	1,4 22, 4
$d =$ $c/4\pi\kappa f$	0,23 nm		0,20 nm		0,19 nm		0,12 nm	

The series of experiments show a correlation between glucose content  $W$  and  $R_{min}$  in the region where  $W$  increases after taking glucose on an empty stomach at frequencies of about 40 and 60 GHz. At the same time just as in [6], where the measurements were carried out in the infrared band, it is needed individual calibration for different persons. Based on this series of measurements were constructed plots, which shows how changes in time module of the reflection coefficient as a function of time elapsed since the adoption of sugar. Fig. 2 presents typical dependences for three different persons. It is evident that these changes are in good accordance with usual “sugar curve” within one hour, which have one maximum and practically the same values for  $t = 0$  and  $t = t_{max}$ .

Figure 3 presents comparison of dependences on time obtained with our noninvasive sensor and standard optical invasive sensor for two different persons.

Note that in the afternoon (after 3–4 p.m.), a variation in  $R$  for close values of  $W$  was much greater than that before the noon. This fact indicates to certain physiological changes in skin at the depth  $d$  that are associated with physical activity, which were pointed out also in [6].

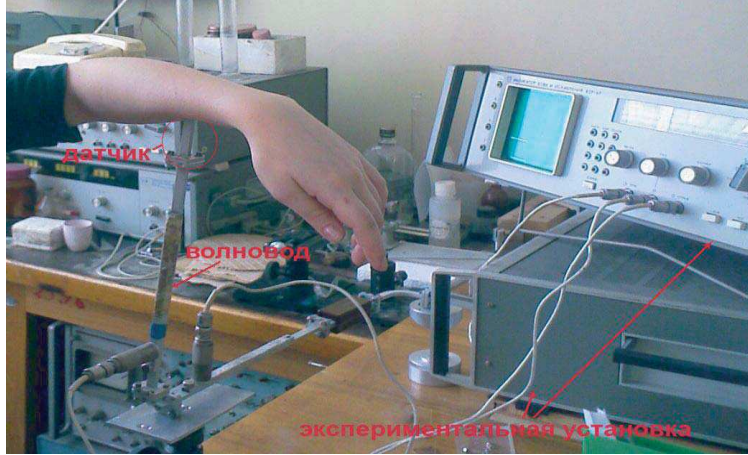


Figure 1: Set up for measurement of reflection from skin.

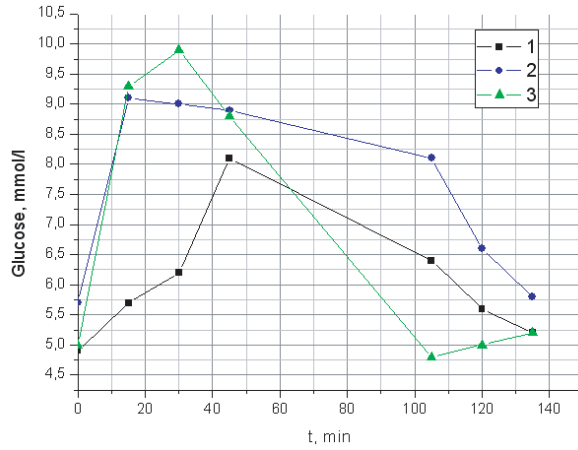


Figure 2: The reflection coefficient as a function of time after OGTT.

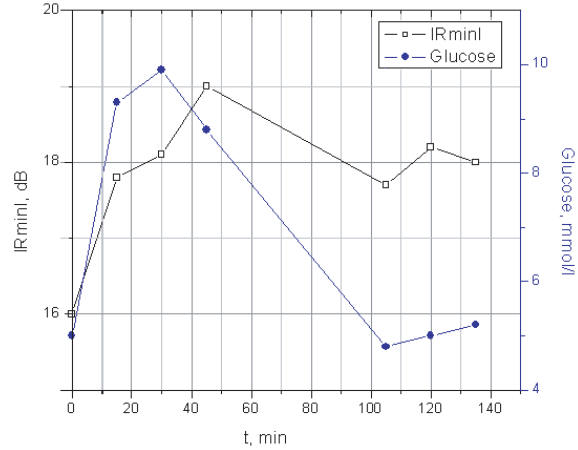


Figure 3: Comparison dependences on time obtained with our noninvasive sensor and standard optical invasive sensor.

### 3. CONCLUSIONS

The values of  $\epsilon'$  and  $\epsilon''$  have been measured near the elbow joint in the frequency range from 30 to 80 GHz. Above 40 GHz, these data have been obtained for the first time. The series of experiments show correlation between glucose content  $W$  and reflection coefficient on skin  $R$  in the region where  $W$  increases after OGTT. It has been established that during OGTT dependences of reflection coefficients from noninvasive resonator sensor have the same shape but different values for different persons.

### ACKNOWLEDGMENT

The work was supported by the Program of the Physical Science Department of the Russian Academy of Sciences "Modern problems of Radiophysics" (Project "Terra-6").

### REFERENCES

- Matsuhiwa, T., M. Yamamoto, and Y. Nikawa, "Basic study on non-invasive monitoring of blood sugar level by measuring transmission coefficient in millimeter waves," *Trans. of the Institute of Electronics, Information and Communication Engineers C*, Vol. J84C, No. 6, 527–530, 2001.
- Nikawa, Y. and D. Someya, "Non-invasive measurement of blood sugar level by millimeter waves," *2001 IEEE MTT-S Intern. Microwave Symposium Digest*, Vol. 1, 171–174, 2001.
- Hochtl, P., S. Boresch, and O. Steinhauser, "Dielectric properties of glucose and maltose solutions," *Journal of Chemical Physics*, Vol. 112, No. 22, 9810–9821, 2000.

4. Meriakri, V. V., E. E. Chigrai, D. Kim, I. P. Nikitin, L. I. Pangonis, M. P. Parkhomenko, and J. H. Won, "Dielectric properties of glucose solutions in the millimetre-wave range and control of glucose content in blood," *Measurement Science and Technology*, Vol. 18, 977–982, IOP Publishing, 2007.
5. Boric-Lubecke, O., Y. Nikawa, W. Snyder, and K. Mizuno, "Skin properties at millimeter waves," *Asia-Pacific Microwave Conf. WEOF35*, 877–880, 2000.
6. Malin, S. F., T. L. Ruchti, T. B. Blank, et al., "Noninvasive prediction of glucose by near-infrared diffuse reflectance spectroscopy," *Chemical Chemistry*, Vol. 45, No. 9, 1651–1659, 1999.

# A Novel Compact Frequency Selective Surface with a Stable Performance Based on Substrate Integrated Waveguide Technology

Hang Zhou<sup>1</sup>, Shaobo Qu<sup>1,2</sup>, Jieqiu Zhang<sup>1</sup>, Jiafu Wang<sup>1</sup>, Baoqin Lin<sup>1</sup>, Hua Ma<sup>1</sup>,  
Zhuo Xu<sup>2</sup>, Peng Bai<sup>3</sup>, and Weidong Peng<sup>3</sup>

<sup>1</sup>College of Science, Air Force Engineering University, Xi'an, Shaanxi 710051, China

<sup>2</sup>Electronic Materials Research Laboratory, Key Laboratory of the Ministry of Education

Xi'an Jiaotong University, Xi'an, Shaanxi 710049, China

<sup>3</sup>Synthetic Electronic Information System Research Department

Air Force Engineering University, Xi'an, Shaanxi 710051, China

**Abstract**— A novel compact frequency selective surface (FSS) with a stable performance is presented. A narrow band-pass circular FSS operating at around 16.6GHz is designed. The unit cell consists of a double-sided metalized substrate with a circular hole in the center as well as 24 metal stubs surrounding the circular hole. In this way, incident EM waves enter the circular cavity formed by the 24 metal stubs and excite a cavity resonance, leading to a narrow pass-band. An approximate analytical formula is introduced to calculate the cavity resonant frequency. The cavity resonance provides a very good wide-angle and polarization-independent stability. Furthermore, there is no other frequency resonance up to 28GHz except the designed frequency. Finally, we get a FSS which has advantages of high selectivity, stable performance and compact volume.

## 1. INTRODUCTION

For more than four decades, Frequency Selective Surfaces (FSSs) have been widely studied for their various applications in spatial microwave and optical filters. They have been used as polarizers, filters, subreflectors, band-pass hybrid radomes for radar cross section (RCS) controlling [1, 2]. In these applications, it is necessary that FSS provide stable performance for different incidence angles and polarization states. Many methods are adopted to improve the performance of FSSs. Munk et al. studied the effects of dielectric loading on FSSs [3]. Three-dimensional structures were designed to obtain isotropic FSSs [4]. Complementary FSSs have been analyzed in [5–8]. References [9–11] made use of resonant structures to design miniaturized FSSs whose dimensions were much smaller than the operating wavelength. In order to get high quality factor of open resonance structures, substrate integrated waveguide (SIW) technology was introduced by Luo et al. [12] to design high performance FSSs. SIW-FSS structures keep the advantages of conventional metallic waveguides, such as high *Q*-factor, high selectivity, cutoff frequency characteristic, high power capacity etc. Base on this method, many excellent SIW-FSSs were studied in [13–15].

In this paper, we proposed a frequency selective surface whose unit cell consists of a double-sided metalized substrate with a circular hole in the center as well as 24 metal stubs surrounding the circular hole. An analytical equation is given to compute the cavity resonant frequencies. In addition, the aperture resonance is adjusted to be far away from the cavity resonance in order not to disturb the cavity resonance. In the end, we obtained a narrow band-pass frequency selective surface with excellent performances. This narrowband FSS owns its advantages to high selectivity, stable performance, compact volume and it is easy to be fabricated by the print circuit board (PCB) technology without post processes.

## 2. THEORY AND DESIGN

Figure 1 shows the geometrical dimensions of the unit cell, where  $p = 15$  mm,  $a = 2.4$  mm,  $b = 6.3$  mm,  $d_2 = 0.2$  mm,  $d_1 = 1$  mm,  $\theta = \pi/12$ . The FSS arrays have a substrate with relative permittivity of  $\epsilon_r = 2.65$ , loss tangent of 0.001 and thickness of  $h_{sub} = 1$  mm. A hole with radius  $a = 2.4$  mm was punched through the substrate.

Finite element method (FEM) was used to calculate its reflection and transmission characteristics. Assume that the SIW-FSS is an infinite periodic structure. The four sides of the unit cell are set to be periodic boundary conditions (PBC) and single SIW-FSS is excited by an incident plane wave. Fig. 2 gives the transmission spectra under normal incidence. We can see from Fig. 2 that an evident resonance occurred at 16.6 GHz. The electric field distributions at 16.6 GHz are

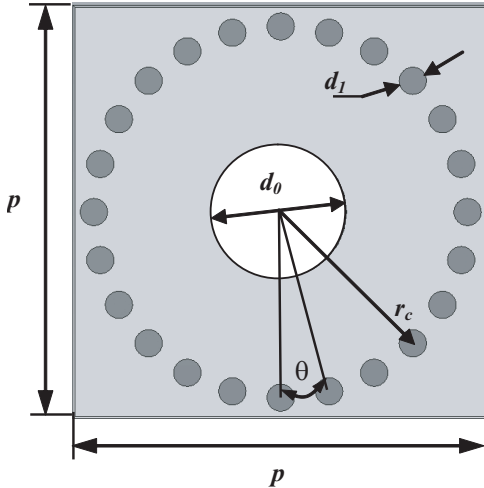


Figure 1: Geometrical configuration of the unit cell.

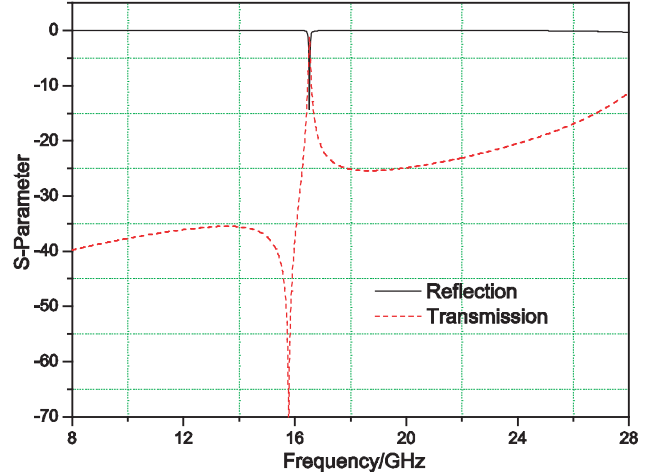


Figure 2: Simulated frequency response of the structure.

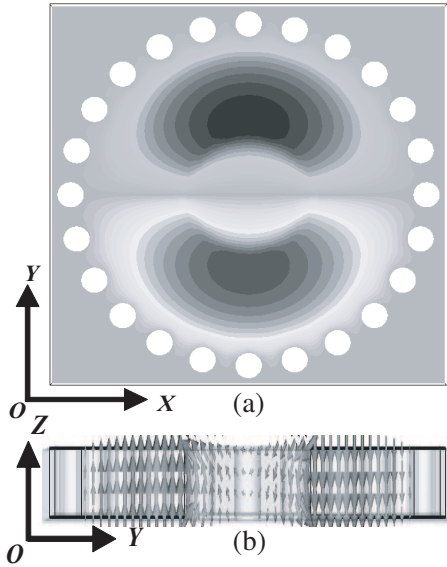


Figure 3: Electric field distribution diagrams of the cavity  $TM_{110}$  resonance in which the white blank corresponds to zero electric field and black corresponds to the strongest electric field. (a) Top view. (b) Side view.

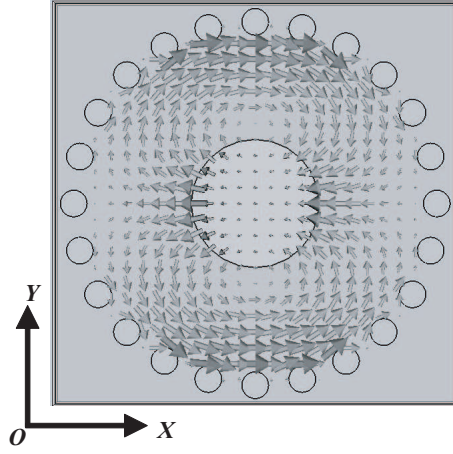


Figure 4: Magnetic field distribution diagrams of cavity  $TM_{110}$  resonance.

plotted in Fig. 3. The first resonance at 16.6 GHz corresponds to a cavity resonance introduced by the circular SIW cavity. The electric field component is mainly  $E_z$  and it is perpendicular to the incident plane as well as the incident field, as shown in Fig. 3(b). Fig. 4 gives the magnetic field distribution at 16.6 GHz under normal incidence. It can be found that the magnetic field at 16.6 GHz exhibits two vortex-like magnetic fields with opposite directions. So we can affirm that it is a  $TM_{110}$  cavity mode which is similar to that of a conventional circular cavity resonance.

The resonance frequency of  $TM_{110}$  cavity model can be approximately calculated by the following formula

$$f_{cav}^{TM_{110}} = \frac{K}{2\pi\sqrt{\epsilon_r\mu_0}} \cdot \frac{v_{11}}{(P \cdot b - Q \cdot a)} \quad (1)$$

where  $v_{11}$  represents the first root to the first-order Bessel function of the first class,  $P$  and  $Q$  are modifying factors that are dependent on the geometry of the FSS unit cell,  $K$  is a constant modifying factor.

For the circular resonant cavity  $TM_{110}$  mode,  $v_{11} = 3.832$ . The two modifying factor are taken

Table 1: Frequency of cavity resonance in SIW cavity ( $d_1 = 1$  mm,  $d_2 = 0.7$  mm).

$b$ (mm)	$a$ (mm)	$f_{cav}$ calculate by (1) (GHz)	$f_{cav}$ calculate by FEM (GHz)	error (%)
3.4	1.1	30.42	31.32	2.87
3.8	1.5	27.82	28.07	0.89
4.8	2.0	22.17	22.14	0.14
6.3	2.4	16.58	16.52	0.36
6.3	2.9	17.12	17.03	0.53
7.8	4.3	14.24	14.08	1.14
7.8	3.3	13.67	13.41	1.94
12.3	5.5	8.73	8.49	2.83
15.3	7.1	6.86	7.06	2.83
17.4	8.4	6.24	6.12	1.96

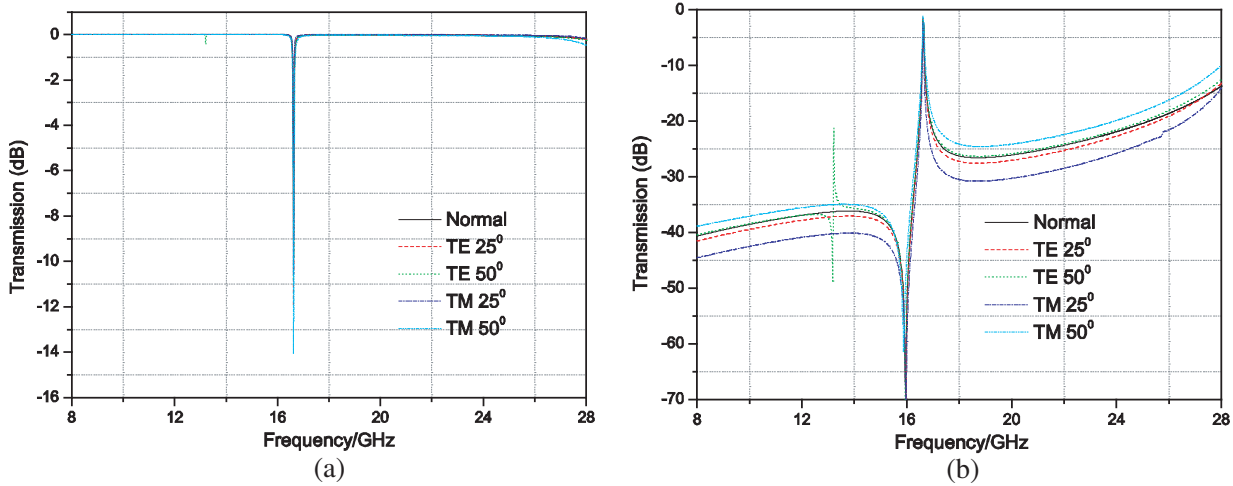


Figure 5: Frequency responses of the FSS with different polarizations and incident angles. (a) Reflection. (b) Transmission.

as  $P = 2.0$  and  $Q = 0.55$ . Because the dielectric part of the region 1 (the inner dielectric cylinder shown in Fig. 1) is removed, so we give  $K = 1.677$  to modify the resonance frequency.

Calculated results of the cavity resonant frequency by formula (1) and FEM method are given in Table 1. The discrepancy between these two methods is less than 3% over a frequency range from 5 to 32 GHz.

### 3. FSS WITH STABLE RESONANCE

As we know that, in practical applications, it is necessary that FSS provide stable performance under different incidence angles and polarizations. Usually, slot FSS based on SIW cavity are constructed to get two resonances and then the two resonances are adjusted so as to be close to each other. A transmission null is caused by the coupling effect of the two resonances. A rapid roll-off edge will be generated by this transmission null. So a higher selectivity than that of conventional slot array FSSs will be obtained at a wide frequency range [12]. Furthermore, multilayer and component FSS-SIW structures are cascaded to obtain quasi-elliptic band-pass response [13, 16].

Figure 5 gives the frequency responses under different incidence angles and polarizations. From Fig. 5 we can find that the resonance frequency of FSS is rather stable under oblique incidence angles from  $0^\circ$  to  $50^\circ$  for both  $TE$  and  $TM$  polarization. Although an additionally unexpected resonance appears under  $50^\circ$  oblique incidence of  $TE$  polarization, its transmission is still below  $-20$  dB, so this anomaly doesn't impact the FSS's performance at all. The central resonance frequency is at 16.6 GHz and the  $-0.5$  dB and  $-3$  dB bandwidth are 10 MHz, 51 MHz, respectively. The bandwidth ratio of different polarizations and different incident angles is very close to 1.0. In addition, even up to 28 GHz, there are no other resonance frequencies.

#### 4. CONCLUSION AND DISCUSSION

In this paper, we proposed a novel compact frequency selective surface with stable frequency-selective performances. The FSS-SIW was fully studied and an approximate formula was derived for the sake of calculating the frequency of the  $TM_{110}$  cavity resonance. The narrow pass-band FSS has advantages of high selectivity, quite stable performance and its thickness is less than  $\lambda/18$ . The presented FSS, by virtue of these advantages, provides practical applications to narrow-band communications, electronic countermeasures, etc.

#### ACKNOWLEDGMENT

This work was supported in part by the National Natural Science Foundation of China under Grant Nos. 50632030, 60871027 and 10804130 and in part by the 973 Project of Science and Technology Ministry of China under Grant No. 2009CB623306.

#### REFERENCES

1. Munk, B. A., *Frequency Selective Surfaces: Theory and Design*, Wiley, New York, 2000.
2. Wu, T. K., *Frequency Selective Surfaces and Grid Arrays*, Wiley, New York, 1995.
3. Luebbers, R. J. and B. A. Munk, "Some effects of dielectric loading on periodic slot arrays," *IEEE Trans. Antennas Propag.*, Vol. 26, No. 4, 536–542, July 1978.
4. Baena, J. D., L. Jelinek, R. Marqués, J. J. Mock, J. Gollub, and D. R. Smith, "Isotropic frequency selective surfaces made of cubic resonators," *Appl. Phys. Lett.*, Vol. 91, 191105, 2007.
5. Wakabayashi, H., M. Kominami, H. Kusaka, and H. Nakashima, "Numerical simulations for frequency-selective screens with complementary elements," *IEE Pro. — Micro. Antennas Propag.*, Vol. 141, No. 6, 477–482, 1994.
6. Lockyers, D. S., J. C. Vardaxoglou, and R. A. Simpkin, "Complementary frequency selective surfaces," *IEE Pro. — Micro. Antennas Propag.*, Vol. 147, No. 6, 501–507, 2000.
7. Marqués, R., J. D. Baena, M. Beruete, F. Falcone, T. Lopetegi, et al., "Ab initio an analysis of frequency selective surface based on conventional and complementary split ring resonators," *J. Opt. A: Pure Appl. Opt.*, Vol. 7, 538–543, 2005.
8. Hu, X.-D., X.-L. Zhou, L.-S. Wu, L. Zhou, and W.-Y. Yin, "A miniaturized dual-band frequency selective surface (FSS) with closed loop and its complementary pattern," *IEEE Antennas Wireless Propag. Lett.*, Vol. 8, 1374–1377, 2009.
9. Sarabandi, K. and N. Behdad, "A frequency selective surface with miniaturized elements," *IEEE Trans. Antennas Propag.*, Vol. 55, No. 5, 1239–1245, 2007.
10. Parker, E. A., J.-B. Robertson, B. Sanz-Izquierdo, and J. C. Batchelor, "Minimal size FSS for long wavelength operation," *Electron. Lett.*, Vol. 44, No. 6, 2008.
11. Liu, H., K. L. Ford, and R. J. Langley, "Miniaturized bandpass frequency selective surface with lumped components," *Electron. Lett.*, Vol. 44, No. 18, 2008.
12. Luo, G. Q., W. Hong, Z. C. Hao, B. Liu, W. D. Li, et al., "Theory and experiment of novel frequency selective surface based on substrate integrated waveguide technology," *IEEE Trans. Antennas Propag.*, Vol. 53, No. 12, 4035–4043, Dec. 2005.
13. Luo, G. Q., W. Hong, Q. H. Lai, K. Wu, and L. L. Sun, "Design and experimental verification of compact frequency-selective surface with quasi-elliptic bandpass response," *IEEE Trans. Micro. Theory Tech.*, Vol. 55, No. 12, 2481–2487, 2007.
14. Luo, G. Q., W. Hong, H. J. Tang, J. X. Chen, et al., "Filtenna consisting of horn antenna and substrate integrated waveguide cavity FSS," *IEEE Trans. Antennas Propag.*, Vol. 55, No. 1, 92–98, Jan. 2007.
15. Luo, G. Q., W. Hong, H. J. Tang, J. X. Chen, and L. L. Sun, "Triband frequency selective with periodic cell perturbation," *IEEE Microw. Wireless Compon. Lett.*, Vol. 17, No. 6, 2007.
16. Yang, H.-Y., S.-X. Gong, P.-F. Zhang, and Y. Guan, "Compound frequency selective surface with quasi-elliptic bandpass response," *Electron. Lett.*, Vol. 45, No. 1, 2010.

# Wave Transformers Based on Transformation Optics Theory

Xin-Hua Wang<sup>1</sup>, Shao-Bo Qu<sup>1,2</sup>, Zhuo Xu<sup>2</sup>, Hua Ma<sup>1</sup>, Jia-Fu Wang<sup>1</sup>,  
Lei Lu<sup>1</sup>, Hang Zhou<sup>1</sup>, Fei Yu<sup>1</sup>, and Yuqing Li<sup>1</sup>

<sup>1</sup>College of Science, Air Force Engineering University, Xi'an 710051, China

<sup>2</sup>Electronic Materials Research Laboratory, Key Laboratory of Ministry of Education  
Xi'an Jiao-Tong University, Xi'an 710049, China

**Abstract**— Transformation optics theory offers a revolutionary way of designing new functional devices. In this paper, the Laplace equations plus Dirichlet boundary conditions are used to obtain the material parameter tensors of the transformation medium. Wave shape transformer, wave splitter and wave synthesizer were designed using this method. Full wave simulations based on the finite element method verified this method. These new functional devices are more favorable than the traditional ones because of their low loss and high transmission efficiency.

## 1. INTRODUCTION

Transformation optics theory [1] gives a revolutionary technique to manipulate the propagation of the electromagnetic wave (EMW). On the basis of the transformation optics theory, Pendry et al. [2] proposed the coordinate transformation method to realize the invisible cloaks. The EMW can be guided around the objects inside invisible cloaks and then return to its original trajectory. The coordinate transformation theory is mainly based on the form-invariance [3] of Maxwell equations during the coordinate transformation. The cloaking effects were verified by full wave simulations [4]. By means of metamaterials design, the cloaking effects were demonstrated at microwave frequency by experiments [5].

By applying the coordinate transformation method, an omni-directional EMW concentrator [3] was proposed, by which EMW was concentrated in the inner region of the concentrator. Chen et al. [6] introduced the rotational coordinate transformation method by transforming the permittivity and permeability of a shell surrounding an enclosed domain. Inside the enclosed domain, the EMW from the outside will appear as if it was coming from a different angle. Cummer et al. [7] proposed the acoustic cloaks by comparing the acoustic equations with Maxwell equations. By applying finite embedded coordinate transformations, adaptive beam bends with arbitrary bend and beam splitters with arbitrary split angles [8] were designed. Anti-cloak [9] was proposed to partially defeat the cloaking effect of the invisible cloak. All the above-mentioned new functional devices are obtained from the coordinate transformation method, so we call them “transformation media.” Such media have some good properties, such as low reflection and good impedance matching. These properties make the transformation medium superior to traditional devices.

Based on the transformation optics theory and the coordinate transformation method [10–13], we designed wave shape transformer, wave splitter and wave synthesizer in this paper. The wave shape transformer can change the EMW's shapes, for example, plane waves to convex waves or concave waves. It can also change the cylindrical waves into plane waves. The wave splitter can divide one plane wave beam into two or three plane wave beams. In contrast, the wave synthesizer can combine two or three plane wave beams into one plane wave beam. In the following sections, we will introduce the design process for such transformation media.

## 2. DESIGN METHODS

For the sake of simplicity, here we just discuss the two-dimensional (2-D) cases which can be easily extended to the three-dimensional (3-D) ones. Consider a two-dimensional (2D) rectangle structure *ABCDE* in the flat space, as shown in Fig. 1. After a finite embedded coordinate transformation [11], the rectangle structure *ABCDE* in the flat space is transformed to a complicated structure *ABCDEFGHI* in the distorted space.

This transformation process is a kind of general embedded coordinate transformation and the transformed structure is very complicated. Here we use the Laplace equation [10] with the corresponding boundary conditions to solve the components of the Jacobian transformation matrix. According to Ref. [10], the inverse form of the Laplace's equations is

$$\left( \frac{\partial^2}{\partial x_1'^2} + \frac{\partial^2}{\partial x_2'^2} + \frac{\partial^2}{\partial x_3'^2} \right) U_i = 0, \quad i = 1, 2, 3 \quad (1)$$

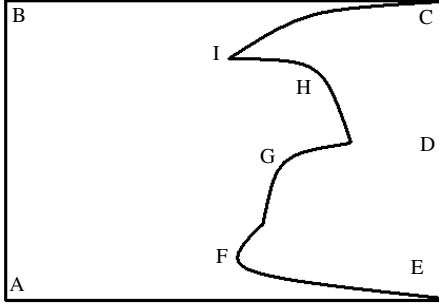


Figure 1: Schematic illustration of constructing wave transformers.

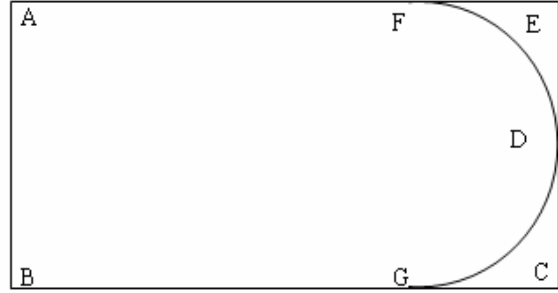


Figure 2: Schematic illustration of the transformation process for the plane wave to convex cylindrical wave.

where  $U_i$  denotes the original coordinates in the original flat space. The corresponding Dirichlet boundary conditions then become  $U(ABCIGHFED) = U(ABCDE)$ . This boundary condition is equivalent to compressing the rectangle  $ABCDE$  to the complicated structure  $ABCIGHFED$ . By solving Eq. (1) plus its boundary conditions, we can obtain  $\lambda_i(i = 1, 2, 3)$ , where  $\lambda_i$  is the eigenvalues of the tensor  $V$  and  $V^2 = AA^T$  ( $A$  is the Jacobian transformation matrix). Thus, we can obtain  $\det A = \lambda_1\lambda_2\lambda_3$ . The material parameter tensors of the transformation media can be solved by

$$\varepsilon' = \varepsilon_0 \text{diag} \left[ \frac{\lambda_1}{\lambda_2\lambda_3}, \frac{\lambda_2}{\lambda_3\lambda_1}, \frac{\lambda_3}{\lambda_1\lambda_2} \right] \quad (2)$$

$$\mu' = \mu_0 \text{diag} \left[ \frac{\lambda_1}{\lambda_2\lambda_3}, \frac{\lambda_2}{\lambda_3\lambda_1}, \frac{\lambda_3}{\lambda_1\lambda_2} \right] \quad (3)$$

This design process falls into two steps. The first step is to solve the Laplace equation with the corresponding boundary conditions in order to obtain the eigenvalues  $\lambda_1, \lambda_2, \lambda_3$ . The second step is to obtain the material parameter tensors of the transformation media.

### 3. WAVE SHAPE TRANSFORMER

Based on Laplace equation [10] to solve the material parameter tensors of the transformation medium, we can design, for example, the wave shape transformers transforming the plane wave to convex cylindrical wave or to the concave cylindrical wave.

The transformation process from the plane wave to the convex cylindrical wave is illustrated in Fig. 2. The rectangle structure  $ABCDE$  is compressed into the complicated structure  $ABGDF$ . The Laplace equation plus the corresponding boundary conditions can describe this transformation process.

Comsol Multiphysics was used to design the wave shape transformer. As mentioned above, the design process falls into two steps. The first step is to solve the Laplace equation with the boundary conditions to obtain the material parameter tensors of the wave transformer. The other step is to design the wave shape transformer. The PDE Module is used to obtain the material parameter tensors firstly and the RF Module is used in the second step.

In the computation domain, all the outer boundary conditions are set as the scattering boundary conditions except one input port while all the inner boundary conditions are continuity boundary conditions. A plane wave is incident on the transformation medium. The simulation results are shown in Fig. 3. As shown in Fig. 3, the plane wave is transformed into the convex cylindrical wave after passing through the transformation medium. After the transformation, EMW radiates into the free space just as a cylindrical wave does. Moreover, just after the transformation medium, the magnitude of transformed cylindrical wave is equal to that of the original plane wave, which indicates low loss during the transformation. These properties are valuable in practical uses.

Similarly, this transformation process can also change the plane wave to a concave cylindrical wave and vice versa. The corresponding simulation results are shown in Fig. 4. From the left panel of Fig. 4, the plane wave is transformed into the concave cylindrical wave after the transformation medium just as if there was a concave mirror. The concave wave focuses firstly and then radiates into

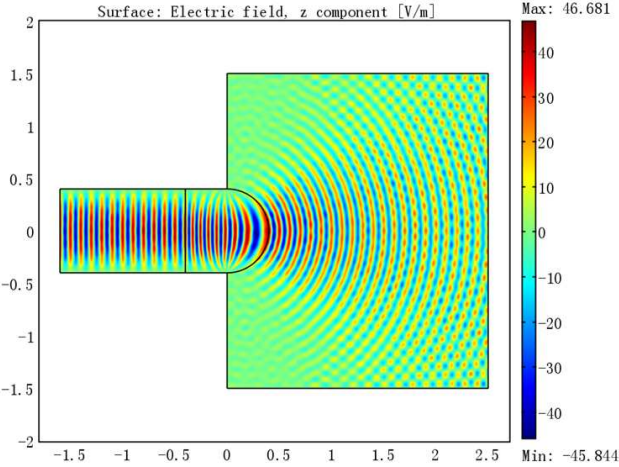


Figure 3: Electric field distributions for the plane-to-concave-cylinder wave transformer.

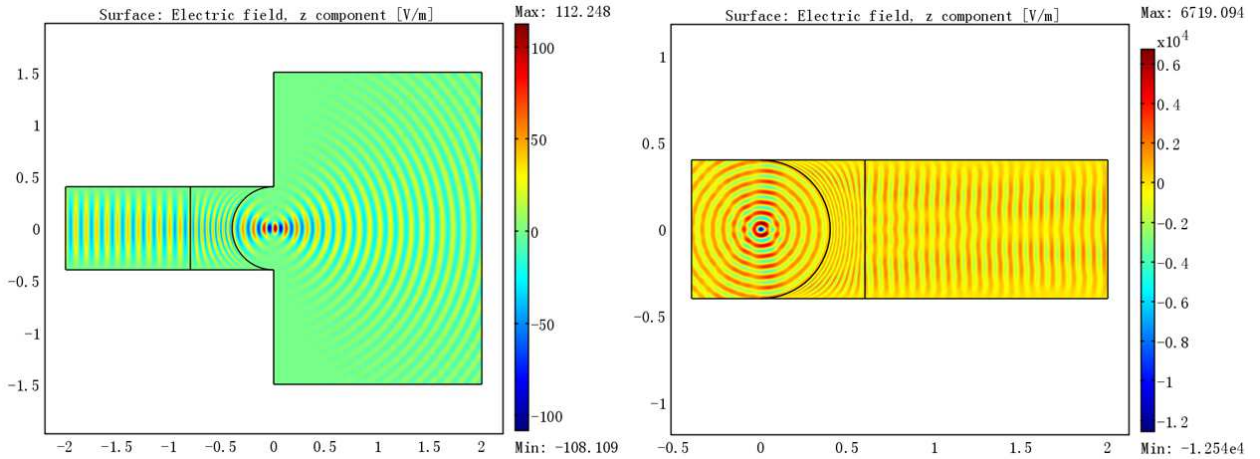


Figure 4: Electric field distributions for (left) plane-to-convex-cylinder wave transformer and (right) cylinder-to-plane wave transformer.

the free space. The right panel of Fig. 4 illustrates the inverse process of the left one. The cylindrical wave is transformed into a plane wave after the transformation medium. This transformation is similar to the Ref. [14]. But our method is easier than the one in Ref. [14]. The material parameter tensors are obtained by solving the Laplace equation and this process can be accomplished by programming.

#### 4. WAVE SPLITTER AND SYNTHESIZER

The transformation process for wave splitter is illustrated in Fig. 5. The rectangle structure  $ABCD$  is compressed into the polygon structure  $ABEFGH$ . By this transformation, a plane wave beam can be transformed into three plane wave beams.

As discussed in the above section, the transformation process can be described by the Laplace equation with the corresponding Dirichlet boundary condition. By solving the above equations, we can obtain the material parameter tensors of the transformation medium easily. A commercial software Comsol Multiphysics is used to design the wave splitter. Here, we take three-output-wave-splitter as an example. By this design, a plane wave beam can be divided into three wave beams, as shown in Fig. 6.

From Fig. 6, a plane wave is split into three wave beams after the transformation medium. The amplitude of the wave does not change after the transformation. This means that the loss of the transformation medium is low. Using the same design idea, we can also design other wave splitters, such as one-to-two and one-to-four wave splitters. Conversely, the method for the wave

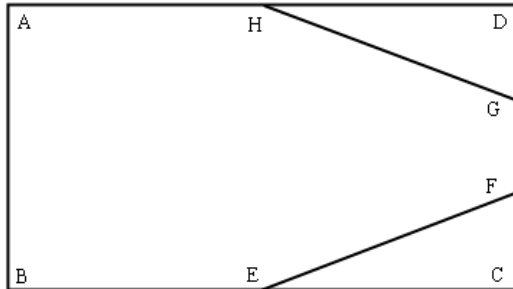


Figure 5: Schematic illustration of the wave splitter transformation.

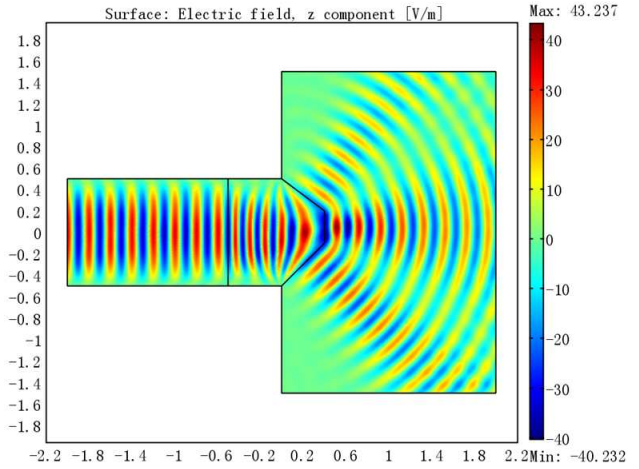


Figure 6: Electric field distribution for one-to-three wave splitter.

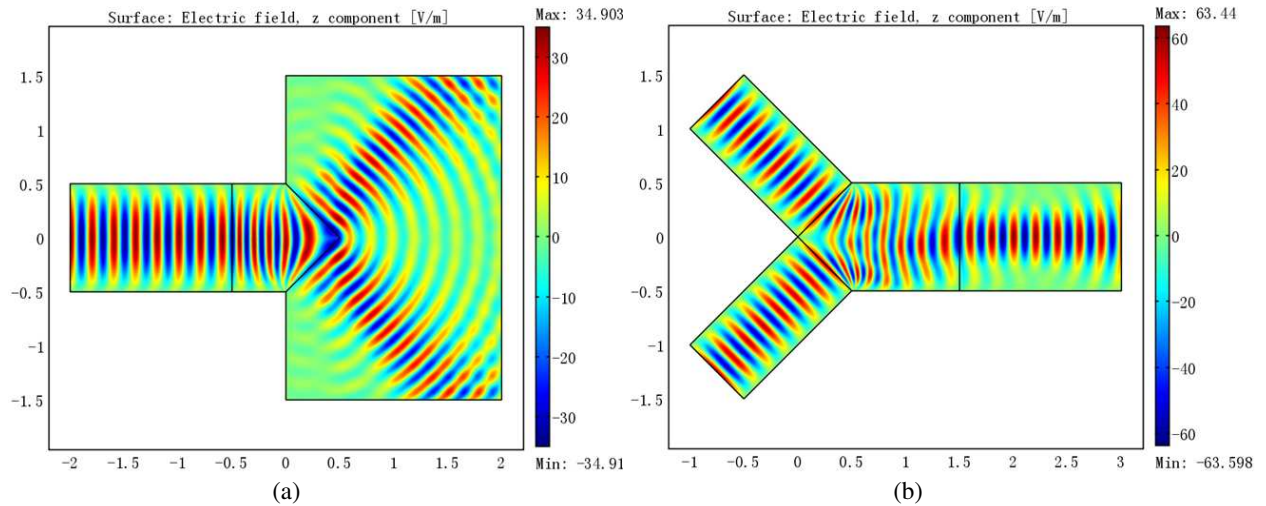


Figure 7: The electric field distribution for (a) one-to-two wave splitter, (b) two-to-one wave synthesizer.

splitter can also be used in designing wave synthesizers. Fig. 7 gives the simulation results for wave synthesizers.

In the left panel of Fig. 7, a plane wave beam is split into two plane wave beams. While in the right panel, two plane wave beams are combined into one plane wave beam after the wave synthesizer. Both devices are useful in the microwave range, especially in the design of waveguides.

## 5. CONCLUSIONS

In this paper, we proposed to obtain the material parameter tensors of the transformation medium by solving the Laplace equation plus its Dirichlet boundary conditions. By applying this method, wave shape transformer, wave splitter and wave synthesizer were designed. The wave shape transformer can transform plane waves into convex cylindrical waves or concave cylindrical waves. Besides, cylindrical waves can also be transformed into plane waves. The wave splitter can split one plane wave beam into two or three plane wave beams. Conversely, the wave synthesizer can combine two plane wave beams into one. Compared with the traditional devices, these transformation devices are of high transmission efficiency and low loss. These properties are valuable in the practice uses.

## ACKNOWLEDGMENT

Project supported partly by the National Natural Science Foundation of China (Grant Nos. 50632030, 10474077, and 60871027), partly by the 973-Project of the Ministry of Science and Technology of

China (Grant No. 2009 CB613306), and partly by the Natural Science Foundation of Shaanxi Province (Grant No. SJ08F01).

## REFERENCES

1. Leonhardt, U., *Science*, Vol. 312, 1777–1780, 2006.
2. Pendry, J. B., D. Schurig, and D. R. Smith, *Science*, Vol. 312, 1780–1782, 2006.
3. Rahm, M., D. Schurig, D. A. Roberts, S. A. Cummer, and D. R. Smith, *Photon. Nanostruc. Fundam. Appl.*, Vol. 6, 87–95, 2008.
4. Cummer, S. A., B.-I. Popa, D. Schurig, D. R. Smith, and J. B. Pendry, *Phys. Rev. E*, Vol. 74, 036621, 2006.
5. Schurig, D., J. J. Mock, B. J. Justice, S. A. Cummer, J. B. Pendry, A. F. Starr, and D. R. Smith, *Science*, Vol. 314, 977–980, 2006.
6. Chen, H. Y. and C. T. Chan, *Applied Physics Letters*, Vol. 90, 241105, 2007.
7. Cummer, S. A. and D. Schurig, *New Journal of Physics*, Vol. 9, 45, 2007.
8. Rahm, M., D. A. Roberts, J. B. Pendry, and D. R. Smith, *Optics Express*, Vol. 16, 11555, 2008.
9. Chan, C. T., *Optics Express*, Vol. 16, 14603, 2008.
10. Hu, J., X. M. Zhou, and G. K. Hu, *Optics Express*, Vol. 17, 1308, 2009.
11. Rahm, M., S. A. Cummer, D. Schurig, J. B. Pendry, and D. R. Smith, *PRL*, Vol. 100, 063903, 2008.
12. Ma, H., S.-B. Qu, J.-F. Wang, Z. Xu, and J.-Q. Zhang, *Chinese Physics B*, Vol. 18, 1850, 2009.
13. Ma, H., S.-B. Qu, J.-F. Wang, Z. Xu, and J.-Q. Zhang, *Chinese Physics B*, Vol. 18, 179, 2009.
14. Jiang, W. X., T. J. Cui, H. F. Ma, X. Y. Zhou, and Q. Cheng, *Applied Physics Letters*, Vol. 92, 261903, 2008.

# Hybrid Electromagnetic Cloaks Mediated by Surface Plasmons: Nonperfect but Practical

Shaobo Qu<sup>1, 2</sup>, Jiafu Wang<sup>1</sup>, Baiyu Yang<sup>1</sup>, Hua Ma<sup>1, 2</sup>, Zhuo Xu<sup>2</sup>, and Song Xia<sup>2</sup>

<sup>1</sup>College of Science, Air Force Engineering University

Xi'an, Shaanxi 710051, China

<sup>2</sup>Electronic Materials Research Laboratory

Xi'an Jiaotong University, Xi'an, Shaanxi 710049, China

**Abstract**— We demonstrated, for the first time ever, a practical hybrid electromagnetic cloak that works effectively under both TE and TM polarizations. To realize such a cloak, a TE cloak and a TM cloak were firstly designed to work at the same frequency. By combining the two cloaks, a hybrid cloak was realized. Different from the transformation-based cloaks, the proposed cloaks are based on the highly surface-confined property of surface plasmons. The cloaking performance of such cloaks is nonperfect. However, such cloaks can be made very thin and moreover are much easier to be realized in practice. Both simulations and experiments verified our design.

## 1. INTRODUCTION

Electromagnetic cloak, which can render a scatter invisible to incident waves, has attracted great attention from the academic world since the first experimental verification at microwave frequency by Smith et al. [1]. Since less-than-1 permeability or permittivity is required, metamaterials are indispensable in implementing such cloaks. By delicately designing the distribution of constitutive parameters of the cloak, perfect invisibility can be realized at a single frequency using the coordinate transformation theory based on the form-invariance of Maxwell's equations [2, 3].

The potent perfect invisibility is a highly desirable performance in many fields such as stealth, un-invasive detection, solar energy harvesting, it is indeed rather a difficult work to realize such cloaks in practice. Three main problems limit the development of EM cloak applications: loss, bandwidth and thickness. Because most metamaterials are realized by resonant structures, the loss is considerable while the bandwidth is rather narrow. Plus the multi-layer parameter matching requirement of adjacent layers, the transformation-based cloaks can only realize single-frequency invisibility theoretically. Gradually varying constitutive parameters of cloaks means multi-layer arrangement and thus means large thickness. To solve the three problems, many schemes have been proposed [4–8], such as plasmonic cloaks, transmission line cloaks. The above-mentioned cloaks either work under TE- or TM-polarized incident waves. While, there is no cloak that can operate both under TE- and TM-polarized waves simultaneously.

In this paper, we reported a thin hybrid EM cloak that can work simultaneously both under TE and TM polarizations. This cloak is based on the surface confinement and surface propagation of surface plasmon polariton (SPP). The strong surface confinement guarantees thin thickness while the surface propagation makes the round-object transmission. A TE cloak and a TM cloak were firstly designed to work under the same frequency, and then the two cloaks were combined to construct the hybrid cloak. Both the simulation and experiment verified the cloaking effect of this hybrid cloak.

## 2. DESIGN AND SIMULATIONS

The designed TE cloak is shown in Figure 1. To couple incident TE-polarized waves into SPPs on the cloak surface, copper strips are arranged periodically along the cylinder axis direction with a periodicity  $h = 12.5$  mm. The strip width is  $h_1 = 11.2$  mm and its thickness is 0.02 mm. The substrate is Rogers 5880, with a thickness  $t = 0.787$  mm and dielectric constant  $\epsilon_r = 2.2$ .

Figure 2 gives the comparison between the simulated electric field distributions with and without the cloak at 8.6 GHz on  $(x, y)$  plane (Figures 2(a) and (b)), as well as the comparison between the power flows with and without the cloak (Figures 2(c) and (d)). As shown in Figure 2, with the cloak, incident waves are coupled into surface mode with strong field intensity around the copper cylinder. This enables EM waves to travel around the copper cylinder so as to arrive at the back region of the copper cylinder, as shown in Figure 2(c). Note since SPP waves are slow waves, there phase fronts in the near field zone behind the copper cylinder is a bit distorted. Nevertheless, after they travel in the far-field zone, the phase fronts restore themselves.

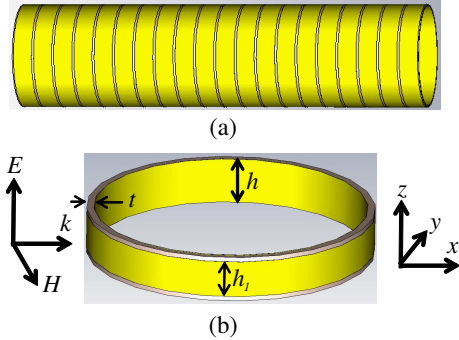


Figure 1: The designed (a) TE cloak and (b) its unit cell.

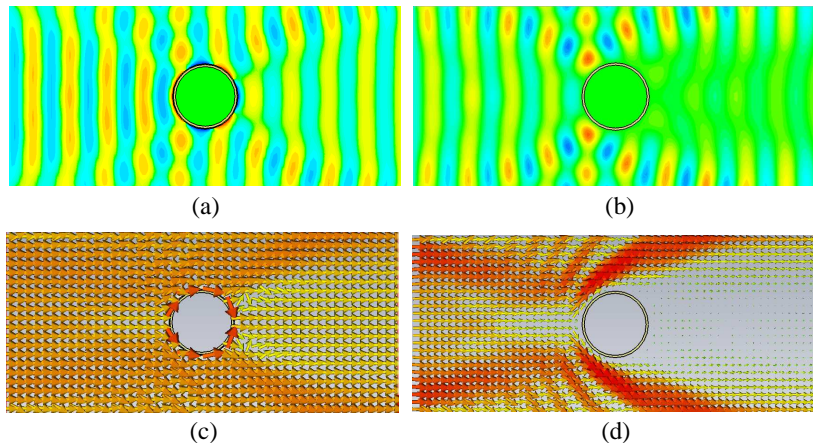
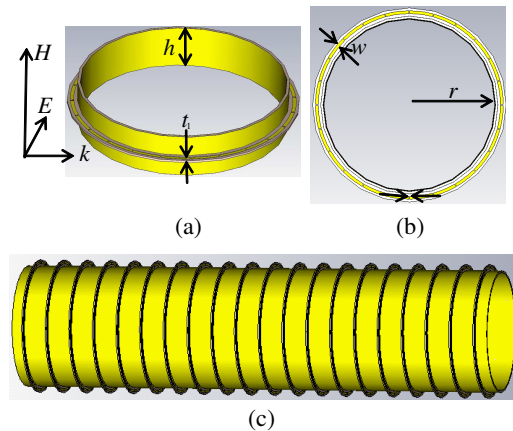
Figure 2: Simulation results: electric field distribution on  $(x, y)$  plane for a copper cylinder (a) with and (b) without the TE cloak at 8.6 GHz; (c) and (d) give, respectively the power flow with and without the cloak at 8.6 GHz.

Figure 3: TM cloak: (a) the unit cell, (b) top view of the unit cell, (c) TM cloak structure

Figure 3 shows the designed TM cloak. To achieve the cloaking effect under TM polarization, circular rings with  $n = 24$  metallic arcs on both sides are arranged periodically along the cylinder axis direction with a periodicity  $h = 12.5$  mm. The gap between each two adjacent metallic arcs is  $s = 0.3$  mm. Strip width of the metallic arc is  $w = 1$  mm. The circular ring uses a substrate with a dielectric constant of  $\epsilon_r = 2.65$  and a thickness of  $t_1 = 1$  mm.

Figure 4 presents the comparison between simulated electric field distributions with and without the TM cloak on  $(x, y)$  plane at 8.6 GHz (Figures 4(a) and (b), respectively), and the power flow

comparison (Figures 4(c) and (d), respectively). By such a comparison, quite good cloaking can be observed in Figures 4(a) and (c). By combining the designed TE and TM cloaks, a hybrid cloak can be implemented, as shown in Figure 5.

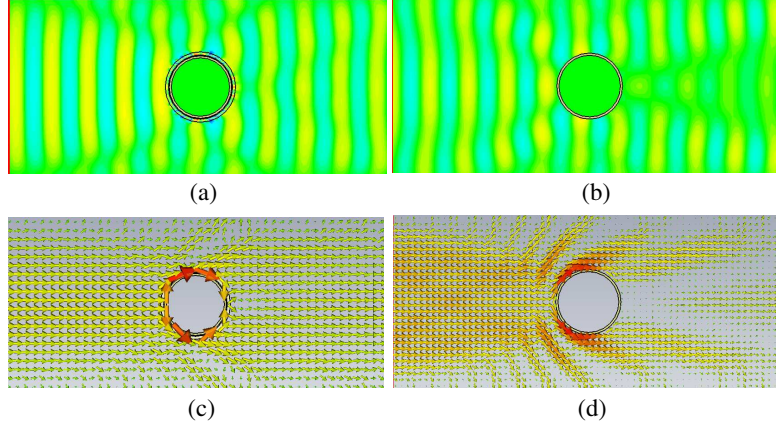


Figure 4: Simulation results of the TM cloak at 8.6 GHz: (a) and (b) show the electric field distribution on ( $x, y$ ) plane for a copper cylinder with and without the TM cloak, respectively; (c) and (d) give the power flow with and without the TM cloak, respectively.

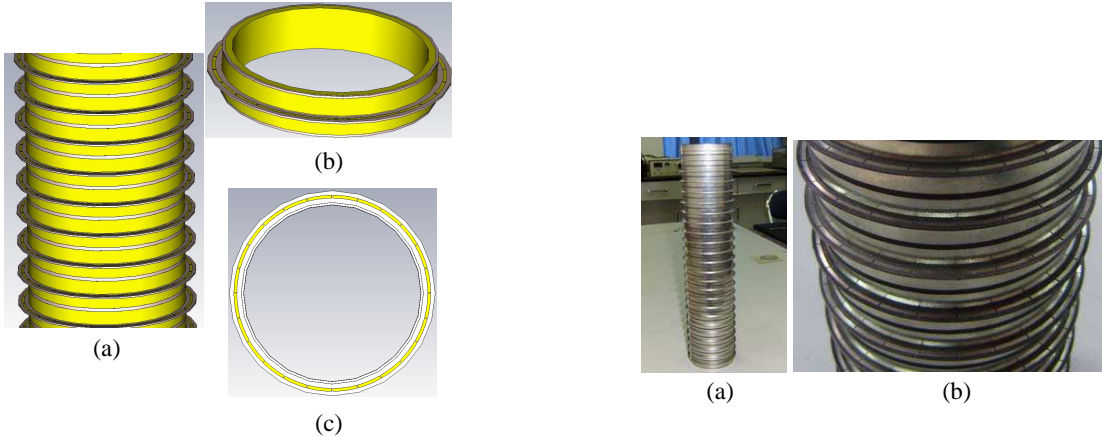


Figure 5: Structure of the hybrid cloak and its unit cell: (a) the hybrid cloak; (b) perspective view of the unit cell; (c) top view of the unit cell.

Figure 6: The fabricated sample.

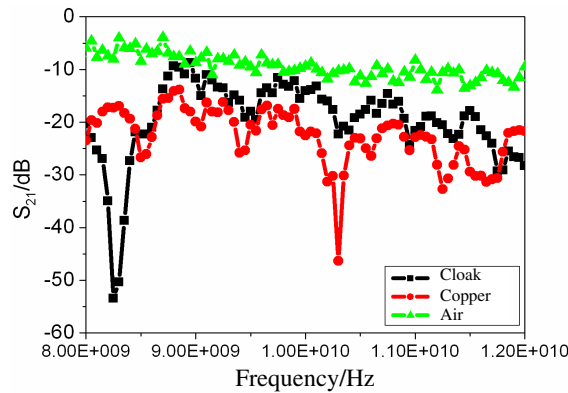
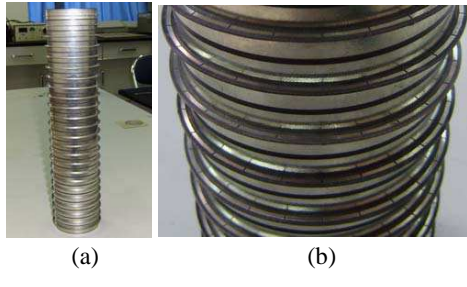


Figure 7: Measured transmission comparison under the same experiment setup.

### 3. FABRICATION AND EXPERIMENT

The designed hybrid cloak was fabricated using the conventional printed circuit board technique. Copper strips were firstly etched on Rogers 5880 substrate. The substrate was rolled up to form a cylinder. Then, the circular rings were put around the cylinder to realize TM cloaking and meanwhile to fix the cylinder, as shown in Figure 6.

The sample was measured using the free space measuring system which consists of two rectangular horn antennas and vector network analyzer. Figure 7 gives the comparison of measured transmission of the cloak, bare copper cylinder and air under the same experiment setup. As shown in Figure 7, the transmission is approximately the same as that in air around 8.7 GHz. This convincingly demonstrates the transparency of the hybrid cloak.

### 4. CONCLUSIONS

In this paper, we reported a thin hybrid EM cloak that can operate simultaneously under TE and TM illumination. The underlying mechanism lies in the excitation of SPPs on the surface of this cloak. The surface confinement of SPP allows the cloak to be thin while the surface propagation property of SPP makes the round-the-object transmission. Both simulation and experiment results verified the cloaking effect of this cloak.

### ACKNOWLEDGMENT

This work is supported in part by the National Natural Science Foundation of China under Grants No. 50632030, 10804130, 60871027 and 61071058 and in part by the 973 Project of Science and Technology Ministry of China under Grant No.2009CB613306.

### REFERENCES

1. Schurig, D., J. J. Mock, B. J. Justice, S. A. Cummer, J. B. Pendry, A. F. Starr, and D. R. Smith, *Science*, Vol. 314, 977, 2006.
2. Pendry, J. B., D. Schurig, and D. R. Smith, *Science*, Vol. 312, 1780, 2006.
3. Ma, H., S. B. Qu, Z. Xu, and J. F. Wang, *Phys. Rev. E*, Vol. 78, 036608, 2008.
4. Ma, H., S. B. Qu, Z. Xu, and J. F. Wang, *Appl. Phys. Lett.*, Vol. 94, 103501, 2009.
5. Wang, X. H., S. B. Qu, S. Xia, B. K. Wang, Z. Xu, H. Ma, J. F. Wang, C. Gu, X. Wu, L. Lu, and H. Zhou, *Photon. Nanostruc. Fundam. Appl.*, Vol. 8, 205, 2010.
6. Chen, H. Y., Z. X. Liang, P. J. Yao, X. Y. Jiang, H. R. Ma, and C. T. Chan, *Phys. Rev. B*, Vol. 76, 241104(R), 2007.
7. Alù, A. and N. Engheta, *Phys. Rev. E*, Vol. 72, 016623, 2005.
8. Tretyakov, P. Alitalo, O. Luukkonen, and C. Simovski, *Phys. Rev. Lett.*, Vol. 103, 103905, 2009.

# Tunable Dual-band Filter Based on Photonic Crystals Doped by Unmagnetized Plasma

Xiang-Kun Kong<sup>1,2</sup>, Shao-Bin Liu<sup>1</sup>, Ping Wang<sup>1</sup>, Xin Li<sup>1</sup>, and Li Liu<sup>1</sup>

<sup>1</sup>College of Electronic and Information Engineering, Nanjing University of Aeronautics and Astronautics  
Nanjing 210016, China

<sup>2</sup>Department of Physics, Zhenjiang Watercraft College, Zhenjiang 212003, China

**Abstract**— A novel tunable dual-band filter from one-dimensional photonic crystals doped by unmagnetized plasma is analyzed. Two defective PCs composed by ZnSe and Na<sub>3</sub>AlF<sub>6</sub> with one defect layer made by unmagnetized plasma stacked in symmetric geometry are considered. By the transfer matrix method and Bloch's theorem, it is found that the frequency of the defect modes can be modulated by plasma frequency and defect thickness. Without changing the structure of the photonic crystal, the defect modes can be modulated in a larger frequency range. These results may provide theoretical instructions for designing new optoelectronic devices.

## 1. INTRODUCTION

Photonic crystals (PCs) have been the object of intensive studies in the last decade due to their unique electromagnetic properties and potential applications [1, 2]. It has been proven that a photonic band gap (PBG) could be formed as a result of the interference of Bragg scattering in a periodical dielectric structure [3, 4]. And the periodicity is broken when introducing a defect into a conventional PC, a localized defect mode can be seen inside the Bragg gap owing to the change of the interference behavior of electromagnetic wave (EM wave). This characteristic can be used to design PC waveguides [5], low-threshold lasers [6], filters [7], etc.

It is noted that this active research area has been extended to plasma photonic crystal (PPC), which contains more particular characteristics than the conventional PCs. Plasma is a kind of dispersive medium with its equivalent refractive index related to the frequency of an incident electromagnetic wave. At the same time, plasma is combined with dielectric material to form PPCs. The dispersion or the transmission properties of one-dimensional PPC (1DPPC) have been studied. Hojo and Mase [8] first considered the dispersion relation of the EM waves in the 1DPPCs, and found that its band gap becomes larger with increasing of the plasma density and thickness. Li et al. [9] analyzed the characteristic of EM wave propagation in the PPCs, and found the PPCs feature the structure of photonic energy band and energy gap. Liu et al. [10, 11] adopted finite-difference time-domain (FDTD) method to study the propagation process with Gauss pulses passing in the unmagnetized and magnetized PPCs. In time-domain, the reflection and transmission electric field of EM waves have been investigated. In frequency-domain, the reflection and transmission coefficients of the pulses through the two kinds of crystals have been computed. Furthermore, Wang [12] and Kong [13] et al. are respectively investigated one dimensional photonic crystal doped by unmagnetized plasma and magnetized plasma. Anomalous dispersion, omnidirectional gap and the effect of random variations of structure parameters of 1DPPC are also discussed [14–16].

In this paper, we theoretically tend to investigate the dependence of the unmagnetized plasma defect mode of the 1DPCs on the plasma parameters. According to the results of the transfer matrix method, in contrast to normal defect mode, the two defect modes caused by one defect layer in this paper can be modulated in a wider frequency range by changing plasma frequency and width without altering the structure of the PCs.

## 2. THE MODEL AND COMPUTATION

In order to acquire a tunable double-band filter, according to reference [16] and [17], consider periodic structure in the 1DPC with  $A/(HL)^N D(LH)^N/A$ , where  $A$  means the usual air,  $H$  and  $L$  respectively represent two kinds of material layers, and  $N$  is the number of periods. The defect layer  $D$ , which generates defect modes inside the photonic band gaps, is the unmagnetized plasma material. Its relative permittivity is a complex number varying with the plasma density or the thickness, as shown in Equation (1)

$$\varepsilon(\omega) = 1 - \frac{\omega_{pe}^2}{\omega(\omega - i\nu)}, \quad (1)$$

The thicknesses of layers  $H$ ,  $L$  and  $D$  are assumed to be  $d_H$ ,  $d_L$  and  $d_D$ , respectively. All the electromagnetic wave (EM wave) is normally incident on the 1DPC.

The transmittance of the finite structure  $A/(HL)^5D(LH)^5/A$  with different plasma frequency and plasma width are calculated through the transfer matrix method. In this paper, only the TE wave is considered. It is noted that the width of photonic band gap is intensively affected by the ratio of permittivity for two dielectric layers in one period. In order to design a photonic crystal with a wide band gap and a tunable defect mode in a wider frequency range, we choose the structure parameters as the follows:  $\varepsilon_H = 6.65(n_H = 2.58)$ ,  $\mu_H = 1$ ,  $d_H = 0.0145$  m,  $\varepsilon_L = 1.82(n_L = 1.35)$ ,  $\mu_L = 1$  and  $d_L = 0.0272$  m. Layers  $H$  and  $L$  refer to ZnSe and Na<sub>3</sub>AlF<sub>6</sub>, respectively. For EM waves with the basic frequency  $f_0 = c/2(n_H d_H + n_L d_L) = 2$  GHz or wavelength  $\lambda_0 = 2(n_H d_H + n_L d_L) = 0.15$  m,  $n_H d_H = n_L d_L = \lambda_0/4$  and the PC structure without defects can be considered a quarter-wave stack.

In the next paper, we will investigate how the defect modes varies with plasma frequency and plasma width amid the fixed structure of 1DPC.

## 2.1. Influence of Plasma Frequency

Here we only focus on the first band gap around 2 GHz, which the parameters are  $\gamma = 10$  MHz, and  $d_D = 1/4\lambda_0 = 0.0375$  m. If the plasma frequency  $\omega_e$  equals zero, the defect layer corresponds to the air layer. For the condition of  $\varepsilon_D = 1$ ,  $\mu_D = 1$  and  $d_D = 0.0375$  m ( $1/4\lambda_0$ ), the defect mode presents itself at the basic frequency  $f_0 = 2$  GHz. Figure 1 and 2 are shown the transmittance of the finite structure  $A/(HL)^5D(LH)^5/A$  for different plasma frequency  $\omega_{pe}$ , in which solid, dashed and dotted lines denote 0,  $2\pi \times 0.8 \times 10^9$  s<sup>-1</sup> and  $2\pi \times 1.6 \times 10^9$  s<sup>-1</sup>, for different  $\omega_{pe}$ , respectively, the frequency of the defect mode rises (from  $f = f_0$ ) with the increase of plasma frequency. According to Equation (1), with the increase of plasma frequency, the refractive index of defect layer decreases. As a result of decreased optical width of defect layer, the resonant wavelength shortens and the resonant EM wave frequency rises. In this case, there are two defect modes, as indicated by the two resonant peaks 1 and 2 within the PBG. The presence of two defect modes can be ascribed to the structural reflection symmetry [17].

It is clear in Fig. 2 that, as the plasma frequency swells from 0 to  $2.6 \times 10^9$  GHz, the two defected modes inside photonic band gap changes swiftly into the higher EM wave frequency. Obviously, the first resonant peak changes faster from 1.70 GHz to 2.15 GHz, while the second resonant peak changes from 2.29 GHz to 2.37 GHz. However, the peak height for the first peak decreases from 1 to 0.35 as the plasma frequency changes.

Figure 3 shows the electric field amplitude distribution for different frequency waves when  $\omega_{pe} = 2\pi \times 0.8$  s<sup>-1</sup>. This feature of symmetry gives rise to two possible field solutions in the defect layer at resonance. One solution proportional to cosine function belongs to an even symmetry which corresponds to the lower energy state, as marked by 1. The other proportional to sine function is an odd symmetry and is indicated by 1. If we choose the EM wave frequency in the PBG range, for example,  $f_p = 1.76$  GHz, the field amplitude and energy distribution decreases to zero. It is noted that from Fig. 4 the electric energy mainly locate at the defected layer for resonance frequencies. When the incident wave has the first resonance frequency ( $f_p = 1.749$  GHz), there is only one

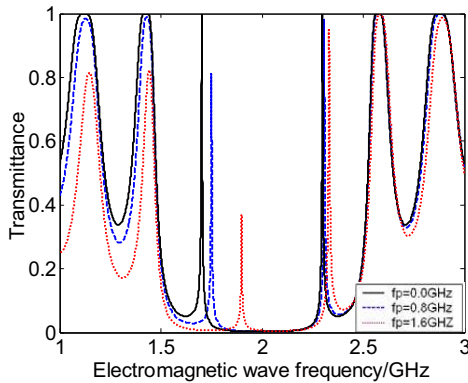


Figure 1: Transmittance of the 1DPC doped by unmagnetized plasma layer with different plasma frequency.

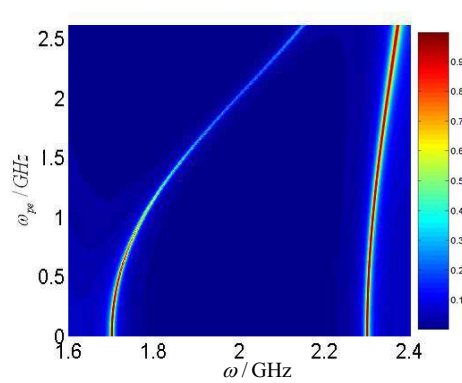


Figure 2: Transmittance of the finite structure  $(HL)^5D(LH)^5$  obtained by the transfer matrix method for different plasma frequency.

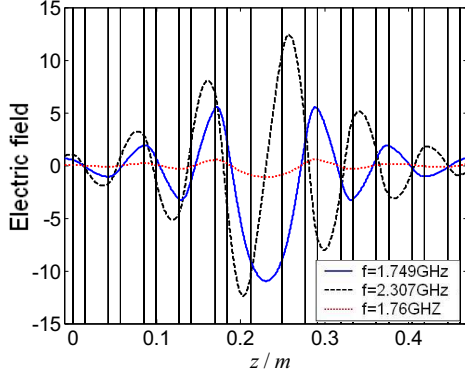


Figure 3: Electric field amplitude distribution for different frequency waves when  $\omega_{pe} = 2\pi \times 0.8 \times 10^9 \text{ s}^{-1}$ .

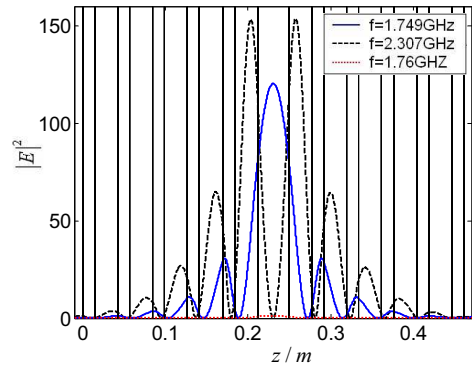


Figure 4: Electric energy distribution for the frequencies in Fig. 3.

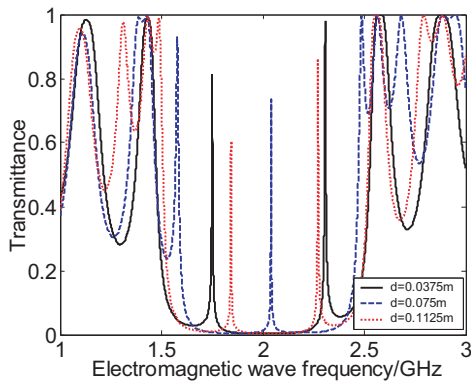


Figure 5: Transmittance of the 1DPC doped by unmagnetized plasma layer with different plasma frequency.

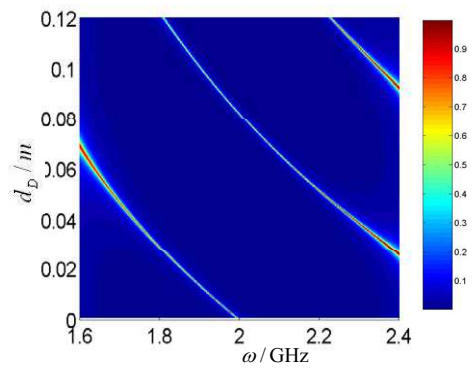


Figure 6: Transmittance of the finite structure  $(\text{HL})^5\text{D}(\text{LH})^5$  obtained by the transfer matrix method for different plasma width.

resonant peak in the defected layer, whereas there are two resonant peaks in the defected layer for the second resonance frequency ( $f_p = 2.307\text{GHz}$ ). From the view point of energy, electromagnetic energy was restricted in the defected layer, which causes resonance effect. When the defected layer is inserted into 1DPC, which leads disturbance to the space symmetry, a microcavity is formed featuring its own resonance frequencies. In controlled conditions, the EM wave having the frequencies near the resonance range will propagate in the 1DPC, otherwise it will be prohibited to cross the PC.

## 2.2. Influence of Plasma Width

Now the effect of the thickness of plasma layer on the transmittance should be considered. For the fixed thickness of layers  $H$  and  $L$  as the same as those in Fig. 2, the transmittances for three values of  $d_D$ , are calculated. The results are shown in Fig. 5. It is shown from Fig. 5 that the positions of defected modes are sensitive to the values of  $d_D$ . With the increase of plasma width from  $0.0375\text{m}$  to  $0.1125\text{m}$ , the two resonance peak can be modulated in a wider frequency range.

Figure 6 shows the results for  $\omega_{pe} = 2\pi \times 0.8 \times 10^9 \text{ s}^{-1}$ , in which the grey scale indicates the transmittance. Obviously, for most plasma width, one value of  $d_D$  has only two transmission peak except in the low plasma width. Outside the channel, all the EM waves are nearly prohibited. With the increase of plasma width, the two resonance peaks move to the lower frequency region. The resonance peak moves to the lower frequency region will vanished in the lower band edge, while the higher band edge generate a new resonance peak. Therefore, for a fixed dielectric width, we can change the thickness of plasma layer to obtain arbitrary frequency channel.

## 3. CONCLUSIONS

In summary, we have analyzed a novel tunable dual-band filter from one-dimensional photonic crystals doped by unmagnetized plasma. Two defective PCs composed by  $\text{ZnSe}$  and  $\text{Na}_3\text{AlF}_6$  with

one defect layer made by unmagnetized plasma stacked in symmetric geometry are considered. By the transfer matrix method and Bloch's theorem, it is found that the frequency of the defect modes can be modulated by plasma frequency and defect thickness. Without changing the structure of the photonic crystal, the defect modes can be modulated in a larger frequency range. These results may provide theoretical instructions for designing new optoelectronic devices.

## ACKNOWLEDGMENT

This work was supported by the supports from the Chinese Natural Science Foundation (Grant No. 60971122), the Innovative and Excellent for Ph.D. Thesis Foundation of NUAA, and the science and technology innovation foundation for NUAA students.

## REFERENCES

1. Yablonovitch, E., "Inhibited spontaneous emission of photons in solid-state physics and electronics," *Phys. Rev. Lett.*, Vol. 58, No. 20, 2059–2061, 1987.
2. John, S., "Strong localization of photons in certain disordered dielectric superlattices," *Phys. Rev. Lett.*, Vol. 58, No. 23, 2486–2489, 1987.
3. Jiang, H. T., H. Chen, H. Q. Li, et al., "Omnidirectional gap and defect mode of one-dimensional photonic crystals containing negative-index materials," *Applied Physics Letters*, Vol. 83, No. 26, 5386–5388, 2003.
4. Wang, L.-G., H. Chen, and S.-Y. Zhu, "Omnidirectional gap and defect mode of one-dimensional photonic crystals with single-negative materials," *Physical Review B*, Vol. 70, No. 24, 245102, 2004.
5. McGurn, A. R., "Intrinsic localized modes in nonlinear photonic crystal waveguides," *Physics Letters A*, Vol. 251, No. 5, 322–335, Feb. 1999.
6. Loncar, M., T. Yoshie, A. Scherer, et al., "Low-threshold photonic crystal laser," *Applied Physics Letters*, Vol. 81, No. 15, 2680–2682, 2002.
7. Lee, H. Y., H. Makino, T. Yao, et al., "Si-based omnidirectional reflector and transmission filter optimized at a wavelength of 1.55 μm," *Applied Physics Letters*, Vol. 81, No. 24, 4502–4504, 2002.
8. Hojo, H. and A. Mase, "Dispersion relation of electromagnetic waves in one-dimensional plasma photonic crystals," *Plasma Fusion Res.*, Vol. 80, No. 4, 89–92, 2004.
9. Li, W., et al., "The dispersive properties of a dielectric-rod loaded waveguide immersed in a magnetized annular plasma," *Chinese Physics*, Vol. 13, No. 1, 54, 2004.
10. Liu, S. B., C. X. Zhu, and N. C. Yuan, "FDTD simulation for plasma photonic crystals," *Acta Physica Sinica*, Vol. 54, No. 6, 2804–2808, 2005.
11. Liu, S. B., C. Q. Gu, J. J. Zhou, et al., "FDTD simulation for magnetized plasma photonic crystals," *Acta Physica Sinica*, Vol. 55, No. 3, 1283–1288, 2006.
12. Wang, S. Y. and S. B. Liu, "Tunable filter using plasma defect in one-dimensional microwave photonic crystal," *Acta Physica Sinica*, Vol. 58, No. 10, 7062–7066, 2009.
13. Kong, X. K., S. B. Liu, H. F. Zhang, et al., "A novel tunable filter featuring defect mode of the TE wave from one-dimensional photonic crystals doped by magnetized plasma," *Physics of Plasmas*, Vol. 17, No. 10, 2010.
14. Kong, X. K., S. B. Liu, et al., "Omnidirectional photonic band gap of one-dimensional ternary plasma photonic crystals," *Journal of Optics*, Vol. 13, No. 3, 035101, 2011.
15. Kong, X. K., S.-B. Liu, H.-F. Zhang, et al., "The effect of random variations of structure parameters on photonic band gaps of one-dimensional plasma photonic crystals," *Optics Communications*, 2–5, in press.
16. Kong, X.-K., S.-B. Liu, H.-F. Zhang, et al., "A novel tunable filter featuring defect mode of the TE wave from one-dimensional photonic crystals doped by magnetized plasma," *Physics of Plasmas*, Vol. 17, No. 10, 103506-5, 2010.
17. Wu, C. J. and Z. H. Wang, "Properties of defect modes in one-dimensional photonic crystals," *Progress In Electromagnetics Research*, Vol. 103, 169–184, 2010.

# Response of Plasma Flow Field to Nuclear Electromagnetic Pulse in Near Space

**Bo-Rui Bian, Shao-Bin Liu, Xiang-Kun Kong, and Chun-Zao Li**

College of Electronic and Information Engineering

Nanjing University of Aeronautics and Astronautics, Nanjing 210016, China

**Abstract**— With the development of national missile defense system, we must rely on new ways to penetrate the existing strategic balance to maintain. Near space vehicle is one of the most promising means of a highly efficient of penetration. Near space vehicle can effectively circumvent the Kinetic Energy Interceptor, but low-yield nuclear detonation may be faced with a typical combat scenario. Nuclear explosions in near space on the impact of near space vehicle are particularly important. In this paper, finite-difference time-domain (FDTD) method has been discussed for complete simulation of nuclear electromagnetic pulse (NEMP) originating from an atmospheric nuclear detonation in near space. The Compton current formula and the simplified model of solving the Maxwell's equations are described. In addition, the typical results that the plasma flow field of near space vehicle is generated by the ionization between high-speed flight and the thin air in near space are presented. The coupling between nuclear electromagnetic pulse (NEMP) in nuclear exploding source region and the plasma flow field of near space vehicle is studied. To achieve this purpose, the radiated field in nuclear exploding source region is calculated using a late-model iterative equation including the electron plasma extra conductivity effect. Because of the free electron plasma extra conductivity, the corresponding conduction current is offset by the Compton current, resulting in significant decline in the peak transverse electric field. The presented results may be used in electromagnetic compatibility analysis of near space vehicle.

## 1. INTRODUCTION

With the development of national missile defense system, we must rely on new ways to penetrate the existing strategic balance to maintain. Near space vehicle is one of the most promising means of highly efficient of penetration [1]. Near space vehicle can effectively circumvent the Kinetic Energy Interceptor, but the intercepting of low-yield nuclear explosion would be a typical combat scenario. Therefore, it is important to research nuclear explosion in near space on the impact of near space vehicle.

For a high-altitude explosion, the effective range of low-yield nuclear explosion shock wave is finite and the irradiation effects such as a variety of high-energy rays and electromagnetic pulse are extremely effective at far distance [2, 3]. In the present paper, the magnitude of electromagnetic field at the distances from the burst point of 500 m to 1000 m under 5-kilotons nuclear explosion is studied and the interaction of the radiated field in nuclear exploding source region with the plasma flow field of near space vehicle is numerically simulated.

## 2. ELECTROMAGNETIC FIELD IN SOURCE REGION

For nuclear explosions below an altitude of 100 or so kilometers the primary source of the electromagnetic pulse is Compton-recoil electrons produced by explosion gamma rays interacting with the atmosphere [3, 4]. The electrons move forward quickly at the speed of light and interact with the geomagnetic field. The Compton current produced by the gamma rays has two components. First, the component in the direction radial from the burst produces principally a radial electric field  $E_r$ . Second, the geomagnetic field causes the Compton current to have transverse current components perpendicular to the radial direction. Transverse current components directly generate transverse electric field  $E_\theta$  and  $E_\varphi$  [4].

According to the relation between the time of explosion electromagnetic field changes with and the space of that, we can retain the main physical quantities and ignore secondary factors, thus the simulated model can be simplified. In spherical coordinates, this approximation mainly includes two aspects. First, we can assume that the field with spherical coordinates in the  $\theta$  direction and  $\varphi$  direction changes slowly relative to the field changes with time. Second, the field which changes in space relative to the field itself is a small amount. Maxwell's equations in the spherical coordinates can be divided into two sets of equations.

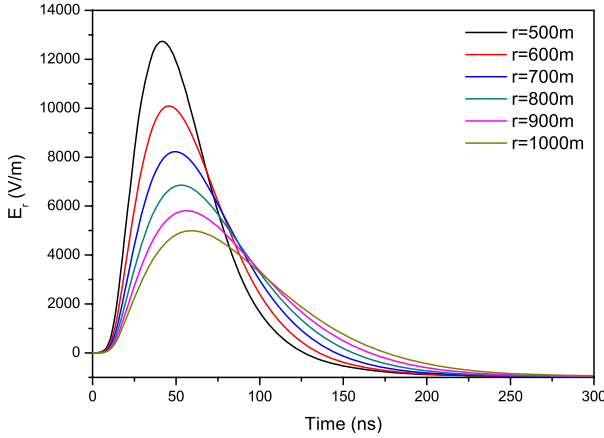


Figure 1: Radial electric field waveform at various distances to the burst point.

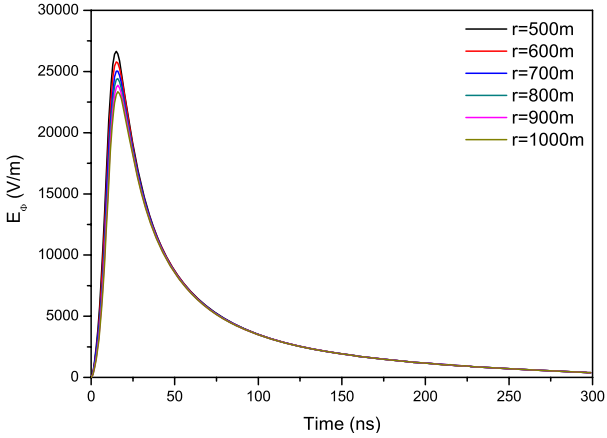


Figure 2: Transverse electric field waveform at various distances to the burst point.

Transverse magnetic wave is described by the following equations

$$\frac{\partial(rH_\varphi)}{\partial r} + rJ_\theta + \sigma rE_\theta = -\varepsilon \frac{\partial(rE_\theta)}{\partial t} \quad (1)$$

$$\frac{\partial(rE_\theta)}{\partial r} = -\mu \frac{\partial(rH_\varphi)}{\partial t} \quad (2)$$

Transverse electric wave is described by the following equations

$$\frac{\partial(rH_\theta)}{\partial r} - rJ_\varphi - \sigma rE_\varphi = \varepsilon \frac{\partial(rE_\varphi)}{\partial t} \quad (3)$$

$$\frac{\partial(rE_\varphi)}{\partial r} = \mu \frac{\partial(rH_\theta)}{\partial t} \quad (4)$$

Nuclear electromagnetic pulse in nuclear exploding source region also contains the radial field which is described by the following equation

$$\varepsilon \frac{\partial E_r}{\partial t} + J_r + \sigma E_r = 0 \quad (5)$$

If we know the calculation formula of Compton current and the temporal and spatial distribution of conductivity generated by the secondary electrons, in accordance with the boundary conditions and the above equations, the distribution of electromagnetic field can be obtained by difference iterative method. Owing to the limitation of the space, the calculation formula of Compton current and conductivity are omitted.

Regarding 5-kilotons nuclear device with explosion height of 60 km off the ground, the time-domain waveforms of the radial electric field and transverse electric field at various distances to the burst point are shown in Fig. 1 and Fig. 2 respectively. Numerical results show that the peak electric field strength is stronger than that of the radial field and the peak value reaches 26000 V/m. This is because that the geomagnetic field deflects the Compton current powerfully in near space, thus the deflected (transverse) Compton current is comparable with the radial current. Fig. 1 shows that the radial electric field decays rapidly along the radial direction. However, the transverse electric field is not sensitive to the distance. As the distance increases, the peak value only slightly decreases (see Fig. 2).

### 3. PLASMA FLOW FIELD OF NEAR SPACE VEHICLE

Plasma flow field is produced by the ionization between the surface of high-speed near space vehicle and the thin air, the distribution region of plasma flow field is not too far away from the near space vehicle [5, 6]. From the simulation results, in the range of the altitude from 40 km to 60 km, the higher the altitude, the lower the plasma electrons density and collision frequency, each rising 10 km, the electron density declined by one order of magnitude. Relatively speaking, the collision

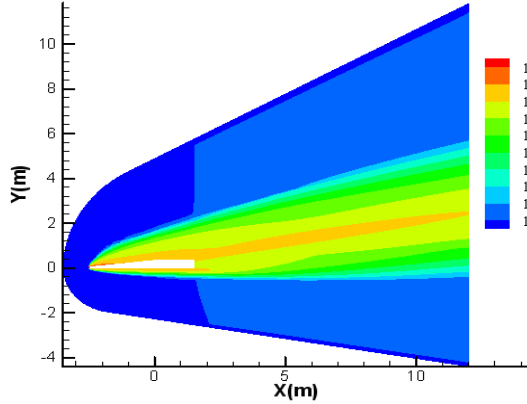


Figure 3: Typical electron density distribution.

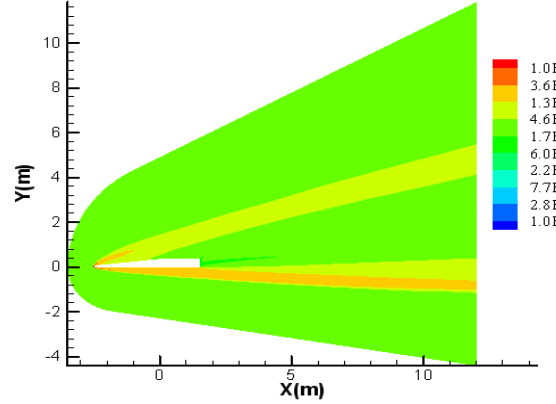


Figure 4: Typical collision frequency distribution.

frequency rate of decline is slightly slower. The typical distributions of electron density and collision frequency are shown in Fig. 3 and Fig. 4. In the figures, wedge shape device is used as near space vehicle.

#### 4. COUPLING OF ELECTROMAGNETIC FIELD AND PLASMA FLOW FIELD

When the plasma flow field exists in the nuclear exploding source region, the plasma flow field will generate additional free electrons conductivity:

$$\sigma_p(\omega) = \varepsilon_0 \frac{\omega_p^2}{j\omega + \nu} \quad (6)$$

where,  $\omega_p = \sqrt{n_e e^2 / m \varepsilon_0}$ ,  $n_e$  is the free electrons conductivity,  $\nu$  denotes the collision frequency of plasma flow field. Thus the plasma flow field current density is

$$J_P(\omega) = \sigma(\omega) E(\omega) \quad (7)$$

Through the inverse Fourier transform, we can get:

$$J_P(t) = \int_0^t E(t - \tau) \sigma(\tau) d\tau \quad (8)$$

$$\sigma_p(\tau) = \varepsilon_0 \omega_p^2 \exp(-\nu\tau) U(\tau) \quad (9)$$

where,  $U(\tau)$  is Unit step function, obviously, as long as substituting  $J = J_\varphi + J_P$  for  $J_\varphi$ , we can concluded impact the transverse current  $J_\varphi$  on the plasma flow field.

$$J_P(t) = \varepsilon_0 \omega_p^2 \exp(-\nu t) \int_0^t \exp(\nu\tau) E(\tau) d\tau \quad (10)$$

After a series of transformation, the convolution equation can change the explicit iterative equation of second order.

$$J_p^{n+1/2}(i) = \exp(-\nu\Delta t) J_p^{n-1/2}(i) + \varepsilon_0 \omega_p^2 \exp(-\nu\Delta t/2) E^n(i) \Delta t \quad (11)$$

#### 5. RESULT OF CALCULATION

Regarding 5-kilotons nuclear device with explosion height of 60 km off the ground, the time-domain waveform of the radial electric field without considering the existence of plasma flow field has been shown in Fig. 1. What follows, we consider the influence of plasma flow field. The distribution of plasma flow field is depicted in Fig. 3 and Fig. 4. We set the observe point located on the up-surface the vehicle and the radial electric field strength is given in Fig. 5. In practice, if the

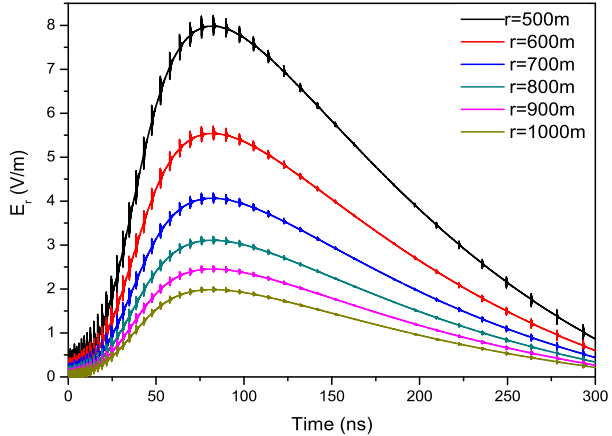


Figure 5: Radial field of the up-surface.

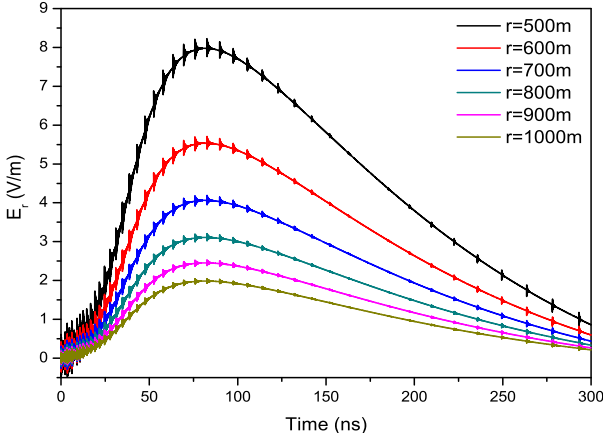


Figure 6: Radial field of the low-surface.

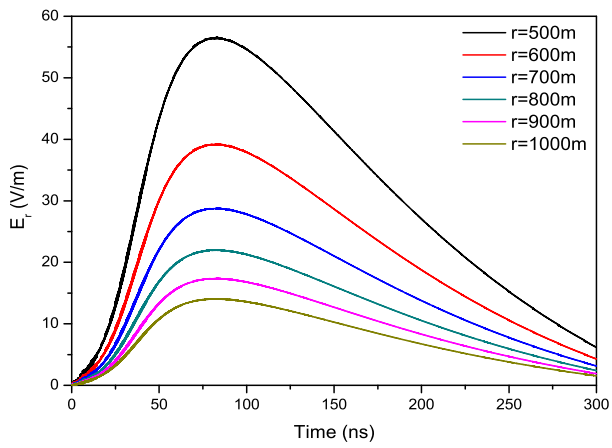


Figure 7: Radial field of the front-surface.

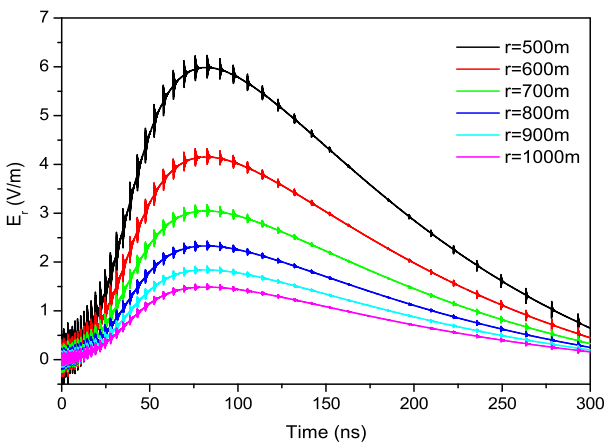


Figure 8: Radial field of the back-surface.

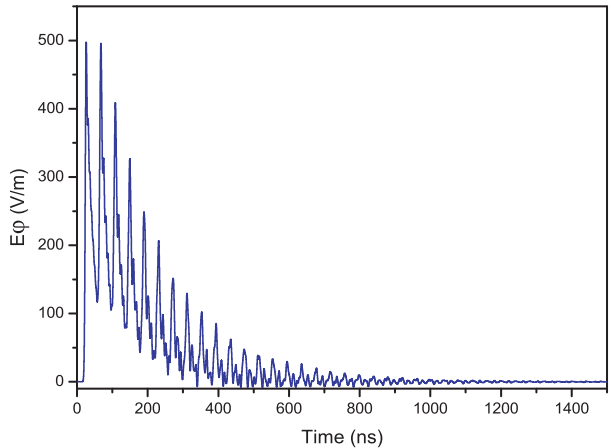


Figure 9: Transverse field of the front-surface.

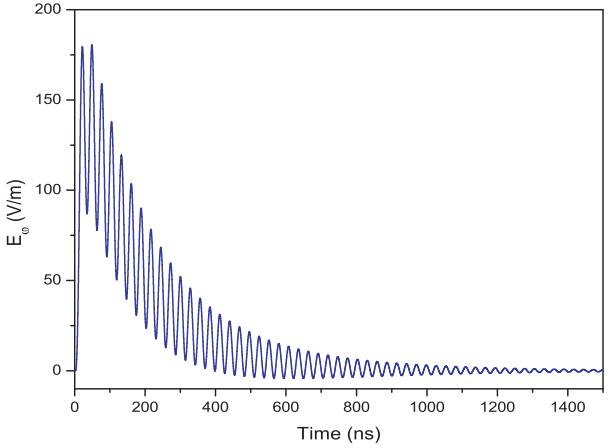


Figure 10: Transverse field of the back-surface.

vehicle is moving above the explosion point, the radial electric field strength of low-surface is given Fig. 6. Considering that the vehicle and the explosion point are in a same height with the observe points located in front-surface and back-surface, Fig. 7 and Fig. 8 depicted the electric field strength. Numerical results show that the radial electric field is influenced by the plasma flow field significantly in source region. The air conductivity increased for the existence of free electrons of plasma, so the total radial current decreases significantly and the large radial electric field can not be generated. Because both the thickness and electron density of plasma flow in the front district of the vehicle are smaller than them in other area, less energy are absorbed in front district and the peak value of electric field reaches 55 V/m as shown in Fig. 7.

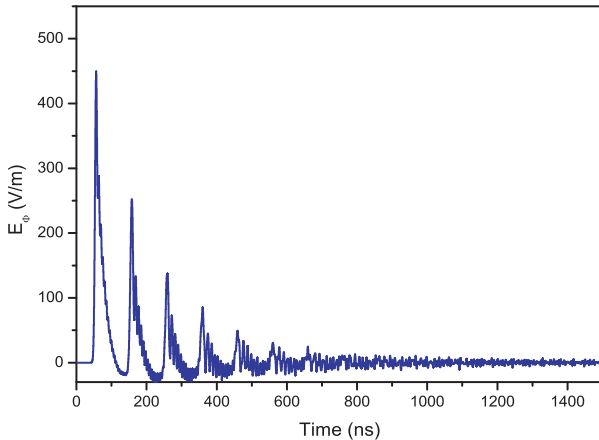


Figure 11: Transverse field of the up-surface.

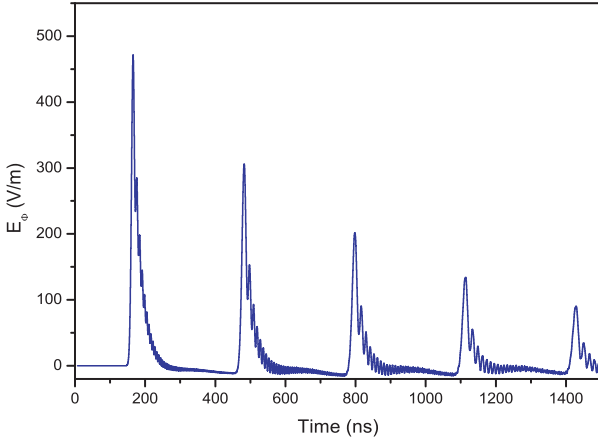


Figure 12: Transverse field of the low-surface.

Because the transverse electric field is not sensitive to the distance, we can take the transverse field of a distance ( $r = 800$  m) as typical value and calculate the propagation characteristic of transverse electric field in the plasma flow field. The transverse electric fields which penetrate through the plasma are shown in Fig. 9 to Fig. 12. Comparing Fig. 9 to Fig. 12 with Fig. 2, it can be seen that the electromagnetic pulse duration is significantly longer when it propagate through the plasma flow field. The relaxation time reaches microsecond level. Because of relaxation response of plasma flow, the transverse electric field which penetrates through the plasma flow field is an oscillating and attenuating waveform. The peak value of transverse electric field is up to 600 V/m after transverse electric pulse reaches the front-surface of the vehicle as given in Fig. 9.

## 6. CONCLUSION

The peak value of electromagnetic field in nuclear exploding source region is tens of thousands of volts. However, because of the existence of the plasma flow field near the surface of near space vehicle, the frequency of the radiation field is much smaller than the plasma cutoff frequency. The energy is mainly reflected or absorbed by the plasma, thus the electric field value which reaches the surface of near space vehicle is order of magnitude smaller than the KV. The presented results may be used in electromagnetic compatibility analysis of near space vehicle.

## ACKNOWLEDGMENT

This work was supported in part by the supports from the Chinese Natural Science Foundation (Grant No. 60971122), in part by the Aviation Science Foundation (Key project 2009ZA52008) and in part by the Open Research Program in China's State Key Laboratory of Millimeter Waves (Grant No. K201103).

## REFERENCES

1. Stephens, H., "Near space," *Air Force Magazine*, Vol. 88, No. 7, 2005.
2. Karzas, W. J. and R. Latter, "Electromagnetic radiation from a nuclear explosion in space," *Physical Review*, Vol. 126, No. 6, 1919–1926, 1962.
3. Karzas, W. J. and R. Latter, "Detection of the electromagnetic radiation from nuclear explosions in space," *Physical Review*, Vol. 137, No. 5, 1369–1378, 1965.
4. Longmire, C. J., "On electromagnetic pulse produced by nuclear explosion," *IEEE Transaction on Antennas and Propagation*, Vol. 26, No. 1, 3–13, 1978.
5. Fujino, T. and M. Ishikawa, "Numerical simulation of control of plasma flow with magnetic field for thermal protection in earth reentry flight," *IEEE Transactions on Plasma Science*, Vol. 34, No. 2, 409–420, 2006.
6. Rybak, J. P. and R. J. Churchill, "Progress in reentry communications," *IEEE Transactions on Aerospace and Electronic Systems*, Vol. 7, No. 5, 879–894, 1971.

# Guided Modes in a Slab Waveguide with Air Core Layer and Left-handed Materials Claddings

Lu Fa Shen<sup>1</sup>, Jia-Cheng Qiu<sup>1</sup>, and Zi-Hua Wang<sup>2</sup>

<sup>1</sup>Science College, Huzhou Teachers College, Zhejiang, China

<sup>2</sup>Key Laboratory of Specialty Fiber Optics and Optical Access Networks  
Shanghai University, Shanghai, China

**Abstract**— A symmetric three-layer slab waveguide with air as core and anisotropic left-handed materials as claddings is investigated. Some dispersion equations are derived and corresponding dispersion curves are plotted, respectively. From these curves, with the increase of the waveguide thickness, their operating frequencies become widely such as surface  $TE_0$  mode, surface  $TE_1$  mode and oscillating  $TM_1$  mode. However, for the surface  $TM_0$  mode, its dispersion curves move down and operating frequencies get narrow, and for oscillating  $TE_1$  mode, its dispersion curves move to left and cutoff frequencies become less. Since all experimental realization of left-handed materials have narrow bands, thus, these new features may give us a direction to increase band width.

## 1. INTRODUCTION

Left-handed materials (LHMs) are artificially fabricated structures possessing certain desirable properties which are not available in natural materials. The typical features include negative refraction, reversed Doppler shift, reversed Cherenkov radiation [1], and reversed Goose-Hanchen shift [2, 3]. Till now, LHMs have been realized successfully in microwaves [4], THz waves and optical waves [5, 6]. An LHMs waveguide has unique properties and becomes one interesting topic. The slab waveguides with the LHM core layer have been discussed and found some typical properties [7–11]. However, LHM is usually constructed by periodic arrays of metallic wire and split-ring resonator (SRR). Therefore, they should have anisotropy and dispersion material feature. Some scholars have studied slab waveguides with anisotropic LHMs. Z. Liu [12] has found the enhancement of photon tunneling by a slab of anisotropic negative refractive index material; T. Pan [13] has obtained the dispersion properties and energy flux properties in a slab waveguide; Hamidreza Salehi etc. [14] have investigated single negative LHM slab waveguide and discussed their device applications. But, they all solved dispersion equations by using a graphical method which can only decide whether the solutions exist. In this paper, we will consider slab waveguides containing anisotropy and dispersion LHMs and calculate numerically dispersion equations of guided modes.

A three-layer slab waveguide with right-handed materials (RHMs) in the core and LHMs in the claddings is examined in this paper. Through Maxwell's equations, considering anisotropy and dispersion LHMs, some dispersion equations for  $TE$  and  $TM$  modes are obtained, respectively. Solving these equations as frequency from 4.0 GHz to 6.0 GHz, we plot corresponding dispersion curves, and find some new dispersion properties.

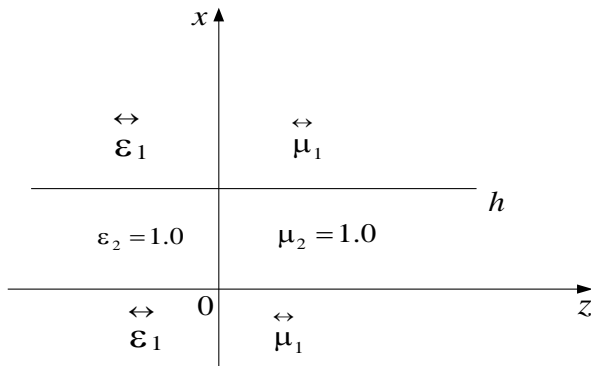


Figure 1: Schematic geometry of a symmetric three-layer slab waveguide including left-handed materials.

## 2. THE DISPERSION EQUATIONS OF THE ANISOTROPIC AND DISPERSIVE LHM SLAB WAVEGUIDE

A three-layer slab waveguide including LHM is shown in Fig. 1. The core layer of thickness  $h$  is air with permittivity ( $\varepsilon_2 = 1$ ) and permeability ( $\mu_2 = 1$ ). The claddings are the anisotropic LHM with permittivity tensor  $\overset{\leftrightarrow}{\varepsilon}_1(\varepsilon_{1x}, \varepsilon_{1y}, \varepsilon_{1z})$  and permeability tensor  $\overset{\leftrightarrow}{\mu}_1(\mu_{1x}, \mu_{1y}, \mu_{1z})$ . For simplicity, we assume that the claddings extend to infinity, and the time-and  $z$ -factor  $\exp[i(\omega t - \beta z)]$  that multiplies all the field components is neglected from all equations. Where  $\omega$  and  $\beta$  denote angular frequency and the longitudinal propagation constant. Usually, slab waveguide can support  $TE$  and  $TM$  modes. For  $TE$  modes, through Maxwell's equations, their electromagnetic fields in the claddings satisfy following equations:

$$-i\beta H_x - \frac{\partial H_x}{\partial x} = i\omega\varepsilon_{1y}E_y \quad (1a)$$

$$H_x = -\frac{\beta}{\omega\mu_{1x}}E_y \quad (1b)$$

$$\frac{\partial E_y}{\partial x} = -i\omega\mu_{1z}H_z \quad (1c)$$

Besides, in the core layer, the corresponding electromagnetic field equations can be obtained by  $\varepsilon_2$  and  $\mu_2$  instead of permittivity and permeability in Eqs. (1a)–(1c). From above equations, after some algebraic manipulations, electric fields of  $TE$  modes in the slab waveguide are written as:

$$E_{y1} = E_1 \exp[-\alpha_1(x - h)], \quad x > h \quad (2a)$$

$$E_{y2} = E_2 \cos(k_2 x - \varphi_s), \quad 0 < x < h \quad (2b)$$

$$E_{y3} = E_3 \exp(\alpha_1 x), \quad x < 0 \quad (2c)$$

where  $E_1$ ,  $E_2$  and  $E_3$  are electric field amplitudes in each layer.  $\alpha_1$  denotes an evanescent coefficient, which can be expressed as  $\alpha_1 = \sqrt{\frac{\mu_{1z}}{\mu_{1x}}}(\beta^2 - k_0^2\varepsilon_{1y}\mu_{1x})$ , and  $k_2$  represents the transverse wave number, which can be expressed by  $k_2 = \sqrt{k_0^2\varepsilon_2\mu_2 - \beta^2}$ . Besides,  $k_0$  and  $\varphi_s$  are wave number in vacuum and a phase constant respectively.

Considering anisotropic LHMs, we assume  $\frac{\mu_{1z}}{\mu_{1x}} < 0$ . This condition can meet easily for example as the case of T. Pan [13]. For real  $\alpha_1 = \sqrt{\frac{\mu_{1z}}{\mu_{1x}}}(\beta^2 - k_0^2\varepsilon_{1y}\mu_{1x})$ , we find that  $\beta < k_0\sqrt{\varepsilon_{1y}\mu_{1x}}$ . Similarly, for real  $k_2 = \sqrt{k_0^2\varepsilon_2\mu_2 - \beta^2}$ , that demands  $\beta < k_0\sqrt{\varepsilon_2\mu_2}$ . But, for imaginary  $k_2 = \sqrt{k_0^2\varepsilon_2\mu_2 - \beta^2}$ , we have  $\beta > k_0\sqrt{\varepsilon_2\mu_2}$ . Therefore, as  $\beta < \min(k_0\sqrt{\varepsilon_{1y}\mu_{1x}}, k_0\sqrt{\varepsilon_2\mu_2})$ , we define these modes as  $TE$  oscillating guided modes, however, as  $\beta$  increases to  $k_0\sqrt{\varepsilon_2\mu_2} < \beta < k_0\sqrt{\varepsilon_{1y}\mu_{1x}}$ , we call these modes as  $TE$  surface modes.

From above discussions, for  $TE$  oscillating guided modes, according to boundary conditions, after some algebraic manipulations, the dispersion equation is obtained as follows:

$$k_2 h - 2 \tan^{-1} \left( \frac{\mu_2 \alpha_1}{\mu_{1z} k_2} \right) = m\pi \quad (2d)$$

For  $TM$  oscillating guided modes, the evanescent coefficient in the cladding can be rewritten as  $\alpha'_1 = \sqrt{\frac{\varepsilon_{1z}}{\varepsilon_{1x}}}(\beta^2 - k_0^2\mu_{1y}\varepsilon_{1x})$ , and the dispersion equation can be obtained that the permeability is replaced by the corresponding permittivity.

A slab waveguide with air core layer and LHM claddings, like a metal waveguide, some surface modes can exist. For  $TE$  surface modes,  $k_2$  in Eq. (3) is an imaginary number and let  $k_2 = i\alpha_2$ , two types of  $TE$  surface modes exist and corresponding dispersion equations are obtained easily as follows:

$$k_2 h + 2 \tanh^{-1} \left( \frac{\mu_2 \alpha_1}{\mu_{1z} \alpha_2} \right) = 0 \quad (4)$$

For the even  $TE$  surface mode or surface  $TE_0$  mode in its field without node in a slab and

$$k_2 h + 2 \coth^{-1} \left( \frac{\mu_2 \alpha_1}{\mu_{1z} \alpha_2} \right) = 0 \quad (5)$$

For the odd  $TE$  surface mode or surface  $TE_1$  mode in its field with one node in a slab.

For  $TM$  surface modes, the corresponding dispersion equations of odd surface mode and even surface mode can be obtained that permeability is replaced by the corresponding permittivity and  $\alpha_1$  replaced by  $\alpha'_1$ , respectively.

### 3. NUMERICAL RESULTS

To the best of our knowledge, the realization of negative-refractive index is by two ways [4, 12]. The first one is by periodic arrays of metallic wire and split-ring resonator (SRR) and the second one employs photonic crystal. In this paper, we consider the first one by the metallic composite LHM with periodic arrays of metallic wire, SRR and glass filled. From above LHM, they should employ some inherent properties, such as material dispersion and material anisotropy, etc. Considering LHM material dispersion, we employ an experimental model in microwave bands [11] with dielectric permittivity and magnetic permeability written as:

$$\varepsilon(\omega) = 1 - \frac{\omega_p^2}{\omega^2}, \quad \mu(\omega) = 1 - \frac{F\omega^2}{\omega^2 - \omega_0^2} \quad (6)$$

where  $F = 0.56$ ,  $\frac{\omega_0}{2\pi} = 4.0$  GHz,  $\frac{\omega_p}{2\pi} = 10.0$  GHz. When frequency increases from 4.0 GHz to 6.0 GHz, permittivity and permeability in Eq. (6) are negative simultaneously. Then, considering extremely anisotropic LHM, which meets  $\frac{\mu_{1z}}{\mu_{1x}} < 0$ , we assume that LHM employs positive permittivity and permeability in the transverse direction and negative ones along the longitudinal direction, such as:  $\varepsilon_{1x} = \varepsilon_{1y} = 2.25 > 0$ ,  $\varepsilon_{1z} = \varepsilon(\omega) < 0$ ; and  $\mu_{1x} = \mu_{1y} = 1 > 0$ ,  $\mu_{1z} = \mu(\omega) < 0$ . Based on above parameters, the oscillating guided modes and surface modes are discussed detail as follows.

#### 3.1. Dispersion Properties for $TE$ Modes

Fixing waveguide thickness  $h = 2$  cm, through Eqs. (3)–(6), dispersion curves (the effective refractive index versus frequency) for  $TE$  oscillating guided modes and surface modes are plotted in Fig. 2, respectively. As frequency from 4.0 GHz to 6.0 GHz, we find only one oscillating  $TE_1$  mode (dashed line), and two surface modes  $TE_0$  and  $TE_1$  (solid lines). Usually, an LHM slab waveguide with air core layer, we regard as a hollow waveguide and only surface modes are exist. However, in this case, both surface mode and oscillating mode can exist. This is because we consider practice dispersion LHM. The curve of surface  $TE_0$  mode is upper than that of surface  $TE_1$  mode. For oscillating  $TE_1$  mode and surface  $TE_1$  mode, their dispersion curves connect smoothly to form a whole curve. Although effective-refractive index of surface  $TE_0$  mode is bigger than that of surface  $TE_1$  mode, they are always between 1.0 and 1.5. But, for oscillating  $TE_1$  mode, its effective-refractive index is

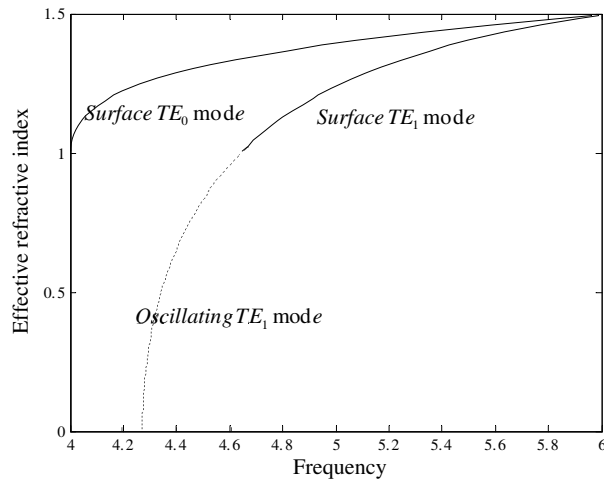


Figure 2: Dispersion curves (the effective-refractive-index as a function with frequency from 4 GHz to 6 GHz) for  $TE$  oscillating guided modes (dashed lines) and surface modes (solid lines).  $h = 2$  cm, the core layer is air, the claddings are the anisotropic-dispersive LHM and filled glass.

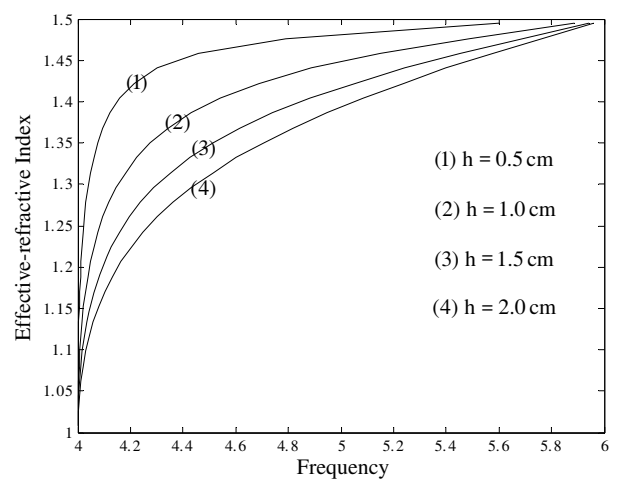


Figure 3: Dispersion curves of surface  $TE_0$  modes (solid lines) for different waveguide thickness.  $h$  equals to 0.5 cm, 1.0 cm, 1.5 cm and 2.0 cm, the other corresponding parameters employed are the same as Fig. 2.

small and between 0 and 1.0. For all guided modes, operating frequency of surface  $TE_0$  mode is the widest and oscillating  $TE_1$  mode the narrowest. As frequency increases, their effective-refractive index increases, too. That shows a normal dispersion property and their group velocities ( $v_g = \frac{d\omega}{d\beta}$ ) are all positive. Moreover, as frequency increases,  $v_g$  becomes fast.

Next we discuss the dependence of mode dispersion properties on waveguide thickness. From Eqs. (3) to (6), some dispersion curves with different waveguide thickness  $h$  are plotted in Figs. 3 and 4, respectively. From Fig. 3, surface  $TE_0$  mode can exist as frequency from 4.0 GHz to 6.0 GHz. As  $h$  increases from 0.5 cm to 2.0 cm, the curves move to down and its effective-refractive index becomes less. But, its operating frequencies become wide. So, we can change the core layer thickness to widen bands and adjust the waveguide effective-refractive index. However, for all these dispersion curves, their index is always between 1.0 and 1.5. With the increase of frequency, their effective-refractive index increases. It reveals normal dispersion properties and positive group velocities. From Fig. 4, both oscillating  $TE_1$  mode (dashed line) and surface  $TE_1$  mode (solid line) exist as frequency from 4.0 GHz to 6.0 GHz. The effective-refractive index for the former is from 0 to 1.0, while for the latter is between 1.0 and 1.5. The group velocity of the former is less than that of the latter. As different  $h$ , two curves of surface  $TE_1$  mode and oscillating  $TE_1$  mode always connect each other to form a smooth curve. As  $h$  increases, the curves move to left. Thus, for oscillating  $TE_1$  mode, its cutoff frequencies become less, and for surface  $TE_1$  mode, its operating frequencies become wide. Wide bands can overcome LHM shortcoming and open a door for practice applications.

### 3.2. Dispersion Properties for $TM$ Modes

Similarly, we choose the same parameters as Section 3.1 and plot some dispersion curves (the effective-refractive index versus frequency) of  $TM$  modes. Firstly, we fix waveguide thickness  $h = 2$  cm., two dispersion curves for  $TM$  modes are plotted in Fig. 5, respectively. As frequency from 4.0 GHz to 6.0 GHz, we only find one oscillating  $TM_1$  mode (dashed line) and one surface  $TM_0$  mode (solid line). But, surface  $TM_1$  mode cannot exist. It is different from that of above  $TE$  modes. Besides, we also find the effective-refractive index for oscillating  $TM_1$  mode is between 0 and 0.8, but, the effective-refractive index for the surface  $TM_0$  modes is in a narrow region (between 1.0 and 1.2). For the surface  $TM_0$  mode, its effective-refractive index increases linearly as frequency. So, they have positive group velocities and almost fixed value as frequency from 4.0 GHz to 6.0 GHz; but, for the oscillating  $TM_1$  mode, its effective-refractive index increases monotonously as frequency from 5.0 GHz to 6.0 GHz. So, it has positive group velocities, furthermore, its group velocity increases with frequency.

For different waveguide thickness, some dispersion curves of  $TM$  modes are plotted in Figs. 6

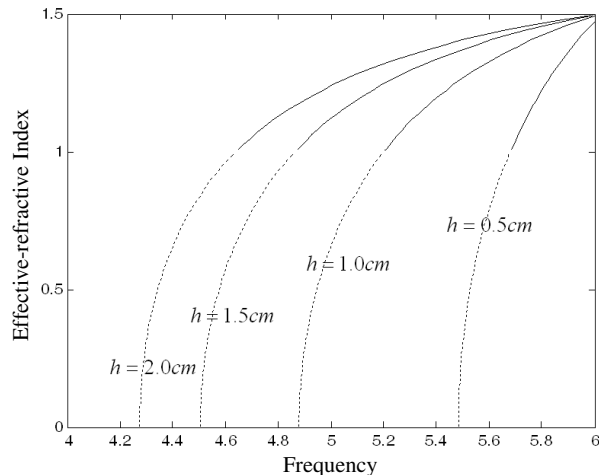


Figure 4: Dispersion curves of oscillating  $TE_1$  guided modes (dashed lines) and surface  $TE_1$  modes (solid lines) for different waveguide thickness.  $h$  equals to 0.5 cm, 1.0 cm, 1.5 cm and 2.0 cm, the other corresponding parameters employed are the same as Fig. 2.

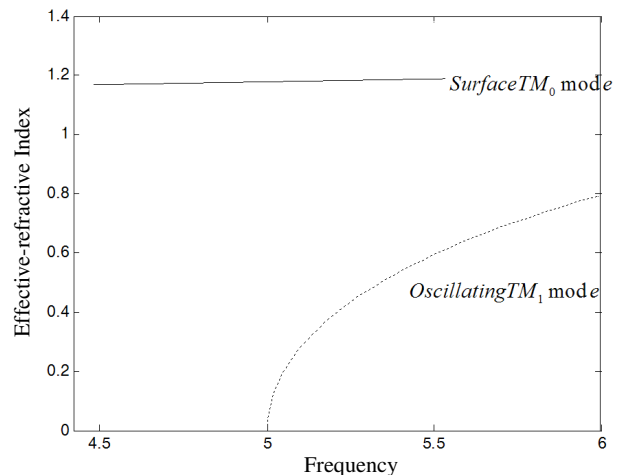


Figure 5: Dispersion curves for the  $TM$  oscillating guided modes (dashed lines) and surface modes (solid lines). The waveguide parameters are the same as Fig. 2.

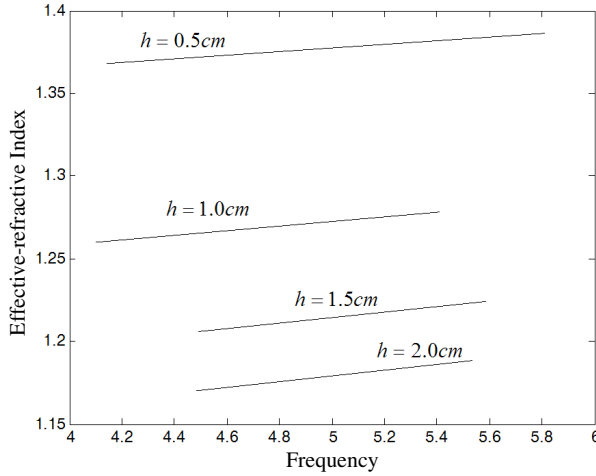


Figure 6: Dispersion curves for the surface  $TM_0$  modes (solid lines) for different waveguide thickness.  $h$  equals to 0.5 cm, 1.0 cm, 1.5 cm and 2.0 cm, the other corresponding parameters employed are the same as Fig. 2.

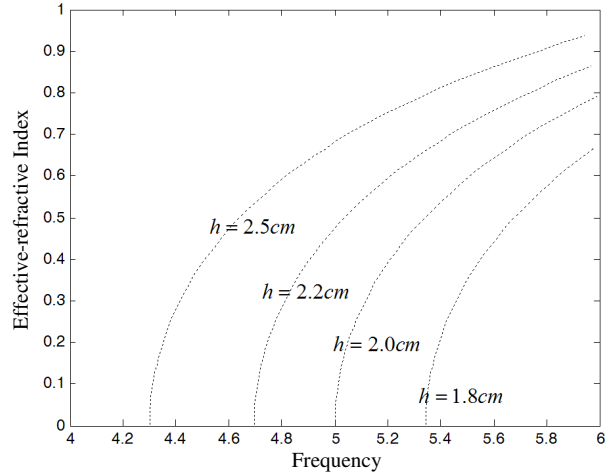


Figure 7: Dispersion curves for the oscillating  $TM_1$  modes (dashed lines) for different waveguide thickness.  $h$  equals to 1.8 cm, 2.0 cm, 2.2 cm and 2.5 cm, the other corresponding parameters employed are the same as Fig. 2.

and 7, respectively. From Fig. 6, as  $h$  changing from 0.5 cm to 2.0 cm, the surface  $TM_0$  mode exists and has following dispersion properties. As  $h$  increases, the curves move down. Its effective-refractive index decreases and operating frequencies become narrow. So, we can decrease waveguide thickness to improve band width and to increase mode effective-refractive index. This is one new feature and may help us realize the wide bands and ultra thin LHM slab waveguide. Besides, all curves almost parallel each other and they may have the same group velocity. So, group velocity of surface  $TM_0$  mode is almost independent of waveguide thickness. From Fig. 7, surface  $TM_1$  mode cannot exist and only oscillating  $TM_1$  mode exists as different waveguide thickness. This is different with above  $TE$  modes. As  $h$  increases, the curves move to left. Thus, its effective-refractive index becomes bigger as same frequency and its cutoff frequencies become less, but its operating frequencies become wide. So, we can increase waveguide thickness to improve band width. This is another new feature and may find a way to realize LHM waveguide practice application.

#### 4. CONCLUSIONS

A symmetric three-layer slab waveguide with air in the core and anisotropic LHMs in the claddings is investigated. Some dispersion equations for oscillating modes and surface modes are obtained and corresponding dispersion curves are plotted, respectively. For  $TE$  modes, as frequency from 4.0 GHz to 6.0 GHz, we find even and odd surface modes ( $TE_0$ ,  $TE_1$ ) and one oscillating guided mode ( $TE_1$ ); for  $TM$  modes, we find only even surface modes ( $TM_0$ ) and one oscillating guided mode  $TM_1$ . They have some important dispersion properties as follows.

(1) The effective refractive index increases with frequency and reveals normal dispersion property.

(2) With the increase of waveguide thickness, for oscillating  $TE_1$  modes, the dispersion curve moves to left and its cutoff frequencies become small; for oscillating  $TM_1$  mode, the dispersion curve moves to left and its cutoff frequencies become small, too. However, its operating frequencies become wide.

(3) With the increase of waveguide thickness, for surface  $TE_0$  and  $TM_0$  modes, the curves move to down and their effective-refractive index becomes less. For surface  $TE_0$  mode, its operating frequencies get wide, but, for  $TM_0$  modes, its operating frequencies get narrower. Besides, for surface  $TE_1$  modes, the curves move to left, so its cutoff frequencies decrease and its operating frequencies become wide.

#### ACKNOWLEDGMENT

This work is supported by Key Project of the National Science Foundation of China (60937003) and STCSM (08DZ2231100).

**REFERENCES**

1. Veselago, V. G., “Electrodynamics of substances with simultaneously negative electrical and magnetic properties,” *Sov. Phys. Uspekhi*, Vol. 10, 509–517, 1968.
2. Berman, P. R., “Goos-Hänchen shift in negatively refractive media,” *Phys. Rev. E*, Vol. 66, 067603, 2002.
3. Qing, D. K. and G. Chen, “Goos-Hanchen shifts at the interfaces between left- and right-handed media,” *Opt. Lett.*, Vol. 29, 872–874, 2004.
4. Smith, D. R., W. J. Padilla, D. C. Vier, et al., “Composite medium with simultaneously negative permeability and permittivity,” *Phys. Rev. Lett.*, Vol. 84, 4184–4187, 2000.
5. Berrier, A., M. Mulot, M. Swillo, et al., “Negative refraction at infrared wavelengths in a two-dimensional photonic crystal,” *Phys. Rev. Lett.*, Vol. 93, 073902, 2004.
6. Soukoulis, C. M., S. Linden, and M. Wegener, “Negative refractive index at optical wavelengths,” *Science*, Vol. 315, 47–495, 2007.
7. He, J. L., Y. Jin, Z. Hong, and S. L. He, “Slow light in a dielectric waveguide with negative-refractive-index photonic crystal cladding,” *Opt. Exp.*, Vol. 16, 11077–11082, 2008.
8. Wu, B. L., T. M. Grzegorczyk, Y. Zhang, and J. A. Kong, “Guided modes with imaginary transverse wave number in a slab waveguide with negative permittivity and permeability,” *J. Appl. Phys.*, Vol. 93, 9386–9388, 2003.
9. Xiao, Z. Y. and Z. H. Wang, “Dispersion characteristics of asymmetric double-negative material slab waveguides,” *J. Opt. Soc. Am. B*, Vol. 23, 1757–1760, 2006.
10. He, Y., J. Zhang, and C. F. Li, “Guided modes in a symmetric five-layer left-handed waveguide,” *J. Opt. Soc. Am. B*, Vol. 25, 2081–2091, 2008.
11. Shadrivov, I. V., A. A. Sukhorukov, and Y. S. Kivshar, “Guided modes in negative-refractive-index waveguides,” *Phys. Rev. E*, Vol. 67, 057602, 2003.
12. Liu, Z., L. Hu, and Z. Lin, “Enhancing photon tunnelling by a slab of uniaxially anisotropic left-handed material,” *Physics Letter A*, Vol. 308, 294–301, 2003.
13. Pan, T., G. Xu, T. Zang, and L. Gao, “Study of a slab waveguide loaded with dispersive anisotropic metamaterials,” *Appl. Phys. A*, Vol. 95, 367–372, 2009.
14. Shen, L. F., Y. Q. Ye, and Z. H. Wang, “Oscillating guided modes in a symmetric five-layer slab waveguide with left-handed materials,” *Acta Photonica Sinica*, Vol. 39, 634–638, 2010.

# New-type Low Power and Anti-interference Transmission Module

Hsien-Wei Tseng<sup>1</sup>, Yih-Gunag Jan<sup>2</sup>, Ming-Hsueh Chuang<sup>3</sup>, Wei Chien<sup>4</sup>, Chih-Yuan Lo<sup>2</sup>, Liang-Yu Yen<sup>2</sup>, and Pei-Jun Chen<sup>1</sup>

<sup>1</sup>Computer and Communication Engineering, De Lin Institute of Technology, Taiwan, R.O.C.

<sup>2</sup>Electrical Engineering, Tamkang University, Taiwan, R.O.C.

<sup>3</sup>Electronic Engineering, National Taiwan University of Science and Technology, Taiwan, R.O.C.

<sup>4</sup>Electronic Engineering Department, De Lin Institute of Technology, Taiwan, R.O.C.

**Abstract**— A new modulation scheme for short range signal transmission is considered. The signal is modulated by sinusoidal waveforms and it is based on the majority of positive or negative waveforms in a symbol interval to determine which symbol, 1 or 0, is transmitted. The system performance implemented with this new modulation scheme is simulated and compares with the traditional BPSK modulation, it has the result that when the system is not synchronized and the transmitted signal suffers a delay greater than a threshold then the new design modulation scheme has a better performance than the traditional BPSK modulation and its allowable delay range is also larger than the BPSK format. With this modulation method we can simplify the receiver terminal hardware structure and to reduce the total system cost.

## 1. INTRODUCTION

As time evolves, many new wireless communications [1–3] have been developed and some wireline communications have been replaced by their equivalent wireless communications. Wireless communications have been applied in our surrounding environments either in the long range transmission or in the short distance communications; however in the wireless transmission it has serious interference problems [4] than that in the wireline transmissions. In this paper it is mainly considers the synchronization problem. In the communication system the goodness of synchronization at the receiving terminal determines the correctness of the demodulated signal and in order to generate correct demodulated signal it needs to know the correct starting position of the received symbols otherwise the system performance will be deteriorated. In this paper for short range transmission we develop a new modulation scheme and compare its performance, such as Bit Error Rate (BER), versus signal transmission delay time with the traditional applied BPSK modulation [5–8]. This paper is organized as follows. A new modulation format and its associated demodulation mechanism are introduced in Section 2. In Section 3 the system performance with the new modulation scheme is performed through MATLAB simulation. Finally a conclusion is drawn in Section 4.

## 2. CONSTRUCTION OF SIGNALS

As shown in Fig. 1 is the definition of the transmitted signals. For the symbol 0 it is the combination of one positive sinusoidal wave and two negative sinusoidal waves while for the symbol 1 it is the combination of two positive sinusoidal waves and one negative sinusoidal wave as shown in Equations (1) and (2) respectively with period of  $3\pi$ .

$$S_1(t) = \begin{cases} \sin(t) & 0 \leq t \leq \frac{T}{3} \\ -\sin\left(t - \frac{T}{3}\right) & \frac{T}{3} \leq t \leq \frac{2T}{3} \\ -\sin\left(t - \frac{2T}{3}\right) & \frac{2T}{3} \leq t \leq T \end{cases} \quad (1)$$

$$S_2(t) = \begin{cases} \sin(t) & 0 \leq t \leq \frac{T}{3} \\ \sin\left(t - \frac{T}{3}\right) & \frac{T}{3} \leq t \leq \frac{2T}{3} \\ -\sin\left(t - \frac{2T}{3}\right) & \frac{2T}{3} \leq t \leq T \end{cases} \quad (2)$$

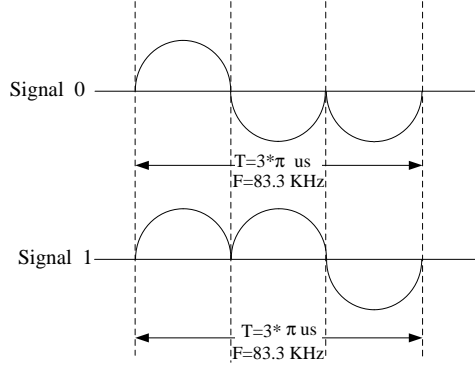


Figure 1: Construction of signals.

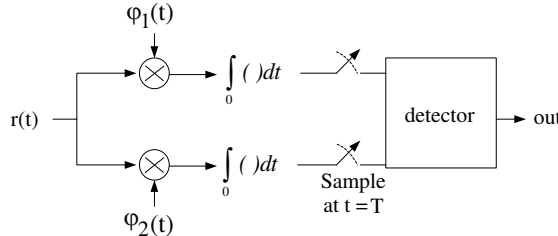


Figure 2: Functional block diagram for demodulation (method I).

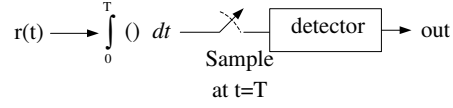


Figure 3: Functional block diagram for demodulation (method II).

In the new modulation design it has two demodulation methodologies and is described in the following: Method I: As shown in Fig. 2 is the functional block diagram for the traditional demodulation process. It first finds the basis  $\varphi_1(t)$  and  $\varphi_2(t)$  for the transmitted symbols,  $S_1(t)$  and  $S_2(t)$  respectively. The basis  $\varphi_1(t)$  and  $\varphi_2(t)$  are entered into the integrator to perform the integration over a symbol time, it uses one bit for one symbol in this paper. After integration, the signal is passed through Detector [9] to determine the symbol is one or zero as illustrated in Equations (3)–(6).

$$\varphi_1(t) = \frac{S_1(t)}{\sqrt{\varepsilon_1}} \quad (3)$$

$$C_{21} = \int_{-\infty}^{\infty} S_2(t)\varphi_1(t)dt \quad (4)$$

$$d_2(t) = S_2 - C_{21}\varphi_1(t) \quad (5)$$

$$\varphi_2(t) = \frac{d_2(t)}{\sqrt{\varepsilon_2}} \quad (6)$$

where  $\varepsilon_1$  is the energy of symbol  $S_1(t)$  and  $\varepsilon_2$  is the energy for symbol  $S_2(t)$ .

Method II: The demodulation method is illustrated in Fig. 3. At the receiver terminal it bases on the number of positive and negatives waveforms it receives in one symbol interval to perform the demodulation process. From the definition of  $S_1(t)$  and  $S_2(t)$ , if it has more positive waveforms then the transmitted signal will be  $S_2(t)$ , otherwise if it has more negative waveforms then the receiver will detect the signal is transmitted from  $S_1(t)$ .

### 3. SIMULATION RESULTS

#### 3.1. Sampling Time

From Sampling theory we know that with a symbol interval of  $3\pi$ , it will meet the Nyquist rate requirement when the sampling interval is less than  $3\pi/2$ . From this consideration if we select 10 samples per symbol interval it would be able to meet this Nyquist rate requirement and it would also be a proper choice from the considerations of BER performance and the hardware cost. From the simulation results as shown in Fig. 4, the system BER almost has the same performance when the number of samples per symbol interval is selected as either 10 or 128. As shown in the figure

the result with 10 sample points is shown with solid line with circle while for 128 sample points it is represented by the solid line.

### 3.2. Simulation Results Without Delay

The system performance, BER vs. SNR, is compared between our proposed new modulation method and the traditional BPSK modulation with a period of  $2\pi$ . The system performance is simulated in the channel with additive white Gaussian noise when the transmitted signal is maintained at the same power level [10, 11]. The simulation result is shown in Fig. 5 where the solid line with hollow circle represents the result from the implementation of Method I modulation, solid line with solid circle is the result from using Method II modulation and the solid line is the result from BPSK modulation. It also reveals from the figure that at the same SNR the BPSK has the lowest BER performance and under no delay assumption it has 2 dB degradation in Method I modulation comparing with the BPSK modulation while it is 13 dB worse in the Method II modulation. Since the new modulation we proposed is for short range transmission we will then consider when the SNR is fixed the delay effect on the system performance when the noise effect is ignored.

### 3.3. The Allowable Delay Range When the SNR Is Fixed

In this subsection we consider when SNR is fixed at certain level the relation between delay and system BER, it has simulation results as shown in Fig. 6 where we maintain the SNR at 16 dB and find how long the delay will be when the BER is so large that we could not successfully demodulate the transmitted signal. In the simulation the period for BPSK is selected as  $2\pi$  while it is  $3\pi$  for the new modulation method and its result is shown in Fig. 6. In the figure the dotted line represents the Method I modulation while Method II results is represented by the line with solid

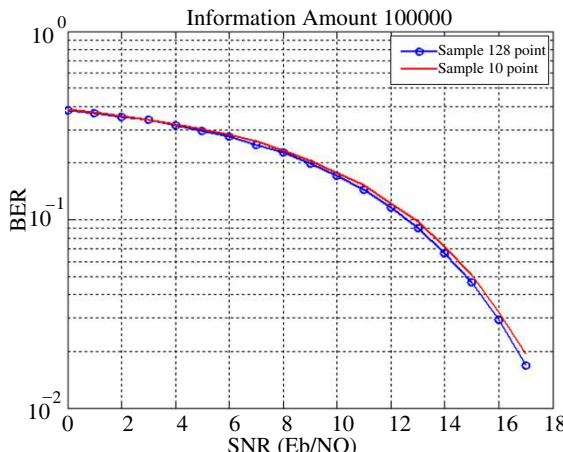


Figure 4: BER vs. SNR with sampling time as a parameter.

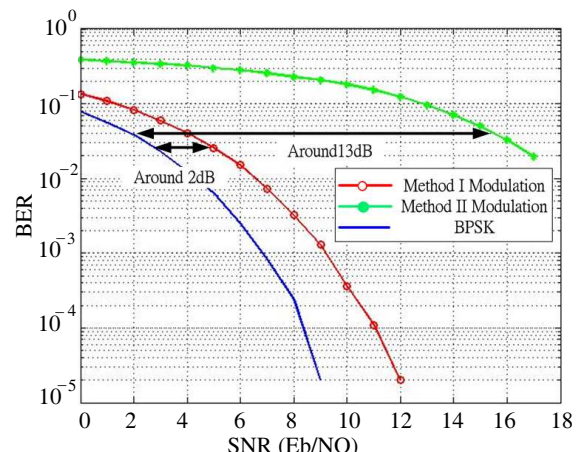


Figure 5: The system performance BER vs. SNR when the system does not introduce delay effect

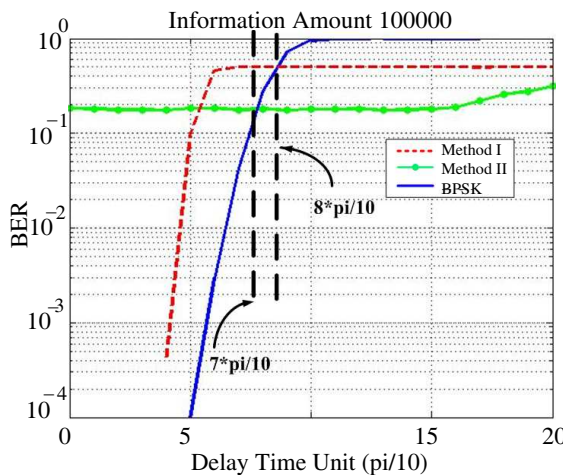


Figure 6: The allowable delay with new modulation methods.

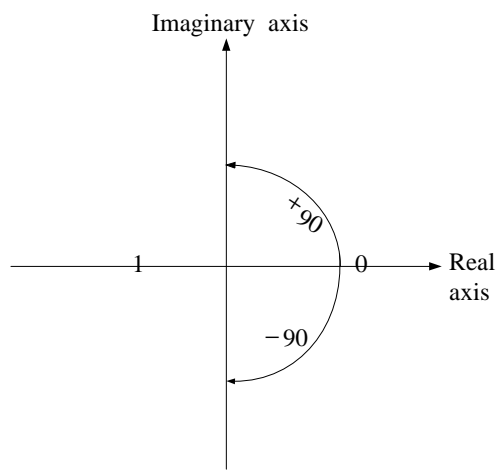


Figure 7: BPSK signal constellations.

circle and the result with BPSK modulation is represented by solid line; it appears that when the delay is around  $7\pi/10$  and  $8\pi/10$  for Method I and Method II respectively, the BPSK will have better performance than both new modulation methods while when the delay is greater than  $7\pi/10$  and  $8\pi/10$  respectively for Method I and Method II modulations the new modulation method has better performance than the traditional BPK modulation.

In the traditional BPSK demodulation when the phase shift is greater than 90 degrees it will incur demodulation error; as shown in Fig. 7 when the received signal is located in the right half of the real axis it is demodulated as a ‘0’ symbol while it is demodulated as a ‘1’ symbol when the received signal is located in the left real axis. Therefore when the signal suffers more than  $\pm 90^\circ$  phase shift in the BPSK modulation it will generate a detected error. However with our new proposed modulation method it makes decision from the waveform point of view when the received waveforms have more positive waveforms then it is detected as the symbol ‘1’ while if it has more negative waveforms it is declared as symbol ‘0’ transmitted and therefore the effect of the phase shift or the delay on the system performance will not be so great than that in the traditional BPSK modulation.

#### 4. CONCLUSION

A new modulation scheme and receiver design was introduced in this paper. The signal was modulated by sinusoidal waveforms and at the receiver terminal it was based on the majority of positive or negative waveforms in a symbol interval to determine which symbol, 1 or 0, was transmitted. Although the system performance vs. noise of our proposed modulation scheme was not as good as the traditional BPSK modulation but since our proposed modulation system was for short range transmission the noise effect on the system was not the main issue in our consideration. On the other hand we used the detection principle based on the majority number of positive or negative waveforms to find the transmitted symbol and we simulated the new system performance and compared its system performance with the traditional BPSK modulation when the system is not synchronized; when the transmitted signal has a delay greater than a threshold then the new design had a better performance than the traditional BPSK modulation and its allowable delay range is also larger than the BPSK format. With this modulation method we can simplify the hardware structure of the receiver terminal and also to reduce the total system cost.

#### ACKNOWLEDGMENT

The authors would like to express their sincere thanks to I.-Yu, Kuo. This study is partially support from the National Science Council, R.O.C. under contracts NSC99-2219-E-009-014, NSC97-2221-E-032-027-MY3.

#### REFERENCES

1. Proakis, J. G. and M. Salehi, *Communication Systems Engineering*, 2nd Edition, 2002.
2. Tachwali, Y. and H. Refai, “Implementation of a BPSK transceiver onhybrid software defined radio platforms,” *Proc. 3rd ICTTA*, 1–5, 2008.
3. Jake, W. C., *Microwave Mobile Communications*, New York, Wiley, 1974.
4. Ziemer, R. E. and W. H. Tranter, *Principles of Communications: Systems, Modulation and Noise*, 5th Edition, 2001.
5. Sobey, C. H., “Probability of error for fault-tolerant byte synchronization detectors,” *IEEE International Conference on Converging Technologies for Tomorrow’s Applications, Conference Record*, Vol. 3, 1528–1532, 1996.
6. Tachwali, Y. and H. Refai, “Implementation of a BPSK transceiver on hybrid software defined radio platforms,” *Proc. 3rd ICTTA*, 1–5, 2008.
7. Ahamed, F. and F. A. Scarpino, “An educational digital communications project using FPGAS to implement a BPSK detector,” *IEEE Trans. Edu.*, Vol. 48, No. 1, Feb. 2005.
8. Proakis, J. G., *Digital Communications*, 5th Edition, McGraw-Hill, New York, 2008.
9. Rezatofighi, S. H., H. Soltanian-Zadeh, R. Sharifian, and R. A. Zoroofi, “A new approach to white blood cell nucleus segmentation based on gram-schmidt orthogonalization,” *International Conference on IEEE Digital Image Processing*, 107–111, 2009.
10. Park, H. C., “Power and bandwidth efficient constant-envelope BPSK signals and its continuous phase modulation interpretation,” *IET Journals*, Vol. 152, No. 3, 288–294, 2005.
11. J. Mitola, “The software radio architecture,” *IEEE Commun. Mag.*, Vol. 33, No. 5, 26–38, May 1995.

# Subgridding Scheme for FDTD in Cylindrical Coordinates

Adam Mock

School of Engineering and Technology, Central Michigan University, USA

**Abstract**— A grid resolution compensation scheme based on subgridding is proposed and evaluated for improving the performance of the finite-difference time-domain method implemented in cylindrical coordinates. The scheme introduces subgrids into the domain with smaller azimuthal grid spacings. This work investigates interpolation methods used for estimating unknown but required field values at the interface between grids with different azimuthal grid spacings. It is found that cubic, cubic spline and trigonometric interpolation cause less than 1% error in estimating the frequencies of the propagating modes of a microstructured optical fiber. Multiple subgrids have the potential for significant domain size reduction and minimum time step enlargement.

## 1. INTRODUCTION

Accurate analysis of the electromagnetics of dielectric structures with complicated wavelength-scale geometry variation most often requires a numerical approach. This work presents a study of subgridding methods for improving the efficiency of the finite-difference time-domain (FDTD) method implemented in cylindrical coordinates. FDTD in cylindrical coordinates is attractive for the analysis of geometries with continuous [1, 2] or discrete [3] azimuthal invariance, and the interest of this work is structures with discrete azimuthal invariance. Examples of structures possessing this symmetry include point defect two-dimensional photonic crystal cavities [4, 5], microgear resonators [6] and microstructured optical fibers [7] (MOFs).

The numerical methods described herein will be applied to the analysis of microstructured optical fibers. MOFs differ from standard optical fibers by the inclusion of micrometer scale geometric features in the fiber cross section that run the entire length of the fiber [8]. Figure 1(a) illustrates the magnetic field associated with a MOF made up of a triangular hole array with 7 holes missing from the center. The field is confined to the central defect region due to both a larger effective index there as well as Bragg reflection from the periodic dielectric distribution surrounding the defect region. These confinement mechanisms along with the highly nonuniform dielectric distribution make the modal properties of MOFs significantly more complicated than the modal properties of standard optical fibers.

However, MOFs are similar to standard fibers in their geometric uniformity along the propagation direction. Because these fiber geometries are uniform along the longitudinal direction, the field behavior along this direction may be characterized by a propagation factor  $\exp(j\beta z)$ . Derivatives with respect to  $z$  can be evaluated analytically which reduces the computational domain from three to two dimensions while still maintaining a fully vectorial solution to Maxwell's equations. This approach has been called the “compact” version of FDTD [9–11] and is applicable to waveguide geometries continuous along the propagation direction [1, 12, 13].

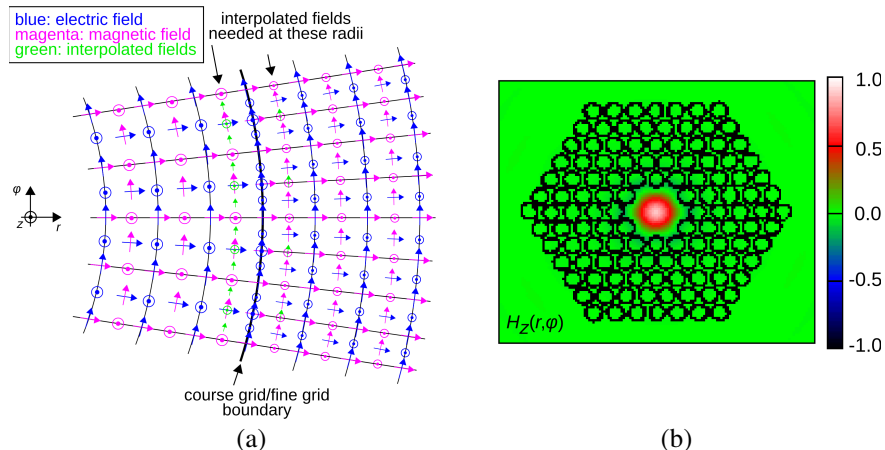


Figure 1: (a) Course grid/fine grid boundary. (b) Field distribution in microstructured optical fiber.

## 2. METHODS

Though several electromagnetic numerical methods exist that are capable of analyzing microstructured optical fibers with varying degrees of accuracy and computational effort [14], the finite-difference time-domain method is advantageous when extending geometry domains to three dimensions and when incorporating nonlinear materials. Semianalytical approaches based on the effective index method [15] require little computational effort but come at the expense of inaccuracies in the vector properties of the fiber modes. The plane-wave expansion method [16] is a fully vectorial approach, but it assumes a periodic geometry. To analyze non-periodic geometries, a supercell must be defined and be large enough to limit cross talk with neighboring cells. Finite-difference methods [17] are fully vectorial mode solvers that solve an eigenvalue problem to obtain the propagating modes as a function of  $\beta$ . Computational domain size is limited in these methods due to the superlinear scaling in execution time for solving large matrix problems [18]. Localized function methods [19] seek to reduce the matrix size with judicious use of spatially local basis functions; however, calculating matrix elements can be computationally intensive, and scaling to three-dimensional problems may still result in large matrices. Furthermore, some prior knowledge of the field solutions must be known to select appropriate localized functions. The finite-element method [20] is popular due to its flexibility in handling arbitrary geometries and efficient discretization of fine geometrical details, but it involves eigenvalue solution, and scaling to three-dimensions can be problematic.

The FDTD method [21] is attractive due to its generality, ease of implementation, linear scaling in execution time with problem size, and ability to handle dispersive and nonlinear materials. FDTD often has the best performance when analyzing structures with three-dimensional material variation.

Previous work has implemented the compact FDTD (cFDTD) method using Maxwell's equations written in cylindrical coordinates [3]. Derivatives with respect to  $z$  can still be evaluated analytically, and the cross section of the geometry is represented in polar coordinates  $(r, \phi)$ . The cylindrical coordinates form of cFDTD has a number of advantages over the more common cartesian coordinates form for analyzing MOFs. Representing the cross section in polar coordinates more naturally conforms to the circular shape of the fiber geometry. This aids in reducing discretization errors at material boundaries as well as enabling a uniform distance between the computational boundaries and the structure under investigation. This uniform spacing can be set at the minimum distance to achieve accurate results, and there are no remaining regions in the domain corresponding to unnecessarily long distances between the boundary and the geometry. For example in cartesian coordinates FDTD, the extra space in the corners of the domain are essentially wasted domain space.

Another advantage of using cylindrical coordinates is the natural ability to implement looped boundary conditions for structures that posses periodicity in the azimuthal direction or discrete azimuthal invariance [3]. In these geometries only the periodic unit sector is required for analysis, and spatially looped boundary conditions can be enforced. For MOFs utilizing a triangular photonic crystal lattice in the cross section, this results in a reduction by a factor of six in the cross sectional domain size.

## 3. SUBGRIDDING

While cFDTD implemented in cylindrical coordinates has several advantages for analyzing MOFs, its performance suffers due to its inherent nonuniform grid spacing. In cylindrical coordinates, the cell size along the azimuthal ( $\phi$ ) direction increases as the radius increases according to  $\Delta s = i\Delta r \Delta \phi$  where  $i$  is the radial index,  $\Delta r$  is the radial discretization length and  $\Delta \phi$  is the azimuthal angular discretization. Even for uniform  $\Delta r$  and  $\Delta \phi$ , the actual FDTD cell size along  $\phi$  (which is  $\Delta s = i\Delta r \Delta \phi$ ) increases as  $i$  increases. This results in high resolution for small  $i$  and low resolution for large  $i$ . Figure 1(b) illustrates the grid resolution compensation strategy to be discussed below. If one considers only the grid region to the left of the coarse grid/fine grid boundary, this inherent grid nonuniformity can be seen.

Although the small resolution for small  $i$  would appear beneficial for resolving detailed geometry near  $r = 0$ , it can also over-resolve the geometry and introduce an unnecessarily small  $\Delta r \Delta \phi$  which

simultaneously causes an unattractive reduction in  $\Delta t$  due to the Courant stability condition

$$\Delta t < \frac{1}{c\sqrt{(\frac{1}{\Delta r})^2 + (\frac{2}{\Delta r \Delta \phi})^2 + (\frac{\beta}{2})^2}}. \quad (1)$$

Ideally a large  $\Delta t$  is sought so that steady state conditions can be reached in a minimum number of time-steps. This inherent non-uniformity in cell size for cylindrical coordinates FDTD motivates the development of techniques for controlling the cell size to compensate the inherent grid nonuniformity. This allows better resolution at large  $i$  and an increase of grid size near the origin so that  $\Delta t$  can be increased.

In order to improve the resolution at large radius, the grid spacing along  $\phi$  can be reduced as  $i$  increases. The result is a computational domain consisting of annular regions with different  $\Delta\phi$  values. The challenge is in handling the interface between these regions. Figure 1(b) illustrates the FDTD gridding scheme implemented in cylindrical coordinates investigated in this work. Both a coarse grid and a fine grid are displayed along with the interface between the two. In the example shown in Figure 1(b), the spatial resolution is improved at a given  $i$  by reducing the azimuthal angular discretization  $\Delta\phi$  by two. Assuming the fine grid represents the necessary grid resolution at a given radius for sufficiently accurate results, utilizing the subgrid approach depicted in Figure 1(b) reduces the number of grid points at smaller radius (in the coarse grid) by a factor of two. If there are an equal number of radial points in the coarse grid as there are in the fine grid, this results in a reduction by 1/4 of the total spatial grid points in the domain and an increase by two of the smallest stable time step. Total execution time is reduced to 3/8 that of a purely fine grid calculation. If more subgrids are included, the reduction in execution time improves. For example, with three interfaces between four regions with different  $\Delta\phi$ , execution times can be reduced by more than a factor of 8.

The spatially staggered arrangement associated with the Yee approach [22] makes interfacing course and fine grids challenging. In particular, the green arrows labeled by “interpolated fields needed at these radii” correspond to vector components of the magnetic field that must be inferred from neighboring values in order to obtain updated values of the electric field along the boundary. To infer the unknown magnetic field components, interpolation along the  $\phi$  direction is used. Linear, cubic, trigonometric and cubic spline interpolations are investigated. Linear interpolation assigns the average value of the two nearest neighboring values to the unknown field value. Cubic interpolation fits a third order polynomial to the four known field values closest to the unknown field value and estimates the unknown field value from this cubic polynomial. Cubic spline interpolation uses a cubic polynomial to interpolate but does so in such a way that the first derivative of the interpolating polynomial is smooth and the second derivative is continuous along the entire interpolation region [18]. Finally, trigonometric interpolation refers to using a truncated trigonometric Fourier series to estimate the unknown field values. This interpolation technique is motivated by observing that the discrete rotational invariance of the structure gives rise to Bloch’s theorem in the  $\phi$  direction which states that the field in this direction can be represented by the product of a complex exponential function and a Fourier series [3].

#### 4. RESULTS

Results for error in the frequency and propagation loss as a function of  $\beta a$  (where  $a$  is the distance between holes in the triangular lattice) when compared to an FDTD calculation run in which the entire geometry is discretized using the fine grid are shown in Figures 2(a) and (b).

Figure 2(a) shows that the subgridding introduces less than 1% error into the calculated propagating mode frequencies for a given  $\beta$  value and that cubic, trigonometric and cubic spline interpolations are all better than linear interpolation. This is consistent with the expectation that higher order interpolation methods will more accurately estimate unknown field values associated with a complicated and rapidly varying field.

Figure 2(b) shows that except for one data point corresponding to trigonometric interpolation at  $\beta a = 3.8$  the subgridding introduces less than 30% error into the calculated propagation loss as a function of  $\beta$ . Although the error in calculating propagation loss is significantly higher than that for propagation frequency, obtaining an accurate value for propagation loss is more sensitive to other variables such as the performance of the perfectly matched layer absorbing boundary conditions. For the propagation loss, it appears that overall the four interpolation methods investigated here perform similarly well with the linear interpolation method exhibiting slightly lower error for some

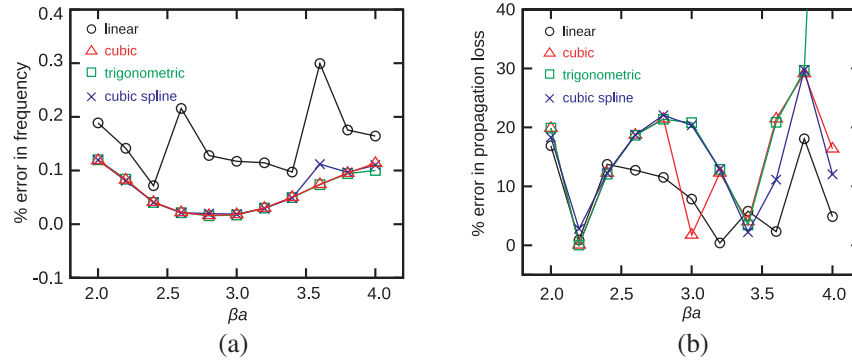


Figure 2: (a) Percent error in propagating frequencies between a uniform fine grid and a subgridded geometry utilizing various interpolation methods. (b) Percent error in propagation constant between a uniform fine grid and a subgridded geometry utilizing various interpolation methods.

$\beta$  values. That the linear interpolation method performs best is surprising, as higher order interpolation methods are expected to better estimate these complicated fields. It should be pointed out that the interpolation may cause charge or current build up at the interface associated with Gauss's laws for electric and magnetic fields. These charges and currents would effect the electromagnetic energy flow in and out of the fiber core and could effect the ensuing propagation constant.

## 5. CONCLUSION

A strategy for nonuniform grid compensation in cylindrical coordinates FDTD is proposed and evaluated. The technique utilizes concatenation of grids along the radial direction with different  $\Delta\phi$  values. At the interface between regions with different  $\Delta\phi$  interpolation of required but unknown field values is used. It is found that cubic, cubic spline and trigonometric interpolation result in the lowest error in estimating the propagation frequency, and that linear interpolation results in the lowest error in estimating the propagation loss. Using a single subgrid as illustrated in this work reduces the overall domain size by one fourth and increases the minimum  $\Delta t$  by two. Using several subgrids will result in significantly lower domain sizes and larger  $\Delta t$ .

## ACKNOWLEDGMENT

Funding is acknowledged from the College of Science and Technology Funds for Advancing Research at Central Michigan University.

## REFERENCES

- Chen, Y. and R. Mittra, "A highly efficient finite-difference time domain algorithm for analyzing axisymmetric waveguides," *Microwave and Optical Technology Letters*, Vol. 15, No. 4, 201–203, 1997.
- Dib, N., T. Weller, M. Scardelletti, and M. Imparato, "Analysis of cylindrical transmission lines with the finite-difference time-domain method," *IEEE Transactions on Microwave Theory and Transactions*, Vol. 47, No. 4, 509–512, 1999.
- Mock, A. and P. Trader, "Photonic crystal fiber analysis using cylindrical FDTD with Bloch boundary conditions," *PIERS Online*, Vol. 6, No. 8, 783–787, 2010.
- Kuang, W., J. R. Cao, T. Yang, S.-J. Choi, P.-T. Lee, J. D. O'Brien, and P. D. Dapkus, "Classification of modes in suspended-membrane, 19-missing-hole photonic-crystal microcavities," *Journal of the Optical Society of America B*, Vol. 22, No. 5, 1092–1099, 2005.
- Tawara, T., H. Kamada, Y.-H. Zhang, T. Tanabe, N. I. Cade, D. Ding, S. R. Johnson, H. Gotoh, E. Kuramochi, M. Notomi, and T. Sogawa, "Quality factor control and lasing characteristics of InAs/InGaAs quantum dots embedded in photonic-crystal nanocavities," *Optics Express*, Vol. 16, No. 8, 5199–5205, 2008.
- Fujita, M. and T. Baba, "Microgear laser," *Applied Physics Letters*, Vol. 80, No. 12, 2051–2053, 2002.
- Russell, P. S. J., "Photonic crystal fibers," *Science*, Vol. 299 358–362, 2003.
- Russell, P. S. J., "Photonic-crystal fibers," *IEEE Journal of Lightwave Technology*, Vol. 24, No. 12, 4729–4749, 2006.

9. Asi, A. and L. Shafai, "Dispersion analysis of anisotropic inhomogeneous waveguides using compact 2D-FDTD," *IEEE Electronics Letters*, Vol. 28, No. 15, 1451–1452, 1992.
10. Xiao, S., R. Vahldieck, and H. Jin, "Full-wave analysis of guided wave structures using a novel 2-D FDTD," *IEEE Microwave and Guided Wave Letters*, Vol. 2, No. 5, 165–167, 1992.
11. Xiao, S. and R. Vahldieck, "An efficient 2-D FDTD algorithm using real variables [guided wavestructure analysis]," *IEEE Microwave and Guided Wave Letters*, Vol. 3, No. 5, 127–129, 1993.
12. Qiu, M., "Analysis of guided modes in photonic crystal fibers using the finite-difference time-domain method," *Microwave and Optical Technology Letters*, Vol. 30, No. 5, 327–330, 2001.
13. Mock, A. and J. D. O'Brien, "Dependence of silicon-on-insulator waveguide loss on lower oxide cladding thickness," *Integrated Photonics and Nanophotonics Research and Applications Topical Meeting*, Boston, MA, USA, Jul. 2008.
14. Saitoh, K. and M. Koshiba, "Numerical modeling of photonic crystal fibers," *Journal of Lightwave Technology*, Vol. 23, No. 11, 3580–3590, 2005.
15. Birks, T. A., J. C. Knight, and P. S. J. Russell, "Endlessly single-mode photonic crystal fiber," *Optics Letters*, Vol. 22, No. 13, 961–963, 1997.
16. Ferrando, A., E. Silvestre, J. J. Miret, P. Andrés, and M. V. Andrés, "Vector description of higher-order modes in photonic crystal fibers," *Journal of the Optical Society of America A*, Vol. 17, No. 7, 1333–1340, 2000.
17. Zhu, Z. and T. G. Brown, "Full vectorial finite-difference analysis of microstructured optical fibers," *Optics Express*, Vol. 10, No. 17, 853–864, 2002.
18. Press, W. H., S. A. Teukolsky, W. T. Vetterling, and B. P. Flannery, *Numerical Recipes in C++*, Cambridge University Press, New York, 2003.
19. Monro, T. M., D. J. Richardson, N. G. R. Broderick, and P. J. Bennett, "Holey optical fibers: An efficient modal model," *Journal of Lightwave Technology*, Vol. 17, No. 6, 1093–1102, 1999.
20. Brechet, F., J. Marcou, D. Pagnoux, and P. Roy, "Complete analysis of the characteristics of propagation into photonic crystal fibers by the finite element method," *Optical Fiber Technology*, Vol. 6, 181–191, 2000.
21. Taflove, A. and S. C. Hagness, *Computational Electrodynamics*, Artech House, Massachusetts, 2000.
22. Yee, K. S., "Numerical solution of initial boundary value problems involving Maxwell's equations in isotropic media," *IEEE Transactions on Antennas and Propagation*, Vol. 14, No. 3, 302–307, 1966.

# Nonlinear Electromagnetics in Negative Index Metamaterials

A. K. Popov

University of Wisconsin-Stevens Point, USA

**Abstract**— The paper reviews several schemes of nonlinear-optical coupling between the ordinary and backward electromagnetic waves in negative-index metamaterials, which meet the requirements of phase matching. They are aimed at applications to compensating strong losses inherent to plasmonic metamaterials and to design of novel photonic devices for optical sensing and data processing. The outlined possibilities of implementation of originally strongly absorbing microscopic samples of plasmonic metal-dielectric composites for the remote all-optically tailoring of their transparency and reflectivity as well as the options for creating of unique ultracompact photonic sensing devices are demonstrated through numerical simulations. Different schemes of coherent energy transfer from strong control field to the negative-index signals described here present the approach to compensating losses in the plasmonic metamaterials alternative to that based on the population inversion. It turned out that similar extraordinary distributed-feedback nonlinear-optical propagation processes are possible through Raman scattering on optical phonons having negative dispersion and negative group velocity.

## 1. INTRODUCTION

Nanostuctured negative-index metamaterials (NIMs) form a novel class of artificial electromagnetic materials that promises revolutionary breakthroughs in photonics. Such metamaterials are expected to play a key role in the development of novel photonic microdevices and all-optical data processing chips. Significant progress has been achieved recently in the design of bulk, multilayered, negative-index, plasmonic slabs. The problem, however, is that these structures introduce strong losses inherent to metals that are difficult to avoid. Unlike ordinary materials, the energy flow and wave vector (phase velocity) are counter-directed in NIMs. Negative-index properties and, therefore, backwardness of electromagnetic waves are usually achievable only within a certain wavelength band. Metamaterials remain ordinary, positive index, outside such interval. This opens the opportunities of unique schemes of nonlinear-optical coupling between the ordinary and backward electromagnetic waves, which meet the requirements of the phase matching. It is because all wave vectors remain parallel, whereas some of the energy flows inside the metamaterial appear counter-directed. Such unusual nonlinear propagation processes exhibit extraordinary properties not achievable in ordinary nonlinear optical materials and not described in the literature [1–3]. The coupling schemes under consideration are also different to phase matching in crystals with periodically poled nonlinearity at the nanoscale [4]. This paper is to propose several phase-matched coupling schemes for ordinary and backward electromagnetic waves to present the analysis of the output properties for one of them in the context of their applications to compensating strong losses inherent to plasmonic metamaterials and to design novel photonic devices for optical sensing and data processing. Each of the schemes provides different distribution of the coupled fields (hot zones) across the originally strongly absorbing metamaterial slab. The outlined possibilities to implement originally strongly absorbing microscopic samples of plasmonic metal-dielectric composites for the remote all-optically tailoring of their transparency and reflectivity as well as the options for creating of unique ultracompact photonic sensing devices is demonstrated through numerical simulations. Different schemes of coherent energy transfer from strong control field to the negative-index signals described here present an approaches to compensating losses in NIMs alternative to that based on the population inversion.

## 2. COHERENT NONLINEAR-OPTICAL COUPLING OF ORDINARY AND BACKWARD ELECTROMAGNETIC WAVES: BASIC CONCEPT

An extraordinary electromagnetic property of the negative-index (NI) metamaterials (NIMs) stems from the fact that energy flow and phase velocity of electromagnetic waves become counter-directed inside the NIM slab. Such phenomenon of backwardness of electromagnetic waves does not exist in naturally occurring materials. The appearance of backward electromagnetic waves (BW) can be explained as follows. The direction of the wave-vector  $\mathbf{k}$  with respect to the energy flow (Poynting vector) depends on the signs of electrical permittivity  $\epsilon$  and magnetic permeability  $\mu$ :

$$\mathbf{S} = (c/4\pi)[\mathbf{E} \times \mathbf{H}] = (c^2\mathbf{k}/4\pi\omega\epsilon) H^2 = (c^2\mathbf{k}/4\pi\omega\mu) E^2. \quad (1)$$

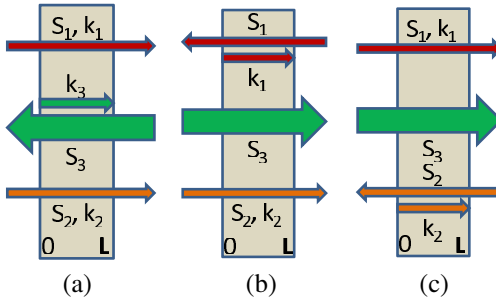


Figure 1: Proposed coupling schemes. (a)  $S_{1,2}$  and  $\mathbf{k}_{1,2}$  are energy fluxes and wavevectors for the ordinary, positive index signal and generated idler;  $S_3$  and  $\mathbf{k}_3$  — for the negative index control field. (b), (c) Alternative prospective schemes. (b) NLO chip amplifies signal travailing against the control beam [ $n(\omega_1) < 0$ ] and frequency upconverts it to the contrapropagating beam. (c) NLO chip shifts frequency and reflects back the signal traveling along the control beam [ $n(\omega_2) < 0$ ].

If  $\epsilon < 0$  and  $\mu < 0$ , refractive index becomes negative,  $n = -\sqrt{\mu\epsilon}$ , and vectors  $\mathbf{S}$  and  $\mathbf{k}$  become contradirected, which is in striking contrast with the electrodynamics of ordinary, positive index (PI) media (PIM). Hence, magnetic response at optical frequencies, including magnetic nonlinear polarization, opens new avenues in electromagnetics and for its numerous revolutionary breakthrough applications. Such property does not exist in naturally occurring materials but becomes achievable in the plasmonic metamaterials. Particularly, nonlinear-optical (NLO) propagation processes intrinsic to mixing of ordinary and backward electromagnetic waves possess unprecedented properties [1–3].

## 2.1. Phase Matching of Counter-propagating Waves: Possible Coupling Schemes

To explain basic principles underlying the proposal, consider nonlinear optical (NLO) coupling of ordinary and backward waves in the most simple case of continuous wave regime. Usually, negative index exist only inside a certain frequency band. The metamaterial remains ordinary, PI, outside that band. Figure 1 depict three possible options of phase matched NLO coupling of the ordinary and backward waves. Consider an example depicted in panel (a). Assume that the wave at  $\omega_1$  with the wave-vector  $\mathbf{k}_1$  directed along the  $z$ -axis is a PI ( $n_1 > 0$ ) signal. Usually it experiences strong absorption caused by metal inclusions. The medium is supposed to possess a quadratic nonlinearity  $\chi^{(2)}$  and is illuminated by the strong higher frequency control field at  $\omega_3$ , which falls into the NI domain. Due to the three-wave mixing (TWM) interaction, the control and the signal fields generate a difference-frequency idler at  $\omega_2 = \omega_3 - \omega_1$ , which is assumed to be a PI wave ( $n_2 > 0$ ). The idler, in cooperation with the control field, contributes back into the wave at  $\omega_1$  through the same type of TWM interaction and thus enables optical parametric amplification (OPA) at  $\omega_1$  by converting the energy of the control fields into the signal. In order to ensure effective energy conversion the induced traveling wave of nonlinear polarization of the medium and the coupled electromagnetic wave at the same frequency must be phase matched, i.e., to meet the requirement of  $\Delta\mathbf{k} = \mathbf{k}_3 - \mathbf{k}_2 - \mathbf{k}_1 = 0$ . Hence, all phase velocities (wave vectors) must be co-directed. Since  $n(\omega_3) < 0$ , the control field is a BW, i.e., its energy flow  $\mathbf{S}_3 = (c/4\pi)[\mathbf{E}_3 \times \mathbf{H}_3]$  appears directed against the  $z$ -axis. This allows to conveniently remotely interrogate the NLO converting chip and to actuate frequency up-conversion and amplification of signal directed towards the remote detector. Such signal can be, e.g., incoming far-infrared thermal radiation emitted by the object of interest, or signal that carries important spectral information about its chemical composition of the environment.

The research challenge is that such unprecedented NLO coupling scheme leads to changes in the set of coupled nonlinear propagation equations and boundary conditions compared to standard ones known from the literature. This, in turn, results in dramatic changes in their solutions and in multiparameter dependencies of the operational properties of the proposed nonlinear-optical photonic devices.

## 2.2. Equations for Slowly-varying Amplitudes of the Coupled Fields

It is convenient to introduce the slowly-varying effective amplitudes of the waves,  $a_{e,m,j}$ , and nonlinear coupling parameters,  $X_{e,m}$ , for both, the electric ( $e$ ) and magnetic ( $m$ ) types of quadratic

nonlinearity,  $\chi_{ej}^{(2)}$ , in the form:

$$a_{ej} = \sqrt{|\epsilon_j/k_j|} E_j, \quad X_{ej} = \sqrt{|k_1 k_2 / \epsilon_1 \epsilon_2|} 2\pi \chi_{ej}^{(2)}; \quad a_{mj} = \sqrt{|\mu_j/k_j|} H_j, \quad X_{mj} = \sqrt{|k_1 k_2 / \mu_1 \mu_2|} 2\pi \chi_{mj}^{(2)}.$$

The quantities  $|a_j|^2$  are proportional to the photon numbers in the energy fluxes. Equations for the amplitudes  $a_j$  are identical for the both types of the nonlinearities:

$$da_1/dz = iX_1 a_2^* a_3 \exp(i\Delta kz) - (\alpha_1/2)a_1, \quad (2)$$

$$da_3/dz = -iX_3 a_1 a_2 \exp(-i\Delta kz) + (\alpha_3/2)a_3. \quad (3)$$

Details can be found in Ref. [3]. We note the following *three fundamental differences* in Eq. (3) as compared with their counterpart in ordinary, PI materials. First, the sign with  $X_3$  is opposite to those with  $X_{1,2}$  because  $\epsilon_3 < 0$  and  $\mu_3 < 0$ . Second, the opposite sign appears with  $\alpha_3$  because the energy flow  $\mathbf{S}_3$  is against the  $z$ -axis. Third, the boundary conditions for the control field are defined at the opposite side of the sample as compared to the signal and idler because the energy flows  $\mathbf{S}_3$  and  $\mathbf{S}_{1,2}$  are counter-directed. Indeed, this leads to *dramatic changes* in in their solution and, consequently, in the propagation properties and in energy-exchange between the coupled waves in double domain PIM/NIM slab compared to those known from textbooks on nonlinear optics for their counterparts in ordinary materials.

### 2.3. Manley-Rowe Relations Extraordinary Spatial Behavior

For loss-free ( $\alpha_{1,2} = 0$ ), off-resonant ( $X_1 = X_2 = X_3 = X = X^*$ ) coupling, one readily derives the following Manley-Rowe relations with the aid of Eqs. (2) and (3):

$$d(|a_1|^2 - |a_2|^2)/dz = 0, \quad (4)$$

$$d(|a_3|^2 - |a_1|^2)/dz = 0, \quad d(|a_3|^2 - |a_2|^2)/dz = 0. \quad (5)$$

Equation (4) predicts that the difference of the numbers of photons  $\hbar\omega_1$  and  $\hbar\omega_2$  remains constant through the sample, which indicates their creation in pairs due to split of photons  $\hbar\omega_3$ . However, Eq. (5) predict that the differences of the numbers of photons  $\hbar\omega_1$  and  $\hbar\omega_3$  as well as of  $\hbar\omega_2$  and  $\hbar\omega_3$  *also remain constant* through the sample. This looks like breaking of energy conservation law and is in seemingly striking difference with the fact that the *sum* of the corresponding photon numbers is constant in the analogous case in a PIM. Actually such unusual dependencies stem from the fact that the waves propagate in the opposite direction. Consequently, *extraordinary distributions* of these fields across the slab and the dependence of their output values on the linear and nonlinear optical properties of the given NIM and on the input intensities of the coupled fields is expected, especially when conversion efficiency become large. Particularly, conversion rate is expected to grow across the slab with a different rate than in the ordinary medium at standard coupling geometry. Eq. (5) indicate unusual feedback, which provides such correlated depletion of the control field on one hand and growth of the signal and the idler on the other hand so that they difference must remain constant along the metaslab. Absorption would change such behavior which may strongly depend on the absorption dispersion and on the phase mismatch.

## 3. PROPERTIES OF THE NONLINEAR OPTICAL REFLECTOR AND AMPLIFIER

Analytical solution is not possible for the problem that underlies the concept of the proposed sensor. Figs. 2 and 3 display the results of numerical simulations for the model depicted in Fig. 1(a). Here,  $z$  is the length across the slab of thickness  $L$ ,  $T_3(z) = |a_3(z)/a_{3L}|^2$  and  $T_1(z) = |a_1(z)/a_{3L}|^2$  are transparency,  $\eta_2(z) = |a_2(z)/a_{3L}|^2$  is photon conversion efficiency,  $g = X a_3(L)$ ,  $X_{ej} = \sqrt{|k_1 k_2 / \epsilon_1 \epsilon_2|} 2\pi \chi_{ej}^{(2)}$ ,  $a_{3L} = a_3(L)$  is amplitude of the input control field. Absorption indices,  $\alpha_j$ , for the coupled field are indicated,  $\Delta k = 0$ . Fig. 2 illustrates the case of weak input signal so that the depletion of the control field due to the conversion becomes significant only in the vicinity of  $z = L$ . Figs. 2(a) and (b) show the possibility to achieve many orders amplification of the signal traveling against the control beam and its conversion to the frequency-shifted wave for the intensity of the income control field corresponding to  $gL \approx 15 \dots 20$ . Then the numbers of the output photons  $\hbar\omega_1$  and  $\hbar\omega_2$  make about 10% of that of the input contra-directed control field, which means amplification on the order of  $10^7$ . Fig. 3 demonstrates stronger energy conversion effect due to higher input intensity of the signal which, however, leads to lower overall amplification. Investigations show significant difference in the operational properties of sensors utilizing the scheme depicted in Fig. 1(a) and those shown in Figs. 1(b), (c).

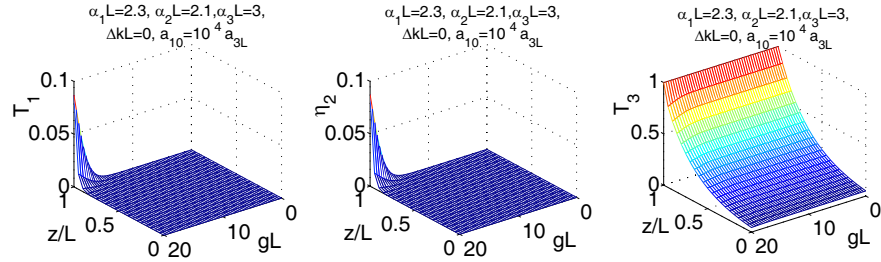


Figure 2: Distribution of the coupled fields across the sensor and output characteristics of the amplified transmitted and generated beams as well as of the depleted control field for the case of weak input signal  $a_{10} = 10^{-4} a_{3L}$ .

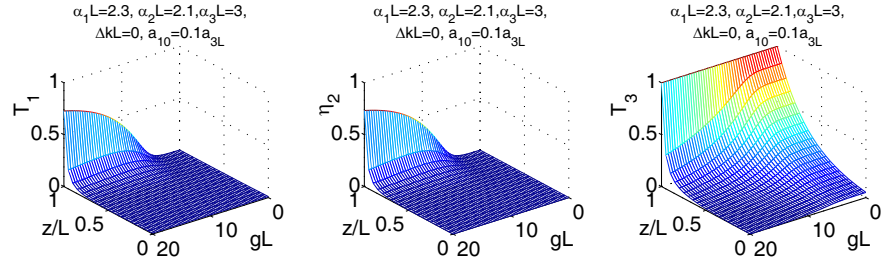


Figure 3: Distribution of the coupled fields across the metaslab, output characteristics of the amplified transmitted and generated beams and of the depleted control field for the case of strong input signal  $a_{10} = 0.1 a_{3L}$ .

### 3.1. Estimations

Estimations of characteristic parameters of sensor and control field based on the outlined simplified models predict that with  $\chi^{(2)} \sim 10^{-5} \div 10^{-6}$  ESU ( $\sim 10^3 \div 10^4$  pm/V), which is on the order of that for CdGeAs<sub>2</sub> crystals, the typical values of the parameter  $gL \sim 1 \dots 10$  required for amplification of the signals can be achieved for the slab thickness in the *microscopic* range and for the power of the control field in the kW range with focusing on the spot of the diameter about 50  $\mu\text{m}$ .

## 4. OPTICAL PHONONS AND DISTRIBUTED FEEDBACK

A different scheme of TWM of ordinary and backward waves (BW) has been proposed in [6]. It builds on stimulated Raman scattering (SRS), where two ordinary electromagnetic waves excite backward elastic vibrational wave in a crystal and TWM. The possibility of such BWs was predicted by L. I. Mandelstam in 1945 [5], who also pointed out that negative refraction is a general property of the BWs. The possibility to replace negative index composites with ordinary crystals and thus to simplify the experimental studies of unparallel properties of coherent NLO energy exchange between the ordinary and backward waves has been shown [6]. Extraordinary nonlinear propagation and output properties of the Stokes electromagnetic wave in one of two different coupling geometries, depicted in Fig. 4, both utilizing the backward elastic waves were investigated. Such unusual properties are in a striking contrast with those attributed to the counterparts in the standard schemes that build on the coupling of co-propagating photons and phonons. They are also different from the properties of the phase-matched mixing of optical and acoustic waves for the case of the latter has energy flux and wave vector directed against those of one of the optical waves. The revealed properties can be utilized for creation of optical switches, filters, amplifiers and cavity-free optical parametric oscillators based on ordinary NLO crystals without the requirement of periodically poling at the nanoscale [4].

The dispersion curve  $\omega(k)$  of phonons in the crystals containing more than one atom per unit cell has two branches: acoustic and optical. For the optical branch, the dispersion is negative, in the range from zero to the boundary of the first Brillouin's zone (Fig. 4) and the group velocity of optical phonons,  $\mathbf{v}_v^{gr}$ , is antiparallel with respect to its wave-vector,  $\mathbf{k}_v^{ph}$ , and phase velocity,  $\mathbf{v}_v^{ph}$ , because  $v_{gr} = \partial\omega(k)/\partial k < 0$ . Optical vibrations can be excited by the light waves due to the two-photon (Raman) scattering. The latter gives the ground to consider crystal as the analog of the medium with negative refractive index at the phonon frequency and to examine the processes of

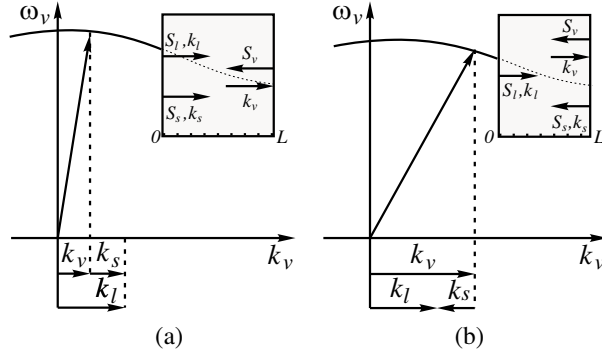


Figure 4: Negative dispersion of optical phonons and two phase matching options, (a) co-propagating, (b) contra-propagating fundamental, control, and stokes, signal, waves. Insets: relative directions of the energy flows and of the wave-vectors.

parametric interaction of the three waves, two of which are ordinary electromagnetic waves and the third is the wave of elastic vibrations with the directions of the energy flow and of the wave-vector opposite to each other.

## 5. CONCLUSION

Extraordinary propagation properties of three-wave mixing and coherent energy exchange between ordinary and backward electromagnetic waves are investigated and the applications to design of ultracompact photonic devices with unparallel function properties are discussed.

## ACKNOWLEDGMENT

Stimulating discussions with V. M. Shalaev and S. A. Myslivets and support of this work by the National Science Foundation under Grant No. ECCS-1028353 are greatly acknowledged.

## REFERENCES

- Shadrivov, I. V., A. A. Zharov, and Y. S. Kivshar, “Second-harmonic generation in nonlinear left-handed metamaterials,” *J. Opt. Soc. Am. B*, Vol. 23, 529–534, 2006.
- Popov, A. K. and V. M. Shalaev, “Compensating losses in negative-index metamaterials by optical parametric amplification,” *Opt. Lett.*, Vol. 31, 2169–2171, 2006.
- Popov, A. K., “Nonlinear optics of backward waves and extraordinary features of plasmonic nonlinear-optical microdevices,” *Eur. Phys. J. D*, Vol. 58, 263–274, 2010.
- Khurgin, J. B., “Mirrorless magic,” *Nat. Photonics*, Vol. 1, 446–448, 2007.
- Mandelstam, L. I., “Group velocity in a crystall lattice,” *ZhETF*, Vol. 15, 475–478, 1945.
- Slabko, V. V., S. A. Myslivets, M. I. Shalaev, and A. K. Popov, “Negative group velocity and three-wave mixing in dielectric crystals,” arXiv:1104.0891v1.

# Numerical Analyses of the Realization of the D'B' Boundary Condition for Planar Surfaces

Ari Sihvola and Ismo V. Lindell

Department of Radio Science and Engineering, School of Science and Technology  
Aalto University, Box 13000, FIN00076 AALTO, Espoo, FINLAND

**Abstract**— In this paper, a realization to synthesize the recently invented concept of a D'B' boundary is studied numerically. The idea behind the realization is to cover a DB boundary by a quarter-wave transformer with strongly uniaxial permittivity and permeability dyadics. In the numerical computations, the extreme parameters are approximated by finite values and the deviation of the behavior of the structure from that of an ideal D'B' boundary is evaluated. It turns out that when the axial constitutive parameters are large but not infinite, the performance degrades for grazing-incidence waves. On the other hand, when the DB boundary below the transforming layer is approximated by a material half space with very-low refractive index, the performance of the D'B' response suffers for wave spectrum close to the normal incidence.

## 1. INTRODUCTION

In electromagnetics, special attention has recently been paid to new boundary conditions. Among interesting novel sets of such electromagnetic boundaries are the so-called DB and D'B' boundaries [1]. At a DB boundary, the normal components of the electric and magnetic flux densities vanish [2, 3], whereas the condition at a planar D'B' boundary is that the normal derivatives of the normal components of these flux densities are zero. This is in contrast with “traditional” boundary conditions, like PEC (perfect electric conductor), PMC (perfect magnetic conductor), and impedance conditions [4], which restrict the freedom of the *tangential* field components.

While there are procedures to create a material realization for the DB boundary using various types of anisotropic and even bi-anisotropic medium structures [5], the realization of a D'B' boundary has turned out to be very difficult to achieve. However, in March 2011 the idea was put forward that making use of a DB boundary, using a strongly anisotropic layer with so-called waveguiding medium, the DB effect is transformed to a D'B' boundary condition [6]. In particular, the axial components (components along the normal to the planes in the structure) of both the permittivity and permeability dyadics have to grow towards infinity in this medium. A quarter-wave thickness of such a planar layer transforms the DB condition into D'B' for the whole spectrum of plane waves, regardless of their transversal wavenumbers.

In this presentation, this theoretical idea to synthesize the D'B' boundary is studied numerically. In particular, the non-ideality aspects are given attention, in other words the question how well a structure can approximate the D'B' behavior even if it is made of real materials that do not have extreme anisotropic parameter ratios.

## 2. REFLECTION CHARACTERISTICS OF A D'B' BOUNDARY

The procedure for checking that a waveguiding material structure works as a D'B' surface is to compute its response to incident plane waves with arbitrary polarization and incidence angle. Since it can be shown that the reflection eigenwaves for the D'B' boundary (and also for the DB boundary) are the TE and TM waves, it is sufficient to restrict the polarization of the incident wave to these two special polarizations. Furthermore, because it is known that the eigenwaves in a uniaxially anisotropic medium are also TE and TM polarized [8], also material structures that are uniaxial with respect to the normal of the boundary are suited for testing the material realizability of D'B' boundaries.

Assuming that the boundary is parallel to the  $xy$ -plane, with unit normal  $\mathbf{u}_z$ , the TE polarized wave is defined as  $\mathbf{u}_z \cdot \mathbf{E} = 0$ , and correspondingly the TM-polarization obeys  $\mathbf{u}_z \cdot \mathbf{H} = 0$ , with the notation of electric  $\mathbf{E}$  and magnetic  $\mathbf{H}$  fields.

Then the boundary conditions read

$$\text{DB boundary : } \begin{cases} \mathbf{u}_z \cdot \mathbf{D} = 0 \\ \mathbf{u}_z \cdot \mathbf{B} = 0 \end{cases} \quad (1)$$

with the electric  $\mathbf{D}$  and magnetic  $\mathbf{B}$  flux densities. For the same planar boundary, the D'B' conditions are

$$\text{D'B' boundary : } \begin{cases} \nabla \cdot (\mathbf{u}_z \mathbf{u}_z \cdot \mathbf{D}) = \partial_z D_z = 0 \\ \nabla \cdot (\mathbf{u}_z \mathbf{u}_z \cdot \mathbf{B}) = \partial_z B_z = 0 \end{cases} \quad (2)$$

where the  $z$ -components of the flux densities are  $D_z = \mathbf{u}_z \cdot \mathbf{D}$  and  $B_z = \mathbf{u}_z \cdot \mathbf{B}$ .

In fact, in addition to the fact that an incident TE wave is reflected as a TE wave and an incident TM wave is reflected as a TM wave for the D'B' boundary, the reflection characteristics are very particular. It turns out that D'B' works as PMC for TE-polarized incidence and as PEC for TM incidence.

Hence the eigenpolarizations of a DB and D'B' plane can be replaced by corresponding PEC and PMC planes. The essentials of this correspondence are condensed in the following Table [7]. Note there also the duality between the DB and D'B' on one hand, and the PEC and PMC on the other.

In the following, the idea is to study how well an approximative waveguiding material realization reproduces the D'B' behavior. The incident wave is assumed TE-polarized and the response is compared to the ideal PMC reflection coefficient, which is  $R = +1$ , for all incidence angles. Due to the duality between the electric and magnetic problems, the same results apply for the TM-polarized excitation, when the electric and magnetic material parameters of the waveguiding structure are interchanged.

### 3. D'B' BOUNDARY FROM AN IDEAL DB BOUNDARY

As mentioned above and shown in detail in [6], the D'B' boundary condition can be mimicked by a layered structure where a planar DB ground plane is covered by a “quarter-wavelength” layer of material according to Figure 1. This medium needs to be anisotropic in both permittivity and permeability such that the normal components are very large, resulting into a “waveguiding” mechanism. The thickness of the layer is  $d = \pi/(2k_t)$  with  $k_t = \omega\sqrt{\mu_t\epsilon_t}$ .

The D'B' boundary appears as a PMC boundary for a TE-polarized wave ( $\mathbf{u}_z \cdot \mathbf{E} = 0$ ) and as a PEC boundary for a TM-polarized wave ( $\mathbf{u}_z \cdot \mathbf{H} = 0$ ). Let us examine in the following how well

Table 1: Boundary conditions involving normal field components can be replaced by effective PEC and PMC conditions for fields with TE and TM polarizations. Note also that the PEC (= D'B) and PMC (= DB') boundaries are “cross-combinations” of the primed and non-primed restrictions for the normal components of D and B.

	TE	TM
DB	PEC	PMC
D'B'	PMC	PEC
DB'	PMC	PMC
D'B	PEC	PEC

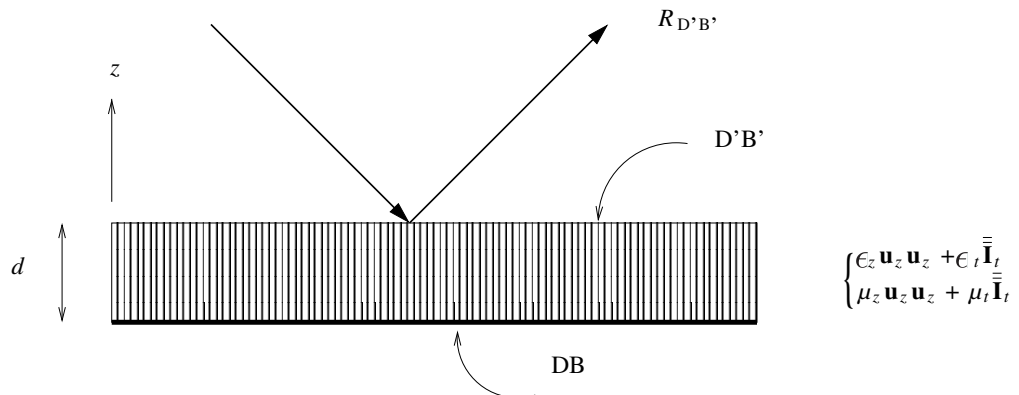


Figure 1: An extremely anisotropic layer transforms a DB-boundary into a D'B' boundary. The axial components  $\epsilon_z$  and  $\mu_z$  tend to infinity. The thickness of the layer is  $k_t d = \pi/2$ .

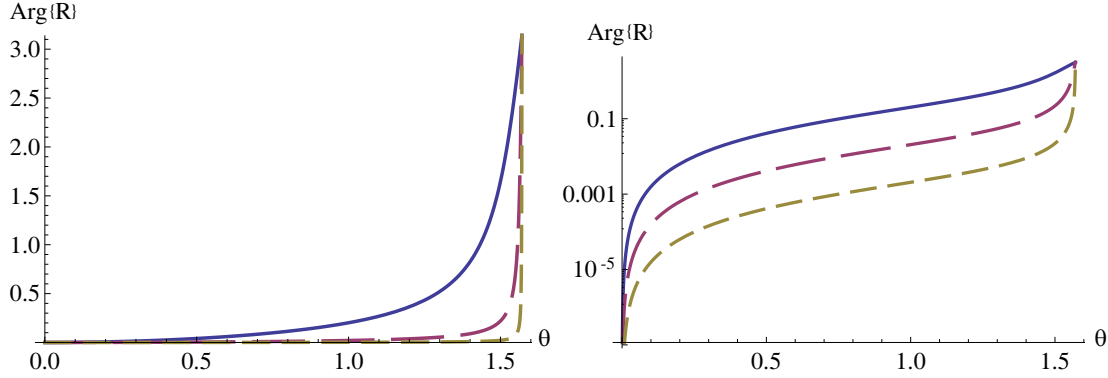


Figure 2: The phase of the TE reflection coefficient from a layer with increasing axial permeability, shown in linear and logarithmic scales, as a function of the incidence angle  $\theta$ . Solid line:  $\mu_z = 10\mu_0$ ; Long-dashed line:  $\mu_z = 100\mu_0$ ; short-dashed line:  $\mu_z = 1000\mu_0$ . The transversal relative permittivity and permeability are assumed to be unity.

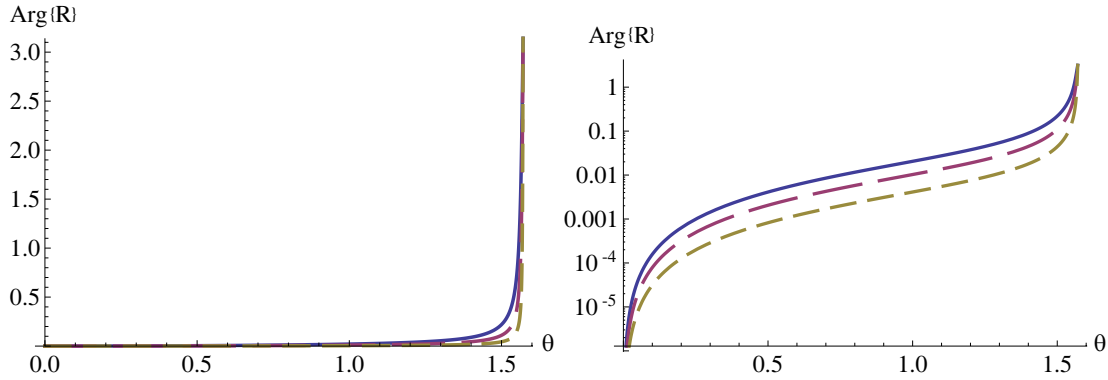


Figure 3: The phase of the TE reflection coefficient from a layer with increasing transversal parameter values, shown in linear and logarithmic scales, as a function of the incidence angle  $\theta$ . Solid line:  $\mu_t/\mu_0 = \epsilon_t/\epsilon_0 = 1$ ; Long-dashed line:  $\mu_t/\mu_0 = \epsilon_t/\epsilon_0 = 2$ ; short-dashed line:  $\mu_t/\mu_0 = \epsilon_t/\epsilon_0 = 5$ . The longitudinal permeability is  $\mu_z = 100\mu_0$  in all cases.

an approximative realization of the D'B' boundary works when the axial components are large but still finite.

The reflection coefficient for the electric field reads in this case as a function of the incidence angle  $\theta$ :

$$R_{TE} = \frac{-\beta\eta_0 + j\tan(\beta d)\mu_t\omega\cos\theta}{\beta\eta_0 + j\tan(\beta d)\mu_t\omega\cos\theta} \quad (3)$$

where  $\beta = k_t\sqrt{1 - \mu_0\epsilon_0 \sin^2\theta/(\epsilon_t\mu_z)}$  and the free-space wave impedance is  $\eta_0 = \sqrt{\mu_0/\epsilon_0}$ .

Figure 2 shows the phase of the E-field reflection coefficient from a boundary where an ideal DB boundary is covered by an anisotropic layer where the transversal material parameters are  $\epsilon_t/\epsilon_0 = \mu_t/\mu_0 = 1$  and the axial permeability parameter  $\mu_z$  grows. The figure shows that with increasing axial permeability parameter, the reflection approaches that of D'B'. Only the grazing incidence ( $\theta = \pi/2$ ) remains a singular limit.

For this TE-polarized incidence, the D'B' boundary should look as a PMC whose electric reflection is  $R = +1$  independently of the incidence angle. Hence the phase is zero over the whole range. The figure shows that with increasing axial permeability parameter, the reflection approaches that of D'B'. Only the grazing incidence ( $\theta = \pi/2$ ) remains a singular limit.

Figure 3 shows the effect of the transversal parameters, whose increase also helps in getting closer to D'B'. This is an interesting result since it means that to achieve an effective waveguiding layer, the axial parameters do not need to be very large *relative to the transversal parameters*, but essential is their magnitude to the free-space parameters. Note also that with increasing transversal parameters, the physical thickness of the layer decreases.

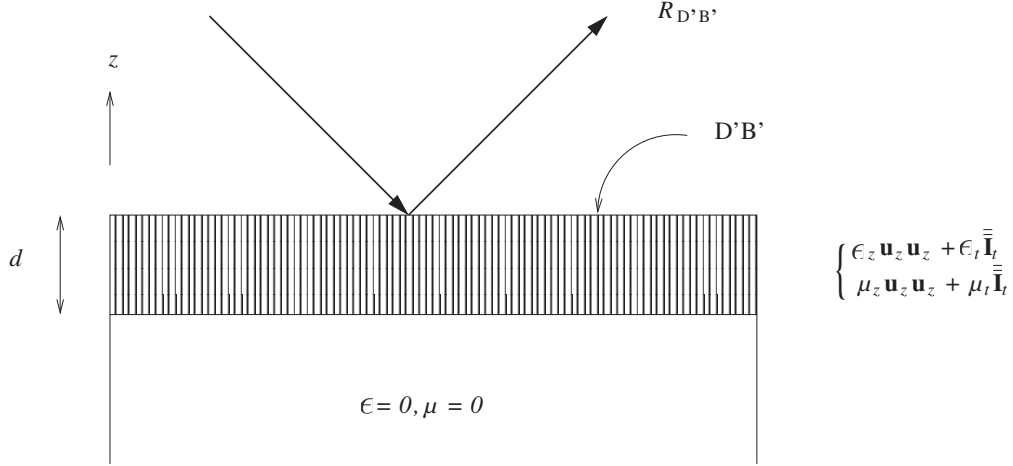


Figure 4: Like in Figure 1, but the bottom DB boundary is replaced by a zero-permittivity, zero-permeability medium.

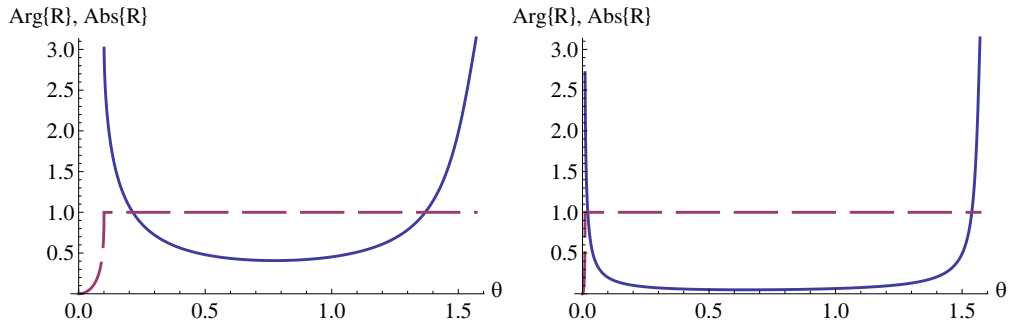


Figure 5: The phase (solid line) and amplitude (dashed line) of the TE reflection coefficient as a function of the incidence angle  $\theta$  when the parameters of the bottom layer in Figure 4 vary. Left panel:  $\epsilon/\epsilon_0 = \mu/\mu_0 = 0.1$ ; right panel:  $\epsilon/\epsilon_0 = \mu/\mu_0 = 0.01$ ; For the anisotropic layer, the longitudinal permeability is  $\mu_z = 100\mu_0$  in all cases, and the transversal relative permittivity and permeability are assumed to be unity.

In these examples, only the TE incidence was analyzed. The TM-case is dual to this one: the curves are exactly the same — for the magnetic field reflection coefficient — when the axial permittivity grows. The results can be directly applied by replacing  $\mu_z/\mu_0$  by  $\epsilon_z/\epsilon_0$  in the figures.

#### 4. FULL-MATERIAL REALIZATION OF THE D'B' BOUNDARY

How, then, to realize the DB boundary on the bottom of the waveguiding layer? As has been shown in [3], a medium with vanishing permittivity and permeability produces the correct boundary conditions (in fact, it suffices that the components of the permittivity and permeability normal to the boundary vanish). This is shown in Figure 4.

But it is difficult to achieve vanishing permittivity and permeability. Figure 5 shows how the small but finite values of the bottom medium affect the D'B' performance of the top surface.

From the figure we can observe that, of course, the reflection is no longer that of PMC if the bottom medium parameters start to grow. In particular, close to the normal incidence, there appears a gap where the structure let part of the incident energy to be transmitted. This is a “filtering effect” similar to the one discussed in [3].

Note that in the above computations, for this TE excitation, the axial permittivity  $E_z$  has no effect. The waveguiding phenomenon is forced by the large value of the axial permeability  $\mu_z$ .

#### 5. CONCLUSIONS

Numerical tests were carried out on the performance of the waveguiding realization of the recently [6] introduced idea to fabricate a planar D'B' boundary using a waveguiding structure. It was shown that with increasing values of the axial permittivity and permeability, the structure converges to D'B'. The most problematic range is grazing incidence. The increase of the transversal parameters

also helps in mimicking D'B': for example for the values of 10 for the relative transversal parameters and 100 for the axial ones, the phase angle is less than 0.06 (around 3 degrees) for all incidence angles less than 85°. If the DB layer on the bottom of the waveguiding structure is realized by an isotropic low-permittivity, low-permeability medium, the structure also works well as D'B' when these parameters approach zero. The effect that this non-ideality causes is that close to *normal* incidence, a “filtering” phenomenon takes place: the structure is no longer a perfect reflector.

## REFERENCES

1. Lindell, I. V., H. Wallén, and A. H. Sihvola, “General electromagnetic boundary conditions involving normal field components,” *IEEE Antennas and Wireless Propagation Letters*, Vol. 8, No. 16, 877–880, 2009.
2. Rumsey, V. H., “Some new forms of Huygens’ principle,” *IRE Transactions on Antennas and Propagation*, Vol. 7, No. 5, S103–S116, December 1959.
3. Lindell, I. V. and A. H. Sihvola, “Zero-Axial-Parameter (ZAP) medium sheet,” *Progress In Electromagnetics Research*, Vol. 89, 213–224, 2009.
4. Lindell, I. V., *Methods in Electromagnetic Field Analysis*, 2nd Edition, Oxford University Press, 2005.
5. Lindell, I. V. and A. H. Sihvola, “Electromagnetic boundary and its realization with anisotropic metamaterial,” *Physical Review E (Statistical, Nonlinear, and Soft Matter Physics)*, Vol. 79, No. 2, 026604, 2009.
6. Lindell, I. V., A. Sihvola, L. Bergamin, and A. Favaro, “Realization of the D'B' boundary condition,” *IEEE Antennas and Wireless Propagation Letters*, submitted for publication, 2011. Also ArXiV:1103.3931v1, March 2011.
7. Lindell, I. V. and A. Sihvola, “Electromagnetic boundary conditions defined in terms of normal field components,” *Trans. IEEE Antennas Propag.*, Vol. 58, No. 4, 1128–1135, April 2010.
8. Chen, H. C., *Theory of Electromagnetic Waves*, McGraw-Hill, New York, 1983.

# Raindrop Size Distribution Model for the Prediction of Rain Attenuation in Durban

P. Owolawi

Department of Electrical Engineering, Mangosuthu University of Technology  
Umlazi, Kwazulu-Natal, South Africa

**Abstract**— The paper is focused on the modeling of raindrop size distribution in Durban, South Africa. The maximum likelihood estimator approach is employed with lognormal distribution to model the dropsize distribution for Durban. The raindrop size is classified into two regimes based on the available data. The goodness-of-fit method (Kolmogorov-Smirnov test (K-test)) is then employed to optimize the selected model for different rain rate regime. The results are compared with the existing models such as the work done in West-Africa, Europe and Asia. The proposed South Africa model seems appropriate for the region to estimate rain attenuation both in terrestrial and satellite links.

## 1. INTRODUCTION

The development of complex radio access networks has resulted in the increase of spectrum occupancy and demand for higher bandwidths; hence it is imperative to employ the advantages of higher frequencies, which are capable of supporting these demands. The obvious candidates are microwave and millimeter bands. The advantages offered by microwave and millimeter waves have attracted immense interest from academia and the communications industry. The main characteristics of both waves include short wavelength (hence small components), large bandwidth, and frequency re-use. An electromagnetic wave propagating through a region containing raindrops suffers two attenuating effects: one is absorption through which part of its energy is absorbed by the raindrops and transformed into heat; and the other is scattering where part of energy is scattered in all directions. The calculation of these two attenuating mechanisms is based on the understanding of the characteristics of raindrops.

The best known raindrop size distribution model is Laws and Parsons [1], which was adopted by the International Telecommunication Union (ITU-R) for the calculation of specific attenuation due to rain. Marshall and Palmer [2] determined raindrop density by analytical method and further extended to other classes of rain type by Joss et al. [3]. Most of the contributors used temperate data to model the DSD which may lead to overestimation of rain attenuation as confirmed by several authors who had carried out measurement in some part of the world [4–6] and compared their results with the temperate counterparts.

In southern part of Africa, less work has been done in this area and need proper attention because of its mixed climatic characteristics that describe most of the southern African regions. Furthermore, in the Southern Africa the advancement in the area of telecommunication at higher frequencies especially satellite communication which operates at bands that are impaired by hydrometeor effects. This paper aims to solve this problem by presenting the results of raindrop size distribution model measured in Durban, South Africa. The results will be useful for telecommunication systems designers in estimating rain attenuation in the region.

## 2. STATISTICAL THEORY OF DSD MODELLING FOR DURBAN

Earlier techniques used in modelling raindrop size distribution seem to have begun with fits to the average drop distributions measured at single rain rates. Most of these fits were applied directly to the drop size distribution data as by Marshall and Palmer [2]. In order to improve the modelling approach and results, there is need to employ a systematic method such as moment and maximum likelihood techniques to estimate modelling parameters. Ajayi and Olsen [4] used the method of moments to estimate modelling parameters for the tropical region of West-Africa while Barclay et al. [7] considered the maximum likelihood method for the Australia. In this paper, the maximum likelihood approach is considered for Durban raindrop size distribution model. The estimator method is then applied to the three-parameter lognormal distribution.

Measured raindrop size distribution can be approximated as the product of total number of drops of all size  $N_T(D)$  and probability density function of lognormal distribution. In this work,

probability density function (pdf) of three-parameter lognormal distribution is used and expressed as:

$$N(D) = N_T(D) \times \text{pdf}(D; \gamma, \mu, \sigma) \quad (1)$$

where random variable mean drop diameter  $D$  is said to have a three-parameter lognormal distribution if the random variable  $Y = \ln(D - \gamma)$ , where  $D$  is greater than  $\gamma$ , is normally distributed  $(\mu, \sigma^2)$ , and  $\sigma$  is considered to be greater than zero. The probability density function of three-parameter lognormal distribution is then given by Pan et al. [8] as:

$$\text{pdf}(D; \gamma, \mu, \sigma) = \frac{1}{\sigma \sqrt{2\pi(D-\gamma)}} \exp \frac{-1}{2\sigma^2} [\ln(D - \gamma) - \mu]^2 \quad \gamma < D < \infty \quad \sigma > 0 \quad (2)$$

and Equation (2) will be zero if the condition in the equation is not met. Parameter  $\sigma^2$  is the variance of  $Y$ ; it is the shape parameter of  $D$  and  $\mu$  is the mean of  $Y$ .

Cohen et al. [9] define the likelihood function for a random sample of drop size distribution as a function of diameter with size  $n$  with  $\text{pdf}(D; \gamma, \mu, \sigma)$  (2) as:

$$L(D_1, \dots, D_n; \gamma, \mu, \sigma^2) = (2\pi\sigma^2)^{-n/2} \cdot \exp \left\{ - \sum_1^n [\ln(D_i - \gamma) - \mu]^2 / 2\sigma^2 \right\} \cdot \prod_1^n (D_i - \gamma)^{-1} \quad (3)$$

Adopting partial differential of logarithm of Equation (3) and equating to zero, results in the following maximum likelihood estimation (MLE) equations:

$$\begin{aligned} \frac{\partial \ln L}{\partial \mu} &= \frac{1}{\sigma^2} \sum_1^n [\ln(D_i - \gamma) - \mu] = 0 \\ \frac{\partial \ln L}{\partial \sigma} &= \frac{n}{\sigma} + \frac{1}{\sigma^3} \sum_1^n [\ln(D_i - \gamma) - \mu]^2 = 0 \\ \frac{\partial \ln L}{\partial \gamma} &= \frac{1}{\sigma^2} \sum_1^n \frac{[\ln(D_i - \gamma) - \mu]}{(D_i - \gamma)} + \sum_1^n (D_i - \gamma)^{-1} = 0 \end{aligned} \quad (4)$$

By elimination,  $\sigma^2$  and  $\mu$  are eliminated from Equation (4), the resulting residual part of the equation as a function of  $\gamma$  becomes:

$$\lambda(\gamma) = \left[ \sum_1^n (D_i - \gamma)^{-1} \right] \left[ \sum_1^n \ln(D_i - \gamma) - \sum_1^n \ln^2(D_i - \gamma) + (1/n) \left( \sum_1^n \ln(D_i - \gamma) \right)^2 \right] - n \sum_1^n \frac{\ln(D_i - \gamma)}{(D_i - \gamma)} = 0 \quad (5)$$

From Equation (4),  $\hat{\mu}$  and  $\hat{\sigma}^2$  are estimated as:

$$\begin{aligned} \hat{\mu} &= (1/n) \sum_1^n \ln(D_i - \hat{\gamma}), \\ \hat{\sigma}^2 &= (1/n) \sum_1^n \ln^2(D_i - \hat{\gamma}) - \left[ (1/n) \sum_1^n \ln(D_i - \hat{\gamma}) \right]^2 \end{aligned} \quad (6)$$

In order to provide a solution for  $\gamma$  in Equation (5), only admissible roots for which  $\gamma < D_1$  are considered. A standard iterative method of Newton-Raphson approximation method is adopted for solving Equation (5) and thus,  $\hat{\gamma}$  is estimated.

Table 1: Classification of  $N(D)$  based on rain rate regimes.

Rain Type	Diameter Range (mm)
Regime one	$0 < R \leq 20$
Regime two	$20 \leq R \leq 100$

### 3. DROPSIZE DISTRIBUTION MEASUREMENT IN DURBAN

In recent years, the introduction of advanced measurement tools has improved modelling techniques and thus more reliable models have been developed. Raindrop size distribution data used in this study was collected with a Joss and Waldvogel distrometer (JWD), specifically RD-80. The equipment comprises: a sensor, which is the outdoor unit, as well as a processor and computer unit which are indoor. RD-80 consists of electromechanical sensors which convert mechanical momentum of falling drops into electrical pulses. The distrometer has  $50\text{ cm}^2$  of sampling area with an accuracy of 5%. It collects raindrop sizes ranging between 0.3 mm to 5.3 mm in diameter with 20 bins or channels of diameter classes. The equipment is placed at latitude  $30^{\circ}58'E$ , longitude  $29^{\circ}52'S$ , and altitude of 139.7 m at the School of Electrical, Electronics and Computer Engineering in the University of KwaZulu-Natal, Howard College, Durban. In the present study the distrometer was installed in December 2008 and commenced full operation in January 2009 till now, with a sampling interval integrated over one minute. In the analysis, the measured data is classified using drop diameter tabulation according to Waldvogel [10], and rain rate regimes according to Timothy et al. [6]. The latter method of classification is adopted in this study. Table 1 summarizes the classifications using diameter as presented by Timothy et al. [6].

The database used in this study consists of a year pool of data with 125 different rain events spread over 6,000 minutes of sampling time. The data sampling months are December 2008 to December 2009, although there were missing events in some months when samples were not recorded by the distrometer data logger. Figure 1 shows a sample profile of total  $N_T(D)$  for all analyzed events at logarithmic scale. The peak of total  $N_T(D)$  recorded was at profile of  $2292\text{ mm}^{-3}$ .

In modelling DSD for Durban, two regimes of DSD evolution were used, which are based on rain rate above and below 20 mm/hr. Three-parameter lognormal probability density function and estimates of its parameters are obtained using MLE as explained using Equations (1) to (6). The MLE method is used to construct estimates of parameters that match the probability density function of lognormal distribution. Forty DSD samples are considered for this work, twenty-four for DSD regime of rain rate lower than 20 mm/hr and sixteen for rain rate above 20 mm/hr. In the

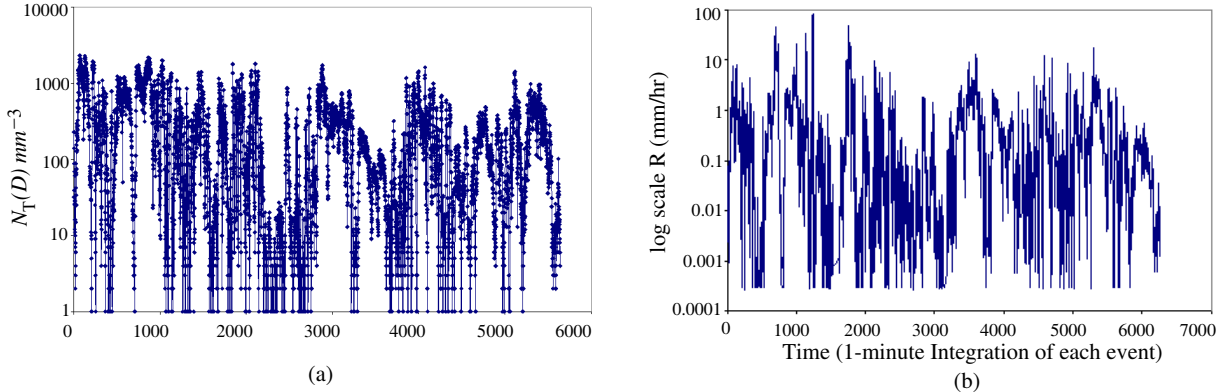


Figure 1: (a) Profile of total  $N_T(D)$ . (b) Profile log of rain rate against time.

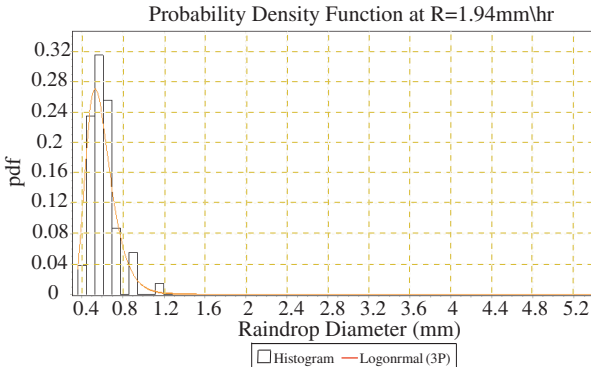


Figure 2: PDF on  $N(D)$  at  $R = 1.94\text{ mm}/\text{hr}$ .

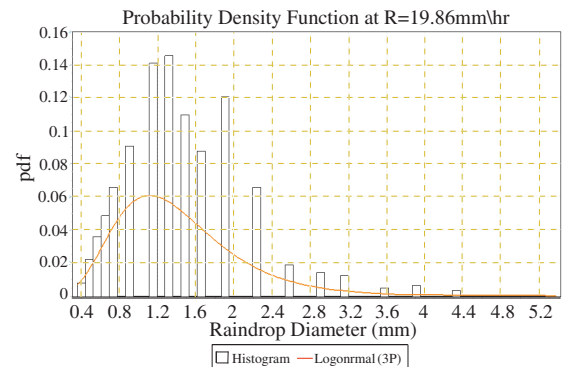


Figure 3: PDF on  $N(D)$  at  $R = 19.86\text{ mm}/\text{hr}$ .

first regime of DSD where rain rate is less than 20 mm/hr, Figure 2 shows one of the samples while Figure 3 represent the second DSD regime where rain rate is greater than 20 mm/hr.

The pdf of regimes with less than 20 mm/hr rain rate show that over 67% of drops fall within diameter range of 0.5 mm and 0.9 mm, while the rain rate regime greater than 20 mm/hr shared 45% of peak drops between 0.5 mm and 0.8 mm, and 20% of remaining peaks were found between 0.9 mm and 2 mm.

In order to see the degree of discrepancy of the chosen estimator with respect to probability density function of the data, a goodness-of-fit test is used to carry out the analysis. In this work, Kolmogorov-Smirnov test (K-test) is chosen because the experimental sample size is small (20 data points) and this is the strength of the K-test over Chi-square whose accuracy depends on large sample size. Press et al. [11] and Massey [12] explain the K-test as a comparison between vertical difference of empirical distribution function (ecdf) and theoretical distribution function (cdf). The empirical cdf is given as:

$$f_n(x_i) = \frac{1}{n} \cdot [\text{number of observations} \leq x] \quad (7)$$

on the vertical difference between the theoretical and experimental cumulative distribution functions. The K-test is mathematically expressed as:

$$D = \max_{1 \leq i \leq n} \text{absolute}(F(x_i) - F_n(x_i)) \quad (8)$$

where  $x_i \dots x_n$  is a random sample cumulative distribution function for either ecdf or cdf.

The hypothesis regarding the distribution under test is rejected provided that test statistics  $D$  in Equation (8) is greater than the critical value as shown in the K-test table. A significance level of 0.05 (5%) is chosen most of the time and sometimes in some other important industrial applications a lower significance level is considered. In this study, 5% significant level is used. Table 2 gives a summary of the K-test with remarks at their various classes of DSD regimes. The table confirms

Table 2: Kolmogorov-smirnov goodness-of-fit test for the DSD modelling.

Classifications Based on two Regimes (mm/hr)	Critical value at 5% significance level	Hypothesis Accepted	Classifications Based on two Regimes (mm/hr)	Critical value at 5% significance level	Hypothesis Accepted
1.94	0.15896	Yes	20.50	0.09522	Yes
2.00	0.17526	Yes	25.32	0.10822	Yes
2.93	0.1362	Yes	34.02	0.0916	Yes
3.08	0.14981	Yes	35.24	0.0777	Yes
3.92	0.16883	Yes	41.90	0.10911	Yes
4.12	0.17859	Yes	46.32	0.08596	Yes
4.15	0.17859	Yes	57.17	0.10445	Yes
5.96	0.13681	Yes	59.33	0.12822	Yes
6.11	0.14734	Yes	61.74	0.10072	Yes
6.73	0.13527	Yes	62.42	0.11006	Yes
6.98	0.15192	Yes	64.65	0.10661	Yes
7.21	0.13527	Yes	64.79	0.10117	Yes
8.36	0.15134	Yes	69.08	0.12026	Yes
8.93	0.12391	Yes	71.07	0.0873	Yes
9.00	0.12078	Yes	77.70	0.08279	Yes
9.79	0.1448	Yes	84.76	0.09737	Yes
11.59	0.14949	Yes			
12.86	0.13451	Yes			
15.02	0.13035	Yes			
16.36	0.12693	Yes			
17.92	0.09455	Yes			
18.26	0.13073	Yes			
19.89	0.1002	Yes			

Sample Size = 20 Channels  
Significant level of 5% = 0.29408

the suitability of lognormal distribution and MLE parameters to be appropriate for describing DSD modelling for Durban. It is noted that at all the chosen regimes, the entire hypotheses were accepted for the MLE estimators.

#### 4. DROPSIZE DISTRIBUTION MEASUREMENT IN DURBAN

Raindrop size distributions have been achieved using the three-parameter lognormal distributions. The parameter  $N_T(D)$  is modeled primarily from the average raindrop data. The results presented in Figures 4(a) and 4(b) are variations of total  $N_T(D)$ , with rain rate obtained at Durban for the two rain rate regimes. The least square regression technique is then applied and their respective power law coefficients are obtained as shown in Equation (9).

$$\begin{aligned} N_T(D) &= 284 R^{0.744} & 1.94 \text{ mm/hr} < R \leq 20.0 \text{ mm/hr} \\ N_T(D) &= 63 R^{0.706} & 20.0 \text{ mm/hr} < R \leq 100.0 \text{ mm/hr} \end{aligned} \quad (9)$$

In the sample for lower rain rate, it is observed that the power fit curve is most influenced by many data points. Rain rates higher than 20 mm/hr are noted to be best represented by the power law; thus the classifications for this power law fit starts for point rain rate of 1.94 mm/hr. In the analysis, 24 selected lower rain rate data points were considered in order to get a reasonable power fit. The square of correlation coefficient for the lower rain rate samples is 0.955, which is reasonable for a good fit. In the case of higher rain rate, the power fit is reasonably accurate and this reflects in the square of correlation coefficient of 0.975.

The resulting parameters  $\mu$ ,  $\sigma^2$  and  $\gamma$  are plotted in Figures 5 to 7 for the two classes of rain rate regimes. Examining Figure 5, the scatter data points are wider apart as rain rate increases. This may be as a result of an internal instability in the raindrops as variation of diameter increases. The square correlation coefficients testify to this: with the lower rain rate, the correlation is 0.4974, while at higher rain rate it gives 0.3426. The following relations are obtained for the mean of the two rain rate regimes:

$$\begin{aligned} \mu &= -1.3652 + 0.6531 \ln(R) & 1.94 \text{ mm/hr} < R \leq 20.0 \text{ mm/hr} \\ \mu &= -0.9663 + 0.4062 \ln(R) & 20.0 \text{ mm/hr} < R \leq 100.0 \text{ mm/hr} \end{aligned} \quad (10)$$

The two parameters  $\sigma^2$  and  $\gamma$  also depend on rain rate and are given as follows for the two regimes of DSD:

$$\begin{aligned} \sigma^2 &= 0.0954 - 0.00121 \ln(R) & 1.94 \text{ mm/hr} < R \leq 20.0 \text{ mm/hr} \\ \sigma^2 &= 0.9486 - 0.2035 \ln(R) & 20.0 \text{ mm/hr} < R \leq 100.0 \text{ mm/hr} \end{aligned} \quad (11)$$

and,

$$\begin{aligned} \gamma &= 0.3345 - 0.2891 \ln(R) & 1.94 \text{ mm/hr} < R \leq 20.0 \text{ mm/hr} \\ \gamma &= 0.1808 - 0.1283 \ln(R) & 20.0 \text{ mm/hr} < R \leq 100.0 \text{ mm/hr} \end{aligned} \quad (12)$$

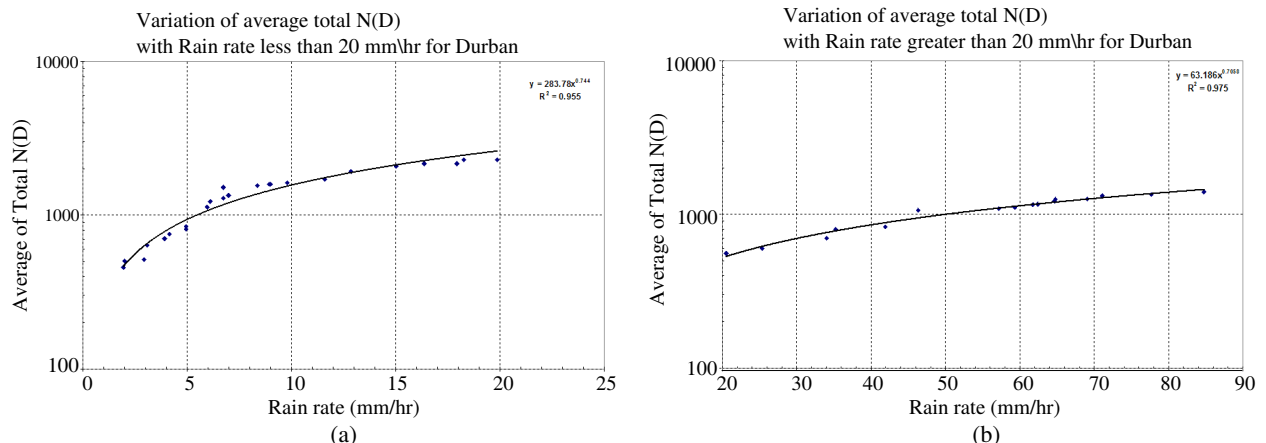
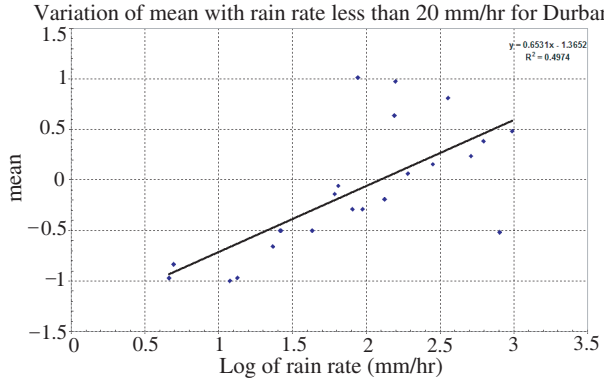
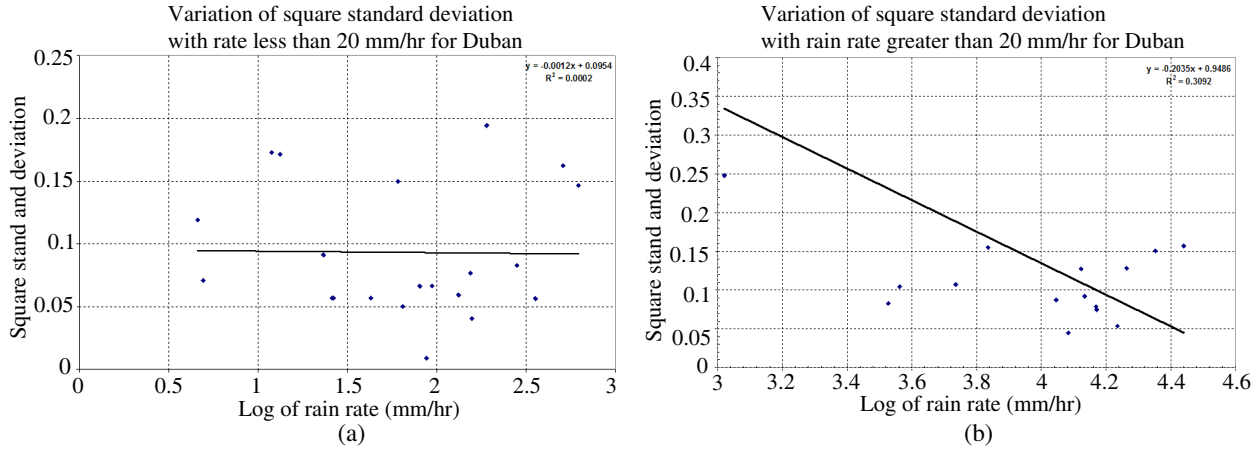


Figure 4: (a) Variation of  $N_T(D) \text{ m}^{-3} \text{ mm}^{-1}$  rate with rain rate less than 20 mm/hr for Durban, (b) variation of  $N_T(D) \text{ m}^{-3} \text{ mm}^{-1}$  with rain rate with rain rate less than 20 mm/hr for Durban greater than 20 mm/hr for Durban.

Figure 5: Variation of mean  $\mu$  mm with log of rain rate less than 20 mm/hr for Durban.Figure 6: (a) Variation of  $\sigma^2$  mm with log of rain rate with log of rain rate greater than 20 mm/hr for Durban, (b) Variation of mean  $\sigma^2$  mm with log of rain rate greater than 20 mm/hr for Durban.

## 5. SELF-CONSISTENCY (SC) OF PROPOSED DSD

The method proposed is validated by comparing the observed rain rates with computed ones using the DSD model, and Gunn and Kinnzer terminal velocity. Self-consistency of the model is determined by the degree of departure from unity of coefficient ratio of the observed to estimated rain rate. The coefficients of self-consistency (*SC*) is computed for all selected rain rates starting from 1.94 mm/hr to 84.76 mm/hr. The minimum coefficient of *SC* considered for regime of rain rate less than 20 mm/hr falls within 12% of unity, while for the regime greater than 20 mm/hr falls within 18% of unity. The expressions for self consistency for the two regimes of rain rate are derived using second order polynomials, and expressed as:

$$\begin{aligned} \text{Normalized}(R) &= 1.2853 - 0.2169X + 0.0082X^2 & 0 < R \leq 20 \text{ mm/hr} \\ \text{Normalized}(R) &= 0.0345 - 3 \times 10^{-3}X + 3 \times 10^{-6}X^2 & 20 < R \leq 100 \text{ mm/hr} \end{aligned} \quad (13)$$

Here  $X = \ln(R)$ .

## 6. COMPARISON OF PROPOSED MODEL WITH EXISTING MODELS

Comparison of proposed models for South Africa is tested against its counterparts from other regions using the Root Mean Square Error (RMSE) method. Figure 8 shows sample of the comparison between the proposed model and other raindrop size distribution models as describe in [13]. RMSE error is calculated for all the compared models by using the following formula::

$$\text{RMSE} = \sqrt{\sum_{i=1}^n \frac{[\text{Measured } N(D_i) - \text{Modeled } N(D_i)]^2}{n}} \quad (14)$$

where,  $N(D_i)$  is raindrop size distribution at different diameter sizes and  $n$  is the number of channels considered. In the overall analysis, the RMSE differences are a bit large for the compared models

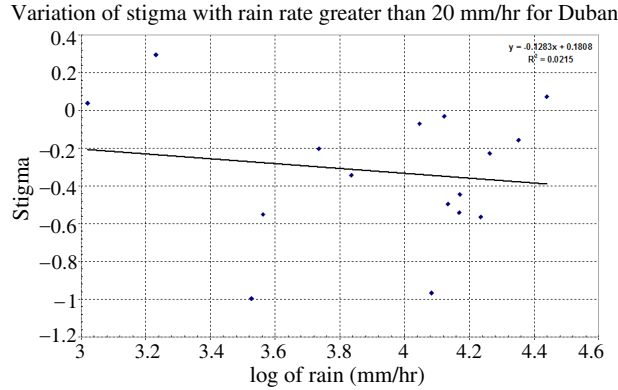


Figure 7: Variation of  $\gamma$  with log of rain rate greater than 20 mm/hr for Durban.

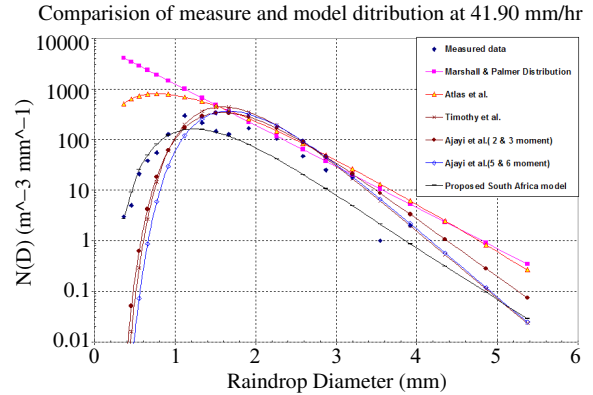


Figure 8: Comparison of measured, proposed and other existing models of  $N(D)$  at  $R = 41.90$  mm/hr.

but the proposed model shows lower values of RMSE between the proposed model and measured DSD. The performance analysis using RMSE at region of rain rate less than 20 mm/hr confirms that the proposed model performs better in all fifteen spectra of DSD samples. The average minimum RMSE is found with proposed model with value of 51.19 while the lowest RMSE is associated with the Marshall and Palmer model [2]. The best performances based on RMSE are rated in ascending order as follows [13]: Marshall and Palmer, Atlas et al., Timothy et al., Ajayi et al., and the proposed South Africa model.

In the case of regime of rain rate greater than 20 mm/hr, the average minimum RMSE is obtained in the proposed model with value of 27.23 and the least is found with Marshall and Palmer. The performance based on RMSE is presented in ascending order as followings: Marshall and Palmer, Atlas et al., Timothy, Ajayi et al., and the proposed model.

## 7. CONCLUSION

The purpose of this paper was to present modelling of raindrop size distribution. The raindrop size distribution spectra showed that the major part of the drop density falls within the 0.3 mm and 4.0 mm diameter range. Using the maximum likelihood regression method on the collected data, the three-parameter lognormal distributions are estimated for two rain rate regimes. The technique employed gives proper description of the DSD distribution curves very well even at lower rain rate. In this study, it was confirmed that Marshall and Palmer and other considered DSD models are not adequate to describe raindrop size distribution in the southern Africa region. A simple lognormal distribution model is proposed to describe the raindrop distribution for Durban using two rain rate regimes. Based on the comparisons carried out, it was found that the proposed model performs better than its counterparts; though at higher rain rates, the distribution patterns of Timothy et al. (Singapore) and Ajayi et al. (West-Africa) seem to give closer representation of distribution. This shows a similarity in the DSD distribution of the South Africa with the two regions. Though, the majority of southern Africa is grouped as sub-tropic region.

## REFERENCES

1. Laws, J. O. and D. A Parsons, "The relation of raindrop-size to intensity," *Transactions Amer. Geophysics Union*, Vol. 24, 452–460, 1943.
2. Marshall, J. S. and W. Palmer, "The distributions of raindrop with size," *Journal of Meteorology*, Vol. 5, 165–166, 1948.
3. Joss, J. and A. Waldvogel, "Raindrop size distribution and sampling size error," *Journal of the Atmospheric Sciences*, Vol. 26, 566–569, 1969.
4. Ajayi, G. O. and R. L. Olsen, "Modelling of a raindrop size distribution for microwave and millimetre wave applications," *Radio Science*, Vol. 20, No. 2, 193–202, 1985.
5. Sekine, M. and G. Lind, "Rain attenuation of centimetre, millimetre and sub-millimetre radio waves," *Proceedings of the 12th European Microwave Conference*, 584–589, Helsinki, Finland, 1982.

6. Timothy, K. I., J. T. Ong, and E. B. L. Choo, "Raindrop size distribution using method of moments for terrestrial and satellite communication applications in singapore," *IEEE Transactions on Antennas and Propagation*, Vol. 50, No. 10, 1420–1424, 2002.
7. Barclay, P., J. A. Bennett, and R. C. Botton, "Properties of rain for microwave propagation studies," Rep.MEE78-1, 35–68, Electrical Engineering Department, Monash University, Melbourne, August 1978.
8. Pang, W.-K., P.-K. Leung, W.-K. Huang, and W. Liu, "On interval estimation of the coefficient of variation for three-parameter Weibull, lognormal and gamma distribution: A simulation-based approach," *European Journal of Operational Research*, Vol. 164, 367–377, 2005.
9. Cohen, A. C. and B. J. Whitten, "Estimation in the three-parameter lognormal distribution," *Journal of American Statistical Association*, Vol. 75, No. 370, 399–404, 1980.
10. Waldvogel, A., "The  $N_0$  jump of raindrop spectra," *Journal of the Atmospheric Sciences*, Vol. 31, 1067–1078, 1974.
11. Press, W. H., B. P. Flannery, S. A. Teukolsky, and W. T. Vetterling, "Kolmogorov-smirnov test," *Numerical Recipes in FORTRAN: The Art of Scientific Computing*, 2nd Edition, 617–620, Cambridge University Press, Cambridge, England, 1992.
12. Massey, F. J., "The Kolmogorov-Smirnov test for goodness-of-fit," *Journal of the American Statistical Association*, Vol. 46, No. 255, 68–78, March 1951.
13. Owolawi, P. A., "Characteristics of rain at microwave and millimetric bands for terrestrial and satellite links attenuation in south africa and surrounding islands," Ph.D. Dissertation, School of Electrical, Electronics and Computer Engineering, University of KwaZulu Natal, Durban, South Africa, 2010.

# Comparison of Aerosol Radiative Forcing Observed by AERONET and MODIS at Xianghe Station — Comparison of the Aerosol Product and Its Radiative Forcing between AERONET and MODIS

Yan Wang<sup>1</sup>, Fengsheng Zhao<sup>2</sup>, and Zhengqiang Li<sup>1</sup>

<sup>1</sup>Institute of Remote Sensing Application, Chinese Academy of Sciences, Beijing 100101, China

<sup>2</sup>Beijing Normal University, Beijing 100875, China

**Abstract**— This paper presents aerosol optical depth (AOD) data and aerosol radiative forcing obtained from AErosol RObotic NETwork (AERONET) and Moderate resolution Imaging Spectroradiometer (MODIS) from September 2004 to September 2005 at Xianghe, China. The results show that aerosol optical depth derived from MODIS has good agreement with AERONET observation at Xianghe station through this period. In average, MODIS AOD showed a small systematical overestimation than that of AERONET. The higher MODIS AOD also results overestimation of aerosol radiative forcing than AERONET one, e.g.,  $12\text{--}17 \text{ Wm}^{-2}$  on the ground,  $2\text{--}3 \text{ Wm}^{-2}$  on the top of atmosphere, and  $9\text{--}12 \text{ Wm}^{-2}$  in the atmosphere respectively.

## 1. INTRODUCTION

The aerosols is the most important factor leading to the air pollution. It's direct and indirect radiative forcing could have a profound impact on climate change. Atmospheric aerosol research is a very active branch for the environment and climate change research. Aerosol properties from the ground measurements and remote sensing retrievals are two common observational approaches. These observations can not only promote knowledge of the aerosol physical, chemical and radiative properties, but also provide an essential input parameter for aerosol model. Satellite observations can give the global distribution of aerosol characteristics for long-term, and even at higher-resolution. The satellite remote sensing can compensate the shortcoming of ground-based observations which can't reflect changes in pollutant spatial distribution and trends of the specific deficiencies. However, satellite observations can't provide as many aerosol physical and chemical properties as the ground based measurements do, and to accurately estimate the optical thickness obtained form satellite is also difficult caused by the surface albedo and aerosol model uncertainty. On the other hand, the current satellite retrieval of aerosol are mainly on dark background such as the marine and land surface with dense vegetation, while in the mainland with high reflectivity, especially in arid and semi-arid areas, satellite retrieval of aerosol information is still scarce.

Many experts have done the comparison between MODIS aerosol data and AERONET observations [3, 6, 7, 9]. Currently many calculations of the aerosols radiative forcing are mainly obtained from satellite data because of its international wide. However, the aerosols radiative forcing from direct observation data is still limited. So comparison the ARF calculated by the observed data and the satellite is very necessary.

## 2. DATA

### 2.1. The Observed Data in Xianghe Station

A CIMEL Sun/sky radiometer was installed in September 2004 and since then Xianghe has become one of the Aerosol Robotic Network (AERONET) sites. AODs at eight wavelengths (340, 380, 440, 500, 670, 870, 1020, and 1640 nm) are retrieved with an uncertainty of  $0.01 \sim 0.02$ . Aerosol size distribution, refractive index and single-scattering albedo are retrieved from the sky radiance measurements and AODs [1].

### 2.2. MODIS Retrieved Aerosol

MODIS is onboard both Terra and Aqua satellites launched by NASA in the United State. Because of its advantage of having 36 spectral channels varying from visible, near infrared to infrared, the highest spatial resolution of 250 m, scanning width of 2330 km, it provide for aerosol remote sensing with a feasible means. NASA MODIS data sets release of aerosol optical depth (AOD) Level 2 products operationally with a resolution of  $10 \text{ km} \times 10 \text{ km}$  [2].

Table 1: The aerosol data in Xianghe station.

Parameters	wavelength (nm)
$\tau$	340, 380, 440, 500, 670, 870, 1020, 1640
$\omega$	440, 670, 870, 1020
$g$	440, 670, 870, 1020
$dV/d(\ln R)$ ( $\mu\text{m}^3/\mu\text{m}^2$ )	50, 65.6, 86.077, 112.939, 148.184, 194.429, 55.105, 334.716, 439.173, 576.227, 756.052, 991.996, 1301.57, 1707.75, 2240.702, 2939.96, 857.452, 5061.26, 6640.745, 8713.14, 1432.290, 15000

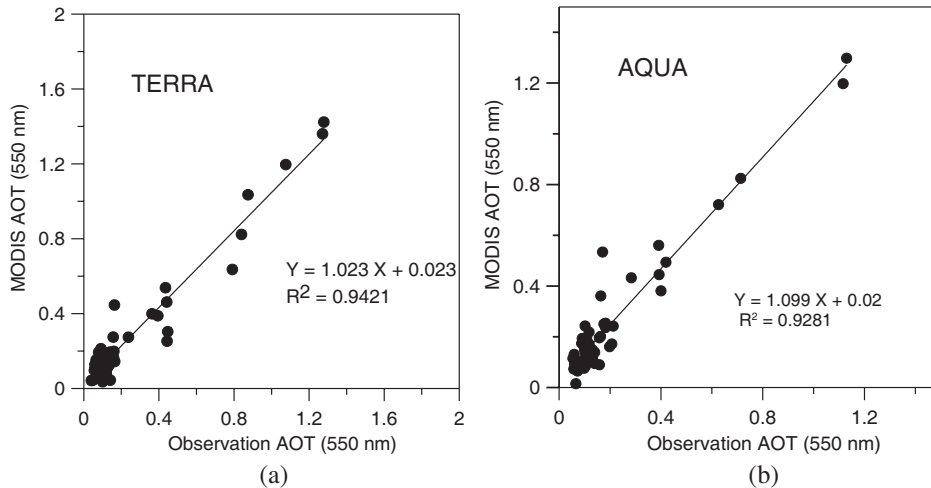


Figure 1: Scatterplots of MODIS versus AERONET aerosol optical thickness (AOT) at 550 nm wavelengths. (a) Terra, (b) Aqua.

### 3. RESULTS

#### 3.1. The Comparison of MODIS and AERONET Aerosol Optical Depth

The frequency of aerosol optical thickness data in Xianghe observation is one minute. In order to compare with MODIS, we averaged the observed AODs which are 30 min before or after the transit time of MODIS. The number of ground-based aerosol observations within that time can be up to 60, then the difference of the averaged ground-based AODs and MODIS retrieved AODs are analyzed.

Figure 1 shows that the aerosol optical thickness of either the Aqua satellite or the Terra satellite have a good correlation with that of ground-based observations. The correlation coefficient  $R^2$  reaches larger than 0.92, indicating that the difference is small. The correlation coefficient of ground-based observations and Terra inversion can get 0.9421, the correlation coefficient of ground-based observations and Aqua inversion can also get 0.9281. The correlation coefficient  $R^2$  of Xianghe station is 0.89 analysed by Li [5]. Levy [4] got the results:  $y = 1.009X + 0.029$ ,  $R^2 = 0.791$  for all land areas. Compares to the two results, the value here is much better. Possible reason is that when compared with satellite the observations data having high frequency: one minute per data. The average value of the samples can be well reflected the state of the atmosphere during satellites transit.

Though both are in good agreement, the aerosol optical thickness of MODIS is larger than that from ground-based observations. It may cause by MODIS's algorithm underestimated surface albedo. Our results show that the MODIS aerosol optical thickness is much larger than ground-based observations in a very clean day. In polluted day (when the aerosol optical thickness is larger) the MODIS results are still larger, but the difference gets relatively small.

#### 3.2. The Comparison of MODIS and AERONET ARF

The  $(\text{ARF})_{\text{surf}}$  terms were determined by the difference between the observed and computed radiation by SBDART without aerosols. The  $(\text{ARF})_{\text{toa}}$  terms were calculated separately with and

without aerosol.  $(\text{ARF})_{\text{suf}} - (\text{ARF})_{\text{top}}$  gives the ARF of the atmosphere,  $(\text{ARF})_{\text{Atm}}$  [8]. When calculating the ARF using MODIS data, both the aerosols Single-scattering albedo and the aerosol asymmetry factor are from AERONET data. Figure 2 show that the ARF calculated by MODIS aerosol is bigger than that calculated by observed data in any conditions.

The  $(\text{ARF})_{\text{suf}}$  of TERRA satellite changes from  $-246 \text{ Wm}^{-2}$  to  $-10 \text{ Wm}^{-2}$ . The  $(\text{ARF})_{\text{suf}}$  calculated by AERONET observed data is  $-196 \text{ Wm}^{-2}$  to  $-14 \text{ Wm}^{-2}$ . The average of  $(\text{ARF})_{\text{suf}}$  is  $-56 \text{ Wm}^{-2}$ ,  $-35 \text{ Wm}^{-2}$ , calculated by TERRA and AERONET respectively. The difference between them is  $21 \text{ Wm}^{-2}$ .

The  $(\text{ARF})_{\text{suf}}$  of Aqua satellite changes from  $-250 \text{ Wm}^{-2}$  to  $-5 \text{ Wm}^{-2}$ . The results of  $(\text{ARF})_{\text{suf}}$  calculated by AERONET observed data vary from  $-192 \text{ Wm}^{-2}$  to  $-14 \text{ Wm}^{-2}$ . The average of  $(\text{ARF})_{\text{suf}}$  is  $-58 \text{ Wm}^{-2}$ ,  $-41 \text{ Wm}^{-2}$ , calculated by Aqua and AERONET respectively. The  $(\text{ARF})_{\text{suf}}$  is overestimated  $17 \text{ Wm}^{-2}$  by the satellite data.

The range of the  $(\text{ARF})_{\text{toa}}$  calculated by TERRA satellite aerosol data is  $-43 \text{ Wm}^{-2}$  to  $8 \text{ Wm}^{-2}$ . The  $(\text{ARF})_{\text{toa}}$  changes from  $-31 \text{ Wm}^{-2}$  to  $7 \text{ Wm}^{-2}$  calculating with AERONET aerosol data. The average  $(\text{ARF})_{\text{toa}}$  of all samples is  $-7 \text{ Wm}^{-2}$ , while the observation value is  $-4 \text{ Wm}^{-2}$ . The difference between them is  $3 \text{ Wm}^{-2}$ .

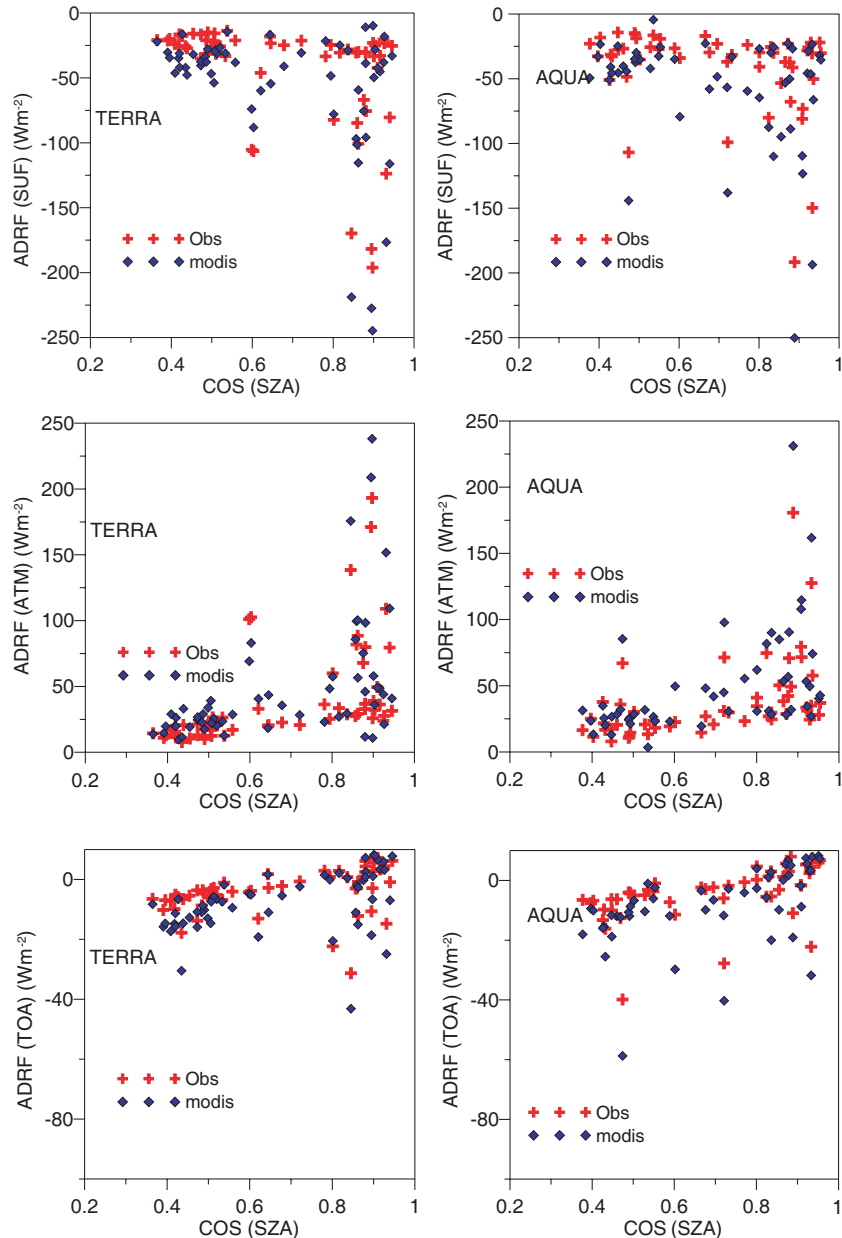


Figure 2: Scatter plots of the ARF and the cosine of the solar zenith angle for (red) observation and (blue) MODIS.

The Aqua satellite (ARF)<sub>toa</sub> range is  $-59 \text{ Wm}^{-2}$  to  $8 \text{ Wm}^{-2}$ , While the AERONET (ARF)<sub>toa</sub> range is  $-40 \text{ Wm}^{-2}$  to  $-8 \text{ Wm}^{-2}$ . The difference of the average (ARF)<sub>toa</sub> between Aqua and AERONET is  $4 \text{ Wm}^{-2}$ .

The (ARF)<sub>atm</sub> calculated by TERRA satellite MODIS aerosol data is  $10 \text{ Wm}^{-2}$  to  $238 \text{ Wm}^{-2}$ , the (ARF)<sub>atm</sub> of AERONET is  $8 \text{ Wm}^{-2}$  to  $193 \text{ Wm}^{-2}$ . The average of (ARF)<sub>atm</sub> is  $49 \text{ Wm}^{-2}$ ,  $40 \text{ Wm}^{-2}$ , calculated by TERRA and AERONET respectively. The (ARF)<sub>atm</sub> of TERRA is  $9 \text{ Wm}^{-2}$  bigger than that of AERONET.

The Aqua satellite (ARF)<sub>atm</sub> range is from  $3 \text{ Wm}^{-2}$  to  $231 \text{ Wm}^{-2}$ , while the ARF of AERONET changes from  $8 \text{ Wm}^{-2}$  to  $181 \text{ Wm}^{-2}$ . The average of (ARF)<sub>atm</sub> is  $50 \text{ Wm}^{-2}$ ,  $37 \text{ Wm}^{-2}$ , calculated by Aqua and AERONET respectively. The (ARF)<sub>atm</sub> of TERRA is  $13 \text{ Wm}^{-2}$  bigger than that of AERONET.

#### 4. SUMMARY

This paper compared the MODIS aerosol optical thickness with the AERONET aerosol optical thickness and a good correlation between these two data sets were found. The square of correlation coefficient between MODIS aerosol optical thickness and the observed aerosol thickness is larger than 0.92, indicating the MODIS measurements are greater than the ground-based observations.

The larger MODIS aerosol optical depth produce high values of ARF accordingly, which are  $17\text{--}21$ ,  $3\text{--}4$ , and  $9\text{--}13 \text{ Wm}^{-2}$  larger than that of the ground-based observations, with respect to the ground, the top of atmosphere and the aerosphere respectively.

#### ACKNOWLEDGMENT

This research was supported by the Multi-scale Comprehensive Observation and Study of Spatial-Temporal Properties of Aerosol Project (MOSTap), National Basic Research Program of China (973 Program), under grant 2010CB950800 (2010CB950801). The authors also would like to thank Wangling's help with the text correction.

#### REFERENCES

- Dubovik, O., et al., "Accuracy assessments of aerosol optical properties retrieved from Aerosol Robotic Network (AERONET) sun and sky radiance measurements," *Journal of Geophysical Research*, Vol. 105, 9791–9806, 2000.
- Kaufman, Y. J., D. Tanré, L. Remer, et al., "Operational remote sensing of tropospheric aerosol over the land from EOS-MODIS," *Journal of Geophysical Research*, Vol. 102, No. 14, 17051–17068, 1997.
- Kaufman, Y. J. and B. N. Holben, "Will aerosol measurements from Terra and Aqua polar orbiting satellites represent the daily aerosol abundance and properties?" *Geophysics Research Letters*, Vol. 27, No. 23, 3861–3864, 2000.
- Levy, R. C., L. A. Remer, S. Mattoo, E. F. Vermote, and Y. J. Kaufman, "Second-generation operational algorithm: Retrieval of aerosol properties over land from inversion of Moderate Resolution Imaging Spectroradiometer spectral reflectance," *Journal of Geophysical Research*, Vol. 112, D13211, 2007, doi:10.1029/2006JD007811.
- Li, Z., F. Niu, K.-H. Lee, J. Xin, W.-M. Hao, B. Nordgren, Y. Wang, and P. Wang, "Validation and understanding of Moderate Resolution Imaging Spectroradiometer aerosol products (C5) using ground-based measurements from the handheld Sun photometer network in China," *Journal of Geophysical Research*, Vol. 11, No. 2, D22S07, 2007, doi:10.1029/2007JD008479.
- Li, C., J. Mao, and J. Chen, "In eastern China using MODIS aerosol optical thickness distribution and seasonal variation," *Science Bulletin*, Vol. 48, No. 19, 2094–2100, 2003.
- Mao, J., C. Li, and J. Zhang, "The comparison of remote sensing aerosol optical depth from MODIS data and ground sun-photometer observations," *Journal of Applied Meteorological Science*, Vol. 13, No. 10, 127–135, 2002.
- Wang, Y., H. Che, J. Ma, Q. Wang, G. Shi, H. Chen, P. Goloub, and X. Hao, "Aerosol radiative forcing under clear, hazy, foggy, and dusty weather conditions over Beijing, China," *Geophysics Research Letter*, Vol. 36, L06804, 2009, doi:10.1029/2009GL037181.
- Xia, X., "Global MODIS aerosol optical thickness over land significantly higher," *Chinese Science Bulletin*, Vol. 51, No. 19, 2297–2303, 2006.

## 2-D Pattern Synthesis for Cylindrical Arrays

C. Liu, Z. Ding, and X. Liu

Department of Communication Engineering, Hefei University of Technology, Hefei, Anhui 230009, China

**Abstract**— A simple algorithm of 2-D pattern synthesis for cylindrical arrays is introduced in this paper. According to the characteristic of cylindrical array, the whole array can be seen as a linear array whose elements are the identical circular arrays. Therefore, the beam pattern can be obtained by the product of the linear and circular arrays' beam pattern and the synthesis process is decomposed into two individual 1-D pattern syntheses of subarrays to approach the desired sidelobe level. Numerical examples illustrate the effectiveness of the proposed method.

### 1. INTRODUCTION

Conformal antenna arrays have extremely wide prospect of application for its low RCS and small effects on aerodynamic performance of the carrier. Because of its curved structure and conformal to the carrier, a more challenging problem has been proposed to synthesize patterns for these arrays, which is more difficult than the synthesis of linear and planar array.

There has been significant attention paid to the area of conformal array pattern synthesis in recent years, and a wide variety of techniques have been developed for the synthesis of conformal arrays. A simple algorithm was proposed in [1] to achieve desired patterns for a wide variety of array geometries. Literature [2] also presented a pattern synthesis method for arbitrary arrays based on adaptive array. However, there is no evidence to indicate their flexibility to conformal arrays. Intelligent optimization algorithms have also been applied in this area. A modified particle swarm optimization algorithm was introduced in [3] to optimize the pattern of cylindrical conformal antenna array for sidelobe level suppression and null control in certain directions. In [4], a synthesis technique was proposed for the optimization of the element excitations of conformal phased array with improved NSGA-II. In [5], the authors indicate that the cylindrical array can be seen as a linear array while beam forming. However, these algorithms are mostly used in the case of 1-D pattern syntheses.

In this paper, a new method is present to solve the 2-D beam pattern synthesis for cylindrical arrays. Due to the geometry feature of cylindrical array, it can be seen as a linear array with its elements of identical circular arrays. Thanks to this characteristic, the 2-D synthesis process can be accomplished by two individual 1-D pattern synthesis of linear and circular array. Compared with previous methods, the new method is simpler for 2-D pattern synthesis with fixed sidelobe level.

### 2. PROBLEM FORMULATION

As one of the most familiar conformal array, the geometry of a finite and periodic cylindrical array of  $M \times N$  is shown in Figure 1. With reference to a Cartesian system  $O(x, y, z)$ , the far-field beam pattern in the generic direction  $(\theta, \varphi)$  can be written as

$$F(\theta, \varphi) = \sum_{i=1}^{MN} w_i \exp\{ik\mathbf{V}_i \mathbf{e}(\theta, \varphi)\} \quad (1)$$

where  $w_i$  is the complex excitation voltage of the  $i$ th element, and  $k = 2\pi/\lambda$  is the phase constant.  $\mathbf{V}_i$  and  $\mathbf{e}(\theta, \varphi)$  are the position vector of the  $i$ th element and the unit vector on the direction  $(\theta, \varphi)$ , which can be expressed as follows

$$\mathbf{V}_i = \mathbf{e}_x x_i + \mathbf{e}_y y_i + \mathbf{e}_z z_i \quad (2)$$

$$\mathbf{e}(\theta, \varphi) = \mathbf{e}_x \cos \theta \cos \varphi + \mathbf{e}_y \sin \theta \cos \varphi + \mathbf{e}_z \sin \varphi \quad (3)$$

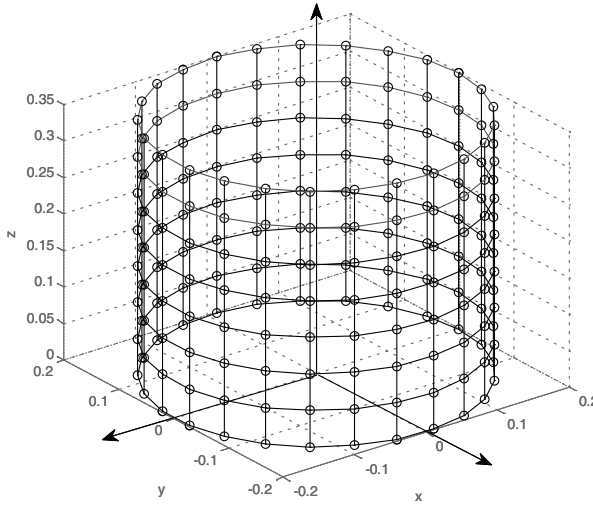


Figure 1: Geometry of cylindrical array.

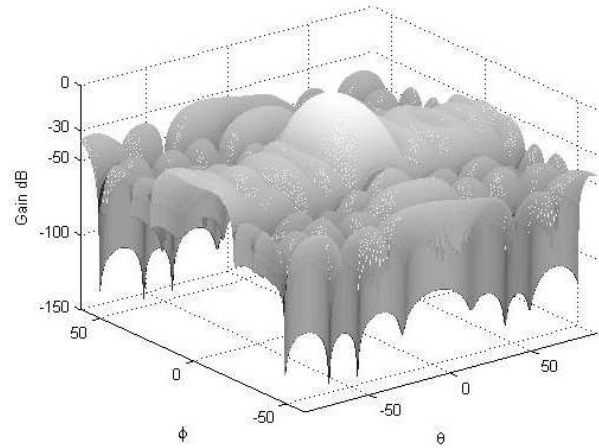


Figure 2: 2-D beam pattern for the cylindrical array.

### 3. PATTERN SYNTHESIS

One of the most differences between conformal array and traditional array is that the beam pattern can not be obtained by the product of array factor and element pattern. However, since the cylindrical array consists of a series of identical circular arrays, the whole array can be seen as a linear array whose elements are these identical circular arrays. Then array beam pattern can still be obtained by the product rule. Therefore, the beam pattern of cylindrical array  $G(\theta, \varphi)$  can be expressed by the following formula

$$G(\theta, \varphi) = G_1(\theta, \varphi) \times G_2(\theta, \varphi) \quad (4)$$

where  $G_1(\theta, \varphi)$  is the beam pattern of the linear array and  $G_2(\theta, \varphi)$  is the beam pattern of the circular array. Assume the complex excitation vector of linear array and circular array are  $\mathbf{w}_1 = [w_{11}, w_{12}, \dots, w_{1M}]^T$  and  $\mathbf{w}_2 = [w_{21}, w_{22}, \dots, w_{2N}]^T$  respectively. Then the beam pattern  $G_1(\theta, \varphi)$  and  $G_2(\theta, \varphi)$  can be written as

$$G_1(\theta, \varphi) = \mathbf{w}_1^T \mathbf{a}_1(\theta, \varphi) \quad (5)$$

$$G_2(\theta, \varphi) = \mathbf{w}_2^T \mathbf{a}_2(\theta, \varphi) \quad (6)$$

where  $\mathbf{a}_1(\theta, \varphi)$  and  $\mathbf{a}_2(\theta, \varphi)$  are the steering vector of the linear array and the circular array respectively. From (4) (5) and (6), we have

$$\begin{aligned} G(\theta, \varphi) &= (\mathbf{w}_1^T \mathbf{a}_1(\theta, \varphi)) (\mathbf{w}_2^T \mathbf{a}_2(\theta, \varphi)) \\ &= (\mathbf{w}_1^T \otimes \mathbf{w}_2^T) (\mathbf{a}_1(\theta, \varphi) \otimes \mathbf{a}_2(\theta, \varphi)) \\ &= \mathbf{w}^T \mathbf{a}(\theta, \varphi) \end{aligned} \quad (7)$$

in which  $\mathbf{a}(\theta, \varphi) = (\mathbf{a}_1(\theta, \varphi) \otimes \mathbf{a}_2(\theta, \varphi))$  is the steering vector of the whole cylindrical array and its weight vector can be obtained as follows

$$\mathbf{w} = \mathbf{w}_1 \otimes \mathbf{w}_2 \quad (8)$$

where “ $\otimes$ ” denotes the Kronecker product.

Usually, there are expected signal, noise and interference embedded in the receiving signal. The adaptive beamformer can control the nulls according to the interference and gets the optimal weight vector:

$$\mathbf{w} = \mu \mathbf{R}_{i+n}^{-1} \mathbf{a}^*(\theta_d, \varphi_d) = \mu \left( \sigma_n^2 \mathbf{I} + \sum_{j=1}^J \sigma_j^2 \mathbf{a}_j \mathbf{a}_j^H \right)^{-1} \mathbf{a}^*(\theta_d, \varphi_d) \quad (9)$$

where  $(\theta_d, \varphi_d)$  is the look direction while  $\sigma_n^2$  and  $\sigma_j^2$ ,  $j = 1, 2, \dots, J$  are the power of noise and interferences respectively. However, when interferences are more than array elements, it will fail to

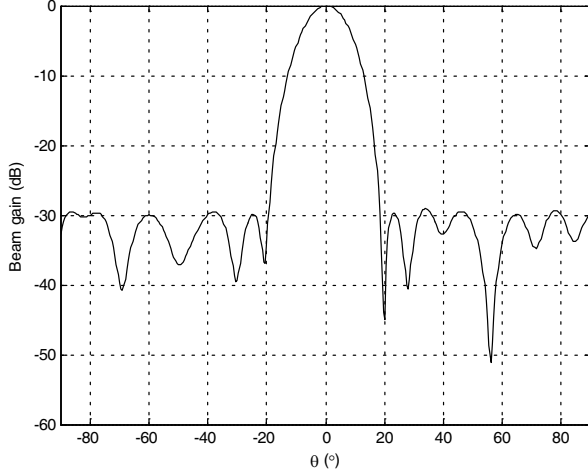


Figure 3: 1-D beam pattern in the azimuth direction, with  $\varphi = 0^\circ$ .

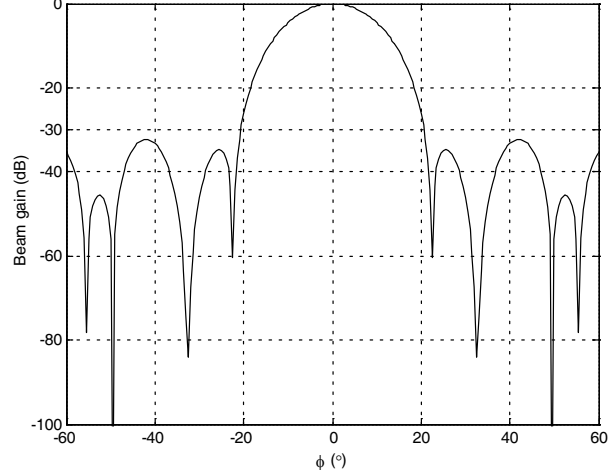


Figure 4: 1-D beam pattern in the elevation direction, with  $\theta = 0^\circ$ .

form nulls adaptively but depress the sidelobe level in the area of interferences [6]. According to this feature, we can control the beam pattern by adjusting the intensity of the interferences.

When the above method is used in 2-D beamforming, we should set a large number of interferences in 2-D angle area, which will lead to a large amount of computation. Since the beam pattern in the elevation direction is mainly determined by the linear array while the beam pattern in the azimuth direction is mainly determined by the circular array, the beam pattern is controlled separately in the direction of azimuth and elevation. Through the following iteration, the optimal weight vector  $\mathbf{w}_1$  and  $\mathbf{w}_2$  for linear and circular array can be obtained respectively.

$$\sigma_j^2(k+1) = \begin{cases} 0 & \theta_j \text{ in mainlobe region} \\ \max\{0, \Gamma_i(k)\} & \theta_j \text{ in sidelobe region} \end{cases} \quad (10)$$

here  $k$  denotes the  $k$ th iteration,  $\Gamma_j(k) = \sigma_j^2(k) + \alpha [G(\theta_j, k) - G_d(\theta_j)]$ , and  $G_d(\theta)$  is the desired beam pattern in the direction of azimuth or elevation. After we get  $\mathbf{w}_1$  and  $\mathbf{w}_2$ , weight vector of the cylindrical array can be obtained by (8).

When the circular arrays arrange equidistantly in the  $z$  axis, the linear array becomes a uniform linear array and Chebyshev polynomials can directly be used as the weight vector.

#### 4. NUMERICAL RESULTS

Consider a uniform cylindrical array with  $M = 8$  and  $N = 25$ , whose space between neighboring elements is half wavelength. Assume the looking direction is  $(\theta_d, \varphi_d) = (0^\circ, 0^\circ)$ , and the desired beam pattern has a sidelobe level of  $-30$  dB. The synthesis process starts with unity values of weighting function. Since the linear array is uniform, Chebyshev polynomials are used as  $\mathbf{w}_1$ . The final synthesized beam pattern with the method above is shown in Figures 2–4. Figure 2 shows the final synthesized 2-D beam pattern for the cylindrical array and Figures 3, 4 show the slices in the azimuth and elevation direction respectively. It can be seen from the figures that the results using our method meet the design requirements well.

#### 5. CONCLUSIONS

In this paper, an efficient 2-D pattern synthesis method is proposed based on cylindrical arrays. According to the geometry characteristics, a cylindrical array can be seen as the integration of linear array and circular array. So that 2-D pattern synthesis process can be accomplished through two 1-D pattern syntheses base on the linear and circular array with the desired sidelobe level, respectively. It can significantly reduce the amount of computation while the finally obtained beam pattern can meet the design requirements well. Validity of the algorithm has been illustrated with simulations.

#### ACKNOWLEDGMENT

This work is supported by China Postdoctoral Science Foundation No. 20100480680.

**REFERENCES**

1. Tseng, C.-Y. and L. J. Griffiths, "A simple algorithm to achieve desired patterns for arbitrary arrays," *IEEE Trans. Signal Process*, Vol. 40, No. 11, 2737–2746, November 1992.
2. Zhou, P. Y. and M. A. Ingram, "Pattern synthesis for arbitrary arrays using an adaptive array method," *IEEE Trans. Antennas & Propag.*, Vol. 47, No. 5, 862–869, May 1999.
3. Lu, Z. B., A. Zhang, and X. Y. Hou, "Pattern synthesis of cylindrical conformal array by the modified particle swarm optimization algorithm," *Progress In Electromagnetics Research*, Vol. 79, 415–426, 2008.
4. Yang, J. O., Q. R. Yuan, F. Yang, et al., "Synthesis of conformal phased array with improved NSGA-II algorithm," *IEEE Trans. Antennas Propag.*, Vol. 57, No. 12, 4006–4009, December 2009.
5. Lin, Z. and H. Zishu, "A beamforming method for cylindrical array based on synthetic pattern of subarray," *International Conference on Image Analysis and Signal Processing*, 667–670, Zhejiang, April 2010.
6. Guo, Q., G. Liao, Y. Wu, and J. Li, "Pattern synthesis method for arbitrary arrays based on LCMV criterion," *Electronics Letters*, Vol. 39, No. 23, 1628–1630, November 2003.

# An Aperture-couple Stack Antenna with Minkoski-island-based Patch for Circular Polarization and Wide-band Applications

Sheau-Shong Bor<sup>1</sup>, Tian-Fu Hung<sup>2</sup>, Chia-Yen Wei<sup>2</sup>, Ji-Chyun Liu<sup>3</sup>, and Hai-Tao Sun<sup>1</sup>

<sup>1</sup>Department of Electrical Engineering, Feng-Chia University, Taichung, Taiwan, R.O.C.

<sup>2</sup>Ph.D. Program in Electrical and Communications Engineering  
Feng-Chia University, Taichung, Taiwan, R.O.C.

<sup>3</sup>Department of Electrical Engineering, Ching Yun University, Chung-Li, Tao-Yuan, Taiwan, R.O.C.

**Abstract**— A stack-structure antenna with Minkoski-islandbased patch for circular polarization and wideband applications has been presented in this paper. The proposed antenna structure is stacked by two FR4 substrates. The bottom substrate is fed by single-feed line coupled with aperture; while the Minkoski-island-based patch is etched on the top substrate which is responsible for the excitation of the wideband response in dual-mode and radiating the circular polarization in orthogonal mode. The stacked form antenna presents the axial ratio (AR) with 3-dB bandwidth of 30 MHz obtaining 1.2% of bandwidth percentage at 2.44 GHz and the wideband response with 10-dB bandwidth of 290 MHz possessing 12% of bandwidth percentage particularly. The radiation patterns show the directional patterns at 2.34 GHz and 2.5 GHz resonance frequencies respectively. The peak power gains are 0.11 dBi and 0.2 dBi correspondingly. The polarization pattern at 2.44 GHz displays the right-hand circular polarization (RHCP) characteristics. It can be properly applied to the WLAN band.

## 1. INTRODUCTION

In recent years, the circular polarization scheme of antenna has been widely used for wireless communications. It has the advantage of solving problems of polarization mismatch and multi-path interference. Owing to the above-mentioned reasons, there are many relevant research results that have been dealt with [1–6]. In addition, the stack-structure antennas and aperture-coupled stack antennas were specifically developed for broad-band, highgain and highefficiency transceiver applications [3–6]. However, the stacked patches were just the square, ring, ring slot or loop features. For the sake of a good orthogonal mode, a Minkoski-island-based patch is thus proposed. The aperture-coupled stacked antenna constructed with single feed line and Minkoski-island-based patch can make a circularly polarized radiation pattern. Details of the antenna design, the simulation and related experimental results are investigated in the following sections.

## 2. ANTENNA CONFIGURATION

The proposed antenna in Fig. 1(a) consists of two FR4 substrates with thickness ( $h_1 = h_2 = 1.6$  mm) and relative permittivity ( $\epsilon_{r1} = \epsilon_{r2} = 4.4$ ). The bottom substrate is fed by a  $50\text{-}\Omega$ -impedance single-feed line coupled with aperture. The Minkoski-island-based patch is done by etching process on the top substrate, which excites the wideband response with dual mode and circular polarization with orthogonal mode. The detailed dimensions in Fig. 1(b) are  $W \times L = 50 \times 44 \text{ mm}^2$ ,  $W_1 \times L_1 = 3.0 \times 17.5 \text{ mm}^2$ ,  $W_2 \times L_2 = 21.3 \times 21.3 \text{ mm}^2$ ,  $G_1 \times L_g = 1.5 \times 28 \text{ mm}^2$ ,  $W_p \times W_p = 2.5 \times 2.5 \text{ mm}^2$  and  $W_3 \times W_3 = 2.3 \times 2.3 \text{ mm}^2$  respectively.

## 3. SIMULATIONS AND EXPERIMENTS

In Fig. 2, the simulated and measured results are quite matching each other. The impedance bandwidth (290 MHz with 12% of bandwidth percentage) of the proposed antenna at center frequency (2.67GHz) is obtained. The measured AR spectrum at resonant frequency of 2.44 GHz (3-dB bandwidth of 30 MHz) is presented in Fig. 3. The minimum AR is 0.51 dB for 2.44 GHz. The surface current distribution shown in Fig. 4 is simulated from HFSS software. Fig 4 also indicates that the vector and scalar current distribution with excited frequencies of 2.34 GHz and 2.5 GHz respectively and the Minkoski-island-based patch can create dual-mode frequency characteristics as orthogonal mode whose phase angle is  $90^\circ$  which can perform the circular polarization (CP) operation for antenna. In field analyses, the 2-D radiation patterns are obtained by an automatic measurement system in an anechoic chamber. The 2-D patterns at resonant frequency of 2.34 GHz and 2.5 GHz are presented in Fig. 5. The directional patterns with peak gains (0.11 dBi and 0.2 dBi respectively) are also exhibited. The circular polarization pattern of 2.44 GHz shows the right-hand circular polarization peak gain (0.3 dBic) in Fig. 6.

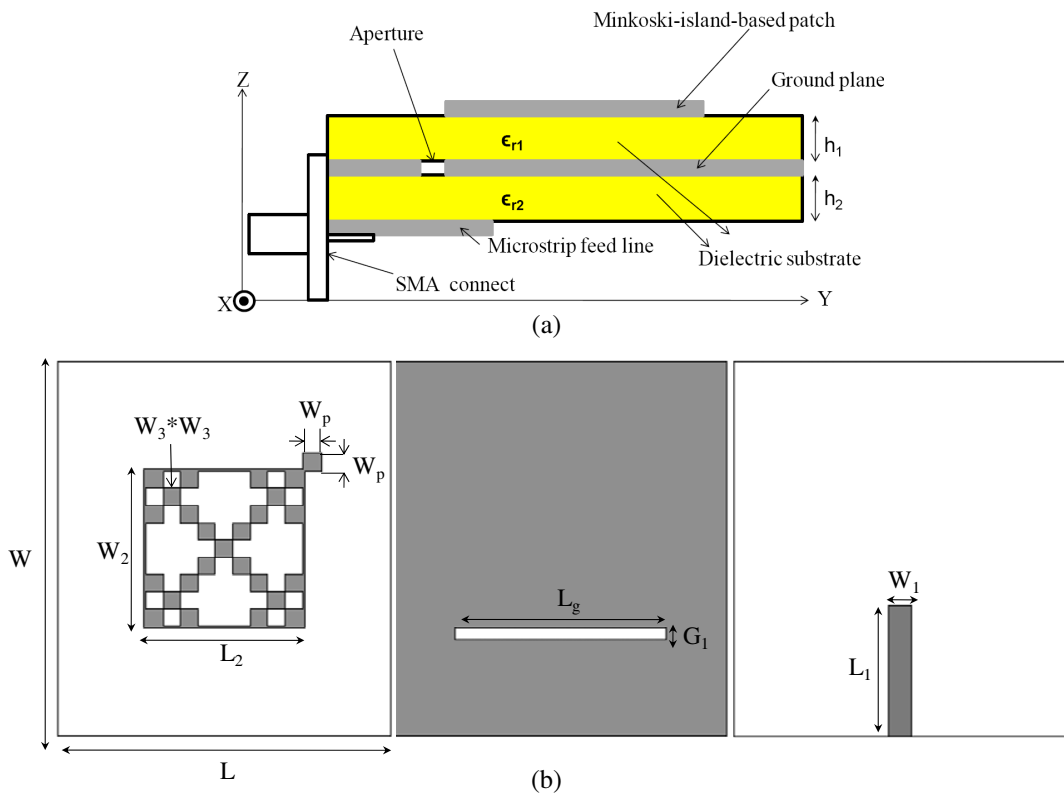


Figure 1: Configurations of the proposed antenna. (a) Structure. (b) Dimensions.

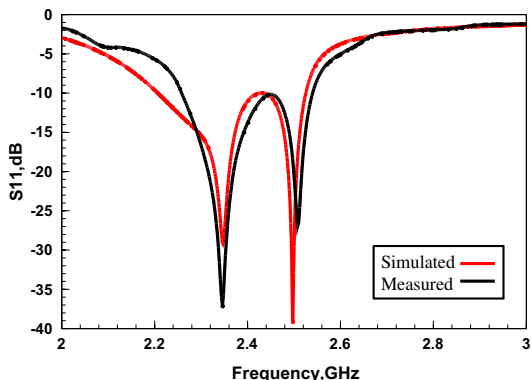


Figure 2:  $S_{11}$  spectrum.

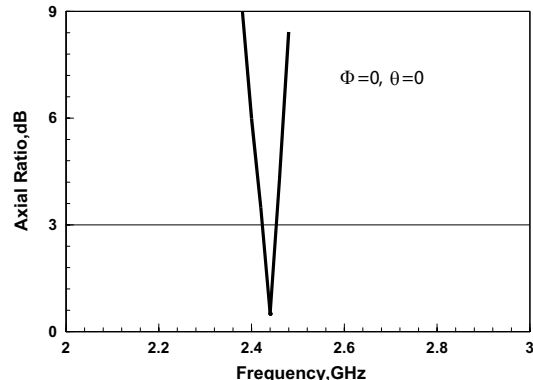


Figure 3: Measured AR spectrum.

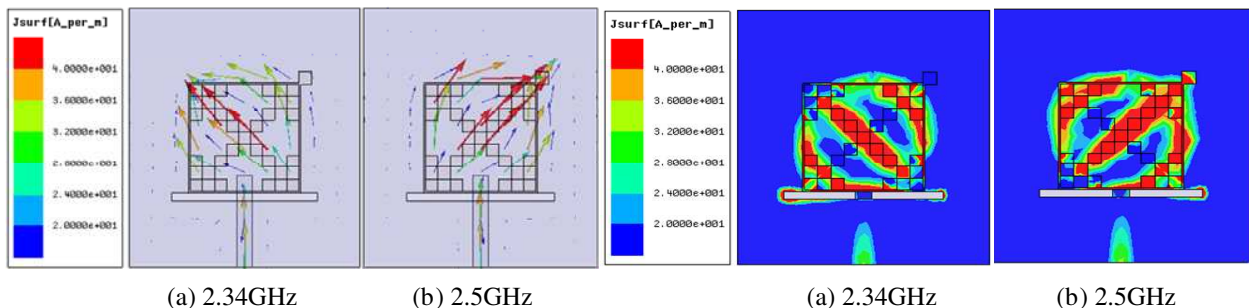


Figure 4: Current distributions of dual mode and orthogonal mode.

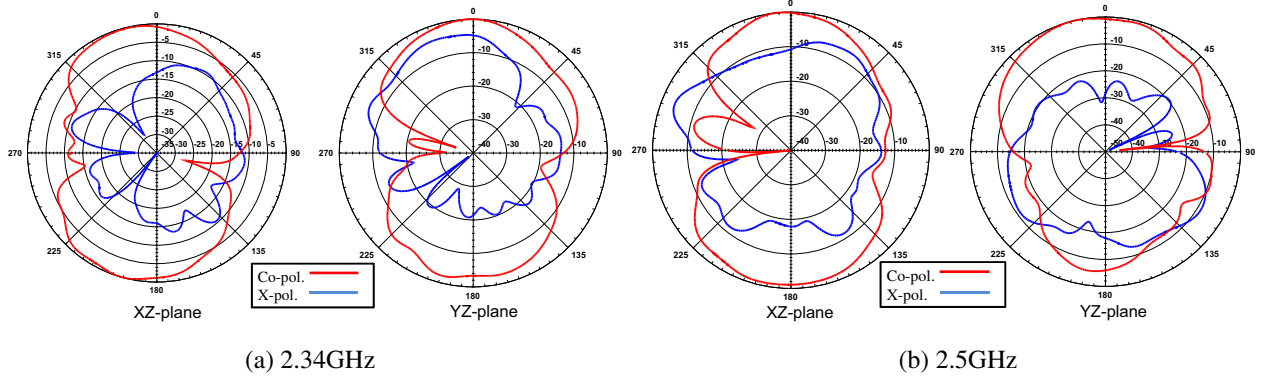


Figure 5: Two-cut radiation patterns of the proposed antenna. (a) 2.34 GHz. (b) 2.5 GHz.

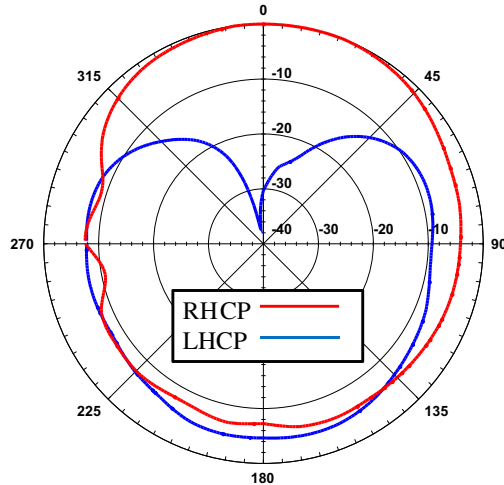


Figure 6: Measured CP radiation patterns of the proposed antenna for 2.44 GHz.

#### 4. CONCLUSIONS

An aperture coupled stack-form antenna with Minkoski-island-based patch for circular polarization and wideband applications has been well presented in this study. A good orthogonal mode can be achievable by using Minkoski-island-based patch technique and the directional radiation patterns are obtained as well. The right-hand circular polarization (RHCP) characteristics are presented. This especially designed antenna can be usefully and properly applied to the WLAN band of wireless communication systems.

#### REFERENCES

- Chi, L. P., S. S. Bor, S. M. Deng, C. L. Tsai, P. H. Juan, and K. W. Liu, “A wideband wide-strip dipole antenna for circularly polarized wave operations,” *Progress In Electromagnetic Research*, Vol. 100, 69–82, 2010.
- Buffi, A., R. Caso, M. R. Pino, P. Nepa, and G. Manara, “Single-feed circularly polarized aperture-coupled square ring slot microstrip antenna,” *Electron. Lett.*, Vol. 46, No. 4, 268–269, Feb. 2010.
- Liu, J.-C., B.-H. Zeng, L. Badjie, S. Drammeh, S.-S. Bor, T.-F. Hung, and D.-C. Chang, “Single-feed circularly polarized aperture-coupled stack antenna with dual-mode square loop radiator,” *IEEE Antennas Wireless Propag. Lett.*, Vol. 9, 887–890, 2010.
- Liu, J.-C., B.-H. Zeng, C. Y. Liu, H. C. Wu, and C.-C. Chang, “A dual-mode aperture-coupled stack antenna for WLAN dual-band and circular polarization applications,” *Progress In Electromagnetics Research C*, Vol. 17, 193–202, 2010.
- Lien, H.-C. and H.-C. Tsai, “A wide-band circular polarization stacked patch antenna for the wireless communication applications,” *PIERS Online*, Vol. 4, No. 2, 255–258, 2008.
- Lien, H.-C., H.-C. Tsai, Y.-C. Lee, and W.-F. Lee, “A circular polarization microstrip stacked structure broadband antenna,” *PIERS Online*, Vol. 4, No. 2, 259–262, 2008.

# UHF SATCOM Broadband CP Antenna: Moxon Type Bent-dipoles over a Ground Plane

Edip Niver<sup>1</sup> and İbrahim Tekin<sup>2</sup>

<sup>1</sup>Electrical Engineering, New Jersey Institute of Technology, Newark, NJ, USA

<sup>2</sup>Electronics Engineering, Sabancı University, İstanbul, Turkey

**Abstract**— In this paper, we investigate and compare two different antenna types for UHF SATCOM applications; proposed Moxon type (bent dipole) and conventional egg beater (loop) antennas in terms of antenna performance and physical size. Bent dipole and egg beater antennas are simulated using HFSS software. Prototype antenna for Moxon type is also fabricated and measured for its return loss using Agilent network analyzer and compared to that of an egg beater antenna. Antenna gains are also simulated. Simulation results show that Moxon type antenna has more impedance bandwidth than egg beater antenna with smaller dimensions and hence can be used for broadband SATCOM applications.

## 1. INTRODUCTION

For UHF SATCOM mobile applications, antennas are required to have high-performance including a broadband operation, circular polarization as well as a large angular coverage from horizon to zenith. For airborne systems at these frequencies, wavelength could be on the order of meters and conventional antennas may be “too big” for deployment. Compact size antennas with desired antenna performance become very crucial part of these airborne systems. In this paper, a novel antenna “Moxon type” bent dipole is proposed for circular polarization and its performance is compared to a conventional egg beater antenna whose dimensions are larger than the proposed Moxon type antenna.

For UHF satcom applications, broadband antennas can be employed such as sleeve dipoles [1]. However, for mobile applications, the antenna size is critical and obtaining a circular polarization with sleeve dipoles will result in complicated antenna structures. Egg beater antennas are another choice for obtaining circular polarization with loop antennas at UHF frequencies [2]. Egg beater antennas may not be easily deployable on mobile platforms due to their dimensions. In this paper, we implement a Moxon type antenna [3] (bent dipole over a ground plane) to obtain circular polarization with its compact size compared to conventional eggbeater antenna which comprises two circular loops fed with a quadrature coupler for circular polarization. Rest of the paper is organized as follows: in Section 2, moxon type bent dipole antenna and egg beater antenna will be described in details, in Section 3, simulation and experimental results are given and finally paper is concluded.

## 2. MOXON TYPE BENT DIPOLE AND EGG BEATER ANTENNAS

### 2.1. “Moxon Type” Bent Dipole Antenna for Circular Polarization

A sketch of one of the bent dipole antenna is shown in Figure 1. The length of the one arm of the dipole is  $L + W$ , the arm is bent toward a ground plane from  $L$  distance away from the center

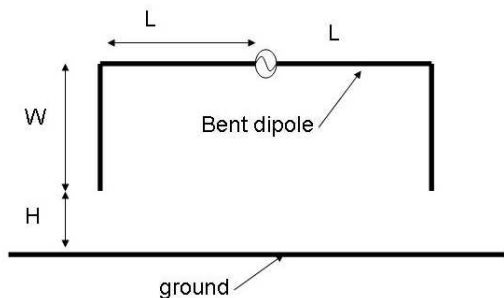


Figure 1: Bent dipole antenna over a ground plane.

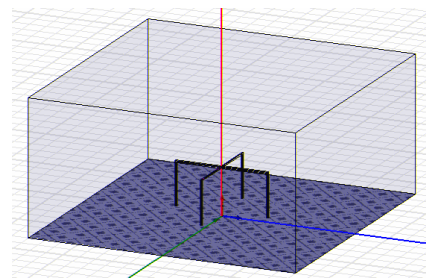


Figure 2: Two perpendicular bent dipole antennas for circular polarization radiation.

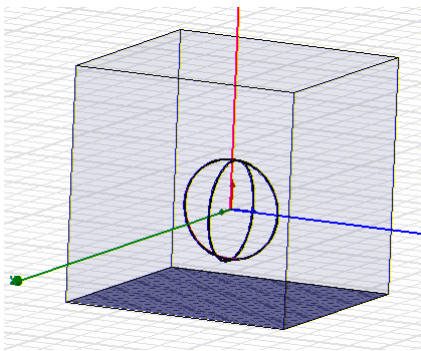


Figure 3: Two circular loop antennas for circular polarization radiatio.

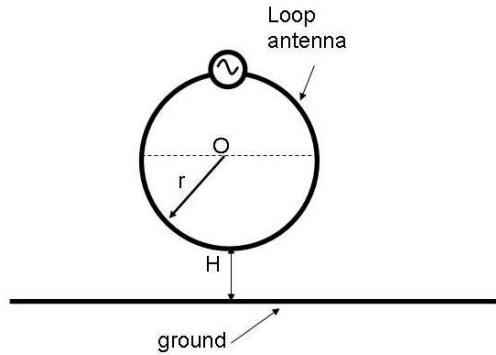


Figure 4: Loop antenna over a ground plane.

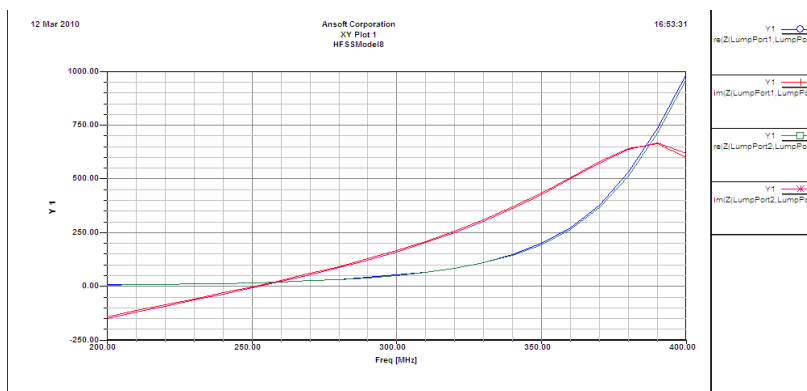


Figure 5:  $Z_{11}$  and  $Z_{22}$ , impedances of the dipole antennas.

of the dipole. The end point of the bent dipole antenna is  $H$  away from the ground plane as in Figure 1. The bent dipole is fed from the center of the antenna with a differential input. The RHCP is obtained simply by placing two dipole bent antennas perpendicular to each other, one in  $x$ - $z$  plane, the other in  $y$ - $z$  plane as in Figure 2. The bent dipole antennas are made of four L shaped metallic rectangular conductors which have square cross-sectional areas.

The electromagnetic simulations are performed using HFSS (for antenna) and ADS (matching circuit) software. For the simulations, the geometrical parameters are chosen as follows to obtain good RHCP properties as well as good impedance matching:  $W$  — length of vertical arms — 126.5 mm,  $H$  — distance from the ground plane — 12 mm,  $L$  — length of horizontal arms — 138.5 mm, Cross sectional area of the antenna is  $4 \times 4$  mm (copper rectangular tubes).

The ground plane is finite and its dimensions are  $4L \times 4L$ . The power handling capability has not been taken into consideration for simulations. The material for the antenna conductor is chosen as copper. The two dipole antennas are fed by a 90 degree phase shift from the two lumped ports in simulations. In real implementation, the antennas are fed by a quadrature coupler connected to the center of the dipole antennas.

## 2.2. The “Eggbeater” Antenna for Circular Polarization

To form the eggbeater antenna, two circular loop antennas are located perpendicular to each other as shown in Figure 3. The loop antennas are made of metallic circular conductors which have square cross-sectional areas. A sketch of one of the loop antenna is shown in Figure 4. The radius of the loop is  $r$  and the loop antenna is  $H$  away from the ground plane as in Figure 4. The RHCP is obtained simply by placing two loop antennas perpendicular to each other, one in  $x$ - $z$  plane, the other in  $y$ - $z$  plane as in Figure 3. One of the loops is shifted in  $z$ -direction with respect to the other loop so that two loops do not intersect.

The electromagnetic simulations are performed using HFSS software. For the simulations, the geometrical parameters are chosen as follows to obtain good RHCP properties as well as good

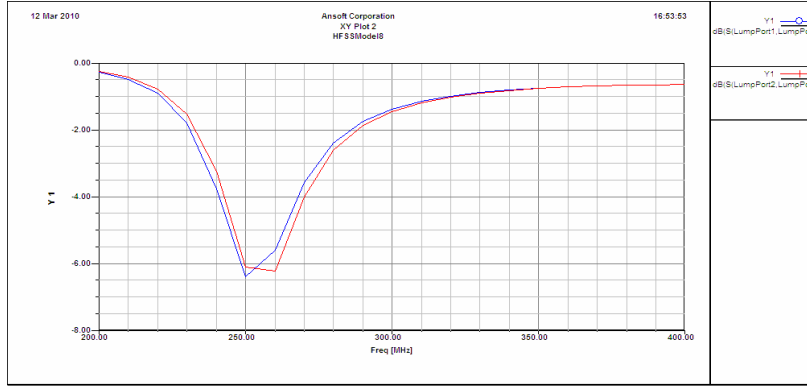
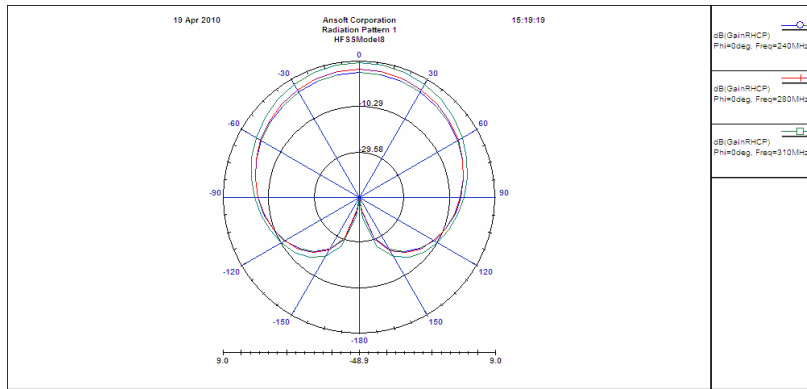
Figure 6:  $S_{11}$  and  $S_{22}$ , input return loss of the bent dipole antennas.

Figure 7: Bent dipole RHCP gain radiation pattern at 240, 280 and 310 MHz.

Table 1: Maximum RHCP and LHCP antenna gains for bent dipoles.

Frequency (MHz)	Max Gain (dB — RHCP)	Max Gain (dB — LHCP)
240	3.98	-9.34
280	5.31	-10.2
310	8.18	-8.85

matching:  $r$  — radius of the loops — 170 mm ( $2 * \pi * r$  is around one wavelength at 280 MHz),  $H$  — distance from the ground plane — 130 mm (approximately 1/8 wavelength at 280 MHz). One of the loop is shifted 5 mm in  $z$ -direction with respect to the other loop. Cross sectional area of the antenna is  $4 \times 4$  mm (copper rectangular tubes). The material for the antenna conductor is chosen also as copper. The two loop antennas are fed by a 90 degree phase shift from the two lumped ports. In real implementation, the antennas will be fed by a quadrature coupler connected to the center of the loop antennas.

### 3. SIMULATION AND MEASUREMENT RESULTS

Figures 5 and 6 displays the input impedances and the  $S$  parameters of the two dipole antennas, real part (green, blue curves) and imaginary parts (red curve). For the above assumed dimensions, it is seen that antennas have series resonance around 250 MHz, and the real part of the impedance is changing from 20 to 60 Ohms between the interested frequency range of 240 to 310 MHz.

With these input impedance values, it seems feasible to be able design a matching circuit such that the two antennas will be matched easily to a single source. The antenna radiation pattern gains are plotted for the three frequency points in the band, at 240, 280 and 310 MHz. RHCP performance at 240, 280 and 310 MHz are shown in Figure 7.

Maximum of the gain patterns for both RH and CH are summarized in Table 1.

Figure 8 displays the input impedances of the two loop antennas, imaginary part (red curve)

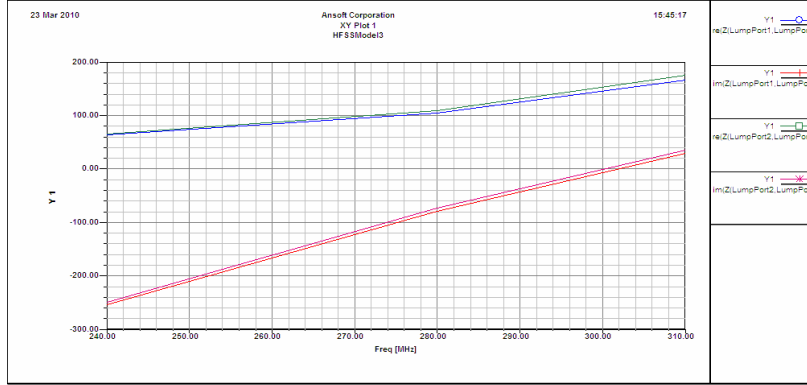


Figure 8:  $Z_{11}$  and  $Z_{22}$ , impedances of the loop antennas.

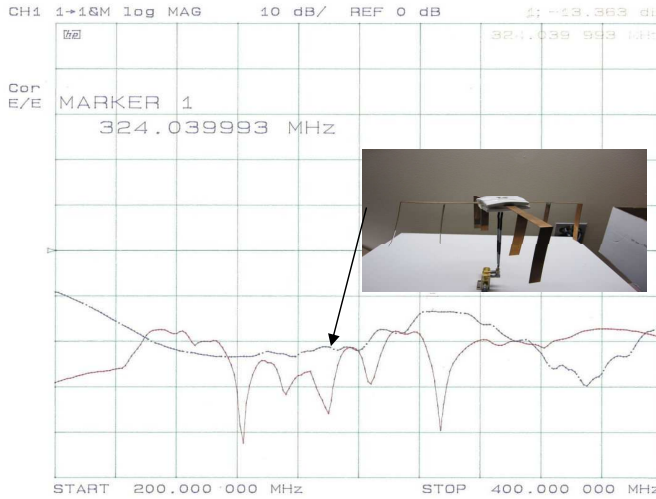


Figure 9: Measured  $S_{11}$  of the Moxon and eggbeater antennas.

Table 2: Maximum RHCP and LHCP antenna gains for eggbeater.

Frequency (MHz)	Max Gain (dB — RHCP)	Max Gain (dB — LHCP)
240	5.59	-4.55
280	5.94	-5.02
310	5.40	-5.18

and real parts (green, blue curves). For the above assumed dimensions, it is seen that antennas have series resonance around 300 MHz, and the real part of the impedance is changing from 60 to 180 Ohms between the interested frequency range of 240 to 310 MHz. One should also look at the  $S$ -parameters of the antenna since the antennas will be fed from a single source. Figure 9 shows the  $S_{11}$  and  $S_{22}$  of the antennas in dB versus frequency.

Maximum of the gain patterns for both RH and LH are summarized in Table 2.

When we compare the bent dipoles to egg beater, we see that size is much smaller for the same frequency band of operation. Polarization ratio (RHCP-LHCP) is also improved for the bent dipole. A prototype antenna was fabricated resulting in a height of 17.5 cm and maximum horizontal length of approximately 25 cm as seen in Figure 9. Double vertical elements are added for broader bandwidth operation. In Figure 9,  $S_{11}$  of both Moxon bent dipoles and egg beater antennas are shown for the band of 240–310 MHz. Both antennas are well matched within the desired band.

#### 4. CONCLUSION

Simulation results show that the bent dipole antenna has good return loss properties within the frequencies of 240–310 MHz UHF satcom band, and its physical size is much smaller compared to

an conventional egg beater antenna.

A prototype antenna is implemented and measured for its return loss and it is shown that  $S_{11}$  is well below  $-10\text{ dB}$  within the UHF satcom band. Simulated antenna gains show that RHCP gain is changing between 4 to 8 dB within the band and show RHCP/LHCP ratio of 13–17 dB within the band.

#### REFERENCES

1. Stutzman, W. L. and G. A. Thiele, *Antenna Theory and Design*, 2nd Edition, Wiley, New York, 1998.
2. Denison, M. and J. Fielding, Editors, *RSGB Radio Communication Handbook*, 9th Edition, UK, 2007
3. Moxon, L. A., *HF Antennas for All Locations*, Radio Society of Great Britain, 1993.

# Wideband Slotted Planar Antenna with Defected Ground Structure

Ayman A. R. Saad<sup>1</sup>, Elsayed E. M. Khaled<sup>2</sup>, and Deena A. Salem<sup>3</sup>

<sup>1</sup>Kosseir Radio, Telecom Egypt, Kosseir, Egypt

<sup>2</sup>Electrical Engineering Department, Assiut University, Assiut, Egypt

<sup>3</sup>Microstrip Department, Electronics Research Institute, Giza, Egypt

**Abstract**— This paper introduces a novel design of a multi-band microstrip antenna based on slot loading technique. Incorporating up to seven slots in the conventional microstrip rectangular patch antenna maintains the multi-band performance and a thin profile characteristic of the antenna. The geometrical configuration of the slots can be chosen according to a certain application to yield the required operational frequencies with wide bandwidths. The frequency range 2–8 GHz which is appropriate for many applications such as WLAN, Mobile WiMAX, and WCDMA is considered. The effect of the structure of the ground plane on the antenna performance is studied by mounting the proposed antenna structure either on a conventional perfect electrical conductor (PEC) ground plane or on a defected ground structure (DGS) ground plane. The antenna is fabricated. The measured data of the return loss versus frequency show very good agreement with the simulated results. The results show that the proposed antenna with DGS ground plane achieves wider bandwidth and high gain than that of conventional PEC ground plane.

## 1. INTRODUCTION

Most of the wireless communication systems are evolving towards miniaturization and multi functionality. Therefore designing multi-band antennas with wide impedance bandwidths while maintaining high radiation efficiency are crucial to construct a wireless communication system. Moreover designing miniaturized antennas are essential to meet wireless industry requirements for portable and mobile communication devices, with the spatial restriction they coerce. The objective of this research is to find out and suggest solutions to design and implement novel multi-band low profile antennas that compromise between the size and the performance of a small size antenna such as a microstrip antenna.

Incorporating slots to the radiating patch of the microstrip antenna enhance the multi-band performance and maintain the antenna's thin profile characteristic. Using slots several configurations can be constructed on the patch [1–3]. In this paper we show that by loading the patch of the conventional microstrip rectangular antenna with up to seven slots through a simple fabrication process, the performance of the antenna can be varied to cover multi-wideband operations. The geometrical configuration of the slots can be chosen according to a certain application to yield the required operational frequencies with wide bandwidths. The frequency band 2–8 GHz which is applicable for many applications such as WLAN, Mobile WiMAX, and WCDMA is considered. The effect of the structure of the ground plane on the antenna performance is studied. The design procedure is described as well as simulated results and measured data are presented.

## 2. DESIGN CONSIDERATIONS

The geometrical configuration of the proposed antenna is shown in Figure 1. It consists of a conventional antenna of an operating center frequency 2.4 GHz. The antenna is constructed on a Duroid 5880 substrate with thickness 1.575 mm, relative permittivity  $\epsilon_r = 2.2$  and a loss tangent  $\tan \delta = 0.0009$ . The ground plane and the patch dimensions are  $50.95 \times 59.00 \text{ mm}^2$  and  $41.35 \times 49.41 \text{ mm}^2$ , respectively. The antenna is fed by a coaxial probe of an inner radius of 0.6 mm. To reduce the size of the conventional antenna and increase the number of its resonance frequencies as well as widen its bandwidths the patch is loaded with up to seven slots that collectively construct a shape of a character or a letter. The loaded slots are indexed from A to G. The horizontal slots A, D, and G have dimensions  $39.35 \times 2.00 \text{ mm}^2$ . The vertical slots B, C, E, and F have dimensions  $2.00 \times 15.71 \text{ mm}^2$ . A strip of width 1.0 mm is considered around the slots to the left, upper, and right edges of the patch, which adds an extra degree of freedom that might be used to control the resonance frequencies and bandwidths of the proposed antenna. Table 1 illustrates examples of shapes of the characters 0, 2, 4, and 5 which constructed by certain arrangement of the slots shown in Figure 1.

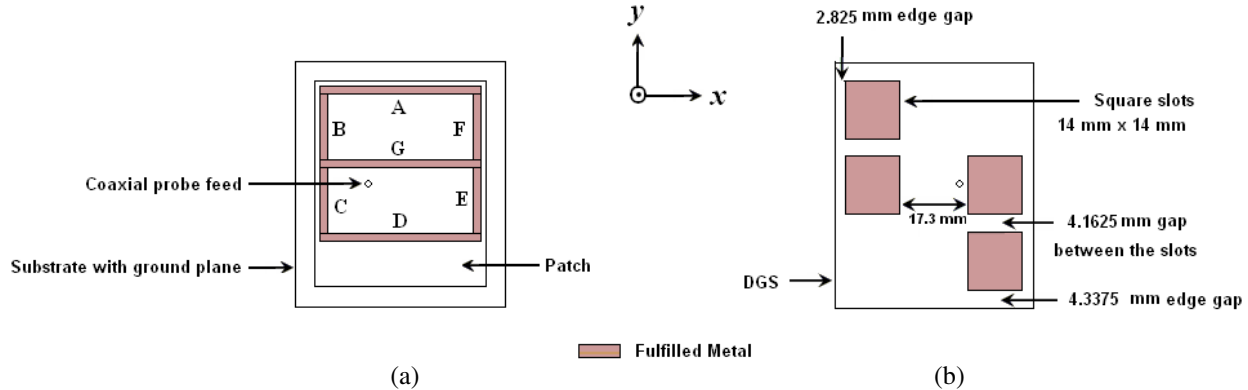


Figure 1: Geometrical configuration and dimensions of the proposed antenna. (a) Top-view with seven slots. (b) Bottom-view with DGS.

Table 1: Slots which are specified in Figure 1 used to construct shapes of some characters.

Geometrical Shape	Corresponding Slots
0	A, B, C, D, E, and F.
2	A, F, G, C, and D.
4	B, G, F, and E.
5	A, B, G, E, and D.

The way that slots are loaded into the patch increases the number of resonant frequencies due to the disturbance caused to the mean current paths of any resonant frequency (a mode). Changing dimensions of a slot causes changes in the effective current paths of a certain mode which in turn causes a shift in the resonant frequency of that mode. Since the radiated fields are created by the currents crossing the radiating edges of the patch, then vertical slots placed close to these edges can control the resonance frequency bands. Horizontal slots can be used to divide the patch into subsections which act as switches. These switches force the currents to travel through different paths according to the positions of the slots causing the antenna to resonate at different frequencies.

The effect of the structure of the ground plane on the antenna performance is also investigated by mounting the proposed antenna structure on either one of two different types of ground planes, the first is a conventional perfect electrical conductor (PEC) ground plane and the other is a defected ground structure (DGS). The DGS plane constitutes of an etched lattice of four squares of  $14 \times 14 \text{ mm}^2$  which are arranged as shown in Figure 1(b). There are two major advantages associated with using DGS planes. First, such structures provide wider bandwidths with enhanced gain and higher radiation efficiency as it will be shown later. Second, these structures forbid the propagation of electromagnetic waves in a certain frequency band. Therefore, they can be used to block surface waves that usually corrupt antenna performance at a certain frequency band [4]. This construction leads to almost a 26% size reduction of the conventional antenna.

### 3. SIMULATED RESULTS AND MEASURED DATA

The proposed antenna is simulated using different combinations of the slots constructing different shapes of characters such as, 0, 2, 4 and 5. The commercial software Zeland IE3D based on Method of Moment (MoM) is used for the simulations. The feeding point is located at  $(X_f, Y_f) = (-6.75, 0)$ , which is chosen by optimization techniques to give the best matching in the frequency range 2–8 GHz.

Figure 2 compares the simulated return loss versus frequency of the proposed antenna with either the PEC or DGS ground plane with different shapes constructed by the slots loading. It is observed that, the simulated return loss and thereby the impedance matching of the patch antenna with DGS ground plane is better than the corresponding return loss of the patch antenna with the conventional PEC ground plane. Also, the figure shows that most of the constructed shapes

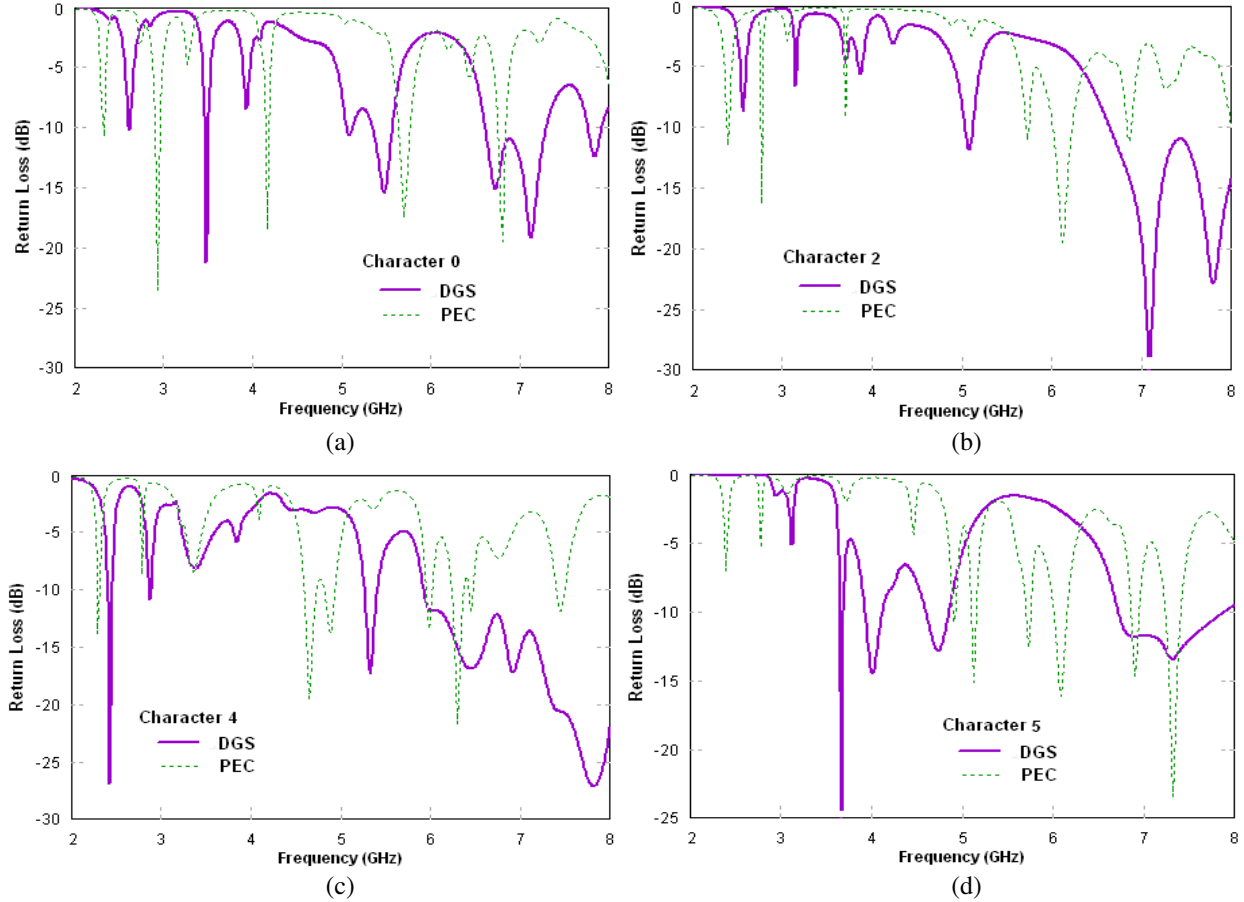


Figure 2: Comparison of the simulated return losses versus frequency for the proposed antenna with either the PEC or the DGS ground plane for different slots loading to form the shapes of, (a) the character 0, (b) the character 2, (c) the character 4, and (d) the character 5.

with slots loading give multi resonances with reasonable bandwidths. These configurations give the antenna the capability to be used for different applications. For a specific application one can decide the required slots loading according to the required resonant frequencies applicable for that application.

In the case of a defected antenna ground plane, the band gap of DGS and the resonant frequency of patch antenna overlaps, therefore inhibiting the surface wave propagation. The feature of the surface wave suppression helps to improve the antenna's performances such as increasing bandwidths and gain as well as reducing back radiations.

The DGS unit cell can be modeled most efficiently by a parallel  $R$ ,  $L$ , and  $C$  resonant circuit as shown in Figure 3(a). The resistance corresponds to both the radiation, and the conductor and the dielectric losses of the defect plane. The equivalent  $R$ ,  $L$ , and  $C$  values are obtained from the following expression [5],

$$C = \frac{\omega_c}{2Z_o(\omega_o^2 - \omega_c^2)} \quad (1)$$

$$L = \frac{1}{4\pi^2 f_o^2 C} \quad (2)$$

$$R(\omega) = 2Z_o / \sqrt{\frac{1}{|S_{11}(\omega)|^2} - \left(2Z_o(\omega C - \frac{1}{\omega L})\right)^2} - 1 \quad (3)$$

where  $f_o$  and  $f_c$  are the resonance, and the cutoff frequency respectively, which can be obtained by simulation and  $Z_o$  is characteristic impedance (50 ohm).

Employing the proposed etched lattice in the ground plane increases the series inductance of the microstrip line. Therefore changing the physical dimensions of the etched lattice can easily

control the effective inductance. This physical arrangement of the lattice provides rejection of some frequency bands, which may be denoted by bandgap or stopband effect. From the simulation results shown in Figure 3(b) it can be seen that, adding a rectangular shaped lattice etched in the ground plane, considerably improves  $|S_{11}|$  to almost  $-15$  dB in the passband around the frequency  $8$  GHz without any other effects at the other frequencies. Simulated  $|S_{21}|$  remains lower than  $-5$  dB in the stopband at  $4.5$  GHz and lower than  $-3$  dB in the passband at  $8$  GHz. The cutoff frequency mainly depends on the etched square area in a ground plane [6].

To validate the idea presented in the paper, the case of loaded slots constructing the shape of the character 0 is implemented. The antenna was fabricated using photolithographic technique with either the PEC ground plane or with the DGS ground plane as shown in Figures 4(a) and 4(b), respectively. The shape of the character 0, in this case, is constructed by placing a pair of U-shaped slots face to face with separation of  $2.0$  mm. The U-shaped slots can be considered as a combination of three slots joint together. The first U-shaped slot is formed from the combination of the slots A, B and F, and the second U-shaped slot is formed from the combination of the slots C, D and E. The simulation and measurement return loss are presented in Figure 5. Very good agreements between the simulated results and the measured data are observed.

The simulated antenna peak gain and radiation efficiency are shown in Figures 6(a) and 6(b), respectively. The figure shows that the antenna gain has improved up to  $10.98$  dBi (from  $-4.04$  dBi to  $6.94$  dBi) at  $3.5$  GHz, and the radiation efficiency increased up to  $16.38\%$  (from  $76.07\%$  to  $92.45\%$ ) at  $3.26$  GHz. This result demonstrates the ability of the DGS ground plane to enhance the gain and radiation efficiency of the antenna. Figure 7 illustrates the simulated far-field radiation patterns of  $E_\theta$  and  $E_\varphi$  for the proposed antenna at the frequency  $6.8$  GHz in the  $yz$  and  $xz$  planes. Nearly omnidirectional patterns have been observed in the both  $yz$  and  $xz$  planes which is suitable for mobile communications.

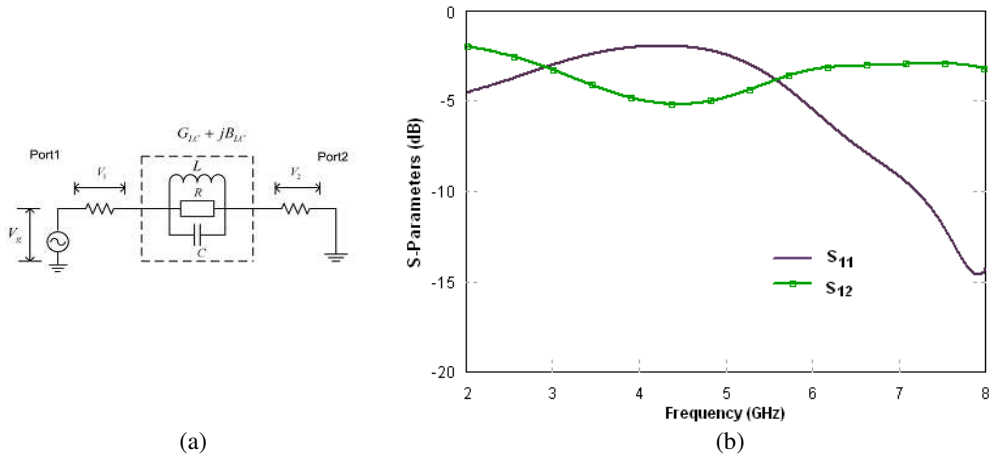


Figure 3: (a)  $RLC$  equivalent circuit model of the DGS unit cell. (b) IE3D full wave simulation of  $S$ -parameters.

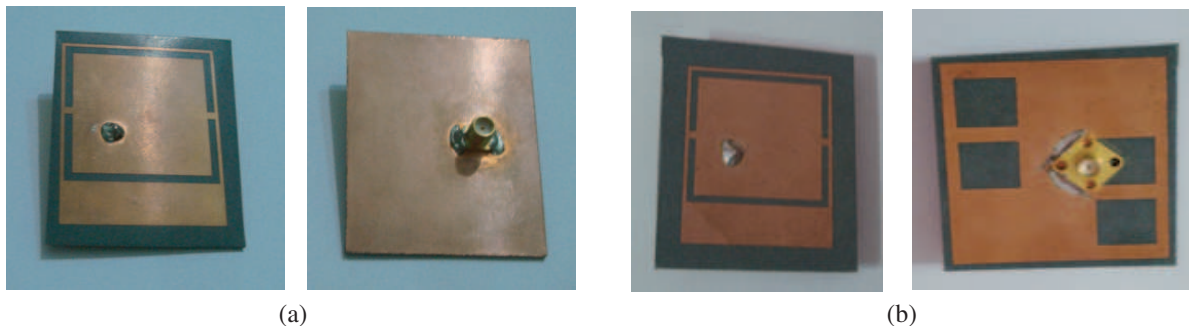


Figure 4: Photograph of the proposed antenna with slots loading constructing the shape of the character 0, (a) slotted patch with PEC ground plane, (b) slotted patch with DGS ground plane.

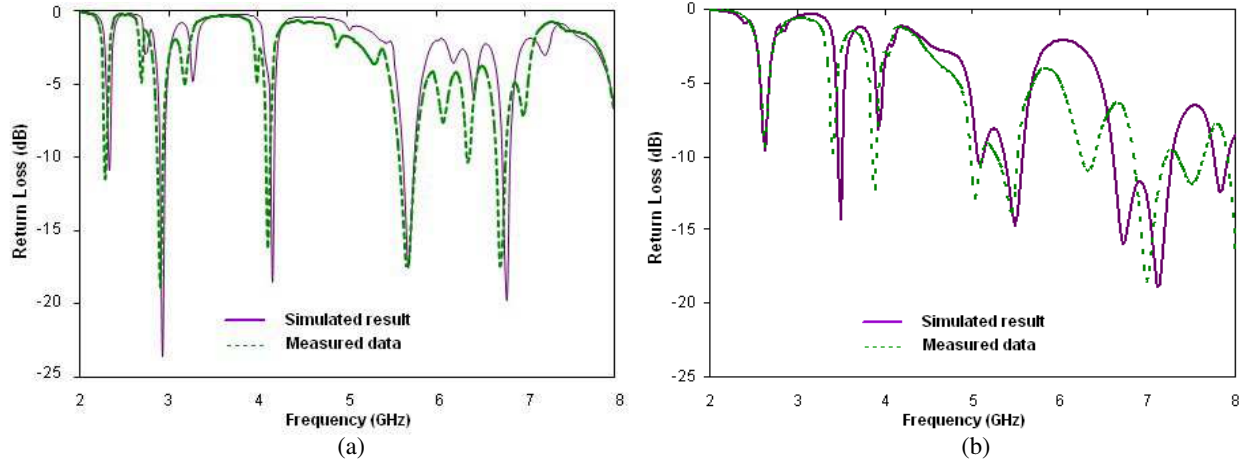


Figure 5: Simulated and measured return loss versus frequency for the proposed antenna with slots loading constructing the shape of the character 0, (a) with PEC ground plane, (b) with DGS ground plane.

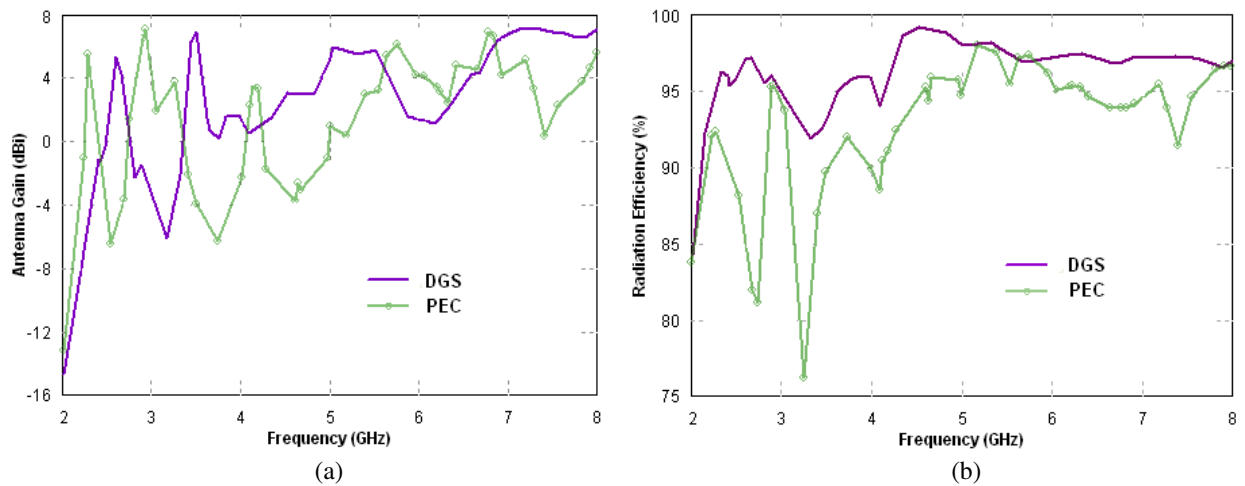


Figure 6: Peak antenna gain (a), and radiation efficiency (b), versus frequency for the proposed antenna with slots constructing the shape of the character 0 with either the PEC or the DGS ground plane.

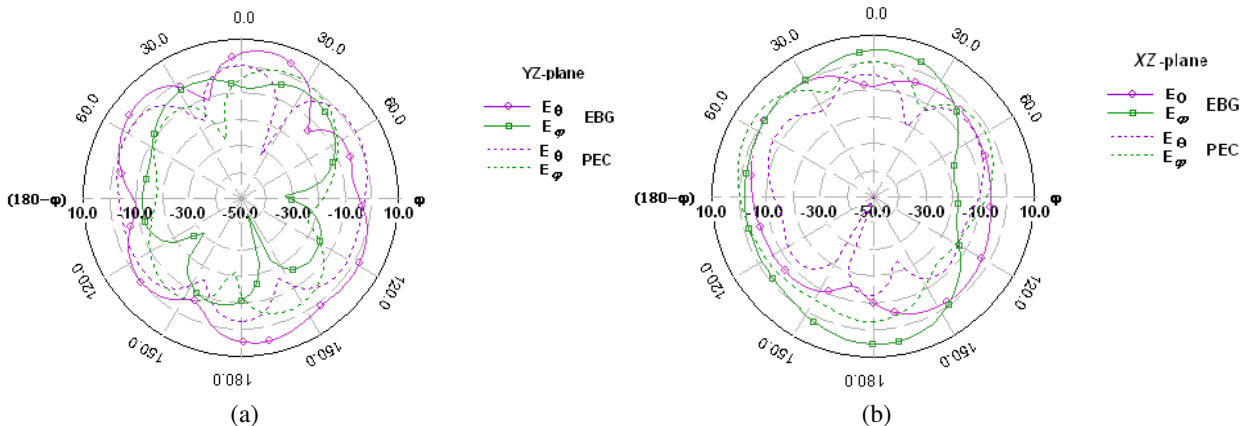


Figure 7: Radiation patterns of  $E_\theta$  and  $E_\phi$  for the proposed antenna with slots constructing the shape of the character 0 with either the PEC or the DGS ground plane at the frequency 6.8 GHz, (a) in the  $yz$  plane (b) in the  $xz$  plane.

#### 4. CONCLUSION

In this paper, loading the patch of the conventional microstrip rectangular antenna with slots enables the designers to control the performance of the antenna to maintain multi-wideband functionality for various applications. Depending on the application the slots arrangement may be decided upon. Comparing the results obtained using the full PEC ground plane and that using the DGS shows that the later enhance the performance of the radiation parameters of the proposed antenna in the required frequency bands. The equivalent circuit model of the DGS unit cell underneath the microstrip line with the parameter extraction method is presented to study the effects of DGS structure on the antenna performance.

The antenna is fabricated and the measured data show very good agreement with the simulated results. The results demonstrate a wider bandwidth and higher gain than that of the conventional antenna with a PEC ground plane. The proposed antenna is capable to achieve multi-wideband operations with return loss (RL) less than 10 dB in the frequency range of 2–8 GHz. Moreover almost a 26% size reduction is achieved which make the antenna suitable for mobile and portable applications.

#### REFERENCES

1. Khaled, E. M. and A. R. Saad, "Multi-wideband compact microstrip patch antennabased on slot matching," *Progress In Electromagnetics Research C*, Vol. 4, 169–177, 2008.
2. Lu, J. H. and K. L. Wong, "Slot-loaded, meandered rectangular microstrip antenna with compact dual-frequency operation," *Electronics Letters*, Vol. 34, No. 11, 1048–1050, May 1998.
3. Sheta, A. F., A. Mohra, and S. F. Mahmoud, "Multi-band operation of compact H-shaped microstrip patch antenna," *Microwave Opt. Tech. Letters*, Vol. 35, No. 5, 363–367, Dec. 2002.
4. Yang, F. and Y. Rahmat-Samii, "Microstrip antennas integrated with electromagnetic bandgap (EBG) structures: A low mutual coupling design for array applications," *IEEE Antennas and Prop.*, Vol. 51, No. 10, 2939–2949, Oct. 2003.
5. Weng, L. H., Y. C. Guo, X. W. Shi, and X. Q. Chen, "An overview on defected ground structures," *Progress In Electromagnetics Research B*, Vol. 7, 173–189, 2008.
6. Boutejdar, A., M. Makkey, A. Elsherbini, and A. Omar, "Design of compact stop-band extended microstrip low-pass filters by employing mutual-coupled square-shaped defected ground structures," *Microwave Opt. Tech. Letters*, Vol. 50, No. 4, 1107–1111, Apr. 2008.

# Adaptive Beamforming Technique for Virtual Antenna Using Modified Interpolated Spatial Smoothing Algorithm

Wenxing Li<sup>1</sup>, Yipeng Li<sup>1</sup>, Lili Guo<sup>1</sup>, Wenhua Yu<sup>2</sup>, and Raj Mittra<sup>2</sup>

<sup>1</sup>Harbin Engineering University, Harbin 150001, China

<sup>2</sup>The Pennsylvania State University, University Park, PA 16802, USA

**Abstract**— In this paper we present an effective algorithm to inhibit the coherent interference with the virtual antenna based on the traditional interpolated spatial smoothing algorithm. Using the interference subspace projection concept, we establish an interference space utilizing the virtual array interfere steering vectors and then project the transformation matrix to it. The theoretical analysis has demonstrated that the interference components in the virtual covariance matrix can be enhanced. Then by employing the minimum variance distortionless response (MVDR) beam forming method, it can improve the robustness of adaptive beamforming with virtual antenna array, and significantly enlarge the inhibition gains on the coherent interference and output signal to interference and noise ratio (SINR).

## 1. INTRODUCTION

The analyses of electromagnetic phenomena in the practical wireless communication environment have become an important topic today. The electromagnetic reflection, refraction and diffraction in a complex terrain is the major issues in the analysis of the coherent interference of incident signal. Since the steering vector of coherent source and the noise subspace are not orthogonal, the subspace approaches such as MUSIC becomes invalid. The spatial smoothing technique [1, 2] is a common decorrelation algorithm, and it recovers the rank of signal covariance, and makes signal subspace and the noise subspace orthogonal again. However, it can only be applied on the antenna array with Vandermonde manifold. The virtual array transformation technique [3] through the interpolationn in the array scanning sector of interest transforms the real array with an arbitrary shape into the virtual array with the Vandermonde manifold. By applying the spatial smoothing technique on virtual array [4–7], the decorrlation problem on a real array can be solved effectively.

When the interpolated spatial smoothing algorithm [4] is used in the virtual antenna adaptive beam forming, the inhibition gains on the coherent interference cannot be satisfied with the practical requirements, and thus the same issue happens to the output SINR [5]. An optimum virtual array beamformer [6] employs the multiple virtual subarrays to conduct dimension recovery, but the system structure is complex, and the real-time performance is not good. In order to enlarge the depth of beam forming null and enhance the anti-interference performance, this paper proposes the modified interpolated spatial smoothing algorithm that imports the interference direction constraint information into transformation matrix based on the subspace projection concept. The robustness of beam forming is reinforced, and a good beam preserving and null forming performance can be provided even in the situation of small snapshots number.

## 2. VIRTUAL ARRAY TRANSFORMATION TECHNIQUES

Considering an array with  $N$  elements [3], when  $M$  far field narrow band signals are incident on an antenna array, the received data  $\mathbf{X}$  can be expressed as follows:

$$\mathbf{X}(t) = \mathbf{A}(\theta)\mathbf{S}(t) + \mathbf{N}(t) \quad (1)$$

where  $\mathbf{X}(t)$  is  $N \times 1$  snap data vector.  $\mathbf{S}(t) = [s_1(t), s_2(t), \dots, s_M(t)]^T$  is a vector containing the complex signal envelops of  $M$  narrow-band signal sources.  $\mathbf{N}(t) = [n_1(t), n_2(t), \dots, n_N(t)]^T$  is a vector of zero-mean spatially white sensor noise of variance  $\sigma_n^2$ ;  $\mathbf{A}(\theta)$  is an array manifold matrix, namely,  $\mathbf{A}(\theta) = [\mathbf{a}(\theta_1), \mathbf{a}(\theta_2), \dots, \mathbf{a}(\theta_M)]$ , where  $\mathbf{a}(\theta_k) = [1, e^{j\beta_k}, \dots, e^{j(N-1)\beta_k}]^T$ ,  $k = 1, 2, \dots, M$  represents a steering vector in the  $\theta_k$  direction and  $\beta_k$  is the information source wave number that can be expressed as:

$$\beta_k = \frac{2\pi}{\lambda}d \sin(\theta_k) \quad (2)$$

Assumed that the signal and noise are linearly independent, then the data covariance is written in the format below:

$$\mathbf{R} = E \{ \mathbf{X}(t) \mathbf{X}^H(t) \} = \mathbf{A} \mathbf{R}_s \mathbf{A}^H + \sigma_n^2 \mathbf{I} \quad (3)$$

where  $E \{ \cdot \}$  denotes the mathematical expectation;  $\mathbf{R}_s = E \{ \mathbf{S}(t) \mathbf{S}^H(t) \}$  represents the autocorrelation matrix of signal complex envelops;  $\sigma_n^2$  is the noise power;  $\mathbf{I}$  is the unit matrix, and  $(\cdot)^H$  denotes the matrix conjugate transposition.

For the coherent signal source, the rank of singular signal covariance matrix  $\mathbf{R}_s$  will decrease to be 1. According to the subspace approaches, after conducting eigen-decomposition on  $\mathbf{R}$ , the dimension of signal subspace will be smaller than the rank of array manifold matrix  $\mathbf{A}(\theta)$ , which will lead to that the steering vector  $\mathbf{a}(\theta_k)$  corresponding to the coherent signal source is not orthogonal to the noise subspace, and the approaches based on the subspace get ineffective completely.

Virtual array transformation is based on the interpolation technique [3] in which the entire antenna array scanning vector is divided into several subregions, and the subregion of interest will be segmented through a certain transformation to realize the mapping from the original to virtual array. Assume that a signal lies in the region  $\Theta$ , we equally divide  $\Theta$  to:

$$\Theta = [\theta_l, \theta_l + \Delta\theta, \theta_l + 2\Delta\theta, \dots, \theta_r - \Delta\theta, \theta_r] \quad (4)$$

where  $\theta_l$  and  $\theta_r$  are the left and right boundary of region  $\Theta$ , respectively.  $\Delta\theta$  is the step length. The real array manifold matrix in the chosen area is expressed as follows:

$$\mathbf{A} = [\mathbf{a}(\theta_l), \mathbf{a}(\theta_l + \Delta\theta), \mathbf{a}(\theta_l + 2\Delta\theta), \dots, \mathbf{a}(\theta_r - \Delta\theta), \mathbf{a}(\theta_r)] \quad (5)$$

where  $\mathbf{a}(\theta_i)$  represents the steering vector in the  $\theta_i$  direction of a real array, and the array manifold matrix of virtual array in the same area  $\Theta$  is expressed as follows:

$$\bar{\mathbf{A}} = [\bar{\mathbf{a}}(\theta_l), \bar{\mathbf{a}}(\theta_l + \Delta\theta), \bar{\mathbf{a}}(\theta_l + 2\Delta\theta), \dots, \bar{\mathbf{a}}(\theta_r - \Delta\theta), \bar{\mathbf{a}}(\theta_r)] \quad (6)$$

where  $\bar{\mathbf{a}}(\theta_i)$  represents the steering vector in the  $\theta_i$  direction of a virtual array, then there exists a fixed transformation relation  $\mathbf{B}$  between the virtual array and the real array that satisfies:

$$\min_{\mathbf{B}} \|\mathbf{BA} - \bar{\mathbf{A}}\|_F \quad (7)$$

where  $\|\cdot\|_F$  is Frobenius mold. When the transformation point number is larger than the real array element number and  $\bar{\mathbf{A}}$  is full-rank, the transformation matrix  $\mathbf{B}$  obtained from (7) can be expressed as:

$$\mathbf{B} = \bar{\mathbf{A}} \mathbf{A}^H (\mathbf{A} \mathbf{A}^H)^{-1} \quad (8)$$

Define the transformation error is:

$$E(\mathbf{B}) = \frac{\min_{\mathbf{B}} \|\mathbf{BA} - \bar{\mathbf{A}}\|_F}{\|\bar{\mathbf{A}}\|_F} \quad (9)$$

When  $E(\mathbf{B}) = 0$ , there is no approximation in the virtual transformation process. If the number of sampling points in the transformation area is finite, there exists an approximation that can be improved by dividing the area further and calculating the transformation matrix again. In practice, as long as the approximation is smaller than the level  $10^{-3}$ , the accuracy can be ensured. The covariance matrix of virtual array can be expressed as:

$$\bar{\mathbf{R}} = \mathbf{B} \mathbf{R} \mathbf{B}^H = \mathbf{B} (\mathbf{A} \mathbf{R}_s \mathbf{A}^H + \sigma_n^2 \mathbf{I}) \mathbf{B}^H = \bar{\mathbf{A}} \mathbf{R}_s \bar{\mathbf{A}}^H + \sigma_n^2 \mathbf{B} \mathbf{B}^H \quad (10)$$

Through the virtual transformation, the white noise received by a real array has already turned into the colored noise. In order to apply the numerical algorithm, the colored noise must be whiten first, and then the virtual array covariance matrix  $\hat{\bar{\mathbf{R}}}$  is calculated in the white noise background. The optimal MVDR weight factor is written as follows:

$$\mathbf{W}_{opt} = \alpha \hat{\bar{\mathbf{R}}}^{-1} \bar{\mathbf{a}}(\theta_0) \quad (11)$$

where  $\bar{\mathbf{a}}(\theta_0)$  is a virtual array steering vector in the desired signal direction and the coefficient  $\alpha = [\bar{\mathbf{a}}^H(\theta_0) \hat{\bar{\mathbf{R}}}^{-1} \bar{\mathbf{a}}(\theta_0)]^{-1}$ .

### 3. MODIFIED INTERPOLATED SPATIAL SMOOTHING ALGORITHM

In this section, we describe the modified interpolated spatial smoothing algorithm. After obtaining the transformation matrix  $\mathbf{B}$ , we establish an interference subspace and then make modulation on the transformation matrix by subspace projection. The detailed procedure is following: 1) pre-estimate the interfere directions  $\theta_1, \theta_2, \dots, \theta_{M'}$ ; 2) calculate the virtual array steering vectors in the interfere directions  $\bar{\mathbf{a}}(\theta_i)$ ; 3) establish the interference subspace, and define the projection matrix  $\mathbf{C}$  as:

$$\mathbf{C} = \left( \sum_{i=1}^{M'} \bar{\mathbf{a}}(\theta_i) \bar{\mathbf{a}}^H(\theta_i) \right)^H \quad (12)$$

4) make modulation on the transformation matrix  $\mathbf{B}$  by projection on the interference subspace:

$$\bar{\mathbf{B}} = \mathbf{CB} \quad (13)$$

The above procedure can enhance the interference components in the virtual covariance matrix [8], then by employing the MVDR adaptive beamforming method, the inhibition gains on the coherent interferes can be enlarged, consequently the output SINR can also be improved. Because the characteristic of MVDR method is: in the desired signal direction the gain is restrained to be 1, and simultaneously array output power is ensured minimum. The higher the interference power is, the stronger inhibition in these directions will be generated. This is the reason why the proposed approach can improve the robustness performance of adaptive beamforming of the virtual antenna array.

### 4. NUMERICAL VERIFICATION

In this section, we use a real array with 4 elements separated by one wavelength as an example to demonstrate the performance of the proposed approach. The expected signal incidents coming from  $0^\circ$  direction, signal to noise ratio is  $SNR = 0$  dB. Three coherent interferers lie in  $-60^\circ$ ,  $-40^\circ$  and  $50^\circ$  directions, respectively. Signal to interference ratio is  $SIR = -40$  dB. The virtual array is uniformly linear array of 10 elements separated by  $\lambda/2$ , and the forward/backward spatial smoothing parameter  $m = 6, p = 5$ . The virtual transformation area is  $[-65^\circ, -35^\circ] \cup [45^\circ, 55^\circ]$ . The coherent interferers eigenvalue, the ccoherent interferers beam forming and the coherent interferers output SINR by using the different approaches are plotted in Figs. 1 to 3.

When the interferes and desired signal are completely correlated, there is only one large eigenvalue after eigen-decomposition using the real array method, the eigenvalues of signal subspace have “spread” into noise subspace, consequently, it cannot generate nulls in interfere directions; however, the modified and original interpolated spatial smoothing algorithm have integrated spatial smoothing technique, the rank of signal covariance matrix can get recovered, therefore, they can be employed to inhibit coherent interferes, via original interpolated spatial smoothing algorithm the

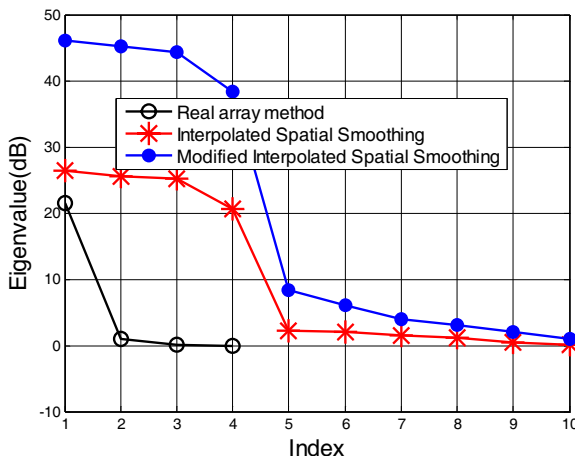


Figure 1: Coherent interferers eigenvalue using different approaches.

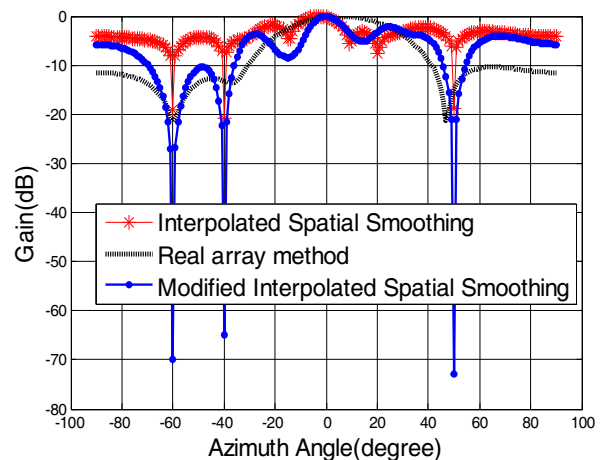


Figure 2: Coherent interferers beam forming using different approaches.

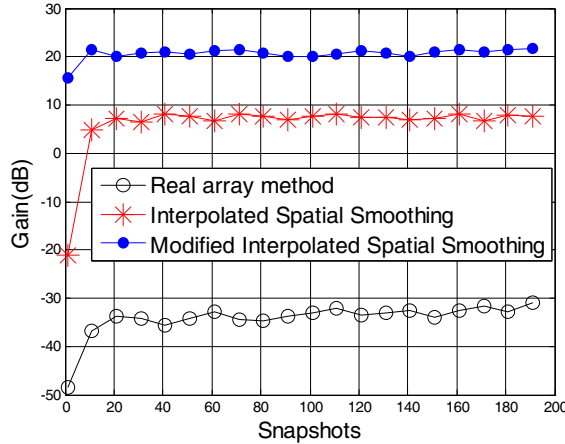


Figure 3: Coherent interferers output SINR using different approaches.

inhibition gains are about  $-20$  dB, and output SINR floats around  $8$  dB; via modified interpolated spatial smoothing algorithm the inhibition gains are about  $-70$  dB, and output SINR is more than  $20$  dB, the performance is fairly good.

## 5. CONCLUSIONS

The modified interpolated spatial smoothing algorithm is presented in this paper. We enhance the interference components in the virtual covariance matrix by introducing the interference subspace projection concept. Through the MVDR adaptive beam forming, the better anti-interference performance can be obtained and the virtual antenna array output SINR is also improved. The effectiveness of our presented algorithm is verified by the simulation results.

## REFERENCES

- Shan, T. J. and T. Kailath, "Adaptive beamforming for coherent signals and interference," *IEEE Trans. on Acoustics, Speech, and Signal Processing*, Vol. 33, No. 3, 527–536, 1985.
- Lu, M. and Z.-Y. He, "Adaptive beamforming for coherent interference suppression," *ICASSP, IEEE International Conference on Acoustics, Speech and Signal Processing*, Vol. 1, 301–304, Apr. 1993.
- Friedlander, B., "The root-music algorithm for direction finding with interpolated arrays," *Signal Processing*, Vol. 30, No. 1, 15–29, 1993.
- Weiss, A. J. and B. Friedlander, "Performance analysis of spatial smoothing with interpolated arrays," *IEEE Transactions on Signal Processing*, Vol. 41, No. 5, 1881–1892, 1993.
- Su, B.-W., "Research on array digital beamforming technology (in Chinese)," Doctoral Dissertation, 39–55, National University of Defense and Technology, 2006.
- Lee, T.-S. and T.-T. Lin, "Adaptive beamforming with interpolated arrays for multiple coherent interferers," *Signal Processing*, Vol. 57, No. 2, 177–194, 1997.
- Lau, B. K., M. Viberg, and Y. H. Leung, "Data-adaptive array interpolation for DOA estimation in correlated signal environments," *ICASSP, IEEE International Conference on Acoustics, Speech and Signal Processing — Proceedings*, Vol. 4, 945–948, 2005.
- Li, W., Y. Li, L. Guo, and W. Yu, "Performance improvement technique of adaptive virtual antenna array," *ACES 2011*, Williamsburg, Virginia, USA, March 2011.

# An Integrated UWB and Bluetooth Antenna with Dual Band-notched Characteristic

K. C. Law, S. W. Cheung, and T. I. Yuk

Department of Electrical and Electronic Engineering, The University of Hong Kong, Hong Kong, China

**Abstract**— This paper presents the design of an integrated Ultrawideband (UWB) and Bluetooth microstrip monopole antenna with a dual band-notched characteristic. The antenna consists of an elliptical ring as the radiator to cover the frequency bands for both the Bluetooth (2.4–2.5 GHz) and UWB (3.1–10.6 GHz) applications. A triangular resonator and a meander defected-ground structure (DGS) are used to generate two notches at the centre frequencies of 2.856 and 5.5 GHz. The return loss, radiation pattern, peak gain and efficiency of the antenna are studied using computer simulation.

## 1. INTRODUCTION

Since the Federal Communication Commission (FCC) assigned 3.1–10.6 GHz frequency band of Ultrawideband (UWB) systems in February 2002 [1], UWB technology has been attracting considerable interests in both the academic and commercial domains due to the potentially high data rate (more than 110 Mbits/s) for short range, low power consumptions and easy connections to different devices such as wireless USB, PCs, high-definition TVs, etc.

In 2006 [2], the Bluetooth Special Interest Group (SIG) selected the WiMedia Alliance multi-band orthogonal-frequency-division multiplexing (MB-OFDM) version of UWB, which could be integrated with the current Bluetooth wireless technology. Nowadays, some portable devices are equipped with the Bluetooth antenna and WLAN antenna. It will be a difficult task to put an additional UWB antenna in the same portable devices due to the limited space available. One of the possible solutions is to use an antenna that can operate in both the UWB and Bluetooth frequency bands.

The current IEEE802.11a/n WLAN systems are occupying a small portion of the UWB. Thus there will be interference between the UWB systems and the IEEE802.11a/n systems. To reduce this interference, the antenna can be designed to have a band-notched characteristic. Different techniques have been studied to produce the band-notched features [3–11]. However, in these designs, the suppressed gains and efficiencies of the antennas at the notched frequency bands were quite limited and far from zero.

In this paper, we propose a planar-monopole antenna using an elliptical ring as the radiator to cover both the UWB and Bluetooth frequency bands with a dual-band notch. As there are other wireless communication systems between the Bluetooth and UWB bands, for example: 3GPP (2.57–2.62 GHz), CDMA2000 (US 2.5 GHz Band) and CMMB (2.635–2.66 GHz), a triangular resonator is placed at the centre of the elliptical-ring radiator to create a notch at 2.856 GHz to reduce interference between the Bluetooth system and these wireless systems. The centre frequency of the notch can be controlled by adjusting the dimensions of the triangular resonator. To reduce interference between the UWB system and the IEEE802.11a/n WLAN system (5.15–5.825 GHz), a meander-DGS is employed to create another notched band at 5.5 GHz. Results show that the peak gain can be suppressed by more than 12 dB at the frequency of around 5.5 GHz, which is deeper than the notches designed for other integrated UWB and Bluetooth antennas [8–11], and the efficiency is close to zero.

## 2. STRUCTURE OF ANTENNA, MODELING OF MEANDER-DGS AND DESIGN OF ANTENNA

### 2.1. Structure of Antenna

Our proposed dual band-notched UWB antenna is shown in Fig. 1. In this design, we use the planar-monopole technology to achieve a compact antenna size for applications in small wireless devices. The antenna has an area of  $31.5 \times 39.75 \text{ mm}^2$  and is designed on a Roger PCB, RO4350B, with a relative permittivity of 3.48, thickness of 0.762 mm and loss tangent of 0.0037. The antenna consists of an elliptical-ring radiator fed by a  $50\text{-}\Omega$  microstrip line printed on one side of the substrate. A triangular resonator is printed inside the elliptical-ring radiator to create a notched

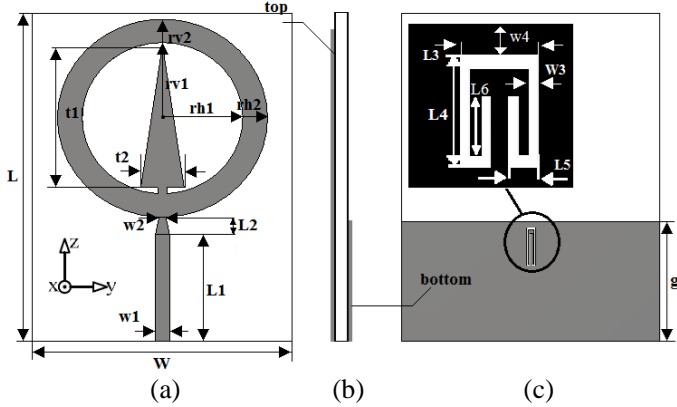


Figure 1: Configuration of proposed antenna: (a) top view, (b) side view and (c) bottom view.

Table 1: Optimized parameters of antenna (mm).

$L$	$L_1$	$L_2$	$L_3$	$L_4$
39.75	13	2.1	1.5	4.58
$L_5$	$L_6$	$g_l$	$t_1$	$t_2$
0.63	3.68	14.5	17.25	5.25
$W$	$w_1$	$w_2$	$w_3$	$w_4$
31.5	1.7	0.8	0.23	0.2
$r_{h1}$	$r_{h2}$	$r_{v1}$	$r_{v2}$	
9.7	12.8	9.1	12	

frequency band at 2.856 GHz next to the Bluetooth band. The other side of the substrate is a ground plane where a meander-DGS is etched under the feed line and acts as an LC resonator to create another notched frequency band centered at 5.5 GHz. To achieve good impedance matching, the distance, gap, between the radiator and the ground plane is set to 0.6 mm and the width of the feed line is tapered, changing gradually from  $w_1 = 1.7$  mm to  $w_2 = 0.8$  mm as shown in Fig. 1. The dimensions of the antenna are optimized using computer simulation, with detailed values listed in Table 1.

## 2.2. Design of Antenna

The meander-DGS etched on the ground plane behaves like a parallel LC resonant [12, 13]. At resonance, the signal from the feed line will be coupled into the meander-DGS, producing a notched characteristic for the antenna. The inductance and capacitance of the LC resonant circuit can be changed by using the dimensions of the meander-DGS and hence used to adjust the notched frequency. As an illustration, Fig. 2(a) shows the simulated notched frequency versus length  $L_4$  of the meander-DGS. To create a notch at a particular frequency, we can simply select the required value from Fig. 2(a).

There is no exact method to design a general microstrip triangular resonator, except for equilateral and isosceles right-angled triangular resonators [14, 15]. Usually, curve fitting is used as a guideline to design the triangular resonators, which is used in our studies here. We first study the effects of the base  $t_2$  and height  $t_1$  of the triangular resonator on the resonant frequency by computer simulation. Fig. 2(b) shows the simulated resonant frequency versus  $t_1$  for different  $t_2$ . It can be seen that  $t_2$  has an insignificant effect on the resonant frequency, but the resonant frequency has a linear relationship with the height  $t_1$ . From these results, we can use linear interpolation to relate the centre frequency in GHz to  $t_1$  by the following equation:

$$f = -0.1893 \times t_1 + 6.122 \quad (1)$$

## 3. RESULTS AND DISCUSSIONS

The antenna has been designed with two notches, centered at 2.856 and 5.5 GHz, on a RO4350B substrate using computer simulation. The simulated return losses of the antenna, with a single

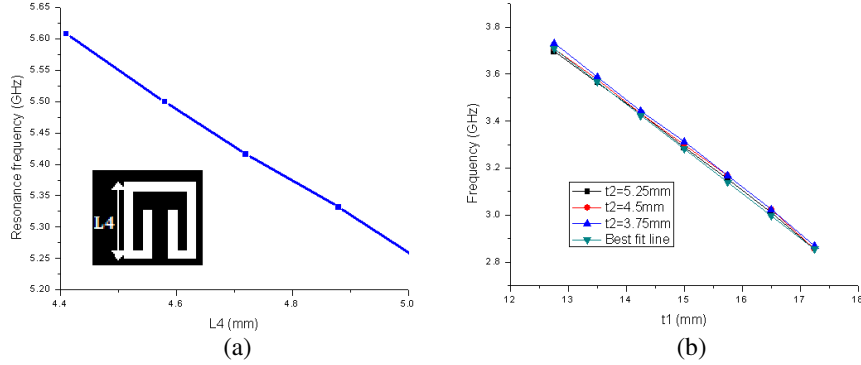


Figure 2: Simulated resonant frequency versus (a) length  $L_4$  and (b) height  $t_1$  for different bases  $t_2$ .

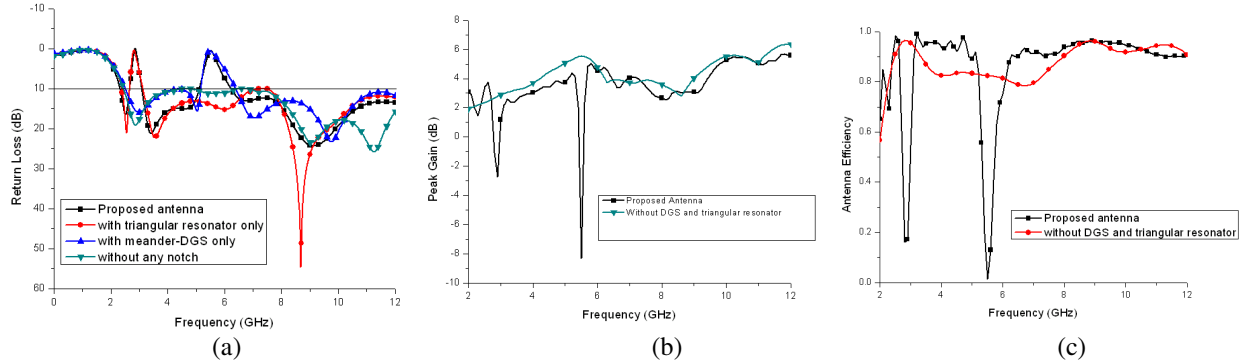


Figure 3: Simulated (a) return losses, (b) peak gain and (c) efficiency with or without notches.

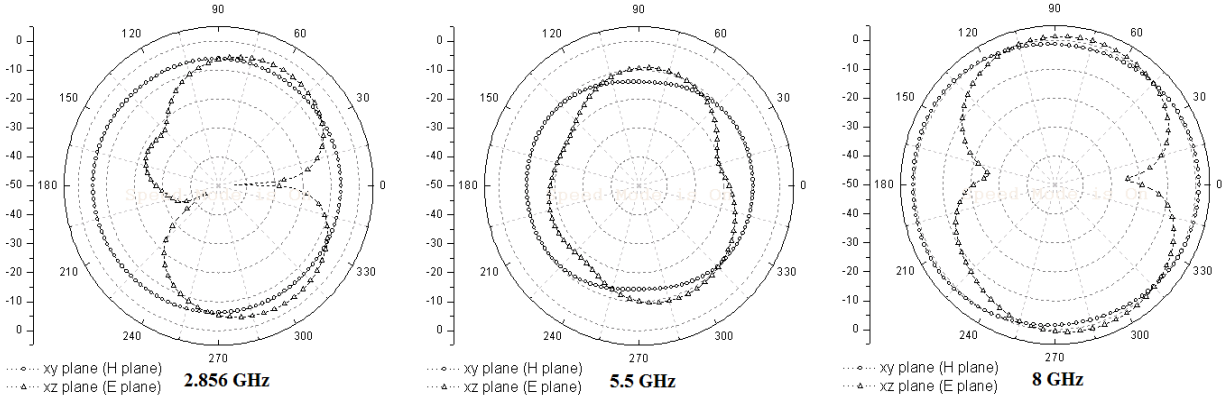


Figure 4: Simulated radiation pattern of proposed antenna.

notch and dual notch are shown in Fig. 3(a). The return loss of the antenna without notch is also shown in the same figure for comparison. It can be seen that, in all these conditions, our proposed antenna has the bandwidths (for return loss  $> 10 \text{ dB}$ ) from 2.31 to over 12 GHz, fully satisfying the bandwidth requirement for UWB applications (3.1–10.6 GHz). For the antenna without any notch, the bandwidth is from 2.44 to over 12 GHz. With the triangular resonator, the lower operating frequency extends to 2.36 GHz and the notch at 2.856 GHz has a bandwidth (for return loss  $< 10 \text{ dB}$ ) from 2.66 to 3.08 GHz. With the meander DGS, the notch is centered at 5.5 GHz with a bandwidth from 5.11 to 6.21 GHz, which can suppress interference to/from the WLAN systems operating in the frequency band from 5.15–5.825 GHz. It should be noted that the triangular resonator and the meander-DGS do not affect each other.

The simulated peak gain and efficiency of our proposed antenna with two notches are shown in Figs. 3(b) and 3(c), respectively. At the notched frequency of 5.5 GHz, the gain and efficiency are significantly dropped by more than 12 dB and to about 1.4%, respectively. Such large drops are due to the high attenuation characteristic of the meander-DGS. At the notched frequency of 2.856 GHz,

the gain and efficiency are dropped by about 5.4 dB and to about 16.8%, respectively. Across the frequency band from 2.5–12 GHz, the gain varies from 2 to 5.5 dB and the antenna efficiency is above 95%.

Figure 4 shows the simulated radiation patterns of the antenna at the notched frequencies of 2.856 and 5.5 and at 8 GHz. The radiation patterns in the *H*-plane at these frequencies are omnidirectional. Radiation is substantially smaller at 5.5 GHz. At 8 GHz, the radiation pattern in the *E*-plane at 8 GHz shows two nulls in the *z*-direction which is typical for a monopole antenna. At 2.856 and 5.5 GHz, the radiation patterns are smaller and distorted.

#### 4. CONCLUSION

The design of an integrated UWB and Bluetooth antenna with a dual band-notched characteristic has been presented. The size of the antenna is only  $31.5 \times 39.75 \times 0.832$  mm<sup>3</sup>. A triangular resonator and meander-DGS have been employed to produce a dual-band notch centered at 2.856 and 5.5 GHz, with the corresponding peak gains dropping by about 5.4 dB and 12 dB and efficiencies to about 16.8% and 1.4%.

#### REFERENCES

1. First Report and Order, Federal Communications Commission (FCC), Feb. 14, 2002.
2. Specifications of Bluetooth System, Profiles, Version 1.1 [Online] Available: <http://www.bluetooth.com>.
3. Abdollahvand, M., H. R. Hassani, and G. R. Dadashzadeh, "Novel modified monopole antenna with band-notch characteristic for UWB application," *IEICE Electronics Express*, Vol. 7, No. 16, 1207–1213, Aug. 2010.
4. Kim, K. H., Y. J. Chao, S. H. Hwang, and S. O. Park, "Band-notched UWB planar monopole antenna with two parasitic patches," *Electron. Letters*, Vol. 41, No. 14, 783–785, Jul. 2005.
5. Li, W. T., X. W., Shi, and Y. Q. Hei, "Novel planar UWB monopole antenna with triple band-notched characteristics," *IEEE Antennas and Wireless Propagation Letters*, Vol. 8, 1094–1098, Oct. 2009.
6. Zhao, Y. L., Y. C. Jiao, G. Zhao, L. Zhang, Y. Song, and Z. B. Wong, "Compact planar monopole UWB antenna with band-notched characteristic," *Microw. Opt. Technol. Lett.*, Vol. 50, No. 10, 2656–2658, Oct. 2008.
7. Weng, Y. F., W. J. Lu, S. W. Cheung, and T. I. Yuk, "UWB antenna with single or dual-band notched characteristic for WLAN band using meandered ground stubs," *Loughborough Antennas & Propagation Conference*, 767–760, Nov. 2009.
8. Kim, C., H. Ahn, J. Kim, X. Cheng, and Y.-K. Yoon, "A compact 5 GHz WLAN notched bluetooth/UWB antenna," *Antennas and Propagation Society International Symposium*, 1–4, Jul. 2010.
9. Zhan, K., Q. Quo, and K. Huang, "A novel kind of bluetooth and UWB antenna," *International Conference on Microwave and Millimeter Wave Technology (ICMMT)*, 1038–1041, May 2010.
10. Li, Z.-Q. and C.-L. Ruan, "A small integrated bluetooth and UWB antenna with WLAN band-notched characteristic," *International Symposium on Signals, Systems and Electronics*, Vol. 1, 1–4, Sep. 2010.
11. Weng, Y. F., S. W. Cheung, and T. I. Yuk, "An antenna for UWB and bluetooth standards with band-notched characteristic," *International Conference on Ultra-wideband*, 170–174, Sep. 2009.
12. Weng, L. H., Y. C. Guo, X. W. Shi, and X. Q. Chen, "An overview on defected ground structure," *Progress In Electromagnetic Research B*, Vol. 7, 173–189, 2008.
13. El Dein, A. Z., A. B. Abdel-Rahman, R. E. Fat-Helbary, and A. M. Montaser, "Tunable-compact bandstop defected ground structure (DGS) with lumped element," *International Multi-conference on Systems Signals and Devices (SSD)*, 1–3, Jun. 2010.
14. Zhao, L.-P., X.-W. Dai, Z.-X Chen, and C.-H. Liang, "Novel design of dual-mode dual-band bandpass filter with triangular resonators," *Progress In Electromagnetic Research*, Vol. 77, 417–424, 2007.
15. Hong, J. S. and S. Li, "Theory and experiment of dual-mode microstrip triangular-patch resonators and filters," *IEEE Trans. Microwave Theory and Techniques*, Vol. 52, 1237–1243, Apr. 2004.

# Side-lobe Searching Algorithm for Measured Antenna Far-field Patterns

Le Kuai<sup>1</sup> and Zhenxin Cao<sup>2</sup>

<sup>1</sup>Department of Electronic Engineering, Chengxian College, Southeast University, Nanjing 210088, China

<sup>2</sup>State Key Laboratory of Millimeter Waves, School of Information Science and Engineering  
Southeast University, Nanjing 210096, China

**Abstract**— According to characteristics of any measured far-field antenna patterns, a side-lobe searching algorithm, based on a special integral method for calculating peak areas and a new decision rule, is proposed in detail, in which both time and space complexities are getting analyzed deeply and effectiveness of the algorithm is confirmed by some typical examples. The algorithm could be applied not only to search for side-lobes in measured far-field antenna patterns with serious spurs, but also to calculate other parameters of antenna patterns such as axis ratio etc. Some special examples show that it's a high-reliable, wide-applicable and high-speed algorithm.

## 1. INTRODUCTION

Generally, antenna radiation pattern contains lots of important information about antenna parameters such as gain, beam width, side-lobe etc. Therefore, it is the most important and basic data in the field of antenna measurement [1]. Based on different measurement principles, at present there are three main ways for measuring patterns including far-field, near-field and compact range measurement where the first one is getting most widely used because of its simplicity and convenience [2]. However, antenna patterns are often distorted by extraneous signal. Some methods by improving measurement system in order to reduce the distortion were proposed [3–5]. But due to be subject to effects of environment, dynamic range and instability of measurement system etc, the obtained far-field patterns are not so smooth as the one measured by the other methods in which there are many irregular and sharp ripples referred as spur. Especially under certain low level such as side-lobe region, the Signal Noise Ratio will become decreasing. Obviously it brings more difficulty for data analyzing and worse influence on extracting and analyzing antenna parameters, such as error positioning of a side-lobe and beam width. Thus, how to obtain main antenna parameters effectively and accurately from radiation patterns with spurs is an important job during antenna measurement.

## 2. DATA PROCESSING ALGORITHM

### 2.1. Features of Some Usual Patterns

Usually there are serious or light spurs in any measured far-field patterns. For the less one, it is acceptable that seeking side-lobes by peak search after making simple smooth processing. But if want to get the higher smoothness, more serious error and distortion will appear. For the rough patterns with serious spurs, the method of peak search may probably lead to wrong result, i.e., some big spurs may be viewed as side-lobes by mistake. For instance, the maximum side-lobe is wrongly positioned at a spur near the main beam by using peak search method on a pattern with many ripples shown in Fig. 1.

### 2.2. Description of Algorithms

For the problems mentioned above, a side-lobe searching method for measured far-field patterns is proposed. It is a combination of a peak search algorithm, a special area integral algorithm and a decision rule for side-lobe and spur.

### 2.3. Peak Search Algorithm

Suppose there are  $n$  data points in a measured pattern and symbol  $a_i$  denotes the  $i$ th data point ( $i \in [1, n]$ ). Let  $j = 1$ , if  $a_{i-j} < a_i$ , and  $a_{i+j} < a_i$  or  $a_{i+j+1} < a_i$  is satisfied,  $a_i$  is a peak value. If  $a_{i-j} = a_i$ , and  $a_{i+j} = a_i$  or  $a_{i+j+1} = a_i$  is satisfied, let  $j$  plus one, and repeat the process above. Otherwise,  $a_i$  is not a peak value. The corresponding flow chart is shown in Fig. 2. This algorithm is also applicable to the patterns with continuous same data point shown in Fig. 1(b). The peak value point can be located at the middle point among them. Each peak value on the pattern corresponds to a side-lobe or a spur. So seeking all the peak values on the pattern is essential.

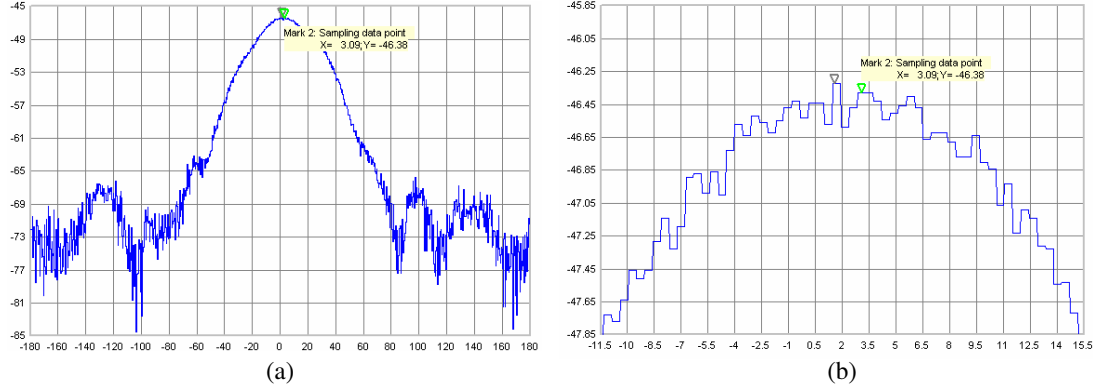


Figure 1: Wrong result obtained by a direct peak search method. (a) Maximum side-lobe is wrongly positioned at a spur near the main beam. (b) Zoomed curve.

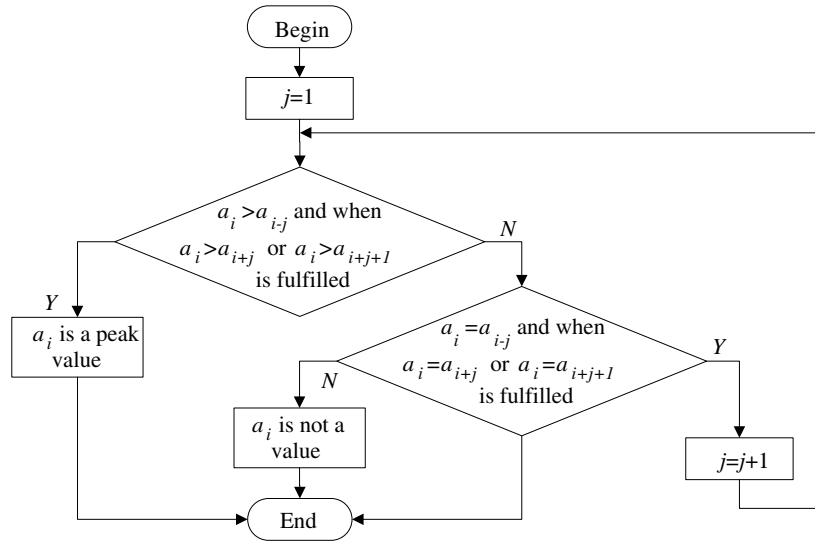


Figure 2: Flow chart of peak search algorithm.

#### 2.4. A Special Area Integral Algorithm

The area integral algorithm is used to calculate area of each peak value region. Its result is a criterion for side-lobe.

Suppose that the lower limit of the integral is  $\alpha$ , the upper limit of the integral is  $\beta$ .  $B$  is the minimum in the integrating range,  $dx$  is the difference between azimuth angles of two adjacent data point. Approximately, a pattern can be considered as a continuous function  $f(x)$ . The area integral is:

$$S_1 = \int_{\alpha}^{\beta} (f(x) - B) dx \quad (1)$$

Let  $L = \beta - \alpha$ ,  $H_1 = |f(\beta) - f(\alpha)|$ . If  $B < \min\{f(\alpha), f(\beta)\}$ , let  $H_2 = \min\{f(\alpha), f(\beta)\} - B$ . Else let  $H_2 = 0$ . The area of peak value region is

$$S = S_1 - \left( \frac{1}{2} \cdot L \cdot H_1 + L \cdot H_2 \right) \quad (2)$$

And some examples are shown in Fig. 3.

#### 2.5. Criterion for Side-Lobe

The maximum peak value is the maximum value of main beam. Its area of 3 dB beam width can be calculated by the above mentioned method.

The criterion for side-lobe is: For a peak value  $a_i$ , if there exist a  $j \in N_+$ , such that the result of area integral whose upper limit is the azimuth angle of  $a_{i+j}$  and lower limit is the azimuth

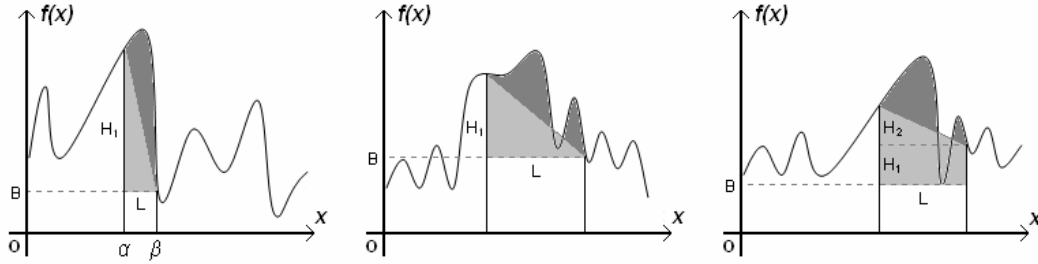


Figure 3: Area calculation for peak value region.

angle of  $a_{i-j}$  is greater than  $1/16$  of the area of  $3\text{ dB}$  beam width, and  $a_{i-j}, a_{i-j+1}, \dots, a_{i-1} < a_i, a_{i+1}, a_{i+2}, \dots, a_{i+j} < a_i$  are fulfilled. Then the peak value is the maximum of a side-lobe. Otherwise, the peak value is a spur. Generally, in the range of  $3\text{ dB}$  beam width, there does not exist a side-lobe. So, the algorithm does not search for side-lobes in the range of  $3\text{ dB}$  beam width in order to enhance the speed of the algorithm.

$1/16$  of the area of  $3\text{ dB}$  beam width is considered as the criterion for side-lobe or spur. It is a suitable constant for most patterns. A pattern with maximum side-lobe of  $-40\text{ dB}$  is simulated by a sampling function where the area of its side-lobe is greater than  $1/16$  of the area of its main beam. And generally, a spur is small ripple, and its corresponding range of azimuth angle is very narrow. Thus, the area of a spur is far less than  $1/16$  of the area of  $3\text{ dB}$  beam width. It shows that  $1/16$  is a suitable constant. Of course, the constant can be adjusted according to practical need.

### 3. ANALYSIS AND VERIFICATION OF THE ALGORITHM [6]

#### 3.1. Time Complexity

Assume that there are  $n$  measured data point and  $m$  peak value in the pattern.

Peak search algorithm analyzes several data points on both left side and right side of each data point. At worst, all data points have the same value. For the  $i$ th data point of left  $n/2$  data points, basic operation will be executed  $i - 1$  times. For the  $i$ th data point of left  $n/2$  data points, basic operation will be executed  $n/2 - i$  times. So the total frequency of basic operation for all data points is

$$\sum_{i=1}^{\frac{n}{2}} \left[ (i-1) + \left( \frac{n}{2} - i \right) \right] = \frac{n^2}{4} - \frac{n}{2} \quad (3)$$

Therefore, the time complexity is  $O(n^2)$ .

For side-lobe criterion algorithm, the worst case is that all peak values are spurs and they have the same value. In this case, assume that the  $i$ th peak value is the  $k_i$ th measured data point, the frequency of basic operation for the  $i$ th peak value is  $f(k_i) = \min\{k_i, n - k_i\}$ . Each integral operation only needs to add two area elements to previous result. So, the frequency of basic operation for a pattern with  $m$  peak value is  $m \cdot \sum_{i=1}^m 2f(k_i)$ . So the time complexity of this algorithm is  $O(n)$ . Therefore, the time complexity of side-lobe searching algorithm for measured antenna far-field patterns mentioned above is  $O(n^2)$ .

#### 3.2. Space Complexity

Assume that there are  $n$  measured data point and  $m$  peak value in the pattern.

There are  $n/2$  peak values when there are only two different values in the pattern. In this case, a pattern has most peak values. In order to have enough storage space, if each peak value is sequential stored in an array which has  $n/2$  elements, the space complexity is  $O(n)$ . If peak values are stored in a link list, much space can be saved, the space complexity is  $O(1)$ , but the speed of searching and analysis will be largely decreased and the programming will be more difficult. And obviously, the space complexity is  $O(1)$  for both area integral algorithm and side-lobe criterion algorithm. Therefore, the space complexity of side-lobe searching algorithm for measured antenna far-field patterns is  $O(n)$  or  $O(1)$ .

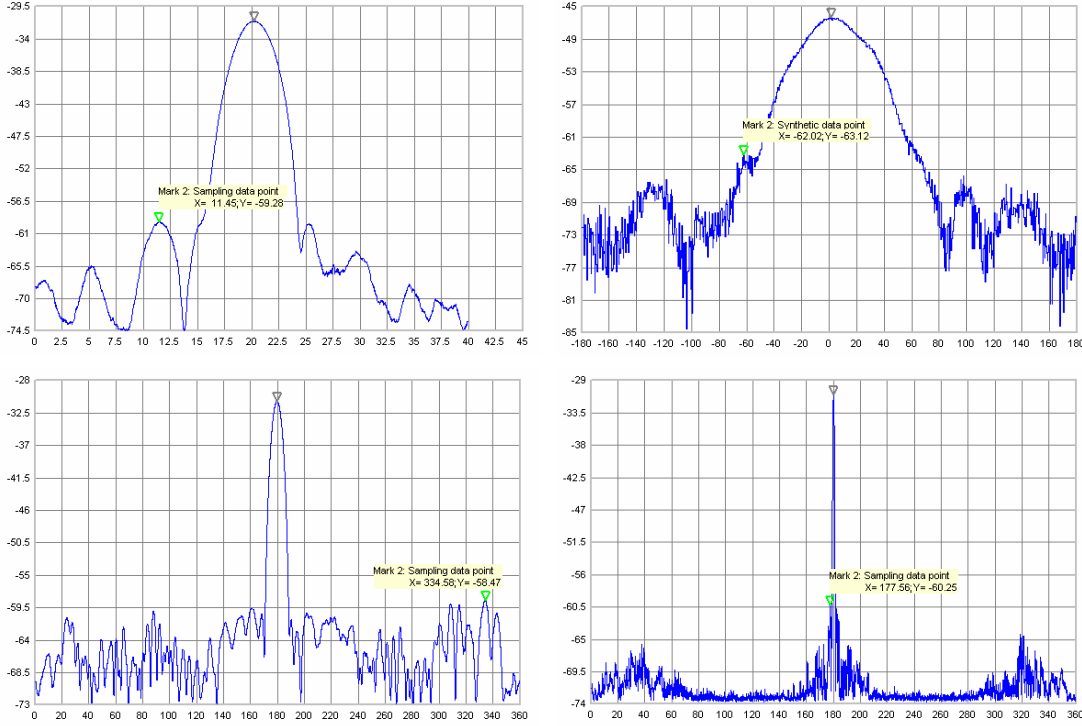


Figure 4: Maximum side-lobes of four representative measure far-field patterns.

### 3.3. Verification

The side-lobes are analyzed for four representative measured far-field patterns by use proposed algorithm, the result as shown in Fig. 4, which show that for these patterns all the results analyzed by use this algorithm are correct.

## 4. CONCLUSIONS

An algorithm based on a special integral method for calculating peak areas and a decision rule is presented here. Analyzed results of radiation patterns confirmed the algorithm is effective and correct for most cases, which overcomes the shortcoming of inaccurate judge in other common data processing algorithm for patterns. It is a high-reliability, wide-applicability and high-operation-speed algorithm for processing measured far-field patterns.

## ACKNOWLEDGMENT

This work was supported in part by NSFC under Grant 60970058 and in part by Jiangsu Natural Science Fund under grant SBK200930425.

## REFERENCES

1. Mao, N. and X. Ju, *Antenna Measurement Handbook*, National Defense Industry Press, 1987.
2. Zhang, Z., J. Lin, and X. Shu, *Radar Antenna Techniques*, Publishing House of Electronics Industry, 2005.
3. Dianat, J., C. Ghobadi, and J. Nourinia, "New method to reduce errors in antenna pattern measurement using RLS algorithm," *APMC 2005, Asia-Pacific Conference Proceedings*, 3081–3083, Suzhou, China, December 2005.
4. Leather, P. S. H., J. D. Parsons, J. Romeu, S. Blanch, and A. Aguasca, "Practical validation of antenna pattern measurement interference cancellation using a correlation technique," *Antennas and Propagation Society International Symposium*, 735–738, Monterey, U.S., June 2004.
5. Wu, R., Y. Wen, and K. Zhou, "Automatic test system of the antenna characteristic," *International Symposium on Electromagnetic Compatibility*, 314–317, Beijing, China, May 2002.
6. Xu, X., *Simple Tutorial of Data Structure*, Tsinghua University Press, 1995.

# Patch Antennas for TTC Applications of Mini-satellites

Nai-Zhi Wang, Xi-Bo Wang, Jianzhou Li, and Jia-Dong Xu

School of Electronic and information, Northwestern Ploytechnical University, Xi'an 710129, China

**Abstract**— In recent years, with the development of miniaturization technologies such as the very large scale integration (VLSI), and the digital signal processing (DSP), small satellites are becoming more and more attractive. And it is known that during both the period of attitude adjustment after the separation and working time of a satellite, TTC (Telemetry, Tracking, and Command) are very important functions necessary for the proper operation of it. In this paper, firstly a design process of a dual-band patch antenna, which can operate at 2 GHz and 2.2 GHz for TTC applications on small satellites is presented, followed by the approach of the placement optimization of the TTC patch antenna onboard for a mini-satellite. In order to obtain one better strategy, the construction of the antenna is discussed and two schemes of antennas placement are introduced. Through the results secured by electromagnetic computation, it is indicated that situating three patch antennas respectively on three adjacent walls and the forth one on the cut-off bottom corner can provide a satisfactory omni-directional radiation pattern. To reduce the complexity, a new method to conform a patch antenna on the mini-satellite is proposed by bending the antenna along one edge of the cube in a top corner. By comparison and analysis, it is concluded that one bended patch antenna can perform as well as four ordinary ones do so that it can effectively cut off the weight and volume of the spacecraft, and facilitate the feeding intricacy. All the S-parameter and radiation pattern results used for analysis were calculated with the CEM software CST Microwave Studio, which is based on the finite integral technique (FIT).

## 1. INTRODUCTION

Miniaturization technologies such as the very large scale integration (VLSI), and the digital signal processing (DSP) make it feasible today to build smaller satellites than those were possible 10 years ago without reducing their capabilities [1]. It can decrease the time of construction and give possibility to launch the spacecraft either as an auxiliary payload by large launchers or with the use of small rockets [2]. The number of planned missions based on small, mini, micro and even pico satellites, referred to henceforth as small satellites, is continuously increasing. Small satellites are attractive because they require lower investments, lower cost mass production while offering greater reliability, lower launch costs and greater launch flexibility. Their use, involving a single or a constellation of satellites, includes earth observation [3–5], the testing of components, communication and educational applications [6]. According to SSTL (Surrey Space Technology Limited) classification [7], mini-satellite is a spacecraft, the weight of which does not exceed 500kg. Due to small dimensions and weight of the mini-satellites, the access to the space is accelerated, but also specific, low profile and small weight communication devices have to be used.

TTC (Telemetry, Tracking, and Command) which are very important functions necessary for the proper operation of a satellite. During the initial acquisition period following the satellite separation from the launcher, the satellite stabilization has usually not been achieved. Thus an omni-directional antenna is required for the communication between space and ground. Sometimes, multiple antennas are mounted on different sides of the satellite to provide better coverage for the TTC link as well as for redundancy. Usually several omni-directional antennas at different frequencies, e.g., UHF and VHF bands, are used for TTC up-link and down-link.

When linearly polarized electromagnetic wave travels through electromagnetic field, under the influence of it, the polarization plane of the incident wave will change. Such phenomenon is known as Faraday rotation. That's why circularly polarized (CP) antennas are necessary for satellites communication in order to obtain the satisfied receiving efficiency. But for TTC antennas, polarization is not pre-requisite, and several antennas located on a satellite make it impossible to achieve circular polarization in all directions. So various linearly polarized antennas such as monopole antennas, inverted F-shaped antenna (PIFA) and microstrip patch antennas have been developed for TTC of small satellites at UHF, VHF, and S-band. These antennas are simple, cheap, easy to fabricate, and have nearly omni-directional or broad-beam radiation patterns, consequently the satellite does not require accurate control of altitude [2].

In this paper two dual-band antennas with compact size are designed and simulated for small satellite TTC mission. And also, schemes of the placement onboard mini-satellite for each antenna

are discussed and compared. The performance requirements of antennas are indicated in Part 2. Design processes of the conventional slotted antenna with corresponding onboard location schemes and numerical simulation results are discussed in Part 3. A novel method to conform a patch antenna on the mini-satellite is proposed in Part 4, which is followed by comparison of the two antenna and conclusion.

## 2. PERFORMANCE REQUIREMENTS

The goal of our work is to design an appropriate antenna for TTC applications, and then optimize the locations of several antennas to obtain omni-directional radiation pattern. The performance requirements of the collective antennas located on the mini-satellite include:

- Operating at two frequencies: 2 GHz and 2.2 GHz respectively for TTC uplink and downlink;
- Low profile, not thicker than 10 mm;
- Small weight as possible;
- Omni-directional coverage range.

Other essential capabilities of the antenna that must be achieved, for instance, the characteristic of heat resistance and the ability to withstand pressure, will be investigated and discussed in the future work.

## 3. 1ST SCHEME: PLANAR PATCH ANTENNA

### 3.1. Antenna Design

Patch antennas are the most suited contender for the TTC application of the mini-satellites, whereas inherently narrow bandwidth is the bottleneck of patch antennas. Some methods have been proposed to solve the problem over the past two decades, such as appending parasitic radiators [8], cavity backed [9], or L-probe feeding [10]. But slotting gaps on the patch to realize dual-band can make the antenna thinner and lighter, so we utilize this strategy to achieve the purpose.

The configuration of the proposed antenna is shown in Fig. 1. The antenna fed by a coaxial-cable consists of a patch with two gaps, the ground plane, a dielectric substrate layer, and is etched on a FR4 substrate with the thickness of 4 mm and the dielectric constant of 4.4. The dimensions of the patch are  $W_1 \times L_1$ , and the spacing between the patch and ground is  $h$ . The feed point is centered with respect to the patch width  $W_1$ , and at a distance  $D$  from one side of the patch. The parameters of the antenna are listed as follows:  $W = 100$ ,  $W_1 = 48$  mm,  $W_2 = 3$  mm,  $W_3 = 21$  mm,  $L_1 = 48$  mm,  $L_2 = 41$  mm,  $D = 13$  mm,  $h = 4$  mm.

The simulation results including  $S_{11}$  and radiation patterns, calculated by the CEM software CST, are shown in Fig. 2. As seen,  $S_{11} < -10$  dB is obtained from 1.975 GHz to 2.025 GHz and from 2.17 GHz to 2.26 GHz, so it can operate well at 2 GHz and 2.2 GHz. Fig. 2(b) shows that the antenna has low gain and wide beamwidth.

A small dimension or weight can cut down the cost of launching. Fig. 3 shows the calculated  $S$ -parameter versus the dimension  $W$  of substrate. There is no acute change along the augment or diminishment of the substrate dimension, so we can choose small  $W$  to make the structure of the antenna lighter and more compact, and here  $W$  is set to 100 mm.

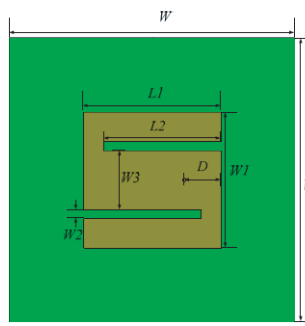
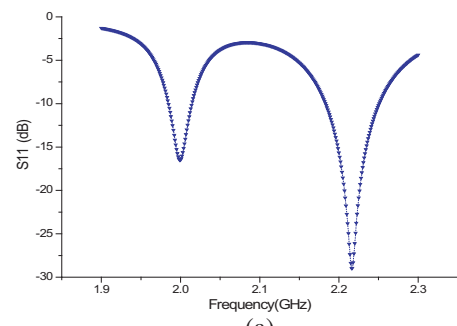
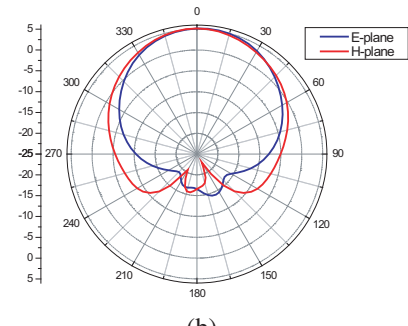


Figure 1: Structure of the antenna.



(a)



(b)

Figure 2: Simulation results. (a)  $S_{11}$  versus frequency. (b) Radiation patterns of 2 GHz.

### 3.2. Antenna Layout

The antenna is with low profile and don't need deployment mechanisms. That's why it can be easily attached to the satellite walls. Here several antennas mounted on a typical mini-satellite with dimension of 500 mm \* 500 mm \* 500 mm will be simulated to evaluate their performance, and minimizing the occurring nulls and improving the omni-directionality of the combined radiation pattern for various configurations are the main goals of optimization of antennas placement.

Analysis of the combined radiation pattern of the antennas set onboard the mini-spacecraft may be accomplished with the use of the Finite Integral Technique (FIT). The FIT is a full-wave method firstly described by Weiland and directly solves Maxwell integral equations [11]. The unknown vector electric and magnetic fields are approximated by specially designed basis functions with unknown coefficients. These basis functions let us satisfy all the required continuity conditions of the electric and magnetic fields at every material boundary. The discretization rate (number of basis cells per wavelength) is one of the main factors that affect the computation time and accuracy. Analysis is not comprehensive because of limited computer memory and processor. For our analysis, the CEM software CST is utilized, and the modeled structures are discretized with at least 20 basis cells per wavelength. The satellite model is modeled as a metallic box with the dimensions of 500 mm \* 500 mm \* 500 mm.

Firstly, create the complete three-dimensional model of the mini-satellite; Secondly, assign conducting materials properties to the parts of the geometrical model.; Then situate three antennas onboard three adjacent walls of the mini-satellite. This scheme leads to fairly omni-directional coverage over the sphere; however some local nulls are visible. Three antennas are not enough for gaining an omni-directional radiation pattern.

Possible antennas locations and their number are usually limited in mini-satellites due to limited dimensions, weight, cable routes etc. Fig. 4 shows four antennas location schemes for cubic satellites. Three of them are amounted in the center of three adjacent walls (Sub-scheme (a)) or clustered in the top corner (Sub-scheme (b)) and the fourth antenna is situated on the cut-off bottom corner. All the transmitting antennas in the top corner should be fed with the same phase to avoid deep nulls in the radiation pattern.

For Sub-scheme (a), the computed combined radiation patterns for the horizontal and the vertical plane at 2 GHz and 2.2 GHz are shown in Fig. 5 and Fig. 6. Placing the fourth antenna on the cut-off corner provides satisfactory omni-directivity of the whole pattern. The deepest nulls for the cut-off corner approach do not exceed  $-10$  dB for both the horizontal plane and the vertical plane.

Sub-scheme (b), three antennas is clustered in the top corner and the fourth antenna situated on the cut-off bottom corner. Fig. 7 and Fig. 8 respectively show the radiation patterns of Sub-scheme (b) at 2 GHz and at 2.2 GHz. Similarly, the deepest nulls for this scheme do not exceed  $-12$  dB for both planes. The  $S$ -parameter of the antennas situated on the mini-satellite is also calculated, which is shown in Fig. 9. All the results indicate that such schemes can provide excellent performance in the mission of TTC. Here choose Sub-scheme (b) as the 1st scheme for its compact distribution and facilitation in feeding intricacy.

## 4. 2ND SCHEME: BENDED PATCH ANTENNA

The radiation pattern of ordinary patch antennas has small sidelobes and the beamwidth is much less than  $180^\circ$ . Because of this characteristic, only mounting one patch antenna on the satellite

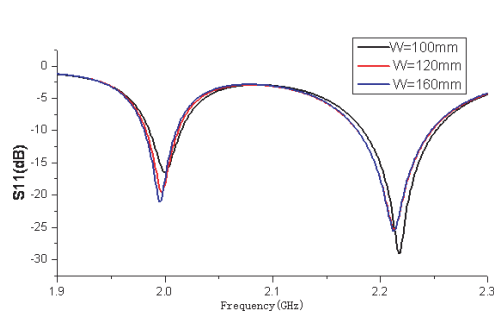


Figure 3:  $S_{11}$  versus  $W$ .

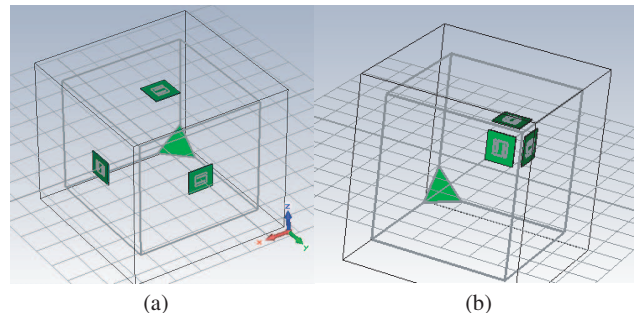


Figure 4: One antenna situated on the cut-off bottom corner.

can not provide an omni-directional radiation pattern. Utilizing the method of mounting several antennas on the small satellite results in accretion of its volume and weight, and feeding all antennas with the same phase to avoid deep nulls in the radiation pattern will also cause troubles.

Here we propose a novel conformal method. Apply the antenna whose structure is as Fig. 1 shown, using an FR4 substrate with thickness of 5 mm and dielectric constant of 4.4. But the dimensions are changed to:  $W = 100$ ,  $W_1 = 53$  mm,  $W_2 = 3$  mm,  $W_3 = 18$  mm,  $L_1 = 52$  mm,  $L_2 = 42$  mm,  $D = 16$  mm,  $h = 5$  mm. Then bend the antenna along one edge of the cube in the top corner and paste the bottom of it to the walls, as shown in Fig. 10.

Similarly, we use the FIT method to analysis the characteristic of the conformal antenna, and discretize the whole structure with at least 20 basis cells per wavelength. Fig. 11 shows the  $S$ -parameter of the antenna conformally mounting on the satellite. As we know the antenna has two operation frequencies 2.0 GHz and 2.2 GHz where  $S_{11} < -10$  dB. Fig. 12 and Fig. 13 are the computed radiation patterns of only one antenna situated on the top corner. Only exiguously numerical difference exists between corresponding radiation patterns. The reason for this phenomenon is that the wavelengths of two operating frequencies are similar in size. The deepest null is about  $-12$  dB for both the horizontal and vertical planes at each operating frequency. Compared to the 1st scheme described previously, it can be seen that one bended patch antenna performs as well as four ordinary ones do. In addition, it also has some advantages such as smaller weight and facilitation in feeding.

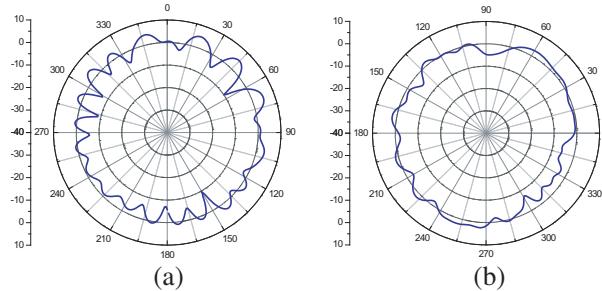


Figure 5: Radiation patterns of sub-scheme (a) at 2 GHz. (a) Horizontal plane. (b) Vertical plane.

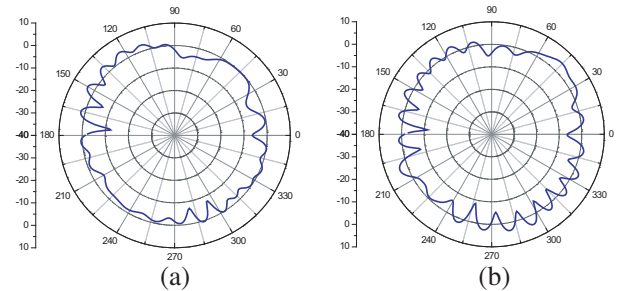


Figure 6: Radiation patterns of sub-scheme (a) at 2.2 GHz. (a) Horizontal plane. (b) Vertical plane.

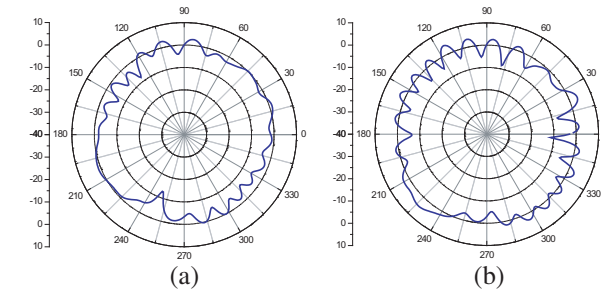


Figure 7: Radiation patterns of Sub-scheme (b) at 2 GHz. (a) Horizontal plane. (b) Vertical plane.

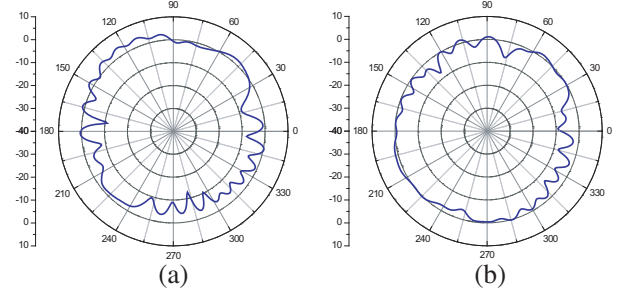


Figure 8: Radiation patterns of Sub-scheme (b) at 2.2 GHz. (a) Horizontal plane. (b) Vertical plane.

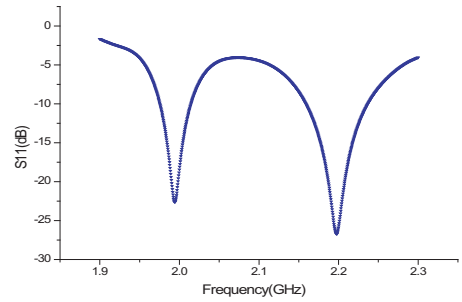


Figure 9:  $S_{11}$  of the antennas situated on the mini-satellite.

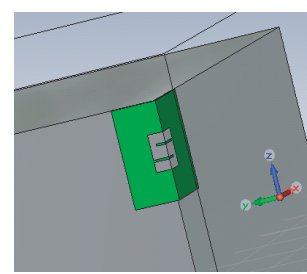


Figure 10: Bend the antenna along the cube edge.

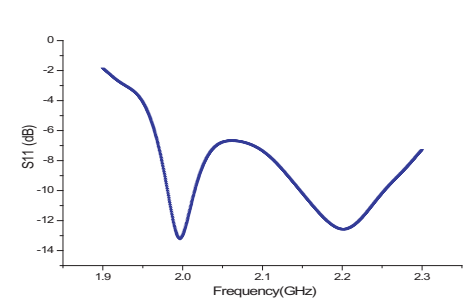


Figure 11:  $S_{11}$  versus frequency.

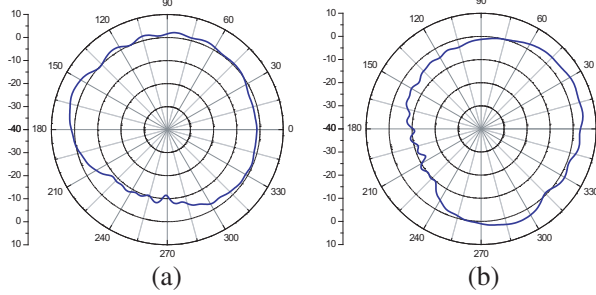


Figure 12: The computed radiation patterns at 2 GHz. (a) Horizontal plane. (b) Vertical plane.

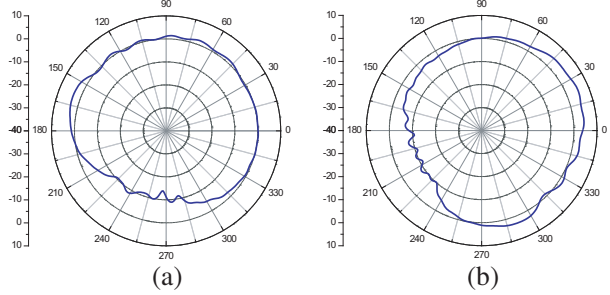


Figure 13: The computed radiation patterns at 2.2 GHz. (a) Horizontal plane. (b) Vertical plane.

## 5. CONCLUSION

Two antennas with different structures and advantages such as compactness, easy fabrication and low cost, have been designed and simulated. Introduced calculations utilizing FIT show some possible approaches to ensure omni-directional radiation patterns, including optimal low gain antennas placement and modifications of the antenna's structure or conformal method. It is concluded that situating three patch antennas respectively on three adjacent walls and the forth one on the cut-off bottom corner can provide better omni-directional radiation patterns, and furthermore, one bended patch antenna can perform as well as four ordinary ones do so that it can effectively cut off the weight and volume of the spacecraft, and facilitate the feeding intricacy. The simulated results of the antennas mounted on the mini-satellite demonstrate the reliable onboard performance and both of them with the corresponding schemes could work well.

## ACKNOWLEDGMENT

This work was supported by the Natural Science Foundation of Shaanxi Province (2009JM8001-2).

## REFERENCES

- Martin, M. and S. Kilberg, “Techsat 21 and revolutionizing space missions using microsatellites [C],” *Proc. 15th Annual AIAA/USU Conf. on Small Satellites*, Logan, UT, Aug. 2001.
- Gao, S., M. Brenchley, M. Unwin, et al., “Antennas for small satellites [C],” *2008 Loughborough Antennas & Propagation Conference*, 66–69, Loughborough, UK, Mar. 17–18, 2008.
- Neeck, S. P., T. J. Magner, and G. E. Paules, “NASA’s small satellite missions for earth observation [C],” *Proc. 4th IAA Symp. Small Satellites for Earth Observation*, Berlin, Germany, Apr. 7–11, 2003.
- Zheng, Y. and Y. Ruliang, “Feasibility study of using small satellite synthetic aperture radar for global 3D imaging [C],” *Proc. Geoscience and Remote Sensing Symp., IGARSS ’02*, Vol. 6, 3162–3164, Jun. 24–28, 2002.
- Wicks, A., A. da Silva-Curiel, J. Ward, and M. Fouquet, “Advancing small satellite earth observation: operational spacecraft, planned missions and future concepts [C],” *14th Annual AIAA/USU Conf. Small Satellites*, Logan, UT, Aug. 21–24, 2000.
- Marchant, W. and E. R. Taylor, “Status of chips: A NASA University astronomy mission [C],” *14th Annual AIAA/USU Conf. Small Satellites*, Logan, UT, Aug. 21–24, 2000.
- [http://centaur.sstl.co.uk/sshp/sshp\\_classify.html](http://centaur.sstl.co.uk/sshp/sshp_classify.html)-Small Satellites homepage.
- Katehi, P. B., N. G. Alexopoulos, and I. Y. Hsia, “A bandwidth enhancement method for microstrip antennas [J],” *IEEE Trans. Antennas Propag.*, Vol. 35, No. 1, 5–12, Jan. 1987.
- Elmezughgi, A. S., W. S. T. Rowe, and R. B. Waterhouse, “Cavity backed hi-lo stacked patch antennas [C],” *IEEE Antenna and Propagation Symp. Dig.*, 2301–2304, 2008.
- Luk, K. M., C. L. Mak, Y. L. Chow, and K. F. Lee, “Broadband microstrip patch antenna [J],” *Electron. Lett.*, Vol. 34, No. 15, 1442–1443, Jul. 1998.
- Weiland, T., “On the numerical solution of Maxwell’s equation and application in the field of accelerator physics [J],” *Particle Accelerator*, Vol. 15, 245–292, 1984.

# Optimal Calculation of the Directivity of Arrays with Azimuthal Element Pattern Symmetry

E. H. Van Lil, J.-W. De Bleser, and A. R. Van De Capelle

Div. ESAT-TELEMIC, K. U. Leuven, Kasteelpark Arenberg 10, Bus 2444, B-3001 Heverlee, Belgium

**Abstract**— A simple analytical formula for the directivity of an array of dipoles is derived. It turns out to be a generalisation of the well known expression for the directivity of an array of isotropic elements. For regular (i.e., equidistant) arrays an efficient algorithm is proposed.

## 1. INTRODUCTION

The directivity function, the proportion between the power density in a certain direction and the average power density, is defined in [1, 2],

$$D(\theta, \phi) = \frac{\left| \vec{F}(\theta, \phi) \right|^2}{\frac{1}{4\pi} \int_0^{2\pi} \int_{-\pi}^{\pi} \vec{F}(\theta, \phi) \vec{F}^*(\theta, \phi) \sin \theta d\theta d\phi} = \left| \vec{F}'(\theta, \phi) \right|^2 D \quad (1)$$

$\vec{F}(\theta, \phi)$  is the complex far-field pattern (\* denotes complex conjugate).

$\vec{F}'(\theta, \phi) = \frac{\vec{F}(\theta, \phi)}{F_{\text{MAX}}}$  and  $D$  is the directivity in the direction of maximum radiation. For an array of  $N$  elements, the far-field pattern can be written as the product of an element pattern and an array factor:  $\vec{F}(\theta, \phi) = \vec{g}(\theta, \phi) f(\theta, \phi)$ . The array factor depends on the (complex) excitation coefficients ( $a_i$ ) and the positions of the elements as well as on the frequency:  $f(\theta, \phi) = \sum_{i=0}^{N-1} a_i e^{j\vec{k}_0(\vec{r}_i - \vec{r}_{ref})}$  (Fig. 1). The worst case maximum value occurs if all amplitudes add up in phase, hence ( $n = N - 1$ )  $f_{\text{MAX}} = \sum_{i=0}^n |a_i|$ . For the most common arrays this occurs within the far-field pattern corresponding with real angles  $\theta$  and  $\phi$ .

If we steer the beam of an array of isotropic elements ( $g(\theta, \phi) = 1$ ) from a given maximal direction  $\mathbf{k}_{\text{MAX}}$  (with coefficients  $a_i$ ) to a new direction corresponding with  $\mathbf{k}'_{\text{MAX}}$ , the new excitation coefficients can be derived from the previous ones:

$$b_i = a_i e^{-j(\mathbf{k}'_{\text{MAX}} - \mathbf{k}_{\text{MAX}}) \cdot \mathbf{r}_i} \quad (2)$$

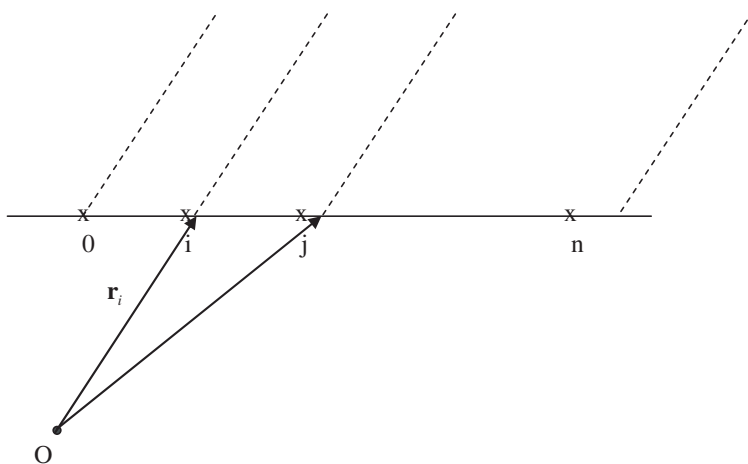


Figure 1: General configuration.

The denominator of (1) then becomes [1]:

$$2 \sum_{i=0}^n \sum_{j=i+1}^n \operatorname{Re}(b_i b_j^*) \operatorname{sinc}(k_o |\vec{r}_i - \vec{r}_j|) + \sum_{i=0}^n |b_i|^2 \quad (3)$$

Note that  $|a_i| = |b_i|$  and hence both  $\sum_{i=0}^n |a_i|^2 = \sum_{i=0}^n |b_i|^2$  and  $f_{\max}$  remain unchanged.

## 2. DIRECTIVITY OF ARRAYS OF HERTZIAN DIPOLES

For the case of a Hertzian dipole  $g(\theta, \phi) = \sin \theta$  the denominator of (1) can be expressed as

$$N_D = \frac{1}{4\pi} \int_0^{2\pi} \int_0^\pi \sum_{i=0}^n \sum_{j=0}^n a_i a_j^* e^{jk_0 \sqrt{(x_i - x_j)^2 + (y_i - y_j)^2}} \sin \theta \cos \phi' e^{jk_0(z_i - z_j)} \cos \theta \sin^2 \theta \sin \theta d\theta d\phi' \quad (4)$$

Using the definition of the Bessel function of the first kind [3, 8.411.1], and noticing that the imaginary part vanishes, we obtain

$$N_D = \sum_{i=0}^n \sum_{j=0}^n a_i a_j^* \int_0^{\pi/2} J_0 \left( k_0 \sin \theta \sqrt{(x_i - x_j)^2 + (y_i - y_j)^2} \right) \cos[k_0 \cos \theta(z_i - z_j)] (1 - \cos^2 \theta) \sin \theta d\theta \quad (5)$$

To solve the second part of this integral we start from [3, 6.688.2] and with  $r = \sqrt{\alpha^2 + \beta^2}$ , we compute the second partial derivative with respect to  $\beta$ .

It is thus possible to derive an analytical formula for arrays of ideal Hertzian dipoles

$$\begin{aligned} N_D &= 2 \sum_{i=0}^n \sum_{j=i+1}^n \operatorname{Re}(a_i a_j^*) [f_1(k_0 |\vec{p}_i - \vec{p}_j|) - f_2(k_0 |\vec{p}_i - \vec{p}_j|) k_0^2 (z_i - z_j)^2] + \frac{2}{3} \sum_{i=0}^n |a_i|^2 \\ f_1(x) &= \operatorname{sinc} x - \frac{\operatorname{sinc} x - \cos x}{x^2} \\ f_2(x) &= \frac{x \sin x + 3 \cos x - 3 \operatorname{sinc} x}{x^4} \\ \vec{p}_i - \vec{p}_j &= (\vec{r}_i - \vec{r}_j) - (\vec{r}_i - \vec{r}_j) \cdot \vec{i}_z \vec{i}_z \end{aligned} \quad (6)$$

Note that  $f_1$  and  $f_2$  are combinations of spherical Bessel functions of the first kind and order 0 and 1 for  $f_1$  and order 2 for  $f_2$ . It can be proven that  $\lim_{r \rightarrow 0} f_1(r) = 2/3$  and  $\lim_{r \rightarrow 0} f_2(r) = -1/15$ .

## 3. GENERAL PLANAR ARRAY CASE

The radiation integral for the planar array case ( $z_i = z_j$ ) and an element power pattern given by  $\sin^{2m} \theta$  is:

$$N_D = \sum_{i=0}^n \sum_{j=0}^n \frac{a_i a_j^*}{2} \int_0^\pi J_0 \left( k_0 \sin \theta \sqrt{(x_i - x_j)^2 + (y_i - y_j)^2} \right) (1 - \cos^2 \theta)^m \sin \theta d\theta$$

The element power pattern can be easily expanded into:

$$(1 - \cos^2 \theta)^m = \sum_{k=0}^m (-1)^k C_m^k \cos^{2(m-k)} \theta = \sum_{k=0}^m (-1)^k \frac{m!}{k!(m-k)!} \cos^{2(m-k)} \theta$$

The integrals

$$I_{m-k} = \int_0^\pi J_0(\alpha \sin \theta) \cos^{2(m-k)} \theta \sin \theta d\theta$$

can be found with [3, 6.683.6] to be:

$$I_{m-k} = 2\sqrt{\frac{\pi}{2\alpha}} \frac{(2(m-k))!}{(m-k)!(2\alpha)^{m-k}} J_{m-k+1/2}(\alpha)$$

It should be noted that this method can be applied to any element power pattern that can be expanded in terms of  $\sin^{2m}\theta$  and  $\cos^{2m}\theta$ , either theoretically or by experimental fitting.

#### 4. FAST FORMULAS FOR LINEAR EQUIDISTANT ARRAYS

For simplicity the procedure for the calculation of the directivity is explained for the case of isotropic elements, but remains valid in the general case.

After the calculation of  $\sum_{i=0}^n |a_i|$  and  $\sum_{i=0}^n |a_i|^2$  we can combine the terms of (3) with constant  $j - i \equiv k$  which gives ( $\mathbf{d}$  is the distance vector between 2 adjacent elements and  $d = |\vec{d}| = |\vec{d}_{i,i+1}|$ )

$$2 \left\{ \sum_{l=1}^n \sum_{i=0}^{n-l} \operatorname{Re}(a_i a_{i+l}^*) \cos \left( l \left( \overrightarrow{k_{\text{MAX}}} - \overrightarrow{k'_{\text{MAX}}} \right) \cdot \vec{d} \right) \operatorname{sinc}(lk_o d) \right. \\ \left. + \sum_{l=1}^n \sum_{i=0}^{n-k} \operatorname{Im}(a_i a_{i+l}^*) \sin \left( l \left( \overrightarrow{k_{\text{MAX}}} - \overrightarrow{k'_{\text{MAX}}} \right) \cdot \vec{d} \right) \operatorname{sinc}(lk_o d) \right\} \quad (7)$$

After defining  $c_l = \sum_{i=0}^{n-l} a_i a_{i+l}^*$  (7) reduces to

$$2 \sum_{l=0}^n \operatorname{Re} \left( c_l e^{-jl \left( \overrightarrow{k_{\text{MAX}}} - \overrightarrow{k'_{\text{MAX}}} \right) \cdot \vec{d}} \right) \operatorname{sinc}(lk_o d) \quad (8)$$

For practical applications (corporate feeding of the array) the coefficients vary little with frequency and hence the  $c_l$ 's can be computed in advance.

To program this efficiently all  $c_l$ 's are computed in advance in one vector, destroying the excitation coefficients. Until the  $(E(N/2) - 1)$ th ( $E$  is the integer just lower than or equal to  $N/2$ ) calculation of  $c_l$  the new element is added in the vector after the end of vector  $a$  ( $c_l$  is added in  $a_{n+1}$ ) (Fig. 2(a)). The total number of memory elements is thus  $N + E(N/2) - 1 = E((3N - 2)/2)$ . After the  $(E(N/2) - 1)$ th coefficient  $c_l$ , the next coefficient  $c_l$  can be placed directly in element  $a_l$ , because those excitation coefficients are not longer required (Fig. 2(b)). At this stage the original excitation coefficients start to be destroyed in the computation. After the buffering the first elements can be copied in place. This means that  $a_{n+1} = c_1$  is put back at memory location  $a_1$ ,  $a_{n+2}$  on  $a_2$  etc (Fig. 2(c)).

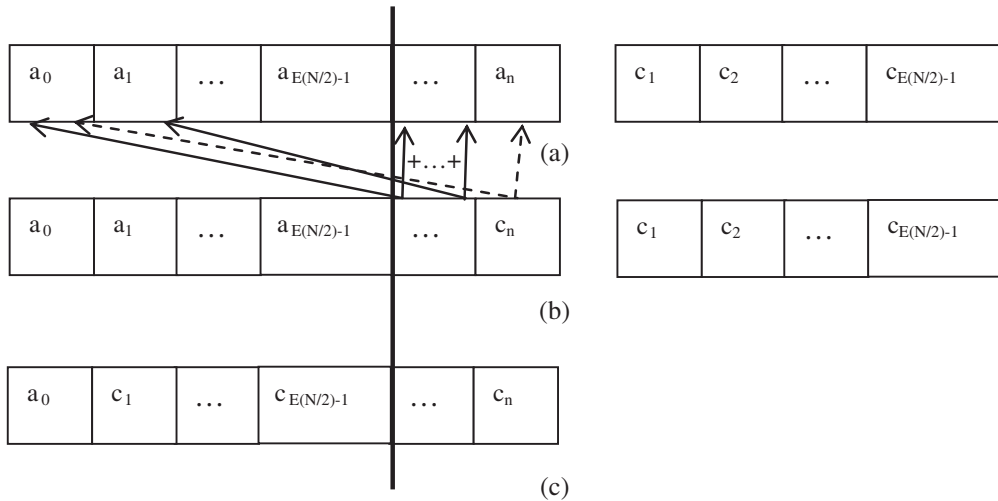


Figure 2: Efficient computation of the coefficients  $c_l$  for equidistant arrays.

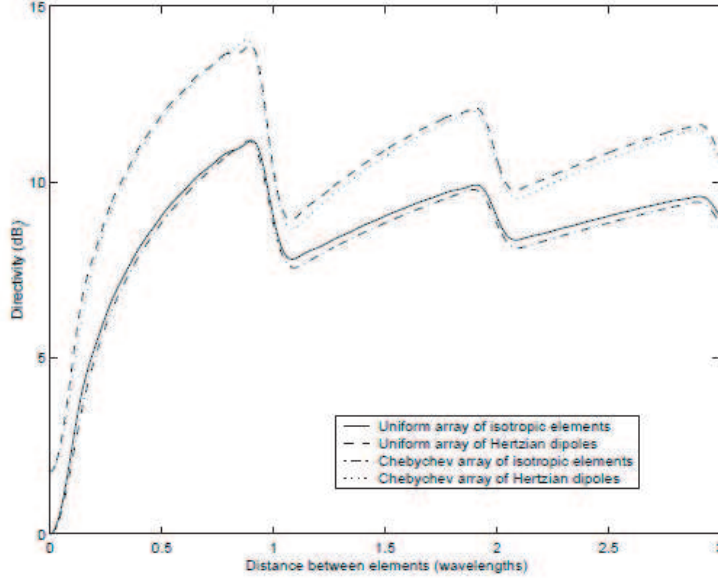


Figure 3: Directivity of a uniform array with 20 elements.

## 5. APPLICATIONS

Figure 3 compares the directivity of uniform and Chebychev arrays of isotropic elements and Hertzian dipoles oriented along the array axis. We notice that the directivity of the uniform isotropic array is equal to  $10 \log_{10} N$  (in this case  $9.03 \text{ dB}_i$ ) for  $d = 0.5m\lambda_0$  ( $m$  is a positive integer). The directivity of the uniform array of Hertzian dipoles at  $0.5\lambda_0$  is  $11.89 \text{ dB}_i$ . For longer distances the directivity of the uniform array of Hertzian dipoles converges in an oscillating way to  $10 \log_{10} (1.5N)$  (in this case  $10.79 \text{ dB}_i$ ). The  $-20 \text{ dB}$  Chebychev pattern leads to a slightly smaller directivity ( $8.84 \text{ dB}_i$  for isotropic elements and  $11.75 \text{ dB}_i$  for Hertzian dipoles at  $0.5\lambda_0$ ). The limit for  $d \rightarrow \infty$  is equal to  $8.84 \text{ dB}_i + 10 \log_{10}(1.5) = 10.60 \text{ dB}_i$ .

## 6. CONCLUSIONS

In this paper a simple analytical formula for the computation of the directivity of an array of Hertzian dipoles was derived. This method turns out to be applicable to most antennas because the power pattern can often be expanded in terms of  $\sin^{2m} \theta$  and  $\cos^{2m} \theta$ . For regular arrays a very efficient procedure is derived.

## REFERENCES

1. Stutzmann, W. and G. Thiele, *Antenna Theory and Design*, John Wiley & Sons, New York, 1981.
2. Ma, M. T., *Theory and Application of Antenna Arrays*, Artech House, 1974
3. Gradshteyn, I. and I. Ryzhik, *Table of Integrals, Series and Products*, Academic Press, New York, 1980.
4. De Coster, I. and E. Van Lil, “Implementation of antenna patterns in EPICS,” *Proc. 9th Cost 259 Meeting*, TD(99)093, 8, Leidschendam, The Netherlands, September 23–24, 1999.

# A Novel UWB Filter with Dual-notch-bands Characteristic Using Radial-multimode Loaded Stub Resonator

C. Y. Liu, T. Jiang, Y. S. Li, and J. Zhang

College of Information and Communications Engineering  
Harbin Engineering University, Harbin, Heilongjiang 150001, China

**Abstract**— this paper presents a novel approach for designing compact ultra-wideband (UWB) band-pass filter with a good dual-notched band characteristic. By using a radial-multimode loaded stub resonator, one notch-band can be got. Another notch-band can be generated by the half-wavelength parasitic micro-strip Resonator. The main advantage of the proposed filter is the frequency of the notched band can be tuned easily in a wide frequency range. The first notch-band can be changed from 4 GHz to 6 GHz. The second notch-band can be changed from 7 GHz to 9 GHz. Electric filed distribution and equivalent model is also given depending on the odd/even excitation resonance condition. The characteristics of the filter are analyzed. To verify the proposed methods, filter is designed and fabricated. Measured results show the proposed UWB properties from 3 to 10.8 GHz. The UWB filter's dual-notch-bands whose center frequencies are 4.5 GHz and 7.7 GHz and have 10 dB fractional bandwidths of about 2.2% and 1.3%, respectively. These filters can be integrated in UWB radio systems and efficiently enhance the interference immunity from undesired signals such as wireless local area network (WLAN) and WiMAX.

## 1. INTRODUCTION

Since the Federal Communications Commission (FCC) released the frequency band from 3.1 to 10.6 GHz for commercial communication applications in February 2002, the ultra-wideband (UWB) radio system has been receiving great attention from both academy and industry [1]. UWB filter is one of the key passive components to realize a UWB radio system. Recently, various methods and structures have been presented to develop UWB BPFs [2–4]. Moreover, the UWB frequency band overlaps with the existing communication such as WLAN and WiMAX which means that those radio signals may interfere with UWB systems and vice versa. Therefore, a compact communication system which operates in UWB frequency band requires a small BPF with single or dual-notched bands in order to avoid being interfered by the undesired radio signals. Recently, there are many methods that have been investigated to design a UWB BPF with notched bands, such as parasitic coupled line [5], mismatch transmission line [6], SCRLH resonator [7] and Asymmetric dual-line coupling structure [8]. Nevertheless, they are still embarrassed by the large electrical size [5], complex structure [6], and the notch band cannot be changed optionally [7, 8].

The present paper provides a new implementation of dual-notch-bands by using a radial-multimode loaded stub. The radial-multimode loaded stub structure can generate dual-notched bands in the pass-band of the UWB BPF. By adjusting the parameters of the radial-multimode loaded stub, the center frequencies of the two notch-bands can be controlled independently. An UWB BPF with dual-notched bands by using the radial-multimode loaded stub structures has been designed, fabricated, and measured. Simulated results agree closely with measured ones.

## 2. FILTER DESIGN AND ANALYSIS

The configuration of the investigated UWB BPF with the dual-notched bands is shown in Fig. 1.

The filter is printed on a substrate with relative permittivity 10.2 and a thickness of 0.635 mm and the characteristic impedance of the input/output micro-strip-line are taken to be  $50\Omega$ . The size of the filter is  $10\text{ mm} \times 10\text{ mm}$ , so they are compact. The proposed BPF is a modified form of [4] and the radial-multimode loaded stub is coupled to the middle MMR section to achieve the dual-notch bands. The radial-multimode loaded stub is composed of two cross-coupled configurations and has signal multiplexed characteristics. The two signal paths incurred from the second cross-coupled configuration are also indicated in Fig. 1. The lower notch-band is generating by the signal path 1, and then the whole electrical length of the single path 1 ( $2 \times L7 + 2 \times L6$ ) is near  $180^\circ$ . The second notch-band is generating by the signal path 2, and the size of the radial-multimode loaded stub can control the second notch frequency.

Figure 2 shows the simulated response  $S_{21}$  of the mentioned filter.  $f_1$  and  $f_2$  are the central frequencies of the lower and upper notched bands, respectively. It can be seen from Fig. 2(a) that

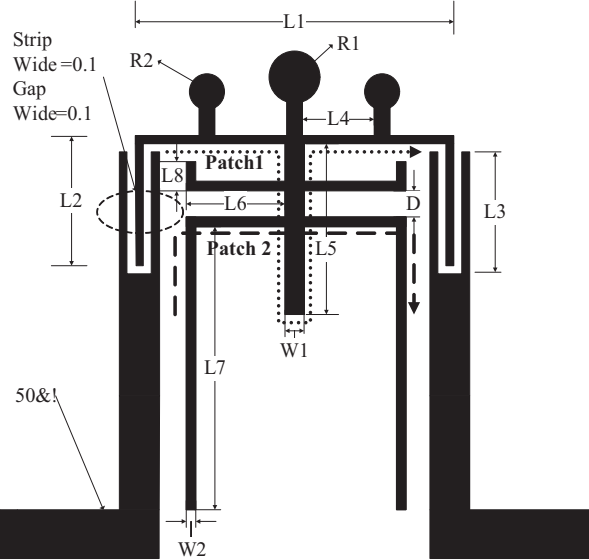
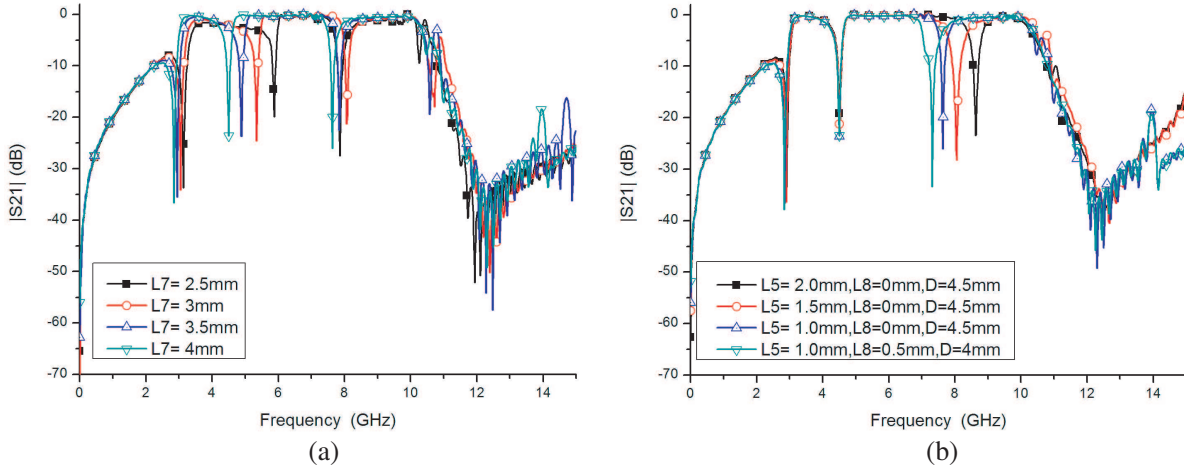


Figure 1: Geometry of the proposed UWB filter.

Figure 2: Simulated response  $|S_{21}|$  of the mentioned filter for varying  $L_7$  and  $L_5$ ,  $L_8$ ,  $D$ . (a)  $L_7$ , (b)  $L_5$ ,  $L_8$ ,  $D$ .

$f_1$  changes dramatically by tuning  $L_7$  with other parameter fixed. Fig. 2(b) shows that  $f_1$  can be kept constant when  $f_2$  changes dramatically by tuning  $L_8$ ,  $L_5$  and  $D$ . According to the above analysis,  $f_1$  can be determined by tuning the structure parameters of the second cross-coupled configuration (such as  $L_7$ ), and the  $f_2$  can be determined by adjusting  $L_8$ ,  $L_5$  and  $D$ . This way, the required two resonant frequencies of the notched bands can be simultaneously obtained and controlled independently.

### 3. EXPERIMENTAL DEMONSTRATION

To verify the effectiveness of the proposed filter, the proposed UWB BPFs with dual-notch-bands using radial-multimode loaded stub is designed, simulated, fabricated and measured. The proposed filter is simulated by using CST. The final dimensions of the filter are as follows:  $L_1 = 6.4$  mm,  $L_2 = 3.7$  mm,  $L_3 = 4$  mm,  $L_4 = 6$  mm,  $L_5 = 4.5$  mm,  $L_6 = 2.5$  mm,  $L_7 = 4$  mm,  $L_8 = 0.5$  mm,  $R_1 = 0.6$  mm,  $R_2 = 0.5$  mm,  $W_1 = 0.3$  mm,  $W_2 = 0.2$  mm,  $D = 1$  mm. Fig. 3 depicts the photograph of the fabricated filters. The proposed tri-wideband BPFs with dual-notch-bands using radial-multimode loaded stub is measured by Anristu 37347D vector network analyzer.

Figure 4 demonstrates the frequency responses and group delay of proposed filters, where excellent agreement is obtained with simulated ones. The result of these filters shows that there are three pass-bands. The three pass-bands of the fabricated BPF centered at 3.8, 6, and 9.2 GHz have 3 dB fractional bandwidths (FBW) of 1.3 GHz (3–4.3 GHz), 3 GHz(4.5–7.5 GHz), and 2.5 GHz

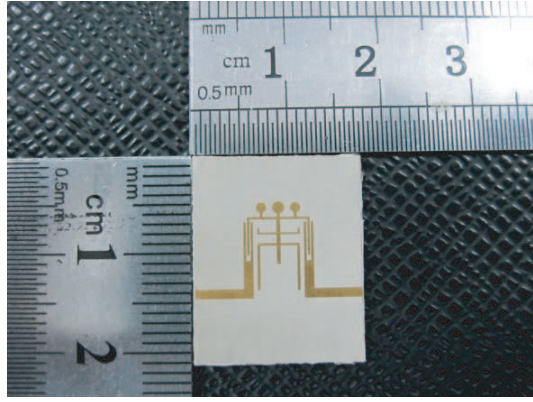
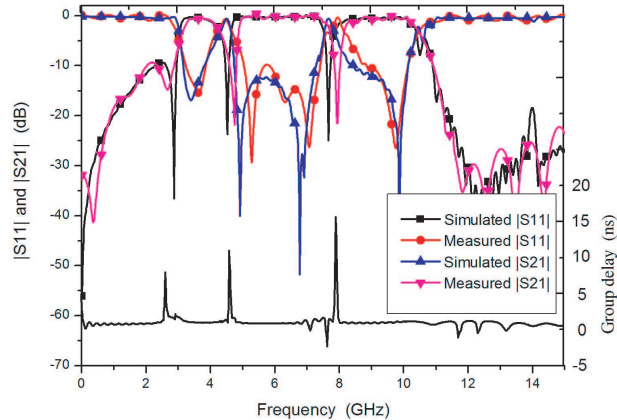


Figure 3: Photo type and of the fabricated filter.

Figure 4: Comparison between simulations and measured results for  $S_{11}$ ,  $|S_{21}|$  and the measured group delay of the fabricated filter.

(7.8–10.3 GHz), and measured minimum insertion losses of 0.42, 0.13, and 0.3 dB, respectively. The two notched bands centered at 4.5 and 7.7 GHz and have 10 dB FBW of about 2.2 and 1.3%. The two rejections between the transmissions bands are more than 20 dB. The measured group delay is between 0.2 and 0.6 ns with a maximum variation of 0.6 ns in the three pass band. At upper rejection band, the presented filters have deeper and wider stop-band attenuation, whose attenuation is more than –20 dB from 11.3 to 15 GHz.

#### 4. CONCLUSION

A Novel UWB filter with dual-notch-bands using radial-multimode loaded stub has been proposed and designed. By tuning the parameters of the structure, there sonant frequencies of the notched bands can be simultaneously obtained and controlled independently. The filter is successfully optimized, fabricated, measured. These filters can be integrated in UWB radio systems and efficiently enhance the interference immunity from undesired signals such as wireless local area network (WLAN) and WiMAX, due to its simple structure, compact size, and excellent performance.

#### ACKNOWLEDGMENT

This is partially supported by the National Nature Science Fund of China (No. 60902014), Nature Science Fund of Heilongjiang (No. 2006F11), Core Young Teacher Fund of Harbin Engineering University (No. 0812).

#### REFERENCES

1. Federal Communications Commission, “Revision of part 15 of the Commission’s rules regarding ultra-wideband transmission systems,” *Tech. Rep.*, ET-Docket 98-153, FCC02-48, April 2002.
2. Huang, X. D., X. H. Jin, and C. H. Cheng, “Compact ultra-wideband filter using coupled-line and short-ended stub,” *Electron. Lett.*, Vol. 46, No. 14, 1033–1035, 2010.
3. Deng, H. W., Y. J. Zhao, L. Zhang, X. S. Zhang, and S. P. Gao, “Compact quintuple-mode stub-loaded resonator and UWB filter,” *IEEE Microw. Wirel. Comp. Lett.*, Vol. 20, No. 8, 438–440, 2010.
4. Yao, B., Y. Zhou, Q. Cao, and Y. Chen, “Compact UWB bandpassfilter with improved upper-stopband performance,” *IEEE Microw. Wirel. Comp. Lett.*, Vol. 19, No. 1, 27–29, 2009.
5. Pirani, S., J. Nourinia, and C. Ghobadi, “Band-notched UWB BPF design using parasitic coupled line,” *IEEE Microw. Wirel. Comp. Lett.*, Vol. 20, No. 8, 444–446, 2010.
6. Jiang, T., C. Y. Liu, Y. S. Li, and M. Y. Zhu, “Research on a novel microstrip UWB notch-band BPF,” *APMC 2009*, 261–264, 2009.
7. Wei, F., C.-J. Gao, B. Liu, H.-W. Zhang, and X.-W. Shi, “UWB bandpass filter with two notch-bandsbased on SCRLH resonator,” *Electron. Lett.*, Vol. 46, No. 16, 1134–1135, 2010.
8. Song, K. and Q. Xue, “Asymmetric dual-line coupling structure formultiple-notch implementation in UWB bandpass filters,” *Electron. Lett.*, Vol. 46, No. 20, 1388–1390, 2010.

# Fast Numerical Simulation of Responses of Array Multicomponent Induction Logging Tool in Horizontally Stratified Inhomogeneous TI Formation by NMM

Hongnian Wang<sup>1</sup>, Ping Hu<sup>1</sup>, and Honggen Tao<sup>2</sup>

<sup>1</sup>College of Physics, Jinlin University, Changchun 130012, China

<sup>2</sup>Wireline Logging Company, Daqing Drilling Engineering Company, Daqing 163412, China

**Abstract**— The computation of the array multicomponent induction logging (AMCIL) responses is transformed into the three axial symmetrical problems about the electrical components through the Fourier series expanding. Through the singularity of the derivative of conductivity functions with respective to the radial distance, the two singular differential operators are introduced to describe the influence of the accumulation surface charges at cylindrical interfaces on the EM fields. The numerical matching mode method (NMM) is used to fast simulate the axial symmetrical problems, and obtain the semianalytic expression of the AMCIL responses in the horizontally layered inhomogeneous TI medium. Numerical results investigate the characteristic of AMCIL responses.

## 1. INTRODUCTION

AMCIL tools as emergent techniques are used to acquire information about the vertical and horizontal resistivities of the formation simultaneously [2, 5]. Differently from the conventional induction tools, the MCIL tool has two mutually orthogonal coplanar transmitter-receiver pairs in addition to the coaxial transmitter-receiver pair. As a result, it provides the nine components of the magnetic field. The EM fields of the coplanar coil pairs are no longer axially symmetrical. Their numerical simulations are often involved with 3D EM problems. Thus their workloads are usually very large. Actually it has become a very important subject to develop a fast and reliable method suitable to computation of the MCIL responses in the variable formations.

In this paper, an efficient and reliable numerical mode matching (NMM) method is developed to simulate the multicomponent induction logging (MCIL) responses in the horizontally layered inhomogeneous transversally isotropic (TI) formations with the borehole and the invasion zone. The computation of AMCIL responses is transformed into three axially symmetrical problems on the Fourier harmonic components of the EM fields. Based on the singularity of the derivative of the conductivity function with respective to the radial distance, the two singular differential operators are given about the horizontally electrical components and the relation between the horizontal EM components to describe the influence of the accumulated charges at the cylindrical interfaces on the EM fields. The first and second kinds of boundary conditions are introduced about the different electrical components to ensure the existence and uniqueness of their solutions. The NMM solves the singular EM problems to obtain the semianalytic tensor expression of AMCIL responses in the horizontally layered inhomogeneous TI formations.

## 2. DECOMPOSITION OF MAXWELL EQUATION

Assume the formation consists of  $N$  horizontally inhomogeneous TI layers (see Fig. 1). The horizontal and vertical conductivities of origin formation (invasion zone), invasion radius and the horizontal interface, borehole radius and mud conductivity are all shown in the Fig. 1. Furthermore, the rectangular coordinate  $(x, y, z)$  is established in Fig. 1. The triaxial co-located unit transmitters ( $\hat{\mathbf{e}}^x, \hat{\mathbf{e}}^y, \hat{\mathbf{e}}^z$ ) and the array triaxial receivers ( $R_{xk}, R_{yk}$  and  $R_{zk}$ ,  $k = 1, 2, 3$ ) with the spacings  $L_k$ , ( $k = 1, 2, 3$ ) are all located at the borehole axis.. The rectangular coordinates  $(x, y, z)$  is easily transformed to the cylindrical coordinates  $(\rho, \theta, z)$ . The AMCIL responses are obtained by solving the Maxwell's equation:

$$\nabla \times \mathbf{E}^p = i\omega\mu\mathbf{H}^p + i\omega\mu\hat{\mathbf{e}}^p\delta(\rho - \rho_s)\delta(z - z_s)/2\pi\rho; \quad \nabla \times \mathbf{H}^p = \bar{\sigma}\mathbf{E}^p, \quad \mathbf{p} = x, y, z. \quad (1)$$

Here, suppose the unit magnetic current  $\hat{\mathbf{e}}^p$ , ( $p = x, y, z$ ), is evenly distributed at the ring with small radius  $\rho_s$ ,  $\bar{\sigma}$  is the conductivity tensor and piece constant. The derivatives of conductivities with respective to  $\rho$  are expressed by:

$$d\sigma_{P,n}(\rho)/d\rho = (\sigma_{PX,n} - \sigma_{md})\delta(\rho - a) + (\sigma_{PT,n} - \sigma_{PX,n})\delta(\rho - r_{xo}), \quad P = H, V, \quad n = 1, 2, \dots, N. \quad (2)$$

## 2.1. The EM Fields of Horizontal Magnetic Dipole (HMD) ( $\hat{\mathbf{e}}^x, \hat{\mathbf{e}}^y$ )

Because the unit HMD is expanded as  $\hat{\mathbf{e}}^p = \sum_{l=\pm 1} \mathbf{M}_l^p e^{il\theta}$ ,  $p = x, y$ , where  $\mathbf{M}_l^p = 0.5(\delta_{xp} - il\delta_{yp})(1 il 0)^T$ , and  $(1 il 0)^T$  is the column vector in the cylindrical coordinates, and  $\delta_{qp} = \begin{cases} 1, & p = q \\ 0, & p \neq q \end{cases}$ , the EM fields due to the  $\hat{\mathbf{e}}^p$  are expanded as

$$\begin{aligned} \mathbf{E}^p(\rho, \theta, z; \rho_s, z_s) &= \sum_{l=-\pm 1} \mathbf{E}_l^p(\rho, z; \rho_s, z_s) e^{il\theta}; \\ \mathbf{H}^p(\rho, \theta, z; \rho_s, z_s) &= \sum_{l=\pm 1} \mathbf{H}_l^p(\rho, z; \rho_s, z_s) e^{il\theta}, \quad p = x, y. \end{aligned} \quad (3)$$

Substitution (2) and (3) into (1) yields the following equation about the components  $\mathbf{E}_{s,l}^p = (\sigma_H E_{\rho,l}^p, E_{\theta,l}^p)^T$ :

$$\tilde{\mathbf{L}}_{E,l} \mathbf{E}_{s,l}^p - \frac{\partial^2}{\partial z^2} \begin{pmatrix} \sigma_H^{-1} & \\ & 1 \end{pmatrix} \mathbf{E}_{s,l}^p = i\omega\mu \frac{(\delta_{xp} - il\delta_{yp})\delta(\rho - \rho_s)}{4\pi\rho} \delta'(z - z_s) \begin{pmatrix} -il \\ 1 \end{pmatrix}, \quad l = \pm 1. \quad (4)$$

Here,  $\tilde{\mathbf{L}}_{E,l}$  is the  $2 \times 2$  singular differential operators defined by

$$\tilde{\mathbf{L}}_{E,l} = \begin{pmatrix} -\frac{\sigma_V^{-1}}{\rho} \frac{\partial}{\partial \rho} \rho \frac{\partial}{\partial \rho} + \frac{l^2 \sigma_H^{-1} + \sigma_V^{-1}}{\rho^2} - i\omega\mu - \frac{d\sigma_V^{-1}(\rho)}{\rho d\rho} \frac{\partial}{\partial \rho} \rho & il \left\{ \frac{\partial \rho}{\rho^2 \partial \rho} - \sigma_V^{-1} \sigma_H \frac{\partial}{\partial \rho} \frac{1}{\rho} + \frac{d[\sigma_V^{-1}(\rho)\sigma_H(\rho)]}{\rho d\rho} \right\} \\ il \left[ \sigma_H^{-1} \frac{\partial}{\partial \rho} \frac{1}{\rho} - \frac{\sigma_V^{-1}}{\rho^2} \frac{\partial}{\partial \rho} + \frac{d\sigma_H^{-1}(\rho)}{\rho d\rho} \right] & -\frac{\partial}{\rho \partial \rho} \rho \frac{\partial}{\partial \rho} + \frac{l^2 \sigma_V^{-1} \sigma_H + 1}{\rho^2} - i\omega\mu \sigma_H \end{pmatrix}. \quad (5)$$

(5) is the singular differential operator because of (2) and reflects the influence of accumulation charges at the cylindrical interfaces on the electrical fields. To solve (4), the internal and outer boundary conditions are essential:

$$\partial \mathbf{E}_{s,l}^p(\rho, z; \rho_s, z_s) / \partial \rho |_{\rho=\rho_{MN}} = 0; \quad \mathbf{E}_{s,l}^p(\rho, z; \rho_s, z_s) |_{\rho=\rho_{MX}} = 0, \quad l = \pm 1. \quad (6)$$

Here,  $\rho_{MN}$  is chosen as a very small number (e.g.,  $10^{-6}$ ),  $\rho_{MX}$  is the bound range in radial direction. The  $l$ -th magnetic components are obtained by

$$\partial \mathbf{H}_{s,l}^p / \partial z = \frac{1}{i\omega\mu} \tilde{\mathbf{W}}_{E,l} \mathbf{E}_{s,l}^p; \quad H_{z,l}^p = \frac{1}{i\omega\mu} \left( -\frac{i\omega\sigma_H^{-1}(\rho)}{\rho} \quad \frac{\partial}{\rho \partial \rho} \right) \mathbf{E}_{s,l}^p, \quad l = \pm 1. \quad (7)$$

Here,  $\tilde{\mathbf{W}}_{E,l}$  is the  $2 \times 2$  known singular differential operators [3].

## 2.2. The EM Fields of the Vertical Magnetic Dipole (VMD)

The electrical field excited by the VMD ( $\hat{\mathbf{e}}^z$ ) is axial symmetric and satisfied with the following equations

$$\left( -\frac{1}{\rho} \frac{\partial}{\partial \rho} \rho \frac{\partial}{\partial \rho} + \frac{1}{\rho^2} - i\omega\mu\sigma_H \right) E_{\theta,0}^z - \frac{\partial^2}{\partial z^2} E_{\theta,0}^z = i\omega\mu \frac{d}{d\rho} \frac{\delta(\rho - \rho_s)}{2\pi\rho} \delta(z - z_s), \quad (8)$$

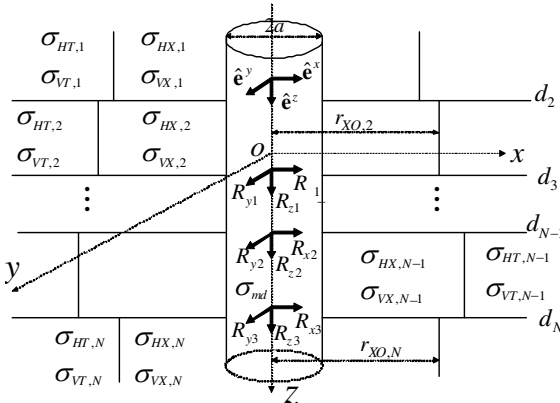


Figure 1: Formation model and the structure of AMCIL tool.

The boundary conditions

$$E_{\theta,0}^z(\rho, z; \rho_s, z_s) |_{\rho=\rho_{MN}} = 0; \quad E_{\theta,0}^z(\rho, z; \rho_s, z_s) |_{\rho=\rho_{MX}} = 0. \quad (9)$$

Magnetic fields are solved by:

$$\partial H_{\rho,0}^z / \partial z = \frac{1}{i\omega\mu} \left( \frac{\partial}{\partial\rho} \frac{1}{\rho} \frac{\partial}{\partial\rho} + i\omega\mu\sigma_H \right) E_{\theta,0}^z; \quad H_{z,0}^z = \frac{1}{i\omega\mu} \frac{\partial}{\partial\rho} E_{\theta,0}^z. \quad (10)$$

### 3. FAST NUMERICAL SIMULATION BY NMM

Divide the bound radial range  $[\rho_{MN}, \rho_{MX}]$  into  $M$  sub-intervals. The radial nodes are denoted by  $\rho_\alpha$ , ( $\alpha = 1, \dots, M+1$ ). The two-order of Newton interpolation polynomials are used as the base functions  $\varphi_\alpha(\rho)$  at the node  $\rho_\alpha$ , and defined by the following:

At the odd nodes  $\alpha = 2k-1$ ,  $k = 1, 2, \dots, [M/2]$ :

$$\varphi_{2k-1}(\rho) = \begin{cases} \frac{(\rho - \rho_{2k-3})(\rho - \rho_{2k-2})}{(\rho_{2k-1} - \rho_{2k-3})(\rho_{2k-1} - \rho_{2k-2})}, & \rho_{2k-3} \leq \rho \leq \rho_{2k-1}, \\ \frac{(\rho - \rho_{2k})(\rho - \rho_{2k+1})}{(\rho_{2k-1} - \rho_{2k})(\rho_{2k-1} - \rho_{2k+1})}, & \rho_{2k-1} \leq \rho \leq \rho_{2k+1}, \end{cases}$$

at the even nodes  $\alpha = 2k$ ,  $k = 1, 2, \dots, [M/2]$ :  $\varphi_{2k}(\rho) = \frac{(\rho - \rho_{2k-1})(\rho - \rho_{2k+1})}{(\rho_{2k} - \rho_{2k-1})(\rho_{2k} - \rho_{2k+1})}$ ,  $\rho_{2k-1} \leq \rho \leq \rho_{2k+1}$ .

#### 3.1. The Solution in Cylindrical TI Model without Horizontal Boundary

Here we solve only the EM field emitted by the HMD because the fields due to the VMD are computed by the similar method. Let  $\mathbf{S}_1(\rho) = (\varphi_1(\rho), \dots, \varphi_{M-1}(\rho), \varphi_M(\rho))^T$ ,  $\tilde{\mathbf{S}}^T(\rho) = \begin{pmatrix} \mathbf{S}_1^T(\rho) & 0 \\ 0 & \mathbf{S}_1^T(\rho) \end{pmatrix}$ . The solution of (4) under (6) is approximated by [1]:

$$\mathbf{E}_{s,l}^p(\rho, z; \rho_s, z_s) = \sum_{\alpha=1}^{2M} \tilde{\mathbf{S}}^T(\rho) \mathbf{E}_{l,\alpha} Q_{l\alpha}(z, z_s) c_{l\alpha}^p(\rho_s); \quad l = \pm 1; \quad p = x, y, \quad (11)$$

where  $\mathbf{E}_{l,\alpha}$  is the  $2M$  unknown column vector,  $Q_{l\alpha}(z, z_s)$  and  $c_{l\alpha}$  are unknown function and constant. Substituting (11) into (4), multiplying  $\rho \tilde{\mathbf{S}}(\rho)$ , and then executing integral on the range  $[\rho_{MN}, \rho_{MX}]$  yield

$$\sum_{\alpha=1}^{2N} c_{l\alpha} Q_{l\alpha}(z, z_s) \left( \tilde{\mathbf{S}}_l - \frac{1}{Q_{l\alpha}(z, z_s)} \frac{d^2 Q_{l\alpha}(z, z_s)}{dz^2} \tilde{\mathbf{V}}_l \right) \tilde{\mathbf{E}}_{l,\alpha}^p = \tilde{\mathbf{F}}_l^p \delta'(z - z_s), \quad l = \pm 1, \quad (12)$$

where  $\tilde{\mathbf{S}}_l$  and  $\tilde{\mathbf{V}}$  are the  $2M \times 2M$  stiff matrix and mass matrix, respectively, and  $\tilde{\mathbf{F}}_l^p$  is the  $2M$  column vector. They are defined by  $\tilde{\mathbf{S}}_l = \int_a^{\rho_{mx}} \tilde{\mathbf{S}}(\rho) \tilde{\mathbf{L}}_{E,l} \tilde{\mathbf{S}}^T(\rho) \rho d\rho$ ;  $\tilde{\mathbf{V}} = \int_a^{\rho_{mx}} \tilde{\mathbf{S}}(\rho) \begin{pmatrix} \sigma_H^{-1}(\rho) & 0 \\ 0 & 1 \end{pmatrix} \tilde{\mathbf{S}}^T(\rho) \rho d\rho$ ; and  $\tilde{\mathbf{F}}_l^x = \frac{i\omega\mu}{4\pi} \begin{pmatrix} -il\mathbf{S}_1(\rho_s) \\ \mathbf{S}_1(\rho_s) \end{pmatrix}$ ,  $\tilde{\mathbf{F}}_l^y = -il\tilde{\mathbf{F}}_l^x$ ;  $l = \pm 1$ .

Executing the separation of variable of (12) leads to the following three independent equations:

$$\tilde{\mathbf{S}}_l \mathbf{E}_{l,\alpha} = \kappa_{l,\alpha}^2 \tilde{\mathbf{V}} \mathbf{E}_{l,\alpha}; \quad \frac{d^2 Q_{l\alpha}(z, z_s)}{dz^2} - \kappa_{l,\alpha}^2 Q_{l\alpha}(z, z_s) = -\delta'(z - z_s); \quad \sum_{\alpha} c_{l\alpha} \tilde{\mathbf{V}} \mathbf{E}_{l,\alpha} = \tilde{\mathbf{F}}_l^p, \quad l = \pm 1, \quad (13)$$

Solving (13) determines the  $2M$  eigenvalues  $\kappa_{l,\alpha}^2$  and the corresponding eigenvectors  $\mathbf{E}_{l,\alpha}$ , the functions  $Q_{l\alpha}(z, z_s)$  ( $\alpha = 1, \dots, 2M$ ) and the vector  $\mathbf{C}_l^p = (c_{l,1}^p, c_{l,2}^p, \dots, c_{l,2M}^p)$ . Thus, the semianalytic solution of (4) is as

$$\mathbf{E}_{s,l}^p(\rho, z; \rho_t, z_t) = \tilde{\mathbf{S}}^T(\rho) \tilde{\mathbf{E}}_l e^{-\tilde{\mathbf{K}}_l |z - z_t|} \text{sign}(z - z_t) \mathbf{A}_l^p(\rho_s, z_s), \quad l = \pm 1, \quad (14)$$

where  $\tilde{\mathbf{E}}_l$  is the  $2M \times 2M$  matrix consisting of  $2M$  eigenvectors  $\mathbf{E}_{l,\alpha}$ ,  $\mathbf{A}_l^p(\rho_s, z_s) = -0.5 \mathbf{C}_l^p$ , and  $\tilde{\mathbf{K}}_l = \text{diag}(\kappa_{l,1}, \kappa_{l,2}, \dots, \kappa_{l,2M})$  is the diagonal matrix composed of the square roots of  $\kappa_{l,\alpha}^2$  and  $\text{Re}(\kappa_{l,\alpha}) > 0$ .

### 3.2. Solution in Horizontally Layered Inhomogeneous TI model

In the horizontally layered inhomogeneous TI model, the EM components ( $\mathbf{E}_{s,l}^p$ ,  $\mathbf{H}_{s,l}^p$ ,  $\mathbf{H}_{z,l}^p$ ) in bed  $n$  due to the HMD [3, 4] have the following semianalytic forms:

$$\mathbf{E}_{s,l}^{p(n)}(\rho, z; \rho_s, z_s) = \begin{pmatrix} \mathbf{S}_1^t(\rho) & \\ & \mathbf{S}_1^t(\rho) \end{pmatrix} \tilde{\mathbf{E}}_l^{(n)} \begin{cases} \tilde{\mathbf{Q}}_{E,l}^{(n)+}(z) \mathbf{A}_l^{p(n)+}(\rho_s, z_s), z > z_s \\ \tilde{\mathbf{Q}}_{E,l}^{(n)-}(z) \mathbf{A}_l^{p(n)-}(\rho_s, z_s), z < z_s \end{cases}, \quad l = \pm 1, \quad (15)$$

$$\mathbf{H}_l^{p(n)}(\rho, z; \rho_s, z_s) = \begin{pmatrix} \mathbf{S}_1^t(\rho) & \\ & \mathbf{S}_1^t(\rho) \\ & & \mathbf{S}_1^t(\rho) \end{pmatrix} \begin{pmatrix} \tilde{\mathbf{H}}_l^{(n)} \tilde{\mathbf{Q}}_{H,l}^{(n)\pm}(z) \\ \tilde{\mathbf{H}}_{z,l}^{(n)} \tilde{\mathbf{Q}}_{E,l}^{(n)\pm}(z) \end{pmatrix} \mathbf{A}_l^{p(n)\pm}(\rho_s, z_s), \quad (16)$$

$$\tilde{\mathbf{Q}}_{E,l}^{(n)+} = \left( e^{-\tilde{\mathbf{K}}_l^{(n)}(z-d_{n+1})} + e^{-\tilde{\mathbf{K}}_l^{(n)}(d_{n+1}-z)} \tilde{\mathbf{R}}_l^{(n,n+1)} \right); \quad \tilde{\mathbf{Q}}_{E,l}^{(n)-} = \left( e^{-\tilde{\mathbf{K}}_l^{(n)}(z-d_n)} + e^{-\tilde{\mathbf{K}}_l^{(n)}(d_n-z)} \tilde{\mathbf{R}}_l^{(n,n-1)} \right). \quad (17)$$

$\mathbf{A}_l^{p(n)\pm}$  is the amplitude of the electrical field in bed  $n$ .  $\tilde{\mathbf{K}}_l^{(n)}$  is the diagonal eigenvalue matrix,  $\tilde{\mathbf{E}}_l^{(n)}$  is the eigenvector matrix,  $\tilde{\mathbf{R}}_l^{(n,n-1)}$  and  $\tilde{\mathbf{R}}_l^{(n,n+1)}$  are the generalized reflection matrixes.  $\tilde{\mathbf{Q}}_{H,l}^{(n)\pm}(z) = (\tilde{\mathbf{K}}_l^{(n)})^{-1} \partial \tilde{\mathbf{Q}}_{E,l}^{(n)\pm}(z) / \partial z$ , and  $\tilde{\mathbf{H}}_l^{(n)}$  and  $\tilde{\mathbf{H}}_{z,l}^{(n)}$  are determined by (7). Supposing the receiver is located at  $\mathbf{r}_R = (\rho_R, \theta_R, z_R)$ , the two main components are given by  $H_{xx} = H_\rho^p(\mathbf{r}_R; \mathbf{r}_s) \cos \theta_R - H_\theta^p(\mathbf{r}_R; \mathbf{r}_s) \sin \theta_R$  and  $H_{yy} = H_\rho^p(\mathbf{r}_R; \mathbf{r}_s) \sin \theta_R + H_\theta^p(\mathbf{r}_R; \mathbf{r}_s) \cos \theta_R$  in the rectangular coordinates.

Similarly, solving (10) through (11) gives the magnetic field  $H_z^p(\mathbf{r}_R; \mathbf{r}_s)$  due to the  $\hat{\mathbf{e}}^z$ . The formula  $\sigma_a^{pp}(z) = 8\pi L \text{Im}(H_{pp})/\omega\mu$ ,  $p = x, y$  and  $\sigma_a^{zz}(z) = 4\pi L \text{Im}(H_{zz})/\omega\mu$  are used to compute the main responses.

## 4. NUMERICAL RESULTS

Using the previous NMM, the codes are developed to compute the AMCIL responses in horizontally layered inhomogeneous TI model. The bound range with  $\rho_{MN} = 10^{-6}$  m,  $\rho_{MX} = 40$  m and  $M = 119$  are chosen during the discretization of (4) through (10). That three different offsets  $L = 0.8, 1.2, 1.8$  m and two operating frequencies  $f = 20, 50$  kHz are assumed. The borehole radius is  $a = 0.1$  m and mud resistivity is the value of  $R_{md} = 1$  or  $1000 \Omega \cdot \text{m}$  for investigation of the influence of the change in the mud on the tool responses.

Figure 2 shows the AMCIL responses in the model with variable bed thickness without invasion zone. Thicknesses of the resistive beds with  $(R_{HT}, R_{VT}) = (5, 22) \Omega \cdot \text{m}$  vary 1, 1.5, 2, 3, and 4 m

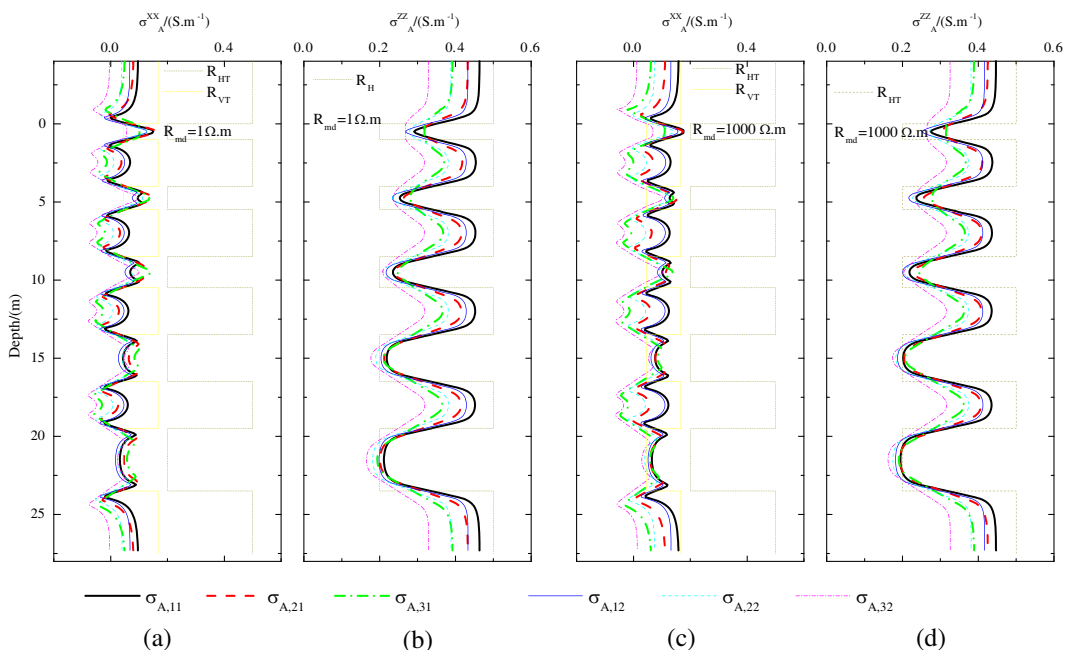


Figure 2: The AMCIL responses in the horizontally layered TI model without invasion zone but the conductive mud or resistive mud.

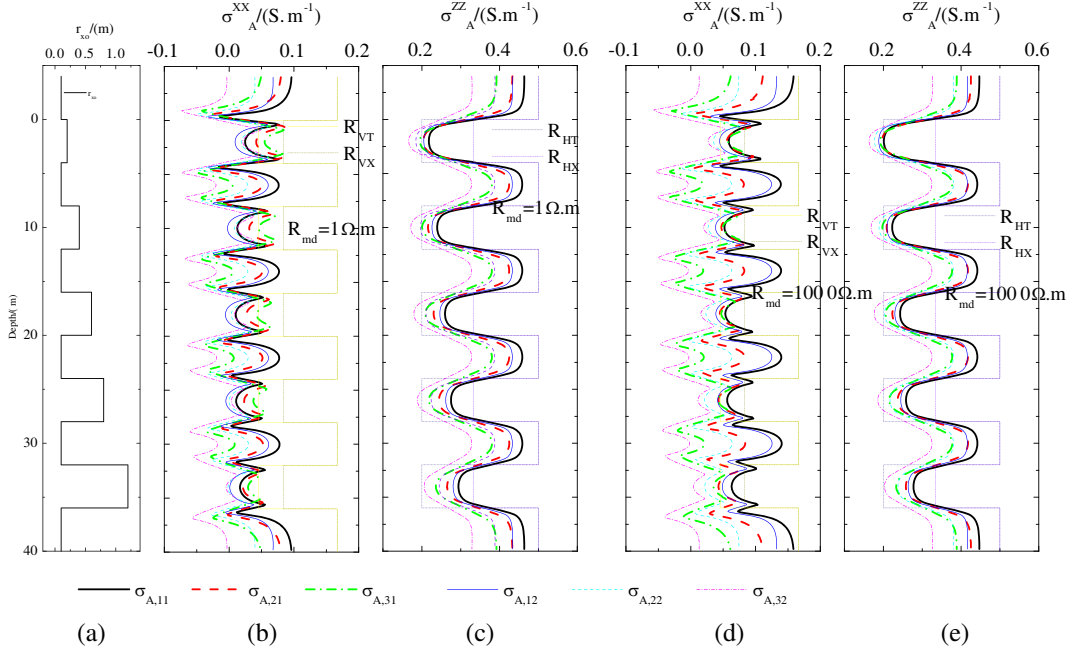


Figure 3: The AMCIL responses in the TI model with variable invasion radii and the conductive mud or resistive mud.

from the top to the bottom, and conductive beds with  $(R_{HT}, R_{VT}) = (2, 6) \Omega \cdot \text{m}$  are 3 m thick. From Fig. 2(a), it is found that the responses of the coplanar coil system seem to be complicated, and their sizes don't directly reveal the true vertical formation conductivity. The array with the short offset spacing of 0.8 m has the highest vertical resolution, and the longer offset spacing, the lower vertical resolution. The change in operating frequencies has the obvious influence on the responses and the high operation frequency helps to enhance the vertical resolution. Comparison of Fig. 2(a) with Fig. 2(d) investigates that the responses corresponding to the resistive mud are larger than that to the conductive mud. In Fig. 2(b) and (c), the responses of coaxial coil system are much simpler than that of the coplanar coil system, and correctly display the change in formation conductivity in the vertical direction.

Figure 3 demonstrates the responses in the model with variable invasion depths. The beds are all 4 m thick except shoulder beds. The invasion radii of resistive beds with  $(R_{HT}, R_{VT}) = (5, 22) \Omega \cdot \text{m}$  and  $(R_{HX}, R_{VX}) = (3, 12) \Omega \cdot \text{m}$  are 0.2, 0.4, 0.6, 0.8 and 1.2 m from the top to the bottom. Conductive beds have  $(R_{HT}, R_{VT}) = (2, 6) \Omega \cdot \text{m}$ . From Fig. 3(a) and 3(c), it is seen that the change in invasion depth has obvious influence on the responses. Longer offset and lower frequency result in deeper investigation depths. The response to the resistive mud seems to more sensitive to the change invasion depth.

## 5. CONCLUSION

The NMM is developed to fast simulate of AMCIL responses in horizontally layered inhomogeneous TI model. The computation of the AMCIL responses located at the borehole axis is transformed into the three axisymmetric problems about the horizontally electrical components. The two extra singular differential operators about the EM components characterize the influence of the accumulation surface charges at the cylindrical interfaces on the EM fields.

The numerical results demonstrate that the tool responses are very complex, and greatly sensitive to the changes in bed thickness, invasion depth and mud resistivity and so on. The change in the offset spacings and operating frequencies has also obvious influence on the responses.

The resistive mud help to improve the responses of the coplanar coil system, and the apparent conductivities to the resistive mud are larger than that to the conductive mud, and closer to the true values of formation conductivity.

## ACKNOWLEDGMENT

The work was supported by National Natural Science Foundation of China (40874058).

**REFERENCES**

1. Liu, Q. H. and W. C. Chew, "Diffraction of nonaxisymmetric waves in cylindrically layered media by horizontal discontinuities," *Radio Sci.*, Vol. 27, No. 4, 616–626, 1992.
2. Wang, H. N., H. G. Tao, et al., "Fast multiparameter reconstruction of multicomponent induction well-logging datum in a deviated well in a horizontally stratified anisotropic formation," *IEEE Trans. on Geosci. and Remote Sensing*, Vol. 46, No. 5, 1525–1534, 2008.
3. Wang, H. N., H. G. Tao, and S. W. Yang, "Study of response of a multicomponent induction logging tool in deviated and layered anisotropic formations by a numerical mode matching algorithm," *Chin. Journal of Geophys.*, Vol. 51, No. 5, 1591–1599, Sep. 2008 (in Chinese).
4. Wang, H. N., "Adaptive regularization iterative inversion of array multicomponent induction well logging datum in a horizontally stratified inhomogeneous TI formation," *IEEE Trans. Geosci. Remote Sens.*, (Accepted).
5. Zhdanov, M. S., W. D. Kennedy, and E. Peksen, "Foundation of the tensor induction well logging," *Periphysics*, Vol. 42, No. 6, 588–610, Jun. 2001.

# Finite Volume Algorithm to Simulate Responses of Multi-component Induction Tools in 3D Inhomogeneous Anisotropic Formation Using Coupled Scalar-Vector Potentials

Ye Zhang, Hongnian Wang, and Shouwen Yang

School of Physics, Jinlin University, Changchun 130012, China

**Abstract**— A novel finite volume method (FVM) is developed for simulation of the responses of multi-component induction logging (MCIL) tool in arbitrarily complex anisotropic formations. To solve the low induction number (LINs) problem and enhance convergent efficiency during the EM modeling, we reformulate Maxwell's equation into Helmholtz equations in terms of coupled scalar-vector potentials of the electric field with Coulomb gauge. Then the new Yee's non-uniform staggered girds, finite volume averaging and interpolation technique is used to discrete the Helmholtz equations and result in an asymmetrical, large, sparse and complex linear system of equations with a block diagonally dominant structure. The combination of BICGSATB with an incomplete LU-decomposition precondition is applied to iteratively solve the system. The FVM results are validated in horizontally layered inhomogeneous TI models against NMM results. The vector graphs demonstrate the spatial distribution of electrical field and investigate electric current in borehole and the accumulation charges at conductivity interfaces.

## 1. INTRODUCTION

Thin laminated sand and shale is very significant potential hydrocarbon reservoirs with visible anisotropic characteristics [1]. As a new generation logging technique, the MCIL tool is composed of the triaxial transmitters and receivers and measure nine components of magnetic field at the same time. Thus it possibly provides much more information about conductivity anisotropy. Because the EM field of coplanar coil system is no longer axial symmetric, the modeling of MCIL responses is substantially involved with the three dimensional (3D) EM problem. In a recent decade, various 3D numerical modeling techniques, such as finite difference method (FDM) [3–5], finite volume method (FVM) [2], integral method (IE) and finite element method (FEM) have been used to compute the MCIL responses in complex formation. Theoretically, each 3D modeling should solve the MCIL responses. However, some 3D modeling often encountered the low induction number (LINs) problem, and its convergent efficiency is greatly reduced in the formation with the large contrast in conductivity.

In this paper, we apply a novel finite volume algorithm to compute MICL's responses in arbitrarily earth formation. The Maxwell equation is reformulated into Helmholtz equation about the coupled scalar-vector potentials of the electric field with Coulomb gauge. Because the coupled scalar-vector potential formulation solves the problems about the slow convergence and LINs, the robust FV method resolves the Helmholtz equation. During the discretization, the Yee's non-uniform rectangular staggered grids, finite volume averaging and interpolation technique is used to result in a large sparse complex linear system on the scalar-vector potentials. The combination of BICGSTAB with ILU preconditioning iteratively determines the solution of the system. The numerical results validate the algorithm against others by the NMM.

## 2. THEROY

Assuming time-harmonic dependence of  $e^{-i\omega t}$ , the vector equation of electrical field is given by

$$\nabla \times \mathbf{E} = i\omega\mu_0\mathbf{H} + i\omega\mu_0\mathbf{M}\delta(\mathbf{r} - \mathbf{r}_s), \quad \nabla \times \mathbf{H} = \bar{\sigma}^*\mathbf{E} \quad (1)$$

Here,  $i = \sqrt{-1}$ ,  $\omega$  is the angular frequency and  $\mu_0$  is a vacuum magnetic permeability,  $\mathbf{M}\delta(\mathbf{r} - \mathbf{r}_s)$  is the known magnetic dipole source located at  $\mathbf{r}_s$ , and  $\bar{\sigma}^*$  is the complex conductivity tensor composed of the conductivity ( $\bar{\sigma}$ ) and relative electrical permittivity ( $\bar{\epsilon}_r$ ) tensors:

$$\bar{\sigma}^* = \bar{\sigma} - i\omega\epsilon_0\bar{\epsilon}_r = \begin{pmatrix} \sigma_{xx}^* & \sigma_{xy}^* & \sigma_{xz}^* \\ \sigma_{yx}^* & \sigma_{yy}^* & \sigma_{yz}^* \\ \sigma_{zx}^* & \sigma_{zy}^* & \sigma_{zz}^* \end{pmatrix}$$

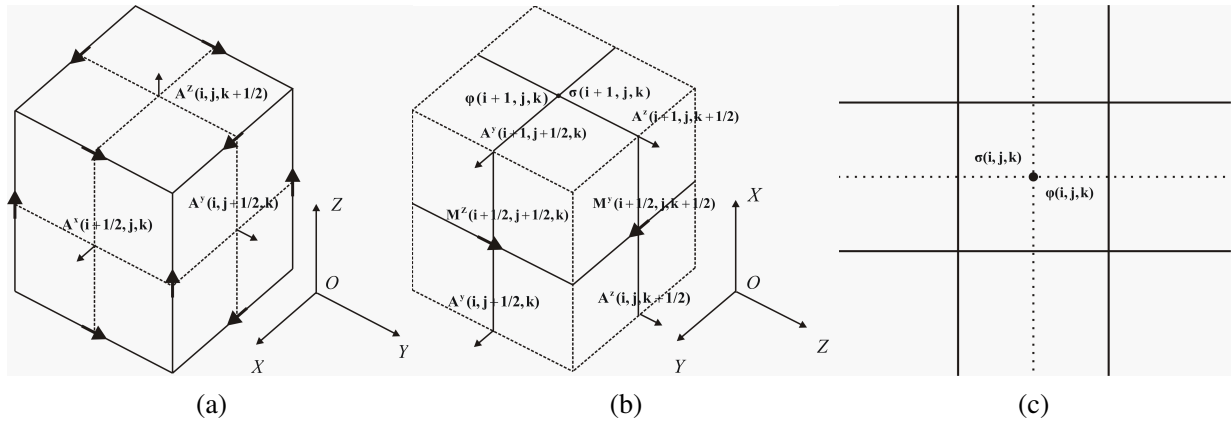


Figure 1: distribution of discrete vector-scalar potentials in staggered grid. (a) cell  $V_{i,j,k}$ . (b) Cell  $V_{i+1/2,j,k}$ . (c) Cross-section of cell  $V_{i,j,k}$ .

Applying Helmholtz decomposition, the electromagnetic fields of (1) is written as [2]:

$$\mathbf{E} = \mathbf{A} + \nabla\phi, \quad \mathbf{H} = \frac{1}{i\omega\mu_0}\nabla \times \mathbf{A} \quad (2)$$

Here, the vector function  $\mathbf{A}$  is referred as the magnetic vector potential that satisfies the Coulomb gauge  $\nabla \cdot \mathbf{A} = 0$ , and the function  $\phi$  is the electric scalar potential. The functions  $\mathbf{A}$  and  $\nabla\phi$  are reasonably considered as the electrical field caused by the magnetic dipole and electrical charges, respectively [2]. Substitution of (2) into (1) yields the following vector Helmholtz equation about coupled potentials

$$\nabla^2 \mathbf{A} + i\omega\mu_0\bar{\sigma}^*(\mathbf{A} + \nabla\phi) = -i\omega\mu_0\nabla \times \mathbf{M}\delta(\mathbf{r} - \mathbf{r}_s). \quad (3)$$

The representations of (3) for the  $x$ -,  $y$ - and  $z$ -components are as follows

$$\nabla^2 A_x + i\omega\mu_0 \left[ \sigma_{xx}^* \left( A_x + \frac{\partial\phi}{\partial x} \right) + \sigma_{xy}^* \left( A_y + \frac{\partial\phi}{\partial y} \right) + \sigma_{xz}^* \left( A_z + \frac{\partial\phi}{\partial z} \right) \right] = -i\omega\mu_0 \langle \nabla \times \mathbf{M}\delta(\mathbf{r} - \mathbf{r}_s) \rangle_x, \quad (4a)$$

$$\nabla^2 A_y + i\omega\mu_0 \left[ \sigma_{yx}^* \left( A_x + \frac{\partial\phi}{\partial x} \right) + \sigma_{yy}^* \left( A_y + \frac{\partial\phi}{\partial y} \right) + \sigma_{yz}^* \left( A_z + \frac{\partial\phi}{\partial z} \right) \right] = -i\omega\mu_0 \langle \nabla \times \mathbf{M}\delta(\mathbf{r} - \mathbf{r}_s) \rangle_y, \quad (4b)$$

$$\nabla^2 A_z + i\omega\mu_0 \left[ \sigma_{zx}^* \left( A_x + \frac{\partial\phi}{\partial x} \right) + \sigma_{zy}^* \left( A_y + \frac{\partial\phi}{\partial y} \right) + \sigma_{zz}^* \left( A_z + \frac{\partial\phi}{\partial z} \right) \right] = -i\omega\mu_0 \langle \nabla \times \mathbf{M}\delta(\mathbf{r} - \mathbf{r}_s) \rangle_z. \quad (4c)$$

Here,  $\langle \nabla \times \mathbf{M}\delta(\mathbf{r} - \mathbf{r}_s) \rangle_x$ ,  $\langle \nabla \times \mathbf{M}\delta(\mathbf{r} - \mathbf{r}_s) \rangle_y$  and  $\langle \nabla \times \mathbf{M}\delta(\mathbf{r} - \mathbf{r}_s) \rangle_z$  are the  $x$ -,  $y$ -, and  $z$ -components of  $\nabla \times \mathbf{M}\delta(\mathbf{r} - \mathbf{r}_s)$ , respectively. The vector potential  $\mathbf{A}$  is not the complete solution to the vector Equation (3). Therefore, an extra scalar equation in addition to (3) is required. We take the divergence of Equation (3) and obtain

$$\nabla \cdot \bar{\sigma}^*(\mathbf{A} + \nabla\phi) = 0 \quad (5)$$

Dirichlet boundary conditions are enforced on the outer boundary  $\partial\Omega$

$$\mathbf{n} \times \mathbf{A}|_{\partial\Omega} = 0, \quad \phi|_{\partial\Omega} = 0$$

After that, we utilize a non-uniform staggered-grid scheme in rectangular coordinates to discrete the Equations (4a)–(4c) and (5). The locations of vector and scalar potential components in the staggered grids are shown in Figure 1.

Vector potential components are defined at the center of the six faces of  $V_{i,j,k}$  and scalar potential is defined at the center of  $V_{i,j,k}$ . Magnetic dipole sources are located at the midpoint of cell's edges. Assuming the conductivity is constant in each volume cell, the equivalent conductivity in each cell is approximated by volume weighted averaging of different conductivity.

$$\sigma_{i,j}^{ave} = \frac{V_1\sigma_{i,j}^1 + V_2\sigma_{i,j}^2}{V_1 + V_2}$$

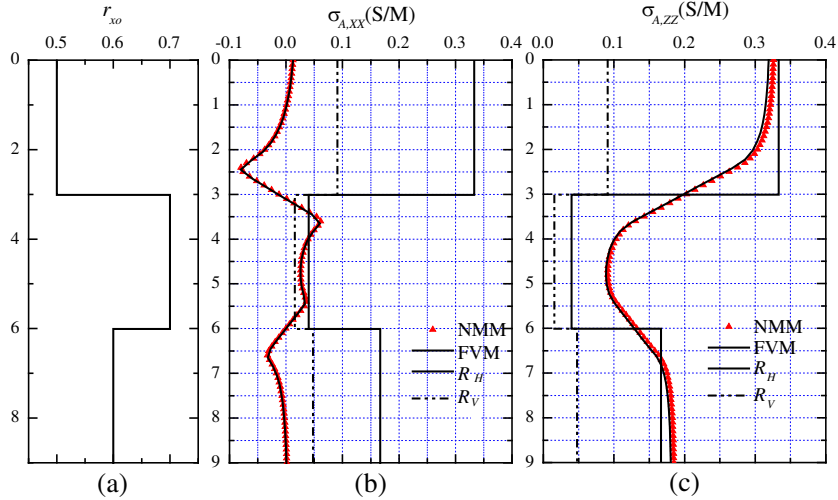


Figure 2: Comparison of numerical results of response of MICL in the 3 horizontal-layer inhomogeneous TI model by NMM method with that by finite volume method using vector-scalar potentials.

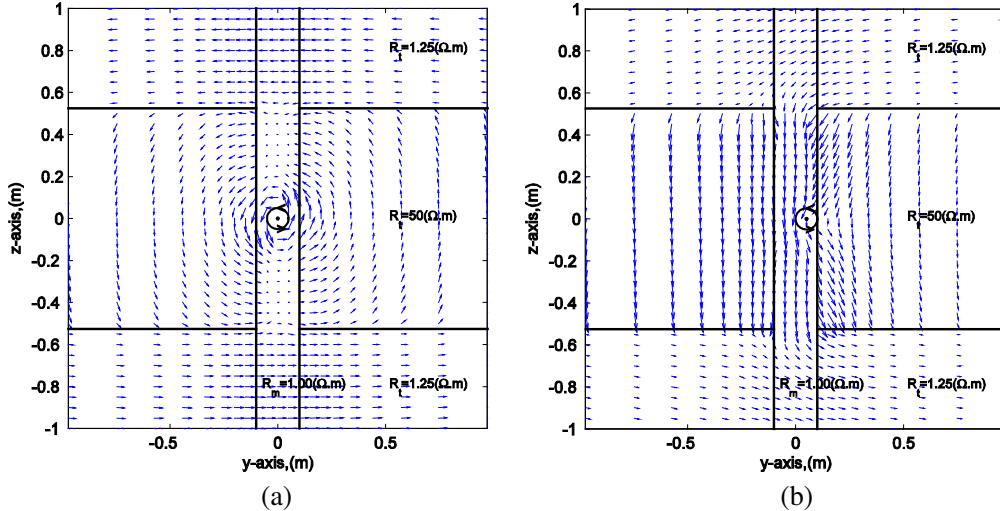


Figure 3: Vector graph of electrical field caused by  $xx$  coupling in vertical well with conductive mud. (a) Vector graph of electrical field when tool is centered in borehole. (b) Vector graph of electrical field when tool is eccentric in borehole.

where ( $i, j = x, y, z$ ),  $\sigma_{i,j}^1$ ,  $\sigma_{i,j}^2$ ,  $V_1$ ,  $V_2$  are respectively the conductivity components and volume of two different material in the cell.  $\sigma_{i,j}^{ave}$  represents the equivalent conductivity component. Applying finite volume averaging and interpolation technique, we can discrete the Equations (4) and (5) as

$$\bar{\mathbf{F}}\mathbf{x} = \mathbf{b} \quad (6)$$

Here,  $\bar{\mathbf{F}}$  is a complex asymmetric large sparse matrix which consists of 16 block sub-matrixes. In order to ensure matrix is diagonal-dominant, the grid size must fulfill the constraint condition as follow [3],  $1/h_{max}^2 \gg \omega\mu_0\sigma_{max}$ , where  $h_{max}$ ,  $\sigma_{max}$  are the max grid spacing and max conductivity respectively. As a fast convergent and stable iterative algorithm, BICGSTAB can solve asymmetrical large sparse complex linear system (6) efficiently. In order to decrease the condition number of matrix  $\bar{\mathbf{F}}$ , the preconditioning technique should be employed. The essence of preconditioning is that the system (6) can be reformulated into another system which has the same numerical result and lower condition number. In this paper, we employ the incomplete-LU decomposition technique with no fill-in (ILU (0)) for preconditioning. Applying incomplete decomposition, the coefficient matrix  $\bar{\mathbf{F}}$  can be written as  $\bar{\mathbf{F}} = \bar{\mathbf{L}}\bar{\mathbf{U}} - \bar{\mathbf{R}}$ . Where  $\bar{\mathbf{L}}$  and  $\bar{\mathbf{U}}$  are the lower triangle matrix and the upper triangle matrix respectively, and  $\bar{\mathbf{R}}$  is the residual matrix. Therefore, system (6) can be written as  $\bar{\mathbf{L}}^{-1}\bar{\mathbf{F}}\bar{\mathbf{U}}^{-1}\mathbf{u} = \bar{\mathbf{L}}^{-1}\mathbf{b}, \mathbf{x} = \bar{\mathbf{U}}^{-1}\mathbf{u}$ . In the process of iterative operation,  $\mathbf{S}$  represents

the residual vector after a ‘Bi-CG step’. We consider that solution had converged to an acceptable accuracy when the norm of  $\mathbf{S}$  is small than  $10^{-4}$ .

### 3. NUMERICAL RESULTS

First, we apply the three-dimensional FV and NMM algorithms to simulate the response of MICL in three-layered inhomogeneous anisotropic media. The model parameters are  $\mathbf{R}_{ht} = (3, 25, 6) \Omega \cdot \text{m}$ ,  $\mathbf{R}_{vt} = (11, 65, 21) \Omega \cdot \text{m}$ ,  $\mathbf{R}_{hx} = (2, 8, 3.5) \Omega \cdot \text{m}$ ,  $\mathbf{R}_{vx} = (7, 24, 1) \Omega \cdot \text{m}$ ,  $\mathbf{R}_{mud} = 1 \Omega \cdot \text{m}$ ,  $\mathbf{d} = (3, 6) \text{ m}$ ,  $\mathbf{r}_{xo} = (0.5, 0.7, 0.6) \Omega \cdot \text{m}$ , and the offset spacing is 1.2 m. Figure 1 shows that the agreement between two algorithms is quite acceptable. Their average relative errors are less than 3%. Unfortunately, the characteristic Curve of  $\sigma_{A,XX}$  is more complicated than  $\sigma_{A,ZZ}$  because of negative responses and horns caused by electric charges accumulation on the bed boundary. Therefore, it is difficult to obtain the horizontal and vertical conductivity from apparent conductivity  $\sigma_{A,XX}$ . In order to obtain the true values of formation conductivity, some inversion method should be applied.

It is well known that the eccentricity effect on transversal components of MICL’s responses is very strong especially in the conductive mud and resistive formation. Applying the vector graph of electrical field, we can explain this phenomenon. As Figure 3(a) shown, the electrical field is circular in the formation when tool is centered. However, the pattern of electrical field is distorted when tool is eccentric. Besides, electrical field in the borehole tends to parallels the direction of

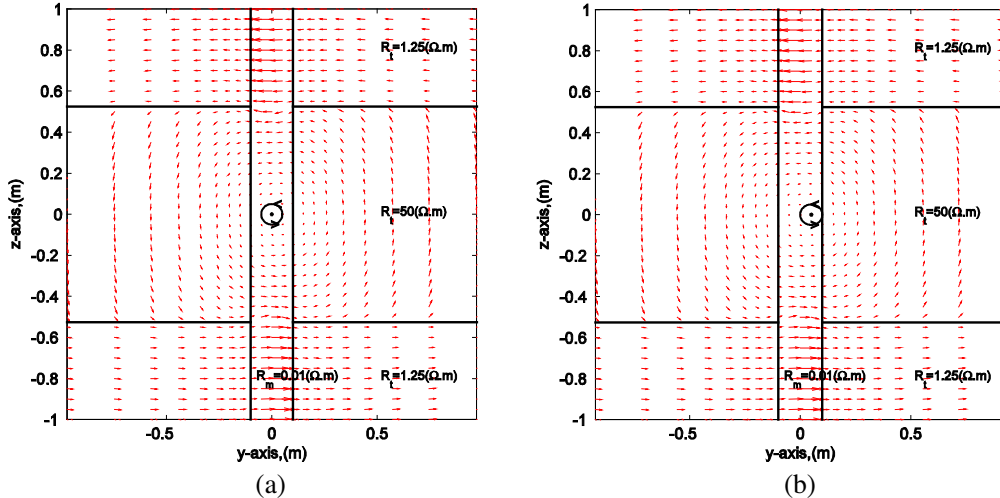


Figure 4: Vector graph of electrical field caused by  $xx$  coupling in vertical well with resistive mud. (a) Vector graph of electrical field when tool is centered in borehole. (b) Vector graph of electrical field when tool is eccentric in borehole.

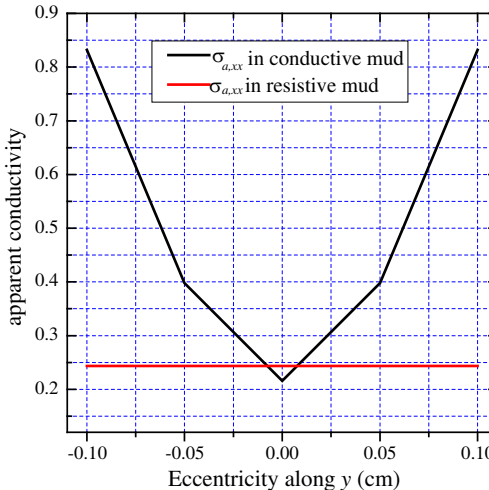


Figure 5: Responses of  $xx$  coupling when tool is eccentric in  $y$ -direction in conductive mud and in resistive mud. (The offset spacing is 1 m).

borehole. As a result, there is net current flow along the borehole. The borehole current produces effect on the receiver. This is why eccentricity effect is enormous, as seen in Figure 5 (black real line). On the contrary, there is little change of electrical field in resistive mud no matter whether tool is centered or eccentric. Thus, the eccentricity effect is very small, as seen in Figure 5 (red real line).

#### 4. CONCLUSIONS

In this paper, a robust FV method based on coupled-potential formulation has been presented to simulate the responses of MICL in 3D inhomogeneous anisotropic formation. The numerical result was validated against NMM method solutions, showing very good agreement. Applying vector graph of electrical field, we can explain that the eccentricity effect is caused by electrical field along the borehole.

#### REFERENCES

1. Wang, H. N. and S. D. Yang, “The response characteristic of resistivity log in anisotropic formations (in Chinese),” *Oil Geophys. Prospect.*, Vol. 34, No. 6, 649–656, 1999.
2. Haber, E. U., M. Asher, D. A. Aruliah, et al, “Fast simulation of 3D electromagnetic problems using potentials,” *Journal of Computational Physics*, Vol. 163, 150–171, 2000.
3. Newman, G. A. and D. L. Alumbaugh, “Three-dimensional induction logging problems, Part 2: A finite-difference solution,” *Geophysics*, Vol. 67, No. 2, 484–491, 2002.
4. Hou, J. S., R. K. Mallan, and C. Torres-Verdin, “Finite-difference simulation of borehole EM measurement in 3D anisotropic media using coupled scalar-vector potentials,” *Geophysics*, Vol. 71, No. 5, 225–233, 2006.
5. Yang, S. W., H. N. Wang, and G. B. Chen, “The 3-D finite difference time domain (FDTD) algorithm of response of multi-component electromagnetic well logging tool in a deviated and layered anisotropic formation,” *Chinese J. Geophysics (in Chinese)*, Vol. 52, No. 3, 833–841, 2009.

# Fast Parameterized Inversion of Multicomponent Induction Logging Data in Horizontally Layered TI Formation

Shouwen Yang and Hongnian Wang

School of Physics, Jilin University, Changchun 130012, China

**Abstract**— We advance a fast parameterized inversion algorithm to simultaneously reconstruct the horizontal and vertical conductivities, the interface depth each bed from the multicomponent induction logging (MCIL) data in horizontal layered TI formations. Applying transmission line method (TLM) gives the analytic solution of tensor Green's function in the frequency-wavenumber domain. The perturbation equations are derived about the changes in responses of MCIL caused by perturbation in model parameters. The computations of the Sommerfeld integrals are solved by the cubic spline interpolation and the recursive formulae of Bessel function. As a result, it is set up the fast computation of the MCIL responses and their Fréchet derivative with respective to all model vectors. Finally, we iteratively reconstruct all the model parameters to realized the best fit of the input logging data with the modeling data by the normalization of Fréchet derivative and singular-value-decomposition (SVD). Theoretical inversion results validate the inversion method and its anti-noise ability.

## 1. INTRODUCTION

The MCIL tool as a new logging technology helps to provide the information about vertical and horizontal resistivity at the same time [1]. Thus, it is very useful to correctly evaluate the sand-shale laminated formation. The tool consists of the triaxial transmitters and receivers, and simultaneously provides all components of magnetic field. Since the responses of the coplanar coil system are very sensitive to borehole environment and formation interfaces [2–4], their sizes don't directly reveal the true values of formation conductivities. It is important to establish the efficient inversion technique of extraction of the formation conductivity from the logs.

The computation of MCIL responses usually involves with the 3D EM problem. The inversion of MCIL responses usually becomes extremely complicated because it requires computation of Fréchet derivative and determination of new model parameters in addition to the forward modeling. Up to now, 1D [5], 2D [6] and 3D [7] inversion algorithms have been studied and established. Especially, the efficient computation of Fréchet derivative is the key problem in the total inversion process. In the literatures [6, 8], the semianalytic solution of EM fields by the NMM has been used to fast compute the MCIL responses, and Fréchet derivative, and efficient 1D and 2D inversions of both MCIL and AMCIL datum have been established.

In this paper, on the basis of the analytic solution of EM field in the frequency-wavenumber domain by TLM [9], we apply the cubic spline interpolation and the recursive formulae of Bessel function to fast compute the Sommerfeld integrals and establish fast computation of MCIL responses in horizontally layered TI formation. We use the perturbation theory and inverse Fourier transform to derive efficient computation of the Fréchet derivative of MCIL responses with respective to all the model vectors. Then a fast iterative parameterized inversion of MCIL data is given to simultaneously reconstruct the horizontal and vertical resistivities and the interfaces.

## 2. THE FAST CALCULATION OF FRÉCHET DERIVATIVE MATRIX

Assume the formation consists of  $N$  horizontally transversally isotropic (TI) layers without borehole for brevity. The conductivity per bed are all the diagonal tensor  $\bar{\sigma}_n = \text{diag}(\sigma_{Hn}, \sigma_{Hn}, \sigma_{Vn})$ , where  $\sigma_{Hn}$  and  $\sigma_{Vn}$  designates horizontal and vertical conductivities in bed  $n$ , respectively. The variable  $d_n (n = 2, 3, \dots, N)$  stands for the horizontal interfaces. The model vector is  $\mathbf{x} = (\sigma_{H1}, \sigma_{H2}, \dots, \sigma_{HN}; \sigma_{V1}, \sigma_{V2}, \dots, \sigma_{VN}; d_2, d_3, \dots, d_N)$ . Because the angular frequency  $\omega$  is usually small, the displacement current can be omitted. The MCIL responses in the model are acquired by solving the following Maxwell equation:

$$\nabla \times \bar{\mathbf{G}}^{ME}(\mathbf{r}, \mathbf{r}_S) = i\omega\mu\bar{\mathbf{G}}^{MH}(\mathbf{r}, \mathbf{r}_S) + \bar{\mathbf{I}}\delta(\mathbf{r} - \mathbf{r}_S); \quad \nabla \times \bar{\mathbf{G}}^{MH}(\mathbf{r}, \mathbf{r}_S) = \bar{\sigma} \cdot \bar{\mathbf{G}}^{ME}(\mathbf{r}, \mathbf{r}_S), \quad (1)$$

where  $\bar{\mathbf{G}}^{ME}(\mathbf{r}, \mathbf{r}_S)$  and  $\bar{\mathbf{G}}^{MH}(\mathbf{r}, \mathbf{r}_S)$  denote the EM tensor Green functions by the unit magnetic currents tensor.  $\bar{\sigma}$  is the conductivity tensor, and  $\bar{\mathbf{I}}$  is the unit tensor. Applying the Fourier

transform of (1) about the variables  $x$ ,  $y$  and TLM give the solutions of (1) in the frequency-wavenumber domain like [9]

$$\tilde{\mathbf{G}}^{MH}(k_x, k_y, z, z_S) = \begin{pmatrix} -\frac{1}{k_\rho^2} [k_x^2 I_v^h(zz_S) + k_y^2 I_v^e(zz_S)] & \frac{k_x k_y}{k_\rho^2} [-I_v^h(zz_S) + I_v^e(zz_S)] & \frac{k_x I_i^h(zz_S)}{\omega \mu} \\ \frac{k_x k_y}{k_\rho^2} [-I_v^h(zz_S) + I_v^e(zz_S)] & -\frac{1}{k_\rho^2} [k_y^2 I_v^h(zz_S) + k_x^2 I_v^e(zz_S)] & \frac{k_y I_i^h(zz_S)}{\omega \mu} \\ k_x V_v^h(zz_S) / \omega \mu & k_y V_v^h(zz_S) / \omega \mu & \frac{1}{i \omega \mu} \left[ \frac{k_\rho^2 V_i^h(zz_S)}{i \omega \mu} + \delta(z - z_S) \right] \end{pmatrix}, \quad (2)$$

$$\tilde{\mathbf{G}}^{ME}(k_x, k_y, z, z_S) = \begin{pmatrix} \frac{k_x k_y}{k_\rho^2} [V_v^e(zz_S) - V_v^h(zz_S)] & -\frac{1}{k_\rho^2} [k_x^2 V_v^e(zz_S) + k_y^2 V_v^h(zz_S)] & \frac{k_y V_i^h(zz_S)}{\omega \mu} \\ \frac{1}{k_\rho^2} [k_y^2 V_v^e(zz_S) + k_x^2 V_v^h(zz_S)] & -\frac{k_x k_y}{k_\rho^2} [V_v^e(zz_S) - V_v^h(zz_S)] & -\frac{k_y}{\omega \mu} V_i^h(zz_S) \\ \frac{i k_y}{\omega \sigma_v} I_v^e(zz_S) & -\frac{i k_x}{\omega \sigma_v} I_v^e(zz_S) & 0 \end{pmatrix}. \quad (3)$$

Here,  $k_x$  and  $k_y$  are the wavenumbers in the  $x$  and  $y$  direction, respectively, and  $k_\rho = \sqrt{k_x^2 + k_y^2}$ .  $V_i^q(z, z_S)$  and  $I_i^q(z, z_S)$  (or  $V_v^q(z, z_S)$  and  $I_v^q(z, z_S)$ ) denote the voltage and current at  $z$  due to a 1-A shunt current (or 1-V series voltage) source at  $z_S$ , respectively. The superscript “ $q = e$  or  $h$ ” represents TM or TE wave to  $z$ . The voltage and current in bed  $n$  are given by [9]

$$V_{i,n}^q(z, z_S) = \begin{cases} A_n^+ \left( e^{ik_{z,n}^q(z-d_{n+1})} + \tilde{R}_{n,n+1}^{(q,v)} e^{ik_{z,n}^q(d_{n+1}-z)} \right), & z > z_S \\ A_n^- \left( e^{ik_{z,n}^q(d_n-z)} + \tilde{R}_{n,n-1}^{(q,v)} e^{ik_{z,n}^q(z-d_n)} \right), & z < z_S \end{cases}, \quad (4)$$

$$I_{i,n}^q(z, z_S) = \begin{cases} B_n^+ \left( e^{ik_{z,n}^q(z-d_{n+1})} + \tilde{R}_{n,n+1}^{(q,i)} e^{ik_{z,n}^q(d_{n+1}-z)} \right), & z > z_S \\ B_n^- \left( e^{ik_{z,n}^q(d_n-z)} + \tilde{R}_{n,n-1}^{(q,i)} e^{ik_{z,n}^q(z-d_n)} \right), & z < z_S \end{cases}$$

where  $A_n^\pm$  and  $B_n^\pm$  are the amplitudes of the voltage and current in bed  $n$ , respectively.  $\tilde{R}_{n,n+1}^{(q,v)}$ ,  $\tilde{R}_{n,n-1}^{(q,v)}$  and  $\tilde{R}_{n,n+1}^{(q,i)}$ ,  $\tilde{R}_{n,n-1}^{(q,i)}$  are the generalized reflection coefficients. The  $k_z^e = \sqrt{k_h^2 - \lambda_e^2 k_\rho^2}$  and  $k_z^h = \sqrt{k_h^2 - k_\rho^2}$  are the propagation wave numbers in the  $z$ -direction.  $\lambda_e = \sqrt{\sigma_H/\sigma_V}$  is the electric anisotropic constant.

Substitution of (4) into (2) and (3) and execution of inverse Fourier transform yield the solutions of the  $\tilde{\mathbf{G}}^{ME}(\mathbf{r}, \mathbf{r}_S)$  and  $\tilde{\mathbf{G}}^{MH}(\mathbf{r}, \mathbf{r}_S)$  whose each component is computed by the Sommerfeld integral like

$$S_{mn} \left[ \tilde{f}(k_\rho) \right] = \int_0^\infty \tilde{f}(k_\rho) J_m(k_\rho \rho) k_\rho^n dk_\rho, \quad m = 0, 1; \quad n = 0, 1, 2, 3. \quad (5)$$

The small perturbation  $\delta\bar{\sigma}$  in the conductivity tensor results in the changes  $\delta\tilde{\mathbf{G}}^{MH}(\mathbf{r}_R, \mathbf{r}_S)$  in the magnetic tensor  $\tilde{\mathbf{G}}^{MH}(\mathbf{r}, \mathbf{r}_S)$  given by [6]

$$\delta\tilde{\mathbf{G}}^{MH}(\mathbf{r}_R, \mathbf{r}_S) = \int_\Omega [\tilde{\mathbf{G}}^{ME}(\mathbf{r}_R, \mathbf{r}_S)]^T \delta\bar{\sigma}(\bar{r}) \tilde{\mathbf{G}}^{ME}(\mathbf{r}_R, \mathbf{r}_S) dV. \quad (6)$$

The perturbation in the conductivity in the horizontally layered TI model has the following expression:

$$\begin{aligned} \delta\sigma(z) = & \sum_{n=1}^{N-1} \delta\bar{\sigma}_n [H(z - d_n^+) - H(z - d_{n+1}^-)] + \delta\bar{\sigma}_N H(z - d_N^+) \\ & + \sum_{n=2}^N \delta d_n [\bar{\sigma}_{n-1} \delta(z - d_n^-) - \bar{\sigma}_n \delta(z - d_n^+)], \end{aligned} \quad (7)$$

where  $H(r) = \begin{cases} 1, & r \geq 0 \\ 0, & r < 0 \end{cases}$  is the Heaviside function, the superscript ‘ $\pm$ ’ denotes its left or right limit,  $\delta\bar{\sigma}_n = \text{diag}(\delta\sigma_{Hn}, \delta\sigma_{Hn}, \delta\sigma_{Vn})$  and  $\delta d_n$  are small perturbations in model parameters of bed  $n$ .

$\delta(z) = H'(z)$  is the Dirac's function. Substituting (7) into (6) obtain the following relation between the changes in the magnetic fields and the perturbations in model parameters:

$$\delta G_{\alpha\beta}^{MH}(\mathbf{r}_R, \mathbf{r}_S) = \sum_{n=1}^N [A_{H,\alpha\beta}(n)\delta\sigma_{Hn} + B_{V,\alpha\beta}(n)\delta\sigma_{Vn}] + \sum_{n=2}^N C_{\alpha\beta}(n)\delta d_n, \quad (8)$$

where

$$A_{H,\alpha\beta}(n) = \int_{d_n}^{d_{n+1}} I_{H,\alpha\beta}(z) dz, \quad B_{V,\alpha\beta}(n) = \int_{d_n}^{d_{n+1}} I_{V,\alpha\beta}(z) dz \quad (9)$$

and  $C_{\alpha\beta}(n) = (\sigma_{H,n-1} - \sigma_{H,n})I_{H,\alpha\beta}(d_n^+) + (\sigma_{V,n-1} - \sigma_{V,n})I_{V,\alpha\beta}(d_n^+).$

The functions  $I_{H,\alpha\beta}(z)$  and  $I_{V,\alpha\beta}(z)$  are defined by

$$I_{H,\alpha\beta}(z) = \int_{-\infty}^{+\infty} \int_{-\infty}^{+\infty} \sum_{\gamma=1}^2 G_{\gamma\alpha}^{ME}(\mathbf{r}, \mathbf{r}_R) G_{\gamma\beta}^{ME}(\mathbf{r}, \mathbf{r}_S) dx dy, \quad (10)$$

$$I_{V,\alpha\beta}(z) = \int_{-\infty}^{\infty} \int_{-\infty}^{\infty} G_{z\alpha}^{ME}(\mathbf{r}, \mathbf{r}_R) G_{z\beta}^{ME}(\mathbf{r}, \mathbf{r}_S) dx dy.$$

Applying inverse Fourier transform

$$G_{\gamma\beta}^{ME}(\mathbf{r}, \mathbf{r}_S) = (2\pi)^{-2} \int_{-\infty}^{\infty} \int_{-\infty}^{\infty} \tilde{G}_{\gamma\beta}^{ME}(k_x, k_y, z, z_S) e^{i[k_x(x-x_S)+k_y(y-y_S)]} dk_x dk_y$$

and the equation  $\int_{-\infty}^{\infty} \int_{-\infty}^{\infty} e^{i[(k_x+k'_x)x+(k_y+k'_y)y]} dx dy = 4\pi^2 \delta(k_x + k'_x) \delta(k_y + k'_y)$ , the integrals of (10) are simplified as

$$I_{H,\alpha\beta}(z) = (2\pi)^{-2} \int_{-\infty}^{+\infty} \int_{-\infty}^{+\infty} \sum_{r=1}^2 \tilde{G}_{r\alpha}^{ME}(-k_x, -k_y, z, z_R) \tilde{G}_{r\beta}^{ME}(k_x, k_y, z, z_S) e^{i[k_x(x_R-x_S)+k_y(y_R-y_S)]} dk_x dk_y, \quad (11)$$

$$I_{V,\alpha\beta}(z) = (2\pi)^{-2} \int_{-\infty}^{+\infty} \int_{-\infty}^{+\infty} \tilde{G}_{3\alpha}^{ME}(-k_x, -k_y, z, z_S) \tilde{G}_{3\beta}^{ME}(k_x, k_y, z, z_S) e^{i[k_x(x_R-x_S)+k_y(y_R-y_S)]} dk_x dk_y$$

It is easy to prove that the integrals of the right hand side of (11) are transformed into the Sommerfeld integrals like (5) and fast computed by Gauss-Legendre quadrature [10]. Based on (4), the integrals of (9) are determined by analytic method. Thus, the coefficients of the right hand side of (8) are efficiently acquired.

Picking the imaginary parts of the three main component of  $\bar{\mathbf{G}}^{MH}(\mathbf{r}_R, \mathbf{r}_S)$ , then dividing the corresponding tool constants, and considering the convenience in inversion process, (8) is written as the form of normalized matrix multiplication [6]:

$$\delta \mathbf{y}_{pp}(z_R) = \bar{\mathbf{F}}_{pp}(z_R) \delta \mathbf{q}, \quad p = x, y, z \quad (12)$$

where,  $\delta \mathbf{q} = (\frac{\delta\sigma_{H1}}{\sigma_{H1}}, \frac{\delta\sigma_{H2}}{\sigma_{H2}}, \dots, \frac{\delta\sigma_{HN}}{\sigma_{HN}}, \frac{\delta\sigma_{V1}}{\sigma_{V1}}, \frac{\delta\sigma_{V2}}{\sigma_{V2}}, \dots, \frac{\delta\sigma_{VN}}{\sigma_{VN}}, \frac{\delta d_2}{d_3-d_2}, \frac{\delta d_3}{d_4-d_3}, \dots, \frac{\delta d_{N-1}}{d_N-d_{N-2}}, \frac{\delta d_N}{d_{N-1}-d_{N-1}})^T$  is the relative perturbation in the model vector,  $\delta \mathbf{y}_{pp}(z_R) = \delta \boldsymbol{\sigma}_{a,pp}(z_R)/\boldsymbol{\sigma}_{a,pp}(z_R)$  is the relative changes in  $\boldsymbol{\sigma}_{a,pp}(z_R)$ ,  $\bar{\mathbf{F}}_{pp}(z_R) = \boldsymbol{\sigma}_{a,pp}^{-1}(z_R) \bar{\mathbf{C}}_{pp}(z_R) \bar{\mathbf{Q}}$  is the normalization Fréchet derivative, where,  $\bar{\mathbf{Q}} = \text{diag}(\sigma_{H,1}, \dots, \sigma_{H,N}, \sigma_{V,1}, \dots, \sigma_{V,N}, h_3 - h_2, (h_4 - h_2)/2, \dots, (h_N - h_{N-2})/2, h_N - h_{N-1})$ .

### 3. THE ITERATIVE INVERSION

Supposing  $\mathbf{y}^{obs} = (y_1^o, y_2^o, \dots, y_M^o)$  is the input data and composed of the two main components  $(\sigma_{a,xx}, \sigma_{a,zz})$  of the MCIL in different positions. The vector function  $\mathbf{y}(\mathbf{x})$  is the theoretical responses of the MCIL due to the model vector  $\mathbf{x}$ . The inversion of MCIL data is to find the some

model vector  $\mathbf{x}^*$  to realize the best fit between  $\mathbf{y}^{obs}$  and  $\mathbf{y}(\mathbf{x}^*)$  in the least square inversion theory, i.e. to minimize the following objective function:

$$J(\mathbf{x}) = 0.5 \left( \mathbf{y}^{obs} - \mathbf{y}(\mathbf{x}) \right)^T \text{diag}^{-2} \left( \mathbf{y}^{obs} \right) \left( \mathbf{y}^{obs} - \mathbf{y}(\mathbf{x}) \right) \quad (13)$$

Suppose that  $\mathbf{x}^{(0)}$  is the initial value of model vector and  $\mathbf{x}^{(k)}$  is the  $k$ -th iteration solution, and expand (13) near  $\mathbf{x}^{(k)}$  as

$$J \left( \mathbf{x}^{(k)} (1 + \text{diag}(\delta\mathbf{q})) \right) \approx 0.5 \left( \Delta\mathbf{y}^{(k)} - \bar{\mathbf{F}}^{(k)} \delta\mathbf{q} \right)^T \left( \Delta\mathbf{y}^{(k)} - \bar{\mathbf{F}}^{(k)} \delta\mathbf{q} \right). \quad (14)$$

Here,  $\delta\mathbf{q}$  is the small relative model vector,  $\Delta\mathbf{y}^{(k)} = \text{diag}^{-1}(\mathbf{y}^{obs})[\mathbf{y}^{obs} - \mathbf{y}(\mathbf{x}^{(k)})]$  is the relative error vector of input data,  $\bar{\mathbf{F}}^{(k)} = \text{diag}^{-1}(\mathbf{y}^{obs}) \nabla \mathbf{y}(\mathbf{x}^{(k)}) \bar{\mathbf{Q}}^{(k)}$  is the  $M \times (3N - 1)$  normalized Fréchet derivative matrix of  $\mathbf{y}(\mathbf{x})$  with respective to the  $\mathbf{x}^{(k)}$  in (12). Based on the condition  $\nabla_{\delta\mathbf{q}} J(\mathbf{x}^{(k)}(1 + \delta\mathbf{q})) = 0$  and the results  $\bar{\mathbf{F}}^{(k)} = \bar{\mathbf{U}} \bar{\mathbf{\Sigma}} \bar{\mathbf{V}}^T$  of the singular value decomposition (SVD), the minimization (13) is  $\delta\mathbf{q}^{(k)} = \bar{\mathbf{V}}^T \bar{\mathbf{\Sigma}}^{-1} \bar{\mathbf{U}} \Delta\mathbf{y}^{(k)}$ . Then the new model vector is given by

$$\mathbf{x}^{(k+1)} = \mathbf{x}^{(k)} \left( 1 + \text{diag} \left( \delta\mathbf{q}^{(k)} \right) \right). \quad (15)$$

Repeat the previous process until getting the some satisfactory result.

#### 4. THE INVERSION RESULTS OF THEORETICAL MODEL

In the following all inversion results, we assume the model consists of ten anisotropic beds, whose horizontal resistivities are 2.0, 6.0, 20.0, 3.0, 5.0, 7.0, 18.0, 30.0, 8.0 and 3.0  $\Omega\text{m}$ , vertical resistivities are 8.0, 24.0, 80.0, 24.0, 40.0, 56.0, 72.0, 120.0, 32.0 and 12.0  $\Omega\text{m}$ , the bed thicknesses are 2.15, 3.0, 1.15, 1.10, 1.25, 2.25, 1.85, 1.95 m from top to bottom, respectively. The MCIL tool's operation frequency is 20 kHz, and the offset of the transmitters and the receivers is 1.0 m. The initial model  $\mathbf{x}^{(0)}$  are determined by the following formulae:  $\sigma_{Hn}^{(0)} = \sigma_{Hn} [1 + (-1)^n \varepsilon_{R_H}]^{-1}$ ,  $\sigma_{Vn}^{(0)} = \sigma_{Vn} [1 + (-1)^n \varepsilon_{R_V}]^{-1}$ ,  $d_n^{(0)} = d_n + (-1)^n \varepsilon_d (d_{n+1} - d_{n-1})$ , where,  $\sigma_{Hn}$ ,  $\sigma_{Vn}$ ,  $d_n$  are the true values of the horizontal and vertical conductivities and interface per bed, respectively. The parameters  $\varepsilon_{R_H}$ ,  $\varepsilon_{R_V}$ ,  $\varepsilon_d$  denote the initial relative errors of the model vector  $\mathbf{x}^{(0)}$  in horizontal and vertical resistivity and interface, respectively, whose values are assumed as 20%, 20% and 10%.

First, we present the inversion results from the MCIL logs without noise. Figs. 1(a) and (b) show the comparison of inversion results of horizontal and vertical resistivities with their true values and initial value, respectively. Fig. 1(c) shows the inversion errors of the horizontal, vertical resistivities, and the interface, respectively. Fig. 1(d) shows the misfit of the input logs with modeling data from the inversion formation model, respectively. From the above results, we can see that the modeling

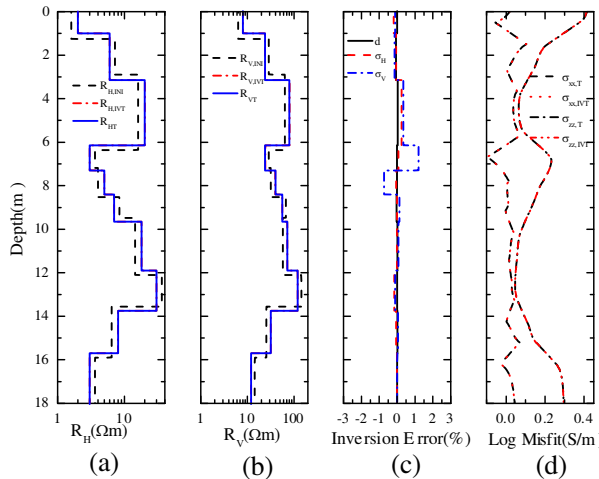


Figure 1: Inversion results from the noiseless log and data misfit.

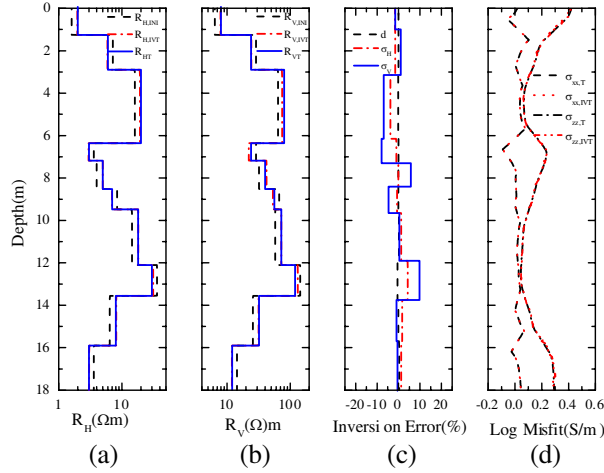


Figure 2: Inversion results from the 5% noise log and data misfit.

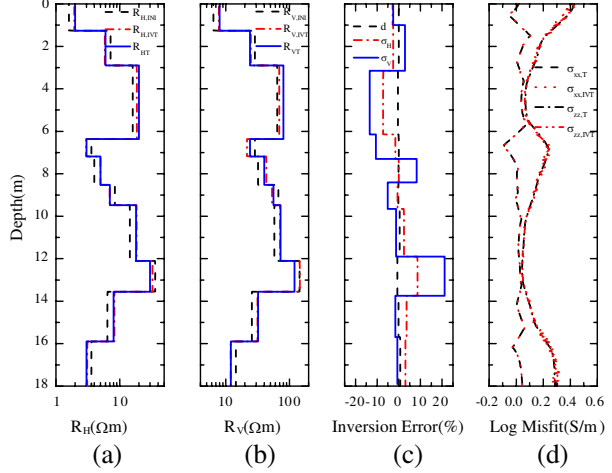


Figure 3: Inversion results from the 10% noise log and data misfit.

data from the inversion model are well consistent with the input logs through 11 times iteration inversion. In contrast, the inversion error of the vertical resistivity is relatively bigger. The main reason is the Fréchet derivative of the vertical conductivity is usually lower, which leads to its having a lower sensitivity in inversion process.

In order to further investigate anti-noise ability of the inversion algorithm, we add a random noise into the input logs, and then invert the formation parameters from the MCIL logs with noise. The input logs with noise are defined  $y'(i) = y(i)[1 + \varepsilon_{NS}R(i)]$ , where  $y(i)$  denotes the logs as Fig. 1,  $R(i)$  is a series of random numbers ranging from  $[-1, 1]$ .  $\varepsilon_{NS}$  is the relative error of the noise. Fig. 2 and Fig. 3 are the inversion results from the input logs with 5% and 10% noise, respectively. The figures show that the inversion errors become larger due to the influence of the noise. However we still can see that the inversion can extremely improve the estimation of all the model parameters even if the noise is up to 10%. The modeled logs from the inversion model also satisfactorily fit the input logs with noise. Similar to the noiseless results, the vertical resistivities still have bigger errors for the logs with noise. It further proves the vertical resistivity is more difficultly reconstructed.

## 5. CONCLUSION

This paper presents a fast iterative parameterized inversion of MICL data to fast reconstruct the horizontal and vertical resistivity and the interface in horizontally layered TI formation without a borehole. We derive the fast algorithm of Fréchet derivative matrix by TLM and inverse Fourier transform, adopt the normalization technology to simultaneous invert all the model parameters, and use the SVD technique to fast update a new formation model. The numerical results validate the inversion algorithm and its anti-noise ability. The vertical resistivity seems to have bigger inversion errors and to be more sensitivity to the influence of noise in logs because of lower sensitivity of the logs to them.

## ACKNOWLEDGMENT

This work was supported by the National Natural Science Foundation of China (40874058, 11047119) and the Basic Research Fund of Jilin University (200903318, 201001006).

## REFERENCES

1. Zhdanov, M. S., D. M. Kennedy, E. Persen, et al., "Foundations of tensor induction well-logging," *Petrophysics*, Vol. 42, No. 6, 588–610, 2001.
2. Wang, H. N., S. Poman, S. W. Yang, et al., "Numerical modeling of multicomponent induction well logging tools in the cylindrically stratified anisotropic media," *IEEE Trans. Geosci. Remote Sens.*, Vol. 46, No. 4, 1134–1147, 2008.
3. Wang, H. N., H. G. Tao, J. J. Yao, et al., "Study on the response of a multicomponent induction logging tool in deviated and layered anisotropic formations by using numerical mode matching method," *Chinese J. Geophys.*, Vol. 51, No. 5, 1591–1599, 2008 (in Chinese).

4. Yang, S. W., H. N. Wang, G. B. Chen, et al., “The 3-D finite difference time domain(FDTD) algorithm of response of multi-component electromagnetic well logging tool in a deviated and layered anisotropic formation,” *Chinese J. Geophys.*, Vol. 52, No. 3, 833–841, 2009 (in Chinese).
5. Zhang, Z. Y., L. M. Yu, B. K. Mauser, et al., “Simultaneous determination of relative angles and anisotropic resistivity using multicomponent induction logging data,” *SPWLA 42nd Annual Logging Symposium*, 2001.
6. Wang, H. N., H. G. Tao, J. J. Yao. , et al., “Fast multiparameter reconstruction of multicomponent induction well logging datum in deviated well in a horizontally stratified anisotropic formation,” *IEEE Trans. Geosci. Remote Sens.*, Vol. 46, No. 5, 1525–1534, 2008.
7. Abubakar, A., T. M. Habashy, V. Drushin, et al., “A 3D parametric inversion algorithm for triaxial induction data,” *Geophysics*, Vol. 71, No. 1, G1–G9, 2006.
8. Wang, H. N., “Adaptive regularization iterative inversion of array multicomponent induction well logging datum in a horizontally stratified inhomogeneous TI formation,” *IEEE Trans. Geosci. Remote Sens.*, (Accepted).
9. Michalski, K. A. and J. R. Mosig, “Multilayered media Green’s functions in integral equation formulations,” *IEEE Transactions on Antennas and Propagation*, Vol. 45, No. 3, 508–519, 1997.
10. Yang, S. W., “Studying on forward and inversion algorithms of multicomponent electromagnetic induction logging data in an anisotropically layered formation,” *The Doctor Thesis of Jilin University*, 2009.